Pramana – journal of physics

Editor

R Nityananda

Raman Research Institute, Bangalore

Associate Editor

H R Krishnamurthy

Indian Institute of Science, Bangalore

Editorial Board

G S Agarwal, *University of Hyderabad, Hyderabad*
V Balakrishnan, *Indian Institute of Technology, Madras*
M Barma, *Tata Institute of Fundamental Research, Bombay*
P Chaddah, *Centre for Advanced Technology, Indore*
B M Deb, *Panjab University, Chandigarh*
P K Kaw, *Institute for Plasma Research, Gandhinagar*
H S Mani, *Indian Institute of Technology, Kanpur*
N Mukunda, *Indian Institute of Science, Bangalore*
T Padmanabhan, *Inter-University Centre for Astronomy and Astrophycs, Pune*
J C Parikh, *Physical Research Laboratory, Ahmedabad*
G Rajasekaran, *Institute of Mathematical Sciences, Madras*
V S Ramamurthy, *Institute of Physics, Bhubaneswar*
R Ramaswamy, *Jawaharlal Nehru University, New Delhi*
K R Rao, *Bhabha Atomic Research Centre, Bombay*
Probir Roy, *Tata Institute of Fundamental Research, Bombay*
A K Sood, *Indian Institute of Science, Bangalore*

Editor of Publications of the Academy

G Srinivasan
Raman Research Institute, Bangalore

Subscription Rates
(Effective from 1989)

All countries except India	1 year	3 years	5 years
(Price includes AIR MAIL charges)	US$ 175	$ 470	$ 700
India	1 year Rs. 100	10 years (1989–1998 only) Rs. 500	

All correspondence regarding subscription should be addressed to the **Circulation Department** of the Academy

---

Editorial Office

Indian Academy of Sciences, C V Raman Avenue,
P.B. No. 8005, Bangalore 560080, India

Telephone: 334 2546
Telex: 845-2178 ACAD IN
Telefax: 91-80-334 6094

© 1994 by the Indian Academy of Sciences. All rights reserved.

"Information for contributions" is printed in the last issue of every volume.

Pramana – journal of physics

Volume 42
1994

Published by The Indian Academy of Sciences
Bangalore 560080

Pramana – journal of physics

Editor

R Nityananda

Raman Research Institute, Bangalore

Associate Editor

H R Krishnamurthy

Indian Institute of Science, Bangalore

Editorial Board

G S Agarwal, *University of Hyderabad, Hyderabad*
V Balakrishnan, *Indian Institute of Technology, Madras*
M Barma, *Tata Institute of Fundamental Research, Bombay*
P Chaddah, *Centre for Advanced Technology, Indore*
B M Deb, *Panjab University, Chandigarh*
P K Kaw, *Institute for Plasma Research, Gandhinagar*
H S Mani, *Indian Institute of Technology, Kanpur*
N Mukunda, *Indian Institute of Science, Bangalore*
T Padmanabhan, *Inter-University Centre for Astronomy and Astrophycs, Pune*
J C Parikh, *Physical Research Laboratory, Ahmedabad*
G Rajasekaran, *Institute of Mathematical Sciences, Madras*
V S Ramamurthy, *Institute of Physics, Bhubaneswar*
R Ramaswamy, *Jawaharlal Nehru University, New Delhi*
K R Rao, *Bhabha Atomic Research Centre, Bombay*
Probir Roy, *Tata Institute of Fundamental Research, Bombay*
A K Sood, *Indian Institute of Science, Bangalore*

Editor of Publications of the Academy

G Srinivasan

Raman Research Institute, Bangalore

Subscription Rates
(Effective from 1989)

All countries except India	1 year	3 years	5 years
(Price includes AIR MAIL charges)	US$ 175	$ 470	$ 700
India	1 year Rs. 100	10 years (1989–1998 only) Rs. 500	

All correspondence regarding subscription should be addressed to the **Circulation Department** of the Academy

---

Editorial Office

Indian Academy of Sciences, C V Raman Avenue,
P.B. No. 8005, Bangalore 560080, India

Telephone: 3342546
Telex: 845-2178 ACAD IN
Telefax: 91-80-3346094

© 1994 by the Indian Academy of Sciences. All rights reserved.

"Information for contributions" is printed in the last issue of every volume.

Pramana – journal of physics

CONTENTS – VOLUME 42

(January–June 1994)

Number 1

Research Articles

Molecular dynamics in chloronitrobenzenes using NQR data
Shanta Sastry, R Shantha Kumari and R Chandramani 1

Lattice vibrational properties of uranium pnictides
Prafulla K Jha and Sankar P Sanyal 9

Electronic structure and high pressure phase transition in LaSb and CeSb
Sankar P Sanyal and S Mathi Jaya 15

The white line in *L* absorption spectra of rare earth oxides
N V Moghe, V S Pai, G G Sahasrabudhe and V B Sapre 23

Estimation of rotational temperature of the source emitting the spectrum of PbO molecule *A B Darji, T M Patel, M B Sureshkumar, N R Shah and P M Shah* 33

Oxide films of copper prepared by the oxidation of copper sulphide films
K S Joseph and B Pradeep 41

Optical design of a toroidal grating monochromator based beam line on Indus-1 *K J S Sawhney and R V Nandedkar* 49

Ray tracing studies of a complete plane grating monochromator beam line
V S Edlabadkar and Ashok Pimpale 65

Brief Report

Photoionization processes in F aggregate centres of LiF crystal
S V Godbole and A G Page 79

Number 2

An identity for R_n embedded into E_{n+1} *Guillermo González, José L López-Bonilla and Marco A Rosales* 85

The Maxwell tensor for the Liénard–Wiechert field as an exact divergence
José L López-Bonilla, Jesús Morales and Marco A Rosales 89

Photon polarisation asymmetries in $(p, p'\gamma)$ experiments
A R Usha Devi, A Sudha Rao and G Ramachandran 97

Leptodermous expansion of nuclear ground state energies and the anomaly in the nuclear curvature energy *S K Kataria, Aruna Nijasure, V S Ramamurthy and A K Dutta* 107

Mass asymmetry dependence of fusion time-scales in $^{11}B + ^{237}Np$ and ^{12}C, ^{16}O, $^{19}F + ^{232}Th$ reactions in a dynamical trajectory model *Kiran Kumar, R K Choudhury and A Saxena* 123

Pre-equilibrium effects in the formation of meta stable states *R Upadhyay, Ch V Sastry, R K Jain and J Rama Rao* 135

Generation of ultrasonic waves in water by an elliptical Gaussian laser beam *M S Sodha, S Konar, M P Verma and V Rai* 141

Local scaling transformation function and atomic shell structure in density functional theory *B M Deb and Bijoy Kr Dey* 149

Hypervirial perturbation theory for eigenenergies for two types of atomic potentials *M R M Witwit* 159

Number 3

Photoelasticity in quasicrystals *K Rama Mohana Rao and P Hemagiri Rao* 167

Elastic anomalies in strontium titanate *K S Viswanathan and B Subramanyam* 175

Relation of coordination number to memory and threshold switching in chalcogenides *Manohar Lal, Navdeep Goyal and Anil Vohra* 187

Magnetic phase diagram of anisotropic layered superconductors via magnetization measurements for $H \| c$ in Bi 2212 *A K Grover, F Iga, Y Yamaguchi, N Aoki, K Ino, N Goyal and Y Nishihara* 193

Self focusing of elliptic Gaussian laser beams: Saturable nonlinearity *S Konar and A Sengupta* 223

High resolution optogalvanic spectrum of N_2-rotational structure of (11, 7) band in the first positive system *P R Sasi Kumar, S S Harilal, V P N Nampoori and C P G Vallabhan* 231

New band system of YbI molecule *K N Uttam and M M Joshi* 239

CH local mode overtone excitations in benzyl chloride—a conformational study *T M A Rasheed and V P N Nampoori* 245

A calorimeter for operation in the temperature range 2–150 K *I Das and E V Sampathkumaran* 251

Losses in pendular suspensions due to centrifugal coupling *Sangita N Pitre, S V Dhurandhar, D G Blair and Ju Li* 261

High pressure measurement with simple piston gauge in static condition *J K N Sharma, Kamlesh K Jain and H N P Poddar* 271

Errata 283

Number 4

Non perturbative effective potentials of quantum oscillators *Rose P Ignatius and K Babu Joseph* 285

Coherent states and squeezed states of real q-deformed quantum oscillators *G Vinod, K Babu Joseph and V C Kuriakose* 299

Squeezed vacuum as an eigenstate of two-photon annihilation operator *C L Mehta, Anil K Roy and G M Saxena* 311

A note on the harmonic plus inverse-harmonic potential in quantum mechanics *R S Kaushal* 315

WKB approximation in complex time II *S Biswas, J Guha and N G Sarkar* 319

An application of hypervirial perturbation theory to calculate energy eigenvalues of the Morse potential for various diatomic molecules *M R M Witwit* 333

Ensemble interpretation of the EPR-Bell correlations *Ravi K Menon and V K Thankappan* 341

Analysis of the excitation functions of $(\alpha, xnyp)$ reactions on natural copper *N L Singh, B J Patel, D R S Somayajulu and S N Chintalapudi* 349

Multiple scattering of gamma rays in water, concrete and sand *G S Bhandal, Vijay Kumar, Rama Rani, Kawaldeep and K Singh* 365

Number 5

Structure and vibrational properties of carbon tubules *N Chandrabhas, A K Sood, D Sundararaman, S Raju, V S Raghunathan, G V N Rao, V S Sastry, T S Radhakrishnan, Y Hariharan, A Bharathi and C S Sundar* 375

The elastic moduli, the volume contribution and the Cauchy ratio for d and f shell metals *N Singh and B S Yadav* 387

Temperature dependence of low angle structure factors of liquid alkali metals using electron-ion plasma model *A Bari, P Pal and R N Joarder* 395

Electronic structure of non-magnetic impurities in dilute alloys of Al *P Singh and S Prakash* 405

Transport phenomena of $SmSe_{1-x}As_x$ *S Ariponnammal and S Natarajan* 421

Modification of spectral characteristics and optogalvanic response in neon hollow cathode under laser excitation
P R Sasi Kumar, V P N Nampoori and C P G Vallabhan 427

Plasma-maser interaction of Langmuir wave with kinetic Alfvén wave turbulence *Bipuljyoti Saikia, B K Saikia, S Bujarbarua and M Nambu* 435

Number 6

Universality in the length spectrum of integrable systems
Debabrata Biswas 447

On phases and length of curves in a cyclic quantum evolution
Arun Kumar Pati 455

On a time-dependent system of noncentral anharmonic oscillators in two dimensions *R S Kaushal* 467

Cosmological models with constant deceleration parameter in Nordtvedt's theory *V B Johri and Kalyani Desikan* 473

Some exact solutions in Bianchi VI_0 string cosmology
Ramesh Tikekar and L K Patel 483

Brief Report

Quark distribution in light nuclei *Nazakat Ullah* 491

Subject Index 495

Author Index 499

Information for Contributors

PRAMANA
— journal of
physics

© Printed in India

Vol. 42, No. 1,
January 1994
pp. 1–7

Molecular dynamics in chloronitrobenzenes using NQR data

SHANTA SASTRY, R SHANTHA KUMARI and R CHANDRAMANI
Department of Physics, Bangalore University, Bangalore 560 056, India

MS received 21 October 1993

Abstract. The torsional frequencies have been rigorously evalulated in the compounds 1,2,4, 5-tetrachloro-3,6-dinitrobenzene and 1,3,5-trichloro-2,4-dinitrobenzene over an extended temperature range (77 K–392 K) using the experimental results of NQR and crystal structure data. The values have been compared with those obtained by using the X-ray thermal parameters.

Keywords. Quadrupole resonance; chloronitrobenzenes.

PACS No. 76·60

1. Introduction

Many poly nitro-substituted aromatic compounds show distortion from planarity. The chlorine atoms exert a steric effect on the nitro groups resulting in its tilting out of the benzene ring plane. The electronegative nitro groups also influence the charge distribution in the molecule. Chloronitro benzenes are suitable to study such changes by ^{35}Cl and by ^{14}N NQR spectroscopy. The temperature dependence of NQR in molecular solids gives useful information about the molecular dynamics (torsional oscillations) and phase transitions.

The temperature dependence of NQR frequency of ^{35}Cl in the range 77 to 400 K were investigated by Wigand *et al* [1] in the compounds 1,2,4,5-tetrachloro-3, 6-dinitrobenzene and 1,3,5-trichloro-2,4-dinitrobenzene. The tetrachloro compound, a centrosymmetric one, gives a single resonance line indicating that all the four chlorine atoms are chemically equivalent. Whereas the trichloro compound answers for three resonance lines due to three chemically inequivalent lattice sites.

In the present paper, the torsional vibration frequencies have been evaluated over an extended range (77 K to 392 K) using the NQR results and the crystal structure data [1] of the compounds. The torsional vibration frequencies have also been evaluated from the mean square angular displacements of various C–Cl bond directions and the available data of X-ray thermal parameters [1].

2. Theory

2.1 The temperature dependence of NQR interaction is mostly due to low frequency torsional vibrations. According to Bayer's [2] theory, the temperature dependence of NQR frequency for the case $I = 3/2$ and $\eta = 0$ is given by

$$\frac{\nu_T}{\nu_0} = 1 - \frac{3h}{8\pi^2}\left[\frac{1}{A_x f_x\{\exp(hf_x/KT) - 1\}} + \frac{1}{A_y f_y\{\exp(hf_y/KT) - 1\}}\right] \tag{1}$$

where ν_T is the NQR frequency at T K, ν_0 that at 0 K. f_x and f_y are the torsional frequencies about X and Y axes of the EFG tensor. A_x and A_y are the moments of inertia of the molecule about X and Y axes respectively. Bayer's theory was later modified by Kushida [3] by taking into consideration all the normal modes. Kushida's equation is given by

$$\nu_T = \nu_0\left[1 - \frac{3h}{8\pi^2}\sum_i \frac{1}{A_i f_i}\left\{\frac{1}{2} + \frac{1}{\exp(hf_i/KT) - 1}\right\}\right] \tag{2}$$

where $i = X, Y$.

Under high temperature approximation $hf_i/kT \ll 1$,

$$\nu_T = a(1 + bT + cT^{-1}) \tag{3}$$

where

$$a = \nu_0, \quad b = -\frac{3k}{8\pi^2}\sum_i \frac{1}{A_i f_i^2}, \quad c = -\frac{h^2}{32\pi^2 k}\sum_i \frac{1}{A_i}.$$

The temperature variation of torsional frequencies f_x and f_y was analysed by following Brown [4]. Assuming a linear temperature dependence for f_i as

$$f_i = f_i^0(1 - g_i T') \tag{4}$$

where T' is the temperature measured from any reference temperature T_0, g_i is the corresponding temperature coefficient of torsional frequency and f_i^0 is the torsional frequency at $T' = 0$ (i.e., at T_0). Introducing the temperature dependence of f_i in (3), the relationship between the first and second derivatives of ν is given by

$$\left[\frac{\mathrm{d}\nu}{\mathrm{d}T'}\right]_{T'=0} \Big/ \left[\frac{\mathrm{d}^2\nu}{\mathrm{d}T'^2}\right]_{T'=0} = \frac{1 + 2T_0\langle g\rangle}{4\langle g\rangle + 6T_0\langle g^2\rangle} \tag{5}$$

where,

$$\langle g\rangle = \sum_i \left[\frac{A_i}{\omega_i^{02}}\right] g_i \Big/ \sum_i \left[\frac{A_i}{\omega_i^2}\right]$$

and

$$\langle g^2\rangle = \sum_i \left[\frac{A_i}{\omega_i^{02}}\right] g_i^2 \Big/ \sum_i \left[\frac{A_i}{\omega_i^2}\right].$$

Here it is assumed that all g_i values are equal. Thus g describes the weighted average of the temperature coefficient for the internal motions. The g values were estimated from the above equation by curve fitting the experimental points to Brown's parabolic equation and calculating the derivatives of ν versus T' curve.

2.2 The NQR motional averaging has been shown to arise from temperature dependent tilting of the Z-axis of the EFG tensor. One can therefore estimate the mean square angular displacements $\langle\theta^2\rangle$ for the various C—Cl bond directions which define the respective EFG Z-direction. Using the high temperature approximation, the expression for $\langle\theta^2\rangle$ is given by

$$\langle\theta^2\rangle = \frac{kT}{4\pi^2 c^2 A f_t^2}.$$

The torsional mode frequency

$$f_t = \left(\frac{kT}{4\pi^2 c^2 A \langle \theta^2 \rangle} \right)^{1/2} \tag{6}$$

where $A = (A_x + A_y)/2 =$ average value of the moment of inertia.

The mean square angular displacement $\langle \theta^2 \rangle$ is evaluated using the thermal parameters in the following manner. Suppose the mean square displacements of two atoms forming a bond are given by $\langle u_1^2 \rangle$ and $\langle u_2^2 \rangle$ and the length of the bond is l_{12}, then the mean square angular displacement of the bond direction would be approximately given by

$$\langle \theta^2 \rangle = \frac{\langle u_1^2 \rangle - \langle u_2^2 \rangle}{l_{12}^2}. \tag{7}$$

3. Method of calculation

3.1 The moment of inertia A_x and A_y were evaluated using the crystal structure data of both the compounds. The principal Z-axis is taken along the C—Cl direction in the centrosymmetric tetrachloro compound whereas it has been taken parallel to C—Cl direction in the other compound. The results are given in table 1. The torsional frequencies f_x and f_y at each temperature were found by solving (2) using the numerical method of Vijaya *et al* [5]. The temperature coefficients of torsional frequencies g are calculated with $T' = 0$ at $T_0 = 200$ K.

3.2 The mean value of $\langle \theta^2 \rangle$ for the three directions of the ellipsoid of thermal vibrations of each atom has been evaluated from thermal parameter data of Wigand *et al* [1] using (7) and is given in table 2. Using these values of $\langle \theta^2 \rangle$ the torsional frequencies have been calculated and shown in table 2.

Table 1. Parameters used in the calculation.

Compound	ν_0 MHz	A_x 10^{-47} kgm^2	A_y 10^{-47} kgm^2	g
1,2,4,5-tetrachloro-3,6-dinitro benzene	39·185	4198·903	1965·744	0·0031167[a] 0·0032900[b]
1,3,5-trichloro-2,4-dinitro benzene				
Line I	39·210	3527·036	1331·487	0·0035[a] 0·00365[b]
Line II	38·082	3521·356	1989·477	0·0034[a] 0·00362[b]
Line III	37·880	3505·022	1945·985	0·00341[a] 0·00330[b]

[a] by Brown's Method
[b] by numerical method

Table 2. Estimated values of $\langle \theta^2 \rangle$ and f_t at $T = 300\,\mathrm{K}$.

Compound	Atom	C–Cl bond length (pm)	$\langle \theta^2 \rangle$ rad^2	Torsional frequency f_t X-ray data cm^{-1}	NQR data
1,2,4,5-tetrachloro 3,6-dinitro benzene	Cl	170·9	0·00695	23	20
1,3,5-trichloro-2,4-dinitro benzene					
Line I	Cl(2)	171·5	0·00453	32	27
Line II	Cl(1)	171·5	0·00927	21	21
Line III	Cl(3)	172·2	0·00874	22	22

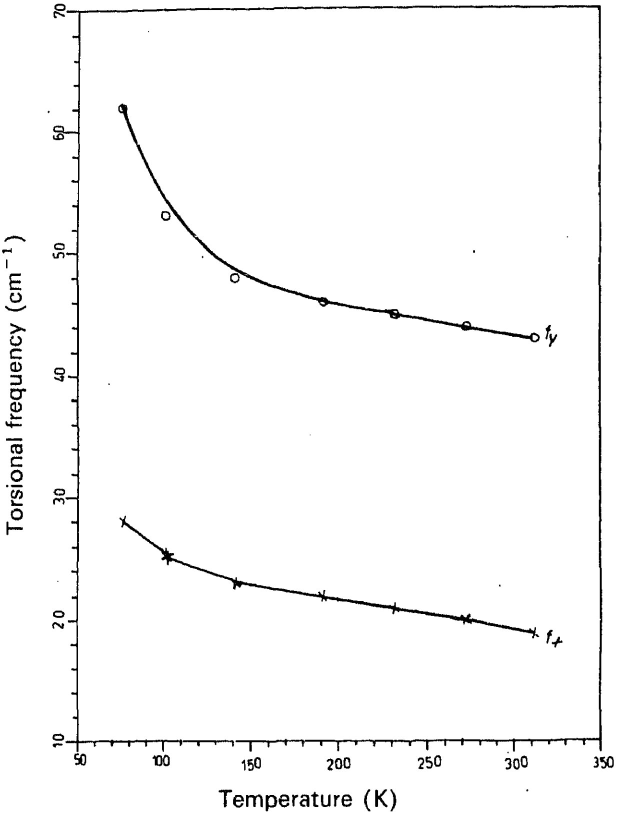

Figure 1. Temperature dependence of torsional frequencies in 1,2,4,5-tetrachloro-3,6-dinitro benzene.

4. Results and discussion

The variation of torsional frequency with temperature is shown in figure 1 for the centrosymmetric tetrachlorobenzene compound. Variation of f_x and f_y with temperature is small and is linear for most of the temperature region studied except at very low temperatures where the variation is slightly larger. For trichloro compound

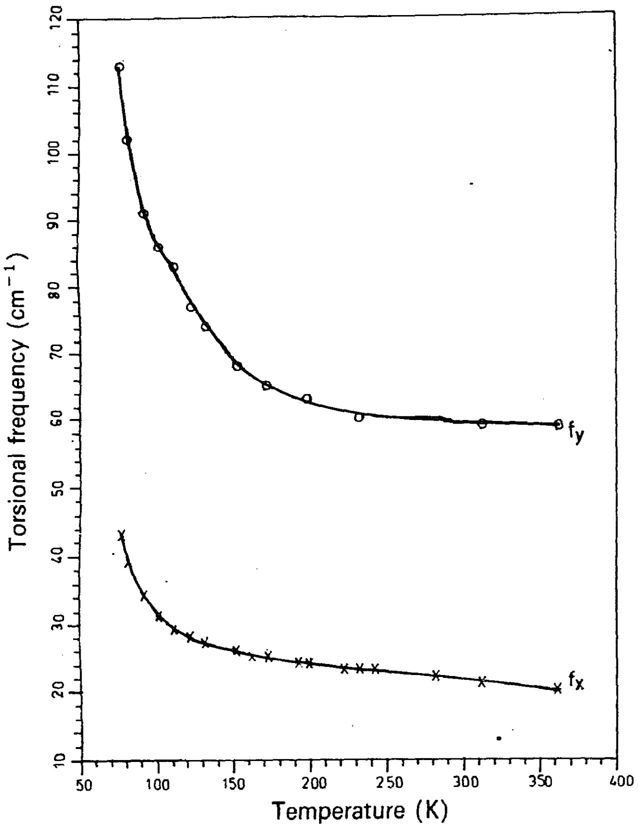

Figure 2. Temperature dependence of torsional frequencies in 1,3,5-trichloro-2,4-dinitro benzene (line I).

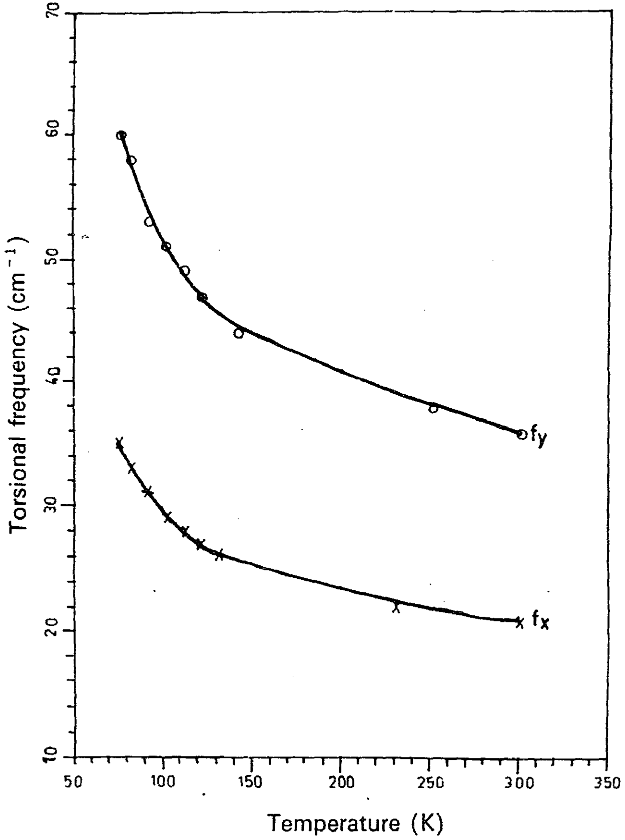

Figure 3. Temperature dependence of torsional frequencies in 1,3,5-trichloro-2,4-dinitro benzene (line II).

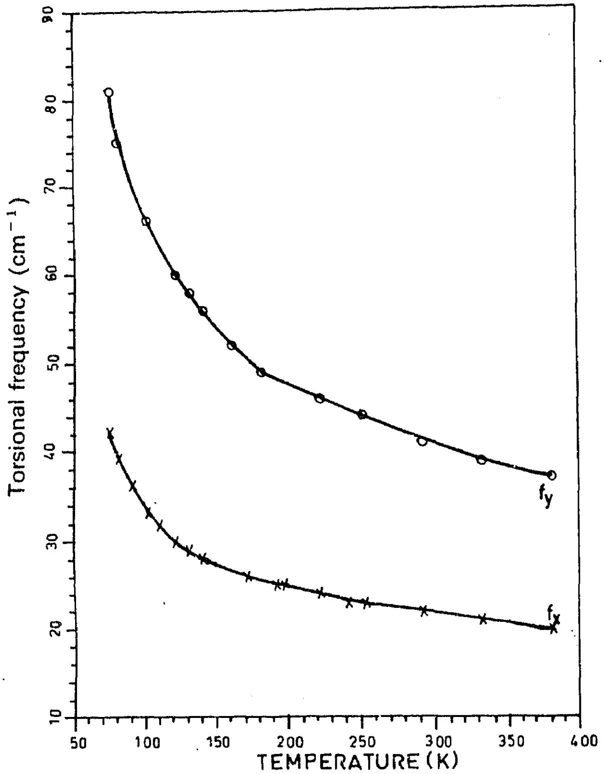

Figure 4. Temperature dependence of torsional frequencies in 1,3,5-trichloro-2,4-dinitro benzene (line III).

the variation of torsional frequencies with temperature for the three lines are shown in figures 2–4. The variation is comparatively more and is linear in most of the temperature region studied. The temperature coefficients g_x, g_y of f_x and f_y and also g, calculated by numerical method are given in table 1. The g value compares well with that obtained by Brown's method. The mean square angular displacements of the C—Cl bond directions and the order of magnitude estimation of the torsional wave numbers are in close agreement with the estimation made on the basis of NQR temperature dependence in both the compounds, as shown in table 2.

5. Conclusion

Generally the torsional frequencies of molecules lie in the range 20 to 100 cm^{-1} [6]. It is also interesting to compare these values with Raman and infrared data. In the present case, good agreement is observed on comparing the values with that obtained by using the X-ray thermal parameters.

The above approach is a good illustration of the supplementary nature of the data from X-ray studies in relation to NQR studies of compounds in the solid state.

Acknowledgement

Authors (SS and RC) are grateful to the University Grants Commission, New Delhi, for the financial support.

References

[1] S Wigand, L Watz, N Weiden and A Weiss, *Ber. Bunsenges Phys. Chem.* (West Germany) **91**, 1189 (1987)
[2] H Bayer, *Z. Phys.* **130**, 227 (1951)
[3] T Kushida, *J. Sci. Hiroshima Univ.*, **A19**, 327 (1955)
[4] R J C Brown, *J. Chem. Phys.* **32** 116 (1960)
[5] M S Vijaya and J Ramakrishna, *J. Mol. Phys.* **19**, 131 (1970)
[6] H D Stidham, *J. Chem. Phys.* **49**, 2041 (1968)

PRAMANA
— journal of
physics

© Printed in India

Vol. 42, No. 1,
January 1994
pp. 9–14

Lattice vibrational properties of uranium pnictides

PRAFULLA K JHA and SANKAR P SANYAL
Department of Physics, C. V. Raman Building, Barkatullah University, Bhopal 462 026, India

MS received 20 July 1993; revised 15 November 1993

Abstract. Lattice vibrational properties of uranium pnictides have been studied using breathing shell model (BSM) which includes breathing motion of electrons of the U-atoms due to $f-d$ hybridization. The phonon dispersion curves of U-pnictides calculated from the present model agree reasonably well with the measured data. A comparison has been made between BSM and our results reported earlier obtained from three-body force rigid ion model to reveal the importance of the short-range electron-phonon interactions in these compounds. We also report, for the first time, the two phonon density of states and specific heat for these compounds.

Keywords. Lattice vibrational; phonons; dispersion curves; breathing shell model; dynamical matrix.

PACS Nos 63·10; 63·20

1. Introduction

The uranium compounds (UX, $X = \mathrm{N}$, P, As, Sb, S, Se, Te) crystallize in rocksalt structure and show wide variety of anomalous behaviour as far as their electronic [1–2], elastic [3–6], magnetic [7] and phonon [8–13] properties are concerned. The phonon properties for these compounds have been studied using rigid ion (RIM) and shell models (SM) by Jackman *et al* [8], three-body force rigid ion model (TRIM) [9] and three-body force shell model (TSM) [10]. Amongst these models, RIM and SM are two-body in nature and fail to explain Cauchy violation ($C_{12} \neq C_{44}$) in the elastic constants. The elastic constant C_{12} for almost all the U-compounds has very small magnitude. Also, the degeneracy in the optical branches along principal symmetry directions and peculiar acoustic behaviour emphasize the necessity of the inclusion of electron-phonon interactions phenomenologically in the dynamical matrix for predicting the anomalous phonon properties in these compounds.

In a recent paper we have considered the many-body interactions arising from charge transfer effects between nearest neighbour ions in the framework of TRIM [9]. The TRIM could explain the gross features of the phonon dispersion curves (PDC), particularly the degeneracy of the optical branches but failed to explain the anomalies observed in the acoustic branches. In addition, this model also neglects the electron ion interactions e.g., electronic polarizabilities which might influence these modes at X-point. The electronic structure and symmetry considerations of the UX compounds depict that inclusion of the breathing motion of the electron shells leading to charge density deformations at U-atom site in the equation of motion might improve our understanding of phonon anomalies in U-compounds. The use of such an approach has also been emphasized earlier by several workers to explain their phonon properties [14–16].

In the present paper we study the lattice vibrational properties such as phonon dispersion curves, BSM [17]. The BSM considers phenomenologically the breathing motion of electron shells resulting into charge density deformation due to $f-d$ hybridization. This model has already been used to study the phonon properties in intermediate valence compounds by Kress *et al* [18] and uranium chalcogenides by us [11].

2. Theory

The breathing shell model considers phenomenologically the short range electron-phonon interactions in terms of electron shell deformations. Depending upon symmetry, it includes dipolar, quadrupolar and breathing deformabilities of the electron shells of the polarizable ions. A detailed review of this model can be found elsewhere [17, 19].

The dynamical matrix corresponding to BSM is

$$D(q)=(R'+ZCZ)-(R'+ZCY)(R'+K+YCY)^{-1}(R'+YCZ) \tag{1}$$

where

$$R'=(R-QH^{-1}Q^{+}) \tag{2}$$

Here C and R are the Coulomb and short-range repulsive interaction matrices. Q is a (6×2) matrix representing the interactions between the ion displacement and breathing mode variables, while H is a (2×2) matrix specifying the interactions between the breathing mode variables of different ions in the lattice. K and Y are the diagonal matrices and represent the core-shell force constants and shell charges, respectively.

The present version of BSM has altogether eight parameters, which can be determined from elastic, dielectric and zone centre phonon properties. We have assumed $Y_1=Y_2=Y$ to minimize the number of parameters. The input data and model parameters are listed in tables 1 and 2, respectively.

Table 1. Input constants for uranium pnictides [8]. Elastic constants are in 10^{12} dyne/cm^2, lattice parameters in Å, frequencies are in THz and polarizabilities in Å^3.

Parameters	UP	UAs	USb
a	5·590	5·779	5·489
C_{11}	—	2·50 ± 0·1	1·60 ± 0·1
C_{12}	—	0·10 ± 0·05	0·07 ± 0·15
C_{44}	—	0·26 ± 0·05	0·20 ± 0·10
$\nu_{TO}(\Gamma)$	9·200	5·990	4·700
α_1	0·550	0·500	0·430
α_2	7·250	7·500	8·200

Table 2. Model parameters for uranium pnictides (for BSM). All are in units of $e^2/2V$ except Y which is in units of e.

Parameters	UP[a]	UAs	USb
A_{12}	34·109	31·261	23·813
B_{12}	5·054	4·804	4·150
A_{11}	2·139	3·142	5·390
B_{11}	−2·237	−1·988	−1·541
B_{22}	0·800	0·933	1·205
Y	−26·610	−22·640	−12·220
$G_1(\times 10^2)$	695·770	575·235	207·328
$G_2(\times 10)$	423·570	288·754	106·206

[a] Values obtained from linear interpolation.

3. Results and discussion

The calculated PDC for U-pnictides (UP, UAs and USb) have been plotted in figures 1–3 and compared with earlier calculated TRIM results [9] and neutron scattering data [8]. In calculating these curves we have, however, not attempted a least square fit to the phonon data but obtained them from the parameters which are physical in nature and derived from crystal properties.

The calculated PDC for UP from TRIM and BSM are plotted in figures 1(a) and (b). In the absence of sufficient measured properties, the force constants for UP are obtained from a linear interpolation of the results of other two members (UAs and USb) of this group. The theoretical results on PDC for UP have also been obtained by Jackman *et al* [8] from RIM using similar method. A close scrutiny of these two results reveals that BSM predicts non-degenerate LO and TO frequencies at X-point, which is not observed in the RIM results [8]. Also, the BSM predicts the LA and TA branches along (qqq) to be nearly degenerate, a feature shown by other members of this family, while the TRIM shows a smooth dispersion of these two branches similar to the RIM results. In the absence of any experimental data, relative merit of either of the model calculations cannot be judged at this moment. We believe that these results will be quite useful to the experimentalists when the PDC for UP are measured.

The PDC for UAs and USb are plotted in figures 2 and 3 from BSM and TRIM and compared with experimental results [8, 13]. The LA and TA branches along (q00) direction for these compounds have been reproduced fairly well by both the models, while a marked disagreement is observed at X-point, particularly in TRIM. Both the models predict degeneracy in the optical branches similar to experiment. All the phonon modes along all the symmetry directions for UAs are explained satisfactorily by BSM, even without any fitting. In UAs, it seems that the BSM predictions are better than those of TRIM along (qqq) direction.

The PDC for USb, plotted in figure 3, reveals that the acoustic modes in all symmetry directions are satisfactorily reproduced by both TRIM and BSM. Large difference between LO and TO along (qq0) direction is a common feature shown by both the models. The difference is maximum at (0·5, 0·5, 0·0). A similar situation is also observed from the RIM fit to the neutron scattering results [8]. The TRIM prediction of large splitting between LO and TO frequencies for USb at L-point

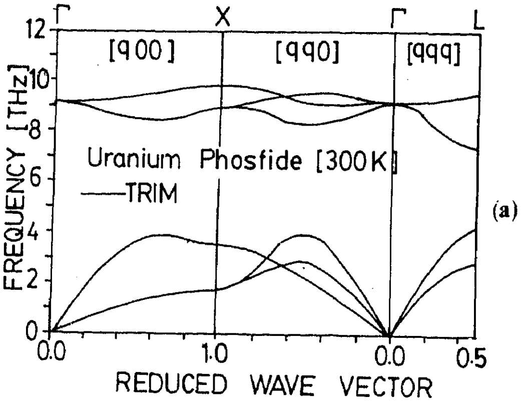

Figure 1(a). Phonon dispersion curves for UP using BSM.

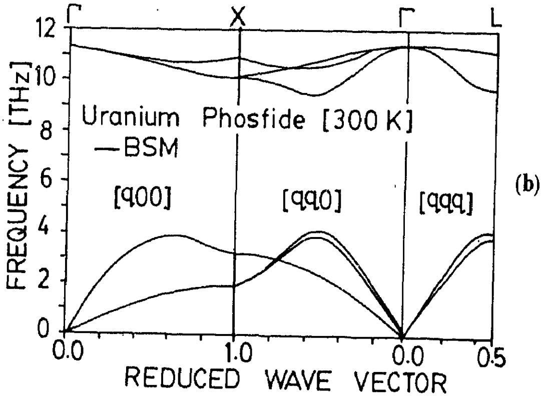

Figure 1(b). Same as in figure 1(a) for UP using TRIM.

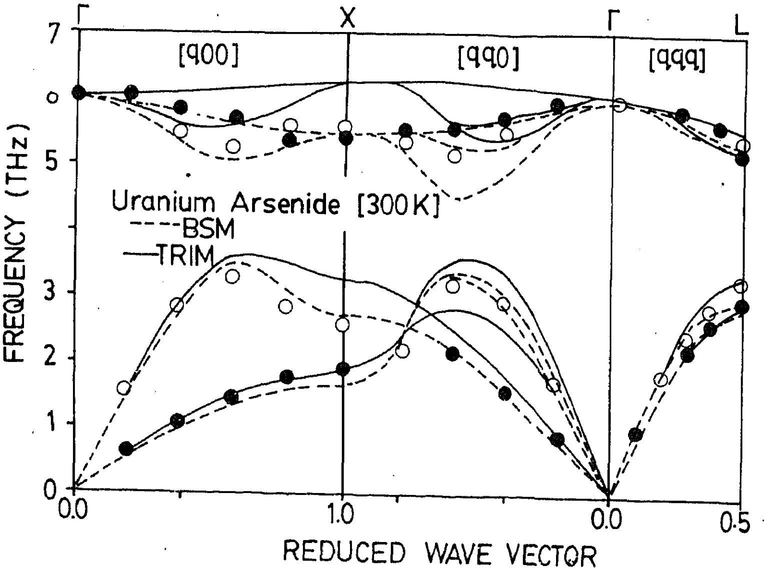

Figure 2. Same as in figure 1 for UAs. Experimental points are taken Jackman *et al* [8] and Stirling *et al* [13].

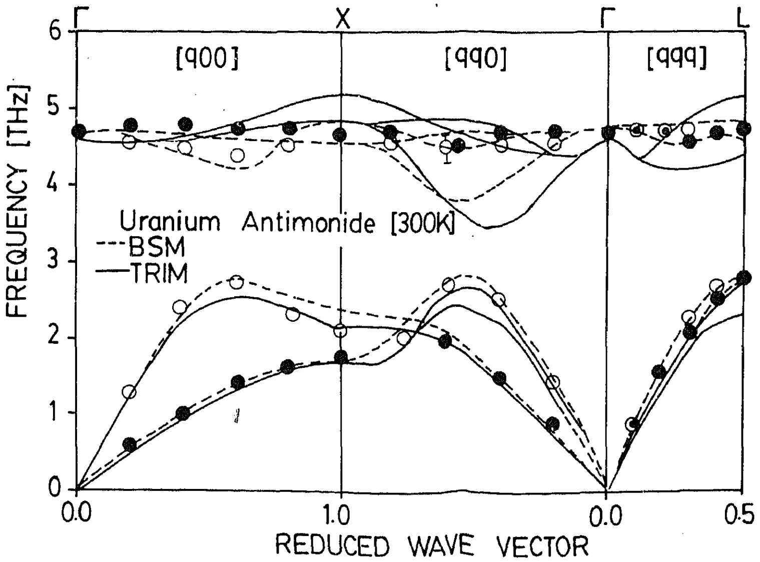

Figure 3. Same as in figure 1 for USb. Experimental points are taken from Jackman *et al* [8] and Stirling *et al* [13].

reveals its failure to take proper account of short-range interactions. In general, the optic branches are less satisfactorily explained by TRIM than BSM for uranium pnictides.

The lattice vibrations in uranium pnictides can be understood convincingly by analyzing the force constants derived from the present model (BSM). We present them in table 2. The salient feature of dominance of U–X (X = P, As, Sb) force constants in all U-pnictides, as is observed from RIM fit [8] has been fairly reproduced by BSM. The U–X force constants derived from BSM are nearly constant across the series. The relatively smaller magnitudes of second neighbour force constants are, to a greater extent, influenced by small magnitudes of bulk modulus of these compounds. Across the pnictide series, our calculated force constants show a similar trend of variation, similar to what is observed in RIM fit to the phonon data.

Finally, in this paper we have presented the results of a systematic study of a few phonon properties of the uranium pnictides. The calculated results point out that the phonon anomalies in these compounds, in general, originate from the breathing motion of the electron shells of uranium ions. The breathing shell model satisfactorily reproduces the gross features of the PDC. These predictions reveal that the polarizabilities of the ions are important and must be included in a realistic model approach. In addition, the short-range deformations due to breathing motion of the electron shells of U-ion contribute significantly to the peculiar phonon dispersion in uranium pnictides.

Acknowledgements

The work is financially supported by the Department of Atomic Energy, Govt. of India. We would like to thank Prof. U Schroder and Prof. W Kress for providing the BSM codes and Prof. R K Singh for valuable discussion. One of us (PKJ) wishes to thank the CSIR for a Fellowship.

References

[1] M Erbudak and F Meier, *Physica* **B102**, 134 (1980) and references therein

[2] M S S Brooks, *J. Phys.* **F14**, 633 (1984) and references therein

[3] C F VanDoorn and P de V DuPlessis, *J. Magn. Magn. Mater.*, **5**, 164 (1977)

[4] J Neuenschwander, H Boppart, J Schoenes, E Voit, O Vogt and P Wachter *14 Journess des Actinidides* edited by Schoenes J (Zurich Edigenossiche Technische Hochschule 1984) p. 30

[5] J S Olsen, S Stenstrup, L Gerward, V Bendict, J C Spirlet and G D Andrectt, *J. Less Common. Met.* **98**, 291 (1984)

[6] J S Olsen, L Geward and V Benedict, *J. Appl. Crystallogr.* **18**, 37 (1985)

[7] G H Lander, W G Stirling, J M Rossat-Mignod, M Hagen and O Vogt *Phys. Rev.* **B41**, 6899 (1990) and reference therein

[8] J A Jackman, T M Holden, W J L Buyers, P De V DuPlessis, O Vogt and G Gemossar, *Phys. Rev.* **B33**, 7144 (1986)

[9] P K Jha and S P Sanyal, *Phys. Rev.* **B46**, 3664 (1992)

[10] P K Jha, R K Singh and S P Sanyal, *Physica* **B174** 101 (1991)

[11] P K Jha and S P Sanyal, *Phys. Rev.* **B** (in press)

[12] W J L Buyers, A F Murray, T M Holden, E C Svensson, P De V DuPlessis, G H Lander and O Vogt, *Physica* **B102**, 291 (1980)

[13] W G Stirling, G H Lander and O Vogt, *J. Phys.* **C16**, 4093 (1983)

[14] P B Allen, *Phys. Rev.* **B46**, 5139 (1977)

[15] H Bilz, G Guntherodt, W Klippmann and W Kress, *Phys. Rev. Lett.*, **43**, 1988 (1979)

[16] N Wakabayashi, *Solid State Commun.* **23**, 737 (1977)

[17] V Nusslien and U Schroder, *Phys. Status. Solidi* **B21**, 309 (1967)

[18] W Kress, H Bilz, G Guntherodt and A Jayaraman, *J. Phys.* **C6–3** (1981)

[19] R K Singh, *Phys. Rep.* **85**, 259 (1982)

PRAMANA
— journal of
physics

© Printed in India

Vol. 42, No. 1,
January 1994
pp. 15–22

Electronic structure and high pressure phase transition in LaSb and CeSb

SANKAR P SANYAL* and S MATHI JAYA**
International Centre for Theoretical Physics, P.O. Box No. 586, Trieste, Italy
*Permanent address: Department of Physics, Bhopal University, Bhopal 462 026, India
**Permanent address: Department of Physics, Anna University, Madras 600 025, India

MS received 29 March 1993; revised 5 October 1993

Abstract. The electronic structure and high pressure structural phase transition in lanthanum and cerium antimonides have been investigated using the tight binding LMTO method. Calculation of the total energy reveals that the simple tetragonal structure is stable at high pressure for both the compounds. In LaSb, the calculated values of the equilibrium cell volume and the cell volume at which phase transition occurs agree with the experimental results. However, in CeSb, the agreement is not so good. We have also predicted the most favoured *c/a* value in the simple tetragonal phase for these compounds. Further, we present the calculated results on the electronic structure of these systems at the equilibrium as well the reduced cell volumes.

Keywords. Electronic structure; high pressure phase transition; lanthanum antimonide; cerium antimonide.

PACS No. 73·40

1. Introduction

The high pressure structural phase transitions in the rare earth (RE) compounds have been an interesting field of research in the last two decades, ever since the discovery of metallization of SmS at high pressure [1]. Most of these RE compounds undergo a structural phase transition, associated with electronic and valence transitions. Several experimental work exists on the RE systems depicting a variety of phenomena at high pressure [1–5]. However the theoretical understanding of such diverse phenomena has been incomplete, particularly in RE-pnictides, which show different behaviour at high pressure, as compared to the RE-chalcogenides.

In this paper we report the results of our investigation on the structural and electronic properties of lanthanum and cerium antimonides (LaSb and CeSb) at high pressures. We have calculated their electronic structures and total energy at different values of the lattice parameter assuming different structures and the results were used in understanding the structural and electronic transitions in these systems. For calculating the electronic structure, we have made use of the tight binding LMTO method, which is convenient for systems having many atoms per unit cell. Especially, in the present work where we calculate the electronic structure at different lattice parameters, this method is most convenient. The details of this method may be found elsewhere [6–8]. In the following sections, we describe the results of our calculations alongwith a brief survey of the earlier work on these systems.

2. Survey of earlier work and outline of the present study

Both these systems, namely LaSb and CeSb crystallize in the NaCl structure at ambient conditions and the values of the lattice parameters are 6·49 Å and 6·42 Å for LaSb and CeSb respectively. Both these systems exhibit a structural phase transition around 11 GPa and transform to simple tetragonal (ST) phase [4, 5]. A volume discontinuity is associated with this phase transition. So far as their electrical properties are concerned, LaSb has a metallic character with a very low density of states at the Fermi energy ($N(E_F)$) and the metallicity in this compound is caused by the slight overlap of the Sb 5*p* bands with the La 5*d* bands. On the other hand CeSb is known to have semi-metallic character with unusual magnetic properties [5].

In the present work we explain the observed structural transition in these systems from the calculation of the total energy as a function of cell volume. In addition, we have obtained the variation of $N(E_F)$ and the integrated density of states with the change in cell volume. We present the calculated band structure and density of states at the normal pressure.

3. The electronic structure

The electronic structures of both these systems were calculated at different cell volumes ranging from 110% to 70% of the equilibrium cell volume, in two different structures, viz. NaCl and simple tetragonal phases. In our calculations, the eigenvalues were calculated at 64 **k**-points uniformly distributed in the irreducible wedge of the Brillouin zone. The sphere radii of the atoms were so chosen that there is a maximum overlap between the spheres and the charge transfers in proper direction. The sphere radii of the atoms used in the calculation at the equilibrium cell volume are 3·704 a.u. for La and 3·899 a.u. for Sb in LaSb and 3·664 a.u. for Ce and 3·857 a.u. for Sb in CeSb. For calculating the electronic structure at different cell volumes, the sphere radii were correspondingly changed keeping the radii ratio same.

The band structure and density of states corresponding to the equilibrium cell volume in NaCl phase for LaSb and CeSb are shown in figures 1 to 4. The low-lying band in both cases is due to the 5*s* orbital of Sb. The conduction bands are formed

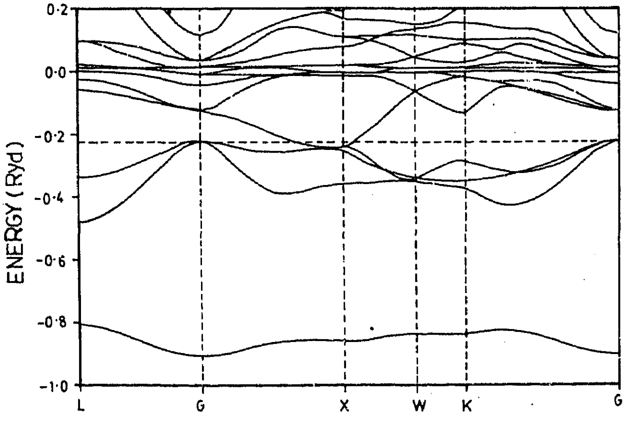

Figure 1. Band structure of LaSb in NaCl phase.

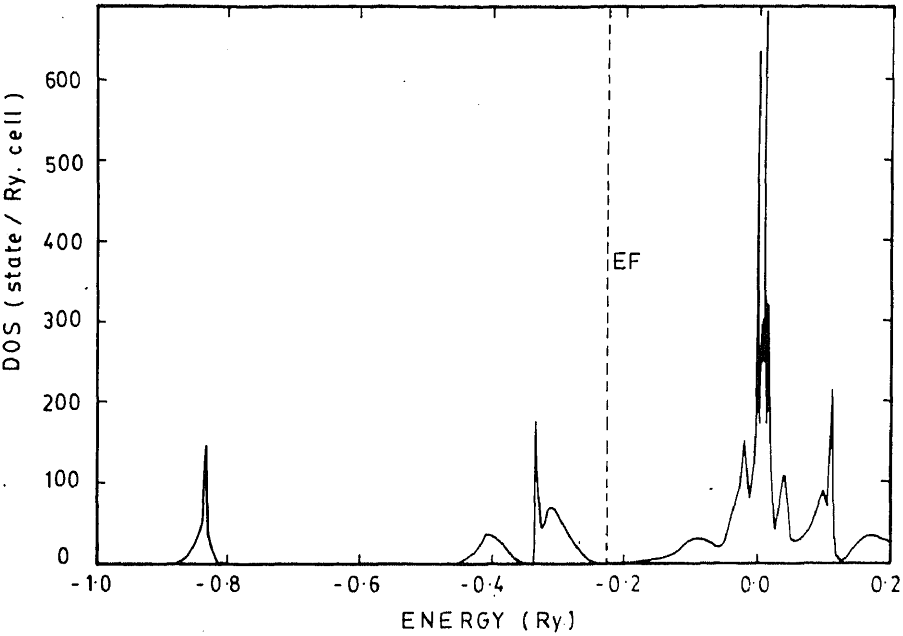

Figure 2. Density of states of LaSb in NaCl phase.

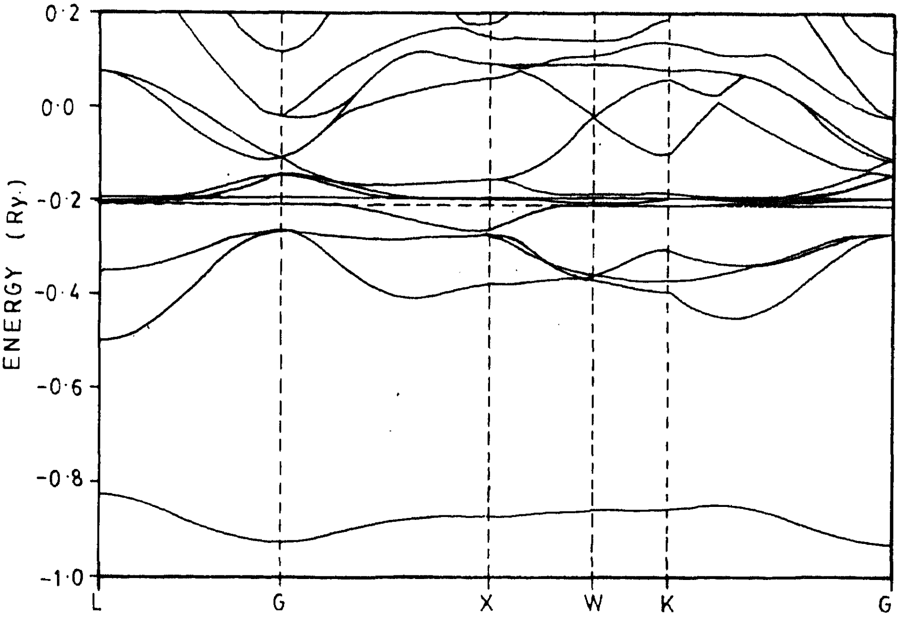

Figure 3. Band structure of CeSb in NaCl phase.

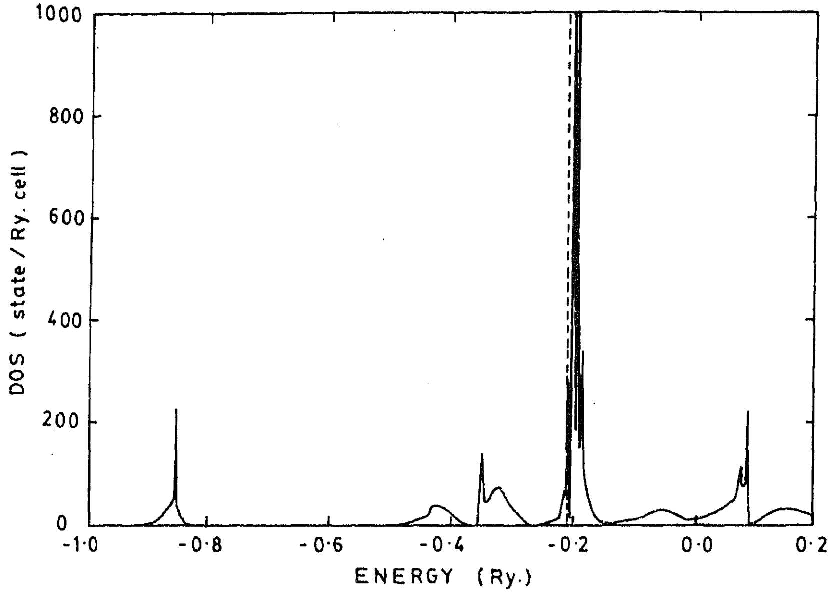

Figure 4. Density of states of CeSb in NaCl phase.

Table 1. $N(E_F)$ and integrated density of states of LaSb and CeSb at two different cell volumes.

LaSb

Cell volume (NaCl) $(\mathrm{a.u})^3$: 444·6935
$N(E_F)$: 0·339 states/Ryd-Cell
Cell volume (ST) $(\mathrm{a.u})^3$: 378·9983
$N(E_F)$: 7·372 States/Ryd-cell

CeSb

Cell volume (NaCl) $(\mathrm{a.u})^3$: 401·6416
$N(E_F)$: 264·508 states/Ryd-cell
Cell volume (ST) $(\mathrm{a.u})^3$: 357·132

NaCl phase

Number of states (electrons/cell)

	La	Sb	Ce	Sb
s	0·3040	1·7451	0·3121	1·738
p	0·5062	3·8713	0·4884	3·7471
d	1·2089	0·1479	1·3793	0·240
f	0·2161	—	1·095	—

Simple tetragonal phase

Number of states (electrons/cell)

	La	Sb	Ce	Sb
s	0·2610	1·7481	0·2681	1·685
p	0·3711	3·6103	0·3931	3·4461
d	1·4229	0·3329	1·6819	0·405
f	0·2531	—	1·121	—

by the Sb *5p* and La (or Ce) *5d* orbitals. It may be seen from figure 1 that in LaSb the hybridization branch of La is substantially above the Fermi level. These factors have resulted in very low density of states at the Fermi level for LaSb. However, in CeSb, the Fermi level lies at the bottom of the narrow Ce *4f* band and hence leads to a large value of the density of states at the Fermi level. The density of states at the Fermi level corresponding to the equilibrium cell volumes are 0·339 states/Ryd-cell for LaSb and 264·508 states/Ryd-call for CeSb. In table 1 we have given the integrated density of states at two different cell volumes corresponding to NaCl and ST phases. It can be noted from table 1 that at high pressures the density of states at the Fermi level is increased in LaSb whereas it is decreased in CeSb. The increase in Sb*5p* and La*5d* hybridization in LaSb and the broadening of the Ce*4f* bands at high pressure are the major causes of decrease in density of states at E_F in CeSb.

As the high pressure phase of both the systems is simple tetragonal (ST), it is desirable to have the band structure and density of states in this phase. Therefore we have calculated the band structures and density of states corresponding to the ST phase and reported them elsewhere [9].

4. Total energy and structural stability

As mentioned earlier, the total energy of these two systems were evaluated at various lattice parameters in two different structures and calculated values of the total energy for LaSb and CeSb are plotted in figures 5 and 6. In these figures the total energies are plotted with respect to the corresponding equilibrium cell volumes. For calculating of the total energy in the ST phase, we have used the *c/a* value of 0·8158 for LaSb and 0·8161 for CeSb, which are the experimental values [4]. It may be seen from

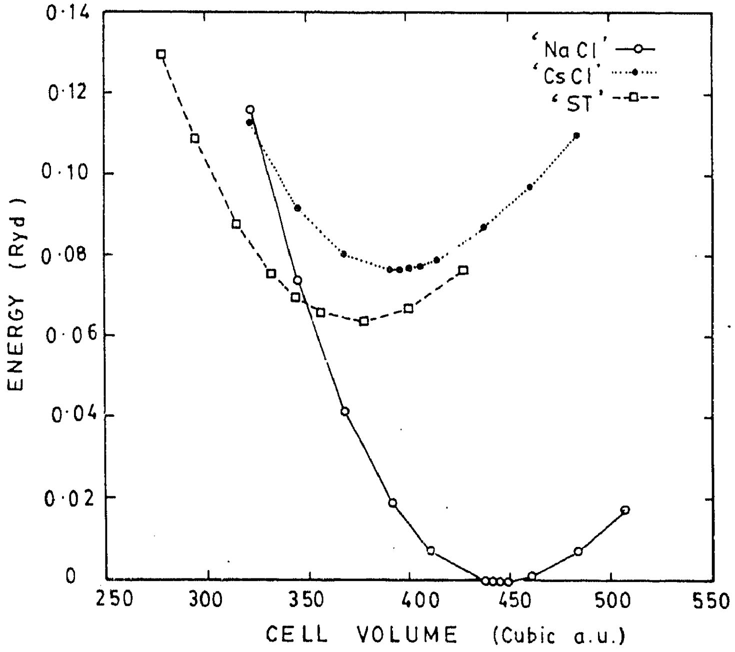

Figure 5. Total energy as a function of cell volume for LaSb.

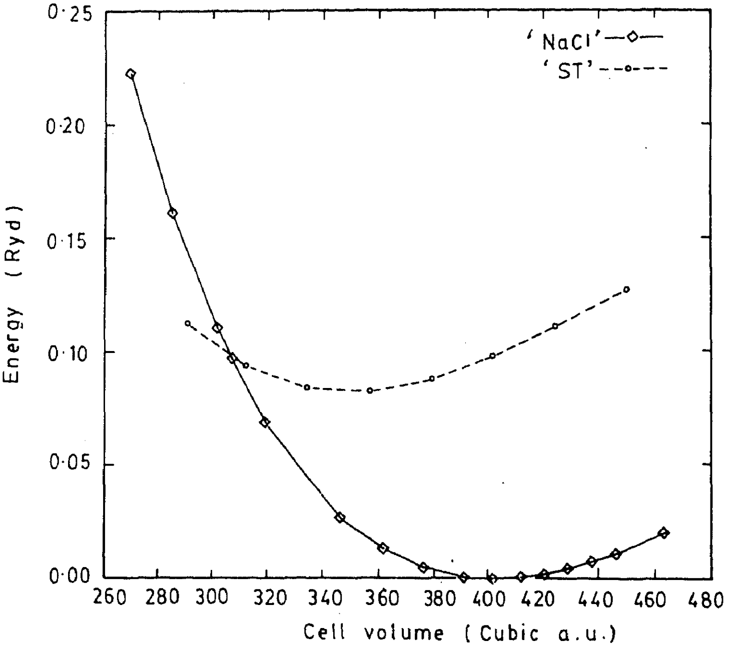

Figure 6. Total energy as a function of cell volume for CeSb.

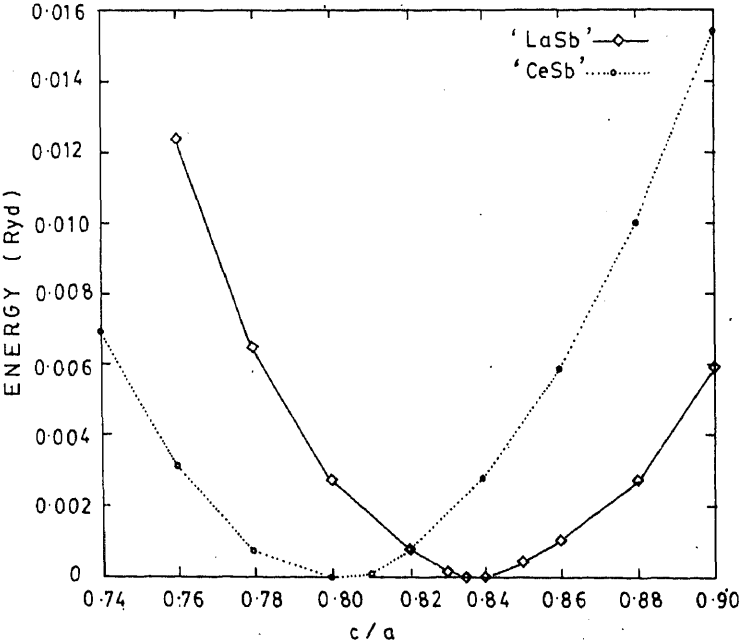

Figure 7. Total energy as a function *c*/*a* ratio for LaSb and CeSb.

figures 5 and 6 that the equilibrium cell volumes for LaSb and CeSb are respectively 444·694 and 401·642 (a.u.)^3. The experimental values of the cell volumes are 461·143 (a.u)^3 and 446·413 (a.u)^3 for LaSb and CeSb respectively. In LaSb, our calculated value of the cell volume agree with the experimental value whereas in CeSb the agreement is not so good. It may be noted from figures 5 and 6 that both the systems transform to the ST phase at high pressure. In LaSb the transition occurs at the cell volume of 351·135 (a.u.)^3 and in CeSb it occurs at 306·425 (a.u.)^3. According to the experimental results, the transition occurs at the cell volume of 357·416 (a.u.)^3 for LaSb and 345·901 (a.u)^3 for CeSb. It may be pointed out that in LaSb, our calculated value of the cell volume at which the phase transition occurs agree with the experimental results. Whereas in CeSb, the predicted cell volume is found to be smaller than that of the experimental one. The discrepancies may be attributed to the limitations of the density functional approach (DFA) to the electronic structure for these systems. However, it may be noted that, our calculations are not fully relativistic. Further, we have not considered any spin splitting in our calculations.

We have also investigated the most favoured value of the c/a ratio in the ST phase for both LaSb and CeSb. To determine the said ratio, we have calculated the total energy as a function of c/a value in the ST phase keeping the cell volume fixed at 351·135 (a.u)^3 for LaSb and 306·425 (a.u)^3 for CeSb. The calculated results are plotted in figure 7 which shows that in LaSb, the most favoured c/a value is 0·837 and for CeSb, it is 0·802. The experimental values are 0·8157 for LaSb and 0·8161 for CeSb. In both cases, our calculated values agree with the experimental observations.

5. Summary and conclusion

The electronic structure and total energy of the rare earth compounds LaSb and CeSb are evaluated at two different structures. The results were used to get the equilibrium cell volume and to predict the possible structural transitions in these systems. Our calculations have shown that both LaSb and CeSb undergo a structural transition from NaCl to ST phase at high pressure. The calculated results agree with the experimental observation. We have also predicted the most favoured c/a ratio in these systems in the tetragonal phase. It may be noted from figure 3 that the narrow Ce $4f$ bands lie very close to the Fermi level and this gives rise to large density of states at the Fermi energy in CeSb. From our study we have found $s \rightarrow d$ and $s \rightarrow f$ electron transfer at high pressure in both compounds. This may be seen from table 1 where the d and f electron numbers have increased in the high pressure ST phase.

Acknowledgement

The authors would like to thank Drs O K Anderson and O Jepsen for providing the computer codes.

References

[1] A Jayaraman, in *Hand Book on the physics and chemistry of rare earths* edited by K A Gschneidner Jr. and Leroy Eyring (North Holland, Amsterdam, 1979)
[2] J M Leger, R Epain, J Loriers, D Ravot and J Rossat-Mignold, *Phys. Rev.* **B28**, 7125 (1983)
[3] M Croft and A Jayaraman, *Solid State Commun.* **35**, 203 (1980)
[4] J M Leger, D Revot and J Rossat-Mignold, *J. Phys.* **C17**, 4935 (1984)

[5] J M Leger, K Oki, D Ravot and, J Rossat-Mignold, *J. Magn. Mater.* **47** and **48**, 277 (1985)

[6] O K Andersen, O Jepsen and M Sob, in *Electronic band structure and its applications* edited by M Yussouf (Springer Verlag, Berlin, 1987)

[7] S K Bose, J K Kudrnovsky, I I Mazin and O K Andersen, *Phys. Rev.* **B42**, 7988 (1990)

[8] O K Anderson, *Workshop on methods of electronic structure calculations*, ICTP, Trieste, (1992)

[9] S Mathi Jaya and Sankar P Sanyal, IC/92/287, ICTP, Trieste, Italy (1992)

PRAMANA
— journal of
physics

© Printed in India

Vol. 42, No. 1,
January 1994
pp. 23–31

The white line in L absorption spectra of rare earth oxides

N V MOGHE, V S PAI, G G SAHASRABUDHE and V B SAPRE
Department of Physics, Nagpur University, University Campus, Nagpur 440010, India

MS received 23 April 1993; revised 17 August 1993

Abstract. The method of curve fitting of the experimentally obtained absorption edge has been developed and successfully adopted to study the precise variation in the density of states responsible for the occurrence of the white line associated with the L_{II} and L_{III} absorption discontinuities of rare earth (RE) in their sesquioxides. The theoretical equation and the curve fitting routine is flexible enough to include all the transitions responsible for XANES as well as other phenomena such as, screening effect, variation in the potential around the metal ion due to surrounding ligand ion, charge transfer etc.

Keywords. Levenberg-Marquardt; Lorentzian; XANES; white line; microdensitometer.

PACS No. 78·70

1. Introduction

The oxides and other compounds of rare earths (RE) have attracted a great deal of attention in recent years [1–5]. Their uses as starting materials for the fabrication of several kind of devices are well-known [6–8]. A lot of work has been reported on the L_{II} and L_{III} X-ray absorption discontinuities of RE metals and their sesquioxides. These studies are known to provide direct method of studying the electronic structure of materials [9–10].

A remarkable feature associated with these discontinuities is the prominent absorption maximum close to the main discontinuity, the so-called white line. This white line can be very clearly seen on the original spectrum recorded photographically.

In the present investigation a systematic study of the intensities of the white line associated with the L_{II} and L_{III} absorption discontinuities in the RE sesquioxides RE_2O_3 (where RE = La, Pr, Nd, Sm, Eu and Gd) has been carried out. A curve fitting routine has been used wherein the experimentally obtained absorption curve has been fitted to a theoretical curve. The nature of the theoretical curve can be expressed by an equation of the type

$$F(Y_i) = \text{arc tangent} + 2 \quad \text{lorentzians}.$$

where, Y_i corresponds to experimentally observed data points and $F(Y_i)$ to data points obtained from the theoretical equation.

After obtaining a close fit we have calculated and compared the full width at half maximum (FWHM) and area under the curve for the Lorentzians. These Lorentzians correspond to the absorption maxima A and A^* associated with the L_{II} and L_{III} absorption discontinuities. This comparison is useful in evaluating the theoretical equation used in the curve fitting routine.

2. Experimental

The experimental technique involves the following aspects:

1. To set and test the performance of the spectrograph
2. To obtain the best possible X-ray spectra on film
3. Use of standard measurement technique, and
4. Use of standard computer programs to derive maximum information from the observations recorded.

In this work a transmission type, focussing X-ray spectrograph of Cauchois geometry of diameter 400 mm, was used. The (100) reflecting planes of a well tested mica crystal were used for obtaining the spectrum. A Chirana X-ray tube with a tungsten target, operated at 18 kV, 15 mA was used as a source of white radiation. Details of the setting of the spectrograph are given in our earlier publications [11, 12].

The performance of the spectrograph was tested by calculating the FWHM of $WL\alpha_1$ line. Our value of $7{\cdot}1 \pm 0{\cdot}36$ eV is in close agreement with those reported by earlier workers [13].

Different thicknesses of the absorbing screen were tried, and the one which gave the best white line was finally selected for recording the spectrum. Care was taken to maintain the uniformity in the thickness of the absorber.

The spectra were recorded on Agfa X-ray film. Minimum possible exposure was given to the film to ensure that the photodensity S of the film was proportional to the incident X-ray intensity, I. This is the most important criterion when one has to study the relative intensities of the spectra recorded on the film. It was found that for an exposure less than 6 h, the above condition was satisfied. The temperature of the developer and fixer was kept at 15°C. Care was taken not to over-develop the film. The microphotometer records of the spectra were obtained using a Carl-Zeiss microdensitometer, MD 100. We [14] have modified the recording technique which has the following advantages.

1. Observations are in a digital format.
2. Energies of data points can accurately be determined due to precise knowledge of their positions.
3. The process of measurement is fast, accurate and has a high degree of repeat reliability.

Observations, in digital format, have paved way for usage of standard computer programs.

The L_{II} and L_{III} absorption curves of RE in their sesquioxide, within 25 eV from the inflection point, can be considered to be significantly dominated by

1. transitions from respective initial levels ($2p_{1/2}$ for L_{II} and $2p_{3/2}$ for L_{III} absorption discontinuities) to the continuum. These are represented by arc tangent curves.
2. On this arc tangent curve are superimposed 2 lorentzians corresponding to the transitions to $2t_{2g}$ and $3e_g$ molecular orbital levels from $2p_{1/2}$ for L_{II} and from $2p_{3/2}$ for L_{III} absorption discontinuities.

The contribution of other effects in this region of absorption discontinuity can be considered to be minimum.

The function which we have fitted to the experimentally observed absorption curve has therefore the following form.

$$A = A(1)*(0{\cdot}5 + 1/3{\cdot}14*(a\tan(E - E_0)/A(2)))$$
$$B = A(3)/(1 + ((E - A(4))^2/A(5)))$$
$$C = A(6)/(1 + ((E - A(7))^2/A(8)))$$
$$F(Y_i) = A + B + C \tag{1}$$

where $A(1)$ is the amplitude constant and $A(2)$ is the width of the arc tangent curve. $A(3)$ and $A(6)$ are the square of the amplitudes, $A(4)$ and $A(7)$ are the positions of absorption maxima A and A^* and $2*A(5)^{1/2}$ and $2*A(8)^{1/2}$ are the full widths at half maximum of first and second lorentzian respectively. E and E_0 are respectively the energy values of the points on the absorption curve and the inflection point on the discontinuity.

This curve fitting is done by utilizing a least square fit minimization technique. i.e.

$$X^2 = (Y_i - F(Y_i))^2 \tag{2}$$

The program minimizes the value of X^2 by adjusting the values of floating parameters $A(1)$ to $A(8)$ in the equation for $F(Y_i)$.

The above problem being a non-linear fitting one, we have used the Levenberg–Marquardt method. This method is one of the standard directional set methods for function minimization [15]. The program is written in Fortran 77 and was implemented on a 386 based LAN.

The error involved in the measurement of $F(Y_i)$ is

$$F(Y_i) \pm (X^2/N\,\text{data})^{1/2} \tag{3}$$

where $(X^2/N\,\text{data})^{1/2}$ is the root mean square (RMS) deviation. For a good fit it is necessary that the order of the RMS value be significantly low as compared to the order of Y_i. For all the L_{II} and L_{III} absorption curves of RE_2O_3 RMS deviation was of the order of 10^{-2} to 10^{-3}, whereas (Y_i) was of the order 1. The degree of close fit is observed from figure 1(a, b).

The expression for B and/or C in (1) has been given by Weiskoff and Wigner [16] for a spectral line which is close to a classical lorentzian. Making use of this form of spectral line, Richtmyer *et al* [17] have discussed the shape of L_{III} absorption discontinuity of gold. They considered the energy continuum of empty states to be formed of regularly shaped discrete levels of equal widths. They also assumed that the transition probability of the inner electron being raised to all these levels is the same. This model then gives rise to a series of absorption lines of the same intensity with equal half widths. Upon integrating these curves, one obtains an arc tangent energy dependence for the absorption coefficient in the region of discontinuity. This arc tangent energy dependence in (1) is represented by expression A.

According to Nordfors [18], the inflection point in the initial rise of an absorption curve (displaying very nearly an arc tangent dependence in most cases) marks the energy value of the onset of allowed energy levels for the ejected inner electrons.

Materlik *et al* [19] while calculating the L_{III} and L_{I} absorption in Gd up to 80 eV above E_f, have taken the E_f point to correspond to the inflection point of the initial rising part of the absorption coefficient. The same procedure has been used by previous workers in our laboratory [9, 10]. We have in this work taken the second derivative

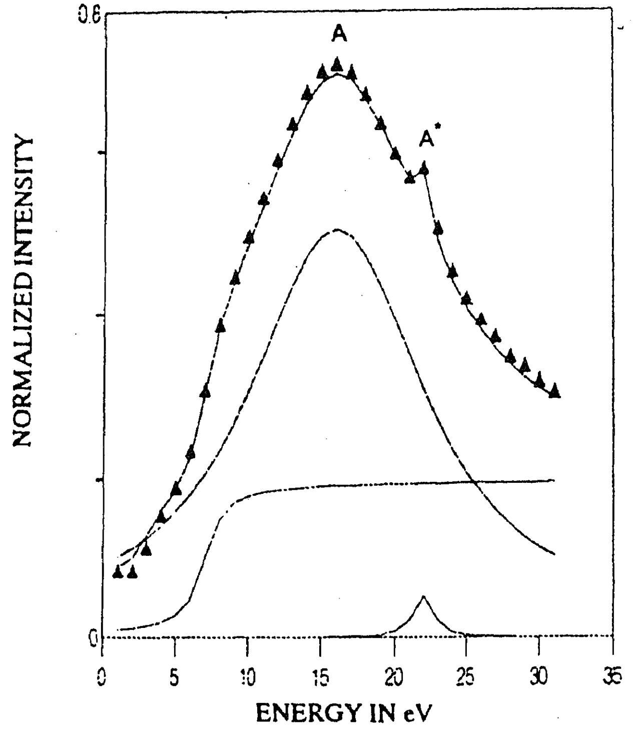

Figure 1(a). L_{II} absorption spectrum of La in La_2O_3. (—) Experimental value, (▲) Theoretical value.

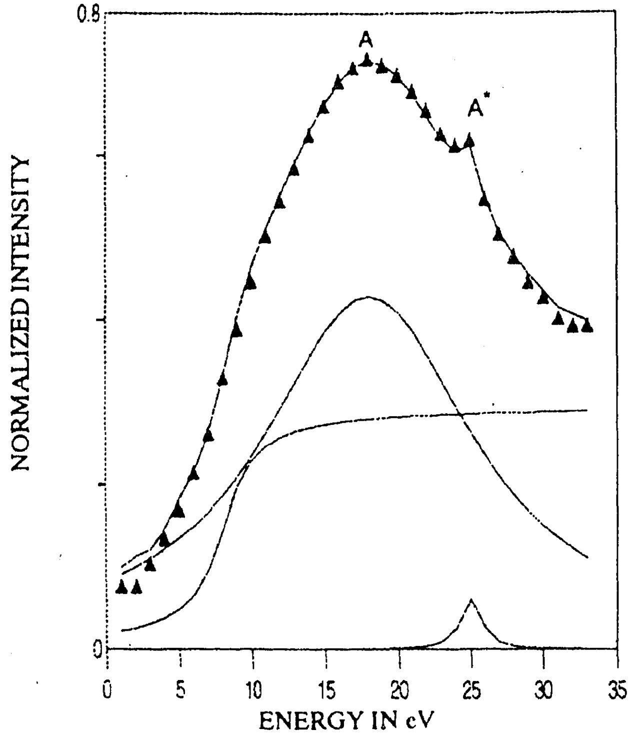

Figure 1(b). L_{III} absorption spectrum of La in La_2O_3. (—) Experimental value, (▲) Theoretical value.

Table 1. L_{II} absorption discontinuity of RE.

Compound	(Width in eV)† A	Area under A	(Width in eV)† A^*	Area under A^*
La_2O_3	5·0	4·05	0·57	0·11
Pr_2O_3	5·8	4·67	0·69	0·15
Nd_2O_3	6·3	4·90	0·75	0·18
Sm_2O_3	6·9	5·80	0·88	0·19
Eu_2O_3	8·2	6·53	0·96	0·22
Gd_2O_3	8·8	6·87	1·1	0·25

† indicates the widths of lorentzians corresponding to the absorption maxima A and A^* (shown in figure 1(a)) associated with the L_{II} absorption discontinuity of rare earths in their sesquioxides.

Table 2. L_{III} absorption discontinuity of RE.

Compound	(Width in eV)† A	Area under A	(Width in eV)† A^*	Area under A^*
La_2O_3	5·3	3·33	0·67	0·08
Pr_2O_3	6·1	3·69	0·81	0·14
Nd_2O_3	7·0	4·64	0·89	0·16
Sm_2O_3	7·5	4·95	0·95	0·18
Eu_2O_3	8·4	5·41	1·1	0·20
Gd_2O_3	9·3	6·47	1·3	0·22

† indicates the widths of lorentzians corresponding to the absorption maxima A and A^* (shown in figure 1(b)) associated with the L_{III} absorption discontinuity of rare earth in their sesquioxides.

of the absorption curve to obtain precise knowledge of inflection point on these absorption curves. The point E_0 corresponding to the energy of the inflection point on the arc tangent curve was fixed at this particular point. The program was then run to adjust the floating parameters from $A(1)$ to $A(8)$ to get the minimum value of X^2.

After successful run of the program we could obtain and compare the widths of the Lorentzians corresponding to the main absorption maxima A and A^* for both L_{II} as well as L_{III} absorption discontinuities. We also calculated the area under the Lorentzians corresponding to the main absorption maxima A and A^* for all the absorption discontinuities studied in the present work.

Tables 1 and 2 give the values of Lorentzian width corresponding to the main absorption maxima A and A^* obtained by using the program, for the L_{II} and L_{III} absorption discontinuities.

3. Results and discussion

The experimentally observed L_{II} and L_{III} absorption curves were normalized by calculating $(I_0 - I)/I_0$. Here I is the intensity at different points in the region of absorption edge and I_0 is the intensity of the continuum over which the absorption edge lies. The intensity of the continuum in the narrow energy region of the discontinuity can be presumed to be constant.

The L_{II} and L_{III} absorption curves for La_2O_3 are shown in figure 1(a, b).

We have obtained a secondary maximum A^* on the higher energy side of the absorption maximum A corresponding to the white line. Similar types of absorption edges are obtained for the rest of the rare earth oxides. The features A and A^* associated with the absorption discontinuities can be explained as follows.

The pronounced white line can be attributed to the transition $2p$ to $5d$ [20–22], highly favoured one due to symmetry consideration. This assignment is also supported by the X-ray isochromat studies [23] of gadolinium sesquioxide. These studies indicate the predominance of d character in its conduction band. The plots of the radial density as a function of r for the $4s$, $5s$, $5p$, $5d$ and $6s$ electrons for tri-positive gadolinium atom are given by Freeman *et al* [24]. The plots vividly demonstrate that the half filled $4f$ shell is indeed deeply embedded within the $5s$ and $5p$ shells. The plot also shows that the atomic state, $5d$, is widely separated from the $4f$ state. According to Rohler [25], the information obtained from the L_{II} and L_{III} absorption spectrum is very local. The measurement probes essentially the $5d$ states of the absorbing atom as modified (from the atomic $5d$ states) by the immediate neighbours. As is well-known, in sesquioxides the RE ions are surrounded by oxygen atoms in an octahedral coordination. The molecular energy level diagram for this system is given in figure 2 [26].

It must be mentioned here that the molecular orbital (MO) diagram is only qualitative and is built on the considerations of LCAO and MO formulation with respect to the first coordination. This first coordination, according to Rohler [25], plays an important and significant part in the atomic orbital modification. The MO diagram does not take into account the several complicating effects, such as interelectronic repulsion, spin orbit coupling, the extend of overlap between the orbitals of the absorbing atom and the concerned ligand ions, etc. Although simplistic, such a diagram enables us to interpret the spectral features associated with the L_{II} and L_{III} absorption edges [27].

The molecular orbital levels $2t_{2g}$ and $3e_g$, have a very significant contribution from the $5d$ atomic orbitals of rare earth ions. These molecular orbital levels will thus be highly favoured for the transition from the initial $2p_{1/2}$ and $2p_{3/2}$ levels in the case of L_{II} and L_{III} absorption respectively.

The probability of transition to MO $3a_{1g}$, which has a contribution from $6s$ atomic orbital of rare earth ion, is comparatively less. The transition to the $4t_{1u}$ molecular level, which has a contribution from the $6p$ atomic levels, is forbidden. We can therefore attribute the main absorption maximum A to the transition to molecular orbital level $2t_{2g}$ and the secondary maximum A^* to the transition to the $3e_g$ molecular orbital level in both the L_{II} and L_{III} absorption spectra.

Tables 1 and 2 show that the width of the Lorentzians corresponding to the absorption maxima A and A^* increases as we go down to the series. This can be explained as follows:

In the lanthanides $(57 < Z < 71)$ it has been shown [28] that the natural widths of the K, L, M and N levels increase more or less monotonously with the increasing atomic number. We expect the same trend to continue in RE sesquioxides. Also, the increase in the width in sesquioxides can be attributed to the fact that as the atomic number of RE increases the life time of the antibonding molecular orbitals of RE sesquioxide, to which the transitions responsible for the absorption maxima A and A^* take place, decreases.

From tables 1 and 2 one observes that the width of the Lorentzian corresponding

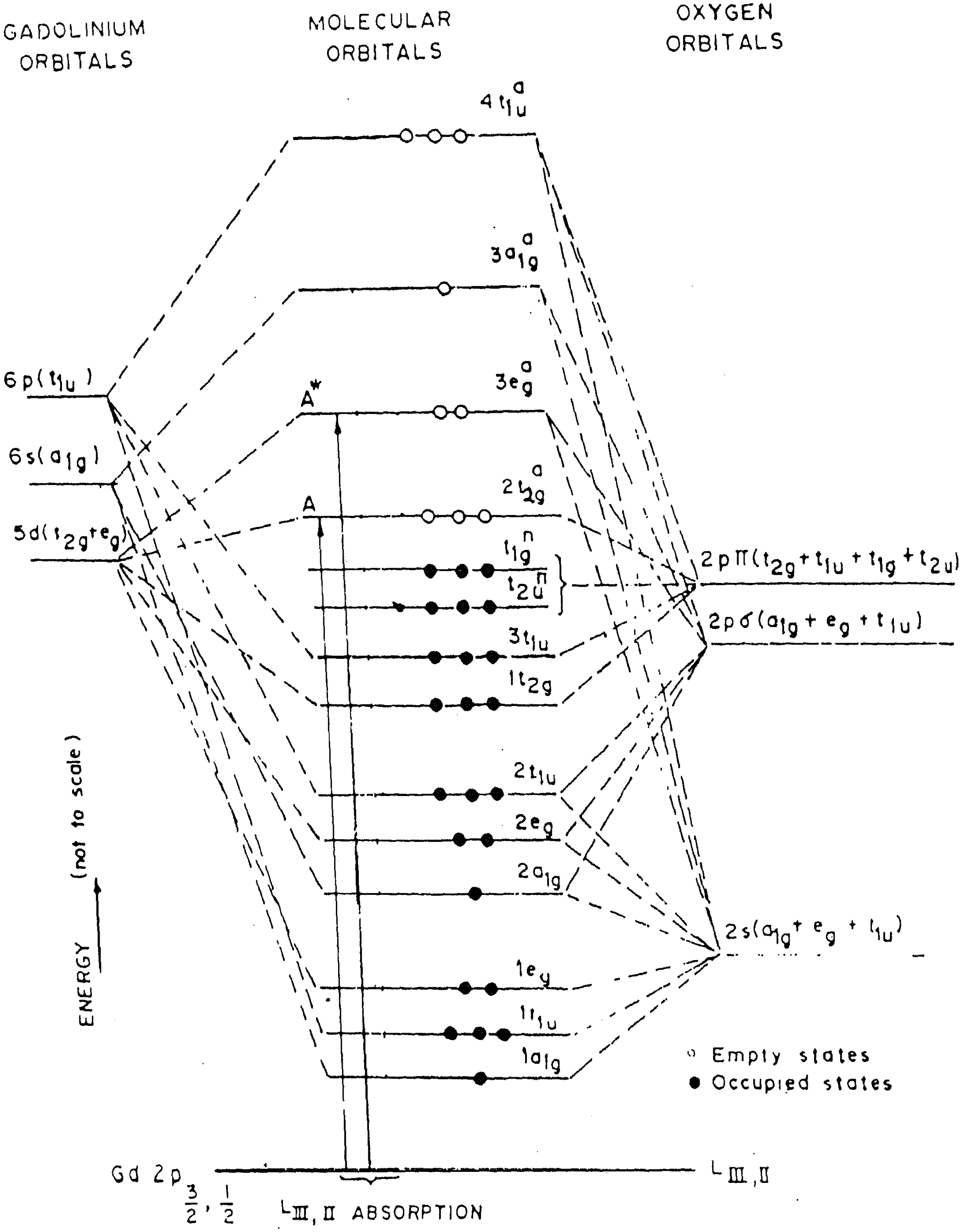

Figure 2. Molecular orbital diagram for Gd_2O_3.

to absorption maxima *A* and *A** is less in L_{II} absorption discontinuity compared to the L_{III} absorption discontinuity for the same RE sesquioxide. This may be attributed to the different initial atomic levels ($2p_{1/2}$ for L_{II} and $2p_{3/2}$ for L_{III} absorption discontinuity) from which the electron makes the transition to the molecular orbital energy levels. The above assumption is based on the fact that, transition probability is the function of the initial as well as the final energy levels. The width of the lorentzian corresponding to these transitions will therefore be affected by the change in these initial levels.

The two peaks, A and A^*, result from the transitions from the inner level $2p_{1/2}$ to the levels $2t_{2g}$ and $3e_g$ respectively for L_{II} and from $2p_{3/2}$ to the same levels $2t_{2g}$ and $3e_g$ for L_{III}. The ratio of the widths and area under the curve of the lorentzians corresponding to the transition to these two levels $2t_{2g}$ and $3e_g$ is thus expected to remain the same for both L_{II}, as well as L_{III} absorption discontinuities. As can be seen from tables 1 and 2 our experimental results corroborate this fact.

4. Conclusion

The agreement between the experimentally observed and theoretically predicted results shows the validity of the theoretical equation as well as the fitting technique used in this work. This technique can be considered as a step towards solving the XANES problem. The theoretical equation is flexible enough to take into account all the transitions responsible for the XANES as well as other phenomena such as, screening effect, variation in the potential around the metal ion due to surrounding ligand ions, charge transfer, etc. The work in this direction is in progress.

Acknowledgement

We are thankful to the University Grants Commission, New Delhi, for financial support.

References

[1] *Handbook of the physics and chemistry of rare earths* edited by K A Gschneidner, Jr L Eyring and S Hufner (Elsevier Science Publishers B V 1987)
[2] J K Lang and Y Baer, *Solid State Commun.* **31**, 945 (1979)
[3] *S. P. S. Systematics and the properties of the lanthanides* edited by Sinha (NATO ASI SERIES D. Reidel Publ. Co., Boston, 1982)
[4] J L Smith and E A Kmetko, *J. Less-Common Met.* **90** 83 (1983)
[5] K N R Taylor, *Contemp. Phys.* **11**, 423 (1970)
[6] R Reisfeld, *Inorg. Chim. Acta* **140**, 345 (1987)
[7] R Reisfeld and C K Jorgenson, *Lasers and exited states of rare earths*, Inorg. Chem. Concepts I (Springer Verlag, 1977)
[8] F H Speeding and A H Daane, *The rare earth* (Wiley, 1961)
[9] A D Vishnoi, V B Sapre and C Mande, *Phys. Status Solidi* **B161**, 891 (1990)
[10] P Deshmukh, P Deshmukh and C Mande, *J. Phys.* **C14**, 531 (1981)
[11] V B Sapre and C Mande, *J. Phys.* **C5**, 793 (1972)
[12] V B Sapre and C Mande, *J. Phys. Chem. Solids* **34**, 1351 (1973)
[13] B G Gokhale, S N Shukla and R N Shrivastava, *Phys. Rev.* **A28** 858 (1983)
[14] N V Moghe, N Mathurkar, G M Bhongale and V B Sapre, *Meas. Sci. Technol.* **3**, 557 (1992)
[15] *Numerical recipes* (*The art of scientific computing*) edited by W H Press, B P Flannery, S A Teukolsky, W T Vetterling, (1988) p. 523
[16] V Weisskoff and E Wigner, *Z. Phys.* **63**, 54 (1930)
[17] P K Richtmyer, S W Barnes and R Ramberg, *Phys. Rev.* **46**, 843 (1934)
[18] *X-ray Spectroscopy*, edited by Leonid V Azaroff (McGraw-Hill, 1974) p. 292
[19] G Materlic, J E Muller and J W Wilkins, *Phys. Rev. Lett.* **50**, 267 (1983a)
[20] J Wong, H L Scott and K J Rao, *EXAFS and NES III* edited by K O Hodgson, B Hedman, and J E Penner Hahn (Springer Verlag, 1984) p. 49

[21] V S Edlabadkar and C Mande, *Pramana – J. Phys.* **20**, 175 (1983)
[22] V S Edlabadkar, Transition rate calculations of some lines in X-ray emission spectra *Thesis* Univ. Nagpur (1981)
[23] S Bergwall and A S Nigawekar, *Phys. Kondens. Mater.* **10**, 107 (1969)
[24] A J Freeman, J O Dimmock and R E Watson, in *Quantum theory of atoms, molecules and the solid state*, edited by Lowdin (Per Olov., Academic Press 1986)
[25] Jurgen Rohler, *Handbook on the physics and chemistry of rare earths* edited by K A Gschneidner, Jr L Eyring and S Hufner, (Elsevier Science Publication, 1987) **10** p. 477
[26] D H Tempaston and C H Dauben, *J. Am. Chem. Soc.* **76**, 5237 (1954)
[27] A V Pendharkar and C Mande, *J. Chem. Phys.* **7**, 244 (1976)
[28] *X-ray absorption and emission spectra, Handbook on the physics and chemistry of rare earths* **10**, 465 (1987)

PRAMANA
— journal of
physics

© Printed in India

Vol. 42, No. 1,
January 1994
pp. 33–40

Estimation of rotational temperature of the source emitting the spectrum of PbO molecule

A B DARJI, T M PATEL, M B SURESHKUMAR, N R SHAH and P M SHAH
Physics Department, M.S. University of Baroda, Baroda 390 002, India

MS received 3 May 1993; revised 31 August 1993

Abstract. The (1, 0), (0, 1) and (0, 2) bands of $D \rightarrow X$ system of lead monoxide have been excited in RF discharge source and photographed in the seventh order of a 2-meter PGS. Intensity records of the rotational lines have been obtained. Rotational constants and the intensity measurements of Q and P branch lines of the above three bands and J numbering are used to calculate the effective rotational temperature of the source emitting the spectrum of ^{208}Pb ^{16}O molecule.

Keywords. Rotational temperature; molecular spectrum; lead monoxide.

PACS No. 33·20

1. Introduction

The spectrum of lead monoxide extending from 6750 to 1700 Å has been extensively studied by earlier workers [1–14] in various degrees of details. They have recorded the spectrum in absorption as well as in flame, d.c. arc, microwave discharge and high frequency discharge. The vibrational analyses of various band systems and rotational analyses of large number of bands have been reported by employing moderate to high dispersions. Rotational constants of X, A, B, C, C' D and E states of the molecule are known. Ram *et al* [14] have reported the rotational analysis of (1, 0) and (1, 1) bands of $B \rightarrow X$ system and (0, 1) and (0, 2) bands of $D \rightarrow X$ system. They have observed several perturbations in the rotational levels associated with $v' = 1$ level of B state and $v' = 0$ level of D state. They have also calculated rotational constants using perturbing rotational levels. The work reported so far on the spectrum of PbO molecule has been well reported by Ram *et al* [14]. Though the study of this molecule is extensive it has been found that there is no report on the intensity measurements of vibrational bands and rotational lines. No one has employed intensity measurements to study the vibrational and rotational temperatures of the molecule. This study makes first attempt to calculate the rotational temperature of PbO molecule. Rotational structure well resolved up to almost the origin of (1, 0), (0, 1) and (0, 2) bands exhibiting sharp rotational lines have been obtained. The rotational analysis of (1, 0) band has also been reported here for the first time. By studying the intensity profiles of the above bands and employing the J numbering and rotational constants, the rotational temperature of the source has been calculated.

Table 1. *J* assignments, vacuum wavenumbers and combination differences of $D \rightarrow X$ system of $^{208}Pb^{16}O$.

J	$Q(J)$ cm^{-1}	$P(J)$ cm^{-1}	$R(J)$ cm^{-1}	$\Delta_2 F'(J)$ cm^{-1}	$\Delta_2 F''(J)$ cm^{-1}
4		30620·19			
5		619·24			
6		618·20			
7		617·08			
8		615·88			
9		614·59			
10	30618·51	30613·22	30624·34	11·12	12·89
11	617·58	611·76	623·94	12·18	14·12
12	616·57	610·22	623·46	13·24	15·35
13	615·48	608·59	622·89	14·30	16·58
14	614·29	606·88	622·24	15·36	17·80
15	613·03	605·09	621·50	16·41	19·03
16	611·68	603·21	620·68	17·47	20·26
17	610·24	601·24	619·77	18·53	21·48
18	608·73	599·20	618·78	19·58	22·70
19	607·12	597·07	617·71	20·64	23·93
20	605·44	594·85	616·55	21·70	25·16
21	603·66	692·55	615·30	22·75	26·39
22	601·80	590·16	613·98	23·82	27·61
23	599·86	587·69	612·56	24·87	28·84
24	597·84	585·14	611·06	25·92	31·15
25	595·16	581·41	608·40	26·99	32·44
26	593·12	578·62	606·83	28·21	32·50
27	590·87	575·90	605·16	29·26	33·80
28	588·57	573·03	603·48	30·45	35·03
29	586·28	570·13	601·75	31·62	36·26
30	584·09	567·22	599·76	32·54	37·49
31	584·41	564·26	597·80	33·54	38·72
32	578·87	561·04	595·42	34·38	39·96
33	575·80	557·84	593·12	35·28	41·28
34	572·93	554·14	590·87	36·73	42·49
35	570·13	550·63	588·28	37·65	43·65
36	566·92	547·22	585·59	38·37	44·91
37	563·66	543·37	582·68	39·31	46·14
38	560·19	539·45	579·95	40·50	47·35
39	556·84	535·33	577·12	41·79	48·58
40	553·39	531·37	574·25	42·88	49·82
41	549·87	527·30	571·29	43·99	51·05
42	546·32	523·20	568·24	45·04	52·29
43	542·73	519·00	565·08	46·08	53·52
44	539·00	514·22	561·83	47·11	54·75
45	535·00	510·33	558·45	48·12	55·97
46	531·11	505·86	555·08	49·22	57·21
47	527·10	501·24	551·58	50·34	58·44
48	523·00	496·64	547·93	51·29	59·67
49	518·80	491·91	544·35	52·44	60·90
50	514·47	487·03	540·55	53·52	62·12

(Continued)

Table 1. (*Continued*)

J	$Q(J)$ cm^{-1}	$P(J)$ cm^{-1}	$R(J)$ cm^{-1}	$\Delta_2 F'(J)$ cm^{-1}	$\Delta_2 F''(J)$ cm^{-1}
51	510·33	482·23	536·88	54·65	63·29
52	505·86	477·26	532·99	55·73	64·57
53	501·54	472·31	529·13	56·82	65·78
54	496·99	467·21	525·15	57·94	67·04
55	492·33	462·09	521·12	59·03	68·27
56	487·53	456·88	516·85	59·97	69·52
57	482·98	451·60	512·54	60·94	70·77
58	478·04	446·13	508·24	62·11	71·90
59	473·20	440·64	503·78	63·14	72·99
60	468·06	435·25	499·18	63·93	74·14
61	463·22	429·64	494·75	65·11	75·41
62	457·95	423·77	490·12	66·35	76·72
63	452·61	418·03	485·15	67·12	77·89
64	447·28	412·23	480·52	68·29	79·04
65	441·78	406·11	475·55	69·44	80·30
66	436·40	400·22	470·56	70·34	81·56
67	430·77	393·99	465·58	71·59	82·78
68	425·26	387·78	460·35	72·57	84·00
69	419·45	381·58	455·25	73·67	85·17
70	413·58	375·18	450·02	74·84	86·32
71	407·68	368·93	444·48	75·55	87·70
72	401·56	362·32	438·90	76·58	88·73
73	395·46	355·75	433·22	77·47	90·01
74	389·32	348·89	427·35	78·46	91·26
75	382·98	341·96	421·56	79·60	92·36
76	376·45	334·99	415·89	80·90	93·56
77	370·20	328·00	410·12	82·12	94·74
78	363·70	321·15	—	—	—
79	357·08	314·13	—	—	—
80	350·32	—	—	—	—
81	343·53	—	—	—	—
82	336·66	—	—	—	—
83	329·57	—	—	—	—

obtained from the present analysis of (1, 0) band are given in table 2. The electronic transition giving rise to the emission of $D \rightarrow X$ system is considered to be $1 \rightarrow 0^+$ both belonging to Hund's case (*c*) as rightly ascribed by Ram *et al* [14]. However, well resolved extremely sharp lines do not show perturbation of any rotational levels as observed in (0, 2) and (0, 1) band structures. The exposures were so adjusted that the rotational isotopic shifts due to ^{206}Pb and ^{207}Pb are not observed. Thus the constants are evaluated for the molecule ^{208}Pb ^{16}O.

(b) *Estimation of rotational temperature of PbO molecule*

Intensity distribution in the rotational structure of (1, 0), (0, 1) and (0, 2) bands together with rotational constants and J numbering has been employed to calculate the rotational temperature of the molecule. The area under the intensity profile of a

Table 2.

(i) Rotational constants of $D \rightarrow X$ system of $^{208}Pb\ ^{16}O$ molecule.

State	Constant	Values	Values reported by Ram et al [14]
D1	B'_1	$= 0{\cdot}26487\ cm^{-1}$	—
	D'_1	$= 2{\cdot}81 \times 10^{-7}\ cm^{-1}$	—
	r'_1	$= 2{\cdot}069$ Å	
	I'_1	$= 105{\cdot}64 \times 10^{-40}\ g\ cm^2$	
$X0^+$	B''_0	$= 0{\cdot}30703\ cm^{-1}$	$0{\cdot}3063\ cm^{-1}$
	D''_0	$= 2{\cdot}34 \times 10^{-7}\ cm^{-1}$	$2{\cdot}27 \times 10^{-7}\ cm^{-1}$
	r''_0	$= 1{\cdot}922$ Å	—
	I''_0	$= 91{\cdot}13 \times 10^{-40}\ g\ cm^2$	—
Band Origin	ν_0	$= 30623{\cdot}15\ cm^{-1}$	—

(ii) Effective rotational temperature of the source emitting the spectrum of PbO molecule

Band	Branch	Rotational temperature (K)
(1, 0)	Q	4897
	P	4605
(0, 1)	Q	5085
	P	4591
(0, 2)	Q	4668
	P	4585

Effective rotational temperature $T = 4738{\cdot}5(\pm 126{\cdot}3)$ K

rotational line is measured by taking the base line corresponding to the background intensity of the emulsion. A standard source of continuous emission spectrum is used for a calibration of temperature T K as well as emulsion. It is assumed that these two parameters remain constant over the small extent of the rotational structure.

The intensities of the rotational lines of rotation-vibration bands in emission is given by

$$I_{em} = \frac{C_{em}\nu^4}{Q_r}\ (J' + J'' + 1)\exp([-B'_v J'(J' + 1)hc]/KT), \tag{1}$$

where C_{em} is a constant depending upon the change of dipole moment and the total number of molecules in the initial vibrational level v and Q_r is the rotational state sum. From (1), one obtains immediately

$$\ln\frac{I_{em}}{J' + J'' + 1} = A - \frac{B'_v J'(J' + 1)hc}{KT}, \tag{2}$$

where

$$A = \ln\frac{C_{em}\nu^4}{Q_r},$$

which may be taken as a constant for a small range of ν.

Estimation of rotational temperature

By ploting log $(I_{em}/(J' + J'' + 1)$ against $J'(J' + 1)$ a straight line is obtained whose slope is $(B'_v hc/KT)$. Thus by measuring line intensities and using rotational constants and J numbering, the temperature of the source can be determined. Strictly speaking (1) holds for emission from a purely thermal excitation. However, it has been found experimentally that the intensity distribution in emission bands in electric discharges is of the same type. Further it is quite clear that the normal intensity distribution in electron discharges results under the situation that the angular momentum is not strongly altered in excitation by electron collision. Considering this we have calculated the rotational temperature of the source emitting the spectrum of lead monoxide molecule.

The well resolved single lines free from any overlapping are considered from Q and P branches of (1, 0), (0, 1) and (0, 2) bands. Area under the peak of each rotational line is measured using a planimeter and the average of area under the peak is used in the calculation. Considering the calibration of the standard source and spectral sensitivity of the emulsion over a small range of wavelength, it is assumed that intensity of rotational lines in emission is proportional to the area under the peak in the intensity records. Thus $\log I_{em}/(J' + J'' + 1)$ is plotted against $J'(J' + 1)$ for Q and P branch lines of (1, 0) band. Using the J numbering and rotational constant B'_1 obtained from the present analysis rotational temperature is calculated. Further the rotational temperature is also calculated using P and Q branches of (0, 2) and (0, 1) bands and rotational constants reported by Ram *et al* [14]. The constants obtained from the present study are given in table 2. The rotational temperature so obtained is an effective one. In electric discharge sometimes rotational intensity distribution deviates from the thermal distribution. Repeated exposures give the position of intensity maxima at the same J number of the rotational lines in the Q and P branches of the above bands. Thus it is believed that the effective rotational temperature obtained from the present study is fairly constant. It is proposed that high dispersion spectrum of PbO molecule existing in the interstellar space and distant stars giving emission be carried out. The band spectroscopic methods for determination of vibrational and rotational temperatures of the interstellar molecules still have interest.

Acknowledgement

Authors are thankful to Dr S H Behere, Marathwada University, Aurangabad for fruitful discussions on the rotational temperature.

References

[1] J M Eder and E Valenta, *Atlas Typishher Spectrum* **17**, 28 (1924)
[2] H Lamprecht, *Z. Wiss. Phot* **33**, 16 (1911)
[3] L Grebe and H Konen, *Phys. Zeit.* **22**, 546 (1921)
[4] R Mecke, *Naturwissenschaften* **17**, 122 (1929)
[5] S Bloomenthal, *Phys. Rev.* **135**, 34 (1930)
[6] H G Howell, *Proc. R. Soc.* (*London*) **A153**, 683 (1936)
[7] E E Vago and R F Barrow, *Proc. Phys. Soc.* **59**, 449 (1947)
[8] A Christy and S Bloomental, *Phys. Rev.* **35**, 46 (1930)
[9] R F Deutsch Barrow and D N Travis, *Nature* (*London*) **191**, 374 (1961)
[10] T Torring, *Z. Naturforsch.* **A19**, 426 (1964)
[11] L Gero, *Z. Phys.* **93**, 669 (1936)

[12] R Schmid and L Gero, *Z. Phys.* **94**, 386 (1935)
[13] I Kovaes, *Z. Phys.* **106**, 431 (1937)
[14] R S Ram, J Singh and K N Upadhya, *Spectrosc. Lett.* **6**, 515 (1973)
[15] G Herzberg, *Molecular spectra and molecular structure 1 spectra of diatomic molecules* (Van Nostrand, New York, 1950)
[16] P Youngner and J G Winans, *J. Mol. Spectrosc.* (USA) **4**, 23 (1960)

PRAMANA
— journal of
physics

© Printed in India

Vol. 42, No. 1,
January 1994
pp. 41–47

Oxide films of copper prepared by the oxidation of copper sulphide films

K S JOSEPH and B PRADEEP
Solid State Physics Laboratory, Department of Physics, Cochin University of Science and Technology, Cochin 682 022, India

MS received 21 October 1993

Abstract. Copper sulphide films prepared by reactive evaporation, when heated in air at 500 K, oxidized to Cu_2O after a series of intermediate chemical transitions. Golden yellow coloured Cu_2O films showed a large absorption before the fundamental absorption edge. The optical band gap was found to be $(2{\cdot}29 \pm 0{\cdot}02)$ eV. When these Cu_2O films were further heated they got converted to CuO and the optical band gap was found to be $(2{\cdot}17 \pm 0{\cdot}02)$ eV.

Keywords. Thin films; optical properties; oxidation; high temperature treatment.

PACS Nos **78·66; 81·60**

1. Introduction

Copper oxide (Cu_2O) is a well-known semiconductor and that its finding renewed interest in the search for low cost materials for solar cell application [1]. It is a defect semiconductor with *p*-type conductivity and through the work carried out in the 1920s, it has become one of the first semiconducting materials to be investigated. Cuprous oxide layers on Cu have been known for many years to be photoconducting and to show photovoltaic effect. The first investigation on photoconductivity of these materials was made by Pfund [2]. More precise photoconductivity study began with the work of Schonwald [3]. He showed that *p*-type conduction in Cu_2O occurs through the presence of copper ion vacancies. Switching phenomenon, similar to that observed in the case of many chalcogenide glasses was observed in Cu_2O crystals by Wang and Weichman [4]. Electrical [5–7] and optical [8–11] properties of Cu_2O have been reported in the literature by various authors. But reports on the electrical and optical properties of CuO are rare.

For use in thin film solar cell technology it must be possible to prepare low resistivity films of Cu_2O with good optical properties in a reproducible manner on a variety of substrates. Preparation methods that are currently being investigated are thermal oxidation [12–14], electrode position [15] and reactive sputtering [16–18]. A problem common to oxidation and electrodeposition methods is that the resulting Cu_2O material tends to be of high resistivity, namely 10^2–10^4 ohm cm in the thermal case [14] and 10^4–10^6 ohm cm in the electro-deposited case [15]. Best films are formed by reactive sputtering of copper in an oxygen-argon mixture which gives films with controlled resistivity over the range 25 to 10^4 ohm cm [16].

Here we report the preparation and optical properties of Cu_2O and CuO films prepared by the oxidation of copper sulphide films in air.

2. Experimental

Copper sulphide films were deposited on glass substrates as described in reference [19, 20]. After deposition the films are taken out of the chamber and oxidized in air at a particular temperature. The set-up used for oxidation of the films in air is given in detail in [21]. The heating rate was approximately $0{\cdot}5\,\mathrm{K\,s^{-1}}$. Both amorphous and crystalline films of CuS were used in these experiments. The criterion used for the oxidation of the final phase of Cu–S (chalcosite, colour yellow) to Cu_2O was the sudden change in the colour of the film to golden yellow. And the criterion used for the further oxidation of Cu_2O into CuO was the change of golden yellow colour to a translucent foggy appearance. These oxidized films contained pin holes and non-uniformities. This was especially severe in the case of thicker films.

Optical measurements of these films were made by using a Hitachi 200-20 UV-Vis spectrophotometer. Films used in the optical study had a thickness around 100 nm. X-ray diffraction measurements were carried out in a Philips PW 1140/90 X-ray diffractometer. About 300 nm thick films were used in X-ray diffraction study.

3. Results and discussion

When CuS films are heated beyond 500 K, after a series of phase transformations [22], the films get oxidized. This oxidation of the film is characterized by a sudden change in the film from yellow of chalcosite to the golden yellow of Cu_2O. The X-ray diffraction pattern of a film so oxidized is given in figure 1. The table 1 lists the *d*-spacings given in JCPDS card and our results. The unidentified lines are not listed

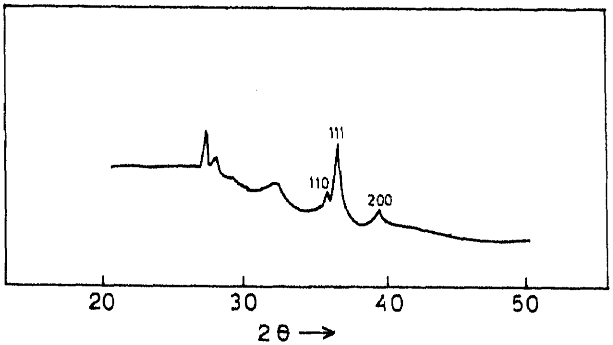

Figure 1. X-ray diffraction pattern of Cu_2O film.

Table 1. X-ray diffraction data for Cu_2O film.

JCPDS (Card No. 5–667)			Present results	
hkl	*d*(Å)	I/I_0	*d*(Å)	I/I_0
110	3·020	9	3·173	8
111	2·465	100	2·456	30
200	2·135	37	2·296	7
211	1·743	1		

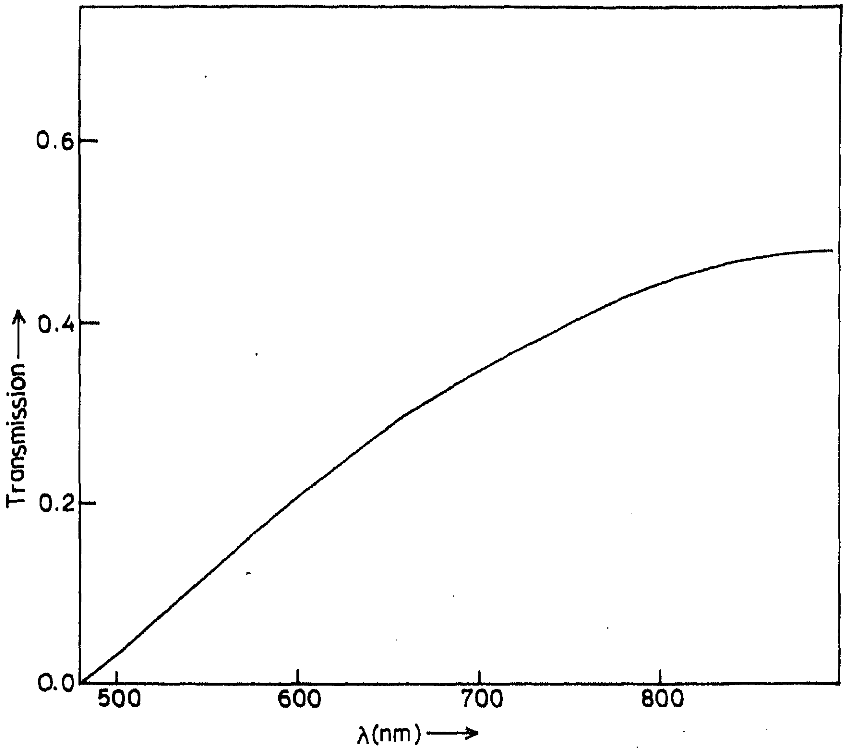

Figure 2. Transmission spectra of a typical Cu_2O film.

in the JCPDS card. It is not clear at present whether these lines are due to the presence of any other unknown phase or was it simply left unlisted in the JCPDS card because of the low inherent accuracy of these lines (low angle diffractions). The uniform colour of the film and the failure to detect two or more phases under crossed polaroids in an optical microscope and also the fact that the unlisted lines are not due to CuO almost rule out the first possibility.

From X-ray diffraction study no preferred orientation of the grains in the films could be found.

The samples obtained show p-type conductivity and were of high electrical resistivity. This is in general agreement with earlier reported data in the literature.

Transmission spectra of a Cu_2O film of thickness ≈ 100 nm is shown in figure 2. It may be seen that this film shows a high absorption ($\alpha \sim 10^4\,\mathrm{cm}^{-1}$) before the onset of band to band transitions. A visual inspection of the film shows that the film is not clear, i.e. they scattered light too much. The absence of interference fringes also shows that the films are not optically perfect. It may also be noted that transmission decreases continuously from 900 nm. This may be due to the existence of large number of levels in the forbidden gap just below the conduction band or just above the valence bands. Weichman and Reyes [23] report that copper inclusions are responsible for absorption peaks in the 1·1 eV to 2·0 eV range. In the present case these absorption peaks may have merged into a single one due to the large number of defects present causing high absorption before the onset of band to band transitions.

Because of the large absorption before the absorption edge, interference fringes were absent and consequently refractive index of the film could not be determined.

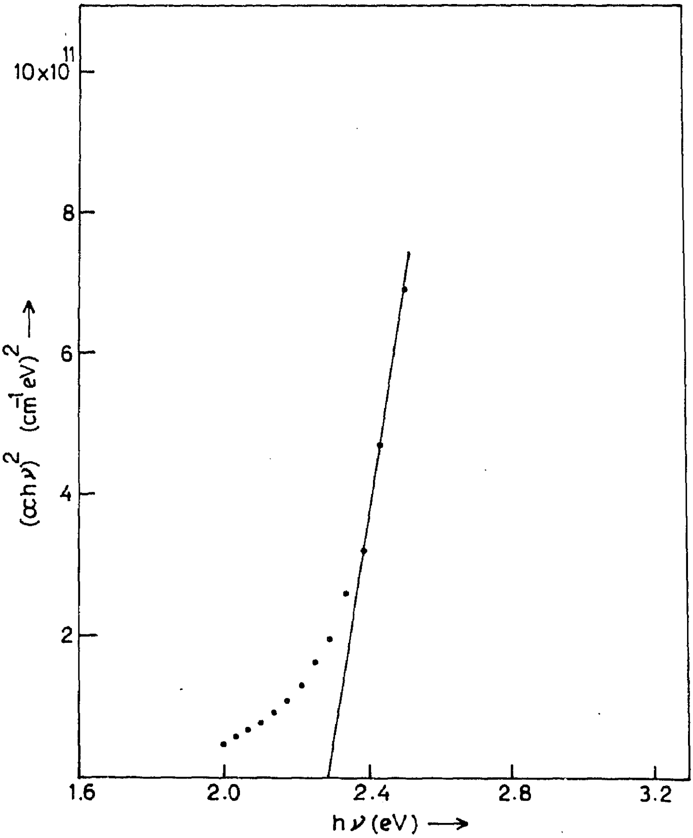

Figure 3. Plot of $(\alpha h\nu)^2$ versus $h\nu$ for a Cu_2O film.

For calculation of absorption coefficient, refractive index data given in [16] was used. The plot of $(\alpha h\nu)^2$ versus $h\nu$ is shown in figure 3. This gives a band gap of $2{\cdot}29 \pm 0{\cdot}02$ eV and the transition leading to this is a direct allowed one. The reported band gap of Cu_2O polycrystalline specimens from photoconductivity data lies between 1·94 eV and 2·14 eV. This band gap corresponds to transitions from valence band to exciton levels [24] just below the conduction band. Since the samples used in the present study show no structure in the transmission curve due to exciton absorption and because of the large absorption coefficients ($\alpha \sim 10^5\,\mathrm{cm}^{-1}$) characteristic of direct transitions, the band gap obtained in the present case may be taken as due to transitions taking place from valence band to conduction band and the band gap obtained as the true gap. This is in agreement with the energy level diagram given in [25] for Cu_2O, where a band gap of 2·3 eV is taken.

When the Cu_2O films are maintained at 500 K for some time, the characteristic golden yellow of Cu_2O disappears and a film with a translucent foggy appearance is obtained. X-ray diffraction pattern of such a film is shown in figure 4. The diffraction data (table 2) shows lines due to monoclinic CuO together with three other lines which are unidentified. It is not clear at present whether this is due to the presence of any other phase.

The transmission spectra of a CuO film at ≈ 100 nm thickness is shown in figure 5. It may be seen that as in the case of Cu_2O films, these films also show high absorption

Table 2. X-ray diffraction data for CuO film.

JCPDS (Card No. 5–661)			Present results	
hkl	d(Å)	I/I_0	d(Å)	I/I_0
110	2·751	12	2·802	9
			2·623	12
002	2·530	49		
$\bar{1}11$	2·523	100	2·520	22
111	2·323	96	2·320	18
200	2·312	30		
$\bar{1}12$	1·959	3		
$\bar{2}02$	1·866	25		

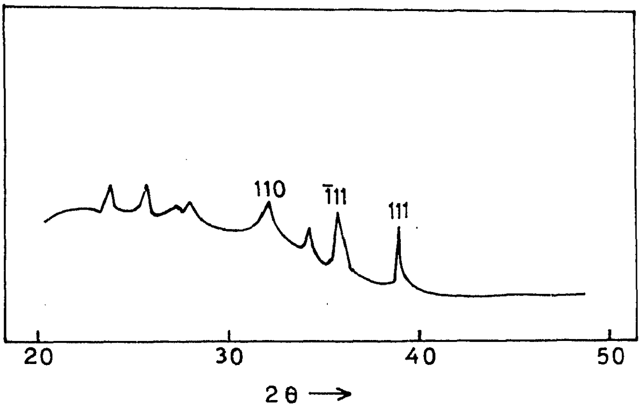

Figure 4. X-ray diffraction pattern of a CuO film.

before the absorption edge. Because of the absence of interference fringes, refractive index in this case also could not be obtained. For the calculation of absorption coefficient, refractive index data given in [16] was used. The plot of $(\alpha h\nu)^2$ versus $h\nu$ for a typical CuO film is shown in figure 6. This gives a direct band gap value of $2{\cdot}17 \pm 0{\cdot}02$ eV and the transition leading to this is an allowed one. Band gap value of CuO films has apparently not been reported in the literature and hence a comparison is not possible. The band gap value obtained in the present case for CuO film is less than that obtained for Cu_2O films. A film of material with a band gap of 2·17 eV should have appeared yellow in transmission as it cuts off wavelengths lesser than yellow. But CuO films obtained in the present case, it seems, does not do this; as mentioned earlier they have a foggy translucent appearance. The apparent transparency suggests a band gap of more than 3 eV. The apparent fundamental absorption shown by these films may be due to a large number of structural and stoichiometric defects which causes band tailing, i.e. impurity bands merging with conduction or valence bands. Evidently more work is needed to clarify these points.

So it can be seen that the effect of heating CuS films in air up to a temperature in excess of 500 K is a series of chemical changes taking place in the structure and composition of the film:

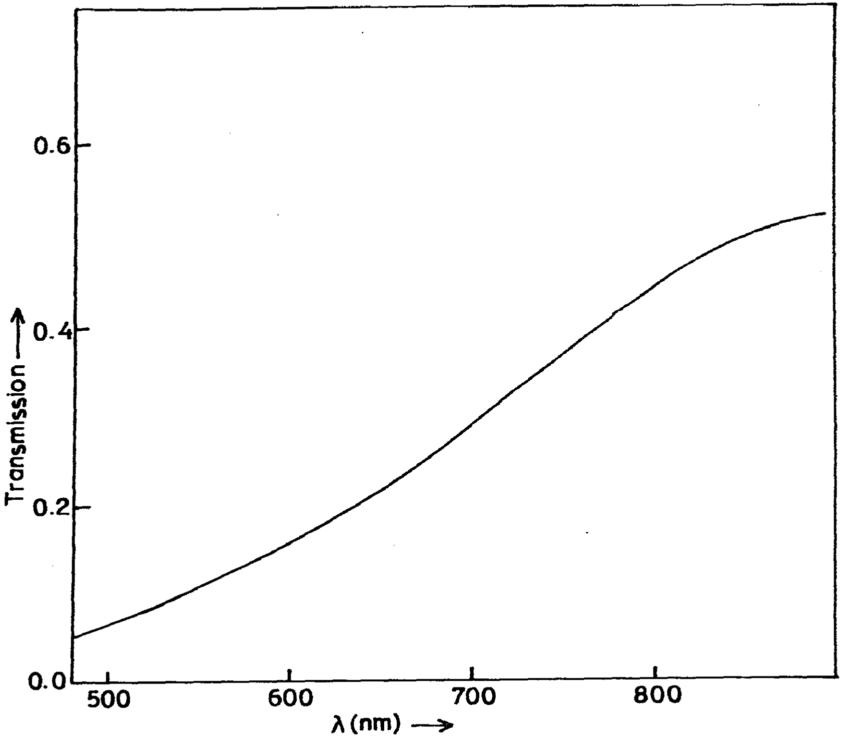

Figure 5. Transmission spectra of a typical CuO film.

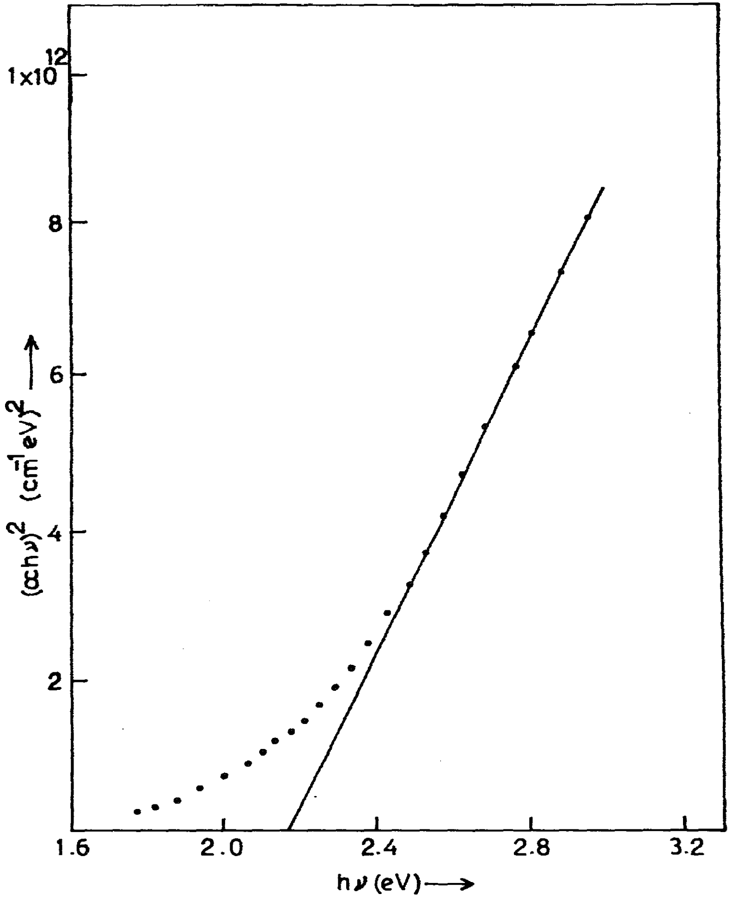

Figure 6. Plot of $(\alpha h\nu)^2$ versus $h\nu$ for a CuO film.

CuS(hexagonal) → djurleite (orthorhombic + S(rhombohedral)) → djurleite (orthorhombic) → chalcosite(orthorhombic) → Cu_2O(Cubic) → CuO(monoclinic).

4. Conclusion

Films of CuS when heated in air at 500 K, after a series of intermediate chemical transitions, get oxidized to Cu_2O. These Cu_2O films are golden yellow and show large absorption edge. The band gap obtained ($2{\cdot}29 \pm 0{\cdot}02$ eV) from optical studies agrees with that reported in the literature for Cu_2O layers. When these Cu_2O films are further heated they get converted to CuO films. These films also show large optical absorption before the absorption edge. The band gap obtained for CuO films is $2{\cdot}17 \pm 0{\cdot}02$ eV. The quality of the films obtained by this method are rather poor.

Acknowledgements

One of the authors (BP) would like to acknowledge the financial assistance by STEC, Trivandrum.

References

[1] F A Shirland and P Rai-Choudury, *Rep. Prog. Phys.* **41**, 1839 (1978)
[2] A H Pfund, *Phys. Rev.* **7**, 289 (1961)
[3] B Schonwald, *Ann. Phys. Lpz.* **15**, 395 (1932)
[4] C J Wang and F L Weichman, *Can J. Phys.*, **60**, 1648 (1982)
[5] J S Anderson and N N Greenwood, *Proc. R. Soc. (London)* **A215**, 353 (1952)
[6] O Bottger, *Ann. Phys.* **10**, 232 (1952)
[7] W Juse and B W Kurtschatow, *Physik. Z. Sowjetunion* **2**, 453 (1932)
[8] T F Gross and N A Karryev, *Dokl. Akad. Nauk. U.S.S.R.* **84**, 471 (1952)
[9] S Nikitine, L Couture, M Seiskind and G Perny, *Comp. rend.* **238**, 1786 (1954)
[10] J H Aptel and L N Hadley, *Phys. Rev.* **73**, 749 (1948)
[11] M Hayashi and K Katsuki, *J. Phys. Soc. Jpn.* **7**, 599 (1952)
[12] L C Olsen and R C Bohara, *Proc. 11th IEEE, Photo. Spec. Conf., 1976, IEEE, New York,* p. 875
[13] D Trivich, E Y Wang, R J Komp and F Ho, *Proc. 12th IEEE Photo. Spec. Conf.*, 1978, IEEE, New York, p. 174
[14] C Nognet, M Tapiero, C Schwab, J P Zielinger and D Trivich, in *Proc. 1st photovoltaic solar energy conference of the commission of european communities*, (D Reidel, Dordrecht, 1977) p. 1180
[15] N A Economiu, R S Toth, R J Koump and D Trivich, in *Proc. 1st photovoltaic solar energy conference of the commission of European communities*, (D. Reidel, Dordrecht, 1977) p. 1180
[16] V F Drobny and D L Pulfrey, *Thin solid films* **61**, 89 (1979)
[17] G Beensh-Marchwicka, L Krol, Stopniewska and M Slaby, *Thin solid films* **88**, 33 (1982)
[18] M Fujinaka and A A Berezin, *J. Appl. Phys.* **54**, 3582 (1983)
[19] Joy George and K S Joseph, *Solid State Commun.* **48**, 601 (1983)
[20] Joy George and K S Joseph, *J. Phys. Chem. Solids* **44**, 341 (1984)
[21] Joy George and K S Joseph, *Solid State Commun.* **46**, 541 (1983)
[22] K S Joseph and B Pradeep (unpublished results)
[23] F L Wichman and J M Reyes, *Can. J. Phys.* **58**, 32[illegible]1980)
[24] R J Elliot and A F Gibson, *An introduction to solid state physics and its applications*, (McMillan, London, 1978) p. 213
[25] G F J Garlick, in *Encyclopedia of physics* (Springer-Verlag, Berlin, 1956) **19**, 379

PRAMANA
— journal of
physics

© Printed in India

Vol. 42, No. 1,
January 1994
pp. 49–64

Optical design of a toroidal grating monochromator based beam line on Indus-1

K J S SAWHNEY and R V NANDEDKAR
Accelerator Program, Centre for Advanced Technology, Indore 452 013, India

MS received 8 April 1993; revised 22 September 1993

Abstract. In this paper, we discuss the detailed optical design of a beam line that is under construction on the synchrotron radiation source, Indus-1. Toroidal mirrors are used as pre- and post- focusing elements and a toroidal grating monochromator as a dispersing element. Using three interchangeable gratings, this monochromator will give, at a moderate resolution, a good throughput on the sample in the wavelength range 40 to 1000 Å. Effect of various parameters and their optimization on the resolution and throughput characteristics have been studied by ray tracing calculations, and presented.

Keywords. Synchrotron radiation; beam line; soft X-ray; vacuum ultraviolet.

PACS No. 42·10

1. Introduction

The measurement of optical properties in vacuum ultraviolet (VUV) and soft X-ray regime (20–2000 Å) is an important area. The measurements in this entire wavelength regime can only be performed using a synchrotron radiation (SR) source. Various sources, detectors and spectrometers are generally required to be calibrated in this wavelength range. The optical constants, viz., the index of refraction and extinction coefficients need to be determined for various polarization components. For these investigations, high intensity monochromatic radiation in the above-mentioned wavelength range is required; however, the resolution requirement is moderate ($\lambda/\Delta\lambda \sim 500$). To carry out this type of studies preliminary design of a multipurpose beam line was conceived [1, 2]. This beam line is being built for setting up on the 450 MeV Indus-1 synchrotron radiation source (SRS). The same beam line will be used for reflectometry to investigate optical constants of materials, multilayers etc in VUV and soft X-ray regime. The purpose of a beam line is to deliver monochromatic light onto a sample. The detailed optical design of this beam line is presented in this paper. The theoretical performance of the beam line has been evaluated using ray tracing calculations.

2. General considerations

In the wavelength range of our interest (40–1000 Å) reflecting optics predominates due to the high absorption of all materials in this wavelength region and the only useful optical elements with good imaging properties are the reflecting mirrors and reflection gratings. Furthermore, to achieve a sufficiently high reflectivity at gratings and mirrors, it is necessary to work at nearly grazing incidence. The imaging quality deteriorates, however, at such grazing angles and even aspherical focusing elements give poor imaging for the off-axial points of an object. There are further problems which arise in this spectral range:

Gratings with high groove densities are needed in order to obtain high angular dispersion and thus high resolution. Such gratings are relatively inefficient and may generate a considerable amount of stray light.

Since SRS is a continuum source of radiation, higher order contributions from diffracting elements may be present and these have to be minimized. This is a severe problem because in general the SR is more intense at short wavelengths.

Aspheric surfaces with very good surface quality are difficult to manufacture.

Furthermore, since the source point is fixed in space, the optical system of the beam line has to be designed in such a way that a fixed exit beam is obtained. Also, to avoid build-up of contamination on the reflecting surfaces, the beam line has to be operated under ultra high vacuum (UHV) conditions. All these considerations have been taken into account in designing the beam line.

3. Optical design

In general, the optical components of a typical beam line consist of a premirror to collect and focus the incident radiation, a monochromator to select a wavelength of interest and a post-mirror to focus the monochromatic radiation onto the sample. We have designed a beam line based on a toroidal grating monochromator and its optical configuration is given in figure 1. Various considerations going into this design are described in the following.

3.1 *Source characteristics*

Indus-1 is a 450 MeV electron storage ring with four bending magnets [3]. A storage ring provides SR by the acceleration of relativistic electrons in the dipole magnetic field of the bending magnets. The radiation is emitted tangentially with 100% linear polarization in the plane of the orbit and is highly collimated in the vertical direction.

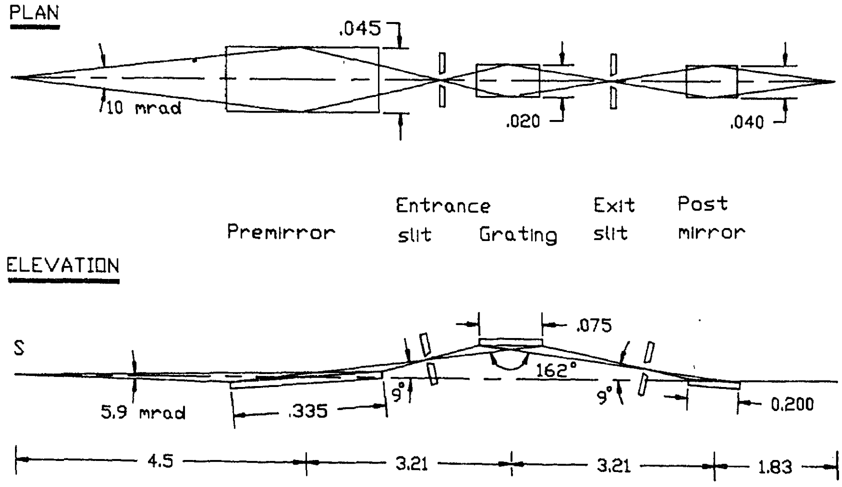

Figure 1. Optical layout of the beam line. All dimensions are in metres.

Table 1. Characteristics of Indus-1 synchrotron radiation source.

Electron energy	: 450 MeV
Source type	: Bending magnet
Bending magnet radius	: 1000 mm
Critical wavelength	: 61 Å
Source size (σ)	: 0·8 mm × 0·1 mm
Horizontal divergence	: 10 mrad
Vertical divergence	: 2–5 mrad

The SR spectrum from Indus-1 consists of a quasi-continuum radiation with a critical wavelength of 61 Å. The SR source size is determined by the cross-section of the electron beam, which in turn depends on the emittance and the angle at which the SR is taken out from the bending magnet. We have considered high emittance mode and our beam line will be on a 10° port on the bending magnet [4]. For this case, the electron beam size is 0·1 mm vertically and 0·8 mm horizontally [5]. Furthermore, the height, width and vertical divergence are not sharply cut-off but follow gaussian distribution. The values quoted above are the σ values of these gaussian distributions. The vertical divergence of the SR beam is wavelength dependent and is given by:

$$\sigma_y = \frac{570}{\gamma}\left[\frac{\lambda}{\lambda_c}\right]^{0\cdot 43} \tag{1}$$

where γ is the electron energy measured in units of the electron rest mass and λ_c is the critical wavelength ($\gamma = 881$ and $\lambda_c = 61$ Å for Indus-1). The vertical divergence increases with increasing wavelength and it is typically in the range of 2–5 mrad. The horizontal divergence is limited by the vacuum port through which the radiation is extracted from the storage ring and for our beam line it is 10 mrad. The various parameters of Indus-1 employed by us for beam line design are given in table 1. The beam power intercepted by this beam line from Indus-1 will be small and hence cooling of the optical elements is not necessary.

3.2 *Pre- and post-focusing mirrors*

For focusing synchrotron radiation, there exists a large choice of mirrors [6]. The simplest option of using spherical mirrors introduces large aberrations at grazing incidence. To reduce these aberrations, aspheric surfaces have to be used for mirrors and gratings. An ellipsoid is an ideal surface to get a stigmatic image of a point source. However, it is rather difficult to fabricate ellipsoidal surfaces and hence they are expensive. An aspheric surface which is easy to fabricate compared to an ellipsoid is a toroid. A toroid is generated by rotating a circle of radius ρ in an arc of radius R. The principal radii of curvature of the toroid are chosen to be equal to those of the ellipsoidal mirror. The principal radii of curvature of the ellipsoidal at the vertex are given by

$$R = \frac{1}{ab}[r_1 r_2]^{3/2} \tag{2}$$

$$\rho = \frac{b}{a}[r_1 r_2]^{1/2} \tag{3}$$

Table 2. Parameters of the toroidal pre- and post-mirrors.

Parameters	Pre-mirror	Post-mirror
R(mm)	38236·5	23400·7
ρ(mm)	235·4	144·1
Angle of incidence (w.r.t. mirror surface)	4·5°	4·5°
Source to mirror distance (mm)	4500	1836
Mirror to focus distance (mm)	2250	1836
Demagnification ratio	2:1	1:1
Size (mm × mm)	335 × 45	280 × 40
Coating	gold/platinum	

where r_1 and r_2 are the object and image distances from the mirror surface and a and b are the semi major and semi minor axes of the ellipsoid. If ψ is the angle of incidence on the mirror surface then a and b are given by

$$a = \frac{r_1 + r_2}{2}, \tag{4}$$

$$b = \sqrt{r_1 \cdot r_2} \cdot \cos\psi. \tag{5}$$

It was shown earlier [7] that for small source size and small horizontal acceptance, the toroidal mirror produces almost as good an image as an ellipsoidal mirror does, and since toroidal surfaces are easier to fabricate we have chosen toroidal mirrors as pre- and post- focusing elements for our beam line. The parameters of these mirrors are given in table 2. Various considerations for choosing the shapes and sizes of these mirrors given in this table are discussed in § 3·4.

3.3 *Toroidal grating monochromator*

The most critical component in the beam line is the monochromator. Unfortunately, the required wavelengths are too long for crystal monochromators and though conventional normal incidence grating monochromators for SR have good stigmatic properties, they cannot be used in the soft X-ray region ($\lambda < 300$ Å). Grazing incidence monochromators are most suitable for operation in the desired wavelength range. Various grazing monochromators [8] are classified according to the type of diffraction grating employed. Monochromators using plane gratings comprise one category, those with spherical gratings a second category and those utilizing aspherical gratings (e.g. toroids) a third category. Every monochromator represents a compromise in acceptance, resolution, spectral range, photon flux and complexity of design [9]. A toroidal grating monochromator (TGM) is the simplest to realize and is characterized by very high efficiency, large collection aperture, moderate resolution and a simple wavelength scanning mechanism. We have chosen a grazing incidence TGM in our beam line design. A number of TGM based beam lines are in operation at the various SR facilities worldwide [10].

When the TGM is used in the fixed deviation geometry, i.e., in a configuration in which the deviation angle between the entrance and exit arms is constant, the grating

Table 3. Parameters of toroidal grating monochromator.

Entrance arm length (mm)	:	1000
Exit arm length (mm)	:	1414
Deviation angle	:	162°
Major radius (mm)	:	7977·0
Minor radius (mm)	:	182·3
Wavelength range		
Grating 1 (1800 grooves/mm)	:	40–120 Å
Grating 2 (600 grooves/mm)	:	120–360 Å
Grating 3 (200 grooves/mm)	:	360–1000 Å
Ruled area of the grating (mm^2)	:	75 × 20
Coating	:	gold/platinum

equation reduces to

$$Nk\lambda = 2\cos\theta\sin(\theta+\beta) \tag{6}$$

where $2\theta = \alpha - \beta$ is the included angle, α is the angle of incidence, β is the angle of diffraction, N is the groove density and k is the diffraction order. α and β are of opposite sign if on the opposite sides of the surface normal. The angle $(\theta+\beta)$ is the deviation of the diffracted ray from the zeroth order, i.e., it is the scanning angle. Equation (6) shows that the wavelength is proportional to $\sin(\theta+\beta)$, implying that a simple sine bar mechanism is sufficient for wavelength scanning.

We plan to use the grating in the first diffraction order since higher orders are not desirable as they require higher angular scan range (due to higher dispersion) which lead to higher aberrations resulting in a net loss of resolution. Also, positive order (exit arm > entrance arm) is preferred as it intercepts more SR with the same size of the grating. Therefore, our monochromator will have $k = +1$. A direct consequence of operating in positive first order at fixed deviation geometry is that a cut-off exists in the long wavelength end of the spectrum corresponding to $\alpha = 90°$ case and hence more than one grating is generally required to cover the full wavelength range.

The design of our beam line is based on a commercially available monochromator TGM1400. Various parameters of the monochromator-like grating radii, included angle 2θ, groove frequency N and object and image distances determines the performance of the monochromator [11]. For instance, the included angle 2θ determines the short wavelength limit of the spectral range. The monochromator chosen has an included angle $2\theta = 162°$, which is sufficiently large to get photons of wavelength 40 Å, and at the same time is as small as possible to reduce the focusing aberrations. Since the aberration corrections are effective in a limited wavelength range, more than one grating is required to be used to cover the full spectral range of interest. The TGM selected utilizes three toroidal gratings which can be interchanged *in situ* without breaking the vacuum. The various parameters of the monochromator are given in table 3.

3.4 *Optical layout*

The optical configuration of the beam line shown in figure 1 comprises of a pre mirror M_1, an entrance slit S_1, a toroidal grating T, an exit slit S_2 and a post mirror M_2. The TGM combines the dispersion and focusing in one optical element, thus minimizing the reflection losses in the system. The various physical constraints such as the length of the front end, thickness of the radiation shielding, etc. restricts the placement of the first mirror M_1 not before 4000 mm from the tangent point of the storage ring. We have therefore kept the first optical element i.e. the pre-focusing toroidal mirror at a distance of 4500 mm from the source. This mirror is inclined at 4·5° to the horizontal plane and it illuminates the entrance slit S_1 by a 2:1 demagnification of the SR source. The grating in the TGM is vertically dispersing at a constant deviation of 162° and has a ruled area of 75 mm × 20 mm. After diffraction by the grating, the monochromatic light passing through the exit slit is deflected back to the horizontal plane (plane of the electron orbit in the storage ring) by a second toroidal mirror at 1:1 magnification which focuses the monochromatised light onto the sample placed at a distance of 1836 mm from the mirror.

The choice of dimensions of the optical elements can be made following several different criteria. Since we plan to use commercially available gratings having ruled area of 75 mm × 20 mm, this becomes our starting point for determining the pre- and post-mirror sizes. For an entrance arm length of 1000 mm, this size of the grating corresponds to a maximum acceptance of the grating of 11·7 mrad vertical × 20 mrad horizontal (corresponding to zeroth order light, $\alpha = -\beta = 81°$). To match this acceptance with a 2:1 demagnification of the pre-mirror, a toroidal mirror of size 335 mm × 45 mm is required. Similarly, to determine the post-mirror size, the vertical and horizontal divergences at the exit slit should be known. These divergence values depend on the acceptance and magnification of the grating. In the dispersive direction, both these quantities depend on wavelength and are given by

$$\sigma_v(\lambda) = \frac{l \cos\alpha}{r_1} \tag{7}$$

and

$$M_v(\lambda) = \frac{\cos\alpha}{\cos\beta} \cdot \frac{r_2}{r_1} \tag{8}$$

where $\sigma_v(\lambda)$ and $M_v(\lambda)$ are the grating acceptance and magnification in the vertical direction, l is the length of the grating and r_1 and r_2 are the entrance and exit arm lengths of the monochromator. From (7) and (8) vertical divergence values of 9·5 mrad and 11·9 mrad are obtained at the exit slit for wavelengths 40 Å and 120 Å, respectively, which are the two extreme wavelength limits of the 1800 grs/mm grating (the other two gratings will also yield the same divergence values). The size of the post-mirror has to be calculated for the larger divergence value which yields a value of 278 mm for the post-mirror length. In the non-dispersive (horizontal) direction the divergence and magnification of the grating are wavelength independent. While the horizontal acceptance of the grating is 20 mrad, the magnification is simply given by r_2/r_1. The horizontal divergence at the exit slit is therefore 14·14 mrad which yields a size of 26 mm for the post-mirror width. We have taken the post-mirror size to be 280 mm × 40 mm which is slightly more than the calculated value. This has been done for manufacturing ease [12].

4. Beam line performance

4.1 *Ray tracing*

To investigate the imaging properties of the beam line, we have carried out simulation studies using ray tracing calculations. The ray tracing calculations enable one to

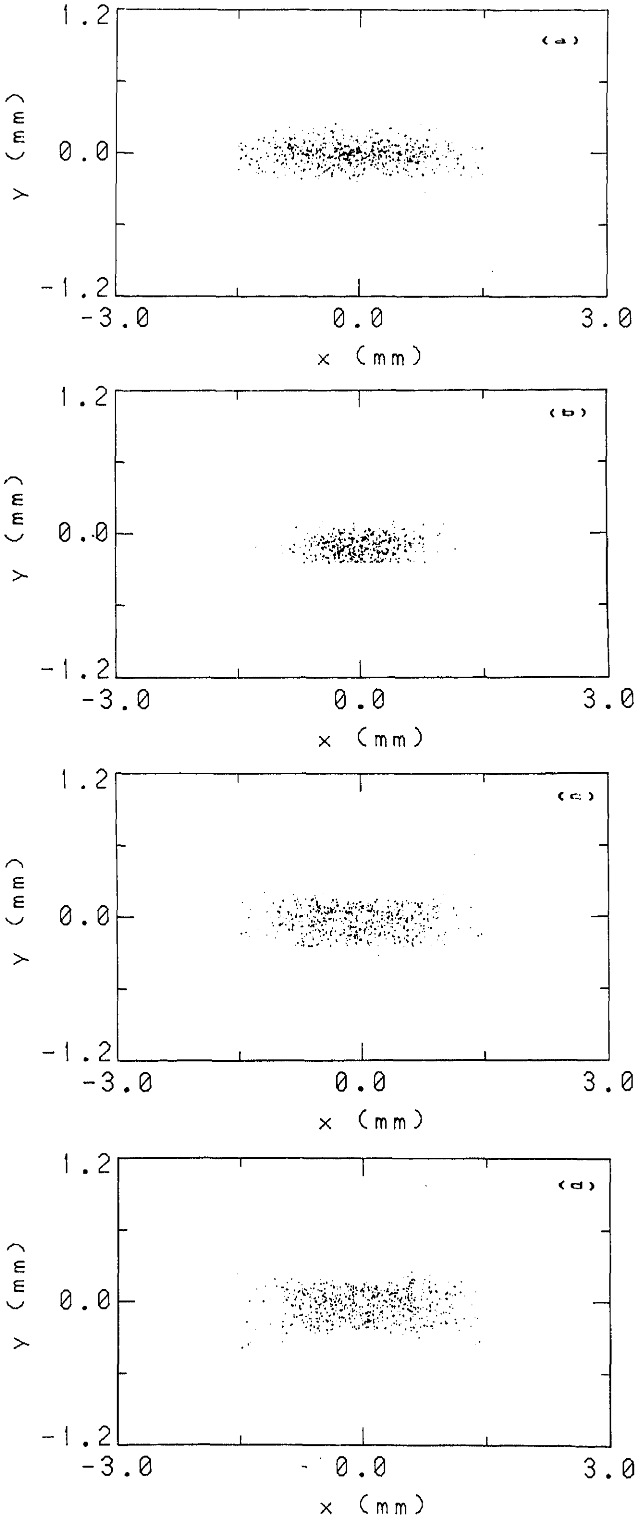

Figure 2. Intensity distribution at various focusing points: (**a**) Source, (**b**) Entrance slit, (**c**) Exit slit, and (**d**) Image plane. Ray tracing performed for 61 Å, 1800 gr/mm grating and for slit settings of 3 mm × 0·5 mm.

visualize actual intensity distributions on all optical elements and on the image planes, and to check the sensitivity of misalignment and shape variations of the optical elements. For this purpose, the ray tracing program RAY [13] has been adopted on the unix based Magnum mini computer in our institute. The program computes the propagation of a photon beam through an optical system. It simulates the SR emitted from a bending dipole magnet of the synchrotron radiation source and traces a set of pseudo random rays through the optical system to find out the intensity reflected and the intensity distribution at various optical elements. The rays are generated statistically taking into consideration the various storage ring parameters such as bending magnet radius, energy of stored electrons, and vertical and horizontal divergences. The values of these parameters for Indus-1 given in table 1 have been used in ray tracing calculations. The beam line optical layout is also specified as an input to the RAY program. These include the object and image distances for the mirrors and the grating, the surface shapes and sizes, incident and reflection/diffraction angles, and the slit sizes, etc. Various parameters of the optical components given in tables 2 and 3 are employed for ray tracing calculations. The ray trace output consists of points on a plot where each ray intersecting a given plane is plotted.

Figure 2a shows a simulation of the bending magnet source using 1000 rays. Figures 2b, 2c and 2d show the image patterns of this source as taken on the entrance slit, exit slit and the image plane, respectively. These results are for 61 Å, the critical wavelength of Indus-1 and the optical elements are assumed to be perfect without any tangent errors. This figure shows that the source is sharply focused at the image plane. The width of the image in the vertical direction at image plane includes the aberrations of the whole system as well as the contributions due to the finite size of the entrance and exit slits. The full width at half maximum (FWHM) of the image in the vertical direction then gives the overall resolution limit of the beam line. A typical intensity profile in the vertical (dispersive) direction at the image plane is shown in figure 3.

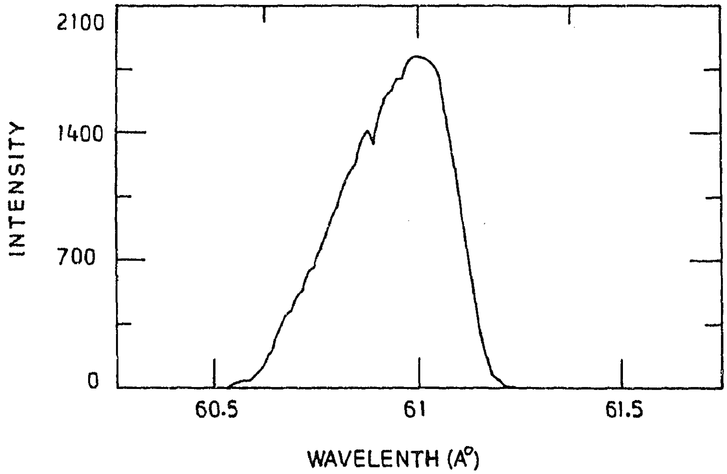

Figure 3. Intensity profile in the vertical (dispersive) direction at the image plane for 61 Å and slit settings of 3 mm × 1 mm.

4.2 *Resolution characteristics*

The resolution achieved by a monochromator in a beam line depends on several factors including the SRS beam size, the photon beam size (S1) at the entrance slit in the dispersive direction, the exit slit size (S2) in the dispersive direction and the geometrical aberration limit of the monochromator. Since our design of TGM utilizes entrance and exit slits at fixed locations the resolution becomes dependent on the wavelength. The attainable resolution of the monochromator is determined by ray tracing as exact analytical evaluation of the various contributions to the resolution is not possible.

In figure 4, the resolution calculated from ray tracing is shown for high energy grating ($N = 1800$ gr/mm) for different slit widths of 200, 500 and 1000 μm. The slit height, which does not influence the resolution, is kept at 3 mm. It can be seen from the figure that for a slit width of 200 μm the resolution is about 0·14 Å between 40 and 120 Å yielding a resolving power ($\lambda/\Delta\lambda$) of 250–700 in this wavelength range. Similar values of the resolving power are obtained for $N = 200$ and $N = 600$ gr/mm gratings. These limiting resolution values have been obtained at slit settings of 200 μm in the dispersive direction which results in a considerable loss of throughput. At higher slit settings, the throughput gets improved significantly though it is at a substantial deterioration of resolution. Theoretically, resolution can be further improved by a factor of 2–4 by masking the outer portions of the grating, since focusing aberrations of the grating limit the resolution rather than the total number of illuminated lines. Horizontally and vertically adjustable apertures are planned to be placed in the entrance arm of the TGM to mask the various regions of the grating. These apertures will also help in reducing the stray light. Furthermore, entrance and exit slits will be continuously adjustable (0–2 mm) in the dispersive direction. In the perpendicular direction also the slits will have adjustable aperture. The effect of the variation of slit widths and the grating masking on the spectral resolution has been systematically investigated and will be reported elsewhere [14].

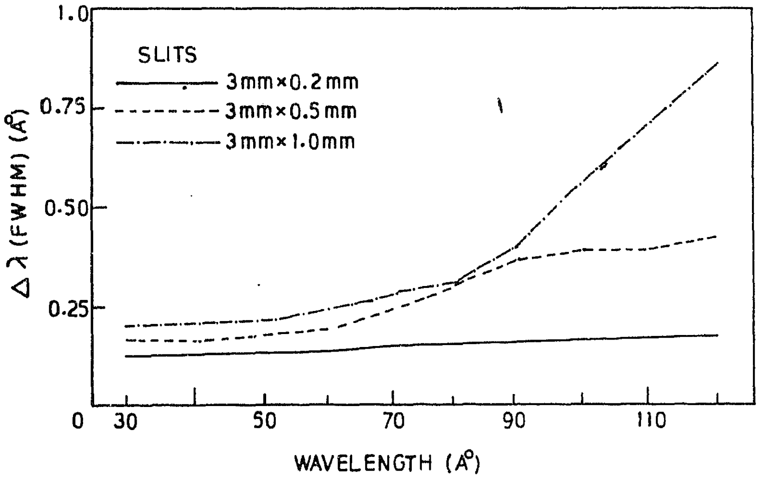

Figure 4. Theoretical resolution curves from ray tracing calculations for different slit setting for 1800 gr/mm grating.

4.3 *Photon flux*

Another parameter of immense interest for experiments using monochromatic light is the maximum photon flux that can be expected on the sample under investigation for a given slit size (or resolution). The flux emitted by the SRS gets attenuated by the beam line because of its nonunity transmission. The transmission is defined as the ratio between the number of rays per unit bandwidth at the image plane and the number of rays per unit bandwidth emitted by the source. It is determined by the pre- and post-focusing mirrors through their reflectivities and dimensions, by the grating through its reflectivity and diffraction efficiency, and by the slit sizes.

Large atomic number elements give substantially higher reflectivities at grazing incidence, nickel being one of the rare exceptions [15]. Platinum, gold or nickel are generally coated on optical elements in the soft X-ray beam lines on SR facilities to get high reflectivity. The reflectivities of these elements are readily calculated using the well documented optical constants data [16, 17]. The reflectivities of these elements at a grazing angle of 4·5° (the grazing angle on toroidal mirrors employed in our beam line) are given in figure 5. This figure shows that gold has higher reflectivity in the 40–300 Å wavelength range, with platinum being marginally worse. Nickel though has a flat response in the wavelength range of our interest, its reflectivity is about 20% lower than that of gold or platinum. We have performed calculations above 300 Å also, and have found that the three elements give almost similar reflectivities in the 300–1000 Å region. Thus, gold is the preferred coating material for the optical elements employed in our beam line.

The grating efficiency is generally measured experimentally as the grating profile parameters required to determine grating efficiency theoretically are not available for the commercially available gratings. However, to get a first order estimate, we have determined the grating efficiency following the procedure outlined by Hellwege [18]. For this, lamellar gratings of groove density (N) of 200, 600 and 1800 grs/mm were taken. To obtain a high diffraction efficiency over a large wavelength range, the grating depth (h) to grating spacing ($1/N$) ratio should have a proper value. After

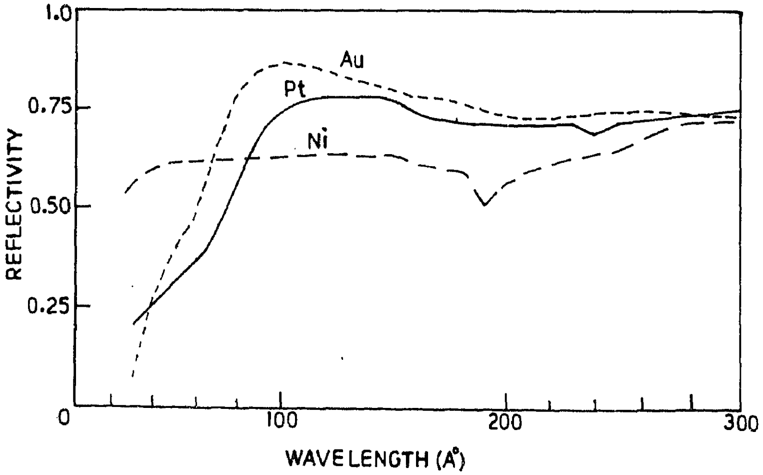

Figure 5. Reflectivities of gold, nickel and platinum at a grazing angle of 4·5°.

performing calculations for grating efficiency for various values of this ratio, we found out that a value of 0·015 gives the best diffraction efficiency in the wavelength range of our interest for three gratings. On the basis of these calculations a maximum of ~ 40% grating efficiency is achieved in the middle of the wavelength range of each grating. Furthermore, to get an accurate idea of the grating throughput, the reflectivity of the grating substrate should also be considered. We have determined the grating reflectivity in a manner similar to the one used for calculating the reflectivities of mirrors with the only difference that proper account has been taken of the varying angle of incidence over the wavelength scan.

The geometrical throughput and the wavelength bandpass of the beam line has been determined through ray tracing. The geometrical throughput of the beam line is wavelength dependent and it reduces as the wavelength increases because of two counts. One, the vertical divergence of the SRS increases with increasing wavelength and second, the grating incidence angle varies with the wavelength scan. Both these factors result in a net loss of geometrical throughput. Our ray tracing results show that the geometrical throughput reduces from 63% to 25% for $N = 1800$ gr/mm grating, from 54% to 16% for $N = 600$ gr/mm grating, and from 41% to 13% for $N = 200$ gr/mm grating as the wavelength is scanned from the minimum to the maximum of each grating's useful wavelength range. The number of rays generated for ray tracing varied from 20,000 to 200,000 depending upon the wavelength, so as to get good statistics at the image plane in each case. To determine the bandpass, intensity profile of the image in the vertical direction was determined through ray tracing at various wavelengths and the FWHM of this profile was taken to represent the band pass.

Following the above considerations, the photon flux has been determined. Figure 6 shows the absolute number of monochromatic photons which will be available at sample with Indus-1 operating at 450 MeV and 100 mA. The calculations have been performed for 10 mrad horizontal acceptance, for slit settings of 3 mm × 0·5 mm, and for gold coating on optical elements. The figure shows that for these typical

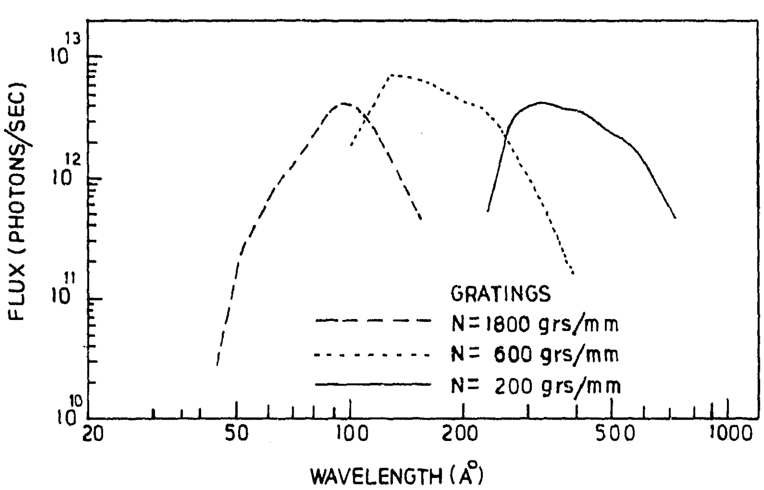

Figure 6. Photon flux as a function of wavelength for all the three diffraction gratings. Calculations have been performed for 10 mrad horizontal acceptance, 100 mA Indus-1 current and slit settings of 3 mm × 0·5 mm.

parameters, photon flux of well over 10^{12} photons/sec can be obtained. At the critical wavelength (61 Å) of Indus-1, one obtains a photon flux of $\sim 8 \times 10^{11}$ photons/sec. Comparing this figure with the number of photons emitted by Indus-1 into the beam line results in a beam line transmission of $\sim 3\%$.

4.4 *Surface figure errors*

The imperfections in the optical elements can severely limit their performance. The acceptable tolerances in the surface figure errors should be evaluated and the mirrors and gratings employed in the beam line should conform to these limits. The main performance limiting imperfections of an optical element are the tangential slope error and the surface micro roughness. While the former deteriorates the resolution, the latter leads to diffused scattering thereby limiting the specular reflectivity. According to Beckmann and Spizzichino [19] the attenuation of the reflectivity due to rms surface roughness of σ is given by an expression of the Debye-Waller form:

$$R = R_0 \exp - \left(\frac{4\pi\sigma \sin\phi}{\lambda} \right)^2 \tag{9}$$

where R_0 is the smooth-surface reflectivity, R is the attenuated reflectivity and ϕ is the glancing angle. This expression indicates that the surface micro roughness greatly limits the performance of optical elements at short wavelengths and large grazing angles. It is readily seen from this expression that a rms surface roughness of 30 Å on the toroidal mirrors (glancing angle $= 4{\cdot}5°$) employed in our beam line will lead to about 40% attenuation in reflectivity.

The effect of tangential slope error has been evaluated in the following way. The presence of a tangential slope error of δ in the given surface element of the mirror can be represented as a deviation of the normal to the surface from the optimal direction by δ, which results in the reflected ray rotating by 2δ. This leads to an increase in the spot size by $2\delta r_2$ where r_2 is the image distance from the mirror. This increase in the spot size should not be greater than the aberration limited spot created by the mirror. To determine the aberrated focal spots created by the toroidal pre and post-mirrors, these mirrors were ray traced individually. The mirrors were assumed to be illuminated by a point source and the acceptance of the pre-mirror was taken to be 10 mrad × 5·9 mrad and that of post-mirror to be 20 mrad × 11·7 mrad. All other parameters were taken to be the same as employed in our beam line (figure 1). The results are shown in figures 7a and 7b for pre-mirror and post-mirror, respectively. From the spot diagrams given in these figures it can be seen that the tangential aberrations are respectively of the order of 550 μm and 100 μm for the two mirrors. These values put a limit of 25 arcsec and 6 arcsec on the tangential slope error tolerable for the pre- and post-mirrors employed in our beam line, respectively.

Extending these arguments for the case of a grating results in a wavelength dependent contribution to the resolution from the tangential slope error, as has been derived by Williams [20]. However, Padmore [21] has shown that a tangential slope error of δ in the grating will lead to a wavelength independent contribution to the resolution given by

$$\Delta\lambda = \frac{2\delta \cos\theta}{Nk}. \tag{10}$$

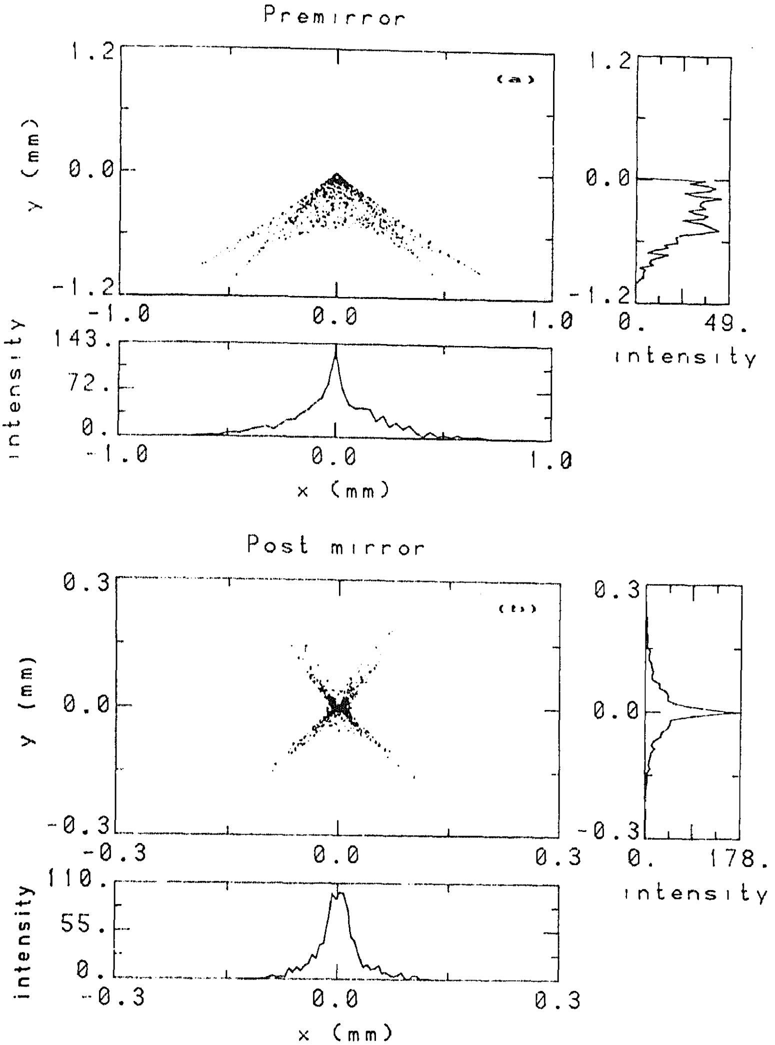

Figure 7. Aberrated focal spots generated by (**a**) pre-mirror and (**b**) post-mirror, when ray traced for point source.

An estimate of the tolerable tangential slope error in the grating can be found out from this equation. It is seen that for a resolving power ($\lambda/\Delta\lambda$) of ~ 1000, the grating should not have a tangential slope error greater than 5 arcsec. The sagittal slope error is seen to have no significant effect on the image quality.

4.5 *Misalignment effects*

The beam line performance can get severely degraded due to incorrect adjustment of optical elements and/or variation in their shapes. To check the sensitivity to misalignment and shape variations of the optical elements ray tracing calculations have been performed at values other than the optimum. The details of these calculations will be reported elsewhere [22]. As a representative case, figure 8 shows the effect

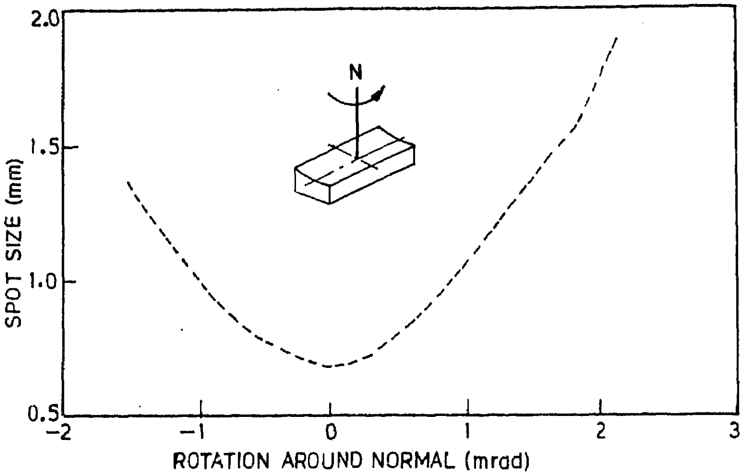

Figure 8. Variation of the spot size created by a single mirror as a function of the adjustment of the mirror in its own plane. The ray tracing calculations have been performed for 61 Å.

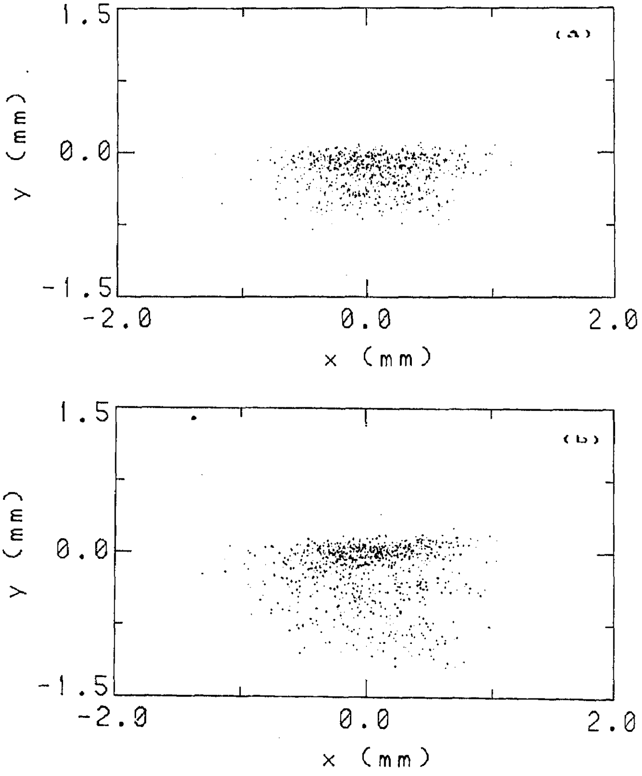

Figure 9. Spot diagram at the focus point of a toroidal mirror: (**a**) Ray traced for a dipole SRS source, (**b**) same as (a) but with a misorientation of the mirror in its plane of 1 mrad.

on spot size at the focusing plane of a single toroidal mirror due to the rotation of the mirror in its plane around an axis perpendicular to its surface. Figure 9a shows the spot diagram obtained from a single mirror with no misalignment errors and figure 9b shows the change in the extent and shape of the focal spot when the mirror is rotated by only 1 mrad. Thus it is evident from figures 8 and 9 that the spot size gets drastically enlarged with only small rotations. Therefore, very fine mechanical controls are being provided [23] in the beam line hardware to permit *in situ* adjustment of the optical elements for optimizing the beam line performance.

5. Summary

Detailed optical design of a TGM-based beam line for Indus-1 storage ring has been described. This beam line will operate in the 40 to 1000 Å wavelength range. The performance of the beam line has been evaluated using ray tracing calculations. The ray tracing results show that a design comprising of proper choice of toroidal pre and post-focusing mirrors and a set of toroidal gratings give optimum performance in terms of resolution and photon flux. Since the beam line has a pre-focusing mirror and an entrance slit, the resolution of the instrument is essentially independent of the source size and the position of the stored electron beam in the SRS. Our calculations show that the beam line will produce a final spot size at the sample of about 2 mm × 0·5 mm and a photon flux of $> 10^{12}$ photons/sec (at 100 mA Indus-1 current).

The effect of various parameters, which may limit the performance of the beam line, has been studied in detail. These include the effect of varying the slit sizes, masking the gratings, presence of surface imperfections and misalignment errors. Also, the resolution of the instrument is wavelength dependent and we have observed that it deteriorates considerably at the high wavelength end of each gratings scan limit. Therefore, to further improve the resolution characteristics, we plan to use, instead of straight groove, constant spacing gratings, the aberration corrected holographically ruled gratings which are commercially available.

This paper gives a reasonable idea about the characteristics of the SR beam, in respect of resolution, photon flux and spot size, which will be available for the users from this beam line and will aid the experimenters to plan their experiments on this beam line.

Acknowledgements

We wish to express our sincere thanks to Dr F Schafers of BESSY for kindly providing the source code of RAY program which enabled us to implement this code on our computer system. We also thank Dr G S Lodha for many useful discussions.

References

[1] R V Nandedkar, K J S Sawhney and G S Lodha, *CAT Report CAT/I/92–01* (1992)
[2] K J S Sawhney and R V Nandedkar, *Proc. Int. Conf. on synchrotron radiation sources*, Indore, India 3–6 Feb 1992, edited by S S Ramamurthi, G Singh and D Angal, 355
[3] G Singh, G K Sahoo, B Singh, D Angal and S S Ramamurthi, *Proc. Internat. Conf. on Synchrotron Radiation Application*, May 9–12, 1989, Hefei, China, edited by H Winick *et al* (Press of Univ. of Science and Technology, Hefei, 1990) 122

[4] R V Nandedkar, *Proc. Int. Conf. on synchrotron radiation sources*, Indore, India 3–6 Feb 1992, edited by S S Ramamurthi, G Singh and D Angal, 279
[5] G Singh, *Private communication* (1990)
[6] D Korsch, *Reflective optics* (Academic Press, Boston, 1991)
[7] K J S Sawhney and R V Nandedkar, *Pramana – J. Phys.* **39**, 177 (1992)
[8] R L Johnson, *Nucl. Instrum. Methods* **A246**, 303 (1986)
[9] H A Padmore, *Rev. Sci. Instrum.* **60**, 1608 (1989)
[10] J B West and H A Padmore, in *Handbook of synchrotron radiation* edited by G V Marr (North-Holland, Amsterdam, 1987) Vol 2, p. 21
[11] W R Mckinney and M R Howells, *Nucl. Instrum. Methods* **172**, 149 (1980)
[12] Personal communication with mirror fabricators
[13] J Feldhaus and F Schafers, *Technical Report BESSY TB-xx-87* (1987)
[14] K J S Sawhney and R V Nandedkar, *to be published* (1994)
[15] V Saile, *SPIE Proceedings* **733**, 126 (1986)
[16] B L Henke, J C Davis, E M Gullikson and R C C Perera, *Lawrence Berkeley Lab. Report LBL-26259* (1988)
[17] E D Palik, *Handbook of optical constants of solids* (Academic Press, Orlando, 1985)
[18] K H Hellwege, *Z. Phys.* **106**, 588 (1937)
[19] P Beckmann and A Spizzichino, *The scattering of electromagnetic waves from rough surfaces* (Pergaman, New York, 1963)
[20] G P Williams, *Nucl. Instrum. Methods* **A246**, 294 (1986)
[21] H A Padmore, *SPIE Proceedings* **733**, 253 (1986)
[22] K J S Sawhney and R V Nandedkar, *to be published* (1994)
[23] A Verma, K J S Sawhney and R V Nandedkar, *Proc. DAE Solid State Phys. Symp.* **C35**, 89 (1992)

PRAMANA
— journal of
physics

© Printed in India

Vol. 42, No. 1,
January 1994
pp. 65–77

Ray tracing studies of a complete plane grating monochromator beam line

V S EDLABADKAR* and ASHOK PIMPALE
Inter University Consortium for DAE Facilities, University Campus, Indore 452 001, India
*G. N. College of Science, Ballarpur 442 701, India

MS received 24 July 1993; revised 11 October 1993

Abstract. Optical design of a plane grating monochromator beam line for X-ray spectroscopic studies to be installed on INDUS-1 is studied using ray tracing technique. The main components of the beam line are pre- and post-elliptical mirrors and the plane mirror-grating dispersing system. The ideal positions of the optical components are decided by using our analytical formulation of the Riemer's kinetic principle for reflecting synchrotron radiation onto the same spot of the dispersing grating. The program is developed indigenously and can be used on a PC. The tangent error and microroughness of the mirrors is explicitly accounted for in the program. The wavelength dependent absorption of radiation at the different reflecting surfaces is also included for calculations of the optical throughput. The dependence of the final image line shape and resolution on various beam line parameters is calculated. The results are useful in deciding the tolerances of the various beam line components and their positions.

Keywords. Synchrotron radiation; ray tracing; image characteristics.

PACS No. 42·15

1. Introduction

Indus-1 is the first synchrotron radiation source in India coming up at the Centre for Advanced Technology, Indore with a 450 MeV electron storage ring. From the bending magnets, useful flux is available in the wavelength range of 15 Å to 1600 Å and beyond, the critical wavelength being 61 Å [1]. One of the beamlines will be used for X-ray spectroscopic studies employing radiation in a wide energy range of 20 to 1200 eV. The beamline is meant for high resolution studies with a good spectral purity i.e. minimal harmonic content. Plane grating monochromator (PGM) of SX-700 type seems to be the best choice for achieving this goal [2–4].

In PGM, the plane grating is preceded by a plane mirror in such a way that the incident radiation falls on the same spot on the grating for different angles of incidence in the grazing incidence geometry. For a fixed exit slit this plane mirror is given linear and rotary motions so that the distance of the virtual source to the focussing post-mirror remains unchanged. Riemer and Torge [5] have demonstrated that these linear and rotary motions can be replaced by a rotation of the plane mirror around a suitable axis of rotation outside the plane of the mirror so that the radiation can be reflected to the same point on the grating, for three angular positions $(\alpha_1, \alpha_2, \alpha_3)$ of the plane mirror. The analytical formulation of this problem was given by Pimpale *et al* [6] which gives an exact algebraic theory of the relationship between the geometric parameters of the plane mirror-grating system and the $\alpha_1, \alpha_2, \alpha_3$ angles.

One can choose the angles based on the wavelength region of interest and reflectivity of the mirror surfaces.

A modification of SX-700 beam line has been discussed by Nyholm *et al* [7] in which an elliptical pre-mirror and an elliptical post-mirror decouple the horizontal and vertical focussing. The line image then has a minimal distortion. We have developed the optical design of a PGM using the analytical formulation of Pimpale *et al* [6] for the plane mirror-grating system and elliptical pre- and post-mirrors. Wavelength scanning is achieved by changing the glancing angle of incidence on the grating and the exit angle consistent with the focussing condition $\sin\beta/\sin\alpha \equiv C =$ constant. The detailed design is reported in [8].

In the present work, ray tracing program is developed indigenously for this beam line. Absorption of intensity at every reflection as a function of incidence angle and the refractive index $(n+ik)$ of the mirror surface is considered for every ray using Fresnel's formulae [9]. The wavelength dependence of the refractive index is explicitly taken into consideration. The tangent error in the reflecting surface is included. Absorption of intensity due to the micro-roughness of the surface is also accounted for [10]. The line shape is obtained from the spot diagram by taking its X and Y profiles. In PGM, different wavelengths are scanned by changing the angle of incidence on the plane mirror. Keeping a particular θ fixed corresponding to a wavelength one can look for the different wavelengths that are admitted at the exit slit, thereby yielding information about the wavelength mixing i.e. resolution governed by geometric factors. Such a resolution is calculated by considering intensities of different wavelengths around the central wavelength for a given slit width. Finally, the program is used for finding the tolerances in positioning of different optical elements.

Programs such as the RAY (Bessy, Berlin) and SHADOW (Wisconsin) are widely used for beam line ray tracing purposes. These programs run on main frame machines and the source code is usually not available. We, therefore, thought it worthwhile to develop indigenously ray tracing program for this work. Our program being based on analytical considerations is simple enough to be implemented on a PC. Further we have also included the features of intensity calculations as well as wavelength resolution as mentioned above. To the best of our knowledge, we are reporting here for the first time the final image shape for a complete PGM beamline comprising the pre- and post-elliptical mirrors and the SX-700 type plane mirror-grating combination with the inclusion of (i) specular reflectivity, (ii) micro-roughness scatter and (iii) wavelength broadening due to geometrical factors.

We have carried out explicit calculations by taking all the reflecting surfaces to be gold. The value of the constant C employed in these calculations is 2·25; this value gives a good grating efficiency and is commonly employed in the design of various SX 700 beam lines. All the calculations correspond to a grating with 1200 grooves per mm and for a good image 10,000 rays are traced.

A preliminary report of part of this work is given in [11].

2. The beam line simulation

The schematic diagram of the PGM beam line under consideration is shown in figure 1. EM1 and EM2 are elliptical pre- and post-mirrors, PM is the plane mirror and G is the plane grating. The extended source S is simulated by taking random points within the source size at S. A ray is simulated by joining a random point at S with another random point on EM1. For ray tracing purposes, the general pre-

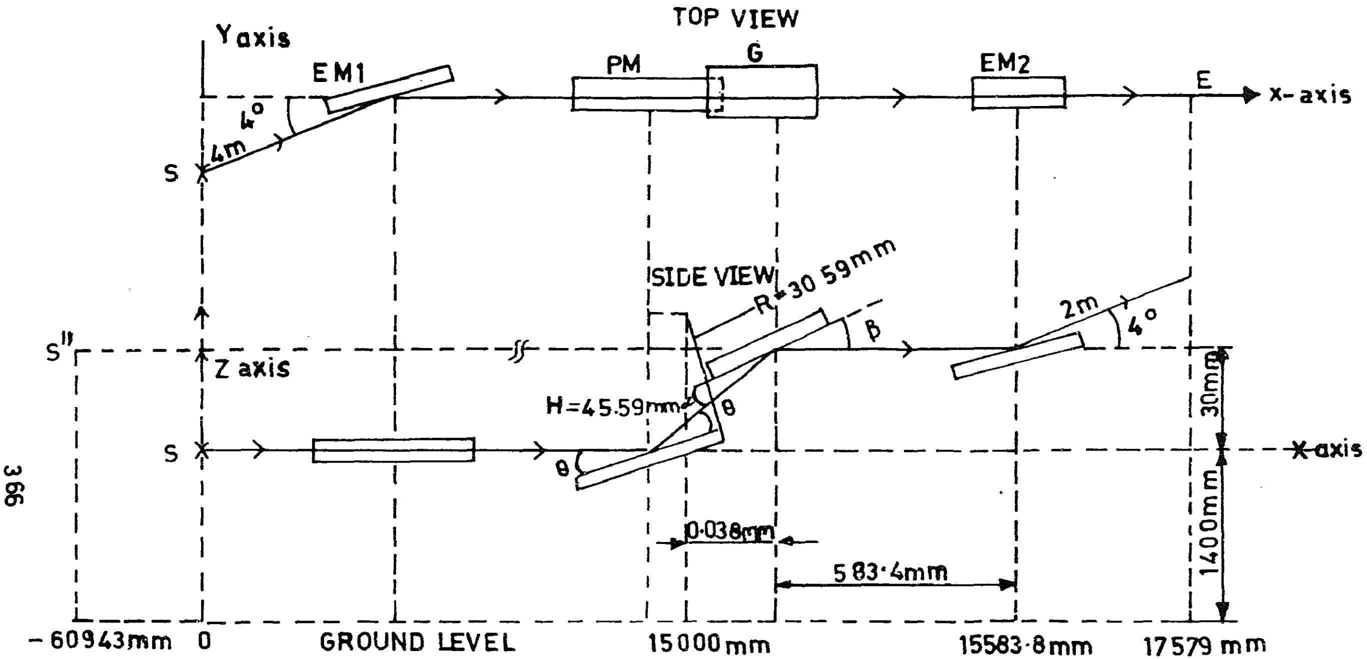

Figure 1. Schematic arrangement of complete beam line with dimensions. S is the exit slit on the storage ring, EM1 and EM2 are the pre- and post-elliptical mirrors, PM and G stand for the plane mirror and plane grating of the dispersing system.

scription of Spencer and Murty [12] is followed. Only the first order diffraction is considered. The mathematical formulation is described in Appendix.

Starting with initial intensity I (say 1) for any ray, the intensity is modified at every reflection as per Fresnel formulae. The electron storage ring orbit is in the horizontal plane and most of the incident radiation is polarized with electric field vector in the same plane. Thus for EM1 the electric vector is in the plane of incidence whereas for PM and EM2 it is orthogonal to the plane of incidence. The change of polarization due to the vertical divergence of the incident beam is ignored for simplicity. The wavelength dependent values of the refractive index $(n+ik)$ for the reflecting surface gold are from Lynch and Hunter [13].

Micro-roughness effect on the reflected intensity I' is calculated using the Johnson formula,

$$I' = I\exp(-(4\pi\sigma\cos\theta/\lambda)^2).$$

Here θ is the angle of incidence, I is the incident intensity at wavelength λ and σ is the RMS micro-roughness.

The tangent error in the surface is simulated by deviating the normal to the plane randomly through an angle within the bounds of maximum tangent error. From the spot diagram of the final image the X- and Y-profiles of the image are obtained.

For wavelength resolution at the central wavelength corresponding to angle of incidence θ on PM, we proceed as follows. Consider a wavelength step of width $\delta\lambda = 0{\cdot}001\lambda$ and calculate explicitly the image at the final image-plane for different wavelengths

$$\lambda_n = \lambda + n\delta\lambda,$$

where n takes a number of integral positive and negative values keeping the same θ. On specifying the upper and lower edges of the exit slit, the program computes intensities of each λ_n within the exit slit. A plot of this intensity as a function of wavelength gives the line shape and resolution.

Positioning of any element can be varied from its ideal value (see figure 1). The spread of the image in horizontal and vertical positions in the final image plane is obtained. From this the tolerances in positioning of the different optical elements in the beamline are found.

3. Results

The ideal positions of the optical components and other parameters used for ray tracing are collected together in table 1. The spot diagram and the vertical and horizontal line shapes for a typical wavelength $\lambda = 48{\cdot}8$ Å are shown in figure 2. The vertical line width is 53 μ and the horizontal line width is 1 mm for a source size of 0·25 mm × 0·25 mm using parameters from table 1.

The reduction in intensity in the final image as a result of (i) absorption during specular reflection and (ii) absorption due to micro-roughness is computed for different wavelengths λ in the region 12·2 Å to 110 Å. Table 2 shows the final % intensity transmitted. For all these calculations, the angle of incidence is always greater than the critical angle for total reflection. We have taken the dimensions of the optical components to be sufficiently large so that no ray is lost during reflection or diffraction. In this situation, the tangent error within the commercially available accuracy of

Table 1. PGM beam line parameters (see figure 1).

Source size	0·25 × 0·25 mm^2
Number of rays traced	10,000
Source to EM1 distance	4,000 mm
Length of EM1	114·6 mm
Breadth of EM1	1 mm
Major axis, *a*1	8,794·2 mm
Minor axis, *b*1	257·2 mm
Tan-error of EM1	1 arc sec
RMS roughness of EM1	2 nm
Glancing angle of incidence of EM1	2 deg.
Lengh of plane mirror	100 mm
Breadth of plane mirror	40 mm
Tan-error of plane mirror	1 arc sec
RMS roughness of plane mirror	1 nm
Length of grating	186 mm
Breadth of grating	40 mm
X-position of centre of rotation, L	15,000 mm
Z-position of centre of rotation, H	45·6 mm
Radius of arm of rotation, R	30·6 mm
Number of grating elements	1,200 grooves/mm
X-position of EM2	15,583·8 mm
Z-position of EM2	30 mm
Major axis of EM2, *a*2	39,263·2 mm
Minor axis of EM2, *b*2	431·5 mm
Length of EM2	350 mm
Breadth of EM2	40 mm
Tan-error of EM2	1 arc sec
RMS roughness of EM2	2 nm
X-position of image plane	17,578·6 mm

Table 2. The percentage intensity, I at the image plane for different wavelengths with and without the inclusion of roughness, σ (2 nm RMS) and the imaginary part of the dielectric constant k of the reflecting coating gold ($I = 100$ when $k = 0, \sigma = 0$).

Wavelength Å	I for $k \neq 0, \sigma = 0$	I for $k = 0, \sigma \neq 0$	I for $k \neq 0, \sigma \neq 0$
12·2	12·5	29·2	3·65
23·9	11·5	69·3	7·97
31·2	12·0	79·1	9·49
48·8	27·6	89·13	24·60
70·3	49·2	93·49	46·00
95·8	76·3	95·94	73·20
110·0	76·8	96·61	74·20

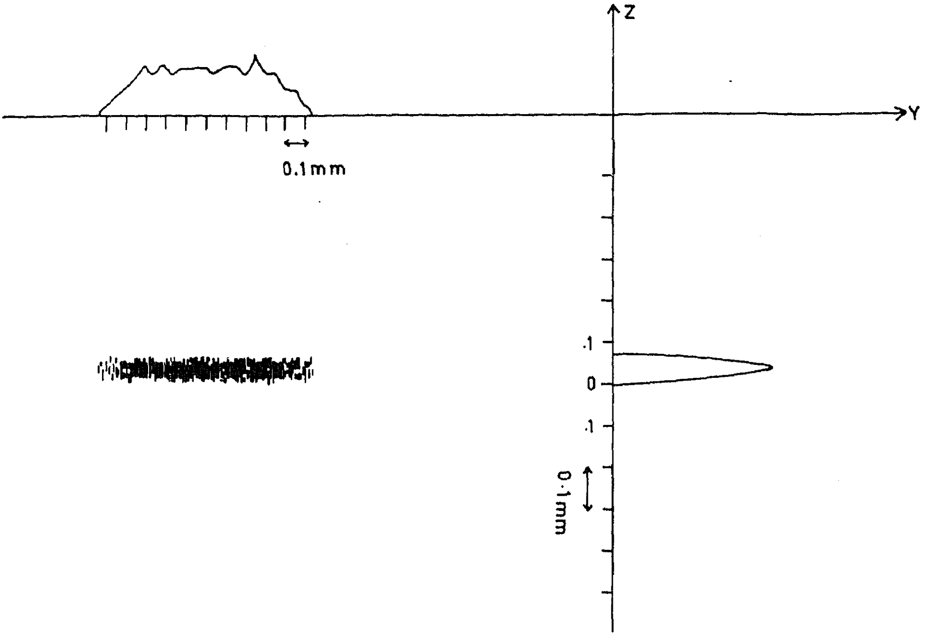

Figure 2. Spot diagram and vertical (Z) and horizontal (X) line profiles for $\lambda = 48{\cdot}8$ A for ideal positions of the optical components.

Table 3. Change in the final image position for changes in the ideal positions of various optical components for three typical photon energies.

Change δd (mm)	Change in image position (mm)		
	1015·7 eV	253·8 (eV)	112·7 (eV)
(a) Changing the source – EM1 distance, $d = 4000$ mm			
1	0·06	0·08	0·08
−1	−0·074	−0·07	−0·05
(b) Changing the x-position of the centre of rotation, $X = 15{,}000$ mm			
150	−0·001	−0·001	−0·001
−150	0·001	0·001	0·001
(c) Changing the Z-position of the centre of rotation, $Z = 45{\cdot}59$ mm			
−0·1	0·016	0·014	0·015
0·1	−0·015	−0·015	−0·015
(d) Changing the radius of the arm of rotation, $R = 30{\cdot}59$ mm			
−0·1	−0·013	−0·012	−0·012
0·1	0·013	0·012	0·011
(e) Changing the X-position of EM2, $X = 15{,}583{\cdot}8$ mm			
−0·5	0·034	0·034	0·034
0·5	−0·035	−0·034	−0·034
(f) Changing the Z-position of EM2, $Z = 30$ mm			
−0·01	−0·011	−0·011	−0·010
0·01	0·009	0·010	0·010

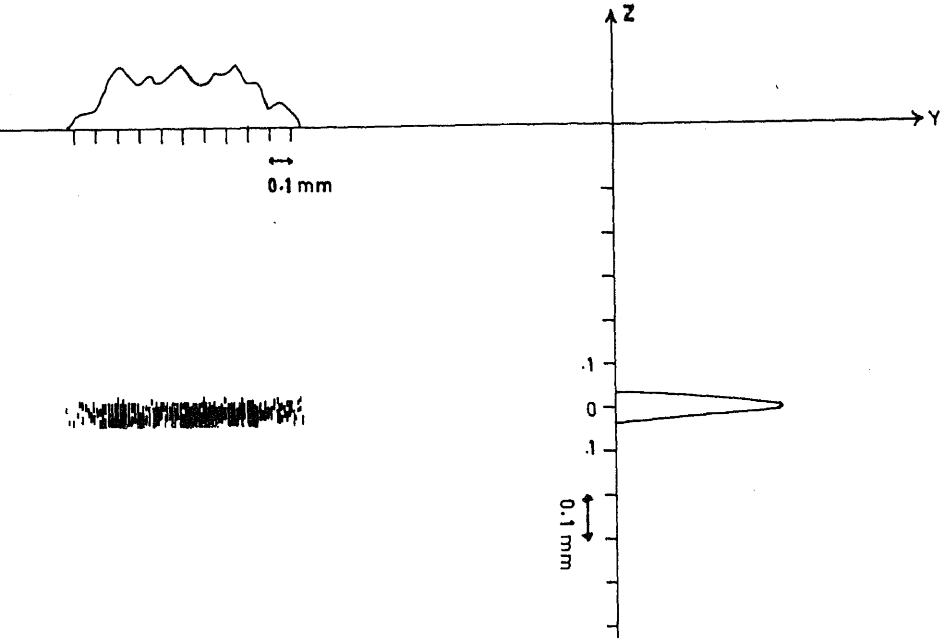

Figure 3. Spot diagram and vertical (Z) and horizontal (X) line profiles for $\lambda = 48{\cdot}8$ A when the X-position of EM2 is varied by $\delta X = -0{\cdot}5$ mm.

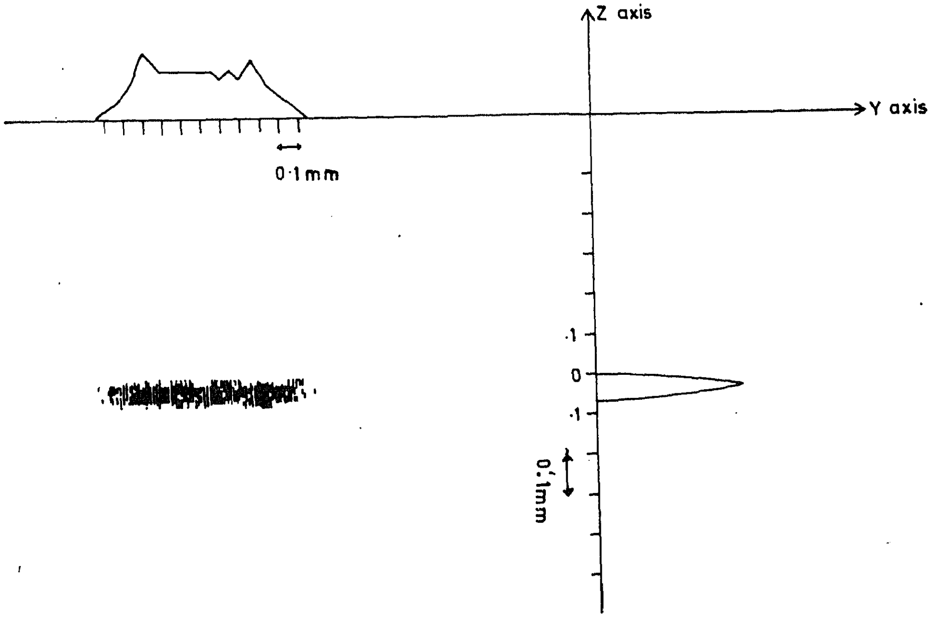

Figure 4. Spot diagram and vertical (Z) and horizontal (X) line profiles for $\lambda = 48{\cdot}8$ A when the X-position of EM2 is varied by $\delta X = 0{\cdot}5$ mm.

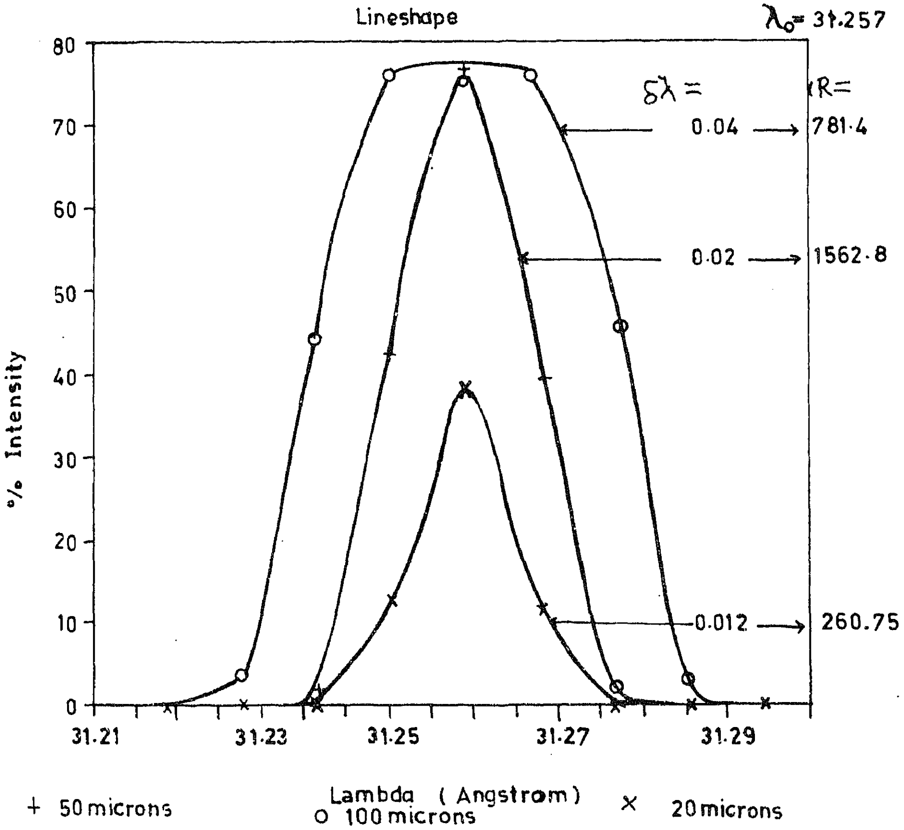

Figure 5. Lineshape for wavelength $\lambda = 31{\cdot}26$ A for three slit widths 20, 50 and 100 microns respectively.

1 arc sec does not affect the intensity. Also, the diffraction grating is assumed to have 100% reflection in the first order. Table 2 clearly shows that both the micro-roughness and absorption effects reduce intensity substantially for lower wavelengths, the latter being dominant for the assumed value of σ.

Table 3 shows the effects of variations in (i) the position of pre-mirror with respect to source S, (ii) the position of mirror-grating system along X-direction, (iii) the position of mirror-grating system along Z-direction, (iv) radius of rotation arm, (v) position of post-mirror along X-direction and (vi) position of post-mirror along Z-direction.

The variations listed are for significant changes in the mean image position and/or the image spread. To exemplify the image shift with variation in a parameter, figures 3 and 4 show the spot diagrams and the horizontal and vertical profiles of the images for typical cases: For $\lambda = 48{\cdot}85$ Å the x-position of EM2 is varied with $\delta x = -0{\cdot}5$ mm (figure 3) and $\delta x = +0{\cdot}5$ mm (figure 4). Figures 5 and 6 show the intensities of wavelengths 95·73 Å and 31·21 Å respectively for three slit-widths 20, 50 and 100 microns. The corresponding line shapes can be discerned from the figures. The resolution $\mathrm{RS} = \lambda/\Delta\lambda$, where $\Delta\lambda$ is half the line width, is given in table 4.

Corresponding to λ the angle θ may be in error, say $\delta\theta$, which causes the shift in the image of λ in vertical direction. Figure 7 gives the vertical position (mean z) of

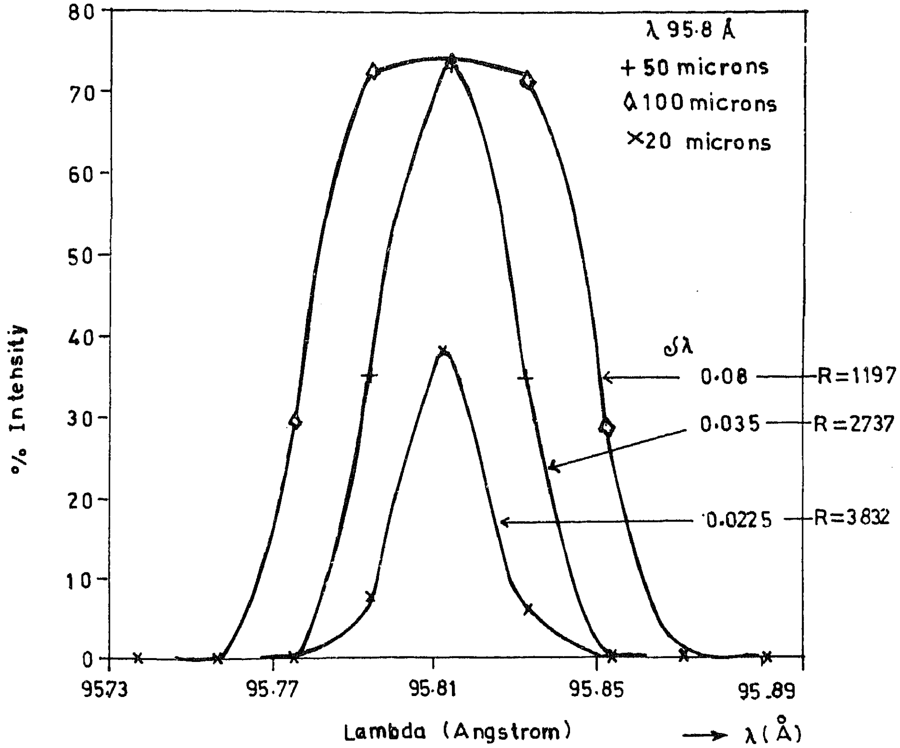

Figure 6. Lineshape for wavelength $\lambda = 95{\cdot}8$ A for three slit widths 20, 50 and 100 microns respectively.

Table 4. Resolution RS ($= \lambda/\Delta\lambda$) as calculated from figures 5 and 6 for different exit slit widths.

Wavelength Å	Slit width (microns) 20	 50	 100
31·257	2604·7	1562·8	781·4
95·8	3832	2737	1197

the image as a function of error $\delta\theta$ for three different wavelengths. We note that the shift is linear with respect to $\delta\theta$ and it is not very sensitive to wavelength.

The size of the image varies with the position of the image plane along the X-direction. Sample chamber may be placed beyond the exit slit to illuminate, say 1 mm × 1 mm sample uniformly. Figure 8 gives the image spread (vertical width) for different image plane positions to facilitate the positioning of the sample.

4. Discussion and concluding remarks

We note that the beam line throughout decreases substantially with increasing energy—hardly 4% of the incident intensity is available at an energy of 1016 eV when

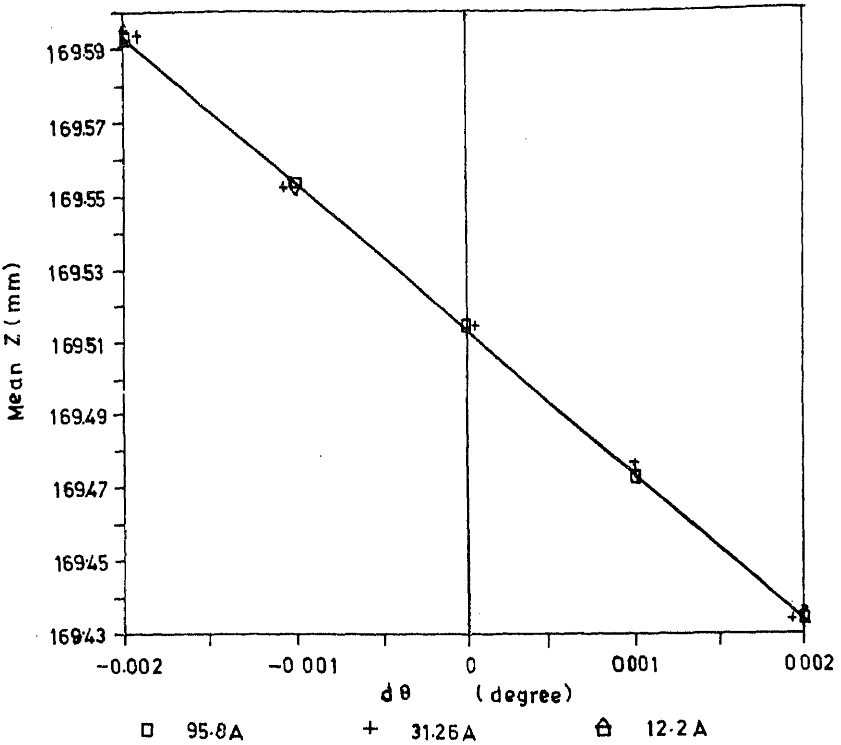

Figure 7. Position (mean Z) of the image as a function of the variation $\delta\theta$ around θ for three different wavelengths.

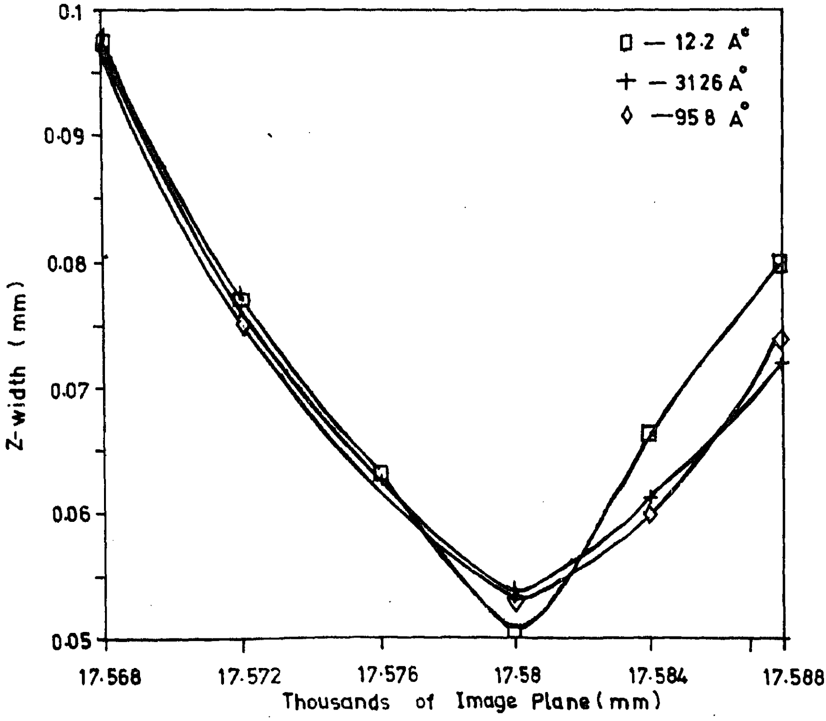

Figure 8. Vertical spread of the image for different image plane positions.

both microroughness and absorption at the reflecting surfaces is taken into account. Within the commercially available smoothness of 2 nm, the absorption effect is the more dominant of the two. Another feature of interest that comes out is the wavelength independence of the positioning accuracy of various optical components. Thus one can do alignment with an optical wavelength, say by employing a laser radiation. The final alignment for XUV radiation from the synchrotron would then require only very minor changes. From amongst the various optical components, an inaccuracy in the x-position of the PM-grating system is not very serious; e.g. a shift of 150 mm changes the image position by only 0·001 mm. On the other hand a change of 0·1 mm in the z-position of the same shifts the image by 0·01 mm.

Acknowledgement

Thanks are due to V G Bhide, R Srinivasan, V B Sapre, S M Chaudhari, S K Deshpande, R V Nandedkar, K J S Sawhney, N C Das and R Nyholm for help during the progress of this work.

Appendix

Schematics of ray tracing formulation

Ray tracing essentially involves determination of the path of light rays through an optical system comprising of various optical elements such as mirrors, lenses, apertures, gratings. This is done with the help of elementary geometry by successive application of the law of reflection (or refraction or diffraction) as the ray encounters the optical element. The incident ray is defined in a coordinate system S_0 [for extended sources we take the central point of the source as origin] as starting from a source point $\mathbf{x}_0$ moving in a direction specified by direction cosines $\mathbf{l}_0$. In our case the source is confined to YOZ plane of S_0. The point $\mathbf{x}_0$ is then generated by two random numbers within the domain specified by the source dimensions, the X-coordinate being identically zero. The central ray is prescribed by the position of the centre of the optical element; in the present case this means

$$\mathbf{l}_0(\text{central ray}) = (1, 0, 0). \tag{A1}$$

Two other random numbers are used to generate an arbitrary direction within pre-assigned horizontal and vertical divergences around the central ray. An arbitrary point $\mathbf{x}$ on the ray is then given by the parametric equations:

$$\mathbf{x} = \mathbf{x}_0 + \mathbf{l}_0 t. \tag{A2}$$

The first optical element, EM1 in the present case, is described by an equation, say,

$$f(\mathbf{x}_1) = 0 \tag{A3}$$

in a coordinate system S_1 with origin at the centre of the optical element and suitably chosen coordinate axes. We transfer the coordinate system from S_0 to S_1 using the transformation equations:

$$\mathbf{x}_1 = \mathbf{a} + T\mathbf{x}_0, \tag{A4}$$

where **a** are the coordinates of the origin of S_0 with respect to S_1 and T is the transformation matrix given by

$$T_{ij} = e_i^1 \cdot e_j^0. \tag{A5}$$

e_i^1, e_i^0 $i = x, y, z$ are the unit vectors along the coordinate axes of S_1 and S_0. The direction cosines are transformed as

$$\mathbf{l}_1 = T\mathbf{l}_0. \tag{A6}$$

The next step is to calculate the point $\mathbf{x}_M$ at which the ray intersects the optical element. For simple systems, this is readily obtained by solving

$$f(\mathbf{x}_1 + \mathbf{l}_1 t) = 0 \tag{A7}$$

for $t = t_M$. Then

$$\mathbf{x}_M = \mathbf{x}_1 + \mathbf{l}_1 t_M. \tag{A8}$$

For simple surfaces, like aperture planes, equation (A7) can be analytically solved. However, for curved surfaces one has to employ an iterative procedure. Using the subscript j to denote the iteration number, we write

$$t_{j+1} = t_j - f(\mathbf{x}_j)/f'(\mathbf{x}_j), \tag{A9}$$

where

$$\mathbf{x}_j = \mathbf{x}_1 + \mathbf{l}_1 t_j \tag{A10}$$

and

$$f'(\mathbf{x}_j) = \mathrm{d}f/\mathrm{d}t|_{t=tj}. \tag{A11}$$

The most useful starting point for the iteration scheme is provided by the point of intersection of the incident ray and the tangent plane at the centre of the optical surface.

The next step is to describe the interaction at the optical surface. In our case we have either reflection or diffraction by a reflection grating. For both we need the unit normal $\mathbf{N}(\mathbf{x}_M)$ to the optical surface at the point of intersection $\mathbf{x}_M$. This is given by

$$\mathbf{N}(\mathbf{x}_M) = \pm \operatorname{grad} f/|\operatorname{grad} f| \Big| (\mathbf{x} = \mathbf{x}_M). \tag{A12}$$

The sign of the normal is so chosen that it points outwards from the reflecting/diffracting surface. For plane mirror and plane grating $\mathbf{N}$ is independent of $\mathbf{x}_M$. For reflection the outgoing rays have direction cosines $\mathbf{l}_r$ given by

$$\mathbf{l}_r = \mathbf{l}_1 + 2|\mathbf{l}_1 \cdot \mathbf{N}|\mathbf{N} \tag{A13}$$

and for diffraction these are given by

$$\mathbf{l}_d = \mathbf{l}_1 - \Lambda \mathbf{u} + \gamma \mathbf{N}, \tag{A14}$$

where

$$\Lambda = n\lambda/d(\mathbf{x}_M) \tag{A15}$$

$$\gamma = -\mathbf{l}_1 \cdot \mathbf{N} + [(\mathbf{l}_1 \cdot \mathbf{N})^2 - \Lambda^2 + 2\Lambda \mathbf{l}_1 \cdot \mathbf{u}]^{1/2} \tag{A16}$$

with **u** the unit normal to the rulings of the diffraction grating, $d(\mathbf{X}_M)$ the grating spacing in the neighbourhood of $\mathbf{x}_M$, n the order of diffraction and λ the radiation wavelength. Equation (A14) simplifies for the case of plane grating since d and $\mathbf{N}$ then become constants. Thus the outcoming ray from the optical element is described parametrically by

$$\mathbf{x} = \mathbf{x}_M + \mathbf{l}_{r(d)}\mathbf{t}. \tag{A17}$$

The above procedure is repeated to trace the rays further until one encounters the final image plane. The points of intersection of the outgoing rays with the image are plotted to get the spot diagram.

References

[1] S S Ramamurthi, *Proc. Int. Conf. Synchrotron Radiation Sources*, Feb. 1992, Centre for Advanced Technology, Indore, p 9

[2] H Petersen, *Opt. Commun.* **40**, 402 (1982)

[3] H Petersen, *Soft X-ray optics and technology*, SPIE **733**, 262 (1986)

[4] M Domke, T Mandel, A Puschmann, C Xue, D A Shirley, G Kaindl, H Petersen and P Kuske, *Rev. Sci. Instrum.* **63**, 80 (1992)

[5] F Reimer and R Torge, *Nucl. Instrum. Methods.* **208** 313 (1983)

[6] A V Pimpale, S K Deshpande and V G Bhide, *Appl. Opt.* **30**, 1591 (1991)

[7] R Nyholm, S Svensson and J Nordgren, *Nucl. Instrum. Methods* **A246**, 267 (1986)

[8] A Pimpale, C Mande, B D Padalia, A S Nigavekar, V B Sapre, R Shankar and V G Bhide, *Beam line for photo-absorption studies using synchrotron radiation source INDUS 1*, Inter-University Consortium for DAE Facilities, Indore, Report (unpublished) June 1990

[9] M Born and E Wolf, *Principles of Optics* (*6th Ed.*) (Oxford, Pergamon Press, 1980)

[10] R L Johnson in *Handbook on synchrotron radiation* edited by E Koch (Amsterdam, North Holland, 1983), Vol. **1A** p. 180

[11] A V Pimpale, S K Deshpande, V S Edlabadkar, V B Sapre and V G Bhide, *Proc. Int. Conf. Synchrotron Radiation Sources, Feb 1991*, Centre for Advanced Technology, Indore, p. 364 (1992)

[12] G H Spencer and M V R K Murty, *J. Opt. Soc. Am.* **52**, 672 (1962)

[13] D W Lynch and W R Hunter in *Handbook of Optical Constants of Solids* edited by E D Palik (Orlando, Academic Press, 1985) p. 275

[redacted]

PRAMANA
— journal of
physics

© Printed in India

Vol. 42, No. 1,
January 1994
pp. 79–84

Photoionization processes in F aggregate centres of LiF crystal

S V GODBOLE and A G PAGE
Radiochemistry Division, Bhabha Atomic Research Centre, Bombay 400085, India

MS received 12 July 1993; revised 20 November 1993

Abstract. Extensive studies have been carried out on the optical conversion of F and F-aggregate colour centres produced in lithium fluoride single crystal on gamma irradiation. Using 308 nm XeCl laser it has been shown that significantly large population build-up of F_3^+ centre and reduction in the population of undesirable F_2 centres can be achieved in gamma irradiated crystal at room temperature due to multistep photoionization processes. These and other investigations have provided a scheme for possible laser action based on F_3^+ colour centres in LiF crystal at room temperature.

Keywords. Photoionization; lithium fluoride; F aggregate centres; XeCl laser; colour centre laser.

PACS Nos 42·55; 81·40; 78·50

1. Introduction

Various types of colour centres such as F and F-aggregate centres are produced in alkali halides on gamma irradiation with large doses at room temperature; however, amongst them the population of F-aggregate centres is quite low [1]. Optical and thermal bleaching behaviour of F centres in various alkali halides has been well investigated [2–4] from dosimetric point of view. With the advent of colour centre lasers based on different types of F-aggregate centres in alkali halides, it has become important to explore all possible means of creating sufficiently large population of the lasing colour centre at an amenable temperature. Extensive reviews on colour centre lasers are available [5, 6] and these deal mainly with the studies on lasers based on $F_A/F_2^+/F_2^-$ colour centres.

A lasing system based on F_3^+ centre, though feasible, has not been studied in detail. Recent reports refer to the feasibility of F_3^+ laser action in LiF single crystal, wherein, low temperature electron bombardment [7, 8] or optical conversion at 77 K [9] has been used for achieving population build-up of F_3^+ centres. Russian workers [10] have also reported Einstein's spectral coefficients for the F_3^+ centre with reference to laser action. In the present work, significantly large build-up of F_3^+ centres has been achieved in optical LiF single crystals at room temperature itself, using a XeCl excimer laser. The work carried out here also includes detailed studies on the thermal stabilities of F-aggregate centres and the mechanism of optical conversion processes.

2. Experimental

Optical quality single crystals of LiF were grown in vacuum (10^{-5} torr) by Stober's method [11] using indigenously developed facilities [12]. During the crystal growth, a cooling rate of 4°C/h was maintained up to 50°C below the melting point and thereafter the rate was stepped up to 20°C/h in stages.

Colour centres were produced in the LiF crystals by irradiation at room temperature using a ^{60}Co gamma source (0·4 M rad/h). These were identified by their well reported spectral characteristics [13–16]. Optical absorption spectra were recorded on a Beckman Du-7 spectrophotometer, while excitation and luminescence spectra were recorded on a Hitachi F-3010 spectrofluorimeter. The optical conversion of colour centres both at 300 K and 77 K was studied using a 308 nm XeCl excimer laser (10 mJ pulse energy, 50 Hz). Thermal stabilities of colour centres were investigated by successively heating the same crystal for 15 min at different temperatures up to 300°C in steps of 25°C. The changes brought about in the population of different colour centres separately by laser irradiation and due to heat treatment were identified from the spectral studies. Using the data obtained on thermal stabilities of different colour centres, specific centres were annihilated by heat treatment and the effects of subsequent laser irradiation were studied in detail.

3. Results and discussion

3.1 *Laser induced conversion of colour centres*

Optical absorption spectra were recorded for the same gamma irradiated crystal at room temperature (a) prior to laser exposure, (b) immediately after laser exposure and (c) 24 h after laser exposure (figure 1). Identical spectra were obtained for the crystals on exposure to laser irradiation at 77 K. As seen from the figure, prior to laser exposure the crystal showed absorption bands with peak positions at 250, 310, 380

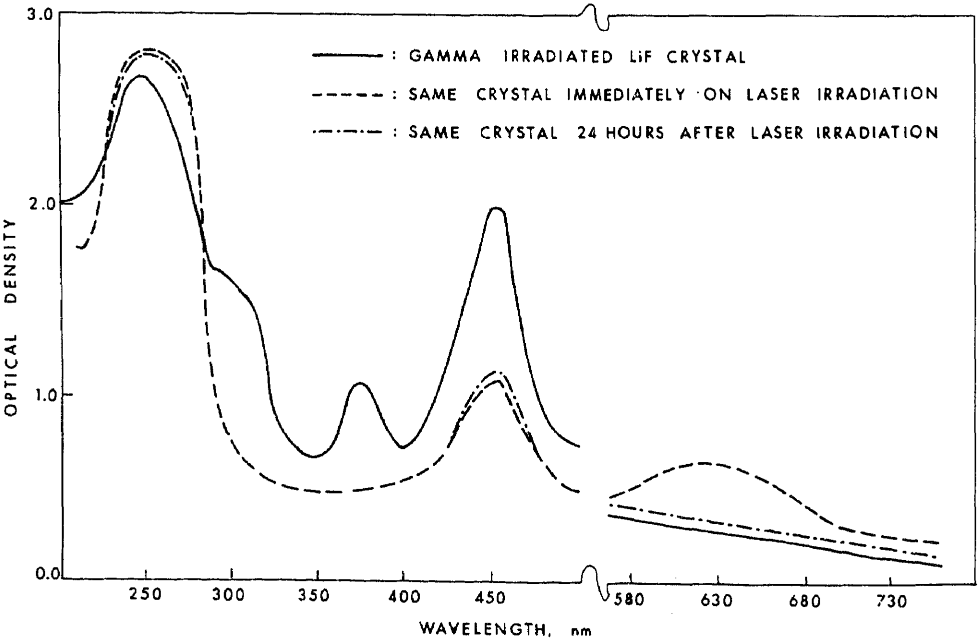

Figure 1. Optical absorption spectra for gamma irradiated LiF crystal at room temperature (a) prior to laser exposure (b) immediately after laser exposure and (c) 24 hours after laser exposure.

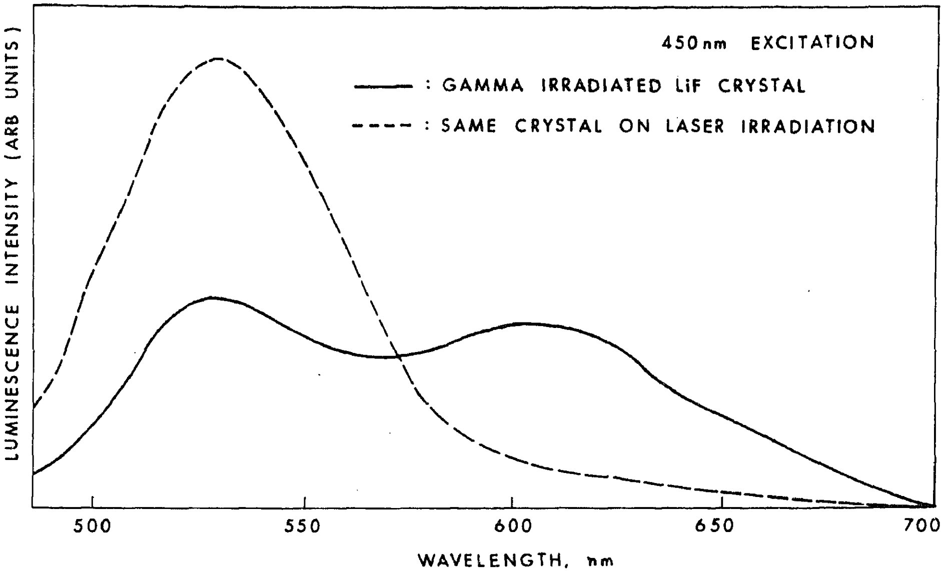

Figure 2. Luminescence spectra with 450 nm excitation for gamma irradiated LiF crystal (a) prior to laser exposure and (b) immediately after laser exposure.

and 450 nm. Of these, a peak at 250 nm corresponding to F centre showed significant increase in intensity on laser exposure at both the temperatures. The peaks at 310 and 380 nm corresponding to F_3 centres, on laser exposure, showed drastic reduction in intensity at both the temperatures. The peak around 450 nm was a composite one corresponding to F_2 and F_3^+ colour centres and also showed significant reduction on laser exposure at two temperatures. An additional peak at 630 nm, which is known to correspond to F_2^+ centre was observed only on laser exposure implying its formation due to optical conversion. On storage the peak at 630 nm was not observable while the peak around 450 nm showed some rise in intensity over the one observed immediately on laser exposure.

The luminescence spectra recorded with 450 nm excitation for the gamma irradiated crystal before and after laser exposure at 300 K is shown in figure 2. As seen from this figure, luminescence intensity around 620 nm corresponding to F_2 centres showed significant reduction, while, luminescence intensity at 530 nm corresponding to F_3^+ centres showed a four-fold increase on laser exposure. On storage of the laser irradiated crystal for 24 h, there was no significant change in the luminescence spectrum in comparison to the one recorded immediately after laser irradiation.

These observations have revealed that on 308 nm laser exposure at 300 K (i) F, F_2^+ and F_3^+ colour centre populations increase and (ii) F_2 and F_3 colour centre populations decrease. On storage of laser irradiated crystal, F_2^+ population decreases significantly leading to further rise in F_3^+ population.

In contrast to 337 nm N_2 laser irradiation reported for the optical conversion [9], the present work is based on the use of 308 nm radiation from XeCl laser. The excitation spectrum recorded at room temperature for the gamma irradiated crystal by monitoring F_3 emission has shown that 308 nm excitation would correspond to resonant absorption for F_3 centres, while, 337 nm would not be so. This would, in turn, reflect in the higher efficiency of the conversion process of F_3 centres with 308 nm laser irradiation.

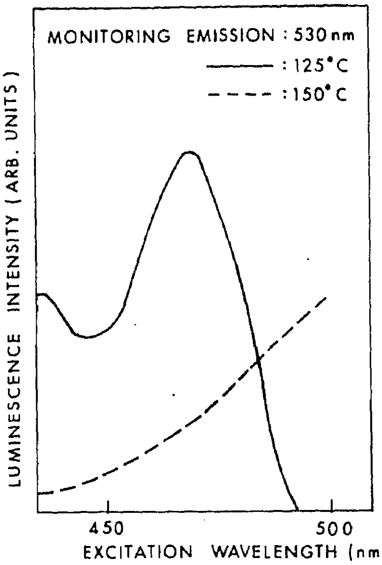

Figure 3. Excitation spectra for F_3^+ centers in gamma irradiated LiF crystal before and after annihilation.

3.2 *Thermal stability of F-aggregate centres in LiF crystal*

Studies carried out on thermal stability of different colour centres have revealed that F_2, F_3 and F_3^+ centres are stable up to 200°C, 250°C and 125°C respectively. A typical excitation spectrum for F_3^+ centres revealing this aspect is shown in figure 3. The feasibility of room temperature operation of F_3^+ centre based laser is evident from the thermal stability of these centres up to 125°C.

3.3 *Mechanism for laser induced conversion of F-aggregate centres*

As seen from the above discussion, laser induced conversion of F-aggregate centres is an involved process with number of changes occurring simultaneously. Additional investigations were carried out to ascertain the pathways for the conversion process. Lithium fluoride crystals of identical dimensions were gamma irradiated at room temperature and by annealing these crystals one at each of the following temperatures viz. 100, 150, 225 and 275°C, for 15 min, different colour centres viz. F_2^+, $F_3^+ + F_2^+$, $F_2 + F_3^+ + F_2^+$ and $F_3 + F_2 + F_3^+ + F_2^+$ were thermally destroyed respectively. Using these crystals laser induced changes were followed by recording absorption and luminescence spectra before and after laser irradiation. The results of these investigations are tabulated below.

Annealing temperature, °C	Colour centers destroyed	Colour centers present	Laser induced change
100	F_2^+	F, F_2, F_3, F_3^+	Increase in F, F_3^+ Decrease in F_2, F_3 Generation of F_2^+
150	F_3^+, F_2^+	F, F_2, F_3	Increase in F Decrease in F_2, F_3 Generation of F_2^+, F_3^+
225	F_2, F_2^+, F_3^+	F, F_3	Increase in F Decrease in F_3 Generation of F_3^+
275	F_2, F_3, F_3^+, F_2^+	F	No change

These observations reveal that (i) F_2^+ centres are formed only when F_2 centres are present in the gamma irradiated crystal prior to laser irradiation and (ii) similarly F_3^+ centres are formed by laser irradiation in gamma irradiated crystal only if F_3 centres are present. Thus the optical conversion process is one of the photoionization, wherein,

$$F_3 \xrightarrow{\text{308 nm laser irradiation}} F_3^+ + e^-$$

and

$$F_2 \xrightarrow{\text{308 nm laser irradiation}} F_2^+ + e^-$$

Free electrons released in these processes are captured at anionic vacancy sites in the crystal leading to formation of additional F centres.

Such a photoionization process for the formation of F_2^+ centres is well reported for alkali halide crystals using two-step photoionization process [5]; however, the process is usually carried out at 77 K due to instability of F_2^+ at room temperature. Similarly the photoionization process for F_3 centres has also been reported to occur only at 77 K using 337 nm N_2 laser excitation [9], while the present studies show that using 308 nm XeCl laser two-step photoionization process can be carried out at room temperature thereby increasing the feasibility of F_3^+ based lasers.

4. Conclusion

Present work conclusively shows that (i) Population build-up of F_3^+ in gamma irradiated lithium fluoride crystal can be achieved at room temperature using 308 nm XeCl excimer laser by photoionization process, (ii) F_2 centre population, detrimental to F_3^+ laser action, due to its overlapping absorption band, can be reduced simultaneously by 308 nm laser photoionization and (iii) F_3^+ laser action is feasible at room temperature as these centres are thermally stable up to 125°C.

References

[1] J H Schulman and W D Compton, *Colour centers in solids* (Macmillan, New York, 1962) Chap. I and III

[2] F Segastibelza and J L Alvarez Rivas, *J. Phys.* **C14**, 1873 (1981)

[3] S W S Mckeever, *Radi. Prot. Dos.* **8**, 3 (1984)
[4] V Ausin and J L Alvarez Rivas, *J. Phys.* **C5**, 82 (1972)
[5] L F Mollaenauer, *Colour center lasers* in Laser Handbook edited by M L Stitch and M Bass (North Holland Publishers, 1985) Vol. 4
[6] W Gellerman, *J. Phys. Chem. Solids* **52**, 24 9 (1991)
[7] L Zheng, S Guo and L F Wan, *Appl. Phys. Lett.* **48**, 381 (1986)
[8] H E Gu, L Qi and L F Wan, *Opt. Commun.* **67**, 237 (1988)
[9] H E Gu, L Qi, L F Wan and H S Guo, *Opt. Commun.* **70** 141 (1989)
[10] A Y Gorkov and V Cheprunoi, *Opt. Spectrosc.* **67**, 642 (1989)
[11] D T J Hurtle, in *Crystal growth*: *An introduction* edited by P Hartmann (North-Holland Publishers, 1972)
[12] S V Godbole, 1989 Ph D Thesis, Bombay University
[13] J Nahum and D A Wiegand, *Phys. Rev.* **154**, 817 (1967)
[14] J Nahum, *Phys. Rev.* **154**, 814 (1967)
[15] J A Okuda, *J. Phys. Soc. Jpn.* **16**, 814 (1961)
[16] Y Farge, M Toulouse and M Lambart, *J. Phys. Radiation* **24**, 287 (1966)

PRAMANA
— journal of
physics

© Printed in India

Vol. 42, No. 2,
February 1994
pp. 85–88

An identity for R_n embedded into E_{n+1}

GUILLERMO GONZÁLEZ, JOSÉ L LÓPEZ-BONILLA and
MARCO A ROSALES*
Area de Física, División de CBI, UAM-Azcapotzalco, Apdo. postal 16-306, 02200 México D.F., Mexico
*Depto. de Física y Matemáticas, Escuela de Ciencias, Universidad de las Américas Puebla, Apdo. Postal 100, Sta. Catarina Mártir, 72820 Puebla, Mexico

MS received 15 November 1993

Abstract. An identity is obtained for a Riemannian n-space (R_n) locally and isometrically embedded into a pseudo-Euclidean $(n+1)$-space (E_{n+1}), relating the corresponding second fundamental form with the intrinsic geometry of R_n. For $n = 4$ such an identity reduces to a previous result by Goenner.

Keywords. Riemannian spaces embedding; local and isometric embedding.

PACS Nos 04·20; 04·90

1. Introduction

We will say that R_n is locally and isometrically embedded into E_{n+1} if and only if there exists the second fundamental form tensor $b_{ac} = b_{ca}$ that satisfies the equations [1]

$$R_{ijkc} = \varepsilon(b_{ik}b_{jc} - b_{ic}b_{jk}) \qquad \text{Gauss} \tag{1a}$$

and

$$b_{ij;k} = b_{ik;j} \qquad \text{Codazzi} \tag{1b}$$

where R_{ajqc} is the curvature tensor for R_n, $\varepsilon = \pm 1$ is the indicator for the normal to this n-space and; c denotes the covariant derivative.

In a usual embedding problem what is known is the R_n intrinsic geometry built from the metric tensor $g_{ab} = g_{ba}$, and the aim is to find out if the tensor b_{ac} satisfying (1a) and (1b) exists. For example, if $n = 4$ and the space-time has a vanishing Ricci tensor, then we know [1–3] that this b_{ac} does not exist and, hence, it may be concluded that no empty R_4 accepts embedding into E_5. Nevertheless, there are other metrics for which such tensor does exist [1, 4–7], and it is in these cases where a relation or identity to explicitly build the b_{ac} is needed.

In § 2 we will show that, using the Gauss equation (1a) only, it is possible to obtain and identity connecting b_{ac} with the intrinsic geometry of R_n, and we will indicate the conditions under which such an identity allows the explicit derivation of the second fundamental form. When $n = 4$ this identity reduces to a relation previously published by Goenner [8] as will be proved in § 3.

2. $\mathbf{b}_{ac}$ and the intrinsic geometry of $\mathbf{R}_n$

The Ricci tensor:

$$R_{jk} \equiv R^i_{jki} = \varepsilon(b^i{}_k b_{ji} - bb_{jk}), \quad b \equiv b^r{}_r \tag{2a}$$

and the scalar curvature:

$$R \equiv R^j{}_j = \varepsilon(b^{ac}b_{ac} - b^2) \tag{2b}$$

are obtained with the help of the Gauss equation. Then, (1a), (2a) and (2b) lead to the identity:

$$pb_{ac} = \frac{R}{2}R_{ac} + \frac{1}{2}R_a{}^r R_{rc} - R_{rc} - R_{arqc}R^{rq} - \frac{1}{4}R_{arqt}R_c{}^{rqt} \tag{3a}$$

that has not been found in the literature thus far. In this equation:

$$p \equiv b^{rq}\left(b^i{}_r b_{iq} - \frac{3}{2}bb_{rq} + \frac{b^2}{2}g_{rq}\right). \tag{3b}$$

But the Einstein tensor is given by:

$$G_{rq} = R_{rq} - \frac{R}{2}g_{rq} \tag{3c}$$

and, hence, (2a), (2b), (3b) and (3c) imply that

$$p = \varepsilon b^{rq}G_{rq} \tag{4a}$$

so that, after multiplying (3a) by εG^{ac} we obtain:

$$p^2 = \varepsilon\left(\frac{1}{2}R_a{}^r R_{rc} - R_{arqc}G^{rq} - \frac{1}{4}R_{arqt}R_c{}^{rqt}\right)G^{ac} \geqslant 0 \tag{4b}$$

which determines the value of ε when $p \neq 0$. From (4b) we learn that p is a function of the intrinsic geometry of R_n only.

Therefore, we can give to the embedding process the following sequence:

1) We have g_{ac} and do not know whether this R_n accepts a local and isometric embedding into E_{n+1}.
2) We compute p through (4b). Then we will have one of the two following cases:
a) If $p \neq 0$ then we determine b_{ac} with the help of (3a). Hence, the R_n does accept embedding into E_{n+1} if and only if *this* b_{ac} fulfils the Codazzi condition, eq. (1b).
b) When $p = 0$ eq. (3a) does not provide any explicit information about b_{ac}. Then, in order to decide if R_n is of class one, and to construct the corresponding second fundamental form, it is necessary to solve (1a) and (1b) directly.

3. The case $n = 4$

For ordinary space-time we can simplify (3a) and (4b) by making the dimension 4 more explicit. Indeed, recalling that the conformal tensor C_{arqt} and the double dual tensor $*R^*_{arqt}$ are related through the expression [9].

$$R_{arqt} = *R*_{arqt} + 2C_{arqt} - \frac{R}{6}(g_{aq}g_{rt} - g_{at}g_{rq}) \tag{5a}$$

this can be introduced into the last term of (3a) to yield

$$pb_{ac} = \frac{1}{4}\left(\frac{K_2}{4} + R^2 - 3R_{qt}R^{qt}\right)g_{ac} - \frac{3}{2}C_{aqtc}R^{qt} + \frac{3}{2}\left(R_{aq} - \frac{R}{6}g_{aq}\right)R^q{}_c \tag{5b}$$

where Lanczos identity [10]

$$*R*^a{}_{cqt}R^{rcqt} = \frac{K}{4}g^{ar}, \quad K_2 \equiv *R*^{ijkr}R_{ijkr} \tag{5c}$$

has been used.

Equation (5b) is valid only for $n = 4$ and it is equivalent to (3.1) of Goenner (1976). Furthermore, (4b) reduces to

$$p^2 = -\frac{3\varepsilon}{2}\left(\frac{R}{24}K_2 + R_{iqtj}G^{ij}G^{qt}\right) \geqslant 0. \tag{5d}$$

As an application of (5b) and (5d) consider Gödel [11] cosmological model (signature + 2):

$$\mathrm{d}s^2 = -(\mathrm{d}x^1)^2 - 2e^{x^4}\mathrm{d}x^1\mathrm{d}x^2 - \frac{1}{2}e^{2x^4}(\mathrm{d}x^2)^2 + (\mathrm{d}x^3)^2 + (\mathrm{d}x^4)^2 \tag{6a}$$

which, together with (5d) imply that $\varepsilon = 1$ and $p = 3\sqrt{2}/4$. Therefore, from (5b) we get $b_{ac} = 0$, except

$$b_{11} = b_{44} = -\frac{\sqrt{2}}{2}, \; b_{12} = -\frac{\sqrt{2}}{2}, \; b_{22} = -\frac{3\sqrt{2}}{4}e^{2x^4} \tag{6b}$$

but this second fundamental form tensor does not satisfy (1b) since, for example, $b_{12;4} \neq b_{14;2}$. Then, due to remark 2 a) at the end of last section, we conclude that Gödel solution does not accept local and isometric embedding into E_5 as was already shown by Szekeres [2] using another technique. It is still ignored if (6a) admits embedding into E_6 (see [6]).

Notice that, when $p = 0$, it is not possible to use (5b) to construct b_{ij} and it is necessary to analyze the Gauss and Codazzi equations directly. An example of such cases can be found in Collinson [5], where Einstein-Maxwell metrics embedded into E_5 are studied.

Acknowledgements

The authors express their gratitude to Dr E Piña-Garza for suggestions that led to identity (3a).

References

[1] D Kramer, H Stephani, M Mac Callum and E Herlt *Exact solutions of Einstein's field equations* (Cambridge: University Press, 1980)
[2] Szekeres, *Nuovo Cimento* **A43**, 1062 (1966)
[3] R Fuentes, J L López-Bonilla, Ovando G and T Matos, *Gen. Relativ. Gravit.* **21**, 777 (1989)
[4] J Rosen, *Rev. Mod. Phys.* **37**, 204 (1965)
[5] C D Collinson, *Commun. Math. Phys.* **8**, 1 (1968a)
[6] C D Collinson, *J. Math. Phys.* **9** 403 (1968b)
[7] A Barnes, *Gen. Relativ. Gravit.* **5**, 147 (1974)
[8] H F Goenner, *Tensor N. S.* **30**, 15 (1976)
[9] C Lanczos, *Rev. Mod. Phys.* **34**, 379 (1962)
[10] C Lanczos, *Ann. Math.* **39**, 842 (1938)
[11] K Gödel, *Rev. Mod. Phys.* **21**, 447 (1949)

PRAMANA
— journal of
physics

© Printed in India

Vol. 42, No. 2,
February 1994
pp. 89–95

The Maxwell tensor for the Liénard–Wiechert field as an exact divergence

JOSÉ L LÓPEZ-BONILLA, JESÚS MORALES* and MARCO A ROSALES[†]
Area de Física, División de C.B.I., Universidad Autónoma Metropolitana-Azcapotzalco, Apdo. Postal 16-306, 02200 México, Mexico
*Instituto Mexicano del Petróleo, Subdirección de Investigación Aplicada. México, D.F.
[†]Depto. de Física y Matemáticas, Escuela de Ciencias, Universidad de las Américas Puebla, Apdo. Postal 100, Sta. Catarina Mártir, 72820 Puebla, Mexico

MS received 16 September 1993; revised 17 November 1993

Abstract. A potential for the bounded part of the Maxwell tensor associated to the Liénard-Wiechert field has been obtained by van Weert. In this paper we explicitly derive the non-local potential for the radiative part of such a tensor.

Keywords. Liénard-Wiechert field; superpotential for the Maxwell tensor; non-local potential for the electromagnetic field.

PACS Nos **03·50; 03·30; 41·10**

1. Introduction

In what follows we will consider the Maxwell field generated by a point charge in Minkowski space. In order to include radiation reaction effects [1–3] on the charge motion it is necessary to compute the electromagnetic energy and momentum fluxes through hypersurfaces (for instance, the Bhabha tube [4, 5]), and it is in these computations where the great usefulness of the superpotential K_{abc} for the Maxwell tensor T_{ab} associated to the Liénard–Wiechert (LW) field [2] is evident.

The concept of superpotential is due to von Freud [6, 7] since he obtained a superpotential for the Einstein energy-momentum canonical pseudotensor [7], greatly used to study the gravitational energy in curved spaces, keeping the idea that if a physical quantity has a vanishing divergence there must exist a potential that generates that quantity (see reference [8]).

In §2 we present a brief summary of the LW field properties, emphasizing the corresponding tensor T_{ab} which admits the splitting [9]

$$T_{ab} = T_{Bab} + T_{Rab} \tag{1a}$$

where T_{Bab} and T_{Rab} are the bounded and radiative parts. These are dynamically independent because they separately satisfy the continuity equation [9] (sum is implied by repeated indices)

$$T^{b}_{Ba}{}_{,b} = 0 \tag{1b}$$

$$T^{b}_{Ra}{}_{,b} = 0 \tag{1c}$$

and, so, it is evident that $T^{b}_{a}{}_{,b} = 0$.

Then, following von Freud [6] it is natural to look for a superpotential $K_{{}_B abc} = -K_{{}_B bac}$ that generates the bounded part

$$T_{{}_B ab} = K^{j}_{{}_B ab,j} \quad \text{with} \quad j = \frac{\partial}{\partial x^j} \tag{2a}$$

from where (1a) follows immediately. Indeed, this was done by van Weert [10] who also showed that (2a) simplifies the computation of the $T_{{}_B ab}$ fluxes through a 3-surface around the charge. Van Weert did not discover the physical meaning of his superpotential, but it was done later [11] where it was found that $K_{{}_B abc}$ is the intrinsic angular momentum density [12] of the electromagnetic field produced by the point charge.

The next step is to construct a superpotential $K_{{}_R abc} = -K_{{}_R bac}$ for the radiative part

$$T_{{}_R ab} = K^{j}_{{}_R ab,j} \tag{2b}$$

and this will be done, using Minkowskian coordinates, in § 3. The $K_{{}_R abc}$ thus obtained results to be non-local since it contains integrals over the past history of the charge, consistently with Rohrlich [13] statement: "... the process of measuring the radiation rate is intrinsically non-local".

Therefore, (1a), (2a) and (2b) imply

$$T_{bc} = (K^{j}_{{}_B bc} + K^{j}_{{}_R bc})_{,j} \tag{2c}$$

and the Maxwell tensor is an exact divergence.

2. The Liénard–Wiechert field

In special relativity a "particle" means a time-like world-line [14] (see figure 1) whose tangent vector is the 4-velocity

$$v^r = \frac{\mathrm{d}q^r}{\mathrm{d}\tau}, \quad v^r v_r = -1 \tag{3}$$

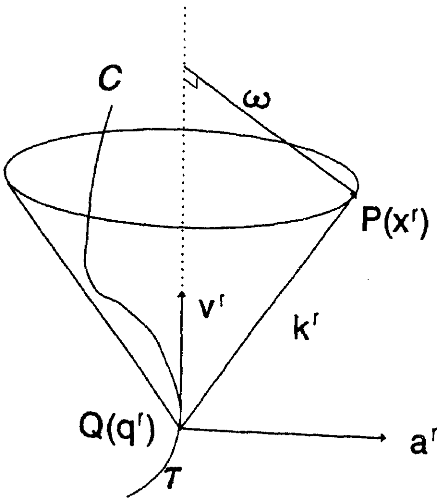

Figure 1. Kinematics of the world line.

where the proper time τ is defined by

$$d\tau^2 = -g_{ab}dx^a dx^b = -dx^2 - dy^2 - dz^2 + dt^2 \tag{4}$$

i.e., the metric is Diag$(1, 1, 1, -1)$ and c (speed of light in vacuum) $= 1$. Then, the 4-acceleration can be written as:

$$a^r = \frac{dv^r}{d\tau}, \quad a^r v_r = 0 \tag{5a}$$

which implies that a^r is space-like:

$$a^2 \equiv a^r a_r \geqslant 0. \tag{5b}$$

If from an event P with coordinates $(x^r) = (x, y, z, t)$ not on the path C we draw the past sheet of its null cone it will intersect C in the point $Q(q^r)$ called the "retarded event associated to P" and

$$q^r = q^r(x^b) \tag{6}$$

because if P is given the retarded point on C is automatically determined as the intersection of C and the null cone with vertex at P. The null vector

$$K^c = x^c - q^c, \quad K^c K_c = 0. \tag{7}$$

For any P we may construct (see figure 1) the retarded distance ω from P to C as proposed by Bhabha [4, 5, 11] and whose expression is:

$$\omega = -K^c v_c \geqslant 0 \tag{8a}$$

Recalling [14] that a null vector cannot be orthogonal to a time-like vector, we obtain from (8a) that:

$$\omega = 0 \text{ if and only if } K^r = 0. \tag{8b}$$

In performing the calculations we will need to know how the physical quantities on C change, but it suffices to have the law of change for τ, since q^r, v^r, a^r, etc depend on that parameter:

$$\tau_{,j} = -\omega^{-1} K_j. \tag{9}$$

All the events P on a given cone are associated with a unique value of τ. This is why the light-cone is the surface $\tau =$ constant and, hence, $\tau_{,j}$ is the vector normal to the cone.

In view of eq. (9) it is simple to obtain the useful relations:

$$\begin{gathered} q^r{}_{,j} = -\omega^{-1} v^r K_j \qquad v^r{}_{,j} = -\omega^{-1} a^r K_j \\ K^r{}_{,j} = \delta^r_j + \omega^{-1} v^r K_j, \quad \omega_{,j} = -v_j + BK_j \end{gathered} \tag{10a}$$

where Plebañski's B invariant [15]:

$$B = \omega^{-1}(1 - W) \text{ with } W = -K^r a_r \tag{10b}$$

appears. Then

$$B_{,c} = \omega^{-1}[U_c - (B^2 + \omega^{-1} K^r S_r) K_c] \tag{10c}$$

where $S^r \equiv \mathrm{d}a^r/\mathrm{d}\tau$ is the superacceleration [5] and U_c is Synge's vector [5]

$$U_c \equiv Bv_c + a_c. \tag{10d}$$

The retarded 4-potential A^r generated by the point charge is the LW field [2, 14, 15] given by:

$$(A^r) = (\mathbf{A}, \phi) = (q\omega^{-1}v^r), \quad q = \frac{\text{charge}}{4\pi\varepsilon_0} \tag{11}$$

which generates the electric and magnetic fields through the well-known relations

$$\mathbf{E} = -\nabla\phi - \frac{\partial \mathbf{A}}{\partial t}, \quad \mathbf{B} = \nabla \times \mathbf{A}. \tag{12a}$$

Recalling the matrix representation of the Faraday tensor $F_{ab} = -F_{ba}$ [2, 7]

$$[F_{ab}] = \begin{bmatrix} 0 & B_z & -B_y & -E_x \\ -B_z & 0 & B_x & -E_y \\ B_y & -B_x & 0 & -E_z \\ E_x & E_y & E_z & 0 \end{bmatrix} \tag{12b}$$

equations (12a) are equivalent to the tensor expression

$$F_{rc} = A_{c,r} - A_{r,c} \tag{13a}$$

and the Maxwell equations become

$$F^{rc}_{\ \ ,c} = 0, \quad F_{br,c} + F_{rc,b} + F_{cb,r} = 0 \tag{13b}$$

or, alternatively.

$$\nabla\cdot\mathbf{B} = 0, \quad \nabla \times \mathbf{B} = \frac{\partial \mathbf{E}}{\partial t}$$

$$\nabla\cdot\mathbf{E} = 0, \quad \nabla \times \mathbf{E} = -\frac{\partial \mathbf{B}}{\partial t}. \tag{13c}$$

Substitution of (10a) and (11) into (13a) yields the Faraday tensor for the LW field [5]

$$F_{bc} = q\omega^{-2}(U_b K_c - U_c K_b) = q\omega^{-2} U_b \times U_c \tag{14a}$$

where we have used Lowry's notation [16]

$$A_b \times B_j \equiv A_b B_j - A_j B_b \tag{14b}$$

With the help of (9), (10c) and (14c) it is easy to prove that

$$F_{rb} = q\tau_{,r} \times B_{,b} \tag{14c}$$

which was first obtained by Plebański [15].

The null vector K^r given by (7) is an eigenvector of (14a) and (14c), i.e.

$$F_{rb}K^b = q\omega^{-2}K_r. \tag{15}$$

Another vector important in electrodynamics of charged particles is [5]

$$p^c \equiv \omega^{-1} K^c - v^c \tag{16a}$$

which, by virtue of (3), (7) and (8a) satisfies

$$p^c p_c = 1, \; p^c v_c = 0 \tag{16b}$$

implying that p^b is unitary and space-like. Furthermore, with (10a) and (16a) it is simple to obtain that

$$p^r_{,j} = \omega^{-1} \delta^r_j + \omega^{-2} v_j K^r + \omega^{-1}(a^r + \omega^{-1} v^r - \omega^{-1} B K^r) K_j \tag{16c}$$

that, together with (14a), implies

$$F^j_c p^r_{,j} = q\omega^{-4} W v^r K_c \tag{16d}$$

Expressions (15) and (16a) are very valuable in deriving the superpotential $K_{R_{abc}}$ for the radiative part of T_{ab}.

It is useful to have an orthonormal tetrad $e_{(a)c}$, $a = 1, \ldots, 4$ on C, because such a tetrad allows the construction of a basis for any tensor object on C. Here, we will use $e^r_{(4)} = v^r$ and the unitary space-like triad $e_{(\gamma)c}$, $\gamma = 1, 2, 3$ will be a "Fermi triad" [17, 18], that is, that it evolves on C according to the transport law:

$$\frac{\mathrm{d}}{\mathrm{d}\tau} e^c_{(\gamma)} = a_{(\gamma)} v^c, \quad a_{(\gamma)} = a^b e_{(\gamma)b} \tag{17}$$

In this equation $a_{(\sigma)}$ are the projections of the acceleration a^r over the spacial triad $e^r_{(\sigma)}$, recalling that (5a) implied the space-like character of a^r. Similarly, we may project (16a) over this triad

$$p_{(\sigma)} = p^r e_{(\sigma)r} \tag{18a}$$

so that (16d), (17) and (18a) imply the equation

$$F^j_b p_{(\gamma),j} = 0 \tag{18b}$$

which will be of fundamental importance in § 3.

All the information about the electromagnetic field energy and momentum is contained in the Maxwell tensor defined [2, 7, 14] by

$$T_{ab} = T_{ba} \equiv F_{ac} F^c_b - (F_{ij} F^{ij}) g_{ab} \tag{19}$$

and substitution of (14a) into (19) leads to Teitelboim splitting [9] indicated in our equation [1a] such that

$$T_{B^{bc}} = e^2 \omega^{-4} \left[\frac{1}{2} g_{bc} + (K_b a_c + K_c a_b) + \widetilde{B}(K_b v_c + K_c v_b) \right.$$
$$\left. - \omega^{-2}(1 - 2W) K_b K_c \right] \tag{20a}$$

and

$$T_{R^{bc}} = e^2 \omega^{-4} (a^2 - \omega^{-2} W^2) K_b K_c \tag{20b}$$

satisfying (1b) and (1c) away from the world-line.

In reference [10] it is not mentioned how eq. (2a) was solved, but in [19, 20] the Newman–Penrose formalism [21] was used to establish the process by which $K_{B_{abc}}$

was obtained, and it was found that

$$K_{Bbjc} = \frac{q^2}{4}\omega^{-4}[\omega^{-1}(4W-3)(v_b \times K_j)K_c - 4(a_b \times K_j)K_c - g_{ci}K_b + g_{cj}K_b] \tag{21a}$$

leads to (20a) through (2a). In the introduction we have already mentioned that the physical meaning of (21a) was determined in [11]. K_{Babc} is said to be local because it depends only on quantities associated to the two events P and Q shown in figure 1. In § 3 we will see that K_{Rabc} will not possess such a locality because it depends on integrals along the world-line of the charge.

Finally, we will mention an interesting identity, related to (21a) and first found by Rowe [22]

$$K_{Bibr} = \left[\frac{q^2}{4}\omega^{-4}(g_{ri}K_bK^c + \delta^c_b K_r K_i - g_{br}K_iK^c - \delta^c_i K_b K_r)\right]_{,c} \tag{21b}$$

3. The potential for the radiative part

The main goal of our work consists of the construction of a superpotential K_{Rabc} satisfying (2b). In this respect, the splitting of T_{Rab} introduced in [23] where it was proved that (20b) can be written as

$$T_{Rbc} = \bar{T}_{Rbc} + \tilde{T}_{Rbc} \tag{22a}$$

where

$$\bar{T}_{Rbc} = e^2\omega^{-4}(a^2 - 3\omega^{-2}W^2)K_bK_c \tag{22b}$$

$$\tilde{T}_{Rbc} = 2e^2\omega^{-6}W^2K_bK_c \tag{22c}$$

satisfying the conservation laws

$$\bar{T}^{b}_{Rc,b} = 0, \quad \tilde{T}^{b}_{Rc,b} = 0 \tag{22d}$$

The physical meaning of the splitting (22a) is the following: As we enclose C by a Bhabha tube [4, 5] and calculate the electromagnetic energy and momentum fluxes of $\bar{T}_{Rab}$ across this tube, it is found that the fluxes vanish. This means that if the Bhabha surface is used to determine the equation of motion [5] the tensor (22b) will not contribute with any term to such equation. Hence, the fluxes of (22a) across the Bhabha cylinder are due only to (22c).

Therefore, to solve (2b) is equivalent to finding solutions to

$$\bar{T}_{Rbc} = \bar{K}^{j}_{Rbc,j}, \tag{23a}$$

$$\tilde{T}_{Rbc} = \tilde{K}^{j}_{Rbc,j}, \tag{23b}$$

from which (22c) follows immediately. We can apply the method presented in references [19, 20] to (23a) to obtain

$$\bar{K}_{Rbjc} = \frac{q^2}{4}\omega^{-2}[\omega^{-2}W^2(g_{cj}K_b - g_{cb}K_j) + \omega^{-1}(v_b \times K_j)(3\omega^{-2}WK_c - a_c)$$
$$+ (a_b \times K_j)(a_c - 4\omega^{-2}WK_c)] \tag{24a}$$

which is local in the same sense as K_{Babc}.

On the other hand, there is no systematic and direct method to solve (23b). We were guided by the analysis of (9), (13b), (15), (17), (18a) and (18b) to construct the non-local superpotential

$$\tilde{K}_{R^{bjc}} = -2eF_{bj}p_{(\sigma)}p_{(\gamma)}\left[\int_0^\tau a_{(\sigma)}a_{(\gamma)}v_c \mathrm{d}\tau + p_{(\beta)}\int_0^\tau a_{(\sigma)}a_{(\gamma)}e_{(\beta)c}\mathrm{d}\tau\right] \tag{24b}$$

with sums over $\sigma, \beta, \gamma = 1, 2, 3$ are implied. The presence of integrals over the past history of the charge must be noticed. Summarizing, (2b) is solved by

$$K_{R^{bjc}} = \bar{K}_{R^{bjc}} + \tilde{K}_{R^{bjc}} \tag{24c}$$

and (2c) is proved.

Acknowledgements

We express our gratitude to Prof. F Rohrlich, Prof. J Plebañski, Dr R Tabensky, Dr C Teitelboim, Dr D Villarroel and Dr Ch G van Weert for their comments on our potential $K_{R^{abc}}$.

References

[1] P A M Dirac, *Proc. R. Soc. London* **A167**, 148 (1938)
[2] F Rohrlich, *Classical charged particles* (Addison-Wesley, Reading, Mass. 1965)
[3] J L Jiménez, *Ciencia* **40**, 257 (1989)
[4] H B Bhabha, *Proc. R. Soc. London* **A172**, 381 (1939)
[5] J L Synge, *Ann. Mat. Pura Appl.* **83**, 33 (1970)
[6] Ph. von Freud, *Ann. Math.* **40**, 417 (1939)
[7] C W Misner, K S Thorne and J A Wheeler, *Gravitation* (W H Freeman, San Francisco, 1970)
[8] R Illge, *Gen. Relativ. Gravit.* **20**, 551 (1939)
[9] C Teitelboim, *Phys. Rev.* **D1**, 1572 (1970)
[10] Ch G van Weert, *Phys. Rev.* **D9**, 339 (1974)
[11] G Ares de Parga, J L López-Bonilla, G Ovando and T Matos, *Rev. Mex. Fís.* **36**, 194 (1990)
[12] C A López and D Villarroel, *Phys. Rev.* **D11**, 2724 (1975)
[13] F Rohrlich, *Nuovo Cimento.* **21**, 811 (1961)
[14] J L Synge, *Relativity: the special theory* (North-Holland, Amsterdam, 1965)
[15] J Plebañski, *The structure of the field of a point charge.* Internal report, CINVESTAV-IPN, México (1972)
[16] E S Lowry, *Phys. Rev.* **117**, 616 (1960)
[17] E Fermi, *Atti. R. Accad. Lincei Rend.* **31**, 21 (1922)
[18] J L Synge, *Relativity: the general theory* (North-Holland, Amsterdam, 1976)
[19] G Ares de Parga, J L López-Bonilla, G Ovando and T Matos, *Rev. Mex. Fis.* **35**, 393 (1989)
[20] G Ares de Parga, O Chavoya, J L López-Bonilla, E Luna, J Morales, *Rev. Mex Fís.* **36**, 184 (1990)
[21] E T Newman and R Penrose, *J. Math. Phys.* **3**, 566 (1962)
[22] E G P Rowe, *Phys. Rev.* **D18**, 3639 (1978)
[23] J L López-Bonilla, *Acta Mex. Cienc. Technol. IPN* **2**, 23 (1984)

PRAMANA
— journal of
physics

© Printed in India

Vol. 42, No. 2,
February 1994
pp. 97–105

Photon polarisation asymmetries in $(p, p'\gamma)$ experiments

A R USHA DEVI, A SUDHA RAO* and G RAMACHANDRAN
Department of Studies in Physics, University of Mysore, Manasagangotri, Mysore 570006, India
*Department of Physics, Teresian College for Women, Mysore 570011, India

MS received 5 July 1993; revised 21 December 1993

Abstract. The Stokes parameters characterising the polarization of the photon in the γ-decay of $^{12}C^*(1^+)$ are examined in correlation with the scattered proton in $^{12}C(p, p')\,^{12}C^*(1^+)$. This opens up the possibility of efficiently determining empirically the six inelastic scattering amplitudes utilizing only 13 measurements. We identify several alternative sets of such measurements to encourage experimental efforts in this direction.

Keywords. Inelastic scattering; amplitude determination; proton polarization; Stokes parameters; correlation observables.

PACS Nos 25·40; 24·70; 23·20; 13·88; 13·40; 29·27

1. Introduction

It is well-known that electron scattering experiments have made important contributions to the study of the electromagnetic structure of the nuclei. It was expected that the study of scattering of hadrons or of reactions involving hadrons on nuclei at intermediate energies would provide useful and complementary information on the nuclear structure. It was initially believed that the hadron interaction with a nucleon bound in the nucleus is not much different from that with a free nucleon at these energies. Alternatively, it was hoped that any deviations in the hadron-nucleon interaction could also be investigated assuming apriori knowledge of nuclear structure derived from electron scattering and other considerations.

After moderate initial successes with cross-section data, a real challenge was posed to these beliefs by the advent of data on the spin observables. It is interesting to note that a similar development took place at high energies, where spin polarization data spelt disaster to Regge Models. In this context, therefore, much work is being done experimentally to determine not only the differential cross-section, but also all the attendant spin observables on hadron-nucleus scattering—both elastic and inelastic.

Of particular interest are the exclusive inelastic nucleon-nucleus scattering studies leading to well-defined excited states of the target nucleus like $^{12}C(p, p')^{12}C^*(1^+)$ on which several experimental studies have been reported recently. Even if we include data obtained by employing polarized protons and measuring the proton polarization, a complete knowledge of the inelastic scattering amplitudes is not forthcoming empirically since the process involves six non-zero amplitudes which are complex. In view of this, suggestions have been made [1, 2] to supplement these measurements with measurements of correlated $(\mathbf{p}, \mathbf{p}'\gamma)$ observables like polarized proton asymmetry, proton polarization and proton spin transfers apart from the coincidence cross-section. Although the measurements already suggested [2] are comprehensive enough to serve the purpose and although measurements of photon polarizations at these energies are probably difficult, it is at least of theoretical interest to investigate $(p, p'\gamma)$ reactions in a more complete manner including those observables associated with photon polarizations. It is encouraging to note in this context that Fasano *et al*, [3] have recently discussed photon polarization-based observables in meson photoproduction involving photons at energies which are even higher by an order of magnitude. The importance of a photon polarization sensitive measurement in $^{12}\mathrm{C}(\mathrm{p},\mathrm{p}'\gamma)^{12}\mathrm{C}$ reaction for the determination of the real part of the density matrix element ρ_{10} was pointed out by Piekarewicz [4]. A special merit in taking photon polarization based observables into consideration in $^{12}\mathrm{C}(p,p'\gamma)^{12}\mathrm{C}$ is that they facilitate direct determination of the magnitudes of the six independent amplitudes, thus effecting reduction in the associated statistical errors. The relative phases can then be determined with greater ease. Alternatively, the photon polarization based observables may also be utilized to economise the number of observables that need to be measured to effect unambiguous determination of the inelastic amplitudes.

In § 2, six independent amplitudes associated with the inelastic scattering process are defined and the Fano statistical tensors t^k_q characterising the $^{12}\mathrm{C}^*(1^+)$ are given explicitly in terms of these amplitudes. In § 3, we outline the conventions adopted in defining the photon observables and discuss the γ-decay of polarized $^{12}\mathrm{C}^*(1^+)$. We also define in full all the photon-proton correlation observables. In § 4, we describe the inversion problem and show how with a proper choice of observables, one can directly determine the magnitudes as well as effect a reduction in the number of observables.

2. Nuclear polarization in the transverse frame

The six independent amplitudes characterising the inelastic scattering $^{12}\mathrm{C}(p,p')$ $^{12}\mathrm{C}^*(1^+)$ can be defined in several ways such that the requirements of rotation and parity invariance are satisfied. If $\mathbf{P}_i$ and $\mathbf{P}_f$ denote the proton momenta in the centre of mass system, Piekarewicz *et al*, [1] define a Cartesian co-ordinate system through

$$\mathbf{N}=\mathbf{P}_i\times\mathbf{P}_f,\quad \mathbf{K}=\mathbf{P}_i+\mathbf{P}_f,\quad \mathbf{Q}=\mathbf{N}\times\mathbf{K} \tag{2.1}$$

and express the amplitude for the nuclear transition $0^+\to 1^+$ through

$$\begin{aligned}T= {}& A_{NO}(\hat{\Sigma}\cdot\hat{N})+A_{NN}(\hat{\Sigma}\cdot\hat{N})(\boldsymbol{\sigma}\cdot\hat{N})+A_{KK}(\hat{\Sigma}\cdot\hat{K})(\boldsymbol{\sigma}\cdot\hat{K})+A_{KQ}(\hat{\Sigma}\cdot\hat{K})(\boldsymbol{\sigma}\cdot\hat{Q})\\ &+A_{QK}(\hat{\Sigma}\cdot\hat{Q})(\boldsymbol{\sigma}\cdot\hat{K})+A_{QQ}(\hat{\Sigma}\cdot\hat{Q})(\boldsymbol{\sigma}\cdot\hat{Q})\end{aligned} \tag{2.2}$$

where $\hat{\Sigma}_M=|1^+M\rangle\langle 0^+|$ is called the polarization operator of the nucleus and $\boldsymbol{\sigma}$, the Pauli spin matrices. With the Z-axis chosen along $\mathbf{Q}$, X and Y respectively along $\mathbf{N}$ and $\mathbf{K}$, the T-matrix is given explicitly by,

$$T^P=\begin{vmatrix} (-1/\sqrt{2})(A_{NO}-iA_{KQ}) & (-1/\sqrt{2})(A_{NN}-A_{KK})\\ (-1/\sqrt{2})(A_{NN}+A_{KK}) & (-1/\sqrt{2})(A_{NO}+iA_{KQ})\\ A_{QQ} & -iA_{QK}\\ iA_{QK} & -A_{QQ}\\ (1/\sqrt{2})(A_{NO}+iA_{KQ}) & (1/\sqrt{2})(A_{NN}+A_{KK})\\ (1/\sqrt{2})(A_{NN}-A_{KK}) & (1/\sqrt{2})(A_{NO}-iA_{KQ})\end{vmatrix} \tag{2.3}$$

where the rows are labelled by the final spin states $|1,1/2\rangle$, $|1,-1/2\rangle$, $|0,1/2\rangle$, $|0,-1/2\rangle$, $|-1,1/2\rangle$, $|-1,-1/2\rangle$ and columns by the initial spin states $|0,1/2\rangle$, $|0,-1/2\rangle$ of the spin zero nucleus and the incident proton.

Helicity formalism is also used in this particular context by Lyndon *et al* [5]. Since invariance under parity for the helicity amplitudes requires

$$T^H_{-\mu',-\mu'_p;0,-\mu_p} = (-1)^{1+\mu_p-\mu'_p-\mu'} \quad T^H_{\mu',\mu'_p;0,\mu_p} \tag{2.4}$$

where μ', μ'_p and μ_p denote the helicities of $^{12}\mathrm{C}^*(1^+)$ nucleus, scattered proton and the incident proton respectively, the T-matrix assumes the form,

$$T^H = \begin{vmatrix} H_1 & -H_6 \\ H_2 & H_5 \\ H_3 & H_4 \\ H_4 & -H_3 \\ H_5 & -H_2 \\ H_6 & H_1 \end{vmatrix} \tag{2.5}$$

where the rows and columns are labelled as in (2.3) but in terms of the helicity states.

We find however that it is more advantageous to choose a special transverse frame, (Z-axis along $\mathbf{N}$) which can be identified with the $(\mathbf{L},\mathbf{S},\mathbf{N})$, $(\mathbf{L}',\mathbf{S}',\mathbf{N}'=\mathbf{N})$ co-ordinate system employed by McClelland *et al* [6]. The advantage inherent in this choice has also been noted by Moravcsik *et al* [7]. The speciality of this transverse frame is that the X-axis for the initial $p-{}^{12}\mathrm{C}$ system is chosen along $\mathbf{P}_i$ whereas it (X') is chosen along the direction $\mathbf{P}_f$ for the $p'-{}^{12}\mathrm{C}^*(1^+)$ system. The respective Y-axes are so chosen to form a right handed co-ordinate system i.e.,

$$\hat{Y} = \frac{\mathbf{N}\times\mathbf{P}_i}{|\mathbf{N}\times\mathbf{P}_i|} \quad \text{and} \quad \hat{Y}' = \frac{\mathbf{N}\times\mathbf{P}_f}{|\mathbf{N}\times\mathbf{P}_f|} \tag{2.6}$$

The requirement of parity conservation in this frame reads as,

$$T^t_{M'm';Om} = (-1)^{M'+m'-m}\, T^t_{M'm';Om} \tag{2.7}$$

so that, the T-matrix assumes the attractive form [1].

$$T^t = \begin{vmatrix} O & D \\ A & O \\ B & O \\ O & E \\ O & F \\ C & O \end{vmatrix} \tag{2.8}$$

where it may be observed that half the number of elements are zero. Though labelled in the same way, it may be noted that the basis states used for T in (2.3), (2.5) and (2.8) are different; but they could be related to each other through appropriate rotations:

$$T^t_{M'm';Om} = \sum_{\substack{M'',m'' \\ m'''}} D^{1^*}_{M''M'}(0,\pi/2,\pi/2+\theta_{\mathrm{cm}}/2)\, D^{1/2^*}_{m''m'}(0,\pi/2,\pi/2+\theta_{\mathrm{cm}}/2)$$

$$T^P_{M''m'';Om'''}\, D^{1/2}_{m'''m}(0,\pi/2,\pi/2-\theta_{\mathrm{cm}}/2) \tag{2.9}$$

and

$$T^{t}_{M'm';Om} = \sum_{\mu',\mu'_p,\mu_p} D^{1^*}_{\mu' M'}(\pi/2,\pi/2,0)\, D^{1/2^*}_{\mu'_p m'}(\pi/2,\pi/2,\pi)\, T^{H}_{\mu'\mu'_p;O\mu_p} D^{1/2}_{\mu_p m}(\pi/2,\pi/2,\pi) \tag{2.10}$$

where θ_{cm} is the centre of mass scattering angle.

The density matrix $\boldsymbol{\rho}$ characterising the final spin state of the $p' - {}^{12}\text{C}^*(1^+)$ system may now be defined in the special transverse frame through its elements

$$\rho_{M'm';Mm} = \sum_{m'',m'''} T^{t}_{M'm';Om''} \rho^{p}_{m''m'''} T^{t^*}_{Mm;Om'''} \tag{2.11}$$

where $\boldsymbol{\rho}^p$ denotes the density matrix characterising the state of polarization of the incident proton beam. Following Ravishankar and Ramachandran [8,9] and observing that $T^{t}_{M'm';Om}$ transforms under rotations in the nuclear spin space as a spherical tensor $\boldsymbol{A}$ of rank 1 i.e.,

$$T^{t}_{M'm';Om} = (-1)^{M'} A_{-M'}(m',m) \tag{2.12}$$

and defining A^+ following Schwinger [10] through $A^+_M = (-1)^M$ times the hermitian conjugate of A_{-M}, the state of polarization of ${}^{12}\text{C}^*(1^+)$ may be characterised by the Fano statistical tensors t^k_q [11] given by

$$t^k_q = (-1)^{k+1}\sqrt{3} \sum_{M,M'} A_M \rho^p A^+_{M'} C(11k; MM'q). \tag{2.13}$$

Writing explicitly

$$A_1 = -\begin{vmatrix} 0 & F \\ C & 0 \end{vmatrix} \quad A_0 = \begin{vmatrix} B & 0 \\ 0 & E \end{vmatrix} \quad A_{-1} = -\begin{vmatrix} 0 & D \\ A & 0 \end{vmatrix} \tag{2.14a}$$

$$A^+_1 = \begin{vmatrix} 0 & A^* \\ D^* & 0 \end{vmatrix} \quad A^+_0 = \begin{vmatrix} B^* & 0 \\ 0 & E^* \end{vmatrix} \quad A^+_{-1} = \begin{vmatrix} 0 & C^* \\ F^* & 0 \end{vmatrix} \tag{2.14b}$$

$$\boldsymbol{\rho}^p = (1/2)(\boldsymbol{1} + \boldsymbol{\sigma}\cdot\mathbf{P}) \tag{2.15}$$

where $\mathbf{P}$ denotes the initial proton (beam) polarization. The scattered proton polarization $\mathbf{P}'$ can be obtained from its density matrix

$$\boldsymbol{\rho}^{p'} = (\text{Tr}\,\boldsymbol{\rho}^{p'}/2)(\boldsymbol{1} + \boldsymbol{\sigma}\cdot\mathbf{P}') \tag{2.16}$$

whose elements are given by

$$\rho^{p'}_{m'm} = \sum_{M} \rho_{Mm';Mm}. \tag{2.17}$$

3. Photon polarization asymmetries

The basis states of polarization [12–18] characterising the photon emitted by ${}^{12}\text{C}^*(1^+)$ can conveniently be chosen to be right circular and left circular,

$$\hat{\varepsilon}_{+1} = (-1/\sqrt{2})(\hat{\varepsilon}_x + i\hat{\varepsilon}_y) \tag{3.1a}$$

$$\hat{\varepsilon}_{-1} = (1/\sqrt{2})(\hat{\varepsilon}_x - i\hat{\varepsilon}_y) \tag{3.1b}$$

so as to satisfy standard conventions [19] for the rotation matrices D^j so that the density matrix $\boldsymbol{\rho}^\gamma$ takes the form,

$$\boldsymbol{\rho}^\gamma = 1/2 \begin{vmatrix} S_0 + S_z & S_x - iS_y \\ S_x + iS_y & S_0 - S_z \end{vmatrix} \tag{3.2}$$

where $S_0 = \operatorname{Tr} \boldsymbol{\rho}^\gamma$ denotes the intensity and $S_x = -s_1$, $S_y = s_2$ and $S_z = s_3$ in terms of the Stokes parameters defined by Born and Wolf [14].

The electromagnetic transition $^{12}\mathrm{C}^*(1^+) \rightarrow {}^{12}\mathrm{C}(0^+) + \gamma$ is governed by the transition matrix element (in the radiation gauge)

$$\langle 0^+; \mathbf{k}\mu | T^\gamma | 1^+ M \rangle = \langle 0^+ | a_{\mathbf{k}\mu} \mathbf{j} \cdot \mathbf{A} | 1^+ M \rangle \tag{3.3}$$

where

$$\mathbf{A} = (2\pi)^{-3/2} \int \mathrm{d}^3 k' (2\mathbf{k}')^{-1/2} \sum_{\lambda = +1, -1} \hat{\varepsilon}_\lambda [a_{\mathbf{k}'\lambda} e^{ik' \cdot x} + a^+_{\mathbf{k}'\lambda} e^{-ik' \cdot x}] \tag{3.4}$$

in terms of the photon creation and annihilation operators $a^+_{\mathbf{k}'\lambda}$ and $a_{\mathbf{k}'\lambda}$ respectively. Carrying out a simple quantum field theoretic calculation and expressing

$$\hat{\varepsilon}_\mu e^{-i\mathbf{k} \cdot \mathbf{r}} = (2\pi)^{1/2} \sum_{L=1}^{\infty} \sum_{M=-L}^{L} (i)^L (2L+1)^{1/2} [-\mu A^{(m)}_{LM} + iA^{(e)}_{LM}] \\ D^L_{M\mu}(\phi_\gamma, \theta_\gamma, 0) \tag{3.5}$$

in terms of the standard multipole solutions [19], we have

$$\langle 0^+; \mathbf{k}\mu | T^\gamma | 1^+ M \rangle = Q(-1)^{1-M} \mu D^1_{-M\mu}(\phi_\gamma, \theta_\gamma, 0) \tag{3.6}$$

where Q collectively denotes all the factors including the reduced matrix element for the nuclear transition and $(\theta_\gamma, \phi_\gamma)$ denote the polar angles of $\mathbf{k}$ with respect to the $p' - {}^{12}\mathrm{C}^*(1^+)$ co-ordinate system defined earlier. The γ-decay of the 15·11 MeV $(J^\pi = 1^+; T = 1)$ state to the $(J^\pi = 0^+; T = 0)$ ground state is a M1 transition with strength $0{\cdot}531 \pm 0{\cdot}011$ W.u [20]. The branching ratio for this transition is 97%, the width of the level being $38{\cdot}5 \pm 0{\cdot}8$ eV. The life time is short enough that the photon can unambiguously be identified with the associated inelastic scattering event and the coincidence cross-section and analysing powers have already been measured experimentally [5, 26].

The density matrix $\boldsymbol{\rho}^\gamma$ for the photon is now defined in terms of its elements,

$$\boldsymbol{\rho}^\gamma_{\mu\mu'} = \sum_{M,M'} \langle 0^+; \mathbf{k}\mu | T^\gamma | 1^+ M \rangle \rho_{MM'} \langle 0^+; \mathbf{k}\mu' | T^\gamma | 1^+ M' \rangle^* \tag{3.7}$$

where the elements $\rho_{MM'}$ of the nuclear density matrix are given in terms of the t^k_qs defined earlier by (2.13) through

$$\boldsymbol{\rho}_{MM'} = 3^{-1/2} \sum_{k=0}^{2} \sum_{q=-k}^{k} (-1)^M (-1)^{k+1} C(11k; -MM'q) \boldsymbol{t}^k_q. \tag{3.8}$$

Substituting (3.8) in (3.7) and making use of the standard properties of the D^j – matrices, we get

$$\boldsymbol{\rho}^\gamma_{\mu\mu'} = (|Q|^2/3^{1/2}) \sum_k \sum_q (-1)^k \boldsymbol{t}^k_q C(11k; \mu - \mu' q') D^k_{qq'}(\phi_\gamma, \theta_\gamma, 0) \tag{3.9}$$

Information regarding all the photon-proton correlation observables are now contained in the matrix elements of

$$S_0(\theta_\gamma,\phi_\gamma;\mathbf{P}) = (2|Q|^2/3^{1/2}) \sum_{k=0,2} \sum_{q=-k}^{k} [4\pi/(2k+1)]^{1/2}$$

$$C(11k;1-10)(\boldsymbol{t}_q^k\, Y_{kq}^*(\theta_\gamma,\phi_\gamma)) = (1/2)[S_{00} + \sum_{j=x,y,z} \boldsymbol{\sigma}_j S_{0j}] \tag{3.10}$$

$$S_x(\theta_\gamma,\phi_\gamma;\mathbf{P}) = (|Q|^2/3^{1/2}) \sum_{q=-2}^{+2} t_q^2 (D_{q2}^2(\phi_\gamma,\theta_\gamma,0) + D_{q-2}^2(\phi_\gamma,\theta_\gamma,0))$$

$$= (1/2)[S_{x0} + \sum_{j=x,y,z} \boldsymbol{\sigma}_j S_{xj}] \tag{3.11}$$

$$S_y(\theta_\gamma,\phi_\gamma;\mathbf{P}) = (i|Q|^2/3^{1/2}) \sum_{q=-2}^{+2} t_q^2 (D_{q2}^2(\phi_\gamma,\theta_\gamma,0) - D_{q-2}^2(\phi_\gamma,\theta_\gamma,0))$$

$$= (1/2)[S_{y0} + \sum_{j=x,y,z} \boldsymbol{\sigma}_j S_{yj}] \tag{3.12}$$

$$S_z(\theta_\gamma,\phi_\gamma;\mathbf{P}) = (-2|Q|^2/3)(2\pi)^{1/2} \sum_{q=-1}^{+1} t_q^1\, Y_{1q}^*(\theta_\gamma,\phi_\gamma)$$

$$= (1/2)[S_{z0} + \sum_{j=x,y,z} \boldsymbol{\sigma}_j S_{zj}] \tag{3.13}$$

which can readily be expressed in terms of A, B, C, D, E and F on making use of (2.13) and (2.14).

4. The inversion problem

To determine empirically the amplitudes A, B, C, D, E and F we need not have to make use of all the observables defined in the previous section. Although there are several ways [2] in which one can choose the requisite observables, all of them require some involved manipulations in order to determine the amplitudes unambiguously. One outstanding advantage in including some of the photon polarization observables is that it enables us to determine straightaway the magnitudes of the six amplitudes through the simple process of solving six linear equations. With this end in view, we first consider the inelastic differential cross-section,

$$(\mathrm{d}\sigma/\mathrm{d}\Omega_p)_{\text{unpol}} = \mathrm{Tr}[\rho^p(\mathbf{P}=0)] = (1/2)(|A|^2+|B|^2+|C|^2+|D|^2+|E|^2+|F|^2) \tag{4.1}$$

for $^{12}\mathrm{C}(p,p')^{12}\mathrm{C}^*(1^+)$ using initially unpolarized protons and

$$(\mathrm{d}\sigma/\mathrm{d}\Omega_p)_{\text{pol}} = \mathrm{Tr}[\rho^p(\mathbf{P}\neq 0)] = (\mathrm{d}\sigma/\mathrm{d}\Omega_p)_{\text{unpol}} + (1/2)P_z(|A|^2+|B|^2+$$

$$+|C|^2-|D|^2-|E|^2-|F|^2) \tag{4.2}$$

with initially polarized protons. We may next choose to take into consideration the measurement of the transverse (or Z) component of the scattered proton polarization given by

$$(\mathrm{d}\sigma/\mathrm{d}\Omega_p)_{\text{unpol}} P'_z(\mathbf{P}=0) = (1/2)(-|A|^2+|B|^2-|C|^2+|D|^2-|E|^2+|F|^2) \tag{4.3}$$

when the initial beam is unpolarised and

$$(\mathrm{d}\sigma/\mathrm{d}\Omega_p)_{\mathrm{pol}}P'_z(\mathbf{P}\neq 0)=(\mathrm{d}\sigma/\mathrm{d}\Omega_p)_{\mathrm{unpol}}P'_z(\mathbf{P}=0)+(1/2)P_z(-|A|^2+|B|^2 -|C|^2-|D|^2+|E|^2-|F|^2) \tag{4.4}$$

with initially polarized proton beam. The above four observables have already been measured experimentally [6, 21–28]. To generate two more linear equations involving the squares of the amplitudes, we suggest here the measurement of the Stokes parameter S_z of forward produced photons. We have

$$S_{z0}(0,0;\mathbf{P}=0)=-(1/2)|Q|^2(|D|^2-|F|^2+|A|^2-|C|^2) \tag{4.5}$$

with initially unpolarized protons and

$$S_{z0}(0,0;\mathbf{P}\neq 0)=S_{z0}(0,0;\mathbf{P}=0)+(1/2)|Q|^2P_z(|D|^2-|F|^2-|A|^2+|C|^2) \tag{4.6}$$

using initially polarized proton beam. It is transparent that equations (4.1) to (4.6) are readily invertible and hence $|A|^2$, $|B|^2$, $|C|^2$, $|D|^2$, $|E|^2$ and $|F|^2$ can be determined. It may be noted that this can be done without introducing large statistical uncertainties in the inversion process. Since the overall phase is anyway not determinable, we are now left with the problem of determining the five relative phases. It is convenient to choose B to be real and positive and the relative phases of A, C, D, E, F may be denoted respectively by δ_A, δ_C, δ_D, δ_E and δ_F. On making use of the observables

$$S_{zx}(\pi/2,0;\mathbf{P}=0)=-(|Q|^2/\sqrt{2})\mathrm{Re}(FE^*+BA^*+CB^*+ED^*) \tag{4.7}$$

$$S_{zx}(\pi/2,0;\mathbf{P}\neq 0)=S_{zx}(\pi/2,0;\mathbf{P}=0) +(|Q|^2/\sqrt{2})P_z\mathrm{Re}(FE^*-BA^*-CB^*+ED^*) \tag{4.8}$$

$$S_{zy}(\pi/2,\pi/2;\mathbf{P}=0)=(|Q|^2/\sqrt{2})\mathrm{Re}(FE^*+BA^*-CB^*-ED^*) \tag{4.9}$$

and

$$S_{zy}(\pi/2,\pi/2;\mathbf{P}\neq 0)=S_{zy}(\pi/2,\pi/2;\mathbf{P}=0) +(|Q|^2/\sqrt{2})P_z\mathrm{Re}(FE^*-BA^*+CB^*-ED^*) \tag{4.10}$$

we can determine the real parts of FE^*, BA^*, CB^*, and ED^* which contain cosines of $(\delta_F-\delta_E)$, δ_A, δ_C and $(\delta_E-\delta_D)$. To avoid discrete ambiguities, we need one more observable [29] which involves a combination of these relative phases and which is linearly independent of equations (4.7), (4.8), (4.9) and (4.10). For this purpose we choose to measure

$$S_{zx}(\pi/2,\pi/2;\mathbf{P}=0)=-(|Q|^2/\sqrt{2})\mathrm{Im}(FE^*+BA^*+CB^*+ED^*) \tag{4.11}$$

We then have δ_A, δ_C, $\delta_E-\delta_D$ and $\delta_E-\delta_F$ unambiguously. To determine δ_D, δ_E and δ_F individually, we can make use of the observables

$$S_{zx}(0,0;P_x,0,0)=-|Q|^2P_x\mathrm{Re}(AD^*-CF^*) \tag{4.12}$$

and

$$S_{zx}(0,0;0,P_y,0)=-|Q|^2P_y\mathrm{Im}(AD^*-CF^*) \tag{4.13}$$

which together readily yield δ_D, δ_E and δ_F unambiguously since the magnitudes of the amplitudes are already known.

It is worth emphasizing that the number of observables chosen here is only 13 as compared to sets suggested earlier [2] each of which contained a total of 16 observables. It may moreover be noted that the inversion procedure suggested here to determine the magnitudes could reasonably be expected to lead to greater precision, provided the Stokes parameters $S_{z0}(0,0;\mathbf{P}=0)$ and $S_{z0}(0,0;\mathbf{P}\neq 0)$ are sufficiently large. To obtain an estimate of these observables we may use the existing non-relativistic [30] or relativistic impulse approximation theories [31]. Using nuclear structure inputs of Cohen and Kurath [32] and Lee and Kurath [33] computer codes DW81 [30] and its relativistic counterpart DREX [31] have already been developed. The estimates for the amplitudes based on these codes have been made available to us by Piekarewicz [34]. We find that the ratio S_{z0}/S_{00} at forward angles of the photon with $\mathbf{P}=0$ vary between ± 40% whereas S_{z0}/S_{00} with $P_z = 0{\cdot}4$ varies between ± 30% [35].

The set of observables (4.1) to (4.13) is by no means unique. Choosing only the Stokes parameter which is connected with the circular polarization asymmetry of the photon polarisation (which is likely to be the easiest to determine experimentally at these energies), we can identify several alternative sets (as many as 16 each of which contain only 13 observables) which can lead to unambiguous determination of inelastic scattering amplitudes. A large number of other sets of possible measurements could also be identified if we take into consideration the other two Stokes parameters. It may also be emphasized finally that a completely empirical programme of determining unambiguously the $^{12}C(p,p')^{12}C^*(1^+)$ scattering amplitudes cannot be envisaged without including at least some observables associated with $^{12}C(p,p'\gamma)^{12}C$.

Acknowledgements

We thank Prof. Piekarewicz for sending us the estimates for the amplitudes based on the computer codes DW81 and DREX. We thank the Referee for the comments in the light of which the paper has been revised. One of us (ARU) thanks the University Grants Commission (India) for financial support through the award of a Research Fellowship.

References

[1] J Piekarewicz, E Rost and J R Shepard, *Phys. Rev.* **C41**, 2277 (1990)
[2] A Sudha Rao, K S Mallesh and G Ramachandran, *Mod. Phys. Lett.* **A7**, 175 (1992)
[3] C G Fasano, Frank Tabakin and Bijan Saghai, *Phys. Rev.* **C46**, 2430 (1992)
[4] J Piekarewicz, *Phys. Rev.* **C37**, 719 (1988)
[5] C R Lyndon *et al*, *Phys. Rev.* **C45**, 308 (1992)
[6] J B McClelland *et al*, *Phys. Rev. Lett.* **52**, 98 (1984)
[7] M J Moravcsik, H M Sinky and G R Goldstein, *Ann. Phys.* **171**, 205 (1986)
[8] V Ravishankar and G Ramachandran, *Mod. Phys. Lett.* **A1**, 333 (1986)
It may be noted that the notation used in this reference for the matrix element is $(-1)^M A^{+}_{-M}$ while the notation used in the present paper follows that of ref. [9]
[9] V Ravishankar and G Ramachandran, *Phys. Rev.* **C35**, 62 (1987)
[10] J Schwinger, in *Quantum theory of angular momentum*, U.S. At Energy Comm. NYO 3071 edited by L C Biedenharn and H VanDam, (Academic Press, New York, 1965) 220
[11] U Fano, *Phys. Rev.* **90**, 577 (1953)
[12] S Pancharathnam, *Proc. Indian Acad. Sci.* **A44**, 247 (1956)
[13] U Fano, *Rev. Mod. Phys.* **29**, 74 (1957)

[14] M Born and E Wolf, *Principles of optics*, (Pergamon Press, London, 1959) Ch. 1 p. 30

[15] W H McMaster, *Rev. Mod. Phys.* **33**, 8 (1961)

[16] G N Ramachandran and S Ramaseshan, *Crystal optics in Encyclopaedia of physics* edited by S Flugge (Springer Verlag, Berlin, 1961)

[17] B A Robson, *Theory of polarisation phenomena* (Clarendon Press, Oxford, 1974)

[18] K Blum, *Density matrix theory and its application*, (Plenum Press, New York and London, 1981)

[19] M E Rose, *Elementary theory of angular momentum* (John Wiley, New York, 1957)

[20] F Ajzenberg-Selov, *Nucl. Phys.* **A433**, 1 (1985)

[21] J R Comfort *et al*, *Phys. Rev.* **C21**, 2147 (1980); **24**, 1834 (1981); **26**, 1800 (1982)

[22] T A Carey *et al*, *Phys. Rev. Lett.* **49**, 266 (1982)

[23] K Jones, Ph D thesis, LAMPF Preprint LA-10064-T, (1984)

[24] J B McClelland, *Proc. LAMPF Workshop on Dirac Approaches to Nuclear Physics*, Edited by J R Shepard, C Y Cheung and R L Boudrie, LA-10438-C; UC-34C, (1985)

[25] O Hausser *et al*, *Nucl. Instrum. Methods* **A254**, 67 (1987)

[26] K H Hicks *et al*, *Phys. Rev. Lett.* **61**, 1174 (1988)

[27] K H Hicks *et al*, *Phys. Lett.* **B201**, 29 (1988)

[28] X Y Chen, J R Shepard, M R Braunstein, T A Carey, K W Jones, J B McClelland, L Rees, T N Taddeucci, N Tanaka, and A D Bacher, *Phys. Rev.* **C44**, 2041 (1991)

[29] N W Dean and Ping Lee, *Phys. Rev.* **D5**, 2741 (1972)

[30] J R Comfort, G L Moake, C C Foster, P Schwandt and W G Love, *Phys. Rev.* **C26**, 1800 (1982)

[31] E Rost and J R Shepard, *Phys. Rev.* **C35**, 681 (1987)

[32] S Cohen and D Kurath, *Nucl. Phys.* **73**, 1 (1965)

[33] T H S Lee and D Kurath, *Phys. Rev.* **C21**, 293 (1980)

[34] J Piekarewicz, Private Communication

[35] J Piekarewicz, A Sudha Rao, M S Vidya, K S Mallesh, G Ramachandran and A R Usha Devi, to be published

[redacted]

PRAMANA
— journal of
physics

© Printed in India

Vol. 42, No. 2,
February 1994
pp. 107–122

Leptodermous expansion of nuclear ground state energies and the anomaly in the nuclear curvature energy

S K KATARIA[1], ARUNA NIJASURE[1], V S RAMAMURTHY[2] and A K DUTTA[3]
[1] Bhabha Atomic Research Centre, Bombay 400085, India
[2] Institute of Physics, Bhubaneshwar 751005, India
[3] Department of Physics, D.A. University, Indore 452001, India

MS received 7 December 1992; revised 2 November 1993

Abstract. The leptodermous expansion of the total ground state energy of a nucleus into volume, surface, curvature and gauss curvature contributions has been studied starting from a semi-classical energy density formalism of extended Thomas Fermi type. A numerical procedure was used to obtain the surface energy and curvature energy contributions from surface moments of energy density profiles $H(r)$ for a sequence of nuclei with $N = Z$ and neglecting the coulomb interaction for the three Skyrme forces. A transition to the liquid drop model type expansion in increasing powers of $A^{-1/3}$ is then made, taking into account the dependence of the central density and the surface structure on the mass of the nucleus. It is found that there is no inconsistency between the curvature contribution to the total energy in the leptodermous expansion and the $A^{-1/3}$ term contribution in the liquid drop model expansion. It has been shown that the earlier apparent anomaly between the above two methods arises due to the use of semi-infinite approximation and the mass dependence of the central density and the surface structure of finite nuclei.

Keywords. Leptodermous expansion; liquid drop model; surface energy; curvature energy; finite nuclei; extended Thomas Fermi calculations; Euler's equations.

PACS No. 21·10

1. Introduction

The concepts of leptodermous system have been extensively discussed in several review articles [1]. Due to the short range of the nuclear forces, the thickness of nuclear surface a is rather small compared to the nuclear radius R except for the very light ones. The ratio a/R can then be used as an expansion parameter in a power series expansion of various quantities in a nucleus such as their ground state energy per nucleon in increasing power of a/R. Such a leptodermous expansion [2] leads to a decomposition of the total ground state energy of a finite nucleus into volume, surface, curvature and Gauss curvature contributions. It is also well-known that nuclear radii exhibit approximately an $A^{+1/3}$ dependence arising from the saturation property of nuclear forces and consequently near constancy of the central density for all the nuclei. This makes it possible to expand several nuclear properties in increasing powers of $A^{-1/3}$. This liquid drop model expansion forms the basis of all semi-empirical mass formulae used to fit experimental ground state masses and fission barriers. While it is customary to associate the leading terms of the liquid drop model expansion a volume, surface and curvature interpretation, this could only be approximate, since the nuclear fluid is not strictly incompressible. Recently, an apparent anomaly has been noticed between the nuclear curvature energies in a leptodermous expansion and the $A^{+1/3}$ term in a liquid drop model expansion of the nuclear ground state energies. Myers and Swiatecki [3] have observed that in the framework of the droplet model best fits to the experimental ground state masses are obtained when the coefficient of the $A^{+1/3}$ term is assumed to be zero. In another study, Seegar and Howard [4] obtained a value of $-0{\cdot}76 \pm 0{\cdot}11$ MeV for the coefficient of the $A^{+1/3}$ term. In the folding model of Krappe *et al* [5], for the surface energy, the curvature energy turns out to be identically zero. On the other hand, leptodermous expansions of the nuclear ground state energies have always yielded much higher values of the nuclear curvature energies, corresponding coefficients of the $A^{+1/3}$ term ranging from 9–15 MeV [6]. Negele and Vautherin [7] using Hartree Fock calculations with Skyrme interactions for a sequence of mirror nuclei without Coulomb interaction obtained the value of curvature contribution as 11·86 MeV. In many recent studies it has been concluded that this anomaly cannot be resolved within the framework of the existing calculations of the ground state energies [8].

In the present work, we have studied in detail leptodermous expansion of the nuclear ground state energies starting [9] from a suitably chosen semiclassical energy density functional. A transition is then made to a liquid drop model expansion taking into account the dependence of the central density, surface diffuseness and surface skewness on the mass number of the nucleus. It is shown that there exists no anomaly between the calculated curvature energies and the coefficient of the $A^{+1/3}$ term in the LDM expansion, if the transition from the leptodermous expansion to the LDM expansion is carried out properly. Previous calculations [1, 6, 8, 10] of curvature contribution have been carried out for semi-infinite surfaces as these only can be carried out analytically. Calculations of curvature energies with semi-infinite model surfaces miss important physical features and result in misleading conclusions.

2. Leptodermous and LDM expansions of nuclear ground state energies

In the framework of energy density formalism [11], the total energy of a nucleus can be written as a volume integral of a suitably chosen energy density $H(r)$

$$E_T = 4\pi \int_0^\infty H(r) r^2 \,\mathrm{d}r \tag{1}$$

where $H(r)$ is a functional of the density $\rho(\mathbf{r})$ and its derivatives. In the present analysis, we restrict ourselves to the case of spherical nuclei with $N = Z$ and without Coulomb interaction. For leptodermous nuclei, the contribution from the surface region to the total energy can be isolated by expanding E_T in terms of the surface moments of $H(r)$ around the nuclear sharp-cutoff radius R_s, defined by the relation:

$$A = 4\pi/3 R_s^3 \rho_0 \tag{2}$$

where central density of a nucleus is denoted by ρ_0 and A is its mass number. For calculation of surface moments around R_s, we substitute $r = R_s + z$ in (1), and obtain

$$\begin{aligned} E_T &= 4\pi \int_{-R_s}^\infty H(z+R_s)(R_s+z)^2 \,\mathrm{d}z \\ &= 4\pi \left[\int_{-R_s}^0 H(z+R_s)(R_s+z)^2 \,\mathrm{d}z + \int_0^\infty H(z+R_s)(R_s+z)^2 \,\mathrm{d}z \right]. \end{aligned}$$

Rewriting the first integral as

$$4\pi\int_{-R_s}^{0}[H(z+R_s)-\varepsilon_0+\varepsilon_0](R_s+z)^2\,\mathrm{d}z$$

where ε_0 is the central energy density corresponding to the density ρ_0, one has

$$E_T=\varepsilon_0\frac{4\pi}{3}R_s^3+4\pi\int_{-R_s}^{0}[H(z+R_s)-\varepsilon_0](R_s+z)^2\,\mathrm{d}z$$
$$+4\pi\int_{0}^{\infty}H(z+R_s)(R_s+z)^2\,\mathrm{d}z$$

and expanding the $(R_s+z)^2$ terms in the integrals, we have

$$\begin{aligned}E_T&=\varepsilon_0V+S\left[\int_{-R_s}^{0}[H(z+R_s)-\varepsilon_0]\,\mathrm{d}z+\int_{0}^{\infty}H(z+R_s)\,\mathrm{d}z\right] \qquad (3)\\&\quad+4\pi R_s\left[\int_{-R_s}^{0}[H(z+R_s)-\varepsilon_0]z\,\mathrm{d}z+\int_{0}^{\infty}H(z+R_s)z\,\mathrm{d}z\right]\\&\quad+4\pi\left[\int_{-R_s}^{0}[H(z+R_s)-\varepsilon_0]z^2\,\mathrm{d}z+\int_{0}^{\infty}H(z+R_s)z^2\,\mathrm{d}z\right]\\&=a_vV+a_sS+a_cC+a_GG;\quad\text{where } G=4\pi \text{ and } C=4\pi R_s\end{aligned}$$

where V is the volume of the nucleus with sharp cutoff radius R_s, S is its surface area, C is its mean radius of curvature and G is its Gaussian curvature. Because of the asymptotic constancy of the energy density $\varepsilon(r)$ for $r \ll R_s$, integrands in all the three terms are sharply peaked around R_s with a range of the order of diffuseness parameter a. The first term in this leptodermous expansion can be identified as the volume energy of the nucleus, the second term its surface energy, the third term its curvature energy and the fourth term corresponds to the Gaussian curvature energy.

In principle, the above expansion could have been carried out around any expansion radius R, e.g. in place of the sharp cut-off radius by half density radius $R_{1/2}$ [10]. To this extent, the decomposition of the total energy into volume and surface contributions is not unique but depends on the choice of the expansion radius. In case expansion is carried out around $R_{1/2}$, the first term will not be proportional to mass number A but will also involve additional contributions of the order of a/R. A similar expansion of the density profile $\rho(r)$ around half density radius $R_{1/2}$ gives the relation between the mass number A and $R_{1/2}$ involving these $a/R_{1/2}$ correction terms in terms of various surface moments of $\rho(r)$ as in eq. (3) for energy density profiles. Hence, for the surface moments of the energy density profiles calculated around this radius, one will have to invert the leptodermous expansion of the density profiles in order to make the transition to the LDM type expansion in $A^{-1/3}$. However, in the present studies, with the choice of expansion radius as the sharp cut-off radius R_s, the volume energy turns out to be proportional to particle number A, which is an advantage in a subsequent transition to liquid drop model expansion. Hence our choice of R_s as the expansion radius. This choice is also consistent with the earlier analysis [6] of surface and curvature energies with model semi-infinite surfaces.

If the nuclear fluid had been incompressible, a transition to the LDM expansion is trivial since

$$R_s = (3A/4\pi\rho_0)^{1/3}$$

and

$$E_T = a_v^* A + a_s^* A^{2/3} + a_c^* A^{1/3} + a_G^* \tag{4}$$

The LDM coefficients a_v^*, a_s^*, a_c^* and a_G^* are uniquely related one-to-one to the leptodermous expansion coefficients a_v, a_s, a_c and a_G. However, the nuclear fluid is compressible with a finite compressibility coefficient. The central density and the structure of the nuclear surface, namely, its thickness and skewness are then dependent on the mass number A of the nucleus. Therefore, the coefficients a_v, a_s, a_c and a_G in (3), are not universal constants but depend on the mass number A. For example, the central density of finite nuclei using semi-classical energy density formalism has been studied in detail earlier [1]. Defining the parameter ε as

$$\varepsilon = -1/3\ (\rho_0 - \rho_\infty)/\rho_\infty \tag{5}$$

where ρ_∞ is the saturation density of nuclear matter. The leptodermous expansion coefficients for the total energy of the nucleus were expanded as

$$\begin{aligned} a_v &= a_v^\infty + 1/2\ K_\infty \varepsilon^2 - 9/2\ \dddot{a}_v \varepsilon^3 \\ a_s &= a_s^\infty - 3\dot{a}_s \varepsilon + 9/2\ \ddot{a}_s \varepsilon^2 \\ a_c' &= a_c^\infty - 3\dot{a}_c \varepsilon + 9/2\ \ddot{a}_c \varepsilon^2 \end{aligned} \tag{6}$$

where dots denote the derivatives with respect to ρ_0; a_v^∞, a_s^∞ and a_c^∞ are the nuclear matter values and K_∞ is the corresponding incompressibility. To the lowest order, the mass dependence of ε can be written as (similar to droplet model)

$$\varepsilon = 3\dot{a}_s A^{-1/3}/K_\infty = -2a_s^\infty A^{-1/3}/K_\infty. \tag{7}$$

It is, therefore, reasonable to express the leptodermous expansion coefficients for finite nuclei as:

$$\begin{aligned} a_v &= a_v^\infty + a_v'' A^{-2/3} + a_v''' A^{-1} \\ a_s &= a_s^\infty + a_s' A^{-1/3} + a_s'' A^{-2/3} \\ a_c &= a_c^\infty + a_c' A^{-1/3} \\ a_0 &= a_0^\infty \end{aligned} \tag{8}$$

where we have used the dashes denoting the derivatives with respect to $A^{-1/3}$, and a_v^∞, a_s^∞ and a_c^∞ are the nuclear matter values. In addition to the variations of the central density with mass number, there could also be mass variations of the surface structure (diffuseness and skewness) for finite nuclei [6] and have not been studied in detail. However, one could use expansions of the type given by the eq. (8) in general. The nuclear matter values for the volume and surface contributions can be evaluated by taking the limit $A^{-1/3} \to 0$. The other coefficients are not of simple nature and are to be evaluated numerically only. A transition to the LDM then implies that the coefficients a_c^* and a_G^* have contributions from lower order terms. For example, the coefficient of $A^{+1/3}$ in (4) has, in addition, to the curvature contribution, has also components from surface and volume terms as given in (8)

$$a_c^* = a_c^\infty + a_s' + a_v''. \tag{9}$$

For a quantitative study of the decomposition of a_c^*, we use the energy density formalism as described below.

3. Numerical studies with semi-classical energy densities

According to the semi-classical energy density formalism any physical quantity can be expressed as a functional of nuclear densities of the two fluids $\rho_q^A(q = n, p)$. The construction of the functional for the total energy requires separate analysis for the kinetic and potential parts. For the kinetic energy part, the second order extended Thomas Fermi Functional involving inhomogeneity corrections up to second order only in the derivatives of the density ρ_q is written as [6]

$$\tau(\rho_q) = \alpha\rho_q^{5/3} + \beta(\nabla\rho)_q^2/\rho_q + \gamma\Delta\rho_q \tag{10}$$

As is well-known, for extended Thomas Fermi (ETF2) functional $\alpha = 3/5(3\pi^2)^{2/3}$ and $\beta = 1/36$ and $\gamma = 1/3$. However, this ETF2 is not a very good approximation at the nuclear surface, where the potential is rapidly varying and one has to go to fourth order corrections in this part. In modified Thomas Fermi (MTF) approach, the nuclear surface properties were shown to be well reproduced [6] using the form given in (10) with $\alpha = 3/5(3\pi^2)^{2/3}$ and $\gamma = 1/3$ and treating β as a free parameter. In the present work, we have used $\beta = 1/18$ and $\beta = 1/36$ for ETF2 calculations.

For the potential part, the use of zero-range Skyrme interaction simplifies the definition of the hamiltonian energy density, which, without any further approximation, depends only on the nuclear density and the kinetic energy density. The Skyrme functional for the total energy density $E(r)$ for a closed shell nuclei with $(\rho_n(r) = \rho_p(r) = 1/2\rho(r))$ can be written as

$$\begin{aligned} E(r) = h^2/2m^*(\mathbf{r})\tau(\mathbf{r}) + 3/8\ t_0\rho^2(\mathbf{r}) + 1/64\ (9t_1 - t_2(5 + 4x_2))(\nabla\rho)^2 \\ + 1/16\ t_3\rho^{2+\alpha}(\mathbf{r}) + 3/4\ W_0(\mathbf{J}\cdot\nabla\rho) \end{aligned} \tag{11}$$

where the effective mass $m^*(r)$ for the Skyrme forces is given by

$$f(r) = m/m^*(r) = 1 + 1/16[3t_1 + t_2(5 + 4x_2)]\rho(\mathbf{r})$$

and $\mathbf{J}$ is the spin current density,
and t_0, t_1, t_2, t_3, x_2 and W_0 are the parameters of the Skyrme forces. There is a whole series of Skyrme force parametrization labelled SI, SII, SIII, SIV, SkM and RATP giving different set of values to the above constants. It is well known that the surface energy coefficient and curvature energy coefficients depend significantly on the choice of these parameter sets. In our calculations, we have studied the leptodermous expansion for the SIII, SkM and RATP Skyrme parameter sets as given in table 1. The densities $\tau(\mathbf{r})$ and $\mathbf{J}(\mathbf{r})$ are universal functional of the local density [11, 12] and in the semi-classical ETF approach, including the terms arising from the effective mass are

$$\tau(r) = \tau_{TF}(\rho(r)) + \tau_2(\rho(r)) \tag{12}$$

Table 1. Parameters of the Skyrme forces used in the present work from refs [1, 6].

Force	t_0 MeVfm^3	t_1 MeVfm^5	t_2 MeVfm^5	t_3 MeVfm$^{3+3\alpha}$	x_0	x_1	x_2	x_3	α	W_0
SIII	−1128·75	395·00	−95	14000	0·45	0·0	0·0	1·0	1	120·00
SkM	−2646·00	385·00	−120	15595	0·09	0·0	0·0	0·0	1/6	130·00
RATP	−2160·00	513·00	+121	11600	0·418	−0·36	−2·29	0·586	1/5	120·00

$$\tau_2(\rho) = 1/36\ (\nabla\rho)^2/\rho + 1/3\ \Delta\rho + 1/6\ \nabla f\cdot\nabla\rho/f + 1/6\ \rho\nabla^2 f/f - 1/12\ \rho(\nabla f/f)^2 + 1/2\ (2m/\hbar^2)^2\rho(W/f)^2 \tag{13}$$

and $\mathbf{J}(\rho) = -2m/\hbar^2\rho/f\,\mathbf{W} = -3/2\ W_0 2m/\hbar^2\rho/f\nabla\rho$.

The minimization of the total energy E_T, written as a functional $H(\rho)$ of matter density $\rho(r)$ leads to the two coupled Euler's equations

$$\frac{\partial H}{\partial\rho_q} - \nabla\cdot\frac{\partial H}{\partial\nabla\rho_q} + \Delta\frac{\partial H}{\partial\Delta\rho_q} = \lambda_q \quad q = n, p \tag{14}$$

where λ_n and λ_p are Langrange multipliers corresponding to the conservation of the number of neutrons and protons. These Euler's equations are second order differential equations which have been solved numerically in the case of finite systems as well as for semi-infinite systems to obtain the density profiles. The density profile systematics for finite nuclear systems have been studied earlier [6]. In our calculations, we have used the same code to obtain the mass dependence of the nuclear surface structure.

Alternatively, the minimization of E_T can be carried out by assuming some analytical form of the semiclassical density $\rho(r)$ and minimizing it with respect to the density profile parameters. This procedure corresponds to a limited variation in some subspace defined by the analytic form of the density profiles. Generalized Fermi functions as given below

$$\rho(r) = \rho_0/\{1 + \exp(r - R)/a\}^{\nu} \tag{15}$$

have been shown to adequately describe the density profiles for the finite nuclei and are very close to the solutions of the Euler's equation. This method has the advantage of the faster convergence over that of Euler equations [12].

We have calculated the total energy E_T, as well as the three surface moments E_s, E_c and E_0 using the density profiles obtained in two ways: (i) by solving the Euler's equations and, (ii) by method of least squares to obtain the parameters of the modified Fermi distributions for a number of nuclei in the mass range $40 < A < 500$. It was found that the differences in the quantities E_T, E_s, E_c and E_0 in these two ways are of the order of 1–5 MeV (see for example E_T values in columns a and b for cases I and III in table 2), and therefore any of these two methods can be used in calculations.

Figure 1 shows the plot of density profile for a very heavy nucleus $A = 500$ calculated using the first method for the SIII interaction. As seen in figure 1, density $\rho(r)$ can be well represented by a generalized Fermi distribution. The plot of corresponding energy density $H(r)$ is also shown in the figure. One observes that the maximum occurs in the vicinity of the nuclear surface and not at the centre of the nucleus, and

Table 2. Total energy of nuclei calculated with SIII interaction and $\beta = 1/18$.

A	Case I (a)	Case I (b)	Case II (a)	Case III (a)	Case III (b)
500	−6703·0	−6704·6	−6560·9	−6423·5	−6428·1
300	−3879·2	−3880·2	−3777·3	−3642·8	−3647·4
200	−2497·2	−2498·0	−2419·0	−2290·6	−2295·2
140	−1685·3	−1685·9	−1623·4	−1501·8	−1506·6
100	−1156·0	−1156·4	−1106·2	−992·0	−997·0
80	−896·7	−896·5	−853·8	−744·6	−749·2
60	−642·8	−642·3	−607·4	−505·4	−508·7
40	−397·0	−397·4	−369·9	−277·0	−281·3

(a) using density profiles calculated from Euler's equation with total $H(r)$. The total energy is calculated using the same density profile with three prescriptions for $\tau(\rho)$.
Case I with complete ETF-2 and MTF values for β and γ parameters,
Case II, $\Delta\rho = \rho''$ was assumed for $\tau(\rho)$ for the calculation of $H(r)$ keeping $\rho(r)$ as in case I estimate.
Case III, E_T was calculated using $\Delta\rho = 0$ in $\tau(\rho)$ expressions.
(b) Same as (a) but using modified Fermi distributions for $\rho(r)$, whose parameters were obtained by minimising the total energy E_T with and without the Δ-term in the calculation of $H(r)$.

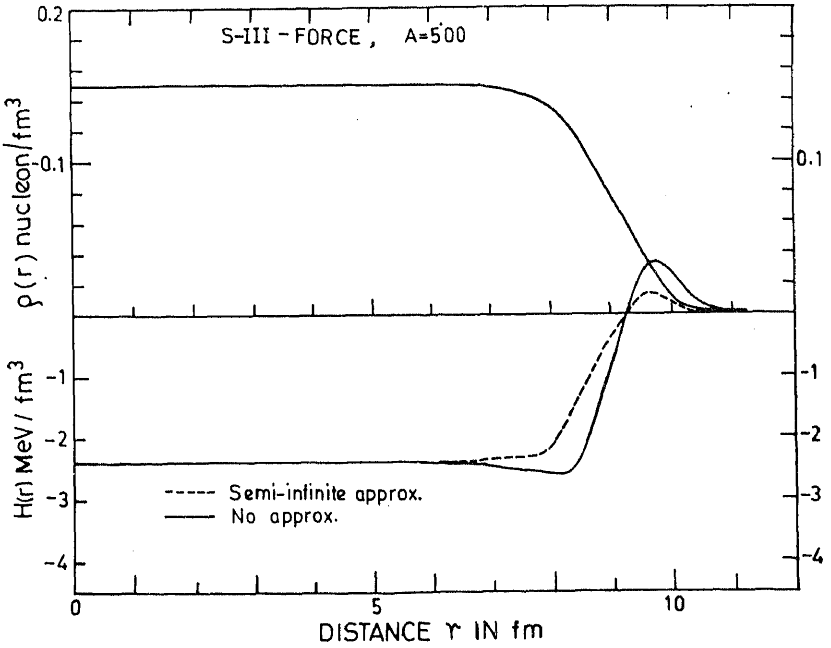

Figure 1. The plots of density distribution $\rho(r)$ and energy density distribution $H(r)$ for $A = 500$, SIII force with $\beta = 1/18$. The continuous curve is for $H(r)$ and dotted curve is obtained by approximating $\Delta\rho = \rho''$ in τ terms and using the same density profile $\rho(r)$ shown in the figure.

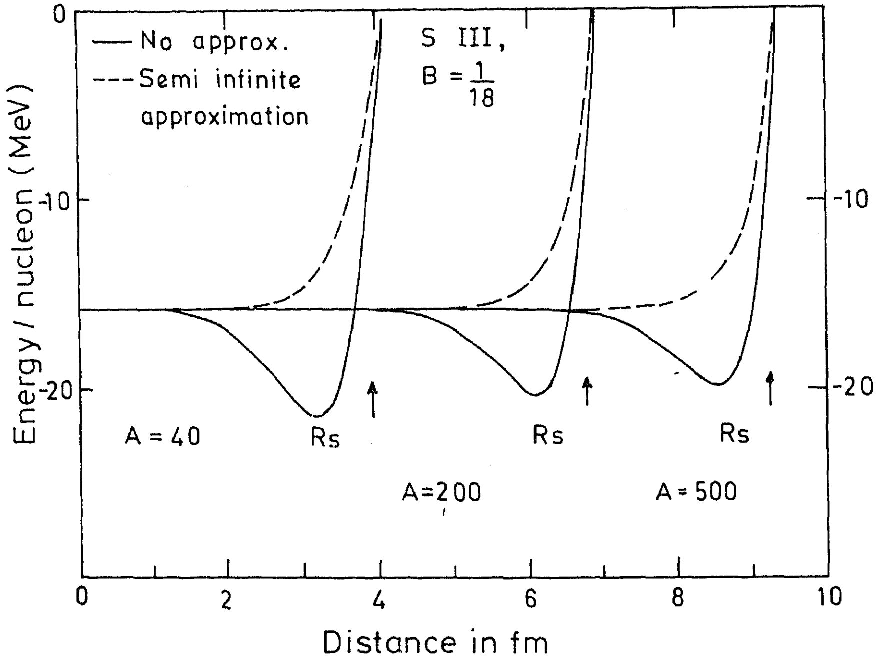

Figure 2. The plot of energy per nucleon $H(r)/\rho(r)$ for $A = 40$, 100 and 500 as a function of r for SIII force as in figure 1. The continuous curve is for total $H(r)$ and dashed curve is obtained under semi-infinite approximation in τ term.

also that the energy density shows positive values outside the sharp cutoff radius. The extra binding energy in the surface region arises due to the Lapalacian term in the kinetic energy term $\tau(r)$, and the contribution of this term increases with decreasing mass number A, due to the presence of $2/r\ \partial/\partial r$ term in the Δ operator. However, the plot of $H(r)$ calculated by approximating $\Delta\rho \simeq \partial^2\rho/\partial r^2$ in its kinetic energy term $\tau(r)$ (termed in this work as semi-infinite approximation) does not show maximum value in the surface region and the positive energy peak is also of much smaller magnitude.

The plots of energy density per nucleon $H(r)/\rho(r)$ as a function of r for three mass numbers $A = 40, 200$ and 500 are shown in figure 2. The surface peaking of the energy density per nucleon is not present when it is calculated in the semi-infinite approximation in the calculation of $H(r)$ and for the same density profiles, shown as dashed curves in figure 2. For the case of smaller nucleus $A = 40$, the maximum in the $H(r)/\rho(r)$ is larger than for the case of very heavy nucleus like $A = 500$. This clearly brings out the dependence of the energy density profiles on the mass number A and also the term responsible for it.

The calculated total energy E_T for a number of nuclei using the density profiles calculated by

(a) solving Euler's equations
(b) the parametrized form given by (15) of $\rho(r)$

are given in table 2 for SIII parameters under different approximations in the kinetic term τ, but using the same density profiles. In this table, case I is for the total energy of the nuclei calculated using τ as given in (10). In case II, E_T is calculated by assuming that the $\Delta\rho = \partial^2\rho/\partial r^2$ in the terms involving τ. In case III, E_T is calculated by neglecting the $\Delta\rho$ terms in the calculation of τ. As can be seen from table 2, the calculated value of E_T under the three cases are significantly different and arise due to the contribution of terms involving the integral $\int \rho\Delta\rho\, d^3r$, and the relative magnitude of this term increases for smaller nuclei.

In earlier self-consistent calculations i.e. solving Euler's equations exactly [6], it was observed that the effective surface diffuseness related to the (10%–90%) distance is almost independent of mass number, although the parameters (r_0, a, ν) of generalized Fermi distribution were found to vary. In order to quantify this mass dependence of nuclear surface structure we have calculated the surface moments of the density profiles around the inflexion point up to fourth order for SkM* force. Figure 3 shows the mass dependence of these surface moments of the density profile, and of the sharp cut-off radius parameter r_0. The skewness parameter μ_3 and μ_4 show large variation with mass number, whereas μ_2 varies rather slowly. The surface tension coefficient is known to depend on the width of the integrand, and therefore, the mass dependence of nuclear surface structure will not alter its estimate significantly. However, the curvature energy, which is the first moment of the surface peaked integrand in (3) and depend on the μ_3 and μ_4 surface moments will show large contribution from

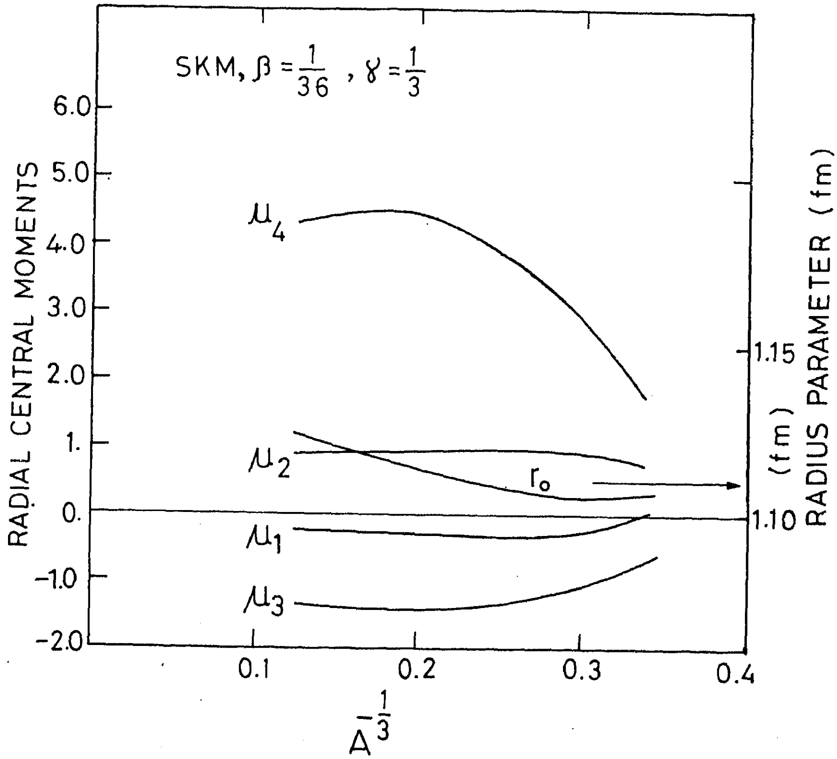

Figure 3. The plot of central moments μ_1, μ_2, μ_3, μ_4 of density distribution $\rho(r)$ around its inflexion point as a function of $A^{-1/3}$. The variation of sharp-cutoff radius parameter r_0 is also shown in the figure.

the mass dependence of the nuclear surface structure. The plot of r_0 as a function of $A^{-1/3}$ shows compressibility effects for larger nuclei $A > 100$ and for smaller masses the compression by the surface tension is compensated by surface structure changes. The magnitude of these quantities are a very sensitive function of the choice of kinetic energy functional and the Skyrme force parameters, but the general trends remain unchanged.

One can also calculate the surface moments of the energy density $H(r)$ for diffuse density distributions [10] $\rho(r)$ as

$$\begin{aligned} E_T = \varepsilon_0 A &+ S\left[\int_{-R_s}^{0} [H(\rho(r)) - \varepsilon_0\rho(r)]\,\mathrm{d}z + \int_0^{\infty} H(\rho(r))\,\mathrm{d}z\right] \\ &+ C\left[\int_{-R_s}^{0} [H(\rho(r)) - \varepsilon_0\rho(r)]\,z\mathrm{d}z + \int_0^{\infty} H(\rho(r))\,z\mathrm{d}z\right] \\ &+ G\left[\int_{-R_s}^{0} [H(\rho(r)) - \varepsilon_0\rho(r)]\,z^2\mathrm{d}z + \int_0^{\infty} H(\rho(r))\,z^2\mathrm{d}z\right]. \end{aligned} \tag{16}$$

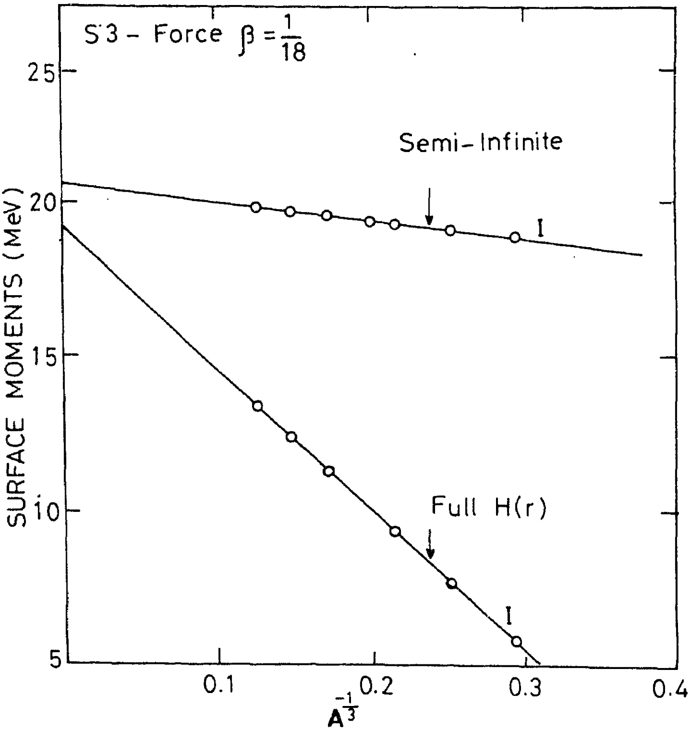

Figure 4. The plot of surface moments of energy density profile $H(r)$ around R_s as a function of $A^{-1/3}$. The semi-infinite values are calculated by $\Delta\rho = \rho''$ approximation in τ-terms.

However, we have calculated the surface moments around sharp cut-off radius using (3) for a number of nuclei and with density profiles calculated in two ways. Figure 4 shows the plot of the surface energy coefficient as a function of $A^{-1/3}$. The extrapolation of these quantities in the nuclear matter limit $A \Rightarrow \infty$, converge to the asymptotic value as expected since the ratio $a/R_s \Rightarrow 0$. The linear extrapolation shown in figure 4 for the nuclear matter limit gives a good estimate for the nuclear matter surface energy coefficient. It can be seen from the figure that the extrapolated value of a_s for full $H(r)$ and the corresponding semi-infinite approximation differ by about 1·5 MeV. In these surface moment calculations, we have used for the ε_0 the value of energy density h_0 at the centre of the nucleus with mass number A, which is to be associated with the volume energy coefficient inclusive of the compressibility effects. Figure 5 shows the plot of this quantity for the two forces RATP and SIII. For semi-infinite approximation case the plot of the volume term coefficient a_v shows the expected parabolic dependence in $A^{-1/3}$ due to compressibility effects. For full $H(r)$, the volume term shows deviations from this simple parabolic dependence for small mass numbers. The increase in this quantity arises only due to the Δ-terms. For

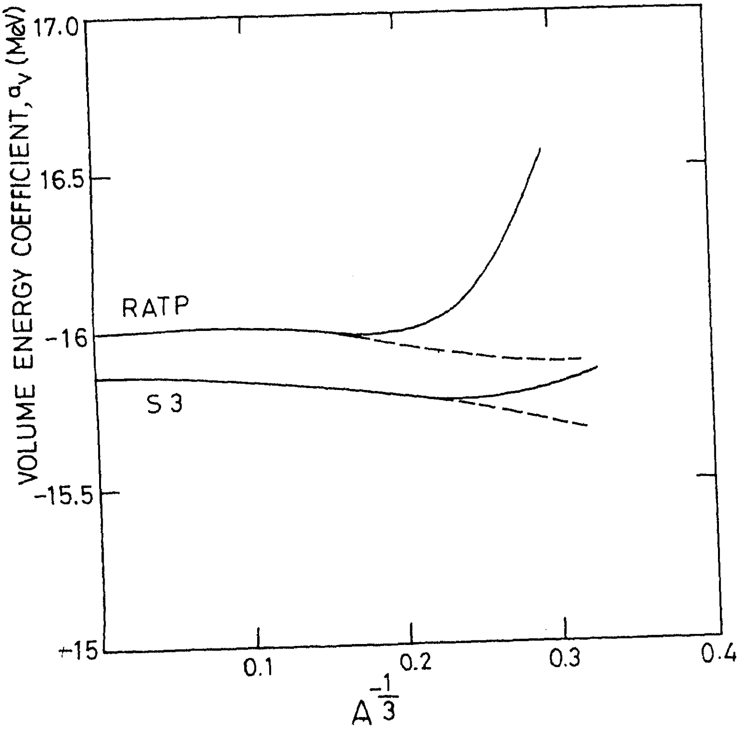

Figure 5. The plot of volume energy coefficient a_v versus $A^{-1/3}$ for SIII and RATP forces. The dashed curve shows the result with semi-infinite approximation in τ expressions.

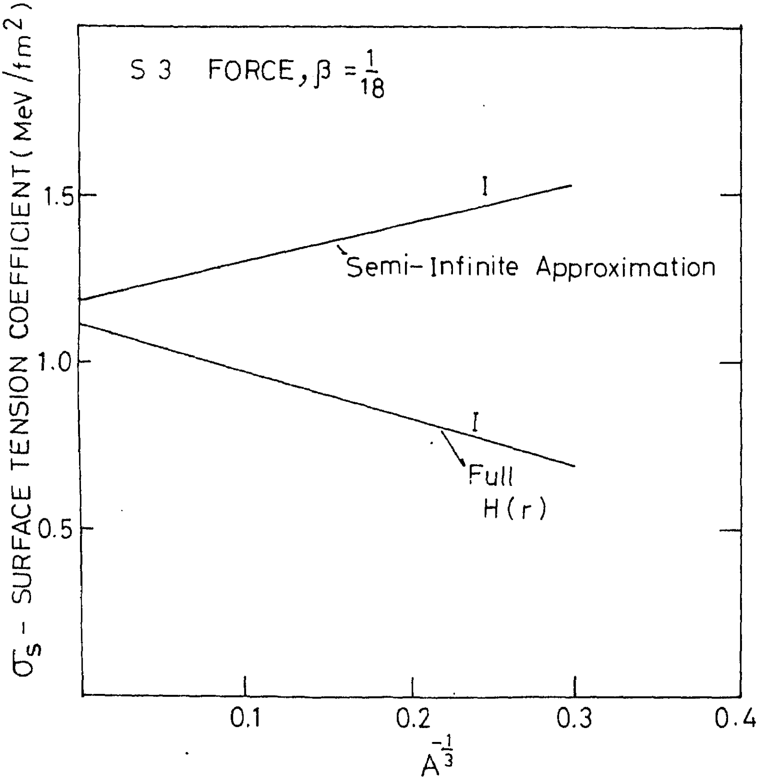

Figure 6. Same as for figure 5, but for surface tension coefficient $\sigma_s(A)$ as a function of $A^{-1/3}$.

RATP force this contribution is rather very large, whereas for SIII and SkM forces these deviations are small and very similar.

The surface tension coefficient σ_s calculated as a coefficient of $4\pi R_s^2$ term in (3) for the total energy density $H(r)$ and is plotted in figure 6 and it almost decreases linearly with $A^{-1/3}$ for SIII force. For semi-infinite approximation $\Delta\rho = \partial^2\rho/\partial r^2$ in the calculation of energy density $H(r)$, the derived surface tension coefficient σ_s increases almost linearly with $A^{-1/3}$. This increase of σ_s with mass number arises due to the diffuseness correction in the sharp cut-off radius R_s. This diffuseness contribution gives rise to geometric contribution from the surface energy term [10] to the curvature energy term.

The effective curvature energy coefficient a_c^* consists of three parts [1, 6, 9] volume compressibility contribution from a_v'' expansion; geometrical component from surface moment expansion of a_s', and the leading term of the curvature moment expansion a_c^∞ as given in (8). The plots of the curvature moments a_c as a function of $A^{-1/3}$ are shown in figure 7 for the full $H(r)$, and for $H(r)$ calculated under the semi-infinite approximation. Table 3 contains the values of a_c^*, and its components obtained by extrapolation of the surface moment a_s, volume term a_v and curvature moment a_c^∞ for the SIII interaction for the two cases shown in the figures 4, 5 and 7. It can be seen from table 3, that the effective a_c^* is smaller in magnitude and even negative for total $H(r)$ density profiles. Whereas, the value of a_c^* for the semi-infinite approximation

Table 3. Three components of effective curvature energy a_c^*, using the surface moments of $H(r)$ around the sharp radius R_s, with and without the semi-infinite approximation in the Δ term in the kinetic energy term $\tau(r)$.

Force	Case	a'_s	a'''_v	a_c^∞	a_c^*
SIII	Total $H(r)$	− 25·73	2·44	22·82	− 0·5
	Semi-infinite	15·94	2·20	− 8·92	9·24

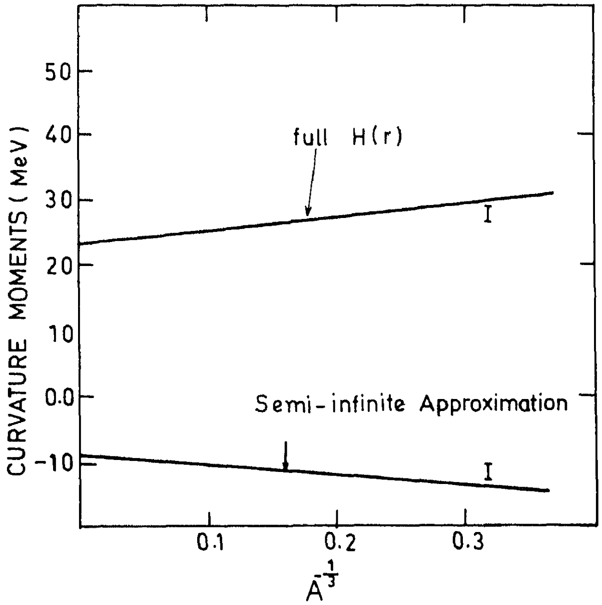

Figure 7. Same as for figure 5, but for curvature moments of $H(r)$.

of $H(r)$ is positive, large $\cong 9$ MeV and is comparable with the values obtained in earlier studies of curvature energies.

The second moments of the surface expansion of $H(r)$ i.e. Gauss curvature moments have been plotted against the $A^{-1/3}$ in figure 8 for SIII forces. It can be seen that for semi-infinite approximation the value of $a_0 \cong 8$ MeV and does not vary much with mass number (variation less than 2 MeV) showing that the shape of the surface peaked integrand does not change with mass number and the accuracy of the surface moments is of the order of 1 MeV. For total $H(r)$, the a_0 values vary from -5 to 8 MeV in the mass range of interest, indicating that in this case the surface structure changes and the second moment brings this out dramatically by changing from negative to positive values. The effective values of a_0^* is a sum of contribution from a_v, a_s, a_c expansions as given in (8).

In order to obtain the surface, curvature energy coefficients for the nuclear matter limit in a more quantitive way, we have used the power series expansions given in eq. (8), and the surface, curvature and gaussian curvature moments calculated for the sequence of nuclei. Table 4 gives these values for the three representative Skyrme parameter sets. The magnitude of curvature energy coefficient in the present

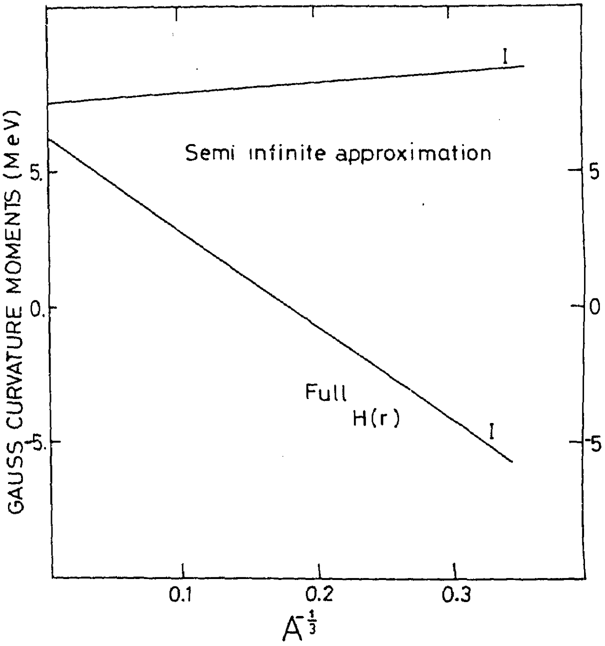

Figure 8. Same as for figure 5, but for Gauss curvature moments of $H(r)$.

Table 4. Nuclear matter values of the volume energy coefficient, surface energy coefficient, effective curvature energy coefficient and Gauss effective energy coefficient for the three Skyrme forces using the total $H(r)$ and the proposed procedure. The second row for each force is obtained by fitting the total energy E_T to the leptodermous expansion of eq. (4).

Force	a_v^∞	a_s^∞	a_c^*	a_0^*
SIII	-15.847	19.26	-0.5	27.0
SIII	—	—	-1.0^+	17.8^+
SkM	-15.71	17.92	2.4	21.0
SkM	—	—	3.8^+	12.0^+
RATP	-15.96	18.90	3.4	20.0
RATP	—	—	4.8^+	12.7^+

calculations is found to be very small, the sign depending on the Skyrme interaction parameters. The values for the a_c^* obtained in the present calculations are very much different from those obtained in earlier studies for all the three Skyrme forces. For some Skyrme forces this term is even negative, whereas all earlier calculations lead to large postive values only.

Another way to obtain the coefficients in the LDM mass relations is to expand the total energy E_T in power series of $A^{-1/3}$ directly as in (4). These fitted constants are highly correlated. However in model masses, one can fix the leading term volume energy a_v^* and surface constant a_s^* depending on the Skyrme interaction chosen, and therefore, one can obtain the remaining curvature terms reliably by fitting directly E_T values. Tables 4, also contains the values (denoted by +) so obtained which are in general agreement with the values deduced from the surface moment expansion, and thus shows the accuracy of the procedure adopted. These calculated coefficients (a_v^*, a_s^*, a_c^*, a_0^*) are consistent with semi-empirical mass fits, which demand small values of a_c^* and non-zero values of a_0^* coefficient.

4. Summary

In conclusion, leptodermous expansion of the ground state energies E_T of finite nuclei has been carried out starting from the semi-classical EDF theory. The surface, curvature and Gauss curvature contributions were obtained from the surface moments of the energy density profile $\mathscr{H}(r)$ around sharp cut-off radius R_s for a sequence of nuclei with $N = Z$ and without any Coulomb interaction. A transition to the LDM type expansion in $A^{-1/3}$ was then made by power series expansion of the surface moments of finite nuclei. The effective curvature energy coefficient a_c^* was found to be very small for the three Skyrme forces S-III, SkM, RATP for LDM type expansion. The calculated total energies E_T when fitted by the least squares to eq. (4) also yielded same values for the LDM coefficients as obtained from the leptodermous expansion method and the power series expansion as in eq. (8). It was also found that the semi-infinite approximation as used in earlier EDF calculations results in overestimates of effective curvature energy. Thus we have resolved the anomaly in the curvature energy coefficient calculated on the basis of EDF formalism and its semi-empirical estimate from the least squares fit to the experimental ground state masses.

Acknowledgements

One of the authors (SKK) is thankful to J Treiner and H Krivine and O Bohigas for use of their code in solving the Euler's equation for density profiles and also for many fruitful discussions on various aspects of this problem in the initial stages of this work during his stay at Institut de Physique Nucleaire, Orsay. We are also thankful to S S Kapoor for many suggestions during the course of these studies. We are greatly indebted to the referee for carefully going through the manuscript and making very useful suggestions in making it concise and clear.

References

[1] M Brack, C Guet and H-B Hakansson, *Phys. Rep.* **123**, 275 (1985)
[2] W D Myers and W J Swiatecki, *Ann. Phys.* **55**, 395 (1969)
[3] W D Myers, *Droplet model of atomic nuclei*, (IFI/Plenum, New York, 1977)
[4] P A Seeger and W M Howard, *Nucl. Phys.* **A238**, 491 (1975)
[5] H J Krappe, J R Nix and A J Sierk, *Phys. Rev.* **C22**, 992 (1979)
[6] J Treiner and H Krivine, *Ann. Phys.* **170**, 406 (1986)
[7] J W Negele and D Vautherin, *Nucl. Phys.* **A207**, 298 (1973)

[8] W Stocker, J Bartel, J R Nix and A J Sierk, **A489**, 252 (1988)
M Brack, *Phys. Rev.* **B39**, 3533 (1989)
M Durand, P Schuck and X Vinas, ISN Grenoble Preprint (1991)

[9] B Grammaticos, *Z. Phys.* **A312**, 99 (1983)

[10] S K Kataria, V S Ramamurthy, S S Kapoor, Aruna Nijasure and A K Dutta, *DAE symp. on Nucl. Phys.*, Bombay, **B31**, 3 (1988)

[11] P Hohenberg and W Kohn, *Phys. Rev.* **136**, B864 (1964)

[12] F Tondeur, A K Dutta, J M Pearson and R Behrman, *Nucl. Phys.* **A470**, 93 (1987)

PRAMANA
— journal of
physics

© Printed in India

Vol. 42, No. 2,
February 1994
pp. 123–133

Mass asymmetry dependence of fusion time-scales in $^{11}B + ^{237}Np$ and ^{12}C, ^{16}O, $^{19}F + ^{232}Th$ reactions in a dynamical trajectory model

KIRAN KUMAR, R K CHOUDHURY and A SAXENA
Nuclear Physics Division, Bhabha Atomic Research Centre, Bombay 400085, India

MS received 14 June 1993; revised 2 November 1993

Abstract. Dynamical trajectory calculations were carried out for the reactions of $^{11}B + ^{237}Np$ and ^{12}C, ^{16}O and $^{19}F + ^{232}Th$, having mass asymmetries on either side of the Businaro–Gallone critical mass asymmetry α_{BG}, in order to examine the mass asymmetry dependence of fusion reactions in these systems. The compound nucleus formation times were calculated as a function of the partial wave of the reaction for all the systems. This study brings out that for systems with $\alpha < \alpha_{BG}$, the formation times are significantly larger than for $\alpha > \alpha_{BG}$, which is caused by the dynamical effects involved in the large scale shape changes taking place in the fusion process as well as due to the interplay between the thermal and the collective motion during the collision process. The calculated time scales are comparable to the experimental values derived from the pre-fission neutron multiplicity measurements.

Keywords. Heavy ion fusion reactions; time scales; dynamical trajectory model; dependence on mass asymmetry.

PACS No. 25·70

1. Introduction

There have been a number of experimental and theoretical investigations in the past [1–9] to determine the role of the entrance channel mass asymmetry in the fusion dynamics of heavy ion induced reactions. Recently, in the work of Ramamurthy *et al* [4] on the fission fragment angular distributions, it was pointed out that the value of α relative to the liquid drop Businaro-Gallone critical mass asymmetry [10] (α_{BG}) may be important in deciding the fusion path in heavy ion reactions. There have been also some experimental studies to determine the fusion-fission time delay from the studies of pre-scission neutron multiplicities in heavy ion induced reactions which seem to suggest the above behaviour. In the work of Saxena *et al* [6], the fusion-fission time scales were determined for $^{11}B + ^{237}Np$ and ^{11}B, ^{12}C, $^{16}O + ^{232}Th$ systems by measuring the pre-scission neutron multiplicities and it was found that for $^{16}O + ^{232}Th$ system ($\alpha < \alpha_{BG}$) the fusion-fission time is larger than that for $^{11}B + ^{237}Np$, $^{11}B + ^{232}Th$ and $^{12}C + ^{232}Th$ systems ($\alpha > \alpha_{BG}$).

The dynamical threshold for the onset of fusion depends critically on the total charge, orbital angular momentum and mass asymmetry of the system. For mass asymmetric reactions, there are two different saddle points in the potential energy surface [7–9]. The first is the Bohr-Wheeler mass-symmetric saddle point and the second is the conditional saddle point which is obtained with the constraint that mass asymmetry is fixed at the initial value of the reaction. During the fusion reaction, the target-projectile system is trapped in the valley of the fusion potential, and the dinuclear system drifts along the mass asymmetry co-ordinate by exchange of mass to form a fused nucleus. During this time the inter-nuclear distance R changes because the distance R_p corresponding to the bottom of the pocket in the potential depends on both the mass asymmetry α and angular momentum. The drift along mass asymmetry α will be governed by the potential energy of the quasi-molecular system which has been formed. The total energy calculated with the potential energy $V(R_p)$ taken for several values of initial mass asymmetry α shows that there are two regions of interest: the one corresponds to the system which will drift towards symmetry for $\alpha < \alpha_{BG}$ and the second region corresponds to the system which will drift towards more asymmetric configuration for $\alpha > \alpha_{BG}$. In other words the initial mass asymmetry of the system may have a great influence on the latter development along the mass asymmetry coordinate. There has not been, however, so far detailed dynamical study of the fusion time scales for systems lying on either side of the critical BG point, to bring out clearly the influence of mass asymmetry in such reactions.

The dynamical evolution of the two colliding nuclei can be described by a sequence of shapes which basically consist of two spheres connected by a conical neck. The three macroscopic variables used are: the distance separating the two centres of mass, the neck co-ordinate and the mass asymmetry co-ordinate. The system is then described by the classical equations of motion for obtaining the mean values of the macroscopic variables and their second moments, with the frictional forces taken to be proportional to the velocities in the collective degree of freedom. We have used the formalism of Feldmeier *et al* [11, 12] to study the fusion dynamics of various target projectile systems with mass asymmetries lying on either side of the liquid drop Businaro-Galline critical mass asymmetry. The systems studied are $^{11}B + ^{237}Np$ and ^{12}C, ^{16}O, $^{19}F + ^{232}Th$ reactions for which the fusion-fission time scales have been experimentally deduced from pre-scission neutron multiplicity measurements [6, 13]. It may be noticed that $^{11}B + ^{237}Np$ and $^{16}O + ^{232}Th$ lead to the same compound nucleus, but have mass asymmetries lying on either side of α_{BG}. The calculated values of the fusion time scales are found to compare well with the experimental values. The details of the calculation procedure are given in the section below. Section 3 gives the results and discussion of the calculations and § 4 contains the summary on the present work.

2. Classical dynamical calculations

We use the model of Feldmeier *et al* [11, 12] where the colliding nuclei are treated as two Fermi gases which exchange particles, momentum and entropy through a window in the mean single particle potential. The time development of the collision trajectories are calculated by solving a Langevin equation with a fluctuating dissipative force. The properties of the fluctuating force are determined from a microscopic picture of particle exchange between two nuclei. The macroscopic shapes of the nuclear system are represented by axially symmetric configurations with sharp surfaces. These shapes are uniquely determined by three macroscopic degrees of freedom: the distance between the nuclei s, the neck coordinate σ, and the mass asymmetry Δ defined as:

$$\begin{aligned} s &= \text{distance between two sphere centres} \\ \sigma &= [V_0 - (4\pi/3)R_1^3 - (4\pi/3)R_2^3]/V_0 \\ \Delta &= [R_1 - R_2]/[R_1 + R_2] \end{aligned} \tag{1}$$

where V_0 is the total volume of the system and is independent of $\{s, \sigma, \Delta)$, R_1 and R_2 are the radii of the two interacting nuclei. If the symmetry axis is taken along z-direction, the shapes of the nuclei can be specified by the profile function $P(s, \sigma, \Delta; z)$ which is defined as [14]

$$P^2(s, \sigma, \Delta; z) = \begin{cases} R_1^2 - z^2 & \text{for} \quad -R_1 \leqslant z \leqslant z_1 \\ a_1 + bz + cz^2 & \text{for} \quad z_1 \leqslant z \leqslant z_2 \\ a_2 + bz + cz^2 & \text{for} \quad z_3 \leqslant z \leqslant z_4 \\ R_2^2 - (z-s)^2 & \text{for} \quad z_4 \leqslant z \leqslant s + R_2 . \end{cases} \tag{2}$$

This representation includes single shapes as well as shapes consisting of two fragments. All the parameters $R_1, R_2, a_1, a_2, b, c, z_1, z_2, z_3, z_4$ depend on the three degrees of freedom defined in (1). In addition there are three rotational degrees of the intrinsic and relative rotation of the di-nuclear complex. Denoting the six macroscopic co-ordinates and their momenta by $(q(t), p(t))$, the Langevin equation can be written as:

$$\begin{aligned} \mathrm{d}\mathbf{p}/\mathrm{d}t &= -\mathrm{d}T/\mathrm{d}\mathbf{q} - \mathrm{d}V/\mathrm{d}\mathbf{q} + \mathbf{X}(t) \\ \mathrm{d}\mathbf{q}/\mathrm{d}t &= M^{-1}\mathbf{p} \end{aligned} \tag{3}$$

where $T = 1/2(\mathbf{p}M^{-1}\mathbf{p})$ denotes the collective kinetic energy and M denotes the mass tensor, while V stands for the conservative potential, and $X(t)$ is the fluctuating force caused by the coupling of the collective degrees of freedom to the intrinsic degrees of freedom. The mass tensor is calculated from the profile function by assuming incompressible and irrotational flow of mass during the shape evolution in the collision. The expression relating the mass parameters to the profile function (eq. (2)) are given in [11]. The potential energy V is calculated by associating with each shape the nuclear and Coulomb energies as follows. The nuclear potential, V_n can be written as a double volume integral of a Yukawa plus exponential folding function [15]:

$$V_n = \frac{-C_s}{8\pi^2 r_0^2 a^3} \int_{\text{shape}} \mathrm{d}^3\mathbf{r}\,\mathrm{d}^3\mathbf{r}' \left(\frac{1}{a} - \frac{2}{|\mathbf{r}-\mathbf{r}'|}\right) \exp\left(-\frac{|\mathbf{r}-\mathbf{r}'|}{a}\right) \tag{4}$$

where

$$c_s = a_s[1 - k_s((N-Z)/A)^2]; \quad a_s = 21{\cdot}7\,\text{MeV}; \quad K_s = 3$$

$$r_0 = 1{\cdot}18\,\text{fm}, \quad a = 0{\cdot}65\,\text{fm}.$$

The Coulomb potential is calculated assuming a uniform charge distribution ρ_c with a sharp surface:

$$V_c = \frac{1}{2}\rho_c^2 \int_{\text{shape}} \mathrm{d}^3\mathbf{r}\,\mathrm{d}^3\mathbf{r}' \frac{1}{|\mathbf{r}-\mathbf{r}'|} \tag{5}$$

The double folding integrals in (4) and (5) are calculated numerically, where the six-fold integral is transformed to a three-fold integral by using a two-fold application of the Gauss divergence theorem for axially symmetric shapes [15]. The energies depend on the three shape degrees of freedom (s, σ, Δ) via the dependence of the profile function $P(q, z)$.

In the above equations, the motion of the system is governed by a strong dissipative force $X(t)$, which is related to the friction and diffusion terms obtained from particle exchange model. One-body dissipation is assumed to be predominant as they have been found to be more relevant for these types of reactions [16].

One-body dissipation: This picture makes use of long mean free path of a nucleon in a nucleus at an excitation energy which is not too high and the mean field of the nucleus acts as a confining vessel. Wall dissipation occurs when particles which are about to hit the wall possess a mean field velocity different from the wall velocity. So after scattering from the wall, their velocity distribution shows a mismatch with the rest of the fluid. The randomisation hypothesis assumes that the bounced particles obtain the velocity distribution of the bulk before they hit the wall again. Window friction occurs for two gases with different velocities in contact at a window. Again particles crossing the window show a mismatch in their velocity distribution with respect to the gas volume in which they are entering. The randomisation assumption implies that the particles have forgotten their original velocity distribution before they return to the window. The fluctuating force $X(t)$ is thus, given by:

$$X(t) = \Sigma R_{ij}(M^{-1}p)_j \tag{6}$$

where R_{ij} is the friction tensor [11]. The energy dissipation rate is given by:

$$\begin{aligned} Q^{\text{wall}} &= \Sigma R_{ij}^{\text{wall}} \dot{q}_i \dot{q}_j \\ Q^{\text{window}} &= \Sigma R_{ik}^{\text{window}} \dot{q}_i \dot{q}_k \\ Q^{\text{w+w}} &= Q^{\text{wall}} + Q^{\text{window}} \end{aligned} \tag{7}$$

As noted earlier, the friction tensor is governed by exchange of nucleons between the interacting nuclei, which results in a fluctuating force (eqn (6)).

To allow a smooth transition between mono and the dinuclear regimes, a form factor f_r is introduced which allows for a smooth transition between the two dissipation mechanisms:

$$Q = (1 - f_r)Q^{\text{w+w}} + f_r Q_{\text{mono}}^{\text{wall}} \tag{8}$$

where the form factor f_r is defined as:

$$f_r(x) = \begin{cases} 0 & 0{\cdot}0 \leqslant x \leqslant 0{\cdot}8 \\ \sin^2\left(\dfrac{x - 0{\cdot}8}{0{\cdot}2}\dfrac{\pi}{2}\right) & 0{\cdot}8 < x < 1{\cdot}0 \\ 1 & x > 1{\cdot}0 \end{cases} \tag{9}$$

where

$$x = \begin{cases} 0 & ;\ \text{for separated shapes} \\ R_{\text{neck}}^2/[\min\{R_1^2, R_2^2\}]; & \text{for shapes with neck} \end{cases} \tag{10}$$

The quantity x is a measure of the ratio between the window area and the wall area surrounding a particle in the smaller part of the shape. We have solved the above equations of motion to study the collision trajectories for various values of the partial waves of the reaction. The results of the calculations are presented in the next section.

3. Results and discussion

We have carried out the calculations for the systems of $^{11}B + ^{237}Np$ and ^{12}C, ^{16}O, $^{19}F + ^{232}Th$ at 77, 86, 104 and 114 MeV bombarding energies respectively, corresponding to nearly same compound nuclear excitation energies for all the systems. The equations of motion (eq. (2)) are solved for a given angular momentum l to determine the time development of the various macroscopic variables defined in eq. (1). The angular momentum l_{crit}, below which the system fuses, is used to calculate the fusion cross-section. For the above systems, the calculated fusion cross sections agree with the experimental systematics [4] within 10%.

Figures 1(a, b, c) show the dependence of s, σ and Δ as a function of time for the four systems for the angular momentum $l = 38\hbar$, which is close to the fusion critical

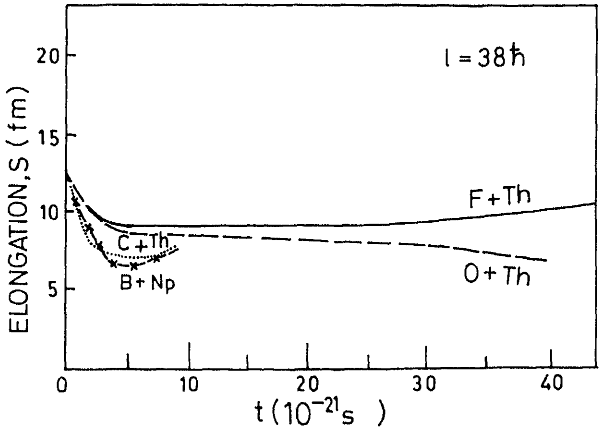

Figure 1a. Time dependence of elongation s for the systems B + Np, C + Th, O + Th and F + Th.

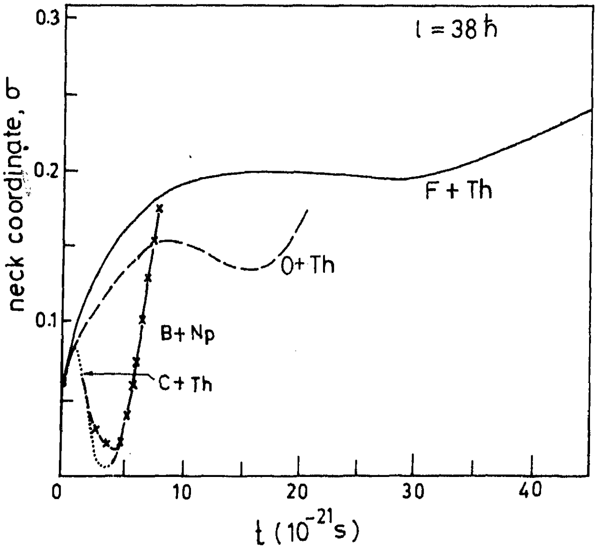

Figure 1b. Same as 1a for neck co-ordinate σ.

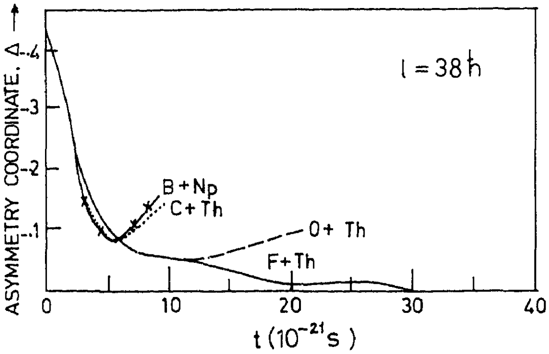

Figure 1c. Same as 1a for asymmetry co-ordinate Δ.

angular momentum l_{crit} for all these target-projectile systems. It is found from figures 1a and 1b that the time development of the elongation and neck coordinates shows quite similar behaviour for the $^{11}B + ^{237}Np$ and $^{12}C + ^{232}Th$ reactions, while for $^{16}O + ^{232}Th$ and $^{19}F + ^{232}Th$ reactions the behaviour is quite different. For the latter cases, there is a significant streching and neck development as the two nuclei fuse, while for $^{11}B + ^{237}Np$ and $^{12}C + ^{232}Th$ reactions, the systems go towards more compact and mononuclear shapes in a shorter time scale. Similarly, as seen from figure 1c, the asymmetry variable Δ decreases sharply with time for $^{16}O + ^{232}Th$ and $^{19}F + ^{232}Th$ systems indicating formation of symmetric shapes while for $^{11}B + ^{237}Np$ and $^{12}C + ^{232}Th$ system Δ shows a minimum value of $-0{\cdot}08$ units at around 5×10^{-21} s and then increases to $-0{\cdot}15$ units before fusion takes place.

Figure 2 shows schematically the time-evolution of the shapes for $l = 38\hbar$ as the two nuclei undergo fusion. This figure brings out clearly differences in the shape evolution as a function of time for the four systems. The fusion time t_{form} (t_{form} is time taken from the beginning of the interaction to compound nucleus formation) for $l = 38\hbar$ is found to be about 8×10^{-21} s for $^{11}B + ^{237}Np$ and $^{12}C + ^{232}Th$ systems, while for the case of $^{16}O + ^{232}Th$ and $^{19}F + ^{232}Th$ systems, it is $\approx 20 \times 10^{-21}$ s and $49{\cdot}3 \times 10^{-21}$ s respectively. As mentioned above, the excitation energies of these systems are roughly same i.e. 59·9, 58·8, 60·8 and 64·0 MeV respectively and one can distinctly visualise the differences in the formation time to be related to the change in the entrance channel mass asymmetry around the B–G mass asymmetry α_{BG}.

Figures 3(a, b, c) shows the typical trajectories in the (s, σ) plane for various l-values for $^{11}B + ^{237}Np$ and ^{16}O, $^{19}F + ^{232}Th$ systems. The numbers indicated are the time taken by the system to reach the end-points in the trajectories. It is seen that for the case of $^{11}B + ^{237}Np$ reaction (figure 3(a)), the mono-nuclear shapes are reached for $l = 38\ \hbar$ and lower l-values, while the system reseparates for $l = 40\hbar$, characterised by deep inelastic behaviour with a very fast transition time of about $0{\cdot}6 \times 10^{-21}$ s. For $^{16}O + ^{232}Th$ and $^{19}F + ^{232}Th$ systems (figures 3b and 3c), the transition between fusion and deep inelastic reactions is not sharply divided in the l-domain. For these systems there is a range of l-values above fusion l-crit for which the composite system goes through substantial amount of stretching and neck formation (being still in the di-nuclear regime) and there is large amount of mass exchange and energy relaxation before the system reseparates into symmetric fragments. For example, as seen from figure 3b, for $^{16}O + ^{232}Th$ system, at $l = 42\hbar$ the neck co-ordinate grows to 0·28 at an elongation of $s = 13$ fm corresponding to the touching distance of the target and

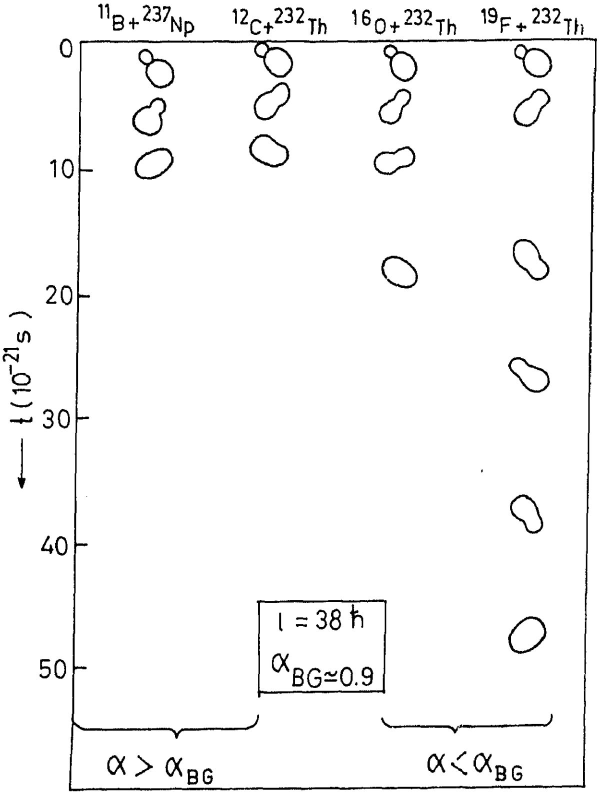

Figure 2. Schematic diagram of the evolution of the nuclear shapes as a function of time.

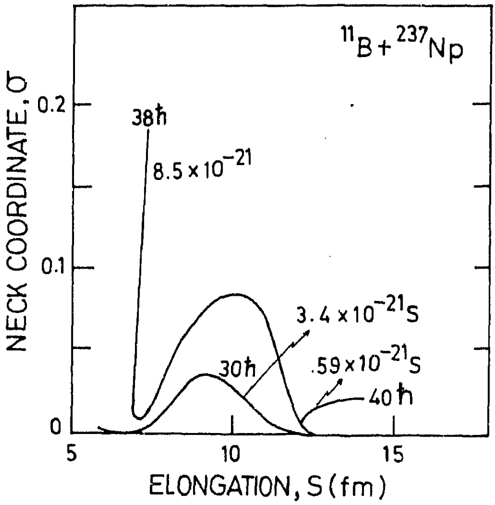

Figure 3a. Typical trajectories in (s, σ) plane for the reaction of B + Np for $l = 30\hbar$, $38\hbar$ and $40\hbar$.

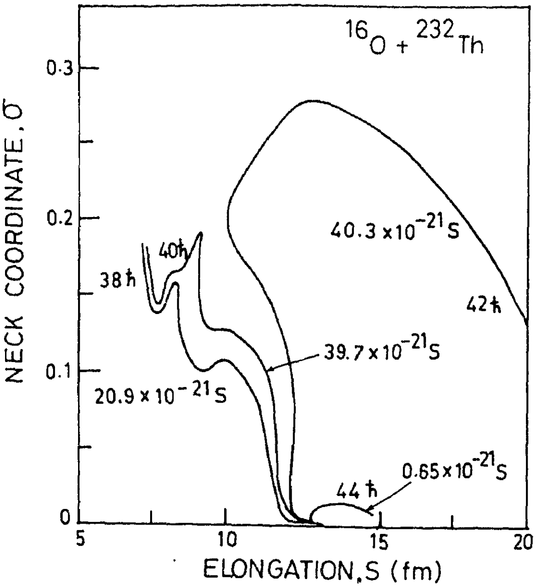

Figure 3b. Same as 3a for O + Th.

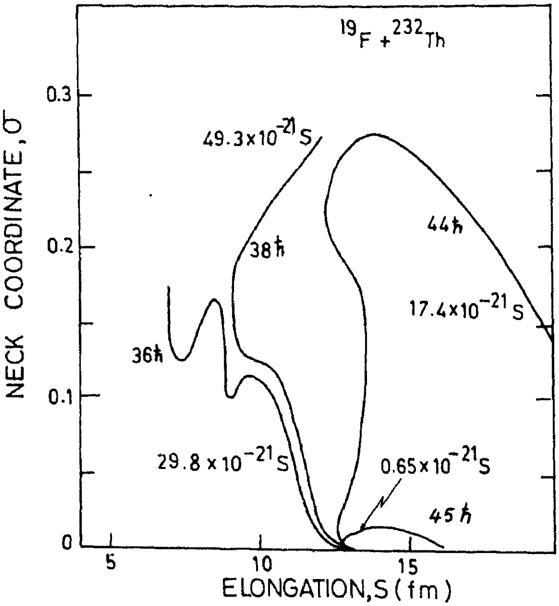

Figure 3c. Same as 3a for F + Th.

projectile, after which the system stretches a lot ($s \approx 20\,\mathrm{fm}$), and the neck co-ordinate decreases to 0·13 before it fragments into two symmetric pieces. At $l = 44\hbar$, however, the system reseparates very quickly as expected for peripheral deep inelastic type of events. Similar behaviour is also observed for $^{19}F + ^{232}Th$ system for trajectories corresponding to l-values between 40 and $44\hbar$, where a large amount of mass exchange as well as stretching of the di-nuclear system takes place before reseparation into symmetric fragments. The transition time for $l = 44\hbar$ in ^{19}F + ^{232}Th reaction is $17·4 \times 10^{-21}$ s indicating that the system undergoes several revolutions, before splitting into two fragments. At $l = 45\hbar$, the system reseparates quickly as a deep inelastic event.

The dependence of t_{form} as a function of the angular momentum of the compound nucleus is shown for all the four systems in figure 4. It is observed that for all l-values, the compound nucleus formation time, t_{form} is higher for ^{16}O + ^{232}Th and ^{19}F + ^{232}Th systems as compared to that for the other two systems. The compound nucleus formation time averaged over the spin distribution for the ^{11}B + ^{237}Np and ^{16}O + ^{232}Th reactions, which lead to the same compound nucleus ^{248}Cf are $2·86 \times 10^{-21}$ s and 11×10^{-21} s respectively. From the measurement of the pre-scission neutron multiplicities [6], it was observed that ^{16}O + ^{232}Th system shows longer fusion-fission time than ^{11}B + ^{237}Np system and the differences in the formation time between the

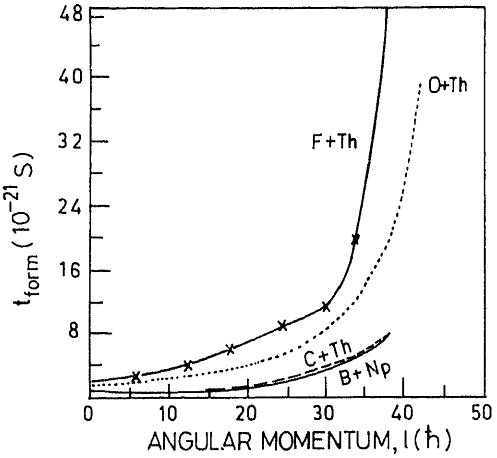

Figure 4. Variation of the compound nucleus formation time with angular momentum for various system.

Table 1. The values of $\alpha/\alpha_{\text{BG}}$ are shown in bracket below each system.

	$t_{\text{form}}(10^{-21}$ s)			
	B + Np	C + Th	O + Th	F + Th
$l\hbar$	1·02	1·01	0·97	0·94
0	0·56	0·60	1·2	1·73
10	0·72	0·80	2·1	3·13
15	0·90	1·00	2·8	5·21
20	1·20	1·35	4·0	7·52
25	1·80	2·20	5·4	9·32
30	3·40	4·00	8·2	11·02
34	4·80	5·20	12·3	20·19
38	8·00	8·00	20·0	49·30
average t_{form}	≈ 2·86	3·35	11·00	$17·2 \times 10^{-21}$

two systems was found to be $\approx(15 \pm 5) \times 10^{-21}$ s which is in agreement with the present calculation.

Table 1 gives a summary of the results of the calculations for the formation time for all the systems. The values of t_{form} averaged over the l-distribution are also shown in the table. It is clearly seen that for the systems studied, the fusion time scales are larger in case of $\alpha < \alpha_{BG}$ as compared to that with $\alpha > \alpha_{BG}$. It is also observed that the difference in the formation time increases significantly for higher partial waves.

4. Conclusion

The present calculations are based on the particle exchange picture and are found to be very effective in describing the dissipative transport phenomena involved in the heavy ion induced reactions leading to fusion. The applicabibity of this model is, however, confined to beam energies such that the mean field picture is valid for the interaction. Also since the calculation does not incorporate dynamic deforamtion, reactions below the Coulomb barrier cannot be described.

One can apply this model to study the detailed features of the peripheral collisions. The energy loss and mass exchange behaviour in such collisions will, however, be very sensitive to the assumptions of the dissipation mechanism assumed in the model.

The present calculations bring out many new features in the behaviour of the fusion reaction as a function of the initial mass asymmetry of target-projectile system near the liquid drop B–G mass asymmetry (α_{BG}). Firstly, compound nucleus formation time is found to be higher for all the l-values for ^{16}O, ^{19}F + ^{232}Th ($\alpha < \alpha_{BG}$) system compared to ^{11}B + ^{237}Np and ^{12}C + ^{232}Th systems ($\alpha > \alpha_{BG}$). The average compound nucleus formation time (summed over all l-values) is larger by $10\text{–}15 \times 10^{-21}$ s for systems having $\alpha < \alpha_{BG}$ as compared to systems with $\alpha > \alpha_{BG}$. Secondly, in the case of ^{16}O, ^{19}F + ^{232}Th reactions, there is a range of l-values beyond fusion l_{crit} for which the di-nuclear system undergoes several rotations and large stretching and neck formation before it reseparates into two symmetric fragments. These new class of events can be verified experimentally by carrying out selective measurements of fragment mass and angular distribution as a function of initial angular momentum of the reaction.

In summary, the calculations carried out in the present work show that the liquid-drop Businaro-Gallone mass asymmetry plays an important role in deciding the reaction dynamics and fusion time-scales in the heavy-ion reactions. The partial wave of the reaction has a strong effect on the reaction times in all the systems.

References

[1] B Haas, D Duchene, F A Beck, T Byrski, C Gehringer, J C Merdinger, A Nourredine, V Rauch, J P Vivien, J Barrette, S Tobbeche, E Bozek, J Styczen, J Keinonen, J Dudek and W Nazarewicz, *Phys. Rev. Lett.* **54**, 398 (1985)

[2] A Ruckelshausen, R D Fischer, W Kuhn, V Metag, R Muhlhans, R Novotny, T L Khoo, R V F Janssens, H Groger, D Habs, H W Heyng, R Repnow, D Schwalm, G Duchene, R M Freeman, B Haas, F Haas, S Hlavac, R S Simon, *Phys. Rev. Lett.* **56**, 2356 (1986)

[3] W P Zank, D Hilscher, G Ingold, U Jahnke, M Lehmann and H Rossner, *Phys. Rev.* **C33**, 519 (1986)

[4] V S Ramamurthy, S S Kapoor, R K Choudhury, A Saxena, D M Nadkarni, A K Mohanty, B K Nayak, S V S Sastry, S Kailas, A Chatterjee, P Singh and A Navin, *Phys. Rev. Lett.* **65**, 25(1990)

[5] G Smith, B Hass, A Alderson, I Ali, C W Beausang, M A Bentley, P Dagnall, P Fallon, G de France, P D Forsyth, U Huttmeier, P Romain, D Santos, P J Twin and J P Vivien, *Phys. Rev. Lett.* **68**, 158 (1992)
[6] A Saxena, A Chatterjee, R K Choudhury, S S Kapoor and D M Nadkarni, 1993 *Phys. Rev.* C (in press)
[7] C Gregoire, R Lucas, C Ngo and B Schurmann, *Nucl. Phys.* **A361**, 443 (1981)
[8] K T R Davies and A J Sierk, *Phys. Rev.* **C31**, 915 (1985)
[9] C Gregoire, C Ngoand and E Tomasi, *Nucl. Phys.* **A387**, 37 (1982)
[10] U L Businaro and S Gallone. *Nuovo Cimento* **5**, 315 (1957)
[11] H Feldmeier, *Rep. Prog. Phys.* **50**, 915 (1987)
[12] H Feldmeier and H Spangenberger, *Nucl. Phys.* **A428**, 223c (1984); **A435**, 229 (1985)
[13] J O Newton, D J Hinde, R J Charity, J R Leigh, J J M Bokhorst, A Chatterjee, G S Foote and S Ogaza, *Nucl. Phys.* **A483**, 126 (1988)
[14] J Blocki and W J Swiatecki, Report LBL-12811, (1982)
[15] H J Krappe, J R Nix and A J Sierk, *Phys. Rev.* **C20**, 992 (1979)
[16] J Blocki, R Planeta, J Brzychczyk and K Grotowski, *Z. Phys.* **A341**, 307 (1992)

PRAMANA
— journal of
physics

© Printed in India

Vol. 42, No. 2,
February 1994
pp. 135–139

Pre-equilibrium effects in the formation of meta stable states

R UPADHYAY, CH V SASTRY, R K JAIN and J RAMA RAO
Department of Physics, Banaras Hindu University, Varanasi 221 005, India

MS received 27 October 1993

Abstract. Isomeric yield ratios have been measured for $^{93}\mathrm{Nb}(\alpha, 2n)^{95m,g}\mathrm{Tc}$ reaction in the energy range 25–60 MeV. The ratios were compared with theoretical values obtained by means of two models one based on compound nucleus mechanism only and the other including pre-equilibrium effects. The trend of experimental ratios is better reproduced by the latter model, although there remains some discrepancy as to the magnitude at higher energies.

Keywords. Isomeric yield ratios; pre-equilibrium effects; moment of inertia; stack foil activation; γ-spectroscopy.

PACS No. 25·90

1. Introduction

Generally in nuclear reactions, the residual nucleus is formed in meta stable states, whenever, between a pair of its levels, the spin difference is large and energy difference small. The study of the cross-section ratio for the formation of the same pair of isomeric states of the residual nucleus, at different projectile energies is of great interest in understanding the reaction mechanism and in determining the spin distribution of nuclear level density [1]. The spin distribution of the compound system is determined by the angular momentum brought in by the projectile which changes with the energy of the projectile. This spin distribution is subsequently altered by particle emission and gamma de-excitation leading to the final spin distribution of the residual nucleus. With the increase in energy pre-equilibrium reaction mechanism dominates and the above picture changes drastically. The importance of this pre-equilibrium or pre-compound process has been emphasized by Blann [2]. The main result of such process is to enhance the emission of particles (nucleons or nuclear clusters) with high energy and predominantly in forward direction. The occurrence of pre-equilibrium reactions will undoubtedly affect the angular momentum distributions of the residual nuclei since high energy nucleons emitted in the forward direction will remove, on an average, much more spin than low energy nucleons evaporated isotropically from an excited compound nucleus in statistical equilibrium. Thus it is to be expected that pre-equilibrium processes would have a measurable influence on the yields of isomers with large difference in spins. For the above reasons it will be interesting to look at the variation of the isomeric yields and their ratio as a function of incident particle energy and to compare the observed trend of variation with those predicted by models based on compound nucleus mechanism only and others including pre-equilibrium effects also, to see the difference.

In literature, for the reaction $\mathrm{Nb}(\alpha, 2n)\mathrm{Tc}^{m,g}$, the individual cross-sections for isomeric and ground states as well as the isomeric ratio were reported (Gadioli *et al*

[3]; Ernst *et al* [4]; Branquinho *et al* [5]) and compared [5] with hybrid model, but only up to 48 MeV. The aim of this paper is to measure the isomer ratios for the reaction ^{93}Nb($\alpha, 2n$)^{95m,g}Tc in the extended energy up to 60 MeV and to compare the results, on the one hand, with the predictions of Huizenga-Vandenbosch model based only on the compound nucleus mechanism, and on the other, with the latest STAPRE model [6] including the pre-equilibrium effects in the framework of exciton model. The standard stack foil activation technique [7] and 60 MeV alpha particle beam from the Variable Energy Cyclotron Centre were employed to obtain the excitation functions of the isomers in the energy range of 25–60 MeV.

2. Experimental details

To obtain the isomer ratio, it is necessary to determine the individual cross-sections for the formation of the meta stable state and the ground state separately. This was done in the present case by taking advantage of their different half-lives, 61*d* for isomeric state and 20 h for the ground state respectively. For the measurement of the individual cross-sections, the stack foil activation technique [7] and HPGe γ-counting method were used. 60 MeV alpha particle beam from Variable Energy Cyclotron Centre, Calcutta, India was used in the experiment. A stack of six spectroscopically pure niobium foils of weight 28 mg/cm^2 each were irradiated. Suitable aluminium degraders were used in between the foils to obtain intermediate energy points. The energy of alpha particles after they had traversed half the thickness of each niobium foil was determined by range energy relations given by Williamson *et al* [8]. Beam currents of the order of 150 nA were used. The energy and efficiency calibration of the detector was performed with a standard ^{152}Eu source. For the flux measurement, ^{27}Al($\alpha, \alpha 2pn$)^{24}Na reaction was used as a secondary standard [9].

In the reaction ^{93}Nb($\alpha, 2n$)^{95}Tc the two isomers formed have widely different spin-parities and half-lives. While ^{95m}Tc has a spin-parity of $(\frac{1}{2})^-$, ^{95g}Tc has an opposite spin parity $(\frac{9}{2})^+$. They almost decay independently of each other except for a weak 4% isomeric transition from 61 day isomer to 20 h ground state. Their cross reactions were, therefore, determined individually using their characteristic gamma rays (204 keV to identify ^{95m}Tc and 1074 keV for ^{95g}Tc) and the cross-section formula:

$$\sigma = \frac{A_i \cdot A_\gamma \cdot \lambda}{\phi \theta_\gamma P_\gamma W_i P_i N_{\mathrm{av}} (1 - e^{-\lambda t_i}) e^{-\lambda t_w} (1 - e^{-\lambda \Delta})}$$

where, σ = reaction cross reaction; A_i = atomic weight of the target element; ϕ = incident flux; θ_γ = absolute abundance of the gamma ray; P_γ = detector efficiency of that gamma ray; W_i = weight per unit area of the foil; P_i = isotopic abundance; N_{av} = Avagadro number; λ = disintegration constant; t_i = time duration of irradiation; t_w = waiting time; Δ = data accumulation time.

Errors: The statistical error is about 2% while the error in the photopeak efficiency is 5%. Error in the uniformity of the thickness is about 2%. Error in the gamma abundances is 4%. The quoted error in the standard monitor reaction cross-section σ_{Al} for ^{27}Al ($\alpha, \alpha 2pn$)^{24}Na was taken to be 6% as given by Probst *et al.* Combining all these errors, the total error on the measured cross-section was estimated to be less than 10%.

3. Theory

Huizenga and Vandenbosch were the first to develop a detailed method for the calculation of the isomeric cross-section ratios based on the statistical compound nucleus theory, with some simplifying assumptions. The calculations are done in three parts: (1) the normalized initial compound nucleus spin distribution is computed, (2) if the compound system decays by particle emission, then the normalized spin distribution following particle emission is calculated and, finally (3) the spin distribution of the nucleus following dipole γ-emission is calculated. The ratio of the high spin state population to the low spin state population will give the corresponding isomeric ratio.

The statistical pre-equilibrium model STAPRE was developed by Uhl and Strohmaier to calculate the cross-sections for particle induced nuclear reactions with several emitted particles and gamma rays under the assumption of sequential evaporation. The evaporation step is treated within the framework of the statistical model with consideration of angular momentum and parity conservation. For the emission of first particle pre-equilibrium decay is taken into account via the exciton model [10]. The individual cross-sections for ground and isomeric states are given by the model from which the corresponding isomer ratio can be calculated.

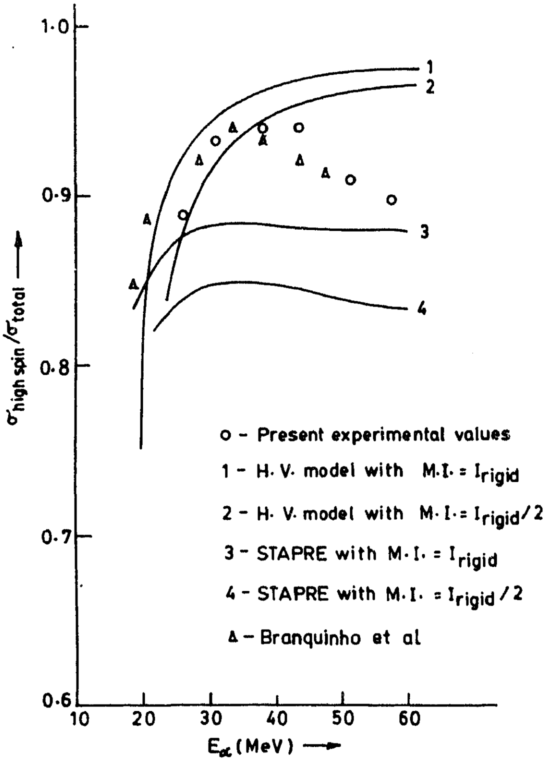

Figure 1. Isomeric cross-section ratio for the reaction $^{93}\text{Nb}(\alpha, 2n)^{95m,g}\text{Tc}$ compared with two theoretical models alongwith previous results of Branquinho *et al* [5].

4. Results and discussion

Figure 1 shows the ratio σ high spin/(σ high spin + σ low spin) as a function of incident alpha particle energy, together with the previous experimental values of Branquinho *et al*, and with the theoretical predictions of Huizenga and Vandenbosch model and STAPRE model.

The individual isomeric cross-sections and their ratios are greatly influenced by the value chosen for the spin cut-off factor σ^2, occurring in the Fermi gas level density formula which determines the spin dependence of the nuclear level density. σ^2 depends on the nuclear temperature and the moment of inertia (MI) of the excited nucleus. It is customary to take rigid body moment of inertia, I_{rigid}. But a deviation of the moment of inertia from rigid body value possible at high excitations is likely to alter the relative populations of high and low spin states and hence the isomer ratio. Therefore, the measured isomeric ratios are compared with the theoretical values, treating the effective moment of inertia (MI) as a variable parameter. So, the experimentally observed values are compared with the theoretical values obtained from the two models, with the effective moment of inertia taken as the rigid body moment of inertia and also half that of a rigid body value, an shown in figure 1.

At the outset it can be seen that the measured ratio increases first with the incident energy up to about 35 MeV, and, later shows a definite decreasing trend up to 60 MeV. The overall trend can be understood quite clearly as the interplay between compound nucleus and pre-equilibrium reaction mechanisms, predominating at different regions of energy. This trend is also confirmed by the results of Branquinho *et al* up to 48 MeV as shown in figure 1. In the energy region up to 35 MeV, the trend can be understood as the tendency to produce residual nucleus at higher and higher spin values in the continuum with increasing bombarding energy, which is a characteristic in CN reactions. Afterwards, pre-equilibrium mechanism dominates. Here, since the pre-equilibrium particles are emitted with higher energy and angular momentum than before, the residual nucleus is left in a region of relatively lower spin in the continuum; hence the ratio decreases with increase in energy in 35–60 MeV region.

As the H–V model is only based on compound nuclear mechanism, it gives fairly good agreement with measured vlaues up to 35 MeV with the moment of inertia (MI) parameter half that of rigid body value but fails at higher energies showing a trend opposite to what is observed.

On the other hand, the theoretical values of the ratio based on the STAPRE model, which takes into account the pre-equilibrium effects in an approximate way, do show a decreasing trend towards higher energies, more so in the calculations with a moment of inertia value half that of the rigid body. However, there still remains a large discrepancy in the magnitude of the ratio between experiment and STAPRE model, indicating the need for further improvements in the model.

Acknowledgements

The authors are thankful to Dr S N Chintalapudi, IUC-CC, Calcutta for co-operation and also to the entire staff of VECC for the smooth running of the accelerator. One of the authors (RKJ) acknowledges CSIR Research Associateship.

References

[1] J R Huizenga and R Vandenbosch, *Phys. Rev.* **120**, 1305, 1313 (1960)
[2] M Blann, *Ann. Rev. Nucl. Sci.* **25**, 123 (1975)
[3] E Gadioli and E Gadioli Erba, *Phys. Rev.* **C29**, 76 (1984)
[4] J Ernst, R Ibowski, H Klampfl, H Machner, T Mayer-Kuckuk and R Schanz, *Z Phys.* **A308**, 301 (1982)
[5] C L Branquinho, S M A Hoffmann, G W A Newton, V J Robinson, H Y Wong, I S Grant and J A B Goodall, *J. Inorg. Nucl. Chem.* **41**, 617 (1979)
[6] M Uhl and B Strohmaier, 1976 Rept. IRK 76/01
[7] J Rama Rao, A V Mohan Rao, S Mukharjee, R Upadhyay, N L Singh, S Agarwal, L Chaturvedi and P P Singh, *J. Phys.* **G13**, 535 (1987)
[8] C F Williamson, J P Boujout and J Picard, 1966 CENS Report CER-R 3042
[9] H J Probst, S M Qaim and R Weinreich, *Int. J. Appl. Radia. Isotope* **27**, 431 (1976)
[10] E Gadioli, E Gadioli Erba and P G Sona, *Nucl. Phys.* **A217**, 589 (1973)

PRAMANA
— journal of
physics

© Printed in India

Vol. 42, No. 2,
February 1994
pp. 141–148

Generation of ultrasonic waves in water by an elliptical Gaussian laser beam

M S SODHA*, S KONAR**, M P VERMA and V RAI
School of Physics, Devi Ahilya Vishwavidyalaya, Khandwa Road, Indore 452 001, India
*Lucknow University, Lucknow 226 007, India
**Present address and for correspondence:
School of Energy Studies, Devi Ahilya Vishwavidyalaya, Khandwa Road, Indore 452 001, India

MS received 24 May 1993; revised 29 September 1993

Abstract. The paper presents an analysis of ultrasonic wave generation in water by intensity modulated elliptical Gaussian laser beams. It is found that generated acoustic radiation is highly directional both in polar and azimuthal directions. An increase in the assymmetry of the transverse intensity distribution from the Gaussian dependence enhances the source directivity considerably. An obvious conclusion is that elliptical Gaussian beams are better choice in applications where it is desired to communicate in an approximately prescribed small solid angle.

Keywords. Thermal generation of sound; thermoacoustic source; far-field directivity pattern; directional acoustic sources.

PACS Nos 42·60; 43·35

1. Introduction

The generation of sound in water by an intensity modulated laser beam has been a fascinating subject since last three decades as it opens up a way to communicate with submarines under water from air. Laser generated acoustic signals are currently being used in optoacoustic spectroscopy [1], in optoacoustic nondestructive testing [2], thermoacoustic medical diagnostics [3], scanning laser acoustic microscopy [4] etc.

There are several mechanisms through which optical energy is converted into the acoustic energy, but the thermal mechanism offers a great advantage over the others because it is easily controllable. This is the reason why it is being used in all the potential applications of laser acoustics. The physics of the process can be easily understood. When an intensity modulated laser beam passes through water it produces an exponentially shaded sound source along its direction of propagation. Since the laser beam is intensity modulated the heating of the medium results in a periodic sequence of condensations and rarefactions which propagate through the medium. The frequency of the acoustic wave is the same as the modulating frequency of the laser beam. Such sources of acoustic perturbation are known as thermoacoustic sources (TS).

Characteristics of TS generated by the absorption of intensity modulated CW laser beams by a water body have been studied by Westervelt and Larson [5], Lyamshev and Sedov [6], Berthelot and Busch-Vishniac [7]. Experimental verification of thermoacoustic radiation has been carried out by various workers [8, 9]. Excitation of acoustic pulses by pulsed laser and moving pulsed laser sources has also been investigated [10–15]. Readers are referred to Lyamshev and Sedov [6] for a review of some of the earlier work in this area.

A common feature of these investigations is the study of the effect of Gaussian intensity distribution in the laser beam on the directional characteristics of the emitted acoustic field. Though such a laser beam produces a highly directional acoustic array its directivity pattern is symmetric around the acoustic array. This symmetry of directivity pattern is a result of the symmetry of the intensity distribution of the laser beam around its axis. Naturally, laser beams with assymmetric intensity distribution will produce acoustic fields which will depend both on polar and azimuthal angles. Since a preferentially directed wave will have its energy confined within a relatively small solid angle, the range is enhanced in certain directions and as a result such sources would be favourable in comparison to symmetric sources for communication in a particular direction. Study of acoustic radiation by an assymmetric array is therefore pertinent.

In this note we have investigated directivity pattern of TS produced by intensity modulated elliptical Gaussian laser beams. Such beams are easy to obtain as for example by sending the circular Gaussian beam through a cylindrical lens [17] and are more suitable for long distance communication as comparatively they spread much less [18]. An expression for acoustic pressure in the far-field approximation is given in § 2. Section 3 provides main results of our study and discusses the benefits achievable by the use of elliptical Gaussian laser beams.

2. Analysis

Consider an intensity modulated laser beam propagating in the positive z-direction and incident normally on the free air-water surface at $z = 0$. We assume that the laser beam is of moderate power so that change of aggregate state of the medium does not take place in the laser absorption zone and hence, the sound generation mechanism is purely thermal in nature. Absorption of laser produces a thermoacoustic array as shown in figure 1. The sound pressure field p satisfies inhomogeneous Helmholtz equation [5]

$$\nabla^2 p - \frac{1}{c^2}\frac{\partial^2 p}{\partial t^2} = -\frac{\beta}{c_p}\frac{\partial q}{\partial t} \tag{1}$$

where c is the velocity of sound in water, β is the coefficient of thermal expansion and c_p the specific heat at constant presure. q is the amount of heat added in water per unit volume per unit time. The required boundary condition for p may be written as

$$p = 0 \text{ at } z = 0 \tag{2}$$

Heat deposition q in the array region may be written as

$$q(x, y, z, t) = A\alpha I(x, y)\exp(-\alpha z)(1 + m\cos\omega t) \tag{3}$$

where A is the transmittivity of laser light in water, α the attenuation coefficient, ω the modulation frequency and m is the modulation index $(0 < m < 1)$. For elliptical Gaussian laser beam I may be written as

$$I = I_0\exp[-(x^2/a^2 + y^2/b^2)] \tag{4}$$

where I_0 is the intensity on the axis and a and b $(a > b)$ are constants; $a = b$ represents a laser beam with Gaussian intensity distribution. In view of (3), (1) may be rewritten as

$$\nabla^2 p + k^2 p = \frac{i\omega m A\alpha\beta}{c_p} I(x, y) e^{-\alpha z} \tag{5}$$

where $k = \omega/c$. The time factor $\exp(-i\omega t)$ is implicit in (5) and only the real part of p is the physical solution.

The solution of (5) may be written as

$$p = -\frac{i\omega m A\alpha\beta}{c_p} \int G(\mathbf{R}|\mathbf{R}') I(x', y') \exp(-\alpha z') \mathrm{d}v' \tag{6}$$

where $G(\mathbf{R}|\mathbf{R}')$ is the Green's function of the homogeneous wave equation (eq. (5)). The Green's function which satisfies the boundary condition at $z = 0$ may be written as

$$G = \frac{1}{4\pi}\left[\frac{e^{ik}|\mathbf{R} - \mathbf{r}_1|}{|\mathbf{R} - \mathbf{r}_1|} - \frac{e^{ik}|\mathbf{R} - \mathbf{r}_2|}{|\mathbf{R} - \mathbf{r}_2|}\right]. \tag{7}$$

Since we are interested in the far field acoustic pattern the following approximations may be appropriate (see figure 1)

$$|\mathbf{R} - \mathbf{r}_1| \approx R_1(z') - r(x', y')\cos\alpha_1$$

$$|\mathbf{R} - \mathbf{r}_2| \approx R_2(-z') - r(x', y')\cos\alpha_2$$

where

$$R_1(z') = \sqrt{(x^2 + y^2 + (z - z')^2)}, \quad R_2(-z') = \sqrt{(x^2 + y^2 + (z + z')^2)}$$

$$r(x', y') = \sqrt{(x'^2 + y'^2)},$$

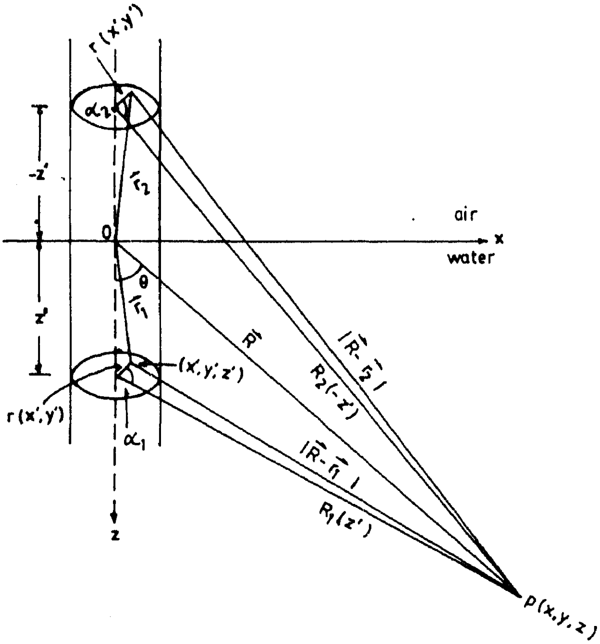

Figure 1. Schematics of thermoacoustic array.

α_1 and α_2 are respectively the angles which $\mathbf{R}_1(z')$ and $\mathbf{R}_2(-z')$ make with $\mathbf{r}(x',y')$. With these substitutions, (6) yields

$$p = -\frac{Am\beta}{2\pi c_p}\frac{e^{ikR}}{R}F(\theta,\Phi) \tag{8}$$

where the directivity pattern $F(\theta,\Phi)$ is given by

$$F(\theta,\Phi) = \frac{\pi\omega\alpha a b I_0 k\cos\theta}{\alpha^2 + k^2\cos^2\theta}\exp\left[-\frac{k^2a^2\sin^2\theta}{4}\left(\cos^2\Phi + \frac{b^2}{a^2}\sin^2\Phi\right)\right] \tag{9}$$

Φ is the angle between xz plane and the plane containing the field point and the z axis. It may be pointed out that setting $a = b$ (reducing to Gaussian beam) reduces the expression for $F(\theta,\Phi)$ to that obtained by Lyamshev [16] as it should. The directivity pattern normalized with the directivity pattern of the acoustic field produced by a Gaussian laser beam of equal power may be cast as

$$F_N(\theta,\Phi) = \exp\left[\frac{k^2a^2\sin^2\theta}{4}\left(b/a - \cos^2\Phi\frac{b^2}{a^2} - \sin^2\Phi\right)\right] \tag{10}$$

3. Discussion

The function $F(\theta,\Phi)$ of (9) represents the angular dependence of the pressure field at a large distance R from the point of incidence of an elliptic Gaussian laser beam incident normally on the water surface. As against this $F_N(\theta,\Phi)$ of (10) expresses the ratio of the fields obtained by two sources, one generated by an elliptic Gaussian beam and the other by a circular Gaussian beam at a point in the direction (θ,Φ) from the point of incidence of the laser beams at a large but equal distance R. The Φ dependence is naturally identical in the two functions. One easily obtains that $\partial F_N/\partial\Phi = \partial F/\partial\Phi = 0$ for the $\Phi = m\pi/2$ where m is an integer. It established that $F(\theta,\Phi)$ (as also $F_N(\theta,\Phi)$) acquires its maximum along $\Phi = \pi/2$ and $3\pi/2$, and minimum along $\Phi = 0$ and π. In addition, towards $\Phi = \pi/2$ and $3\pi/2$, $F_N(\theta,\Phi)$ is always greater than one. Thus, one finds that the sound field of the source generated by the elliptic Gaussian beam has an enhanced intensity towards $\Phi = \pi/2$ and $3\pi/2$ directions.

The dependence on θ can also be analysed from (9). For this let us choose $\Phi = \pi/2$ or $3\pi/2$ the directions in which most of the sound is propagating. In that case $\partial F/\partial\theta = 0$ demands

$$k^2\cos^2\theta = \left(\frac{1}{b^2} - \frac{\alpha^2}{2}\right) \pm \left[\left(\frac{1}{b^2} - \frac{\alpha^2}{2}\right)^2 - \frac{2\alpha^2}{b^2}\right]^{1/2}.$$

For $k^2\cos^2\theta$ to be real and positive we must have $\alpha^2b^2 < 2/3$. For lasers with small attenuation coefficients α and a reasonable size of the beam diameter this condition is invariably satisfied. For example for an Nd-glass laser $\alpha \approx 0{\cdot}17\,\mathrm{cm}^{-1}$. If the radius of the beam is even 2 cm (b is always < 2 cm), we shall have $\alpha^2b^2 \approx 0{\cdot}1 < 2/3$. For such a system one can easily obtain for the maximum of $F(\theta,\Phi)$ an approximate relation $k^2\cos^2\theta \approx \alpha^2$, which for a sound wave of 60 kHz yields $\theta \approx 86{\cdot}1^\circ$.

Figure 2 shows angular plot of $F_N(\theta,\Phi)$ versus Φ for different values of a and b, the frequency of the generated acoustic wave is $f = 60$ kHz ($f = \omega/2\pi$) and the field point is located at a polar angle $\theta = 75^\circ$. For $f = 60$ kHz and $\theta = 75^\circ$, values of

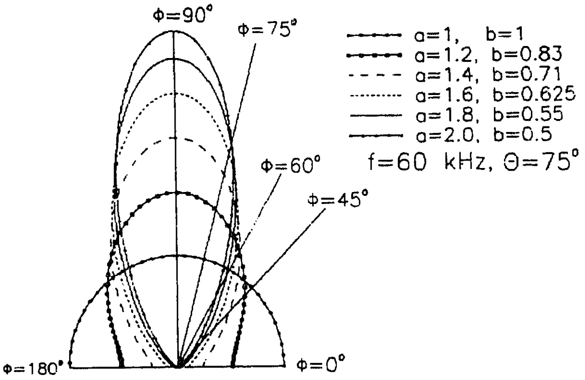

Figure 2. Angular plot of $F_N(\theta, \Phi)$ as a function of Φ.

Table 1. $F_N(\theta, \Phi)$ for different values of b/a and Φ; $f = 60\,\text{kHz}$, $\theta = 75°$ and $ab = 1$; Φ in degrees.

	b/a					
Φ	1·0	0·69	0·51	0·39	0·30	0·25
0	1·00	0·52	0·24	0·10	0·04	0·01
15	1·00	0·56	0·28	0·12	0·05	0·02
30	1·00	0·69	0·41	0·22	0·11	0·05
45	1·00	0·91	0·71	0·50	0·32	0·19
60	1·00	1·19	1·20	1·10	0·94	0·76
75	1·00	1·46	1·78	1·98	2·07	2·08
90	1·00	1·57	2·06	2·45	2·77	3·01
105	1·00	1·46	1·78	1·98	2·08	2·09
120	1·00	1·19	1·21	1·11	0·94	0·76
135	1·00	0·91	0·71	0·50	0·32	0·19
150	1·00	0·69	0·42	0·22	0·11	0·05
165	1·00	0·56	0·28	0·13	0·05	0·02
180	1·00	0·52	0·24	0·10	0·04	0·01
195	1·00	0·56	0·28	0·12	0·05	0·02
210	1·00	0·69	0·41	0·22	0·11	0·05
225	1·00	0·90	0·70	0·49	0·32	0·19
240	1·00	1·19	1·20	1·10	0·93	0·75
255	1·00	1·45	1·78	1·97	2·06	2·07
270	1·00	1·57	2·06	2·45	2·77	3·01
285	1·00	1·46	1·79	1·99	2·08	2·10
300	1·00	1·19	1·21	1·11	0·95	0·77
315	1·00	0·91	0·71	0·50	0·32	0·19
330	1·00	0·69	0·42	0·23	0·11	0·05
345	1·00	0·56	0·28	0·13	0·05	0·02
360	1·00	0·52	0·24	0·10	0·04	0·01

$F_N(\theta, \Phi)$ for different values of Φ and b/a are given in table 1. Figure 3 shows angular plot of $F_N(\theta, \Phi)$ which modulation frequency f for $\theta = 45°$, $a = 1{\cdot}4\,\text{cm}$ and $b/a = 0{\cdot}507$. Figure 4 shows angular plot of $F(\theta, \Phi)$ with θ for $f = 60\,\text{kHz}$, $\Phi = \pi/2$, $\alpha = 0{\cdot}17\,\text{cm}^{-1}$, $a = 2\,\text{cm}$ and $b = 0{\cdot}5\,\text{cm}$. For $\Phi = \pi/2$, $\alpha = 0{\cdot}17\,\text{cm}^{-1}$ and $f = 60\,\text{kHz}$, values of $F(\theta, \Phi)/B$ (where $B = I_0 \pi c$) for different values of θ and b/a are given in table 2. It is

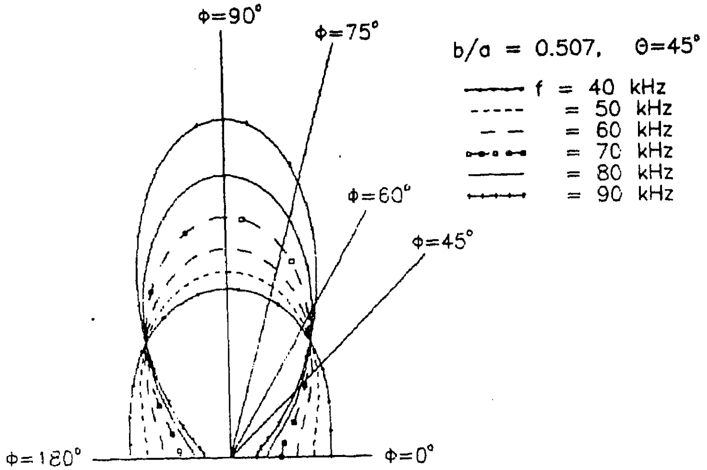

Figure 3. Angular plot of $F_N(\theta, \Phi)$ as a function of f.

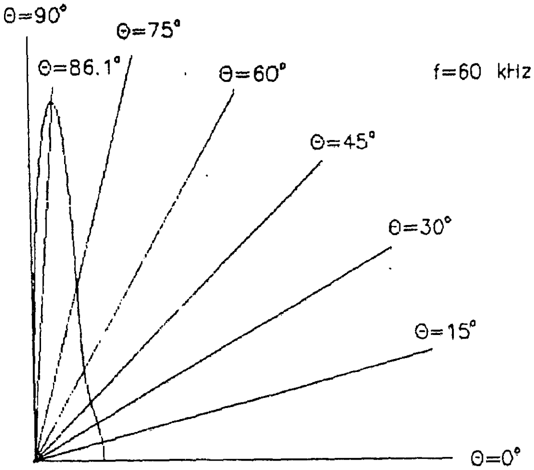

Figure 4. Angular plot of $F(\theta, \Phi)/B$ as a function of θ. $\alpha = 0{\cdot}17\,\mathrm{cm}^{-1}$, $a = 2\,\mathrm{cm}$, $b = 0{\cdot}5\,\mathrm{cm}$, $\Phi = 90^\circ$ and $f = 60\,\mathrm{kHz}$. $B = I_0 \pi c$ and $F(\theta, \Phi)/B$ in cgs units.

obvious from these figures and tables that the sound field has a preferential direction in the $\theta \approx 86{\cdot}1^\circ$, $\Phi = \pi/2$ and $3\pi/2$, and the solid angle carrying most of the sound field narrows as the sound frequency and the ellipticity of the laser beam are increased.

Thus it is clear from the above discussion that using an elliptic Gaussian beam one can get an acoustic field which depends both on polar (θ) as well as azimuthal (Φ) directions. Particularly, towards $\Phi = \pi/2$ and $3\pi/2$ acoustic field enhances whereas towards $\Phi = 0$ and π it diminishes. Since, acoustic field also depends on $1/R$, acoustic field generated by an elliptic Gaussian laser beam can travel larger distance towards $\Phi = \pi/2$ and $3\pi/2$, and less distance towards $\Phi = 0$ and π in comparison to acoustic field generated by a Gaussian laser beam of equal power. Thus using elliptic Gaussian laser beam one can get acoustic field above noise level to larger distances towards $\Phi = \pi/2$ and $3\pi/2$. Once acoustic field above noise level is available, one can easily electrically amplify it, but no amplifier can detect/amplify acoustic signals unless it

Table 2. $F(\theta, \Phi)/B$ for different values of b/a and θ. $f = 60\,\mathrm{kHz}$, $\Phi = 90°$, $ab = 1$ and $\alpha = 0{\cdot}17\,\mathrm{cm}^{-1}$; $F(\theta, \Phi)/B$ in cgs units and θ in degrees.

			b/a			
θ	1	0·69	0·51	0·39	0·3	0·25
0	0·17	0·17	0·17	0·17	0·17	0·17
5	0·17	0·17	0·17	0·17	0·17	0·17
10	0·16	0·17	0·17	0·17	0·17	0·17
15	0·16	0·16	0·17	0·17	0·17	0·17
20	0·15	0·16	0·16	0·17	0·17	0·17
25	0·14	0·15	0·16	0·17	0·17	0·17
30	0·13	0·15	0·16	0·17	0·17	0·18
35	0·12	0·14	0·16	0·17	0·18	0·18
40	0·11	0·14	0·16	0·17	0·18	0·19
45	0·11	0·14	0·16	0·18	0·19	0·20
50	0·10	0·14	0·16	0·18	0·20	0·21
55	0·10	0·14	0·17	0·19	0·21	0·22
60	0·10	0·15	0·18	0·21	0·23	0·25
65	0·11	0·16	0·20	0·24	0·26	0·28
70	0·12	0·18	0·24	0·28	0·31	0·34
75	0·14	0·22	0·29	0·35	0·39	0·43
80	0·18	0·29	0·39	0·47	0·53	0·58
84	0·24	0·39	0·52	0·62	0·71	0·78
85	0·25	0·41	0·55	0·66	0·75	0·82
86	0·26	0·42	0·56	0·68	0·77	0·85
87	0·25	0·41	0·54	0·66	0·75	0·82
88	0·21	0·34	0·45	0·55	0·62	0·68
89	0·12	0·20	0·26	0·32	0·36	0·39
90	0·00	0·00	0·00	0·00	0·00	0·00

exists above noise level. The elliptic Gaussian beam provides a simple means of availability of acoustic field over noise level to larger distances in comparison to a Gaussian laser beam of equal power. Hence, it is a positive advantage as far as underwater sound communication via laser source is concerned.

Acknowledgement

This work is supported by Department of Electronics, Government of India. We would like to thank the referee for many valuable suggestions.

References

[1] V P Zharov and V S Letokhov, *Laser optoacoustic spectroscopy* (Springer-Verlag, Berlin, 1986)
[2] C B Scruby, R J Dewhurst, D A Hutchins and S B Palmer, *J. Appl. Phys.* **51**, 6210 (1980)
[3] R J Von Gutfeld, *Ultrasonics* **18**, 175 (1980)
[4] B Cretin and D Hauden, *IEEE Ultrason. Symp.* **2**, 656 (1984)
[5] P J Westervelt and R S Larson, *J. Acoust. Soc. Am.* **54**, 121 (1973)
[6] L M Lyamshev and L V Sedov, *Sov. Phys. Acoust.* **27**, 4 (1981)
[7] Y H Berthelot and I J Busch-Vishniac, *J. Acoust. Soc. Am.* **78**, 2074 (1985)
[8] T G Muir, C R Culbertson and J R Clynch, *J. Acoust. Soc. Am.* **59**, 735 (1976)

[9] F V Bunkin, A I Malyarovski, V G Mikhalevich and G P Shipulo, *Sov. J. Quantum Electron.* **8** 270 (1978)
[10] S G Kasoev and L M Lyamshev, *Sov. Phys. Acoust.* **23**, 510 (1977)
[11] S G Kasoev and L M Lyamshev, *Sov. Phys. Acoust.* **24**, 302 (1978)
[12] L M Lyamshev and L V Sedov, *Sov. Phys. Acoust.* **25**, 510 (1979)
[13] Y H Berthelot and I J Busch-Vishniac, *J. Acoust. Soc. Am.* **81**, 317 (1987)
[14] A D Pierce and H A Hsieh, in *Progress in underwater acoustics* edited by H M Merklinger (Plenum, New York, 1987), pp 595
[15] Y H Berthelot, *J. Acoust. Soc. Am.* **83**, 1399 (1988)
[16] L M Lyamshev, *Sov. Phys. Usp.* **24**, 977 (1981)
[17] A Yariv, *Quantum electronics* (John Wiley and Sons, 3rd Ed, 1989) pp 129
[18] I G Zakharova, Yu N Karamzin and V A Trofimov, *Sov. J. Quantum Electron.* **17**, 1172 (1987)

PRAMANA
— journal of
physics

© Printed in India

Vol. 42, No. 2,
February 1994
pp. 149–157

Local scaling transformation function and atomic shell structure in density functional theory

B M DEB* and BIJOY KR. DEY
Theoretical Chemistry Group, Department of Chemistry, Panjab University, Chandigarh 160014, India
*Also from the Jawaharlal Nehru Centre for Advanced Scientific Research, Indian Institute of Science Campus, Bangalore 560012, India

MS received 2 August 1993; revised 17 January 1994

Abstract. The method of local scaling transformation in density functional theory calculates a transformation function (TRF) in order to generate an optimized atomic N-electron wave function from a trial density and a reference density/wave function. The TRFs $f(r)$ for several atomic systems are studied and it is observed that the number of minima in $\mathrm{d}f(r)/\mathrm{d}r$ equals the number of atomic shells, except when $\rho = \rho_0$ and $f = r$.

Keywords. Local scaling transformation; atomic shell structure; density functional theory.

PACS Nos 31·10; 31·20; 71·10; 71·45

1. Introduction

Recently, the method of local scaling transformations (LST) in density functional theory (DFT) has attracted some attention [1–5]. Starting from a reference N-electron wave function $\Psi_0(\mathbf{r}_1, \ldots, \mathbf{r}_N)$, corresponding to a reference one-electron density $\rho_0(\mathbf{r})$, the method generates an N-electron wave function $\Psi_\rho(\mathbf{r}_1, \ldots, \mathbf{r}_N)$ from a given (trial) one-electron density $\rho(\mathbf{r})$ through a unique one-electron transformation T, where $\rho(\mathbf{r}) = T\rho_0(\mathbf{r})$. If $\rho(\mathbf{r})$ contains adjustable parameters then these would enter into Ψ_ρ, enabling one to variationally optimize the parameters. It has been shown [3–5] that even if one uses a trial density $\rho(\mathbf{r})$ which is considerably simpler than the Hartree-Fock (HF) density, the method can deliver atomic density and energy of near-HF accuracy. It is also interesting to note that for the ground states of two-electron atomic systems Ψ_ρ is independent of Ψ_0 [3]. Apart from numerical accuracy, a principal advantage of this method is the retention of the wave function concept within DFT (see also [6]). It has been opined [7] that discarding the wave function concept in DFT is the primary reason for the latter's discomfiture while being extended to excited and time-dependent states.

2. The method

The LST method has been described in detail by others [1–5]. Here we summarize the essential equations which are useful to us, for the ground states of spherically symmetric systems.

The transformation function (TRF) $f(r)$ which is of primary interest in this report is defined and calculated through the following expressions:

$$\rho(r) = J(f/r)\rho_0(f), \tag{1}$$

$$J(f/r) = \frac{f^2}{r^2}\frac{\mathrm{d}f}{\mathrm{d}r}, \tag{2}$$

$$\frac{\mathrm{d}f}{\mathrm{d}r} = \frac{r^2\rho(r)}{f^2\rho_0(f)}, \tag{3}$$

$$\int_0^r \rho(x)x^2\,\mathrm{d}x = \int_0^f \rho_0(y)y^2\,\mathrm{d}y \tag{4}$$

$$f(r) = [\rho(0)/\rho_0(0)]^{1/3}r + O(r^2), \text{ for small } r \tag{5}$$

$$\Psi_\rho(r_1,\ldots,r_N) = \left[\prod_{i=1}^{N} J(f_i/r_i)^{1/2}\right]\Psi_0(f_1,\ldots,f_N). \tag{6}$$

Thus, Ψ_ρ yields the one electron-density $\rho(r)$. In case Ψ_0 is constructed from a set of orthonormal orbitals $\{\psi_{0i}(r)\}$, $i = 1,\ldots,N$, then one obtains the following set of transformed orthonormal orbitals $\{\phi_{\rho i}(r)\}$ for constructing Ψ_ρ:

$$\phi_{\rho i}(r) = J(f/r)^{1/2}\psi_{0i}(f) \tag{7}$$

Thus, the structures of Ψ_ρ and Ψ_0 are the same, and

$$E[\rho] = E[\rho;\Psi_0] = \langle\Psi_\rho|H|\Psi_\rho\rangle/\langle\Psi_\rho|\Psi_\rho\rangle \tag{8}$$

where H is the Hamiltonian of the system.

The TRF $f(r)$ can be ascribed the same physical meaning as that of the radial coordinate r, i.e., f is a distance quantity, $0 \leqslant f \leqslant \infty$. Thus, $\rho_0(f)$ is obtained by simply replacing r in $\rho_0(r)$ by f. The TRF in effect implies a mapping between r-space and f-space. The plots of $f^2\rho_0(f)$ as functions of $\sqrt{f}$ and $\sqrt{r}$ have been shown later.

Apart from the statement [4] that $f(r)$ is a monotonically increasing function of r, no attention seems to have been paid to the detailed structure of $f(r)$ which, as shown by (3), is dependent on ρ_0 and ρ. In particular, the number of minima in $\mathrm{d}f/\mathrm{d}r$ is observed by us to correspond to the number of shells and hence the number of maxima in atomic radial density.

Although the calculations reported in this paper correspond to the ground states of spherically symmetric systems, it is worthwhile to note that, in principle, the LST method is also applicable to excited states and to non-spherical systems, e.g., diatomic molecules. While no calculations seem to be reported for molecules, Koga [5] has reported LST calculations on the $2\,^1S$ excited state of the He atom, by taking a configuration-interaction wave function as Ψ_0 and satisfying both Hamiltonian and wave-function orthogonalities.

3. Results and discussion

In order to examine the structure of $f(r)$, we have repeated Koga's calculations, using his optimized electron densities for the ground states of H^-, He, Li^+, Be^{++}, Li and Be [3, 4]. The reference density ρ_0 and the wave function Ψ_0 for He, Li^+, Li and Be were taken from the single-zeta calculations of Clementi and Roetti [8] while those

Table 1. Calculated kinetic energies (a.u.) for atoms and ions containing 2–4 electrons by the local scaling transformation method. The electron density is normalized up to the fifteenth decimal place. In columns 3 and 4, the negative of total energy is taken as the kinetic energy (values from table 3 of Koga [3], tables 1 and 3 from Koga [4]).

	Kinetic energy		
Atom/Ion	Present value	Koga's value	Hartree-Fock value
H^-	0·4885550[a]	0·4879262	0·4879297
He	2·8615775[a]	2·8616799	2·8616800
Li^+	7·2349501[a]	7·2364148	7·2364152
Be^{++}	13·613227[a]	13·611299	13·611299
Li	7·4328695[b]	7·431530	7·432727
Be	14·565166[c]	14·568511	14·573023

[a] Using the optimized electron density from table 3 of Koga [3]; [b] Using the optimized $\rho_2(r)$ from table 1 of Koga [4]; [c] Using the optimized $\rho_2(r)$ from table 3 of Koga [4].

Table 2. Comparison of calculated position moments (a.u.) with the corresponding values from table 2 of Koga [3] for the He atom as well as with the Hartree-Fock values [3]. The present Ψ_ρ has been normalized to unity up to the fifteenth decimal place.

Position moment	Present value	Koga's value	Hartree-Fock value
$\langle r^{-2} \rangle$	5·9936	5·9959	5·996
$\langle r^{-1} \rangle$	1·6873	1·6873	1·6873
$\langle r \rangle$	0·9273	0·9273	0·9272
$\langle r^2 \rangle$	1·1847	1·1849	1·1846
$\langle r^3 \rangle$	1·9396	1·9407	1·9398
$\langle r^4 \rangle$	3·8810	3·8882	3·8838

for H^- and Be^{++} were taken from the single-zeta calculations of Roothaan and Soukup [9]. Table 1 compares our kinetic energy values with Koga's and HF values [3,4]. We see that although our kinetic energy value has occasionally gone slightly above the HF value, our computed values are in excellent agreement with the HF and Koga's values. We also compare our calculated position moments, by using Ψ_ρ, for the He atom with those of Koga [3] in table 2. The agreement is again excellent and in fact our values generally show better agreement with the HF values than those of Koga [3]. All calculations were performed in double precision.

Figures 1 and 2 depict $f(r)$ and df/dr for H^- ion and Be atom respectively. The plots for the other two-electron systems, He, Li^+ and Be^{++}, are qualitatively similar to those for H^- while the plots for Li atom are qualitatively similar to those of Be.

Several remarks can be made regarding these plots:

1. $f(r)$ is depicted as a monotonically increasing function of r [4]; $f = 0, \infty$ corresponding to $r = 0, \infty$.
2. df/dr plots show the effects of both Z and N. As r increases, df/dr increases with Z from H^- to Be^{++}. The same is true from Li to Be.

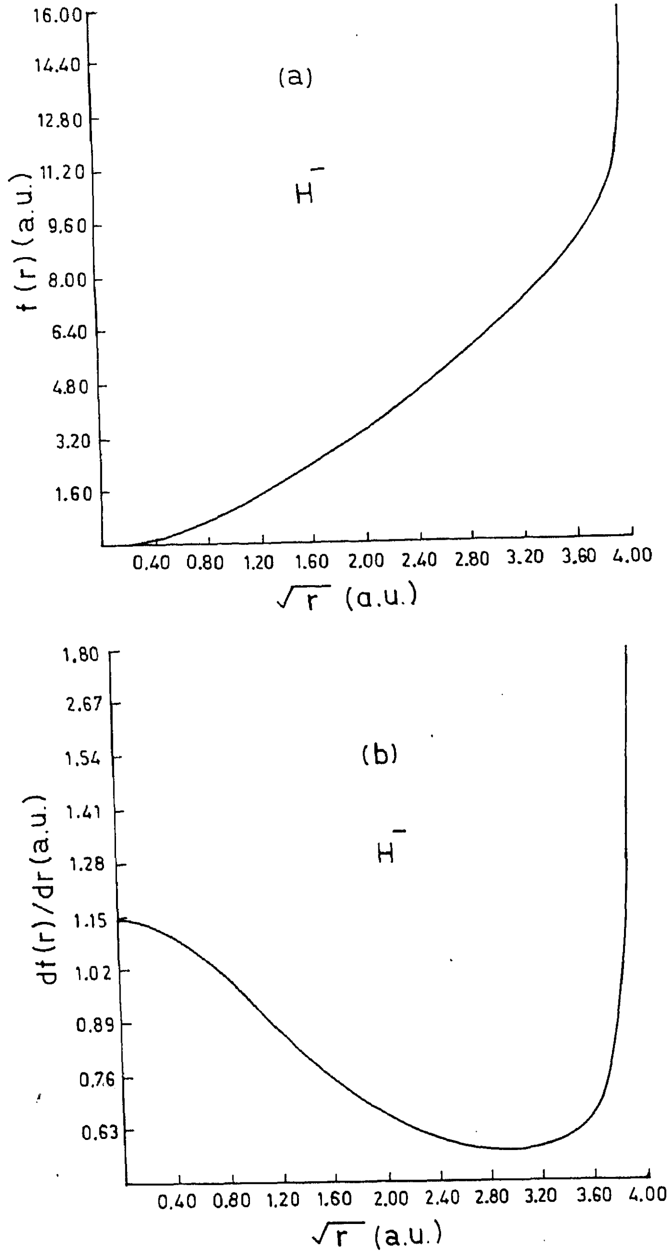

Figure 1. Plot of (**a**) $f(r)$ against $\sqrt{r}$ and (**b**) df/dr against $\sqrt{r}$, in a.u., for the H^- ion. The plots for other two-electron systems, He, Li^+ and Be^{++}, are similar. Normalized transformed orbital is employed.

3. $f(r)$ increases rapidly with r so that at an r-value where the electron density is very small f is quite large, leading to a rapid increase in df/dr which tends to ∞ as $r \to \infty$.
4. From (5), $[df/dr]_{r=0} \simeq 1$, since $\rho_0(0)$ and $\rho(0)$ are quite close to each other. This is always true in our calculations.

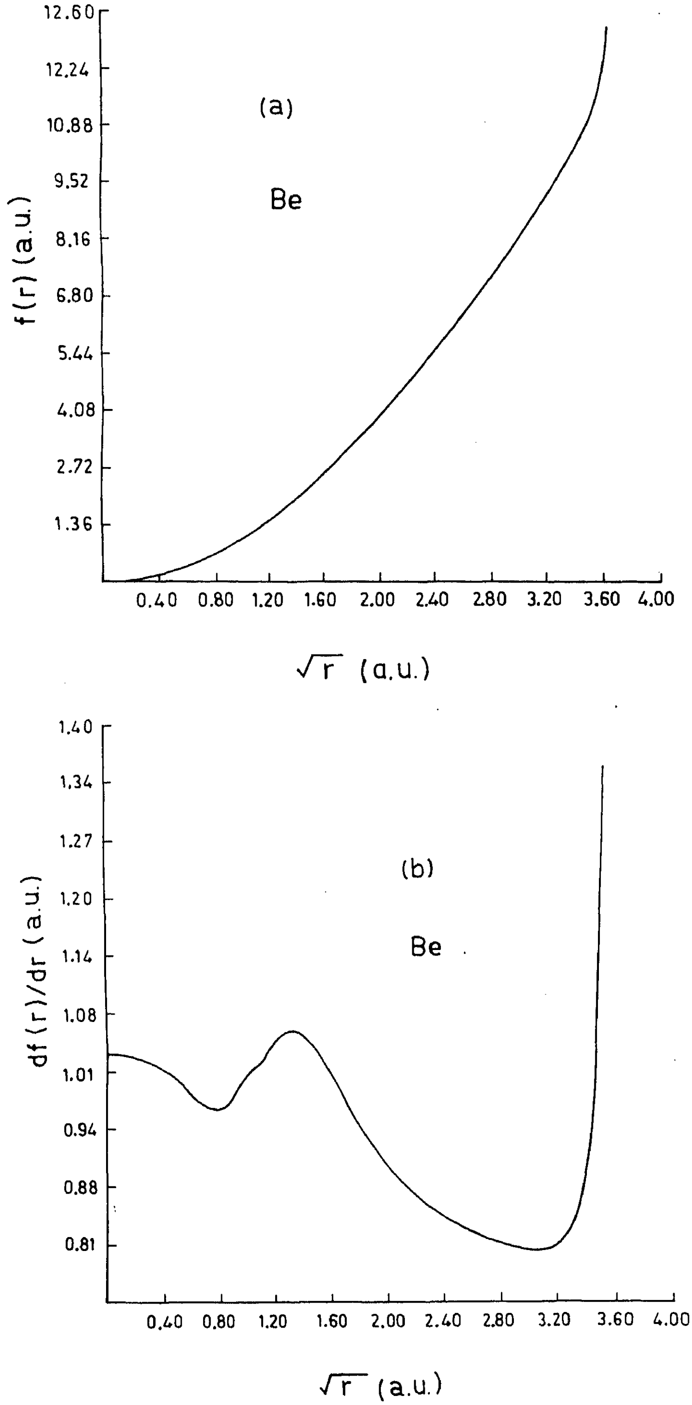

Figure 2. Plot of (**a**) $f(r)$ against $\sqrt{r}$ and (**b**) $\mathrm{d}f/\mathrm{d}r$ against $\sqrt{r}$, in a.u., for the **Be** atom. The plots for the Li atom are similar. Orthonormalized transformed orbitals are employed.

5. df/dr shows one minimum for H^-, He, Li^+ and Be^{++} and two minima for Li and Be, corresponding to the presence of one and two shells respectively. However, the locations of these minima do not coincide with the maxima or minima in the radial density. The first minimum occurs at 9·042 (H^-), 3·652 (He), 2·217 (Li^+), 2·350 (Be^{++}), 1·024 (Li), 0·575 (Be) a.u. while the second minimum occurs at 12·96 (Li) and 9·248 (Be) a.u. respectively.
6. Thus $f(r) = f(r, Z, N)$, as also df/dr.

Although no LST calculation has been reported so far on atomic systems containing three shells, we feel that our observation of the number of minima in df/dr being equal to the number of atomic shells should be of general validity. This observation is of interest for two reasons: (a) Observation of shell structure in a distance quantity, f. This is different from the familiar shell structure in density quantities. (b) Although (3) indicates that df/dr should contain information about shell structure since both $r^2\rho(r)$ and $f^2\rho_0(f)$ contain such information, it is not clear how such information is encoded in df/dr. Equation (3) gives

$$\frac{d^2 f}{dr^2} = \frac{1}{f^2\rho_0(f)}\left[\frac{d}{dr}\left\{r^2\rho(r)\right\} - \frac{r^4\rho^2(r)}{f^4\rho_0^2(f)}\frac{d}{df}\{f^2\rho_0(f)\}\right] \tag{9}$$

This means that d^2f/dr^2 vanishes when

$$f^4\rho_0^2(f)\frac{d}{dr}\{r^2\rho(r)\} = r^4\rho^2(r)\frac{d}{df}\left\{f^2\rho_0(f)\right\} \tag{10}$$

Such vanishing need not be at the maxima or minima of the radial density. However, $d^2f/dr^2 = 0$ at $r = 0$, from (9), since $d/df\{f^2\rho_0(f)\} = 0$ at $r = 0$ and f varies linearly as r for very small r. Figures 1(b) and 2(b) verify these conclusions.

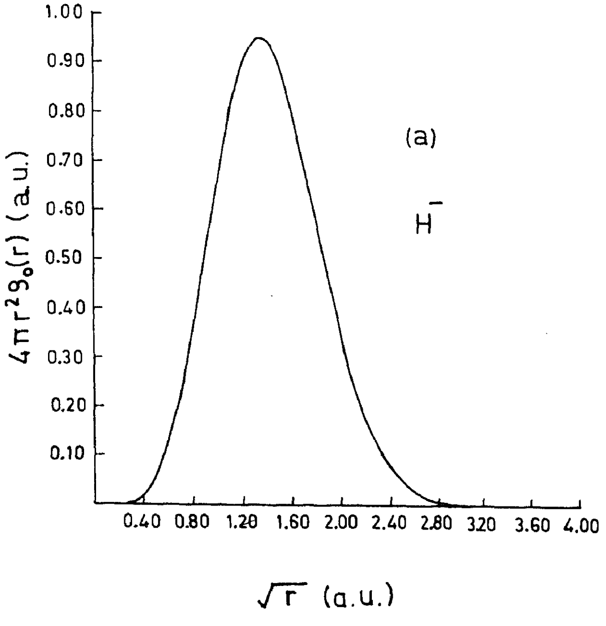

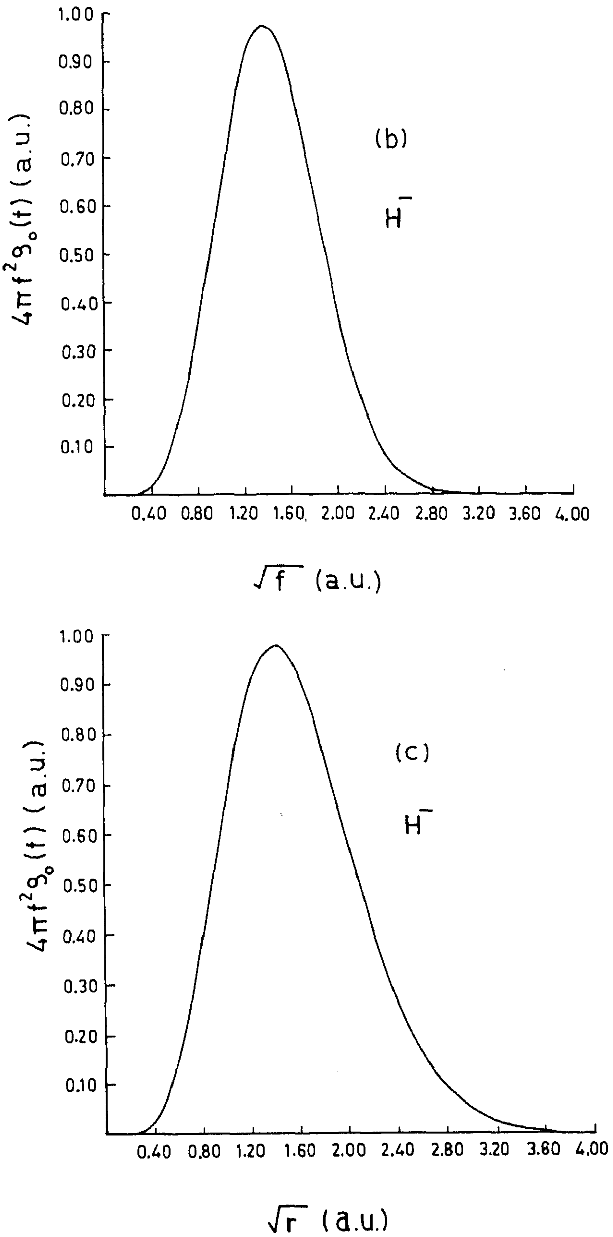

Figure 3. Plot of (**a**) single-zeta [8] $4\pi r^2 \rho_0(r)$ against $\sqrt{r}$, (**b**) $4\pi f^2 \rho_0(f)$ against $\sqrt{f}$ and (**c**) $4\pi f^2 \rho_0(f)$ against $\sqrt{r}$, in a.u., for the Li^+ ion. The plots for the other two-electron systems, H^-, He and Be^{++}, are similar. Plots (a) and (b) are identical but (c) is different. Normalized transformed orbital is employed.

Furthermore, figures 3 and 4 depict $4\pi f^2 \rho_0(f)$ as functions of $r^{1/2}$ and $f^{1/2}$, for Li^+ ion and Be atom. They are also compared with the corresponding single-zeta $4\pi r^2 \rho_0(r)$ plotted against $r^{1/2}$. The plots of $4\pi f^2 \rho_0(f)$ against $f^{1/2}$ and $4\pi r^2 \rho_0(r)$ against $r^{1/2}$ obviously coincide. But those of $4\pi f^2 \rho_0(f)$ against $f^{1/2}$ and $r^{1/2}$ are not identical; the locations of the maxima and minima in the last two plots are slightly different. Also, the plot against $r^{1/2}$ has a longer tail. This explains why $\mathrm{d}f/\mathrm{d}r$ in (3) goes to ∞ as $r \to \infty$.

In summary, atomic shell structure has been observed in a distance quantity like $f(r)$ whose behaviour is such that $f(r) = 0, \infty$ at $r = 0, \infty$; $\mathrm{d}f/\mathrm{d}r \simeq 1$ at $r = 0$ and goes to ∞ as $r \to \infty$. These conclusions are valid except in the special case of $\rho = \rho_0$ and $f = r$.

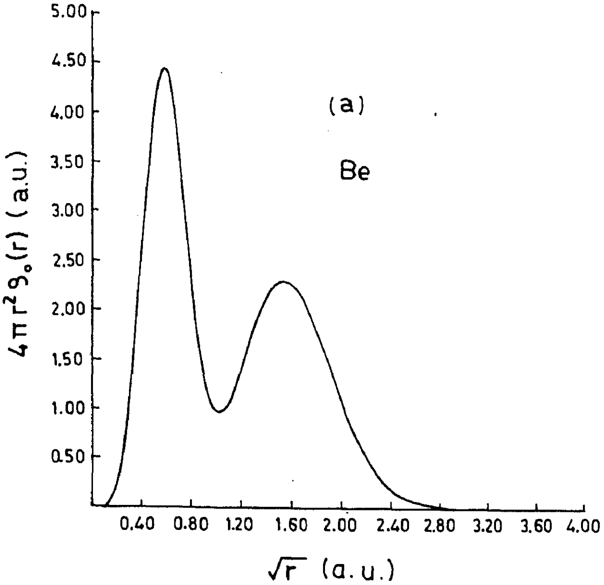

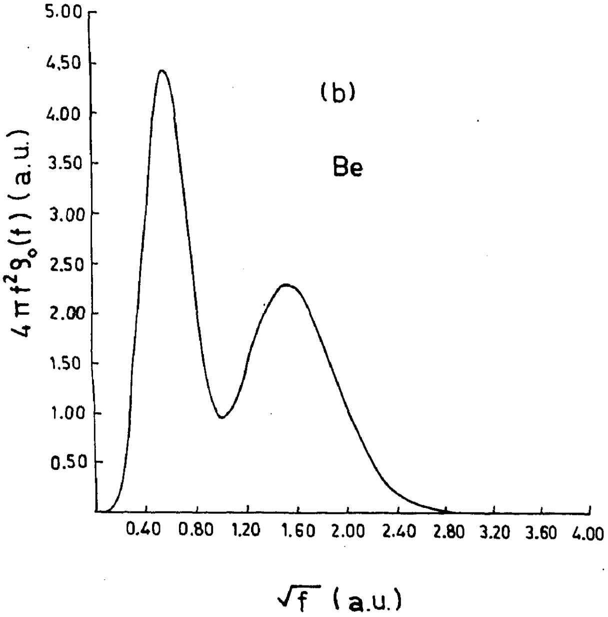

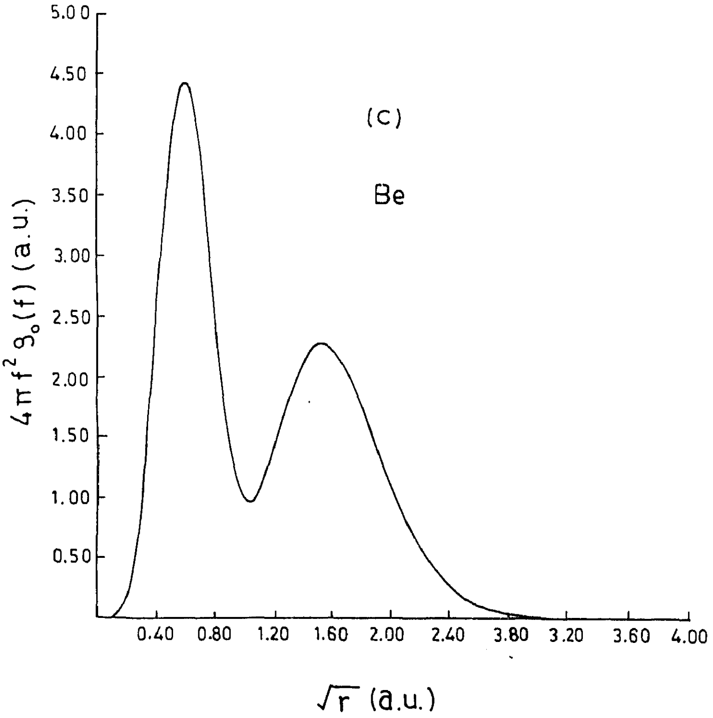

Figure 4. Plot of (**a**) single-zeta [8] $4\pi r^2 \rho_0(r)$ against $\sqrt{r}$, (**b**) $4\pi f^2 \rho_0(f)$ against $\sqrt{f}$ and (**c**) $4\pi f^2 \rho_0(f)$ against $\sqrt{r}$, in a.u., for the Be atom. The plots for the Li atom are similar. Plots (a) and (b) are identical but (c) is different. Orthonormalized transformed orbitals are employed.

Acknowledgement

The authors thank the Department of Atomic Energy, Government of India, for financial support.

References

[1] I Zh Petkov, M V Stoitsov and E S Kryachko, *Int. J. Quantum Chem.* **29**, 149 (1986)
[2] E S Kryachko and E V Ludena, *Energy Density Functional Theory of Many-Electron Systems*, (Kluwer Academic Press, Dordrecht, 1990) Ch. 7
[3] T Koga, *Phys. Rev.* **A41**, 1274 (1990)
[4] T Koga, *Phys. Rev.* **A42**, 3763 (1990)
[5] T Koga, *J. Chem. Phys.* **95**, 4306 (1991)
[6] R G Parr and M B Chen, *Proc. Natl. Acad. Sci. USA* **78**, 1323 (1981)
[7] B M Deb, P K Chattaraj and S Mishra, *Phys. Rev.* **A43**, 1248 (1991)
[8] E Clementi and C Roetti, *At. Data Nucl. Data Tables* **14**, 174 (1974)
[9] C C J Roothaan and G A Soukup, *Int. J. Quantum Chem.* **15**, 449 (1979)

[redacted]

PRAMANA
— journal of
physics

© Printed in India

Vol. 42, No. 2,
February 1994
pp. 159–165

Hypervirial perturbation theory for eigenenergies for two types of atomic potentials

M R M WITWIT
Department of Applied Mathematics, University of Hull, HU6 7RX, UK

MS received 23 August 1993; revised 15 December 1993

Abstract. Eigenenergies are calculated for the potentials $V_1(r) = -(a/r)[1+(1+br)e^{-2br}]$ and $V_2(r) = -(v/r)[1-\lambda r(1-Z^{-1})(1+\lambda r)^{-1}]$, using renormalized series technique. Accurate results produced here for various eigenstates agree with those available in the literature.

Keywords. Schrödinger equation; two types of potentials; eigenenergies.

PACS No. 3·65

1. Introduction

In quantum mechanics calculation of the eigenvalues of the Schrödinger equation is a very important task. These eigenvalues can be obtained analytically for a few potentials, e.g., for the Coulomb potential, the Morse potential, the square-well potential and the harmonic oscillator. On the contrary large majority of potentials belong to a class of quantum-mechanical potentials which cannot be solved exactly in general, such as the potentials given by equations (2, 3). There is a wide range of approaches, such as variational techniques, the Padé approximant method, the finite difference method and perturbations schemes, to calculate the energy eigenvalues of the Schrödinger equation.

In the present work we apply the hypervirial perturbation theory to study the discrete spectra of Schrödinger equation of the form

$$\left[-\frac{1}{2}\frac{d^2}{dr^2}+\frac{l}{2}(l+1)r^{-2}+V_L(r)\right]\Psi(r)=E\Psi(r), \quad L=1,2. \tag{1}$$

We use atomic units ($m=\hbar=1$). Two examples dealt with and for which there are several comparable studies [1–6] in the atomic physics literature are given by

$$V_1(r) = -\frac{a}{r}[1+(1+br)e^{-2br}] \tag{2}$$

with appropriate values of a and b, $V_1(r)$ represents the potential experienced by the second electron in a helium atom, due to the nucleus and the first electron. Besides its importance for the helium problem, the potential $V_1(r)$ is of special interest being the prototype of more general potentials used in atomic problems [7]. The potential (2) has been studied by many workers [1–3] who have computed its bound state energies, using different numerical techniques.

The second example is the screened Coulomb potential of the form

$$V_2(r) = -\frac{v}{r}[1-\lambda r(1-Z^{-1})(1+\lambda r)^{-1}]. \tag{3}$$

The problem of the screened Coulomb potential is of great importance in all atomic phenomena involving electronic transitions because these potentials are known to adequately describe the effective interaction in many-body atomic phenomena. The potential (3) has been studied by many workers using different types of numerical techniques [4–6]. In the atomic physics application the coupling constant v and the screening parameter λ for the non-Coulombic factor are given by $v = \alpha Z$, $\lambda = \lambda_0 \alpha Z^{1/3}$, $\lambda_0 = 0{\cdot}98$, where $\alpha = 1/137{\cdot}037$ is the fine-structure constant and Z is the atomic number. The potential (3) is almost Coulombic everywhere for it is like $-v/r$ for small r and like $-v/Zr$ for large r.

In the present paper we shall treat the potentials (2 and 3) in the context of renormalized series technique based on the hypervirial theorem and a renormalization parameter β. This technique has previously been used to treat many potentials such as Yukawa, Hulthen potential and other screened Coulomb potentials [8].

2. The hypervirial method and recurrence relations for potential $V_1(r)$

To calculate the eigenvalues for the Schrödinger equation with the potential (2) using hypervirial perturbation theory, it is necessary to write the potential (2) in terms of the perturbation parameter λ as

$$V_1(r) = -\frac{a}{r} - a\left(r^{-1} + \frac{\lambda}{2}\right)e^{-\lambda r}, \quad b = \frac{\lambda}{2}. \tag{4}$$

The central idea of this is to expand the potential function $e^{-\lambda r}$ in a Taylor series around $r = 0$, and solve the resulting approximate problem by hypervirial perturbation theory. The expansion of $V_1(r)$ can be written as

$$V_1(r) = -\frac{a}{r} - a\left[\sum_{m=0}^{\infty} \frac{(-\lambda)^m r^{m-1}}{m!} + \frac{\lambda}{2}\sum_{m=0}^{\infty} \frac{(-\lambda)^m r^m}{m!}\right], \tag{5}$$

$$\equiv -\frac{a}{r} - a\left[\sum_{m=0}^{\infty} \frac{(-\lambda)^m}{m!} r^{m-1} + \frac{1}{2}\sum_{m=0}^{\infty} \frac{(-)^m(\lambda)^{m+1}}{m!} r^m\right]. \tag{6}$$

If we change summation limit of the first term in (6), we obtain

$$V_1(r) = -\frac{2a}{r} - a\left[\sum_{m=1}^{\infty} \frac{(-\lambda)^m}{m!} r^{m-1} + \frac{1}{2}\sum_{m=0}^{\infty} \frac{(-)^m(\lambda)^{m+1}}{m!} r^m\right]. \tag{7}$$

To improve the convergence properties of perturbation series we rearrange terms in the expanded potential (7). To illustrate this technique it is necessary to write the potential appearing in (7) in renormalized form

$$V_1(r) = -2a[\mu + \lambda\beta]r^{-1} - a\left[\sum_{m=1} \frac{(-\lambda)^m}{m!} r^{m-1} + \frac{1}{2}\sum_{m=0} \frac{(-)^m(\lambda)^{m+1}}{m!} r^m\right] \tag{8}$$

where $\mu = 1 - \beta\lambda$. Let us assume that the energy E and the expectation $\langle r^N \rangle$ can be expanded in power series of the perturbation parameter λ as

$$E = \sum E(I)\lambda^I, \tag{9}$$

$$\langle r^N \rangle = \sum H(N, M)\lambda^M. \tag{10}$$

If we use the perturbation expansions given by (9) and (10) in the hypervirial relation given by [8] in the form

$$2E(N+1)\langle r^N \rangle = \sum V_m(2N+2+m)\langle r^{N+m} \rangle - \frac{N}{2}(N^2-1)\langle r^{N-2} \rangle, \tag{11}$$

we obtain the following recurrence relation after some algebra

$$\begin{aligned}(2N+2)\sum_0^M E(I)H(N, M-I) &= N[l(l+1) - \tfrac{1}{4}(N^2-1)]H(N-2, M)\\ &- 2a[2N+1][\mu H(N-1, M) + \beta H(N-1, M-1)]\\ &+ V_{m1}[2N+m+1]H(N+m-1, M-m)\\ &+ V_{m2}[2N+2+m]H(N+m, M-m-1).\end{aligned} \tag{12}$$

The coefficients V_{m1} and V_{m2} can be written as

$$V_{m1} = -a\sum_{m=1}^{\infty}\frac{(-)^m}{m!}, \tag{13}$$

$$V_{m2} = -\frac{a}{2}\sum_{m=0}^{\infty}\frac{(-)^m}{m!}. \tag{14}$$

We have expanded the potential coefficients (13) and (14) to the limit in which any term beyond that limit makes no difference to our calculations. For the present calculations this limit was reached for ($m = 16$). The two coefficients (13 and 14) in general alternate in sign and the coefficients decrease with increasing m.

Applying the Hellmann–Feynman theorem in the form

$$\frac{\partial E}{\partial \lambda} = \left\langle \frac{\partial V}{\partial \lambda} \right\rangle \tag{15}$$

we obtain a recurrence relation for the energy coefficients of the form

$$\begin{aligned}(M+1)E(M+1) = -2a\beta H(-1, M) &+ mV_{m1}H(m-1, M-m+1)\\ &+ [m+1]\,V_{m2}H(m, M-m)\end{aligned} \tag{16}$$

where the energy of the unperturbed nth state is

$$E(0) = -\frac{a^2\mu^2}{n^2}. \tag{17}$$

The recurrence relations (12) and (16) can be used to calculate the energy coefficients from a knowledge of $H(0,0) = 1$ and $E(0)$.

3. The hypervirial method and recurrence relations for potential $V_2(r)$

In this section we calculate the bound state energies of the screened Coulomb potential $V_2(r)$ for different eigenstates, by applying the hypervirial and Hellmann–Feynman theorems to calculate perturbatively the bound state energy levels without using perturbed wavefunctions, the potential $V_2(r)$ may be written in the form

$$V_2(r) = -\frac{v}{r} + \lambda v(1 - Z^{-1})(1 + \lambda r)^{-1}. \tag{18}$$

The potential (18) can be expanded as

$$= -\frac{v}{r} - v(1 - Z^{-1}) \sum_{m=0}^{\infty} (-\lambda)^{m+1} r^m. \tag{19}$$

The potential (19) can be expressed in renormalized form

$$V(r) = -v[\mu + \lambda\beta] r^{-1} - v(1 - Z^{-1}) \sum_{m=0}^{\infty} (-\lambda)^{m+1} r^m \quad \mu = 1 - \lambda\beta \tag{20}$$

If we use the hypervirial relation (11) as in the previous section together with perturbation expansions given by (9) and (10) for potential (20) leading to the following recurrence relation

$$\begin{aligned}(2N+2)\sum_{0}^{M} E(I)H(N, M-I) &= N[l(l+1) - \tfrac{1}{4}(N^2-1)]H(N-2, M)\\ &\quad - v[2N+1][\mu H(N-1, M) + \beta H(N-1, M-1)]\\ &\quad + V_m[2N+m+2]H(N+m, M-m-1)\end{aligned} \tag{21}$$

where

$$V_m = -v(1 - Z^{-1}) \sum_{m=0}^{\infty} (-)^{m+1} \tag{22}$$

If we apply the Hellmann–Feynman theorem which is given by (15) and use the energy and the expectation value $\langle r^N \rangle$ series as given by (9) and (10) we obtain the following recurrence relation

$$(M+1)E(M+1) = -\beta H(-1, M) + [m+1]\, V_m H(m, M-m). \tag{23}$$

The recurrence relations (21) and (23) with unperturbed energy $E(0) = -v^2\mu^2/2n^2$ and initial condition $H(0,0) = 1$ can be used to evaluate the energy coefficients $E(M)$.

4. Numerical results and discussion

In the present work we show how the renormalized series technique can be used for solving the eigenvalue problem. Our technique has been tested for the Schrödinger equation involving two types of atomic potentials. This technique has been shown to be very effective and more accurate than other methods which have been used to handle the same calculations [1–6]. We have calculated energy levels for potentials (2) and (3), for several eigenstates, different values of λ and over a wide range of values of an atomic number Z.

Table 1. Eigenvalues of the potential $V_1(r)$, for several states and different values of the perturbation parameter λ. The empty spaces mean that the corresponding eigenvalues cannot be reached by our technique.

	$-E_{nl/a^2}$			
S	$\lambda = 0{\cdot}010$	$\lambda = 0{\cdot}015$	$\lambda = 0{\cdot}018$	$\lambda = 0{\cdot}020$
1*s*	1·990000506306924	1·985001719575	1·982002982696	1·98000410184407
2*s*	0·490007282474012	0·485025075092	0·482043856739	0·48006064920319
3*s*	0·212259757166784	0·207354504983	0·204456932941	0·20254999056173
4*s*	0·115125251146804	0·110457274703	0·107830352762	0·10617901123446
5*s*	0·070331611296376	0·066279398685	0·06442855	0·063592
6*s*	0·046323898496	0·04388		
7*s*	0·0324852			
2*p*	0·490005179368098	0·485017794813	0·482031082486	0·48004294593839
3*p*	0·212254715472863	0·207336473486	0·204424654765	0·20250464670232
4*p*	0·115115441929899	0·110420433374	0·107762271451	0·10608116832868
5*p*	0·070314330389804	0·066209366162	0·06429074	0·06338
6*p*	0·04629474917	0·04374		
7*p*	0·0324354			
3*d*	0·212244709229763	0·207300827916	0·204360999606	0·20241537041801
4*d*	0·115095975575826	0·110347620894	0·107628061997	0·1058886351467
5*d*	0·070280041156948	0·066071034235	0·06401954	0·062967
6*d*	0·04623692646	0·043467		
7*d*	0·0323367			
4*f*	0·115067156077349	0·110240576818	0·107431630061	0·10560771699417
5*f*	0·070229288635185	0·065867869543	0·06362375	0·062369
6*f*	0·046151382507	0·043063		
7*f*	0·032191			
6*h*	0·0460395458168	0·042546		
7*h*	0·03200107	0·03		
8*h*	0·0241			

	$-E_{nl/a^2}$			
λ	1*s*	2*s*	2*p*	3*s*
0·025	1·975008062303	0·475120894718	0·475085416748	0·19789232491473
0·030	1·970014020431	0·470213255371	0·470150337166	0·19343652031976
0·035	1·965022406241	0·465345779041	0·465243213018	0·18924939238
0·040	1·960033660542	0·460527177763	0·460369961841	0·18541468
0·045	1·955048235217	0·455766900334	0·455536956196	0·182044
0·050	1·950066593503	0·451075221633	0·450751076828	0·17931
0·055	1·945089210289	0·446463354484	0·446019778919	0·1775
0·060	1·940116572432	0·441943592771	0·441351176185	0·176
0·065	1·935149179084	0·4375294994	0·43675415007	
0·070	1·930187542037	0·433236162	0·4322384959	
0·075	1·925232186087	0·42908056	0·427815128	
0·080	1·920283649421	0·4250822	0·42349639	
0·085	1·915342484017	0·42164	0·4192965	
0·090	1·910409256077	0·41765	0·415233	
0·095	1·905484546482	0·4143	0·41133	
0·100	1·900568951274	0·41119	0·40759	
0·150	1·852057405331			
0·200	1·80525132			
0·250	1·76114			
0·300	1·7213			
0·400	1·67			

In table 1, we present the eigenvalues for the potential $V_1(r)$ for different values of λ and different state numbers. The renormalized series provides extremely accurate eigenvalues at low λ. But, at larger values of λ and higher excited states, the accuracy

Table 2. Bound-state energies (in keV) for the potential $V_2(r)$ for the states $(1s, 2s, 2p, 3s, 3p, 3d)$. The values of the renormalization parameter β are given. M is the order of the perturbation expansion with which we obtain convergence.

Z	$-E_{1s}$	M	$-\beta$	$-E_{2s}$	M	$-\beta$	$-E_{2p}$	M	$-\beta$
4	0·13523	12	1·2	0·0138	40	26	0·0123	10	2·6
9	0·766002	14	1	0·0828	48	18	0·0697	16	2·5
14	1·993278	16	1	0·2448	54	15	0·2142	17	2·4
19	3·8419428	17	0·9	0·5172	60	14	0·4674	18	2·2
24	6·3241426	16	0·8	0·9107	70	14	0·8411	19	2·1
29	9·44728452	17	0·7	1·4324	73	13	1·3428	18	1·9
34	13·21643035	16	0·6	2·0873	74	12	1·9779	19	1·9
39	17·635292381	16	0·5	2·87934	75	11	2·7503	20	1·8
44	22·706727619	18	0·5	3·81148	75	10	3·6631	19	1·7
49	28·4330136113	40	0·4	4·88617	80	10	4·7187	17	1·6
54	34·81601545815	39	0·3	6·10552	70	8	5·91934	18	1·4
59	41·857292885107	28	0·2	7·47117	65	7	7·26647	18	1·2
64	49·558172935606	28	0·2	8·98457	70	7	8·76162	18	0·9
69	57·919800654238	32	0	10·64701	62	6	10·406027	17	0·9
74	66·9431758274224	34	0	12·45959	69	6	12·200809	16	0·8
79	76·6291802637234	34	0	14·42328	44	4	14·1469203	17	0·7
84	86·9785985081688	31	0	16·53894	43	4	16·2452164	16	0·7
89	97·9921338756381	28	0	18·80734	38	3	18·4964652	16	0·6
94	109·670421069675	20	0	21·229208	16	0	20·9013591	15	0·6
100	124·562645734566	21	0	24·338872	15	0	23·99092361	16	0·5
110	151·514471031952	20	0	30·0173678	16	0	29·63648765	15	0·5
120	181·133721056460	17	0	36·3189465	16	0	35·905799803	16	0·4

Z	$-E_{3s}$	M	$-\beta$	$-E_{3p}$	M	$-\beta$	$-E_{3d}$	M	$-\beta$
14	0·0476	12	1·8	0·0381	11	1·5	0·0228	14	1·4
19	0·1049	12	1·4	0·0876	14	1·4	0·0576	12	1·2
24	0·19477	15	1·3	0·16832	16	1·2	0·12033	12	0·8
29	0·32191	16	1·3	0·28526	14	1·1	0·217001	14	0·8
34	0·49007	16	1·2	0·44249	16	1·1	0·352318	16	0·8
39	0·70223	16	1·2	0·64317	15	1·1	0·529913	14	0·6
44	0·96083	15	1·1	0·88987	16	1·1	0·752687	14	0·6
49	1·26792	16	1·1	1·184772	16	0·9	1·023009	14	0·6
54	1·625248	17	0·9	1·529661	16	0·8	1·342859	12	0·5
59	2·034299	14	0·8	1·926106	15	0·7	1·7139192	12	0·5
64	2·4963937	16	0·7	2·3754626	16	0·7	2·1376324	15	0·5
69	3·0126824	16	0·6	2·8789179	17	0·7	2·6152581	14	0·5
74	3·5841909	14	0·6	3·4375239	17	0·5	3·1479033	14	0·5
79	4·2118361	15	0·5	4·0522190	15	0·5	3·7365502	15	0·5
84	4·8964437	15	0·4	4·7238464	14	0·4	4·3820766	16	0·5
89	5·6387619	15	0·5	5·4531682	16	0·5	5·08527290	14	0·4
94	6·4394719	12	0·5	6·24087711	14	0·5	5·84685424	14	0·3
100	7·47827502	14	0·5	7·26408595	14	0·5	6·83873299	14	0·3
110	9·401082478	14	0·5	9·160952213	15	0·5	8·68350120	15	0·3
120	11·56665076	17	0·4	11·30067818	15	0·5	10·77134969	13	0·3

decreases, exactly as in our previous renormalized series calculations [8]. The accuracy of our results in general is better than that of previous studies [1–3].

Our confidence in the accuracy of our results comes from the checks, the agreement between our results and with those results produced by using finite difference technique [9]. Also by two separate computations for some eigenstates with slightly increasing or decreasing the value of the renormalization parameter β, yielded eigenenergy agreeing to all digits.

In table 2, we list the energy of states ($1s$, $2s$, $2p$, $3s$ $3p$, $3d$), for different values of $Z (4 \leqslant Z \leqslant 120)$. For a given shell the results improve with increasing Z, and this behavior is clear from our listed results. The degree of agreement between our results and those arising form other methods [4–6] is good, but for $Z > 84$ numerical results are not reported. We state that the renormalized series technique work equally for $\lambda = \lambda_0$ and $\lambda = \lambda_0 \alpha Z^{1/3}$ as perturbation parameter; we used two values of λ to verify the accuracy of renormalized series.

For comparison with the results available in literature [1–6], the energy in table 1 is given as $-E_{nl/a^2}$. Also using other parameters such as $v = \alpha Z$, $\lambda = \lambda_0 \alpha Z^{1/3}$ in our calculations and listed energies E_{nl} in keV in table 2 we obtain the relation

$$\begin{aligned}\text{Energy} &= [2 \times 13{\cdot}6047][1000\alpha^2]^{-1} E \ \text{keV} \\ &= 510{\cdot}969 E \ \text{keV}. \qquad (24)\end{aligned}$$

References

[1] R Sever and C Tezcan, *Phys. Rev.* **A36**, 1045 (1987)
[2] R Sever and C Tezcan, *Phys. Rev.* **A37**, 3158 (1988)
[3] Y P Varshni, *Phys. Rev.* **A38**, 1595 (1988)
[4] C H Mehta and S H Patil, *Phys. Rev.* **A17**, 34 (1978)
[5] R L Hall, *Phys. Rev.* **A32**, 14 (1985)
[6] R Roychoudhury, B Roy and Y P Varshni, *Phys. Rev.* **A38**, 3944 (1988)
[7] A Hibbert, *Adv. At. Mol. Phys.* **18**, 309 (1982)
[8] M R M Witwit, *J. Phys.* **A24**, 4535 (1991)
[9] M R M Witwit, *J. Phys.* **A25**, 503 (1992)

[redacted]

PRAMANA
— journal of
physics
© Printed in India
Vol. 42, No. 3,
March 1994
pp. 167–173

Photoelasticity in quasicrystals

K RAMA MOHANA RAO and P HEMAGIRI RAO*
Department of Applied Mathematics, Andhra University Post-Graduate Centre, Nuzvid 521 201, India
*Department of Mathematics, Bapatla Engineering College, Bapatla 522 101, India

MS received 31 August 1993; revised 1 January 1994

Abstract. The maximum number of non-vanishing and independent second order photoelastic coefficients required by the seven pentagonal and the two icosahedral point groups $5(C_5)$, $\bar{5}(S_{10})$, $\overline{10}(C_{5h})$, $\overline{10}\,m2(D_{5h})$, $52(D_5)$, $5m(C_{5v})$, $\bar{5}\,2m(D_{5d})$; $235(I)$, $2/m\,\bar{3}\,\bar{5}(I_h)$—that describe the quasicrystals symmetry groups in two and three dimensions—is obtained. The schemes of non-vanishing and independent coefficients have been calculated and listed. Finally the results of this group-theoretical study are briefly discussed.

Keywords. Quasicrystals; pentagonal and icosahedral point groups; photoelasticity, non-vanishing and independent tensor coefficients.

PACS No. 78·20

1. Introduction

The discovery of Al–Mn quasicrystal by Schectman *et al* [1] representing the first real life example with non-crystallographic rotational symmetry has jolted our notions about the structure of solids. This experimental evidence and the theoretical reasons [2] made the scientists world-over believe that although periodic crystals with pentagonal symmetry in two-dimensions (2D) and icosahedral symmetry in three-dimensions (3D) cannot exist, quasicrystals with such symmetries can and do exist. The hunt for stable icosahedral phases resulted in the solidification of Al–Cu–Fe, Al–Pd–Mn [3, 4, 5]; Al–Cu–Li; Al–Cu–Ru [6] and Al–Pd–Cr–Fe [7] systems. The discovery of these materials, in addition to giving a better understanding of the microstructure of the quasicrystals, has indeed provided an opportunity for studying the dislocations, hydrodynamic theory, elasticity [8, 9, 10] and electronic properties such as resistivity, magneto-resistance and Hall-effect [11] etc. of some stable icosahedral quasicrystals.

The discovery of optically active and transparent quasicrystals such as the rare-earth pyrogermanate ($R_2Ge_2O_7$) quasicrystal and the thulium pyrogermanate (Tm PG) one, with unique crystal field potential of $\overline{10}\,m2(D_{5h})$ site symmetry [10] have paved the way for the group-theoretical physicists to study some optical properties such as photo-elasticity. Yi-Jian Jiang *et al* [12] calculated the (first order) photoelastic tensor coefficients for all the nine point groups: $5(C_5)$, $\bar{5}(S_{10})$, $\overline{10}(C_{5h})$, $\overline{10}\,m2(D_{5h})$, $52(D_5)$ $5m(C_{5v})$, $\bar{5}\,2m(D_{5d})$; $235(I)$, and $2/m\,\bar{3}\,\bar{5}(I_h)$ with five-fold rotational axes of symmetry. In this communication, exploring the group-theoretical methods, we have obtained the maximum number of non-vanishing and independent tensor coefficients required by the aforesaid nine point groups, which describe the symmetry groups of the quasicrystals in 2D and 3D, to describe the second order photoelasticity. The obtained schemes of non-vanishing and independent second-order photoelastic tensor coefficients have been listed in table 1, employing an elegant and simple notation adopted by Vedam and Srinivasan [13] in respect of such coefficients for the 32 crystallographic point groups. Finally a brief summary of the results obtained vis-a-vis the importance of photoelastic tensor schemes, is provided in §3.

2. Second order photoelastic coefficients: Evaluation and results

It is well known that substances that are optically isotropic initially, become birefringent under the application of stress and stress alters the birefringence in substances which already possess it. This phenomenon known as photoelasticity is thus a physical property arising from an action and effect relation between a symmetric second rank tensor and another symmetric second rank tensor. The strain optical coefficients and stress optical coefficients are related between themselves as

$$p_{ik} = q_{ij}C_{jk}; \quad q_{ik} = p_{ij}S_{jk}. \tag{2.1}$$

In (2.1) the C's and S's are respectively the elastic stiffness and elastic compliances. Since the relation $p_{ik} = p_{ki}$ or $q_{ik} = q_{ki}$ do not hold good in respect of photoelasticity, in the general unsymmetrical case, there are 36 independent first order photoelastic coefficients. The maximum number of first order coefficients for each of the nine aforesaid point groups were obtained by Yi Jian Jiang *et al* [12].

The second order photoelastic tensor P_{ijklmn} is a product of symmetric tensor (C_{ij}) and square of the symmetric tensor (C_{klmn}). Following a two suffix notation, it can be written as a sixth rank tensor p_{ijk} that is symmetric with respect to the last two suffixes j and k. Hence the compound character $\chi_\rho(R)$ for the second order photoelastic tensor can be expressed as:

$$\chi_\rho(R) = (4C^2 \pm 2C)(16C^4 \pm 8C^3 - 4C^2 + 1). \tag{2.2}$$

In (2.2), C stands for the cosine of the angle of rotation ϕ, represented by the symmetry operation R under consideration. The positive or negative sign is to be taken according to whether the symmetry operation R is a pure rotation or a rotation reflection.

The maximum number of non-vanishing and independent photoelastic coefficients (n_i) of the property tensor under consideration, for each of the nine point groups with five fold rotations, are determined using the well-known formula:

$$n_i = \frac{1}{g}\sum_\rho h_\rho \chi_\rho(R)\chi_\rho^{(\Gamma_i)}(R) \tag{2.3}$$

with the usual notation.

To identify the non-vanishing tensor coefficients, the transformations corresponding to the pentagonal and icosahedral symmetries under consideration cannot be applied adopting the ordinary (direct inspection) method of Nye [14]. Hence we resorted to the analytical method of writing the transformation equations and finding the governing relations between the coefficients. Following the application of a symmetry operation on these relations, which is normally a generating element of the point group under consideration, a transformation of the kind $x'_i = a_{ij}x_j$ is obtained. This

Table 1. Second order photoelastic coefficients.

Quasi-crystal class/ constant	$5, \bar{5}$	$\overline{10}$	$52, \bar{5}2m$	$5m$	$\overline{10}m2$	$235, 2/m\bar{3}\bar{5}$
111	111	111	111	111	111	111
112	112	112	112	112	112	112
113	113	113	113	113	113	113
114	114	0	114	0	0	a
115	115	0	0	115	0	0
116	116	116	0	0	0	0
122	122	122	122	122	122	122
123	123	123	123	123	123	123
124	−114	0	−114	0	0	−a
125	−115	0	0	−115	0	0
126	116	116	0	0	0	0
133	133	133	133	133	133	b
134	0	0	0	0	0	0
135	0	0	0	0	0	0
136	136	136	0	0	0	0
144	144	144	144	144	144	c
145	145	145	0	0	0	0
146	−115	0	0	−115	0	0
155	155	155	155	155	155	d
156	114	0	114	0	0	a
166	e	e	e	e	e	e
211	122	122	122	122	122	122
212	112	112	112	112	112	112
213	123	123	123	123	123	123
214	−114	0	−114	0	0	−a
215	−115	0	0	−115	0	0
216	−116	−116	0	0	0	0
222	111	111	111	111	111	111
223	113	113	113	113	113	113
224	114	0	114	0	0	a
225	115	0	0	115	0	0
226	−116	−116	0	0	0	0
233	133	133	133	133	133	b
234	0	0	0	0	0	0
235	0	0	0	0	0	0
236	−136	−136	0	0	0	0
244	155	155	155	155	155	d
245	−145	−145	0	0	0	0
246	115	0	0	115	0	0
255	144	144	144	144	144	c
256	−114	0	−114	0	0	−a
266	e	e	e	e	e	e
311	311	311	311	311	311	f
312	312	312	312	312	312	123
313	313	313	313	313	313	g

(Continued)

Table 1. *(Continued)*

Quasi-crystal class/ constant	$5, \bar{5}$	$\overline{10}$	$52, \bar{5}2m$	5m	$\overline{10}m2$	$235, 2/m\bar{3}\bar{5}$
314	0	0	0	0	0	0
315	0	0	0	0	0	0
316	0	0	0	0	0	0
322	311	311	311	311	311	f
323	313	313	313	313	313	g
324	0	0	0	0	0	0
325	0	0	0	0	0	0
326	0	0	0	0	0	0
333	333	333	333	333	333	h
334	0	0	0	0	0	0
335	0	0	0	0	0	0
336	0	0	0	0	0	0
344	344	344	344	344	344	i
345	0	0	0	0	0	0
346	0	0	0	0	0	0
355	344	344	344	344	344	i
356	0	0	0	0	0	0
366	j	j	j	j	j	j'
411	411	0	411	0	0	a
412	−411	0	−411	0	0	−a
413	0	0	0	0	0	0
414	414	414	414	414	414	k
415	415	415	0	0	0	0
416	416	0	0	416	0	0
422	411	0	411	0	0	a
423	0	0	0	0	0	0
424	424	424	424	424	424	l
425	425	425	0	0	0	0
426	−416	0	0	−416	0	0
433	0	0	0	0	0	0
434	434	434	434	434	434	m
435	435	435	0	0	0	0
436	0	0	0	0	0	0
444	0	0	0	0	0	0
445	0	0	0	0	0	0
446	n	n	0	0	0	0
455	0	0	0	0	0	0
456	p	p	p	p	p	p'
466	−411	0	−411	0	0	−a
511	−416	0	0	−416	0	0
512	416	0	0	416	0	0
513	0	0	0	0	0	0
514	−425	−425	0	0	0	0
515	424	424	424	424	424	l
516	411	0	411	0	0	a
522	−416	0	0	−416	0	0
523	0	0	0	0	0	0

Table 1. (*Continued*)

Quasi-crystal class/ constant	$5,\bar{5}$	$\overline{10}$	$52,\bar{5}2m$	$5m$	$\overline{10}m2$	$235, 2/m\bar{3}\bar{5}$
524	−415	−415	0	0	0	0
525	414	414	414	414	414	k
526	−411	0	−411	0	0	−a
533	0	0	0	0	0	0
534	−435	−435	0	0	0	0
535	434	434	434	434	434	m
536	0	0	0	0	0	0
544	0	0	0	0	0	0
545	0	0	0	0	0	0
546	p	p	p	p	p	p'
555	0	0	0	0	0	0
556	−n	−n	0	0	0	0
566	416	0	0	416	0	0
611	−2(116)	−2(116)	0	0	0	0
612	0	0	0	0	0	0
613	−136	−136	0	0	0	0
614	−115	0	0	−115	0	0
615	114	0	114	0	0	a
616	q	q	q	q	q	q
622	2(116)	2(116)	0	0	0	0
623	136	136	0	0	0	0
624	115	0	0	115	0	0
625	−114	0	−114	0	0	−a
626	q	q	q	q	q	q
633	0	0	0	0	0	0
634	0	0	0	0	0	0
635	0	0	0	0	0	0
636	k	k	k	k	k	k
644	145	145	0	0	0	0
645	r	r	r	r	r	p'
646	−114	0	−114	0	0	−a
655	−145	−145	0	0	0	0
656	−115	0	0	−115	0	0
666	0	0	0	0	0	0
Maximum No. of independent constants 126	26	22	18	18	16	5

Table 2. Key to alphabetical symbols used in table 1.

Symbol	Expression	Symbol	Expression
a	112 − 113		
b	112 − 113 + 122		
c	− 1/2[112 − 113 − 122 + 123]		
d	1/4[111 − 6(112) + 4(113) + 122]		
e	1/4[111 − 2(112) + 122]		
f	− [112 − 113 − 122]		
g	2(112) − 113		
h	111 − 3(112) + 3(113)		
i	1/4[111 + 2(112) − 4(113) + 122]		
j	1/2[311 − 312]	j$^{\text{l}}$	− 1/2[112 − 113 − 122 + 123]
k	1/2[113 − 123]		
l	1/4[111 − 4(112) + 4(113) − 122]		
m	1/4[111 + 4(112) − 4(113) − 122]		
n	1/2[415 − 425]		
p	− 1/2[414 − 424]	p$^{\text{l}}$	1/8[111 − 4(112) + 2(113) − 122 + 2(123)]
q	1/4[111 − 122]		
r	− 1/2[144 − 155]		

induces a transformation in the components of the second order photoelastic tensor P_{ijklmn} which may be written as

$$P'_{ijklmn} = a_{io} a_{jp} a_{kq} a_{lr} a_{ms} a_{nt} P_{opqrst}, \quad 1 \leqslant i, j, k, l, m, n \leqslant 3. \tag{2.4}$$

By giving different values for the suffixes in (2.4) and demanding invariance of the tensor components under the considered transformation, we obtain a set of simultaneous equations, which when solved give the desired tensor coefficients. The non-vanishing and independent schemes of second order photoelastic tensor coefficients derived for all the nine quasicrystalline classes are listed in table 1, adopting tabulation method due to [13] in respect of the second order photoelastic coefficients of crystals.

The second-order photoelastic tensor P_{ijklmn} is invariant with respect to an interchange of i, j or k, l or m, n and also under the interchange of $k\, l$ and $m\, n$. Although a sixth rank tensor in three variables can possess $3^6 = 729$ components, intrinsic symmetry reduces the maximum number to 126. When the tensor components are written in three suffix notation P_{ijk}, the independent components are P_{ijk} whose suffixes take values from 1 to 6 such that $j \leqslant k$. Table 2 gives the key to symbols used in table 1. To avoid the excessive use of suffixes, the letter P is omitted from tables 1 and 2; an entry 111 in the table, for example, stands for P_{111} and an entry $\frac{1}{4}[111 - 6(112) + 4(113) + 122]$ for $\frac{1}{4}[P_{111} - 6P_{112} + 4P_{113} + P_{122}]$.

3. Results and discussion

It can be observed that the number of photoelastic coefficients increase with the order of the effect. Whereas for the first order effect [12] the maximum number obtained was only five, for the second order effect it is 26. The seven pentagonal classes separate into five sets 5, $\bar{5}$; $\overline{10}$; 52, $\bar{5}$ 2*m*; 5*m*; $\overline{10}$ *m*2 requiring 26; 22; 18; 18; 16 coefficients respectively and the two icosahedral classes 235; 2/*m* $\bar{3}\,\bar{5}$ forming a single set, require 5 coefficients each.

Yi Jian Jiang *et al* [12] obtained the maximum number of independent first order photoelastic coefficients for icosahedral class and found it to be two. They have verified that the corresponding number for the isotropic medium was also two. But we find here that the maximum number of independent second order photoelastic tensor coefficients for the icosahedral class is five, whereas the corresponding number for the isotropic medium is four.

From table 1, one can observe that the photoelastic tensor coefficients obtained for the icosahedral class in this work are fewer than such coefficients needed by any one of the 32 crystal classes [13].

The maximum number of non-vanishing and independent tensor coefficients obtained for the quasicrystalline classes for the second order photoelasticity, which is a sixth rank cross property type tensor has been listed in the last row of table 1. In view of the importance of photoelasticity and as the same schemes are applicable to a few other properties, namely, piezoresistance, magnetoresistance and magnetothermal conductivity, the full schemes obtained for all the nine physically interesting point groups are listed in table 1. We hope that condensed matter physicists shall evaluate the utility of these coefficients.

Acknowledgements

The authors thank Professor L S R K Prasad, AUPG Centre, Nuzvid for his constant encouragement. They are also grateful to the referee for his constructive comments.

References

[1] D Schectman, I Blech, D Gratias and J W Cahn, *Phys. Rev. Lett.* **53**, 1951 (1984)

[2] D Levine and P J Steinhandt, *Phys. Rev. Lett.* **53**, 2477 (1984)

[3] T Klein, C Berger, D Mayou and F Cyrot Lackman, *Phys. Rev. Lett.* **66**, 2907 (1991)

[4] A P Tsai, A Inoue and T Masumoto, *Mat. Trans. JIM*. **31**, 98 (1990)

[5] A P Tsai, Y Yokoyama, A Inoue and T Masumoto, In *Proc. Intl. Symp. physics and chemistry of finite systems* edited by P Jena, S N Khanna and B K Rao (Kluewer, Dordrecht, 1992) pp. 177

[6] A P Tsai, A Inoue and T Masumoto, *Jpn. J. Appl. Phys.* **26** L1505 (1987)

[7] Z Wang, R A Dunlap and D W Lawther, *J. Phys. Condens. Matter.* **5** 663 (1993)

[8] P Bak, *Phys. Rev.* **B32**, 5764, (1985)

[9] D Levine, T C Lubensky, S Ostlund, S Rama Swamy and P J Steinhandt, *Phys. Rev. Lett.* **54**, 405 (1985)

[10] A Sen Gupta, S Bhattacharya, D Gosh and B M Wanklyn, *Indian J. Phys.* **62**, 900 (1988)

[11] Takeo Fujiwara, *J. Non-Cryst. Solids*, **156**, 865 (1993)

[12] Yi-Jian Jiang, Liao Li-Ji, Chen Gang and Zhang Peng-Xiang, *Acta Crystallogr.* **A46**, 772 (1990)

[13] K Vedam and R Srinivasan, *Acta Crystallogr.* **22**, 630 (1967)

[14] J F Nye, In *Physical properties of crystals* (Clarendon, Oxford, 1985) p. 116

PRAMANA
— journal of
physics

© Printed in India

Vol. 42, No. 3,
March 1994
pp. 175–185

Elastic anomalies in strontium titanate

K S VISWANATHAN and B SUBRAMANYAM
Department of Physics, Indian Institute of Technology, Madras 600036, India

MS received 1 October 1993

Abstract. The anomalies of the second and third-order elastic constants have been considered for the phase transition of strontium titanate within the framework of Landau's theory. All the anomalies of the second-order elastic constants have been obtained in a single formula using Kronecker delta functions and relations among them have been established. The real parts of C^*_{11} and C^*_{44} decrease steeply across the transition temperature and thereafter flatly tend to their asymptotic values in the low temperature phase agreeing qualitatively with experimental observations. We have also derived expressions for the third-order elastic anomalies and discussed the temperature variation of the real part of C^*_{111}. We have derived expressions for the attenuation of the longitudinal and transverse waves along certain simple symmetry directions and have shown that there is nearly good agreement with experimental observations.

Keywords. Elastic anomalies; phase transition; strontium titanate

PACS Nos 64·70; 62·20

1. Introduction

Strontium titanate has a cubic perovskite structure and undergoes an improper ferroelastic second order-phase transition near a temperature of 105 K. While at normal temperature, $SrTiO_3$ is paraelectric, it transforms on cooling to a tetragonal phase with a c/a ratio of 1·00056. The optical, dielectric, thermal and elastic properties associated with the phase transition have been investigated by many workers and these have been reviewed by various authors [1–4]. Experimental studies in $SrTiO_3$ as well as in similar crystals like $KMnF_3$, $LaAlO_3$, $PAlO_3$ and $NdAlO_3$ have demonstrated that spontaneous optic mode displacements and spontaneous strains appear during the phase transition at the low temperature phase [5–6].

Another aspect of the phase transition that has been extensively studied relates to second harmonic generation and the third-order elastic constants [7]. Peters and Arnold [8] studied the temperature variation of the third-order elastic constant C_{111} in the range 103–300 K using ultrasonic harmonic generation technique. Meeks and Arnold [9] used the second harmonic generation technique to measure combinations of several third-order elastic constants over a wide range of temperatures. The work of Bell and Rupprecht [10] showed that there were pronounced variations in the second-order elastic constants besides, large changes in ultrasonic attenuation occur near the phase transition. The attenuation of elastic waves and the changes in their velocity during phase transition have been investigated by Fossum and Fossheim [11] and also by Schwabl and Iro [12].

In this paper, we study systematically the anomalies near the phase transition of $SrTiO_3$ of the second and third-order elastic constants within the framework of the Landau theory. While the initial strains and the components of the order parameter in the low temperature phase can be obtained from the stability conditions, the fluctuations in these parameters from their equilibrium values have been derived by an appeal to the Landau-Khalatnikov equations in irreversible statistical mechanics. In §4 we derive the anomalies for all the second-order elastic constants in a single formula and discussed the temperature variation of the second-order elastic constants. In §5, we derive expressions for the anomalies in third-order elastic constants in terms of the coupling constants and discuss the temperature variation of C^*_{111} near the transition temperature. In §6, we make comments about the attenuation of the longitudinal and transverse modes along the principal axis and face diagonal of the crystal.

2. The equilibrium values of the order parameters and the strains

Strontium titanate undergoes a structural phase transition from cubic to tetragonal class at a temperature of 105 K. The transition is induced by the softening of the phonon mode at (π/a) $(1,1,1)$ corner of the Brillouin zone. Below transition temperature, there is coupling of the unit cell and the symmetry of the crystal changes from O_h to D^{18}_{4h}. The order parameter is the rotation of the alternate oxygen octahedra TiO_6 around cubic axes. The phase transition is an improper ferroelastic transition.

The free energy of the crystal is the sum of the elastic energy F_{el}, the Landau energy F_Q and the coupling energy F_c

$$F = F_{el} + F_Q + F_c \tag{1}$$

The elastic energy of the crystal in the cubic phase is the sum of the second-order (E_2) and third-order (E_3) deformation energies. Further,

$$E_2 = \frac{1}{2}\{C_{11}(\eta_1^2+\eta_2^2+\eta_3^2) + 2C_{12}(\eta_2\eta_3+\eta_3\eta_1+\eta_1\eta_2) + C_{44}(\eta_4^2+\eta_5^2+\eta_6^2)\} \tag{2}$$

where $\eta_1, \eta_2, \ldots, \eta_6$ are the six components of the strain tensor. The expression E_3 for the third-order deformation energy is well known and is not reproduced here for lack of space. It can be shown that the corrections brought about by third-order deformation energy to equilibrium values of order parameter and strain variables are smaller by a factor $Q^2_{30}C_{ijk}(C_{ij})^{-2}$ in comparison with the contribution from second-order deformation energy. We shall therefore neglect them in future calculations. The order parameter is the octahedra rotation. The three components of the order parameter are denoted by Q_1, Q_2, Q_3 such that $Q^2 = Q_1^2 + Q_2^2 + Q_3^2$. The Landau free energy is given by Lemanov [1]

$$F_Q = \frac{1}{2}\alpha Q^2 + \frac{1}{4}\beta_1 Q^4 + \frac{1}{4}\beta_2(Q_2^2Q_3^2 + Q_3^2Q_1^2 + Q_1^2Q_2^2) \tag{3}$$

where $\alpha = \alpha'(T - T_c)$, α' being a constant. The coefficients β_1 and β_2 are constants, very nearly independent of temperature.

The term F_c due to coupling between the order parameter and the strains had been evaluated using symmetry consideration and is given by Lemanov [1]

$$F_c = d_1\{(Q^2-3Q_1^2)\eta_1+(Q^2-3Q_2^2)\eta_2+(Q^2-3Q_3^2)\eta_3\}$$
$$+d_t\{(Q_2Q_3\eta_4+Q_3Q_2\eta_5+Q_1Q_2\eta_6\} \tag{4}$$

where d_1 and d_t are coupling constants.

The free energy is a function of the three components of the order parameter and the six strain components. For the stability of the crystal, the partial derivatives of F with respect to all these nine parameters should vanish.

It can be seen that the solution of these nine equations for the high temperature paraelectric phase corresponds to the case in which all the three components of the order parameter as well as the six strain components vanish.

The phase transition of $SrTiO_3$ to the tetragonal phase is ferroelastic and corresponds to the case in which the order parameter along the c-axis is nonzero while the other two components are zero. Hence the case $Q_1 = Q_2 = 0$ and $Q_3 \neq 0$ needs to be discussed. Solving the nine equations for the stability conditions, we find that the equilibrium values of the order parameter as well as the nonvanishing strain components are given by

$$Q_{30}^2 = (\alpha/a), \tag{5}$$

$$\eta_{10} = \eta_{20} = -d_1(C_{11}-C_{12})^{-1}Q_{30}^2, \tag{6}$$

$$\eta_{30} = 2d_1(C_{11}-C_{12})^{-1}Q_{30}^2. \tag{7}$$

3. The Landau–Khalatnikov equation and the fluctuations in the order parameter

The Landau–Khalatnikov equation expresses the fact that the time rate of change $\mathrm{d}Q/\mathrm{d}t$ of the order parameter fluctuation towards equilibrium is proportional to the thermodynamic restoring force $\partial F/\partial Q$. From the Landau–Khalatnikov equation, the expressions for the fluctuations induced by an ultrasonic wave in order parameters from their equilibrium values can be obtained.

The Landau–Khalatnikov equation for the order parameter components can be written as

$$\dot{Q}_i = -\Gamma_i(\partial F/\partial Q_i) \quad (i = 1,2,3) \tag{8}$$

where $\Gamma_1, \Gamma_2, \Gamma_3$ are the three kinetic coefficients. The symmetry of the tetragonal phase ensures that $\Gamma_1 = \Gamma_2$. We shall consider the solution of the Landau–Khalatnikov equation for the ferroelastic phase and write

$$Q_i = Q_{i0} + q_i^* \quad (i = 1,2,3) \tag{9a}$$

$$\eta_i = \eta_{i0} + \eta_i^* \quad (i = 1 \text{ to } 6) \tag{9b}$$

Then q_i^* and η_i^* represent the time dependent fluctuations of these parameters from their equilibrium values.

By expanding $(\partial F/\partial Q_i)$ for $i = 1$ to 3 about the equilibrium values of the order parameter components and the strain variables and setting q_i^* proportional to $\exp(i\Omega t)$, we find that the solution of the Landau–Khalatnikov equations turn out to be

$$q_1^* = A_1 \eta_5^* \tag{10}$$

$$q_2^* = A_1 \eta_4^* \tag{11}$$

$$q_3^* = \sum_{i=1}^{6} \alpha_i \eta_i^* \tag{12}$$

where

$$A_1 = -(\Gamma_1/P_1)\mathrm{d}_t Q_{30}, \tag{13a}$$

$$P_1 = i\Omega + \Gamma_1(\partial^2 F/\partial Q_1^2)_0, \tag{13b}$$

$$\alpha_1 = \alpha_2 = -(2\Gamma_3 Q_{30}\mathrm{d}_1)/P_3, \tag{13c}$$

$$P_3 = i\Omega + \Gamma_3(\partial^2 F/\partial Q_3^2)_0, \tag{13d}$$

$$\alpha_3 = -2\alpha_1;\ \alpha_4 = \alpha_5 = \alpha_6 = 0. \tag{13e}$$

The above equations show that the fluctuations in the components of the order parameter about their equilibrium values are linearly related to the fluctuations in the strain variables.

4. Anomalies in the second-order elastic constants

If we substitute the equations (9a) to (13e) in the expression for the free energy, we find

$$F = F_0 + F_2 + F_3 + F_4 \tag{14}$$

where F_0, F_2, F_3 and F_4 denote the zero, second, third and fourth-order energies respectively. In view of the stability condition, F_1 vanishes. The zeroth order term F_0 gives the shift in the zero point energy at the transition temperature and its derivative with respect to temperature gives the specific heat anomaly at the transition temperature. By collecting all the terms which are quadratic in the strain variables, the expression for F_2 becomes

$$\begin{aligned} F_2 = \frac{1}{2}\sum_{ij} C_{ij}^* \eta_i^* \eta_j^* &= \frac{1}{2}\sum_{ij} C_{ij}\eta_i^*\eta_j^* \\ &+ \alpha/2(q_1^{*2} + q_2^{*2} + q_3^{*2}) \\ &+ (\beta_1/4)\{2Q_{30}^2(q_1^{*2} + q_2^{*2} + q_3^{*2}) + 4Q_{30}^2 q_3^{*2}\} \\ &+ (\beta_2/4)Q_{30}^2(q_1^{*2} + q_2^{*2}) \\ &+ d_1\{\eta_{10}(q_3^{*2} + q_2^{*2} - 2q_1^{*2}) + \eta_{20}(q_3^{*2} + q_1^{*2} - 2q_2^{*2}) \\ &+ \eta_{30}(q_1^{*2} + q_2^{*2} - 2q_3^{*2}) + 2Q_{30}q_3^*(\eta_1^* + \eta_2^* - 2\eta_3^*)\} \\ &+ d_t Q_{30}(q_2^*\eta_4^* + q_1^*\eta_5^*) \end{aligned} \tag{15}$$

where C_{ij}^* represents the modified second-order elastic (SOE) constants arising from the coupling of the order parameters with strains. By writing

$$C_{ij}^* = C_{ij} + \Delta C_{ij}^* \tag{16}$$

ΔC_{ij}^* represents the anomalies in the SOE constants. Using Kronecker delta functions, one can in fact write the anomalies for all the elastic constants in a single formula as

$$
\begin{aligned}
\frac{1}{2}\Delta C_{ij}^{*} = {} & \{A_1^2(\delta_{i5}\delta_{j5}+\delta_{i4}\delta_{j5})+\alpha_i\alpha_j\} \times \\
& \{\alpha/2+(\beta_1/2)Q_{30}^2+(\beta_2/4)Q_{30}^2\} + \\
& + Q_{30}^2\{(\beta_1-\beta_2/4)\}\alpha_i\alpha_j \\
& - 3d_1\{A_1^2(\eta_{10}\delta_{i5}\delta_{j5}+\eta_{20}\delta_{i4}\delta_{j4})+\eta_{30}\alpha_i\alpha_j\} \\
& + d_1Q_{30}\{\alpha_i(\delta_{j1}+\delta_{j2}-2\delta_{j3})+\alpha_j(\delta_{i1}+\delta_{i2}-2\delta_{i3})\} \\
& + d_tQ_{30}A_1(\delta_{i4}\delta_{j4}+\delta_{i5}\delta_{j5}).
\end{aligned}
\tag{17}
$$

The existence of anomalies in the SOE constants shows that the velocities of the elastic waves undergo a change during phase transition, and further the waves are attenuated as ΔC_{ij}^{*} is complex. One can notice that there exist relations among the elastic anomalies in the low temperature phase and all of them can be expressed in terms of two, namely ΔC_{11}^{*} and ΔC_{44}^{*}. The relations are

$$\Delta C_{11}^{*} = \Delta C_{22}^{*} = \Delta C_{12}^{*} \tag{18}$$

$$\Delta C_{23}^{*} = \Delta C_{13}^{*} = -2\Delta C_{11}^{*} \tag{19}$$

$$\Delta C_{33}^{*} = 4\Delta C_{11}^{*} \tag{20}$$

$$\Delta C_{44}^{*} = \Delta C_{55}^{*} \tag{21}$$

$$\Delta C_{11}^{*} = (8\Gamma_3^2 d_1^2\alpha^2\beta_1)/(P_3^2a^2) - (8d_1^2\Gamma_3\alpha)/(P_3a) \tag{22}$$

$$\Delta C_{44}^{*} = (2\Gamma_1^2 d_t^2\alpha^2)/(P_1^2a^2)\{(\beta_2/4)+(3K/4)\} - 2\Gamma_1^2 d_t^2\alpha/(P_1a) \tag{23}$$

where

$$K = 12d_1^2(C_{11}-C_{12})^{-1} \tag{24a}$$

and

$$a = -(\beta_1 - K). \tag{24b}$$

The expressions P_1 and P_3 given by (13b) and (13d) can be expressed in terms of the relaxation time τ. In terms of this parameter, the above expressions for ΔC_{11}^{*} and ΔC_{44}^{*} turn out to be

$$\Delta C_{11}^{*} = -(2d_1^2/\beta_1)(1+2i\Omega\tau)(1+i\Omega\tau)^{-2} \tag{25}$$

$$\Delta C_{44}^{*} = -\{2d_t^2/(\beta_2+3K)\}(1+2i\Omega\tau)(1+i\Omega\tau)^{-2} \tag{26}$$

where

$$\tau = \tau_0/|T_c - T|.$$

The numerical values of τ_0, (d_1^2/β_1), $d_t^2/(\beta_2+3K)$ for $SrTiO_3$ have been given by Lemanov [1] as $1{\cdot}6 \times 10^{-11}$sK, $1{\cdot}6 \times 10^9\,N/m^2$ and $1{\cdot}9 \times 10^9\,N/m^2$ respectively. For numerical calculations, we shall choose experimental value of Ω as $1{\cdot}6 \times 10^9\,s^{-1}$ so that $\Omega\tau_0 = 10^{-2}$. We notice that both ΔC_{11}^{*} and ΔC_{44}^{*} are complex and temperature dependent. The real parts of the elastic anomalies are given by

$$R(\Delta C_{11}^{*}) = -(2d_1^2/\beta_1)(1+3\Omega^2\tau^2)(1+\Omega^2\tau^2)^{-2} \tag{27}$$

$$R(\Delta C_{44}^{*}) = -\{2d_t^2/(\beta_2+3K)\}(1+3\Omega^2\tau^2)(1+\Omega^2\tau^2)^{-2}. \tag{28}$$

From these expressions, it is possible to discuss the temperature variation of these anomalies numerically. At the transition temperature, $T = T_c$, $\tau \rightarrow \infty$ so that both $R(\Delta C^*_{11})$ and $R(\Delta C^*_{44})$ vanish. Next $\Omega\tau$ reaches the value unity when $(T_c - T) = \Omega\tau_0 = 10^{-2}$. For this value as well as for the point $\Omega\tau = 0$, we find that

$$R(\Delta C^*_{11}) = -2d_1^2/\beta_1 \tag{29}$$

and

$$R(\Delta C^*_{44}) = -2d_1^2/(\beta_2 + 3K). \tag{30}$$

Again the stationary values of these anomalies are reached for the temperature $T = T_c + \sqrt{3}10^{-2}$.

For this value

$$R(\Delta C^*_{11}) = -(9/8)(2d_1^2/\beta_1); \tag{31}$$

$$R(\Delta C^*_{44}) = -(9/8)\{2d_1^2/(\beta_2 + 3K)\} \tag{32}$$

With these numerical values, we notice that the elastic constants have uniform values in the paraelectric state, fall steeply within a range of the order 10^{-2} K to the values given in (31) and (32), and reach asymptotic values within a range of 10^{-1} K. The

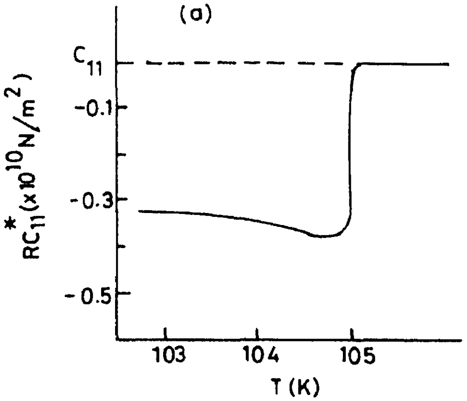

Figure 1a. Variation of the real part of C^*_{11} with respect to temperature close to the phase transition (theoretical).

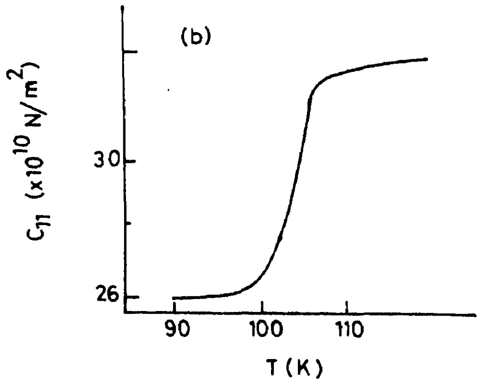

Figure 1b. Temperature variation of C_{11} near phase transition (experimental).

temperature variation of real parts of C^*_{11} and C^*_{44} has been plotted in figures (1a) and (2a) respectively.

Slonczewski and Thomas [5] have investigated the elastic anomalies of strontium titanate close to the transition temperature. They have derived the following relations among the elastic anomalies;

$$C_{11} = C^c_{11} - D;\ C_{33} = C^c_{11} - 4D \tag{33}$$

$$C_{12} = C^c_{12} - D;\ C_{13} = C^c_{12} + 2D \tag{34}$$

$$C_{44} = C^c_{44} - E \tag{35}$$

where

$$D = (4B^2_e Q^2_s / M\omega^2_3); \tag{36}$$

$$E = (B^2_t Q^2_s / M\omega^2_1). \tag{37}$$

Comparing the set of equations (33) to (35) with (18) to (21) we find that we have recovered all the relations for the elastic anomalies given by them. However, our formulae for the anomalies are different and go deeper than the results of Slonczewski

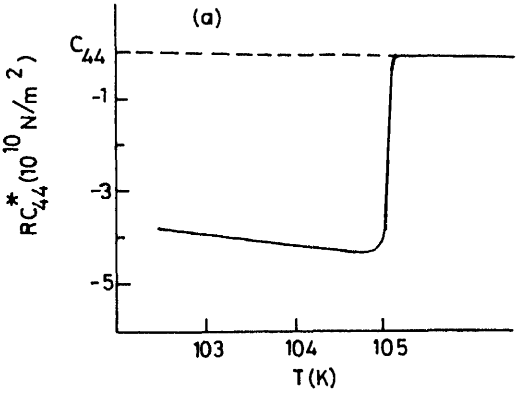

Figure 2a. Variation of the real part of C^*_{44} with respect to temperature close to the phase transition (theoretical).

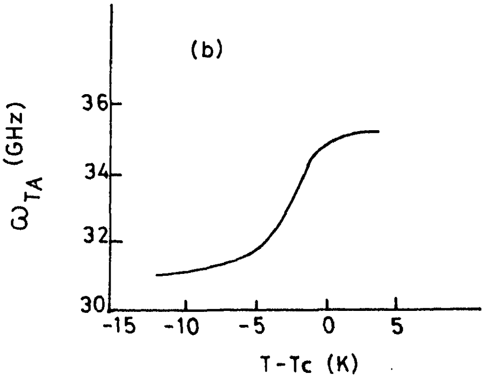

Figure 2b. Transverse acoustic mode ω_{TA} frequency as a function of $(T - T_c)$ (experimental).

and Thomas. If we substitute the expression for the soft mode frequencies from the formula

$$M\omega_1^2 = M\omega_2^2 = \left(\frac{\partial^2 F}{\partial Q_1^2}\right)_0 = \frac{\alpha}{2a}(\beta_2 + 3K) \tag{38}$$

$$M\omega_3^2 = \left(\frac{\partial^2 F}{\partial Q_3^2}\right)_0 = (2\alpha\beta_2/a) \tag{39}$$

in the formulae for D and E, we obtain

$$D = (2B_e^2/\beta_1) \text{ and } E = (2B_t^2)/(\beta_2 + 3K). \tag{40}$$

Comparing these with (27) and (28), we see that their formulae give the first factor in (27) and (28), but lack the factor depending on the relaxation time. Without this factor, it is not possible to explain the steep dip in the elastic constants occurring at the transition temperature.

The temperature variation of C_{11} near the transition temperature has been evaluated by Luthi and Moran [13] experimentally. The shape of our curve agrees qualitatively with their curve (1b). Similarly the shape of our curve agrees qualitatively with the experimental curve in figure (2b) for the variation of C_{44} near the transition temperature by the Brillouin scattering method given by Lyons and Fleury [14].

5. Anomalies in the third-order elastic (TOE) constants

The expression for the free energy contains cubic terms in the order parameters and strain variables. The anomalies in the TOE constants can be obtained by collecting the coefficients of all the third-order terms $\eta_i^* \eta_j^* \eta_k^* (i, j, k = 1 \text{ to } 6)$. Several of the anomalies become equal to each other and it can be verified that the following relations exist among the individual TOE constants

$$\Delta C_{111}^* = \Delta C_{222}^* = \Delta C_{112}^* = \Delta C_{122}^* = -\frac{1}{8}\Delta C_{333}^* \tag{41}$$

$$\Delta C_{123}^* = -2\Delta C_{111}^* \tag{42}$$

$$\Delta C_{144}^* = \Delta C_{255}^* \tag{43}$$

$$\Delta C_{344}^* = \Delta C_{355}^* \tag{44}$$

$$\Delta C_{155}^* = \Delta C_{244}^* \tag{45}$$

$$\Delta C_{456}^* = (d_t^3 \Gamma_1^2 \alpha)(P_1^2 a)^{-1}. \tag{46}$$

The real part of ΔC_{111}^* can be written as

$$R(\Delta C_{111}^*) = -\frac{6d_1^3(\beta_1 - K)(\Omega\tau)^2(3 - \Omega^2\tau^2)}{\beta_1^2(T_c - T)\alpha'(1 + \Omega^2\tau^2)^3} \tag{47}$$

It is seen that $R(\Delta C_{111}^*)$ is zero when $T = T_c$ and it is positive for all values of $\Omega\tau$ from infinity up to $\sqrt{3}$ where it becomes zero again. The graph for real part of C_{111}^* very close to the phase transition is given in figure 3a. It is seen that the real part of C_{111}^* decreases steeply close to the transition temperature and then increases within

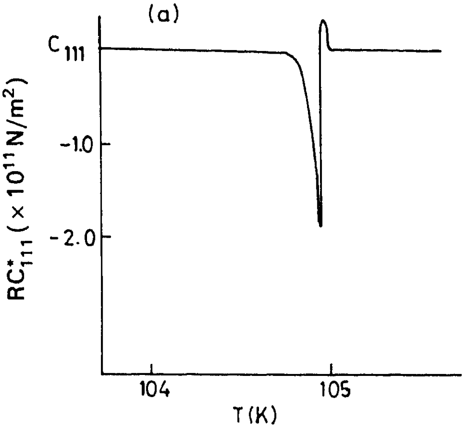

Figure 3a. Variation of the real part of C^*_{111} with respect to temperature close to the phase transition (theoretical).

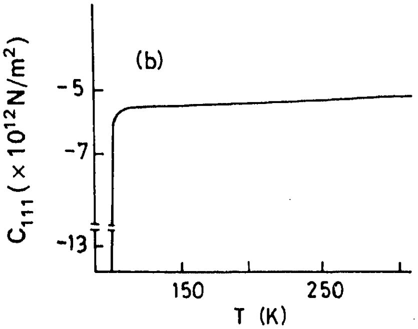

Figure 3b. Temperature variation of C_{111} as a function of temperature (experimental).

a range of the order 10^{-1}K to become zero again. Meeks and Arnold [9] have investigated experimentally (figure 3b) the temperature dependence of C_{111} at the transition temperature. They found that at the transition temperature C_{111} decreases steeply and our curve qualitatively agrees with their results. However, our theoretical results predict that the anomaly in $R(\Delta C^*_{111})$ will become zero again within a very small range of temperature.

6. Attenuation of elastic waves

Apart from the anomalies in elastic constants of various orders, which determine the sound wave velocities, another major effect of the phase transition is the attenuation of the sound waves. In this section, we give expressions for the attenuation of the elastic waves close to the transition temperature.

Let us write

$$C_{ij} = C'_{ij} + C''_{ij} \tag{48}$$

where C'_{ij} and C''_{ij} denote the real and imaginary parts of C^*_{ij}. Let us denote by α_1 the

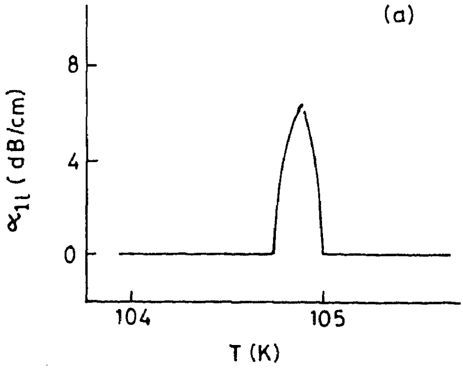

Figure 4a. Variation of attenuation of the longitudinal wave (α_{1l}) with respect to temperature close to the phase transition (theoretical).

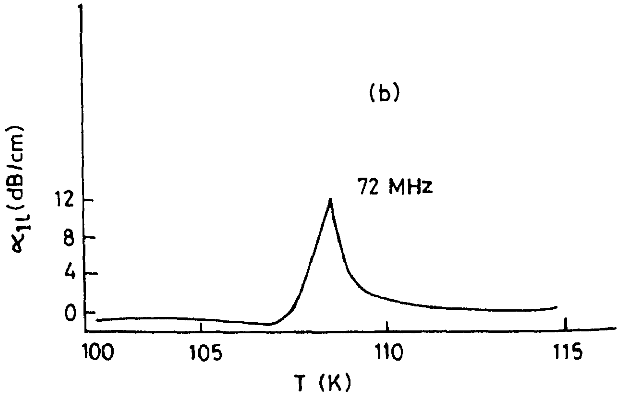

Figure 4b. Ultrasonic attenuation α_{1l} of longitudinal wave as a function of temperature at high biaxial pressure (experimental).

attenuation of the elastic waves. Then we have the following expressions for the attenuation of the longitudinal and transverse waves along the principal directions.

(1) (100) direction

$$\alpha_{1l} = (\Omega/2)(C''_{11}/C'_{11}) \tag{49a}$$

$$\alpha_{1t} = (\Omega/2)(C''_{44}/C'_{44}) \tag{49b}$$

(2) $\left(\frac{1}{\sqrt{2}}, \frac{1}{\sqrt{2}}, 0\right)$ direction

$$\alpha_{1l} = (\Omega/2)(C''_{11} + C''_{12} + 2C''_{44})/(C'_{11} + C'_{12} + 2C'_{44}) \tag{50a}$$

$$\alpha_{1t_1} = (\Omega/2)(C''_{11} - C''_{12})/(C'_{11} - C'_{12}) = \alpha_{1t_2} \tag{50b}$$

From the equation (49a), we find that the attenuation of the longitudinal wave along the [100] direction is given by

$$\alpha_{1l} = \frac{2\Omega d_1^3}{\beta C'_{11}} \frac{(\Omega\tau)^3}{(1 + \Omega^2\tau^2)^2} \tag{51}$$

The attenuation anomaly vanishes when $\Omega\tau \rightarrow \infty$ or at $T = T_c$. The attenuation steeply increases from zero to its maximum value and then again decreases to its asymptotic value of zero. Since C_{44}^* also has the same dependence on temperature, the variation with temperature of the transverse mode along [100] and the corresponding mode along [110] is also similar. The attenuation of longitudinal wave (72 MHz) as a function of temperature at high biaxial pressure of $SrTiO_3$ has been measured by Fossheim and Berre [15]. There is good agreement between the experimental curve (figure 4b) and our prediction (figure 4a).

References

[1] V V Lemanov, *Proceedings of the second international conference on Condensed Matter Physics* (1982) 190–228 edited by M Borissov (Varna, Bulgaria) World Scientific, Singapore
[2] W Rehwald, *Adv. Phys.* **22**, 721 (1973)
[3] B Luthi and W Rehwald, *Topics in current physics*, Vol. 23: *Structural phase transitions*, edited by K A Muller and H Thomas, (Springer-Verlag, Berlin, Heidelberg, 1981)
[4] B Dorner, *Topics in current physics*, Vol. 23, Structural Phase Transition, edited by K A Muller and H Thomas (Springer-Verlag, Berlin, Heidelberg, 1981)
[5] J C Slonczewski and H Thomas, *Phys. Rev.* **B9**, 3599 (1970)
[6] R A Cowley, *Phys. Rev.* **A134**, 981 (1964)
[7] A G Bettie and G A Samara *J. Appl. Phys.* **42**, 2376 (1971)
[8] R D Peters and R T Arnold, *J. Appl. Phys.* **42**, 980 (1971)
[9] E L Meeks and R T Arnold, *Phys. Rev.* **B1** 982 (1970)
[10] R O Bell and G Rupprecht, *Phys. Rev.* **129**, 90 (1963)
[11] J O Fossum and K Fossheim, *Solid State Commun* **51**, 839 (1984)
J O Fossum and K Fossheim, *Ferroelectrics* (G.B.) **54**, 629 (1984)
[12] F Schwabl and H Iro, *Ferroelectrics* (*G.B.*), **35**, 215 (1981)
[13] B Luthi and T J Moran, *Phys. Rev.* **B2**, 1211 (1970)
[14] K B Lyons and R T Arnold, *Solid State Commun.* **23**, 477 (1977)
[15] K Fossheim and B Berre, *Phys. Rev.* **B5**, 3292 (1972)

PRAMANA
— journal of
physics

© Printed in India

Vol. 42, No. 3,
March 1994
pp. 187–191

Relation of coordination number to memory and threshold switching in chalcogenides

MANOHAR LAL, NAVDEEP GOYAL and ANIL VOHRA*
Department of Physics, Panjab University, Chandigarh 160014, India
*Department of Electronic Science, Kurukshetra University, Kurukshetra 132119, India

MS received 22 June 1993; revised 13 October 1993

Abstract. The paper reports a structural study of some memory and threshold chalcogenides in terms of coordination number C, defined by $C=8-N$, and is the average coordination number for covalently bonded materials. The average number of nearest neighbours surrounding a central atom, obtained for As–Ge–Te (memory) and Se–Ge–Te (threshold) systems have been used to estimate the cohesive energies, assuming simple additivity of bond energies. The bonding pattern so obtained, explains certain properties of these glasses.

Keywords. Chalcogenides; chemical bonds; memory; threshold.

PACS Nos 72·20; 71·55

1. Introduction

The recognition that chalcogenides were both understandable and potentially useful, stimulated an intense research effort. Insights have accumulated and continue to accumulate, as a result of interdisciplinary efforts involving theory and experimentation in diverse areas of physics, chemistry, electrical engineering and material science [1–5].

Considerations of the fundamental nature of chemical bonding in chalcogenide glasses, have been a very important part of this research effort [6–8]. A chemically ordered network model for the atomic arrangement in the glasses, wherein the maximum number of heteronuclear bonds are formed first and the remaining part of the valence requirement is met with by homonuclear bonding at random, was found to account satisfactorily, for the connectedness dependence of switching observed in As–Ge–Te and Se–Ge–Te chalcogenides. The amount of connectedness of an alloy determines whether it will have threshold or memory switching properties. It also explains the difference between them in terms of relative rigidities of atomic networks formed by different percentages of divalent, trivalent and tetravalent alloying elements. Weaker bonds and more flexible network containing an abundance of divalent atoms, provide lower energy barriers to reversible local order changes and structural phase transition, whereas more rigid threshold switches can undergo electronic transitions which are automatically reversed when applied voltage causing excitation is removed.

The approach through chemical bond studies suggested by Bicerano and Ovshinsky [9–10], has been used in present paper to study some chalcogenides. Results based on quantitative analysis suggest that coordination number is related to memory and threshold switching in chalcogenides.

2. Model

The chemical bond approach as suggested by Bicerano and Ovshinsky [9] is based on the following assumptions:

(i) There is normal structural bonding with preferred coordination number C for each element in an alloy. For example, $C(\mathrm{Ge})=4$; $C(\mathrm{As})=3$; and $C(\mathrm{Se})=C(\mathrm{Te})=2$. It is equivalent to neglecting dangling bonds, Van der Waals interactions and some other valence defects.
(ii) Atoms combine more favourably with atoms of different kind than with the same kind, which assumes maximum amount of chemical ordering possible. Here atoms with identical valencies are considered to be of same kind.
(iii) Bonds are formed in sequence of decreasing bond energy until all the available valencies are saturated provided $D(\mathrm{A-B}) \gg D(\mathrm{A-C})$ (where D is bond energy), and on the other hand if $D(\mathrm{A-B})=D(\mathrm{A-C})$ the weighing factor $e^{D/kT}$ decides the ratio of bonds to be formed.
(iv) The bond energies $D(\mathrm{A-B})$ for heteronuclear bonds are calculated using the Paulings relation [11]

$$D(\mathrm{A-B})=[D(\mathrm{A-A}).D(\mathrm{B-B})]^{1/2}+30(x_{\mathrm{A}}-x_{\mathrm{B}})^2 \quad (1)$$

where $D(\mathrm{A-A})$ and $D(\mathrm{B-B})$ are the energies of homonuclear bonds [12] in kcal/mol and x_{A} and x_{B} are the electronegativities of atoms involved [13]. The values of x_{A} and $D(\mathrm{A-A})$ for alloys studied are listed in table 1.

The model as stated above clearly uses two sets of parameters, viz. coordination number C (a measure of connectedness) of the elements and the bond energy D between elements.

3. Results and discussion

The application of the method has been illustrated using threshold and memory materials $\mathrm{Se_{25}Ge_{20}Te_{75}}$, $\mathrm{As_5Ge_{10}Te_{85}}$ and $\mathrm{As_{15}Ge_{10}Te_{75}}$ abbreviated as T, M1 and M2, respectively.

Table 1, enlists the types of bonds expected to occur in T, M1 and M2 together with their bond energies. The average number of neighbours for each type of central atom is listed in table 2. The cohesive energies (CE) calculated for these alloys and their constituent elements, assuming simple additivity of bond energies, are listed in table 3. The results are CE(T) = 2·10 eV/atom, CE(M1) = 1·65 eV/atom and CE(M2) = 1·72 eV/atom.

Table 1. Energies of bonds expected to occur in T, M1, M2 materials.

T		M1 and M2	
A–B	D(A–B)*	A–B	D(A–B)
Ge–Se	49·4	As–Ge	35·6
Ge–Te	35·5	Ge–Te	35·5
Te–Te	33·0	As–Te	32·7
		Te–Te	33·0

* kcal/mole.

Table 2. Average expected number of neighbours.

Central atoms	Its neighbours	Average number for material T	M1	M2
As	Ge	—	3·0	1·51
	Te	—	—	1·49
Ge	Te	1·50	2·50	1·76
	As	—	1·50	2·24
	Se	2·50	—	—
Te	As	—	—	0·30
	Se	—	0·29	—
	Ge	0·45	1·71	0·23
	Te	1·45	—	1·47
Se	Ge	2·0	—	—
	Te	—	—	—

Table 3. Cohesive energies (CE) in eV/atom.

Material	C	CE_2^a	CE_1^b	Percentage
T	2·40	2·10	2·56	82·0
M1	2·25	1·65	2·43	67·9
M2	2·35	1·72	2·50	73·2
As	3·0	2·09	2·96	70·6
Ge	4·0	3·26	3·85	84·7
Te	2·0	1·43	2·23	64·2
Se	2·0	1·90	2·25	84·4

[a] CE_2 = Cohesive energies of materials assuming additivity of bond energies.

[b] CE_1 = Cohesive energies obtained by weighted averaging over the elements.

[c] Percentage = $100 \times CE_2/CE_1$.

As observed from table 3 the magnitude of C and CE follow the same behaviour as would be expected from qualitative arguments concerning relative rigidities of the network containing different percentages of divalent, trivalent and tetravalent atoms i.e. the cohesive energy should increase/decrease with the increase/decrease in the coordination number.

The results of C and CE are also consistent with the general mechanism suggested for switching [8] which expects the threshold voltage for switching to decrease with increase in temperature and to increase with increase in coordination number.

On comparing calculated values of CE with those obtained by assuming that the actual CE values are weighted averages of CE values of elements listed in table 3, we find that the calculated values (2·10, 1·65 and 1·72 eV/atom) for T, M1 and M2 are 82%, 67·9% and 73·2% respectively.

Underestimation is expected from the fact that while assuming simple additivity of non-interacting bond pair in bond activity assumption, one neglects electron correla-

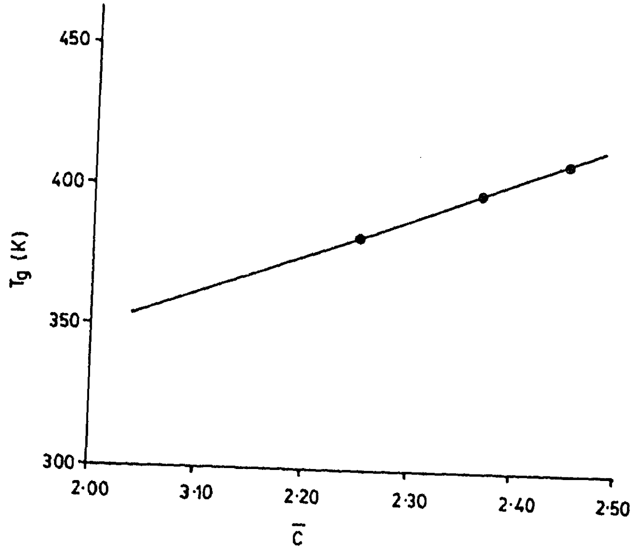

Figure 1. Demonstration of equation 2.

tion, self consistency and electron delocalization effects, which are the stabilizing effects. Further, the order of underestimation varies M1 > M2 > T. A similar trend of results was observed by Bicerano and Ovshinsky [9, 10] for materials $Se_{18}Ge_7As_{35}Te_{40}$ (threshold), $Ge_{15}Te_{81}Sb_2S_2$ and $Ge_{24}Te_{72}Sb_2S_2$ (both memory type). The glass-transition temperature (T_g) was determined for the materials reported in this paper. The values are: $As_5Ge_{10}Te_{85}$ ($T_g = 383°C$); $As_{15}Ge_{10}Te_{75}$ ($T_g = 398°C$) and $Se_{25}Ge_{20}Te_{75}$ ($T_g = 413°C$). Thus T_g increases in the same order as CE and C and the validity of the relation

$$T_g = T_g^0 + (C - 2)E_{04} \tag{2}$$

suggested by deNeufville and Rockstad [6] has been tested and demonstrated through figure 1.

Another observation about these glasses is that they all contain Te–Te bonds. An appreciable amount of Te–Te bonding is unavoidable for memory materials since Te atoms are present in large excess. Due to excess of Te content in the memory alloys the unswitched as well as the switched materials are dominated by Te-chains cross linked by tetravalent Ge atom which in turn are bridged by As atoms. However the length of exclusive Te chains in the unswitched material is likely to be smaller because its average coordination number has been found to be relatively large. A reduction in coordination number for switched materials coupled with an increase in Te contents, not only indicates the existence of relatively larger Te chains but also increases the possibility of formation of localized micro crystallites of Te.

Average coordination number (C) of a network may fundamentally be related to its vitrification properties. A bond percolation threshold C^P for average coordination number of the network is suggested. The materials above $C > C^P$ would be too rigid to set the memory transition. They would undergo threshold transition which does not require structural rearrangement.

The above study reveals that simple chemical bond considerations can be used to develop an understanding of structural properties of chalcogenide glasses.

References

[1] S R Ovshinsky, *Phys. Rev. Lett.* **21**, 1450 (1968)
[2] K Tanaka, S Iizima and M Suzi, *Solid State Commun.* (USA) **8**, 75 (1970)
[3] J Feinlib, S Iwasa, S C Moss and J P deNeufville, *J. Non-Cryst. Solids* (Netherlands), **8–10**, 909 (1972)
[4] C B Thomas and A F Frat, *Philos. Mag.* **B26**, 617 (1972)
[5] S R Ovshinsky and P H Klose, *J. Non-Cryst. Solids* (Netherlands) **8–10**, 892 (1972)
[6] J P deNeufville and H K Rockstad, *Proceedings of The fifth Int. Conf. Amorphous Semiconductors* edited by J Stuke and W Brinig (London: Taylor and Francis, 1974) 419–429
[7] M Persin, D Kuntelz and A Persin, *Thin solid films* (Switzerland), **36**, 475 (1976)
[8] S R Ovshinsky, *Phys. Rev. Lett.* **36**, 1469 (1976)
[9] J Bicerano and S R Ovshinsky, *Proceedings of The Noble Laureates Symposium on applied quantum chemistry*, held on Dec, 16–21, 1984 at Honolulu, Hawaii (D. Reidel Publishing Co.)
[10] J Bicerano and S R Ovshinsky, *J. Non-Cryst. Solids* (Netherlands), **74**, 75 (1985)
[11] L Pauling, *The Nature of the chemical bonds* 3rd edition (Cornell University Press, 1960) p. 91
[12] L Pauling, *The Nature of the chemical bonds.* 3rd edition (Cornell University Press, 1960) Tables 3–4, p. 85
[13] A L Alfred, *J. Nucl. Chem.* **17**, 215 (1961)

PRAMANA
— journal of
physics

© Printed in India

Vol. 42, No. 3,
March 1994
pp. 193–222

Magnetic phase diagram of anisotropic layered superconductors via magnetization measurements for $H \| c$ in Bi2212

A K GROVER[1,2], F IGA[1], Y YAMAGUCHI[1], N AOKI[3], K INO[3],
N GOYAL[2] and Y NISHIHARA[1]
[1] Electrotechnical Laboratory, Tsukuba, Ibaraki 305, Japan
[2] Centre of Advanced Study in Physics, Panjab University, Chandigarh 160014, India
[3] Meiji University, Kawasaki, Kanagawa 216, Japan

MS received 22 December 1993; revised 4 February 1994

Abstract. The $Bi_2Sr_2CaCu_2O_8$ system is viewed as an archetypal of superconductors modelled as Josephson coupled CuO_2 bilayers. The isothermal and temperature dependent DC and AC magnetization measurements for $H \| c$ in a single crystal of Bi2212 have been performed. Qualitative changes are observed to occur over a narrow range of temperature values before reaching the superconducting-normal transition. The observed behaviour can be ascribed to the rapid variation in the strength of the coupling between the superconducting CuO_2 planes (i.e., bilayers in the case of Bi2212). Strongly coupled planes behave like a 3D superconductor, whereas weakly coupled planes have a two component response attributable to 2D planes and interplanar couplings. We believe that this paper is a plethora of new findings. Our observations imply that resistivity across the planes becomes zero earlier than that within the planes. A new line (designated as $H_{2D}(T)$) above which the change in the electromagnetic response is dominated by quasi 2D-planes has been determined for the first time. This paper also contains the first observation of Differential Diamagnetic Effect (DDE) in the In-phase AC susceptibility data which signals the onset (at $T_{2D}(H)$) of dominance of response from 2D-planes. In addition to a host of interesting thermomagnetic history effects which are a consequence of interplay between the diamagnetic responses from the two components, a comparison of irreversibility lines (of the 3D state) determined by different methods on the same specimen of a HTSC is also being presented for the first time. We have come across Paramagnetic Meissner Effect (PME), first recognized in ceramic samples of Bi2212, in the temperature region of dimensional crossover in our single crystal sample, which *inter-alia* confirms our labelling of the two component behaviour. A schematic phase diagram summarizing the various transformations that can occur near T_c in the electromagnetic response of an anisotropic layered system has been drawn.

Keywords. Layered superconductors; dimensional crossover; magnetic phase diagram; Bi2212.

PACS Nos 74·25; 74·50; 74·60; 74·72

1. Introduction

The difference in the electromagnetic response of high temperature superconductors (HTSC) vis-a-vis conventional low temperature superconducting alloys (e.g., the slower rate of decrease of electrical resistance with temperature at the superconducting transition and the absence of noticeable shift in the superconducting onset with moderate fields, etc.) have led to the pursuit of answers to the questions, like, whether

HTSC materials ever attain $R = 0$ state, what the nature (topological character, size, etc.) of so called vortex lines in these materials is, and how the vortices arrange themselves, etc. (for a review, see [1]). A hallmark of cuprate HTSC is their layered structure and the accompanying large anisotropy. In recent years, a consensus appears to have emerged [1] that cuprate superconductors, with or without large anisotropy do really superconduct ($R = 0$) in the vortex glass phase at low temperatures, and up to moderate field values. The glassy phase is believed to be a consequence of an inevitable presence of imperfections at the atomistic level in these materials. However, the details of the magnetic phase diagram in high field values at low temperatures or even in low fields at the elevated temperatures remain to be clearly revealed. In particular, in highly anisotropic compounds, like bismuth cuprates (BSCCO), where it is considered that vortices comprise of "wiggly flux lines" or "pancake" vortices confined to individual planes with correlations amongst them, the issue of the intrinsic strength of these correlations (and the influence of applied field and temperature on them) is in contemporary focus.

Kadowaki [2] and Kes *et al* [3] had been the first to point out a change in the character of diamagnetic response (i.e. the transformation in the sign of dM/dH from positive to negative value, before reaching the nominal zero field superconducting-onset temperature $T_c(0)$), in temperature dependent magnetization measurements for $H \| c$ in single crystal samples of $Bi_2Sr_2CaCu_2O_8$ (Bi2212). The Bi2212 system has been shown to comprise of Josephson coupled CuO_2 bilayers [4]. In this system, the diamagnetism increases as H increases at T close to $T_c(0)$ [2, 3]. A conventional analysis of such data implies that nominal $T_c(H)$ (or $H_{c2}(T)$) increases as H (or T) increases. However, such a response, since the initial works of Kadowaki [2] and Kes *et al* [3], has been considered to emanate from superconducting fluctuations confined to individual copper oxide planes (a two dimensional (2D) superconductivity *a la* 2D magnetism). The 2D superconductivity is full of exotic possibilities (e.g. see, [5, 6]), with novel features anticipated in the electromagnetic response of Josephson coupled planes (i.e., CuO_2 bilayers in the case of Bi2212). Of particular interest is the existence of a Kosterlitz-Thouless (KT) type of a transition, and the manifestations of possible spontaneous creation of vortex-antivortex pairs in individual planes [6]. From a theoretical treatment, suitable for bismuth and thallium cuprates, which incorporates the entropy contribution to the free energy due to thermal distortion, Bulaevskii, Ledvij and Kogan (to be referred as BLK) [6] showed that KT type transition can occur in these systems at a temperature $T_s < T_c(0)$. Their analysis also identifies a temperature at which the change in character of diamagnetic response occurs. It is argued that at $T \approx T^*$, the magnetization becomes field independent for $H \gg H_{cr}$. This, in turn, implies that temperature dependent magnetization ($M(T)$) curves for $H \gg H_{cr}$ would intersect at $T = T^*$. Above T^*, diamagnetic response is predicted to increase logarithmically with field, whereas somewhat below T^* the diamagnetic values decrease with field as in usual 3D superconducting materials. The temperature T^* is believed to lie below T_s and both of them lie in the region where coherence length ξ_c is much less than interplanar spacing s. The electrical resistivity and lower critical field H_{c1} are anticipated to fall to zero value at T_s instead of $T_c(0)$ [6].

Vacaru *et al* [7] found that H_{c1} data for $H \| c$ in a single crystal specimen of $Tl_2Ba_2CuO_6$ (Tl 2201) indeed linearly extrapolate to zero value at a temperature smaller than its $T_c(0)$. The temperature at which H_{c1} extrapolates to zero value is observed to lie in between $T_c(0)$ and the temperature at which change in character of diamagnetic response occurs in their sample. More recently, Brawner *et al* [8] have reported that, in a single crystal sample of Bi2212 (for $H \| c$), changes in slope values of $\mathrm{d}H_{c1}/\mathrm{d}T$ and $\mathrm{d}J_c/\mathrm{d}T$ occur at a temperature below $T_c(0)$. Their H_{c1} and $J_c(H=0)$ (as deduced from isothermal hysteresis value in zero field) values indeed collapse to zero at a temperature smaller than the nominal $T_c(0)$ in their sample. They attribute the sudden change in slope values $\mathrm{d}H_{c1}/\mathrm{d}T$ and $\mathrm{d}J_c/\mathrm{d}T$ to dimensional crossover effect. Brawner *et al* [8] further surmise that, after the collapse of H_{c1} and J_c, the diamagnetic susceptibility is *reversible*. Such an inference appears to be in contrast to the behaviour exhibited by a single crystal sample of Tl 2201 of Vacaru *et al* [7]. In Tl 2201, the irreversibility temperature $T_r(H)$ in $H = 1$ Oe lies above the temperature of collapse of H_{c1}. Another notable difference between the analysis made by Vacaru *et al* [7] and Brawner *et al* [8] is that the former group designates the temperature of $H_{c1} = 0$ as T_s, whereas, the latter group identifies T_s (the onset-temperature of K-T type of a transition) with the temperature at which slope value $\mathrm{d}H_{c1}/\mathrm{d}T$ exhibits a drastic change. In any case, the experimental data of both these groups and the scenario sketched by BLK [6] provide many interesting leads which must be followed to unravel the details of the magnetic phase diagram near $T_c(0)$. We have been concerned with the determination of irreversibility lines and lower critical fields by different magnetization techniques and methods in samples of Bi2212 [9–11]. We have reinitiated a series of new investigations by AC and DC magnetization techniques in high quality single crystal samples of Bi2212 for the said purpose. Our initial data show that as 3D to 2D crossover occurs, the magnetic response of a crystal transforms from that of a one-component system to two-component system corresponding to 2D planes and interplanar links. The two-component response is highly irreversible and the irreversibility persists up to $T_c(0)$. We identify the T^* and H_{cr} values of BLK [6] with (T_{2D}, H_{2D}) line (i.e., $\mathrm{d}M/\mathrm{d}H = 0$ line), above which the changes with field and temperature in the diamagnetic response are dominated by the response from 2D planes. Below this line, we see clear manifestations of interplay between diamagnetism of two components. Our new results lead us to schematically sketch the details of the magnetic phase diagram near $T_c(0)$. The key result and a summary of our new findings have been communicated earlier [12, 13]. The purpose of this paper is to report the details of new experiments which vividly elucidate the changes in magnetic response that occur during the dimensional crossover in highly anisotropic layered superconductors.

2. Experimental details

Our single crystal sample of $Bi_2Sr_2CaCu_2O_8$ ($1{\cdot}9 \times 1{\cdot}5 \times 0{\cdot}4\,\mathrm{mm}^3$) is cut from a boule grown by travelling solvent floating zone technique [14]. The DC and AC magnetization data for $H \| c$ have been recorded using a Quantum Design SQUID magnetometer ($MPMS_2$-system) and a home built mutual inductance bridge, respectively. The AC susceptibility system has a variable frequency 2-phase lock-in amplifier and a superposed DC field is produced using a superconducting solenoid and can be swept at a rate of 0·5 to 100 Oe/s at fixed temperatures. The bridge is usually operated at 119 Hz.

This paper is based on the following experimental runs.

2.1 *Temperature dependent DC magnetization curves*

We recorded magnetization data in $H = 0{\cdot}3$, 0·5, 1·3, 10, 50, 100 and 300 Oe, respectively along zero field cooled warm-up (M_{ZFC}, cycle 1), (very slow) field cool cool-down (M_{FCC}, cycle 2), field cool warm-up (M_{FCW1}, cycle 3) and warm-up after rapid (in 3 to 5 minutes) cool-down to 10 K in field (M_{FCW2}, cycle 4). No measurements can be made during rapid cool-down cycle in field. The T-dependent data have been recorded in small steps of 100 to 200 mK in the temperature regions of interest, and at each temperature a minimum wait time of 300 s was maintained. It was checked that a wait time longer than 600 s did not produce any further measurable change in magnetization values. The thermal equilibrium gets established rather slowly in Quantum Design SQUID magnetometer. Further, the overshoots and undershoots are not the same during warm-up and cool-down cycles. During cool-down, minimum undershoot is about 1 K in 60 to 90 K interval even when the set temperature is decreased by only 0·1 K. The overshoot/undershoot values during warm-up can be limited to less than 0·5 K provided the step size is not greater than 0·2 K.

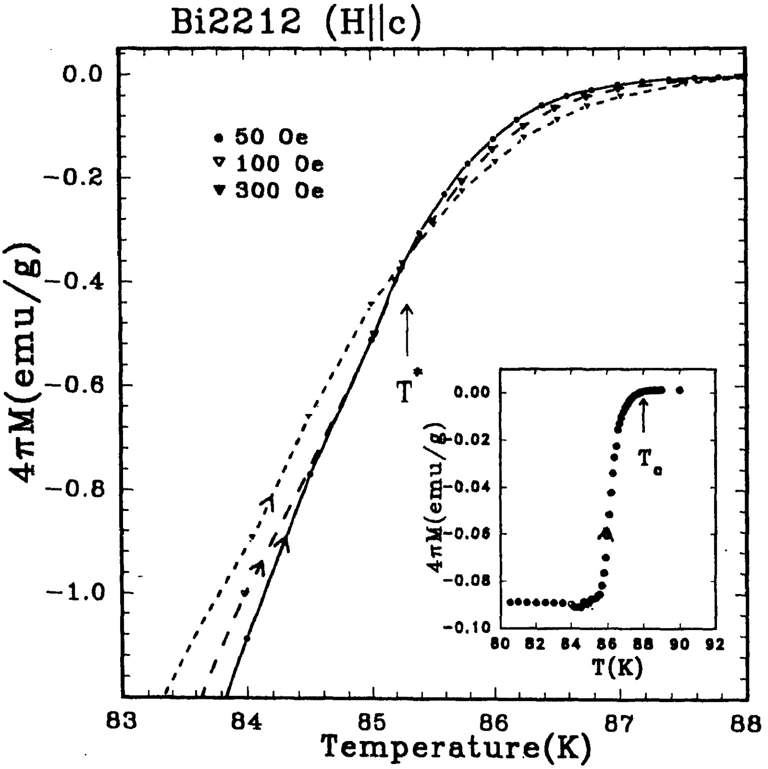

Figure 1. Zero field cooled magnetization curves, M_{ZFC} vs T, in a single crystal specimen of $\mathrm{Bi_2Sr_2CaCu_2O_8}$ for $H(\| c) = 50$, 100 and 300 Oe, respectively. The temperature T^* identifies the midpoint of the temperature range encompassing the region of intersection of curves for 50 Oe $< H <$ 300 Oe. The inset shows the identification of so-called zero field transition temperature T_c via the onset of diamagnetic response in the temperature dependent magnetization curve recorded in the warm-up mode in the nominal residual field ($\approx 0{\cdot}3$ Oe) of the magnet. The sample was initially rapidly cooled down to 10 K in the same field.

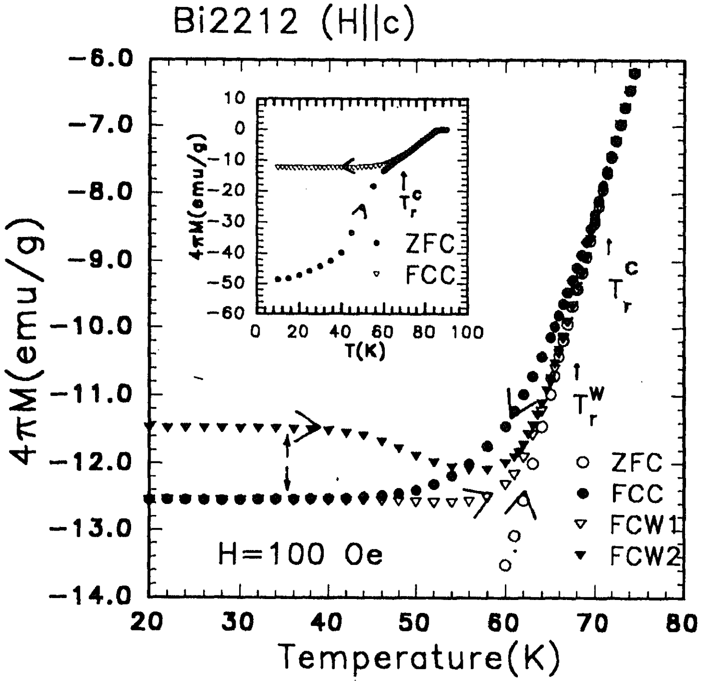

Figure 2. Temperature dependence of magnetization data in $H(\| c) = 100\,\mathrm{Oe}$ in Bi2212 sample. The acronyms ZFC, FCC, FCW1 and FCW2 identify the cycles zero field cooled warm-up, (slow) field cooled cool-down, (first) field cool warm-up and (second) field cool warm-up (after rapid field cool cool-down), respectively. The temperatures T_r^c and T_r^w identify the merger of M_{FCC} and $M_{\mathrm{FCW1}}/M_{\mathrm{FCW2}}$ curves with M_{ZFC}. The temperature at which M_{FCW1} curve starts to bifurcate from M_{FCC} data can identify the limiting value of the lower critical field via the criterion suggested by Clem and Hao [19]. The inset shows $M_{\mathrm{ZFC}}(T)$ curve over the entire temperature range.

The temperature dependent data can be used to determine the limiting values of irreversibility temperature and the lower critical field. These data also identify the temperature region across which the change in character of diamagnetic response occurs (i.e., change in $\mathrm{d}M/\mathrm{d}H$ from positive to negative values, e.g., see figure 1). The merger temperature of M_{ZFC} with M_{FCC} and $M_{\mathrm{FCW1}}/M_{\mathrm{FCW2}}$ identify the values of irreversibility temperatures $T_r^c(H)$ and $T_r^w(H)$ (e.g., see figure 2). In general, $T_r^c(H) > T_r^w(H)$ [11, 15–18] and Clem and Hao [19] have sought to provide an understanding of the difference between M_{FCC} and M_{FCW1} curves in the framework of critical state model. Clem and Hao [19] argue that M_{FCW1} values in an applied field H would start to differ from M_{FCC} values at a temperature T_{c1} such that the lower critical field at T_{c1} equals H. Following such a procedure, we may choose to pick out $H_{c1}(T)$ values also from the temperature dependent magnetization data.

2.2 *Isothermal DC magnetization hysteresis curves*

Magnetization hysteresis curves in fields up to ± 10 kOe have been recorded at close temperature intervals in the range 73 K to 86·7 K. For every run, the specimen was cooled down to a given temperature in nominal zero field, i.e., the residual field values

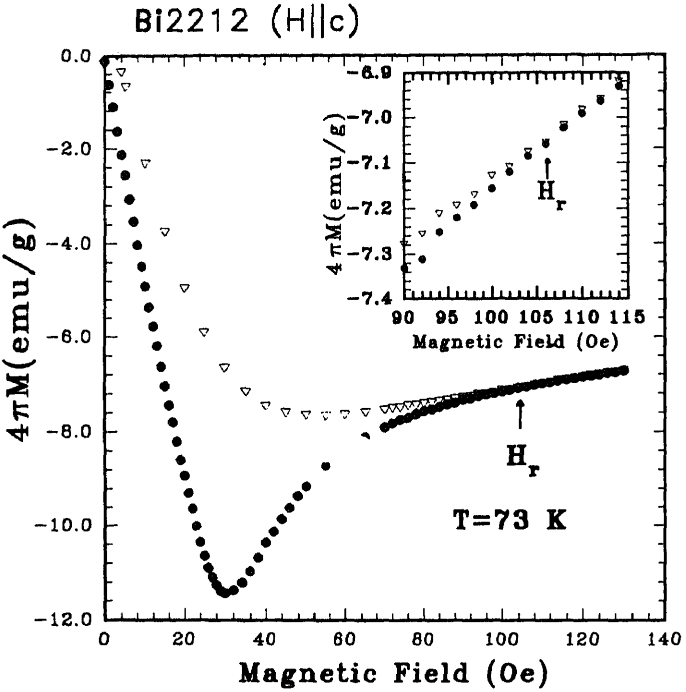

Figure 3. Isothermal magnetization curve in a Bi2212 sample ($H \parallel c$) at 73 K. The inset highlights the identification of irreversibility field H_r(73 K) = 106 Oe. It may be noted that T_r^c (100 Oe) = 72·5 K in figure 2.

of magnet (which were measured to lie between 0·3 to 0·4 Oe). For observing the details of magnetization curves in the low field region, the residual field of the magnet was specifically reduced to $\approx$ 1 mOe using Fluxgate option supplied by Quantum Design Inc. However, the smallest absolute field value which the power supply can reproducibly set is limited to 0·3 Oe and the smallest step size thereafter is limited to 0·1 Oe. The field values were incremented in non-overshoot mode, and without invoking the *hysteresis-option software*. The field increments using *hysteresis-option software* were completely avoided as it leads to various artifacts [20]. A minimum wait time of 60 s was observed at each field value.

The isothermal hysteresis curves are used to determine the values of irreversibility field $H_r(T)$ via the merger of $M-H$ curve recorded during the forward cycle with that recorded during the reverse cycle (e.g., see figure 3). The isothermal magnetization data also help to identify the field-temperature region across which dramatic changes occur in the shape and nature of hysteresis loops (e.g. see figures 4 and 5). During this changeover, the hysteresis curve appears to be a superposition of two components instead of the usual behaviour expected in an irreversible type II superconductor (cf. loops at 83 K and 86·7 K in figure 4).

2.3 *Temperature dependent in-phase (χ') and out-of-phase (χ'') AC susceptibility*

$\chi'(T)$ and $\chi''(T)$ data at a frequency of 119 Hz and with a peak amplitude in the range of 0·6 Oe to 1·3 Oe in superposed DC field values of nominal zero, 100 Oe and 300 Oe, respectively, have been recorded.

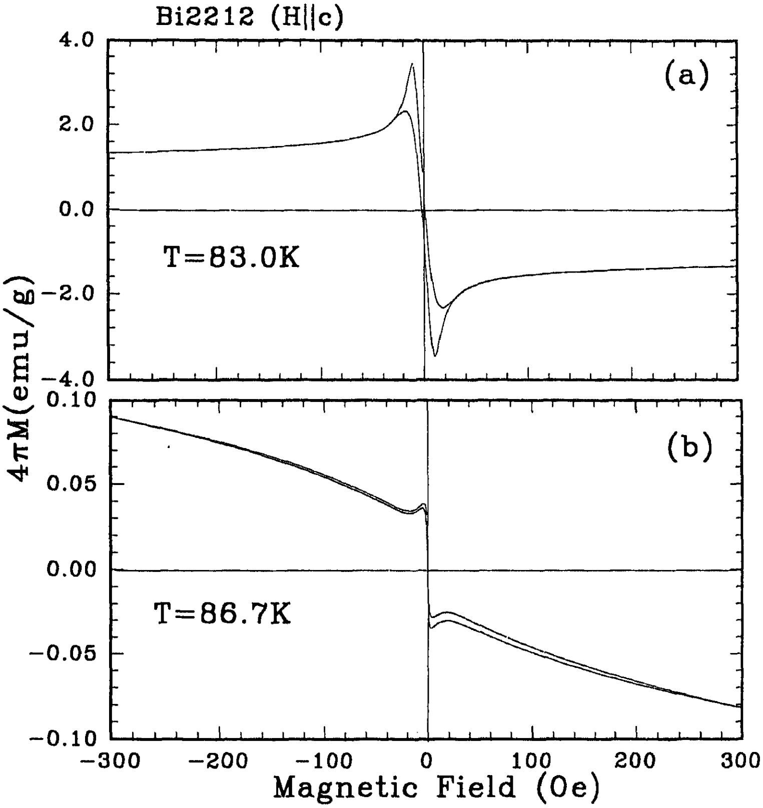

Figure 4. Comparison of magnetization hysteresis loops obtained between ± 300 Oe at 83 K ($< T^*$) and 86·7 ($> T^*$), respectively. Note the change in shape, increase in irreversibility field value and the loss of symmetry as the temperature crosses T^* value of about 85·3 K.

The $\chi'_H(T)$ data at fixed H identify the irreversibility temperature [21–24] as the onset-temperature (designated as $T_r^{\mathrm{DPE}}(H)$) of differential paramagnetic effect (DPE) (e.g., see figures 6 and 7).

From $\chi''_H(T)$ data in different H (e.g., see figure 7), one can pick out the temperature values of peak positions ($T^{\chi''}_{\mathrm{peak}}(H)$).

2.4 *Isothermal in-phase and out-of-phase AC susceptibility*

χ'_H and χ''_H data as a function of superposed DC field (up to 300 Oe) have been recorded at several temperature values lying between 60 K and T_c.

The χ'_H vs H plots at different T identify the irreversibility field as the field values of the onset of DPE (designated as $H_r^{\mathrm{DPE}}(T)$, e.g see figure 8), whereas χ''_H vs H data are used to pick the field values of peak positions in χ''_H (designated as $H^{\chi''}_{\mathrm{peak}}(T)$, e.g. see figure 9). In principle, the isothermal χ'_H and χ''_H data can also be used to confirm the 'temperature and field' values across which the qualitative changes in the shape of DC magnetization hysteresis loops occur. The detailed results and the analysis of AC susceptibility studies shall be reported elsewhere [24]. Only a part of AC susceptibility data necessary for the present objective have been included here.

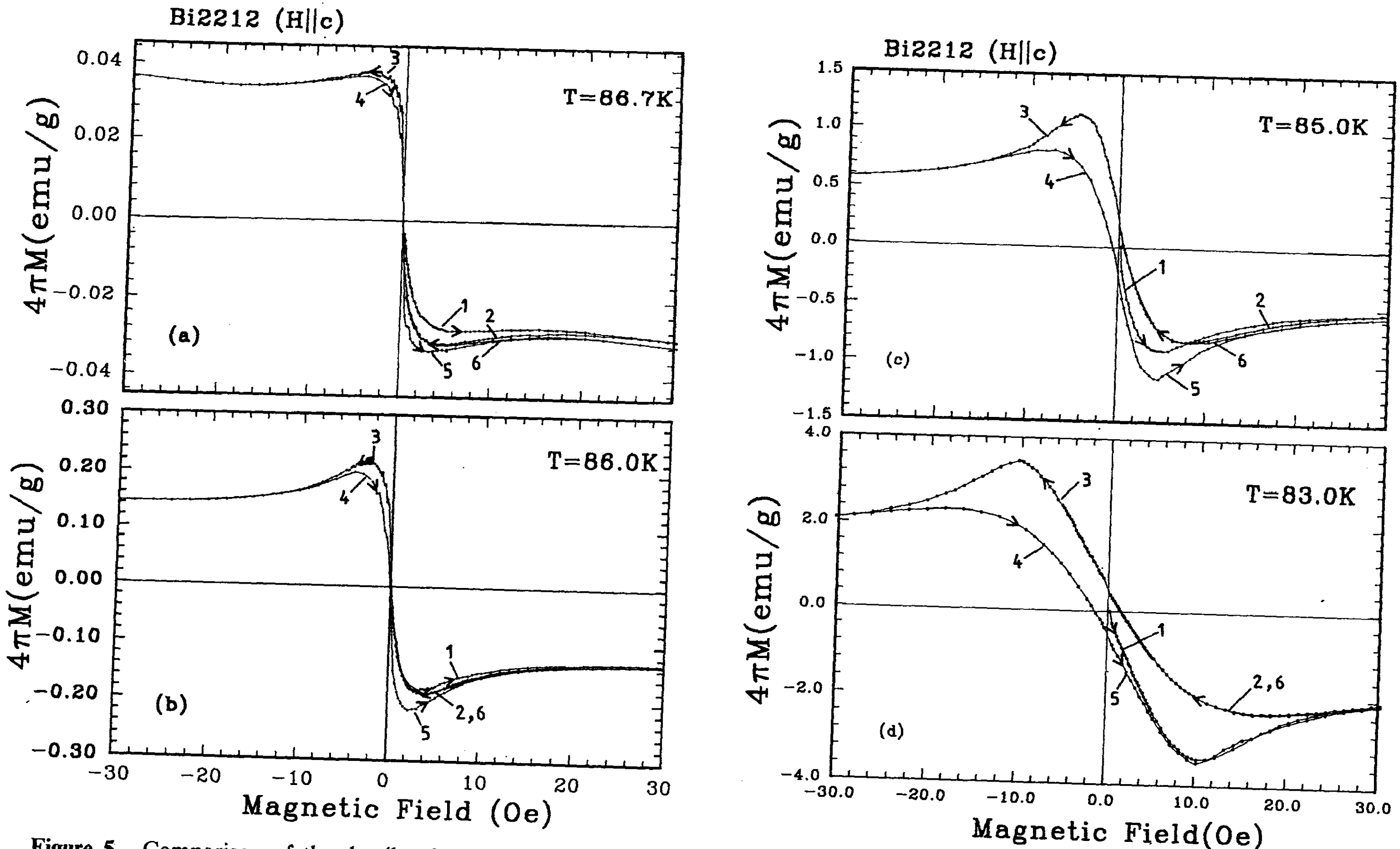

Figure 5. Comparison of the details of the magnetization hysteresis curves obtained at (a) 86·7 K, (b) 86 K, (c) 85 K and (d) 83 K, respectively. Each time the sample was cooled down to a given temperature in a residual field of about 1 mOe. Each of the complete cycles is as follows: 0 to + 30 Oe (1), + 30 Oe to 0 Oe (2), 0 to − 30 Oe (3), − 30 Oe to 0 (4), 0 to + 30 Oe (5) and 30 Oe to 0(6). Note the difference between curves 1 and 2 as the temperature changes from 86·7 K to 83 K. The irreversibility field as defined by merger of curves 3 and 4 would appear to decrease as T changes from 83 K to 86·7 K. However, the differences between curves 1 and 2 may imply otherwise.

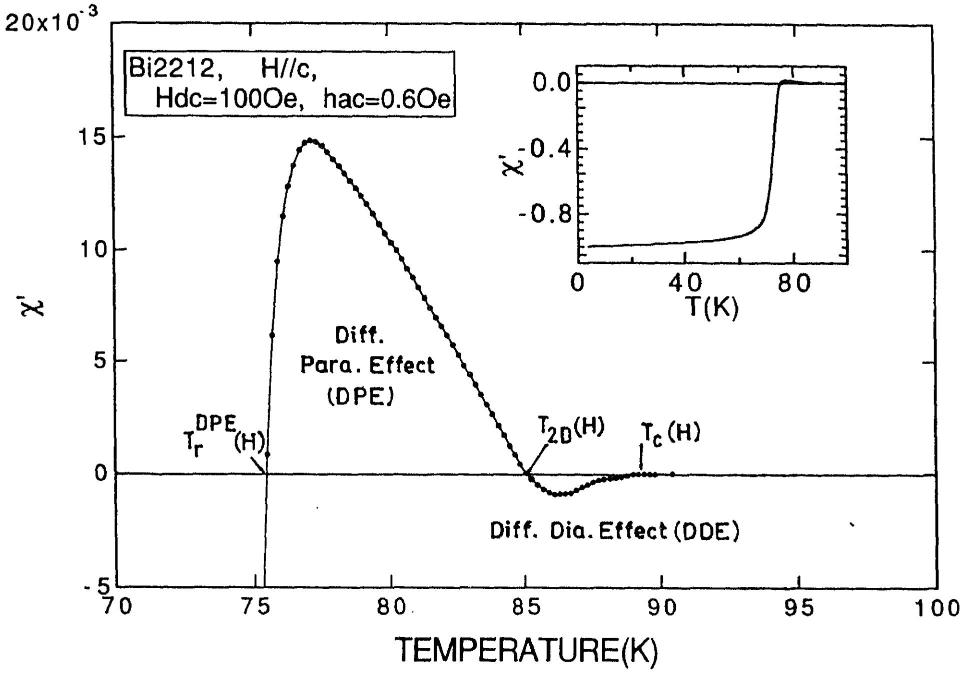

Figure 6. The in-phase AC susceptibility $\chi'(T)$ vs T near T_c in $H(\| c) = 100$ Oe. The onset and offset of positive response in $\chi'(T)$ identify the values of $T_r^{\mathrm{DPE}}(H)$ and $T_{2\mathrm{D}}(H)$, respectively. The amplitude of AC field was 0·6 Oe and frequency = 119 Hz.

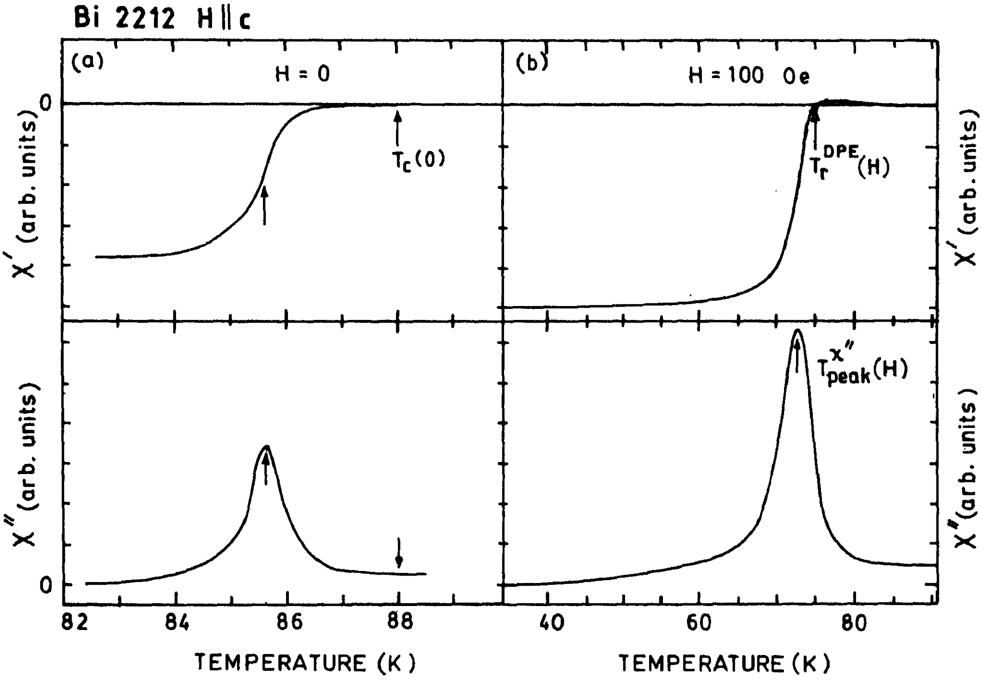

Figure 7. Comparison of in-phase and out-of-phase AC susceptibility in $H = 0$ and 100 Oe in Bi2212 sample.

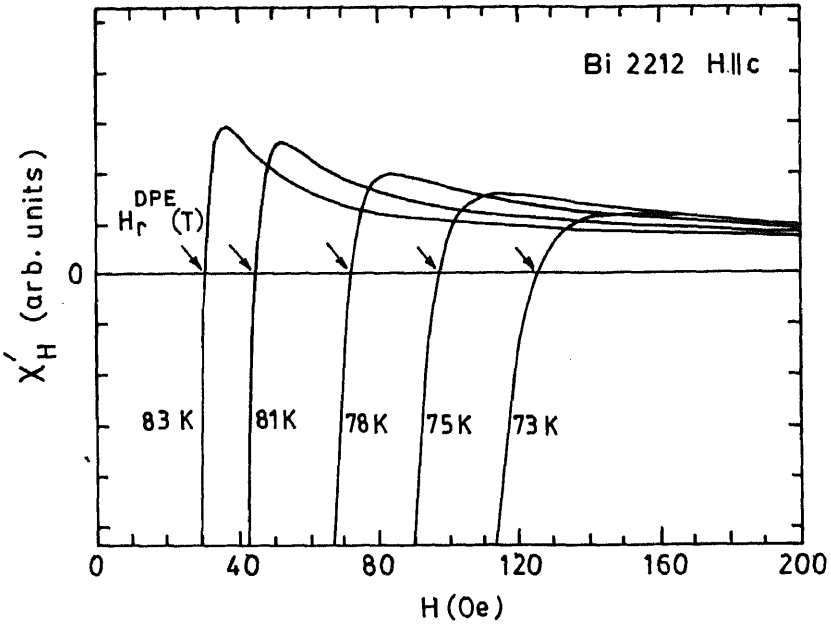

Figure 8. The in-phase AC susceptibility vs H data at different temperatures. The arrows identify the values of irreversibility field at different temperatures. These data have been obtained at a frequency of 119 Hz, the irreversibility fields are seen to increase as frequency increases (data not shown here).

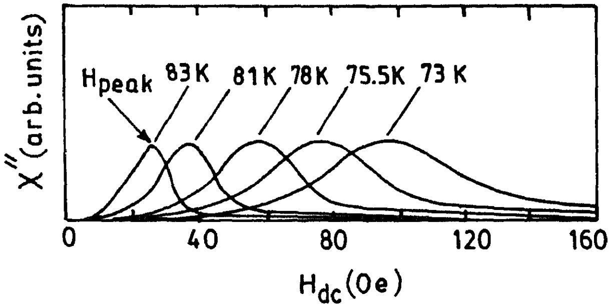

Figure 9. The out-of-phase AC susceptibility data vs H at different temperatures.

3. Results and discussion

3.1 *Dimensional crossover effect*

Figure 1 shows M vs T curves for $H = 50$, 100 and 300 Oe, respectively. It is apparent that these curves intersect at a temperature of $85{\cdot}3 \pm 0{\cdot}1$ K. At any temperature value below this, dM/dH values are positive whereas above this the dM/dH values cross over to the negative regime. The positive values imply a behaviour usually seen in the mixed state of any type-II superconductor. Figure 4 shows magnetization hysteresis loops in ± 300 Oe, at temperature values below and above the intersection temperature of 85·3 K. At 83 K, the hysteresis loop (figure 4(a)) has the shape and features normally ascribable to a hard type-II superconductor, whereas at 86·7 K, it is tempting to view the observed hysteresis curve (figure 4(b)) as the superposition of a minor hysteresis loop (limited to low field values) on the continuously increasing irreversible diamagnetic response extending to high field values. The isothermal magnetization data of figure 4 confirm that dM/dH values for $H \geqslant 30$ Oe are positive and negative at 83 K and 86·7 K, respectively. As remarked in the introduction, the response with negative dM/dH values is being perceived to arise from fluctuation effects confined to individual quasi-2D copper oxide planes. Taking a clue from well documented 2-component behaviour (ascribed to intragrain and intergranular regions) observed in magnetization hysteresis curves of ceramic samples of HTSC [25–28] or fine multi-filament wires of alloy superconductors (see, for instance, discussion in §4 of [29] or [30]), we identify the hysteresis loop confined to lower field values with the response from interplanar linkages. At any temperature, as the applied field increases the interplanar links are expected to get severed resulting in response from only decoupled planes.

Two more noteworthy differences in the hysteresis loops displayed in figures 4(a) and (b) are, (i) the change (i.e., increase) in the irreversibility field value on increasing the temperature from 83 K to 86·7 K and (ii) the appearance of marked asymmetry (i.e., the absence of time reversal symmetry) in the hysteresis loop at 86·7 K. Both these changes are of considerable significance. The irreversibility in a hard type-II superconductor correlates with the macroscopic currents that flow in a hard type-II superconductor. Since the critical current density J_c decreases with increase of temperature or the field, the irreversibility field values are expected to decrease as T increases. The absence of time reversal symmetry has hitherto been noted in ceramic samples of $YBa_2Cu_3O_7$ by Roy *et al* [30] and is ascribed by them to the interplay between the diamagnetic responses from intragrain and intergranular regions. The explanation uses an idea due to Evetts and Glowacki [31], that in sintered samples, the intra-grain diamagnetic response M_g in an applied field H_o provides an additional field $H_g(M_g)$ in the intergrain region. The additional field value $H_g(M_g)$, thus, depends on the history of application of H_o via the history dependent magnetization value of the grain in field H_o.

The inset of figure 1 depicts warm-up M vs T curve obtained after rapidly cooling the sample in nominal residual field ($\approx 0{\cdot}3$ Oe) of the magnet. The nominal zero field transition temperature $T_c(0)$, identified with the onset of curvature (w.r.t. base line) in the diamagnetic response, is reckoned as 88 K in our sample of Bi2212. The mid-point of sharp fall in diamagnetic response is located just above 86 K. The transition width of this specimen is very narrow and it correlates well with similar data reported in the literature in good quality samples of the highly anisotropic layered compounds (e.g., see figure 4 of [7]). The magnetization data contained in figures 1 and 4 motivates us to view the observed changes (e.g., at 85·3 K in figure 1) in magnetization behaviour before reaching the $T_c(0)$ value as the consequence of dimensional cross-over effect. So long as the inter-planar coupling is strong, the specimen has a response identifiable with a 3D type-II superconductor. The weakening of the coupling results in a quasi-two component behaviour with interesting interplay between the two components.

3.2 *Irreversibility line*

The fact that the flux pinning has to vanish at a temperature below $T_c(H)$ in a hard type-II superconductor inevitably leads to the existence of pinning-depinning transition (or an irreversibility line) above which the value of macroscopic critical current density J_c is zero (see schematic description in §3 of [9]). Ever since the determination of an irreversibility line in a specimen of HTSC by Müller *et al* [32], a variety of techniques and procedures have been employed to determine quasi-irreversibility lines in HTSC as well as in conventional alloy superconductors. It is an experimental reality that irreversibility lines determined by different methods in the same sample do not overlap. However, all the irreversibility lines concur in conveying the message that values of irreversibility field/irreversibility temperature decrease as temperature/field increases. A systematic study in the samples of niobium (an elemental superconductor with $T_c = 9{\cdot}3$ K) have indicated a hierarchy amongst the irreversibility lines determined from different DC and AC magnetization measurements [9, 21, 22]. A complete understanding of this hierarchy is still to be attained. In any case, we find the existence of similar hierarchy in the quasi-irreversibility lines determined from different measurements in our single crystal sample of Bi2212.

Figures 2, 3, 6, 7, 8 and 9 exemplify the determination of values of temperature and field, in T-dependent and isothermal DC and AC magnetization measurements, which are considered to mark the transition from irreversible to reversible response. Figure 10 summarizes all the data obtained on irreversibility temperatures and fields for $T > 70$ K and $H < 300$ Oe. The hierarchy that $H_r^{\mathrm{DPE}}(T)$ line defines the upper boundary and $T_r^c(H)$ line is the lower limit of the irreversible to reversible transition region is clearly evident in figure 10. Clem and Hao [19] have argued that merger temperatures $T_r^w(H)$ at which M_{ZFC} data become indistinguishable from M_{FCW} data do not identify the real boundary of reversible to irreversible transition. $T_r^w(H)$ data points are observed to lie below the corresponding $T_r^c(H)$ data points in figure 10.

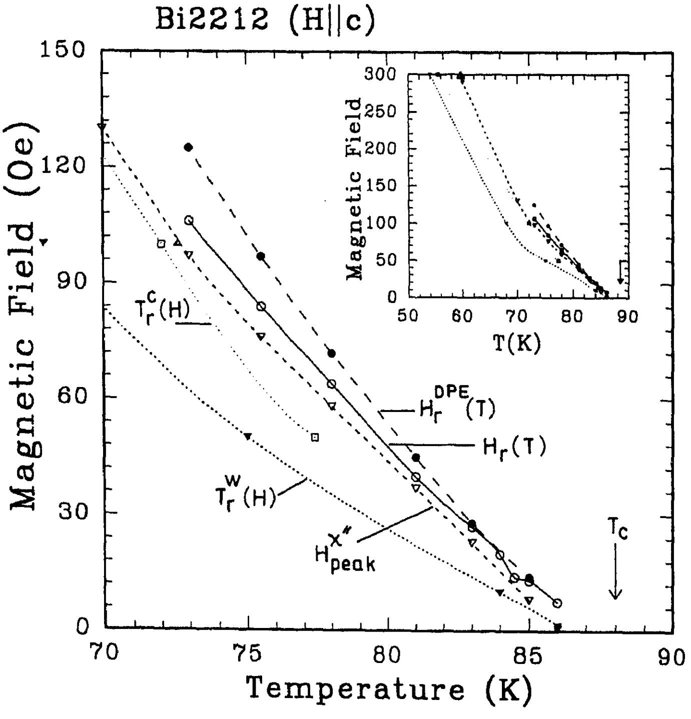

Figure 10. Comparison of quasi-irreversibility lines near T_c obtained by different procedures and techniques. The inset shows such data over an extended temperature range.

Also, the peaks in χ'' data are considered to identify the line that should lie below the true reversible to irreversible boundary [9]. However, $H^{\chi''}_{\text{peak}}(T)$ line is observed to lie above the $T^{c}_{r}(H)$ line. This in turn implies that $T^{c}_{r}(H)$ line is located sufficiently below the actual irreversible to reversible boundary.

For our purpose it suffices to reckon here that $H_r(T)$ and $H_r^{\text{DPE}}(T)$ lines would nearly linearly extrapolate to zero at a temperature value which is definitely smaller than the nominal $T_c(0)$ value of the sample. We have not included data points above 86 K in figure 10 because a little below this temperature the qualitative changes that occur in the irreversibility behaviour at low fields start to make the determined values of $H_r(T)$ depend on the maximum field to which the sample is exposed. This point is exemplified by a comparison of two hysteresis loops at 86·7 K displayed in figures 4(b) and 5(a), respectively. In figure 4(b), the irreversibility is seen to persist up to maximum field of 300 Oe, whereas, from figure 5(a), the irreversibility field value may be picked out to be equal to or less than 30 Oe. A similar comparison of hysteresis loops at 83 K in figures 4(a) and 5(d) shows that H_r values in the two figures are nearly the same.

3.3 *Two-component behaviour*

As stated earlier, the asymmetry in the hysteresis loop at 86·7 K (figure 4(b)) is a signature of interplay between the diamagnetism of two components. Several other interesting thermomagnetic history effects which are a consequence of interplay between the responses from two components in sintered samples of HTSC have been documented in the literature [33–36]. Two of these are the observed increase in transport $J_c(H)$ (i) on reversing the field, and (ii) on field cooling the sample in the given H. Both these are ascribable to additional field values arising from intragrain diamagnetism. The $J_c(H)$ values during the first ramp-up of applied field (after initially cooling the sample in zero field) are lower because the effective field (at a given applied H) experienced by intergrain regions during the first forward run is larger than that during the reversal of the applied field or after cooling the sample in a given applied field. We see somewhat analogous effects in $M-H$ data in the temperature region of dimensional crossover in our single crystal sample of Bi2212.

Figure 5(a) shows the details of the $M-H$ curves obtained at 86·7 K after ensuring the cool-down of the sample in a field of ≈ 1 mOe. The complete cycle is as follows: 0 to ± 30 Oe (curve 1), $+30$ to 0 Oe (curve 2), 0 to -30 Oe (curve 3), -30 to 0 Oe (curve 4), 0 to $+30$ Oe (curve 5) and $+30$ to 0 Oe (curve 6). It may be noted that curve 2 lies below curve 1, which was completely unexpected. This implies that diamagnetic values are larger on reversal of field from $+30$ Oe to 0 Oe as compared to those during the virgin ZFC run (0 to $+30$ Oe). On further cycling the field between ∓ 30 Oe, the hysteresis loop comprises of curves 3, 4, 5 and 6. It may also be noted that the difference between curves 1 and 2 is larger than that between curves 3 and 4 or curves 5 and 6. The irreversibility field value determinable from curves 3 and 4 or 5 and 6 is much smaller than that evident from curves 1 and 2. On subsequent repeated cycling the field between ± 30 Oe, the hysteresis loop would consist of curves equivalent to curves 3, 4, 5 and 6. We further find that, if the sample gets cooled down to 86·7 K in a nominal residual field of the magnet ($\approx 0{\cdot}3$ Oe), the hysteresis loop nearly comprises of curves 5, 6, 3 and 4, and no anomalous increase in diamagnetic response is evident on reversal of field after the first forward run. This point is well illustrated by a comparison between the two sets of data contained in figure 11. In

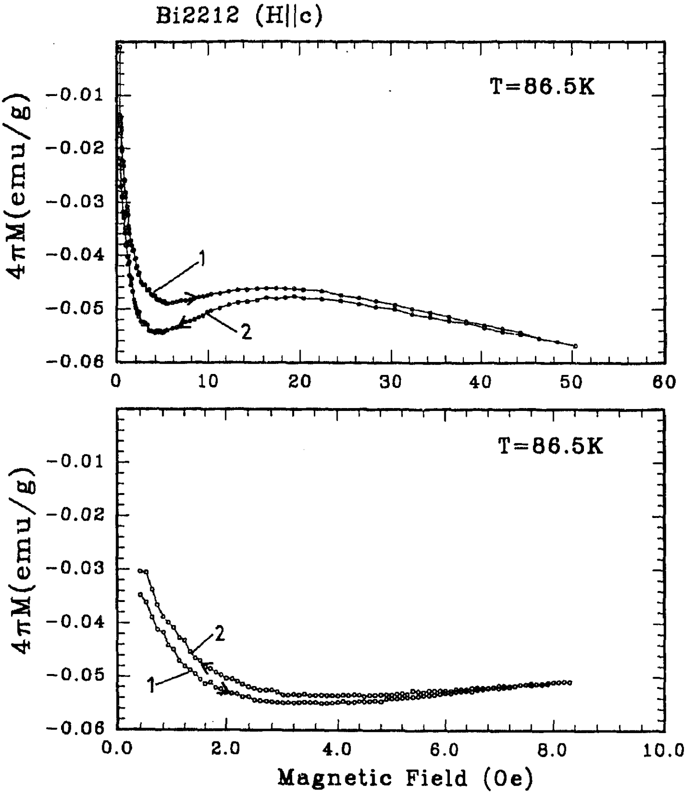

Figure 11. Comparison of magnetization curves obtained at 86·5 K in two different initial conditions. In figure 11(a), the sample has been cooled-down to 86·5 K in a residual field of 1 mOe, whereas the curves in figure 11(b) correspond to an initial cool-down to the same temperature in a nominal residual field of the magnet which was measured to be about 0·4 Oe.

figure 11(a), we have depicted $M-H$ curves up to 50 Oe after cool down of the sample in a field of 1 mOe, whereas figure 11(b) shows $M-H$ curves obtained after cool down of the sample to 86·5 K in nominal zero field ($\approx$ 0·3 Oe). In any case, the complete hysteresis loop obtained on repeated cycling the field between $\pm H_{\max}$ is independent of the initial thermomagnetic history of the specimen. The complete loop comprises the asymmetry property reflecting the interplay between the diamagnetic responses from the two components.

A careful examination of the details of the magnetization curves obtained at 86 K, 85 K and 83 K (see, figures 5(b) to 5(d)) shows that vivid effects which reflect the interplay between the two components become less spectacular as the temperature is lowered from 86·7 K to 83 K. As remarked earlier, the irreversibility field value at 83 K is found to be nearly independent of the thermomagnetic history and the maximum field values between which the sample is cycled. It may be mentioned here that $H_r(T)$ values at 85 K and 86 K contained in figure 10 correspond to those obtained by ramping the field up to a maximum of 20 Oe.

3.4 *Dimensional crossover line*

The experimental data and their analysis presented so far implies that the imprints of two component response and the dimensional crossover effect are present before reaching $T_c(0)$ value. Further, if we accept the argument that response from 2D planes has the characteristic that dM/dH is always negative, we can look for this signature in the isothermal $M-H$ curves. For instance, it may be noted from $M-H$ curves at 86·7 K and 86·5 K (see, figure 4(b), 5(a) and 11(a)) that after the initial peak in magnetization located between 3 and 4 Oe, the magnetization curves turn over again at about 15 Oe and 20 Oe, respectively and above these field values the diamagnetic values increase as H increases (i.e., dM/dH is negative). We may take the second field value at which $dM/dH = 0$ to signify the onset of dominance of 2D like response and designate this field as H_{2D}. Figure 12 shows $M-H$ curves obtained at 83·5 K and 85·5 K, respectively. In this figure, the H_{2D} value at 85·5 K has been identified, whereas at 83·5 K, dM/dH values continue to remain positive up to 10 kOe (highest field up to which data have been recorded) and as such H_{2D} value cannot be ascertained at 83·5 K. We may remark here that some of H_{2D} values at $T < 85$ K evident in reference 13 are erroneous due to an inadvertent omission of subtraction of sample holder diamagnetism.

Figures 13(a) and (b) show the plots of H_{2D} values vs temperature on linear as well as semi-log scales. It is apparent that H_{2D} values show a slow increase as temperature is progressively lowered down from 86·7 K to 85·75 K. The fast rise in H_{2D} values sets in only below 85·5 K. The temperature interval between the drastic change in dH_{2D}/dT value (the dotted line in figures 13(a) and (b)) and the $T_c(0)$ value nominally

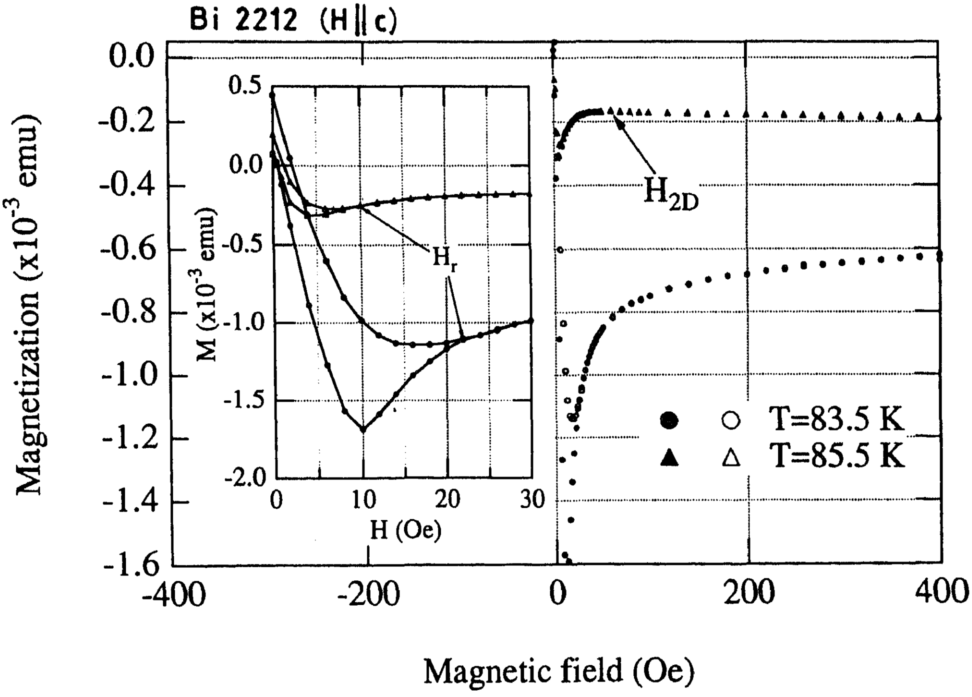

Figure 12. Isothermal M vs H curves at 83·5 K and 85·5 K, respectively.

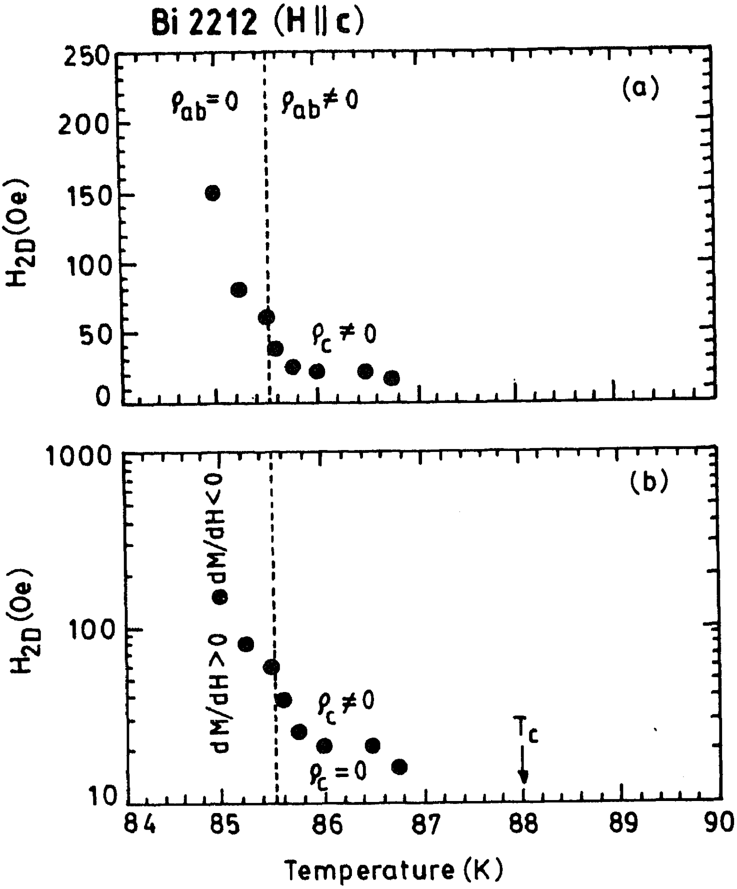

Figure 13. Plot of H_{2D} vs T values on (a) linear and (b) semilog scales. The temperature at which rapid rise in H_{2D} values sets in can be easily seen in these data.

marks the dimensional crossover region. From (H_{2D}, T_{2D}) line of figure 13(b), we note that H_{2D} value at the temperature of intersection ($= 85{\cdot}3 \pm 0{\cdot}1$ K) of $M - T$ curves (depicted in figure 1) is about 50 Oe. This immediately tempts us to identify T_{2D} values of figure 13 with T^* of BLK [6]. As remarked in the introduction section, in the framework of BLK treatment, T^* is the temperature at which $\mathrm{d}M/\mathrm{d}H = 0$ for $H > H_{cr}$ and above which $\mathrm{d}M/\mathrm{d}H$ values are negative. If our T_{2D} and T^* of BLK [6] are the same, it would imply that $M - T$ curves for all H would not intersect at the same T^*. As H values increase, the temperature-band of intersection of $M - T$ curves would expand towards the lower temperature. The overall shape of (H_{2D}, T_{2D}) line comprising of rapid build up of H_{2D} with T_{2D} in figure 13 indicates that the said temperature-band of intersection of $M - T$ curves is reasonably narrow for the range of laboratory field values across which $M - T$ curves are usually recorded by experimentalists (e.g., see figure 1 of BLK [6]). Recent high field ($1\,\mathrm{kOe} < H < 50\,\mathrm{kOe}$) $M - T$ curves (for $H \parallel c$) in our Bi2212 sample show that these curves intersect at $85{\cdot}5 \pm 0{\cdot}2$ K [37]).

BLK [6] have also talked of temperature T_s at which electrical resistance (and consequently J_c as well) and H_{c1} values vanish and above which electromagnetic response arises only from 2D planes. As found in § 3·2, the irreversibility lines of strongly coupled quasi-3D superconductor extrapolate to zero at a temperature larger than T^* but smaller than $T_c(0)$. We shall present our H_{c1} data in the next section. However, we wish to remark here that low field hysteritic behaviour attributed to interplanar links continues to persist up to $T_c(0)$, this implies that the imprints of two component behaviour probably survive up to $T_c(0)$. Lastly, it is not of place to recall here that BLK [6] have predicted that above T^*, the diamagnetic response increases logarithmically with field and Martinez *et al* [38] have sought to provide magnetization data from torque measurements in Bi2212 supporting this prediction. But, a cursory look at $\mathrm{d}M/\mathrm{d}H$ values at $H > H_{2D}$ in our specimen of Bi2212 shows that diamagnetic values increase in a quasi-linear manner.

It is pertinent to also recall here an assertion recently made by Wan *et al* [39] on the basis of their electrical transport studies for $H \parallel c$ in Bi2212. They noted that the deduced values of resistivity (in zero applied field) within the planes (ρ_{ab}) go to zero at a temperature T_c^{ab} which is lower than the temperature T_c^c at which the resistivity across the planes ρ_c goes to zero. This led them to surmise that in the temperature interval $T_c^{ab} < T < T_c^c$ Josephson supercurrents flow across the resistive planes (which are presumably in the dissipative fluctuating superconducting state). It is tempting to correlate the temperature interval T_c^{ab} to T_c^c with the interval over which we observe spectacular manifestations of two component response in the $M-H$ data. Our identification of normal looking minor hysteresis loop confined to low field values with the component corresponding to interplanar links inherently implies the existence of supercurrents across the planes. We think that the temperature $T_c^{ab}(H=0)$ at which the resistivity within the planes goes to zero probably marks the transition from weakly coupled to strongly coupled response (from Josephson coupled quasi-2D planes) in the magnetization data. The (H_{2D}, T_{2D}) line of figure 13a appears to be made up of two parts corresponding to slower and faster increase in $H_{2D}(T)$ values. The temperature $T_c^{ab}(H=0)$ perhaps demarcates the two parts. In the nominal dimensional crossover region (temperatures above dotted line figures 13(a) and (b)), the (H_{2D}, T_{2D}) line is such that $\rho_c = 0$ below it but ρ_c values would become non-zero at somewhat above it. At temperatures lower than $T_c^{ab}(H=0)$, the (H_{2D}, T_{2D}) line is such that above this line the change is diamagnetic response ($\mathrm{d}M/\mathrm{d}H$ values are negative) of the strongly coupled system is dominated by the response from quasi-2D planes. At $T < T_c^{ab}(0)$, the (H_{2D}, T_{2D}) line determined via $\mathrm{d}M/\mathrm{d}H = 0$ values does not bifurcate the regions of $\rho_c = 0$ and $\rho_c \neq 0$. The line demarcating the regions $\rho_{ab} = 0$ and $\rho_{ab} \neq 0$ probably lies below it whereas the line demarcating the region $\rho_c = 0$ and $\rho_c \neq 0$ would exist above it. These lebellings have been schematically depicted in figures 13(a) and (b).

3.5 *Paramagnetic Meissner effect*

Braunisch *et al* [40] reported observation of field independent positive magnetization value (designated as Paramagnetic Meissner Effect PME) in certain ceramic samples of Bi2212 on field cooling in very low field values (< 100 mOe). Their initial observations have since been confirmed by them [40] as well as others [41] in several other varieties of ceramic samples of Bismuth cuprates. The PME is believed [40, 41] to be a consequence of the occurrence of spontaneous orbital (superconducting) currents in certain loops containing weak links (the so called "π" junctions). For our purpose, it is enough to consider that PME is an attribute of the existence of weak links of certain strength in loops of certain geometrical shape and size. In view of the observation that the single crystal specimen of Bi2212 has two component response, like, the ceramic samples, in the temperature interval of dimensional crossover, we may expect to see the signature of PME in our single crystal sample as well.

One way to look for presence of PME is to measure FC magnetization in small fields at different temperatures. We measured FC magnetization in a field value of ≈ 1 mOe in the temperature range 83 K to 87·7 K. The positive magnetization signals with $4\pi M$(emu/cm^3) ≈ 50 mOe are observed at $T > 85$ K. This magnitude compares

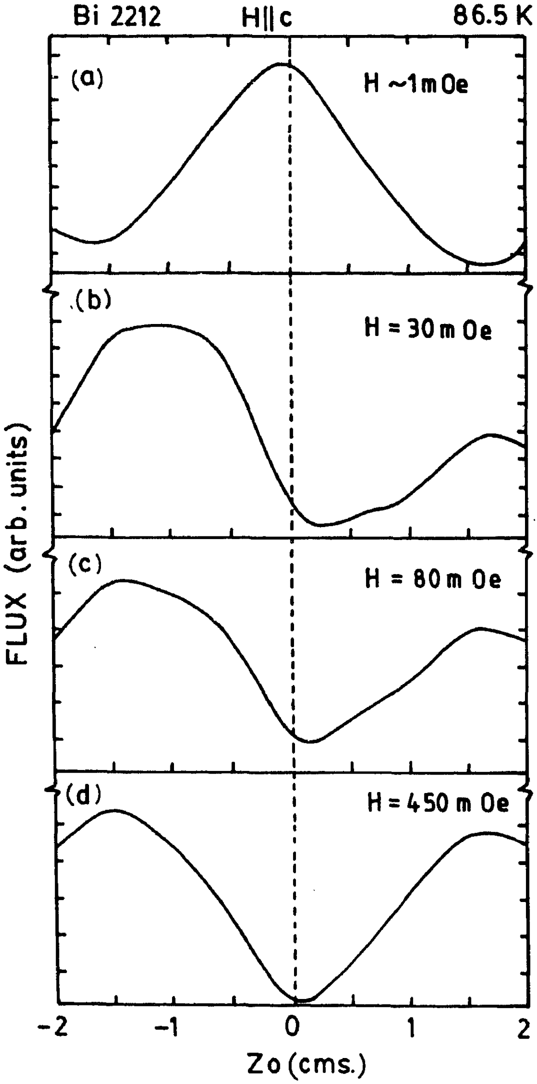

Figure 14. Flux detected as a function of distance from the centre of "second derivative" coil array of Quantum Design SQUID magnetometer at 86·5 K for $H \parallel c$ in Bi2212 at different values of field. The sample is initially cooled down to 86·5 K in a field of ≈ 1 mOe and flux profile is recorded over 4 cm scan (figure 14(a)). The field is then ramped up. Figures 14(b), (c) and (d) show the flux profiles in nominal field values of 30 mOe, 80 mOe and 450 mOe.

favourably with the values of such signals reported earlier [40–42]. After cooling the sample in $H \approx 1$ mOe, a further increase in applied field values up to a few hundered mOe pushes the sample magnetization towards negative values. At such fields, the diamagnetism due to surface screening current starts to dominate over positive magnetization from spontaneous orbital currents.

The magnet power supply of Quantum Design SQUID magnetometer ($MPMS_2$ system) is such that in its usual mode of operation, it does not reproducibly generate low filed values ($H < 300$ mOe). Hence, we are not confident of absolute values of field at $H < 0{\cdot}3$ Oe. In any case, we made a record of flux profiles as the applied field is slowly ramped up from nominal 10 mOe to 500 mOe at 86·5 K. Figure 14 shows flux profiles recorded in nominal field values of 1 mOe, 30 mOe, 80 mOe and 450 mOe. The profiles in 1 mOe (figure 14(a)) and in 450 mOe (figure 14(d)) are essentially dipolar like [9] with magnetization ($4\pi M$) values of $+8 \times 10^{-3}$ emu/g and $-1{\cdot}4 \times 10^{-2}$ emu/g, respectively. The profiles in figures 14(b) and 14(c) show large deviation from dipolar like response, thereby implying that the magnetization signal originating from states of superposition of spontaneous orbital currents and the surface screening current in low field values have significant contributions from quadrupolar moment [9, 43]. In view of our past experience with the analysis of deviations from dipolar like response in superconducting samples [43], we can confidently state that the profiles in figures 14(b) and (c) are neither an artifact of any inhomogeneity in the field along the axis of the magnet, nor the smallness of the absolute value of the magnetization signal.

3.6 *Critical fields*

It is now widely appreciated that the determination of precise values of lower critical field in HTSC is a daunting task for experimentalists (e.g., see remarks in [38] and description in § 8·2 of [9]). The simplest procedure of picking out field values at which isothermal M vs H curve deviates from linearity provides an upper limit on H_{c1} values, when the pinning is strong. We have stuck to this procedure only to ascertain values of $(1 - N_{\|})H_{c1}$ in our sample of Bi2212, where $N_{\|}$ is the demagnetization factor for $H \| c$. It suffices for our limited purpose here as we are interested in knowing the behaviour of H_{c1} vs T near T_c, where the pinning effects are not anticipated to be very strong.

Figure 15 shows a plot of values of $(1 - N_{\|})H_{c1}$ for $T > 70$ K, determined via nominal deviation from linearity criterion. It is apparent that $H_{c1}(H \| c)$ values linearly extrapolate to zero between 86·5 and 87 K. We are not confident of the occurrence of any drastic change (i.e., increase) in value of the slope dH_{c1}/dT just before the collapse of H_{c1} in our data. As stated in § 1, such a behaviour has been noted by Brawner *et al* [8] in Bi2212. In the usual mode of operation the Quantum Design SQUID magnetometer, even with the Fluxgate option facility, does not provide accurate values of deviation from linearity field lying in the range $\leqslant 1$ Oe. The value of $(1 - N_{\|})H_{c1}$ falls to $2{\cdot}0 \pm 0{\cdot}5$ Oe at 84 K in our data and above this temperature, our error bars are so large that they preclude any inference regarding the increase in values of the slope dH_{c1}/dT between 84 K and 87 K. Even in the absence of this effect in our data, it is satisfying to note that the $H_{c1}(T)$ values extrapolate to zero at a temperature value $\leqslant 87$ K. This temperature appears to be not very different from the temperature region of steep increase in diamagnetic response in the lowest field (see, inset of figure 1). This leads us to surmise that the latter identifies the

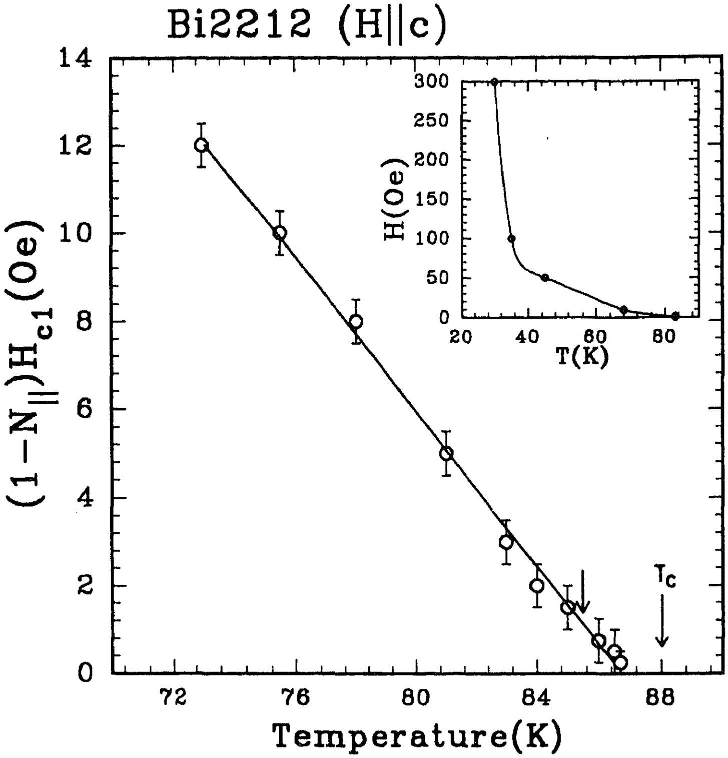

Figure 15. Plot of $(1-N_{\|})H_{c1}$ vs temperature for $H \| c$ in Bi2212. $N_{\|}$ is the demagnetization factor for $H \| c$. The values of $(1-N_{\|})H_{c1}$ have been determined via deviation from linearity criterion. The inset shows the field dependence of temperatures at which M_{FCC}/M_{FCW1} curves start to bifurcate or M_{FCW2} curve starts to show a downward trend.

temperature region of the occurrence of rapid change in the strength of the interplanar coupling (i.e., thermally induced dimensional crossover) in zero field. We feel that above 86 K, the strength of interplanar coupling stands considerably reduced, but, as stated earlier, some imprints of the two component response appear to survive up to $T_c(0)$.

The inset of figure 15 shows the field dependence of temperature values at which M_{FCW1} data start to differ from M_{FCC} data and the M_{FCW2} data start to show a downward trend (see figure 2 for data in $H = 100$ Oe). If we identify the $H - T$ curve in the inset of figure 15 with $H_{c1}(T)$ as per the suggestion of Clem and Hao [19], these limiting values of $H_{c1}(T)$ are somewhat smaller than the corresponding values determined from deviation from linearity criterion. Further, it may be noted that the temperature dependence of the curve in the inset of figure 15 shows a steep rise at $T < 40$ K. Such a behaviour has often been noted in temperature dependence of H_{c1} in HTSC. Burlachkov *et al* [44] have recently pointed out that the steep rise in H_{c1} at lower temperatures is caused by an additional surface barrier effect which becomes effective at high pinning strength. They argue that if a correct analysis of the data is made, the actual H_{c1} values would show the usual saturation effect in the lower temperature region.

The $H - T$ curve in the inset of figure 15 identifies the boundary at which M_{FCW1}

and M_{FCW2} data (as in figure 2) start to show the so-called negative peak effect, i.e., increase in diamagnetic response with increase in temperature. It may be mentioned that the negative peak effect stands enhanced in the warm-up data recorded after rapid cool down in field (cf. M_{FCW2} and $\mathrm{M}_{\mathrm{FCW1}}$ data sets in figure 2). The negative peak feature has earlier been noted in ceramic samples of HTSC or specially prepared porous polycrystalline samples of an alloy superconductor Nb_3Sn [18]. Huyn [18] has sought to explain this effect in terms of interplay between responses from two components (i.e., grains and intergranular regions or weak links at grain boundary contacts in HTSC or alloy superconductor, respectively) in conjunction with thermal hysteresis of diamagnetism of first component, viz., grains. The central idea is that during cool-down, the flux escaping from the grain region gets trapped in intergranular regions. On warm-up, the flux movement inside and outside the grain regions is such that more net flux escapes from the entire sample resulting in enhanced diamagnetism. The two facts, that (i) the field cool magnetization value after rapid cool-down (the first data point of the data set marked FCW2 in figure 2) differs from the corresponding value after slow cool-down and (ii) the negative peak effect, can be qualitatively understood in terms of a scenario described by Huyn [18], which also implicitly confirms the existence of interplay between the responses from two components in a single crystal of Bi2212. When the interplanar coupling is strong, the usual electromagnetic response of the coupled system is indistinguishable from that of a 3D type-II superconductor. However, coupling manifests itself via the effects, like the two pointed out above. As stated in the introduction, Kleiner *et al* [4] have been the first to directly observe dc and ac Josephson effects at 4·2 K in Bi2212. More recently Nakamura *et al* [45] have described another manifestation of the coupling between planes via the drastic change in the initial magnetization curve at 10 K, when the applied field stood slightly misaligned w.r.t. a–b plane.

The assignment of upper critical field for the coupled 2D superconductor poses new issues. It is generally accepted that there is no well defined H_{c2} line for the highly anisotropic HTSC system, instead, there perhaps exists only a dimensional crossover region (e.g., see figure 3(b) of [1]). Kadowaki [2] has been amongst the firsts to point out that T-dependent magnetization data cannot be used to identify the said H_{c2} values as the onset of diamagnetism in these systems is gradual, rounded and somewhat obscure and the conventional analysis leads to an unusual inference that $T_c(H)$ increases with H [3].

When we consider the electromagnetic response of a layered HTSC in terms of a 2-component system, the above remarks regarding the absence of any signature and the difficulty in defining H_{c2} would apply to the component corresponding to 2D planes. The other component attributed to interplanar links and identified with the hysteresis loop confined to low field values does possess a feature which can be used to pick out a limiting value of the upper critical field of that component. In the temperature interval of dimensional crossover, $H_{2\mathrm{D}}$ is physically the field above which all interplanar links may be considered broken. Thus, $H_{2\mathrm{D}}$ at any T, as identified with the field value at which $\mathrm{d}M/\mathrm{d}H = 0$ in isothermal DC magnetization curve, defines a (lower) limit, which must correlate with the upper critical field H_{c2} of the interplanar component.

In principle, one can see a signature of $H_{2\mathrm{D}}$ via differential paramagnetic effect (DPE) in the in-phase AC susceptibility data as well. Figure 16 shows a schematic plot of isothermal DC magnetization and χ'_H vs H curves. The first field value at which χ'_H crosses from negative to positive values identifies $H_r(T)$, whereas the second

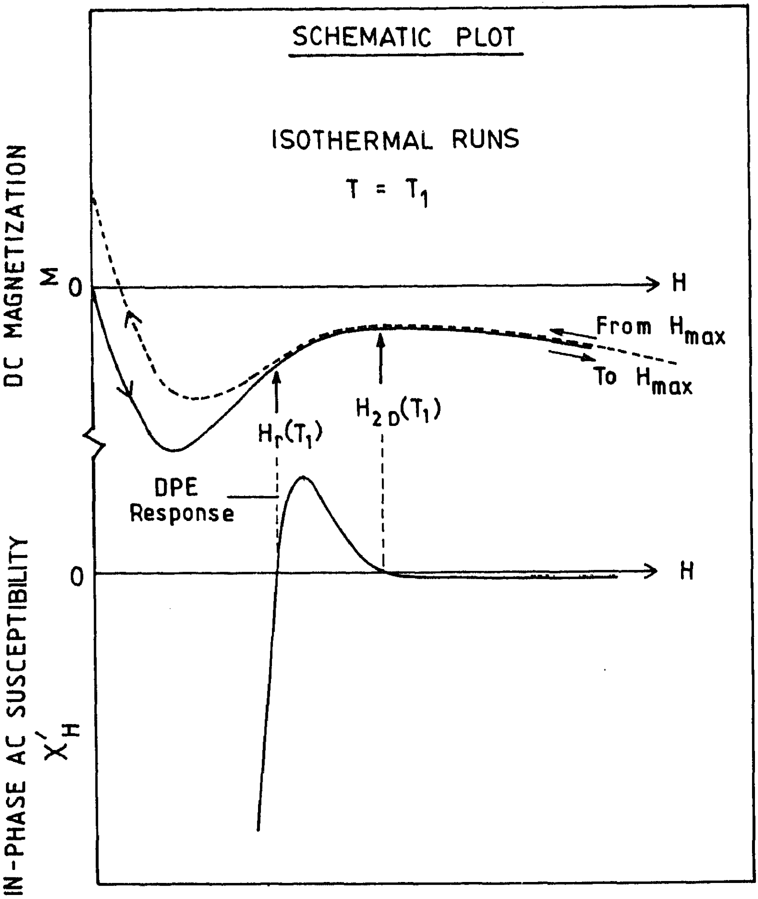

Figure 16. Schematic plot of isothermal M vs H and χ' vs H behaviour expected in a situation which encompasses dimensional crossover. The signatures of irreversibility field $H_r(T)$ and the dimensional crossover field $H_{2D}(T)$ are identified.

crossover, after which χ'_H saturates to a very small negative value, should identify the H_{2D} value. The second crossover is difficult to unambiguously pick out from the isothermal χ'_H data. However, it is possible to pick out the analog of second crossover corresponding to $T_{2D}(H)$ value in very carefully recorded temperature dependent $\chi'_H(H)$ runs [cf. figure 6]. Figure 6 shows DPE peak in χ' vs T data in $H = 100$ Oe. We feel that in T-dependent measurements, the temperature at which DPE signal crosses the baseline second time identifies $T_{2D}(H)$. Above $T_{2D}(H)$, the differential susceptibility ($\mathrm{d}M/\mathrm{d}H$) is negative and we choose to call the tiny negative peak as *Differential Diamagnetic Effect* (DDE). The DDE is a hallmark of dominance of diamagnetic response from decoupled 2D planes. The temperature at which DDE signal merges into base line identifies the so-called $T_c(H)$ value which correlates well with the similar value evident in DC magnetization data of figure 1. It may be appreciated that DPE and DDE responses are so small that DPE and DDE signals being reported in the present paper would rank amongst the first such observations in any single crystal specimen of HTSC. The presence of DPE and DDE type peaks in polycrystalline samples of Bi2212 can be noted in some of the data of Couach and Khoder [23]. Kadowaki *et al* [46] have also recently reported the field dependence of the temperature values (designated as $H_{c2}(T)$ by them) at which DPE signals merge into the base line in their single crystal sample of Bi2212 for $H \parallel c$. They find a steep fall in "$T_c(H)$" values (as H increases) across a narrow temperature region lying below $T_c(0)$. We feel that their "H_{c2}" vs T behaviour echoes the H_{2D} vs T dependence of our sample (figure 13) in the temperature interval of dimensional crossover. They have not succeeded in observing DDE peaks in their data.

If we examine the hysteresis loop at 86·7 K in figure 4(b) in the light of above discussion, we may note that irreversible behaviour continues up to field values much larger than the identified H_{2D} at this temperature. We find that the hysteritic behaviour asymptotically vanishes at $H \approx 1$ kOe (data not shown here). We speculate that the field value at which the irreversibility in diamagnetic response disappears may play the role of "H_{c2}" for the component representing the response from decoupled 2D planes.

3.7 *Irreversible behaviour near T_c at low fields*

The occurrence of dimensional crossover and the interplay between diamagnetism of two components bestows this system with anomalous looking features just below T_c in temperature dependent DC magnetization measurements. For instance, figure 17 displays M_{ZFC}, M_{FCC} and M_{FCW} curves obtained in 1·3 and 10 Oe in our sample of Bi2212. We note that whereas M_{FCW} curves merge into the respective M_{ZFC} curves, and the M_{FCC} curve do not do so. M_{FCC} curves cross the respective M_{ZFC} curves; above the crossover temperature, the M_{FCC} data points lie below the M_{ZFC} data. The anomaly that $M_{FCC}(T) > M_{ZFC}(T)$ is somewhat analogous to the observation that diamagnetic response during the reverse cycle is larger than that during the virgin ZFC run at 86·7 K (cf. curves 1 and 2 in figure 5(a)). Two interrelated inferences which further emerge from the observed anomalous behaviour are as follows: (i) Irreversible behaviour at low fields appears to survive up to T_c and (ii) $T_r^c(H)$ as defined by merger of M_{FCC} data into M_{ZFC} data is not relevant at small H.

We do not see anomalous behaviour in temperature dependent magnetization data at $H = 50$ Oe for which $T_r^c(H) = 77{\cdot}5$ K and $T_r^w = 75$ K. The (minimum) limiting value of the field in which we shall not observe anomalies in temperature dependent runs on our sample lies between 10 and 50 Oe. This leads us to surmise that the field value $H_{2D}(T^*)$ perhaps defines an upper limit below which anomalous effects would be visible. Figure 18 schematically sketches the anticipated behaviour in temperature dependent magnetization data across such a limiting field. The data of figure 17(a) and figure 2 can be identified with the schematic plots in figures 18(a) and (b), respectively.

Figure 19 summarizes further manifestations of the hysteritic response at low fields. The magnetization curves in field values smaller than $H_{2D}(T^*)$ are not expected to intersect, they asymptotically approach each other near the superconducting transition temperature (e.g., see $M_{ZFC}(T)$ data in 1·3 Oe and 10 Oe, respectively in figure 19(a)). Figure 19(b) shows a comparison of magnetization data recorded during warm-up (after initial rapid cool-down to 10 K in a field of about 0·3 Oe) with the data recorded during slow cool-down in the same field. These data exemplify the survival of irreversible behaviour in a small field of 0·3 Oe up to the nominal T_c value.

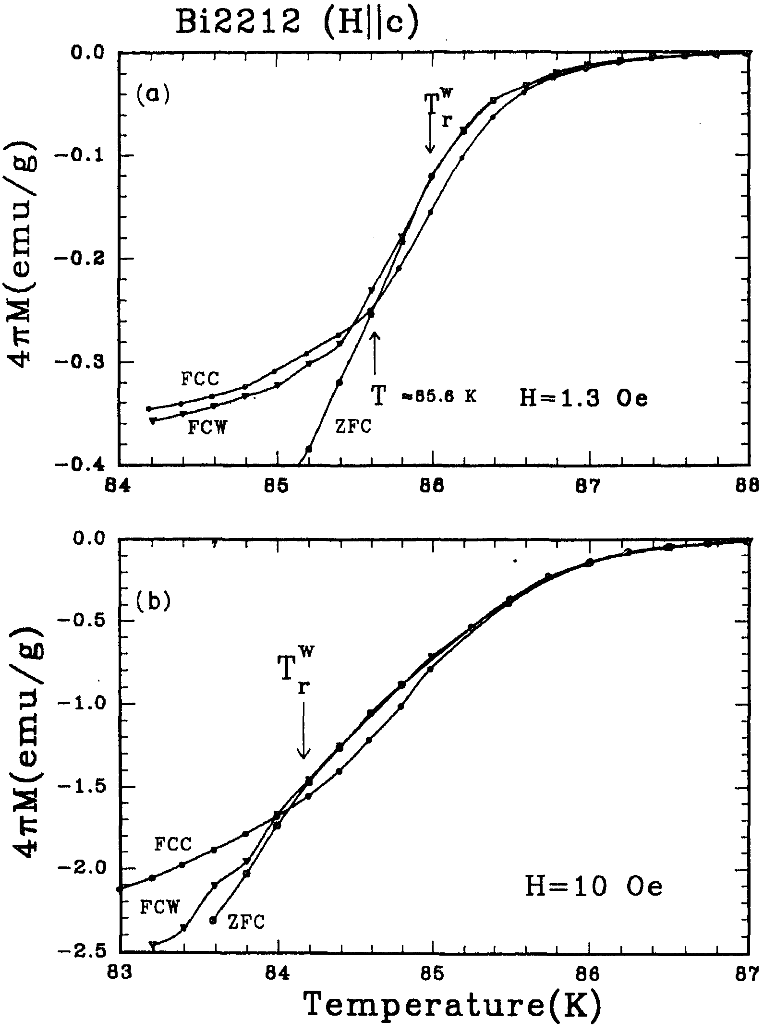

Figure 17. Temperature dependence of magnetization data in (a) $H \approx 1{\cdot}3$ Oe and (b) = 10 Oe, respectively.

3.8 *Magnetic phase diagram*

The magnetization data presented so far (for instance, see figures 10, 13 and 15) motivate us to propose revision and additions in the schematic phase diagrams drawn by Brawner *et al* [8] and Huse *et al* [1]. Our proposed schematic phase diagram near T_c is depicted in figure 20. We feel that on cooling down a specimen from higher temperature end, the superconducting fluctuations start to cause a deviation from the normal state resistivity $\rho(T)$ in the "H_{c2}" crossover region. Below this region there broadly exist three regions corresponding to response from strongly coupled 2D planes (≡ 3D superconductor), weakly coupled 2D planes (two-component response) and decoupled 2D planes. The usually determined irreversibility lines approximately demarcate the regions of reversible and irreversible response from the 3D superconductor. The H_{2D} line lies above the $H_r(T)$ line. The temperature at which

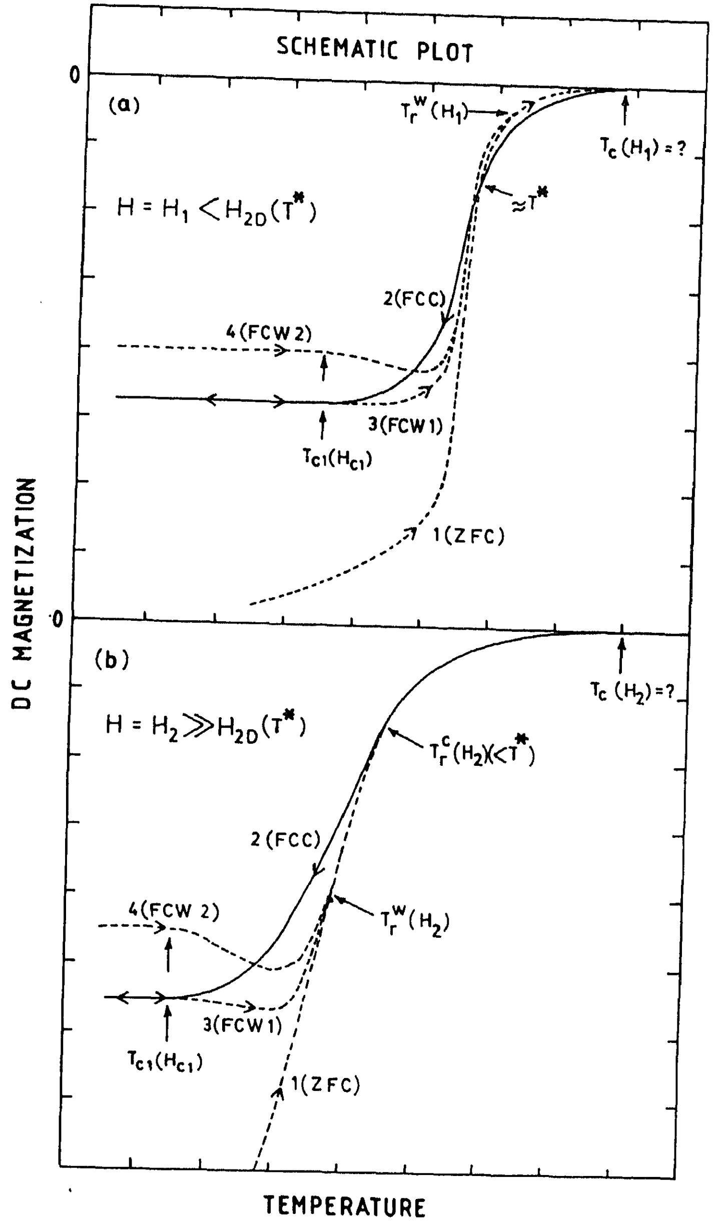

Figure 18. Schematic plot of temperature dependent magnetization data expected in (a) very small and (b) large applied fields. In (b), $T_r^c(H) > T_r^w(H)$ and no further anomalies are anticipated. In (a), $T_r^w(H) > T^*$, $T_r^c(H)$ cannot be defined and many anomalies are anticipated near T.

drastic change in the value of the slope dH_{2D}/dT (also, that of dH_{c1}/dT) occurs approximately identifies the onset of transformation from one component (3D superconductor) to two component (weakly coupled 2D planes) response. The $H_{2D}(T)$ line in the temperature interval of two component response approximately demarcates the field-temperature regions of $\rho_c = 0$ and $\rho_c \neq 0$.

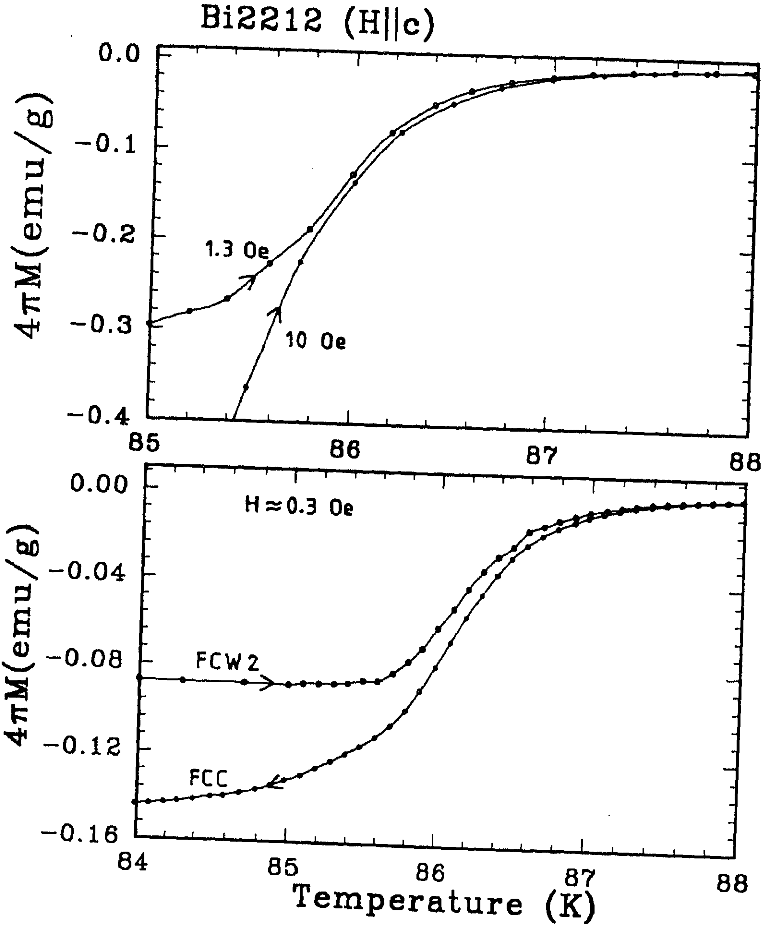

Figure 19. Temperature dependence of magnetization values near T_c in small field values. Figure 19(a) shows that warm-up magnetization curves obtained in $H = 1{\cdot}3$ Oe and 10 Oe, respectively, asymptotically meet at T_c. Figure 19(b) shows a comparison of field cool warm-up (after initial rapid cool down) and slow field cool cool-down magnetization data in the residual field of magnet ($\approx 0{\cdot}3$ Oe).

For the strongly coupled 2D planes, the $H_{2D}(T)$ line probably lies in between the $T_c^{ab}(H)$ and $T_c^c(H)$ lines. We have not extrapolated the $H_r(T)$ line across the transformation region of one component to two component response in view of the observed enhancement in the irreversibly field values due to interplay between the responses from two components. Further, the measured $H_{c1}(T)$ and $H_{2D}(T)$ in the region of 2-component response, may be taken as the lower and upper critical fields of the component describing the response from interplanar couplings.

It is also worthwhile to stress that our proposed phase diagram, in concept, is consistent with two other experimental facts about cuprate variety of HTSC, as enunciated by Geballe [47] and Chien *et al* [48], respectively. A unit cell of Bi2212 comprises of a pair of CuO_2 bilayers Josephson coupled to each other. The experimental data on BSCCO superlattice structures supports the view [47] that $\rho_{ab} = 0$ transition at about 85 K is a property of double pyramidal sequence (i.e., one CuO_2 bilayer). In $YBa_2Cu_3O_7$ system, one needs to consider at least two unit cells to

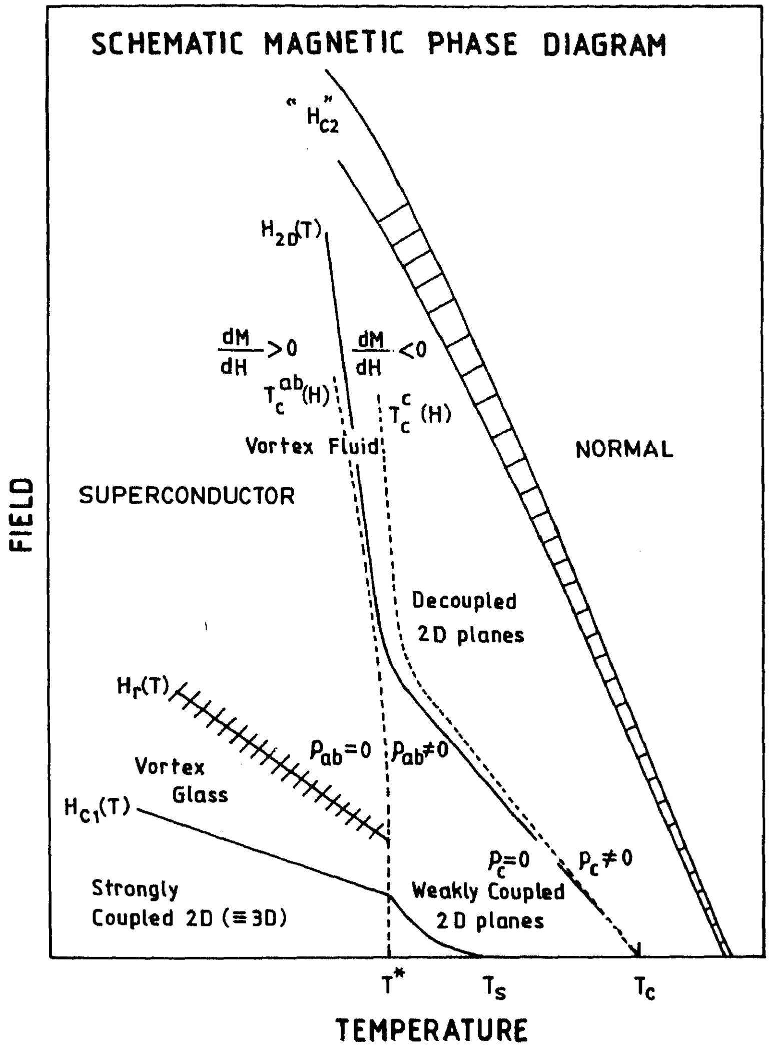

Figure 20. Schematic plot of proposed phase diagram in an anisotropic layered superconductor. For explanation of various lines, see text.

visualize the presence of a double pyramidal sequence (two CuO_2 layers separated by a Y layer). Chien *et al* [48] have reported that within the vortex liquid state of $YBa_2Cu_3O_7$ ($H \parallel c$), qualitative changes in dissipation behaviour occur across some identifiable field-temperature lines. The vortex motion correlated over a certain length scale gives way to a diffusive behaviour across a specific field-temperature line (see, H_k line in figure 4 of [48]). In our phase diagram, we expect the diffusive behaviour to occur above $T_c^c(H)$ line. The vortex motion may continue to remain correlated across $T_c^{ab}(H)$ line, somewhat analogous to the behaviour across H_0 line of Chien *et al* [48].

4. Summary

We have performed extensive isothermal and temperature dependent magnetization measurements for $H \| c$ in a high quality single crystal sample of $Bi_2Sr_2CaCu_2O_8$. The new results presented in this paper include the following:

1. Comparison of irreversibility lines (for $H \| c$) determined by different DC and AC magnetization methods and procedures in the same single crystal sample of a HTSC.
2. Identification and labelling of two component response across the dimensional crossover region and determination of $H_{2D}(T)$ line.
3. Identification of effects due to the interplay between the diamagnetic responses from two components.
4. Recognition of occurrence of qualitative changes in the irreversibility behaviour across the dimensional crossover.
5. Observation of paramagnetic Meissner effect in the temperature interval of dimensional crossover. This effect *inter alia* confirms our labelling of two component response.
6. Schematic representation of the observed anomalies near T_c in the temperature dependent magnetization data at low fields.

5. Conclusion

The modelling of highly anisotropic copper oxide superconductors as stacks of two dimensional superconducting planes Josephson coupled to each other is so appealing, that for long experimentalists have sought to provide evidences in favour of such a scenario in all sorts of magnetic and transport measurements. We feel that the results presented in this paper convincingly reaffirm the validity of Josephson coupled models. The isothermal and temperature dependent magnetization data near the superconducting to normal transition temperature comprehensively elucidate the changes that occur in the electromagnetic response over a narrow range of temperature values. The schematically sketched phase diagram in figure 20, in a sense, summarizes our present understanding of such systems. More experiments are in progress at the moment and the sketched diagram may undergo further revisions on analysis of newer results. We have refrained from making any quantitative contact with different theoretical models, including the one due to BLK [6], at this stage, as by and large no model predicts several of the key features of the scenario that appears to emerge from the results in our specimen of Bi2212.

Acknowledgements

We would like to acknowledge Dr P Chaddah (CAT, Indore) for communicating to us the confirmation of our new finidings on their single crystal sample of Bi2212. We thank Prof. T V Ramakrishnan and Prof. Deepak Kumar for fruitful discussions. We acknowledge Mr Mahesh Chandran for pointing out the simultaneous presence of DPE and DDE peaks in the data of Couach and Khoder. One of us (AKG) thanks STA of Japan for the grant of research award for foreign specialists. He also gratefully acknowledges the enviable warm hospitality of members of Electron Physics Section of Electrotechnical Laboratory, Tsukuba during the tenure of this award.

References

[1] D A Huse, M P A Fisher and D S Fisher, *Nature* (*London*) **358**, 553 (1992) and references therein
[2] K Kadowaki, *Physica* **C185–189**, 2249 (1991)
[3] P H Kes, C J van der Beek, M P Maley, M E Mchenry, D A Huse, M J Menken and A A Menovsky, *Phys. Rev. Lett.* **67**, 2283 (1991)
[4] R Kleiner, F Steinmeyer, G Kunkel and P Müller, *Phys. Rev. Lett.* **68**, 2394 (1992)
[5] S Sengupta, C Dasgupta, H R Krishnamurthy, G I Menon and T V Ramakrishnan, *Phys. Rev. Lett.* **67**, 2249 (1991)
[6] L N Bulaevskii, M Ledvij and V G Kogan, *Phys. Rev. Lett.* **68**, 3773 (1992) and references therein
[7] D Vacaru, F Zuo, H M Duan and A M Herman, *Physica* **C203**, 393 (1992)
[8] D A Brawner, A Schilling, H R Ott, R J Haug, K Ploog and K von Klitzing, *Phys. Rev. Lett.* **71**, 785 (1993)
[9] A K Grover, in *Studies of high temperature superconductors* edited by A V Narlikar (Nova Science Publishers, Inc., New York, 1993) Vol. 14
[10] Y Yamaguchi, D H Ha, F Iga and Y Nishihara, *Advances in superconductivity V* (Proc. ISS'92) edited by Y Bando and Y Yamaguchi (Springer-Verlag, 1993) p 183
[11] Ravi Kumar, A V Volkozub, P A J de Groot, S K Malik and A K Grover, *Proc. of 20th Int. Conf. Low Temp. Phys.* (Eugene, Oregon, USA, 1993), *Physica* **B** (In press)
[12] A K Grover, F Iga, Y Yamaguchi and Y Nishihara, *Phys. Rev. Lett.* (submitted)
[13] A K Grover, F Iga, Y Yamaguchi, N Aoki, K Ino and Y Nishihara, *Physica* **C220**, 353 (1994)
[14] D H Ha, K Oka, F Iga and and Y Nishihara, *Jpn. J. Appl. Phys.* **32**, L778 (1993)
[15] C V Tomy, Ravi Kumar and A K Grover, *Solid State Commun.* **80**, 117 (1991)
[16] Ravi Kumar, C V Tomy, A K Grover and S K Malik, *Applied Superconductivity* **1**, 1115 (1993)
[17] J Deak, M McElfresh, J R Clem, Z Hao, M Konczykowski, R Muenchausen, S Foltyn and R Dye, *Phys. Rev.* **B47**, 8377 (1993)
[18] O B Hyun, *Phys. Rev.* **B48**, 1244 (1993)
[19] J R Clem and Z Hao, *Phys. Rev.* **B** (In press)
[20] A K Grover, F Iga, Y Nishihara *et al* (to be published)
[21] A K Grover, S Ramakrishnan, Ravi Kumar, P L Paulose, G Chandra and P Chaddah, *Physica* **C192**, 372 (1992)
[22] S Ramakrishnan, Ravi Kumar, C V Tomy, A K Grover, P Chaddah and S K Malik, in *Magnetic susceptibility of superconductors and other spin systems*, edited by R A Hein, Thomas L Francavilla and Donald H Leibenberg (Plenum Press, New York, 1991) pp 389–404
[23] M Couach and A F Khoder, in *Magnetic susceptibility of superconductors and other spin systems*, edited by R A Hein, Thomas L Francavilla and Donald H Leibenberg (Plenum Press, New York, 1991) pp 25–48 and references therein
[24] Y Yamaguchi *et al* (to be published)
[25] A K Grover, C Radhakrishnamurty, P Chaddah, G Ravi Kumar and G V Subbarao, *Pramana – J. Phys.* **30** 569 (1988)
[26] P Chaddah, G Ravi Kumar, A K Grover, C Radhakrishnamurty and G V Subbarao, *Cryogenics* **29** 907 (1989)
[27] C Radhakrishnamurthy, A K Grover, P K Mishra, P Chaddah and G V Subbarao, *Physica* **C162–164**, 333 (1989)
[28] S Senoussi, M Oussena, M Rebault and G Collin, *Phys. Rev.* **B36**, 4003 (1987)
[29] P Chaddah, in *Studies of high temperature superconductors*, edited by A V Narlikar (Nova Science Publishers, Inc., New York, 1993) Vol. 14, and references therein
[30] S B Roy, S Kumar, A K Pradhan, P Chaddah, R Prasad and N C Soni, *J. Appl. Phys.* **73**, 1539 (1993) and *Physica* **C218**, 476 (1993)
[31] J E Evetts and B A Glowacki, *Cryogenics* **28**, 641 (1988)
[32] K A Müller, M Takashige and J G Bednorz, *Phys. Rev. Lett.* **58**, 1143 (1987)

[33] H Morita, K Watanabe, Y Murakami, Y Koyanagi, K Noto, H Fujimori and Y Muto, *Jpn. J. Appl. Phys.* **28**, L628 (1989)
[34] H Obara, H Yamasaki, Y Kimura and S Kosaka, *Appl. Phys. Lett*, **55**, 2342 (1989)
[35] S Kumar, S B Roy, P Chaddah, R Prasad and N C Soni, *Physica* **C191**, 450 (1992)
[36] S B Roy, S Kumar, P Chaddah, R Prasad and N C Soni, *Physica* **C198**, 383 (1992)
[37] Y Nishihara, A K Grover, F Iga, Y Yamaguchi, N Aoki and K Ino, *Proc. of ETL Workshop on HTSC*, Dec. 6–8, 1993 (to be published)
[38] J C Martinez, S H Brongersma, A Koshelev, B Ivlev, P H Kes, R P Griessen, D G de Groot, Z Tranavski and A A Menovsky, *Phys. Rev. Lett.* **69**, 2276 (1992)
[39] Y M Wan, S E Hebboul, D C Harris and J C Garland, *Phys. Rev. Lett*, **71**, 157 (1993)
[40] W Braunisch, N Knauf, V Kataev, S Neuhausen, A Grütz, A Kock, B Roden, D Khomskii and D Wohlleben, *Phys. Rev. Lett.* **68**, 1908 (1992)
[41] W Braunisch, N Knauf, G Bayer, A Kock, A Becker, B Freitag, A Grütz, V Kataev, S Neuhausen, B Roden, D Khomskii, D Wohlleben, J Bock and E Preisler, *Phys. Rev.* **B48**, 4030 (1993)
[42] Ch Heinzel, Th Theilig and P Zeimann, *Phys. Rev.* **B48**, 3445 (1993)
[43] A K Grover, Ravi Kumar, S K Malik and P Chaddah, *Solid State Commun.* **77**, 723 (1991)
[44] L Burlachkov, Y Yeshurun, M Konczykowski and F Holtzberg, *Phys. Rev.* **B45**, 8193 (1992)
[45] N Nakamura, G D Gu and N Koshizuka, *Phys. Rev. Lett.* **71**, 915 (1993)
[46] K Kadowaki *et al* (to be published)
[47] T H Geballe, in *Physics of high temperature superconductors*, edited by S Maekawa and H Sato (Springer-Verlag, 1992) p 339 and references therein
[48] T R Chien, T W Jing, N P Ong and Z Z Wang, *Phys. Rev. Lett.* **66**, 3075 (1991)

Post script

Isothermal magnetic hysteresis data for $H \| c$ in our specimen between 10 and 75 K (obtained since the submission of this manuscript) reveal the presence of additional two component responses at temperatures 25 K and 75 K. The magnetic response is one component like between 5 and 15 K, 35 K and 65 K, 78 K and 83 K. We now believe that in addition to intra-unit cell weak link there also exist inter-unit cell weak links having a certain heirarchy in any Bi2212 single crystal specimen. The Bi2212 single crystals are never perfectly stoichiometric and HREM pictures also reveal the presence of stacking faults as well as the intergrowth of unit cells of Bi2201 and Bi2223 in them. The inter-unit cell weak links are a material property whereas the intra-unit cell weak link is intrinsic (exists within a unit cell) and is the strongest. The breakage of intra-unit cell weak link gives rise to dimensional crossover phenomenon just below T_c, whereas the breakage of inter-unit cell weak links amount to division and further sub-division of a given crystal into aligned microcrystallites of progressively smaller dimension. The microcrystallites and the Josephson coupling across them can give rise to two component response, each of which is like a 3D type-II superconductor. In view of above scenario, it may be difficult to uniquely label the weak link responsible for negative peak effect in our figure 18 as well as for the effects described in references [4] and [45].

PRAMANA
— journal of
physics

© Printed in India

Vol. 42, No. 3,
March 1994
pp. 223–230

Self focusing of elliptic Gaussian laser beams: Saturable nonlinearity

S KONAR and A SENGUPTA
School of Energy Studies, Devi Ahilya Vishwavidyalaya, Indore 452001, India

MS received 23 August 1993; revised 15 November 1993

Abstract. An analysis of self focusing of an elliptic Gaussian laser beam, propagating through a medium with saturable nonlinearity has been presented. It has been established that stationary self trap propagation of the beam is not possible. Though stationary self trap propagation does not occur, one can define a virtual threshold power for self focusing. Above this threshold power value, but not far from it, the beam focuses; below this threshold value it defocuses. As a whole three different defocusing zones and two focusing zones have been identified. It is also shown that effective beam radius never reaches zero.

Keywords. Self focusing; saturable nonlinearity; elliptic laser beams; self trapping; virtual threshold.

PACS No. 42·65

1. Introduction

The self focusing of a laser beam has been a subject of many theoretical and experimental investigations in dielectrics as well as in plasmas [1–13], mainly because it has considerable influence on other nonlinear phenomena. Most of the theoretical investigations of self focusing of laser beams in nonlinear media have been confined to cylindrical Gaussian beams. In a few recent publications cylindrical off axis modes [10], spiral self trapping [4], elliptic Gaussian beam [5] and nonisotropic media have been considered. Particularly, in a classic paper Cornolti *et al* [5] have considered the self focusing of elliptic Gaussian laser beams in a Kerr nonlinear medium. It is pointed out that the self trapping threshold is a growing function of ellipticity, and like Gaussian beams, depending on laser power collapse of the beam width parameter takes place too.

Collapse of a laser beam is a characteristic of the medium whose intensity dependent dielectric constant is similar to Kerr-law nonlinearity. However, for any nonlinear medium there exists a maximum change in the intensity dependent dielectric constant, i.e., the intensity dependent dielectric constant saturates to a certain level; and in many cases, the optical power density required for saturation can be attained easily. The self focusing of elliptic Gaussian laser beams in such a medium has not been considered so far.

This paper presents an analysis of self focusing of elliptic Gaussian laser beams in a saturable nonlinear medium. In § 2 we obtain equations for laser fields in a lossless homogeneous saturable nonlinear medium. Numerical results and discussion are presented in § 3. A brief conclusion is given in § 4. The present theory, like many earlier ones, makes use of the paraxial and WKB approximations.

2. General equations for self focusing

Consider the propagation of an elliptic Gaussian laser beam in a homogeneous nonlinear medium along the z-direction. The electric field of the beam at $z = 0$ may be represented by

$$|E|^2_{z=0} = \frac{E_0^2}{a(0)b(0)} \exp[-\{2(x/ra(0))^2 + 2(y/rb(0))^2\}] \tag{1}$$

where $ra(0)$ and $rb(0)$ are the initial width parameter of the beam in x and y directions respectively; r is assumed to be constant throughout along the propagation direction; and a and b are variable width parameters, $a = a(0)$ and $b = b(0)$ at $z = 0$. E_0 is the constant electric field.

We choose a model for dielectric constant of the form

$$\varepsilon = \varepsilon_0 + \Phi(|E|^2) \tag{2}$$

where ε_0 and Φ are the linear and nonlinear parts of the dielectric constant ε. For saturable nonlinearity we assume Φ in the form [13]

$$\Phi = \varepsilon_s[1 - \exp(-\alpha|E|^2)] \tag{3}$$

where ε_s and α are two constants of the medium concerned. The analytic form of Φ has been chosen to satisfy two basic conditions viz., $\Phi \to \varepsilon_s \alpha |E|^2$ at low intensity and $\Phi \to \varepsilon_s$, the saturation value in the limit $\alpha|E|^2 \gg 1$.

Assuming a time harmonic dependence of the electric field, $E \sim e^{i\omega t}$, neglecting the term $\nabla(\nabla \cdot \mathbf{E})$, which is justified if $(c^2/\omega^2)|(1/\varepsilon)\nabla^2 \ln \varepsilon| \ll 1$, the time independent scalar wave equation takes the form

$$\nabla^2 E + \frac{\omega^2}{c^2} \varepsilon E = 0. \tag{4}$$

Assuming $E = A(x, y, z)\exp(-ikz)$, and employing the WKB approximation, (4) yields

$$-2ik\frac{\partial A}{\partial z} + \nabla_\perp^2 A + k^2 \frac{\Phi(AA^*)}{\varepsilon_0} A = 0 \tag{5}$$

where $k = (\omega/c)\sqrt{\varepsilon_0}$ and $\nabla_\perp^2 = (\partial^2/\partial x^2) + (\partial^2/\partial y^2)$. Putting $A = A_0 \exp(-ikS(x, y, z))$ in (5) and separating real and imaginary parts one obtains

$$2\frac{\partial S}{\partial z} + \left(\frac{\partial S}{\partial x}\right)^2 + \left(\frac{\partial S}{\partial y}\right)^2 = \frac{1}{k^2 A_0} \nabla_\perp^2 A_0 + \frac{\Phi}{\varepsilon_0}(\Phi), \tag{6a}$$

$$\frac{\partial A_0^2}{\partial z} + \frac{\partial S}{\partial x}\frac{\partial A_0^2}{\partial x} + \frac{\partial S}{\partial y}\frac{\partial A_0^2}{\partial y} + A_0^2 \nabla_\perp^2 S = 0. \tag{6b}$$

The solutions of eqs (6a–b) can be written as [1, 3]

$$A_0^2 = \frac{E_0^2}{(ab)} \exp[-\{2(x/ra)^2 + 2(y/rb)^2\}], \tag{7a}$$

$$S=\frac{x^2}{2}\beta_1+\frac{y^2}{2}\beta_2+\eta(z), \tag{7b}$$

$$\beta_1=\frac{1}{a}\frac{\mathrm{d}a}{\mathrm{d}z},\ \beta_2=\frac{1}{b}\frac{\mathrm{d}b}{\mathrm{d}z}. \tag{7c}$$

Substituting for A_0, S in (6a), using the paraxial ray approximation, separately equating coefficients of x^2 and y^2 in both sides of the resulting equation and substituting for β_1, β_2 one obtains

$$M\frac{\mathrm{d}^2a}{\mathrm{d}\xi^2}=\frac{1}{a^3}-\frac{gpM^{1/2}\exp(-p/ab)}{a^2b} \tag{8a}$$

$$M\frac{\mathrm{d}^2b}{\mathrm{d}\xi^2}=\frac{1}{b^3}-\frac{gpM^{1/2}\exp(-p/ab)}{b^2a} \tag{8b}$$

where $g=(\varepsilon_s/\varepsilon_0)$, $p=\alpha E_0^2$, $M=((1/2)(\omega^2/c^2)r^2\varepsilon_0)^2$ and $\xi=kz$. Equations (8a, b) can now be used to study self focusing of the beam in the nonlinear medium.

3. Results and discussion

Case a: Small nonlinearity

Here the self focusing in a Kerr law medium is discussed briefly [5]. When $\alpha|E|^2\ll 1$, (2) reduces to $\varepsilon=\varepsilon_0+\varepsilon_s\alpha|E|^2$; i.e., the medium is a Kerr law medium. For such a medium equations corresponding to (3a, b) can easily be obtained as

$$M\frac{\mathrm{d}^2a}{\mathrm{d}\xi^2}=\frac{1}{a^3}-\frac{gpM^{1/2}}{a^2b}, \tag{9a}$$

$$M\frac{\mathrm{d}^2b}{\mathrm{d}\xi^2}=\frac{1}{b^3}-\frac{gpM^{1/2}}{b^2a}. \tag{9b}$$

It is obvious that eqs (9a, b) have the same form of Newtonian equation of motion of a particle of mass M in a potential well $V(a,b)$ which does not depend on ξ explicitly. The potential can easily be found as

$$V(a,b)=\frac{1}{2a^2}+\frac{1}{2b^2}-\frac{gpM^{1/2}}{ab}. \tag{10}$$

The energy H_K of the system is a constant of motion and can be expressed as

$$H_K=\frac{M}{2}(\dot{a}^2+\dot{b}^2)+\frac{1}{2a^2}+\frac{1}{2b^2}-\frac{gpM^{1/2}}{ab}=\text{constant} \tag{11}$$

where dot over a and b represents derivative with respect to ξ and the subscript K is used to represent Kerr nonlinear medium. It can easily be shown that

$$\frac{\mathrm{d}^2\rho^2}{\mathrm{d}\xi^2}=\frac{4H_K}{M} \tag{12}$$

where $\rho = (a^2 + b^2)^{1/2}$ is the effective beam radius. Equation (12) implies

$$\rho^2 = \frac{2H_K}{M}\xi^2 + 2(a(0)\dot{a}(0) + b(0)\dot{b}(0))\xi + \rho^2|_{\xi=0}. \tag{13}$$

Equation (13) determines the overall behaviour of the beam. For an initially parallel beam, initial conditions are $\dot{a}(0) = \dot{b}(0) = 0$. The value of H_K completely determines the behaviour of the beam as it propagates through the medium. When $H_K > 0$, the beam expands; for $H_K < 0$, the beam collapses and it occurs at a distance $\xi = \xi_c = (-\rho^2|_{\xi=0}/2H_K)^{1/2}M^{1/2}$. When $H_K = 0$, the beam neither expands nor collapses but propagates as a self trapped beam.

Case b: Saturating nonlinearity

The situation is somewhat different in the case of a saturable nonlinear medium. For such cases, from (8a, b) one can easily obtain

$$\frac{d^2\rho^2}{d\xi^2} = \frac{4H_S}{M} - F(ab) \tag{14}$$

where

$$H_S = \frac{M}{2}(\dot{a}^2 + \dot{b}^2) + \frac{1}{2a^2} + \frac{1}{2b^2} + gM^{1/2}\exp(-p/ab) = \text{constant} \tag{15}$$

and

$$F(ab) = \frac{4g}{M^{1/2}}[1 + p/ab]\exp(-p/ab)$$

For initially parallel beam $\dot{a}(0) = \dot{b}(0) = 0$; hence $\left.\frac{d\rho^2}{d\xi}\right|_{\xi=0} = 0$. A necessary condition for stationary self trapping is $\left.\frac{d^2\rho^2}{d\xi^2}\right|_{\xi=0} = 0$, which implies

$$\frac{1}{2}\left(\frac{1}{a^2(0)} + \frac{1}{b^2(0)}\right) = \frac{gP_{cr}M^{1/2}}{a(0)b(0)}\exp(-P_{cr}/a(0)b(0)) \tag{16}$$

where P_{cr} is the value of p when $\left.\frac{d^2\rho^2}{d\xi^2}\right|_{\xi=0} = 0$. For an initially parallel Gaussian beam it can easily be shown that the above condition is also the sufficient condition for stationary self trapping. For stationary self trapping to take place, in addition to $\left.\frac{d\rho^2}{d\xi}\right|_{\xi=0} = 0$ and $\left.\frac{d^2\rho^2}{d\xi^2}\right|_{\xi=0} = 0$ all other higher order derivatives of ρ^2 should also vanish at $\xi = 0$. It is easy to show from (14) that, though a third order derivative of ρ^2 readily vanishes at $\xi = 0$, a vanishing fourth order derivative at $\xi = 0$ require $a(0) = b(0)$, i.e., the initial beam should be Gaussian. Hence, stationary self trapped propagation of an initially parallel elliptic Gaussian laser beam in a saturable nonlinear medium is forbidden. This is one of the main contributions of this paper.

It is very difficult to obtain analytical solutions of eqs (8a, b) and thereby to predict the development of the beam as it propagates. One may therefore resort to numerical computation to study beam dynamics. Though it is not possible to stationary self trap an elliptic Gaussian laser beam in a saturable nonlinear medium, numerical analysis of eqs (8a, b) may tempt one to define a virtual threshold. This is done in the following way. Equation (16) has two roots, P_{cr1} and $P_{cr2}(p_{cr1} < p_{cr2})$. For a Gaussian beam (i.e., $a(0) = b(0)$) these two roots are the threshold values of p for self trapping; for $p < p_{cr1}$ or $p > p_{cr2}$, the beam defocuses, and for $p_{cr1} < p < p_{cr2}$, the beam focuses. For an elliptic Gaussian beam one may notice numerically that, when $p < p_{cr1}$, the beam defocuses (see figure 1) and when $p = p_{cr1}$ or slightly greater than p_{cr1}, the beam focuses (see figure 2). Therefore, one can argue that $p = p_{cr1}$ can be treated as a virtual threshold though stationary self trapping does not occur at this value. For example, for $a(0) = 2{\cdot}0$, $b(0) = 0{\cdot}5$, $g = 0{\cdot}1$ and $M^{1/2} = 501$, value of this virtual threshold turns out to be $p = 0{\cdot}044$. It must be pointed out that, though on either side of p_{cr1}, the beam behaves differently, one does not notice such type of behaviour on either side of p_{cr2}; hence, p_{cr2} cannot be treated as a virtual threshold.

However, a comprehensive numerical study shows that p_{cr1} is not the only threshold value of p. For instance, if one increases the value of p further from p_{cr1} one would notice that for $p = 1{\cdot}0$, the beam defocuses. This is shown in figure 3(a, b). This clearly suggests a defocusing zone near $p = 1{\cdot}0$. Similarly, figure 4 suggests a focusing zone

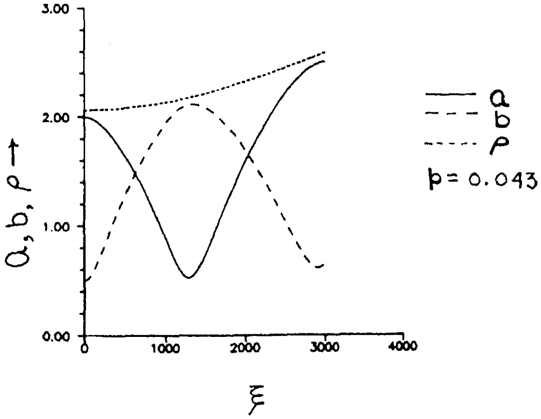

Figure 1. Variation of a, b and ρ with ξ for $p = 0{\cdot}043$, $g = 0{\cdot}1$, $M^{1/2} = 501$, $a(0) = 2{\cdot}0$, $b(0) = 0{\cdot}5$. $p_{cr1} = 0{\cdot}044$.

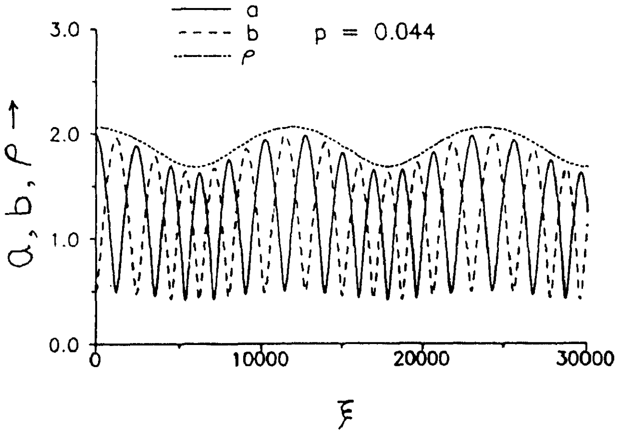

Figure 2. Variation of a, b and ρ with ξ for $p = 0{\cdot}044$, $g = 0{\cdot}1$, $M^{1/2} = 501$, $a(0) = 2{\cdot}0$, $b(0) = 0{\cdot}5$. $p_{cr1} = 0{\cdot}044$.

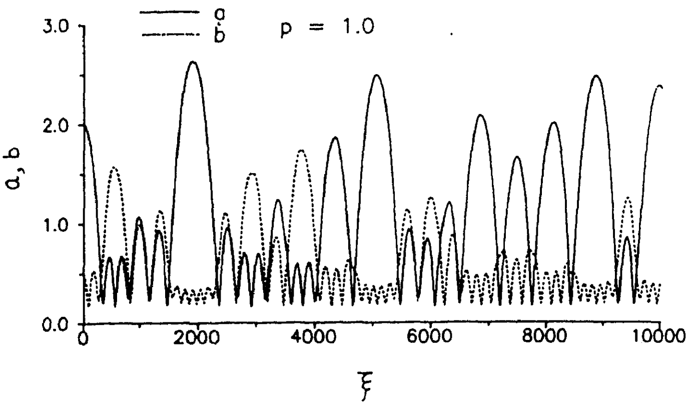

Figure 3a. Variation of a and b with ξ for $p = 1{\cdot}0$, $g = 0{\cdot}1$, $M^{1/2} = 501$, $a(0) = 2{\cdot}0$, $b(0) = 0{\cdot}5$.

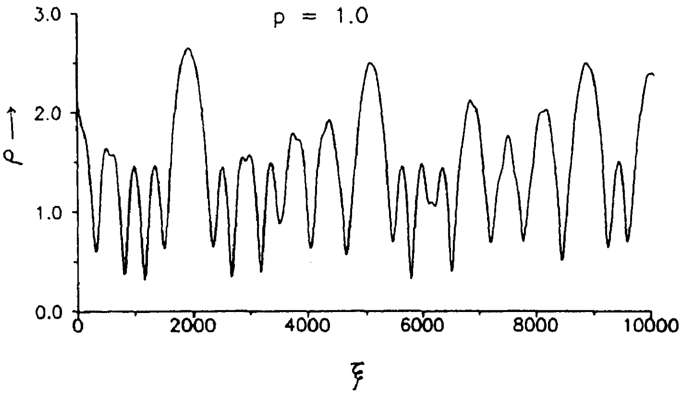

Figure 3b. Variation of ρ with ξ for $p = 1{\cdot}0$, $g = 0{\cdot}1$, $M^{1/2} = 501$, $a(0) = 2{\cdot}0$, $b(0) = 0{\cdot}5$.

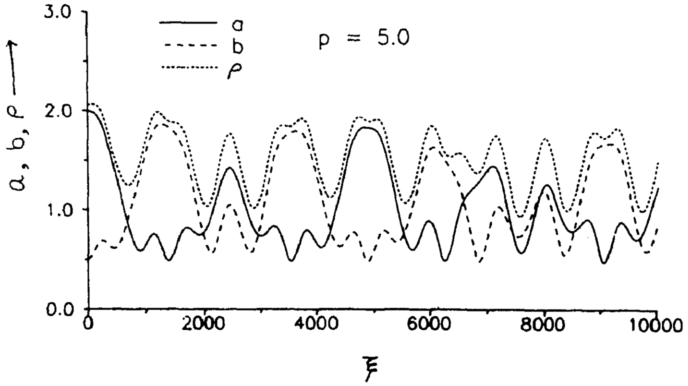

Figure 4. Variation of a, b and ρ with ξ for $p = 5{\cdot}0$, $g = 0{\cdot}1$, $M^{1/2} = 501$, $a(0) = 2{\cdot}0$, $b(0) = 0{\cdot}5$.

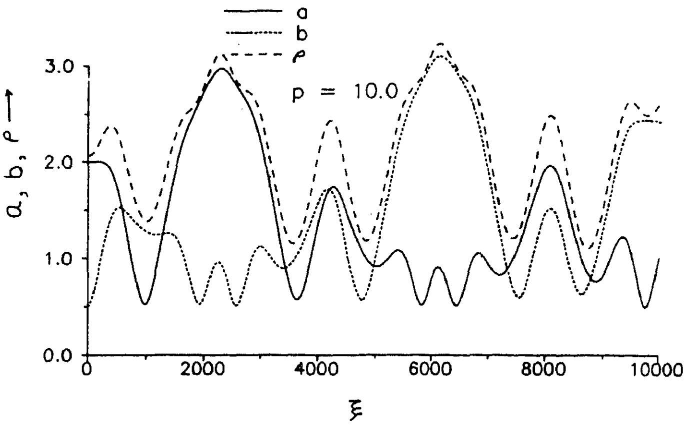

Figure 5. Variation of a, b and ρ with ξ for $p = 10{\cdot}0$, $g = 0{\cdot}1$, $M^{1/2} = 501$, $a(0) = 2{\cdot}0$, $b(0) = 0{\cdot}5$.

in the neighbourhood $p = 5{\cdot}0$, while figure 5 suggests another defocusing zone in the neighbourhood of $p = 10$. For further increase of p, the beam always defocuses. Thus, it is clear that, though a definite self trapped threshold does not exist for elliptic Gaussian beam, three power regimes exist where the beam defocuses, while in two other power regimes the beam focuses. This is in contrast to the behaviour of a Gaussian beam for which only three power regimes exist; in two of these regimes the beam defocuses, while in another one, the beam focuses. Another point to be noted is that unlike Gaussian beam, where, in the focusing regime, the beam parameter always oscillates between a minimum and a maximum value and the oscillation repeats maintaining constant values of these maxima and minimas as the beam propagates; there are, however, two basic differences in the present case, (i) oscillations of beam parameters are highly irregular, (ii) there exists several maxima and minima of different values. It must be pointed out that, whenever the beam focuses or defocuses its effective value never reaches zero. This property is similar to that of a Gaussian beam.

4. Conclusion

To conclude one may say that, an elliptic Gaussian laser beam cannot be stationary self trapped in a saturable nonlinear medium. Though stationary self trapping does not occur, one can define a virtual threshold below which the beam defocuses and above this threshold, but not far from it, the beam focuses. As a whole three different defocusing zones and two focusing zones have been identified. Whenever the beam focuses or defocuses the beam width parameter oscillates asymmetrically without repetition. Moreover, the effective beam radius never reaches zero.

The present theory should find its application in many nonlinear optical processes like stimulated Raman scattering, stimulated Brillouin scattering, two photon absorption, optical breakdown of gases, etc. where self focusing has strong influence on these processes. It is also applicable to space communication, atmospheric propagation of laser beams, laser fusion and propagation of laser beams in nonlinear fibers. It should find application in microwave heating of tokamak plasmas wherein the intensity distribution along the wavefront of the externally launched microwave becomes elliptic Gaussian after entering inside plasma.

Acknowledgement

We thank the referee for valuable suggestions.

References

[1] S A Akhmanov, A P Sukhorukov and R V Khokhlov, *Sov. Phys. Usp.* **10**, 609 (1968)
[2] M S Sodha, A K Ghatak and V K Tripathi, *Self focusing of laser beams in dielectrics, plasmas and semiconductors*, (Tata McGraw Hill, New Delhi, 1974)
[3] M S Sodha, A K Ghatak and V K Tripathi, *Progress in optics*, edited by E Wolf (North Holland, Amsterdam 1976) **Vol. XIII**, p. 171
[4] V I Kruglov and R A Vlasov, *Phys. Lett.* **A111**, 401 (1985)
[5] F Cornolti, M Lucchesi and B Zambon, *Opt. Commun.* **75**, 129 (1990)
[6] H Hora, *Z. Phys.* **226**, 156 (1969)
[7] P K Kaw, G Schmidt and P Wilcox, *Phys. Fluids* **16**, 1522 (1973)
[8] E L Kane and H Hora, *Laser interaction and related plasma phenomena*, edited by H J Schwartz and H Hora, (Plenum, 1977) **Vol. 4B**, 913
[9] G Schmidt and W Horton, *Comments on Plasma Phys. Controlled Fusion* **9**, 85 (1985)
[10] R R Jones, W C Mead, S V Coggeshal, C H Aldrich, L Norton, G D Pollak and J M Wallace, *Phys. Fluids* **31**, 1249 (1988)
[11] D P Garuchava, N L Tsintsadze and D D T Tskhakaya, *Proceedings of the 1989 International Conference in Plasma Physics* edited by A Sen and P K Kaw, (Indian Academy of Sciences, 1991) p. 329–348
[12] M S Sodha, S Konar and K P Maheshwari, *J. Plasma Phys.* **48**, 107 (1992)
[13] Yijiang Chen, *Opt. Lett.* **16**, 4 (1991)

PRAMANA
— journal of
physics

© Printed in India

Vol. 42, No. 3,
March 1994
pp. 231–237

High resolution optogalvanic spectrum of N_2-rotational structure of (11, 7) band in the first positive system

P R SASI KUMAR, S S HARILAL, V P N NAMPOORI and C P G VALLABHAN
Laser Division, Department of Physics, Cochin University of Science and Technology, Cochin 682 022, India

MS received 10 August 1993; revised 20 November 1993

Abstract. High resolution optogalvanic spectrum of the (11, 7) band in the first positive system of nitrogen molecule has been recorded from 17179 to 17376 cm^{-1}. Assignment of 432 rotational lines belonging to the 27 branches of this band has been carried out.

Keywords. Optogalvanic spectroscopy; nitrogen molecule

PACS Nos **82·80; 33·10**

1. Introduction

Optogalvanic spectroscopy (OGS) using tunable lasers has proven to be a highly useful and sensitive method for detecting transitions of excited states of atoms and molecules [1, 2]. In OGS, when the incident laser radiation is resonant with a transition of some species present in the gaseous discharge, a change in impedance of the plasma can occur. This change in impedance of the discharge is monitored as a function of the irradiating laser wavelength. Such laser-induced impedance changes manifest as current changes and can be detected as a signal voltage across a suitable ballast resistance connected in series with the discharge cell.

First positive system ($B^3\Pi_g$–$A^3\Sigma_u^+$) of nitrogen molecule is the most prominent band system and has been the subject of many detailed investigations [3, 4]. OGS has been successfully applied to investigate transitions of N_2 with low as well as high resolution techniques. OG spectrum of the first positive system of nitrogen molecule in the wavelength region of 560–600 nm under low resolution has been studied by many researchers [2, 5]. Certain results of the investigations on rotational structure of various band systems of N_2 by using this technique have also been reported [6–8]. This paper reports the recording of well resolved rotational lines in the 17179–17376 cm^{-1} region of the (11, 7) band of the $B^3\Pi_g$–$A^3\Sigma_u^+$ system using high resolution optogalvanic spectroscopy.

2. Experimental

The experimental set up employed to record Doppler-limited high resolution OG spectrum is reported earlier [6]. In brief, a positive column N_2 discharge was maintained at a current of 2·8($\pm$0·1) mA and a pressure of 0·8 mbar. Modulated beam from a frequency stabilized single mode ring dye laser (Spectra Physic 380D), at about 225($\pm$15) mW power, was axially passed through the cell without allowing to

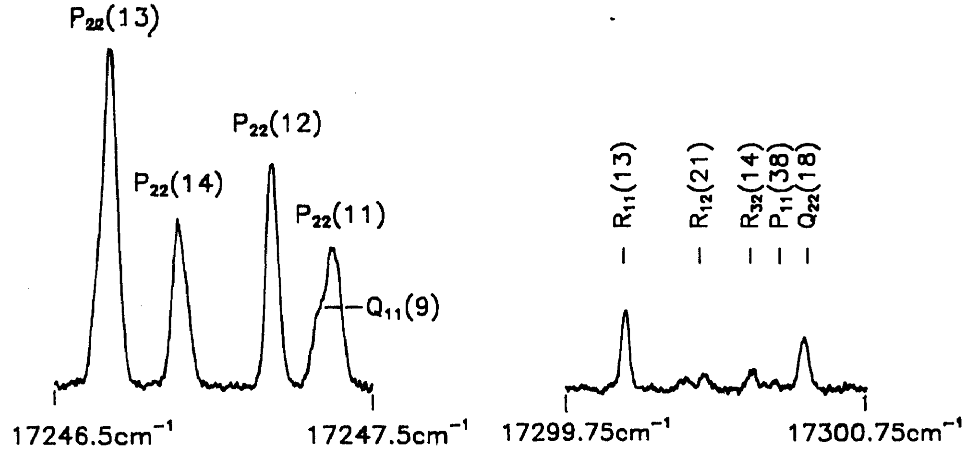

Figure 1. High resolution OG spectrum of some main and satellite lines.

fall on the electrodes. The laser was scanned in steps of 30 GHz, and the OG signal generated was detected using a lock-in amplifier which is interfaced with a computer for data acquisition. Figure 1 shows such a spectrum obtained in a single scan. Effect of variation in intensity of the dye laser on scanning was eliminated by normalizing the OG signal intensity with the photo diode output of the dye laser. The wavelength was measured using a commercial wave meter and the frequency of the measured lines is accurate to $\pm 0{\cdot}06\,\mathrm{cm}^{-1}$.

3. Analysis of the OG spectrum

The digitized OG spectrum, which is obtained by joining a number of 30 GHz spectra, and the Fortrat parabola of all branches are shown in figure 2. The first positive system of nitrogen molecule, which corresponds to the transition $B^3\Pi_g - A^3\Sigma_u^+$, consists of three subsystems namely $^3\Pi_0(F_1) - A^3\Sigma_u^+$, $^3\Pi_1(F_2) - A^3\Sigma_u^+$ and $^3\Pi_2(F_3) - A^3\Sigma_u^+$. These transitions are composed of 27 branches with three main and six satellite branches in each of the subsystems. Details of the energy level diagram and the rotational analysis are discussed in literature [9]. About 648 rotational lines have been observed and 432 of these have been identified as members of the (11, 7) band belonging to all of the 27 branches of the $B^3\Pi_g - A^3\Sigma_u^+$ system. These are listed in table 1. A few transitions belonging to the (12, 8) band are also observed in this region. The correctness of the J number assignment of rotational line is tested by a number of standard combination relations [9].

In conclusion, optogalvanic spectrum of (11, 7) band of the $B^3\Pi_g - A^3\Sigma_u^+$ system of N_2 is recorded and J values of rotational lines were assigned in the spectral region from 17179 to $17376\,\mathrm{cm}^{-1}$.

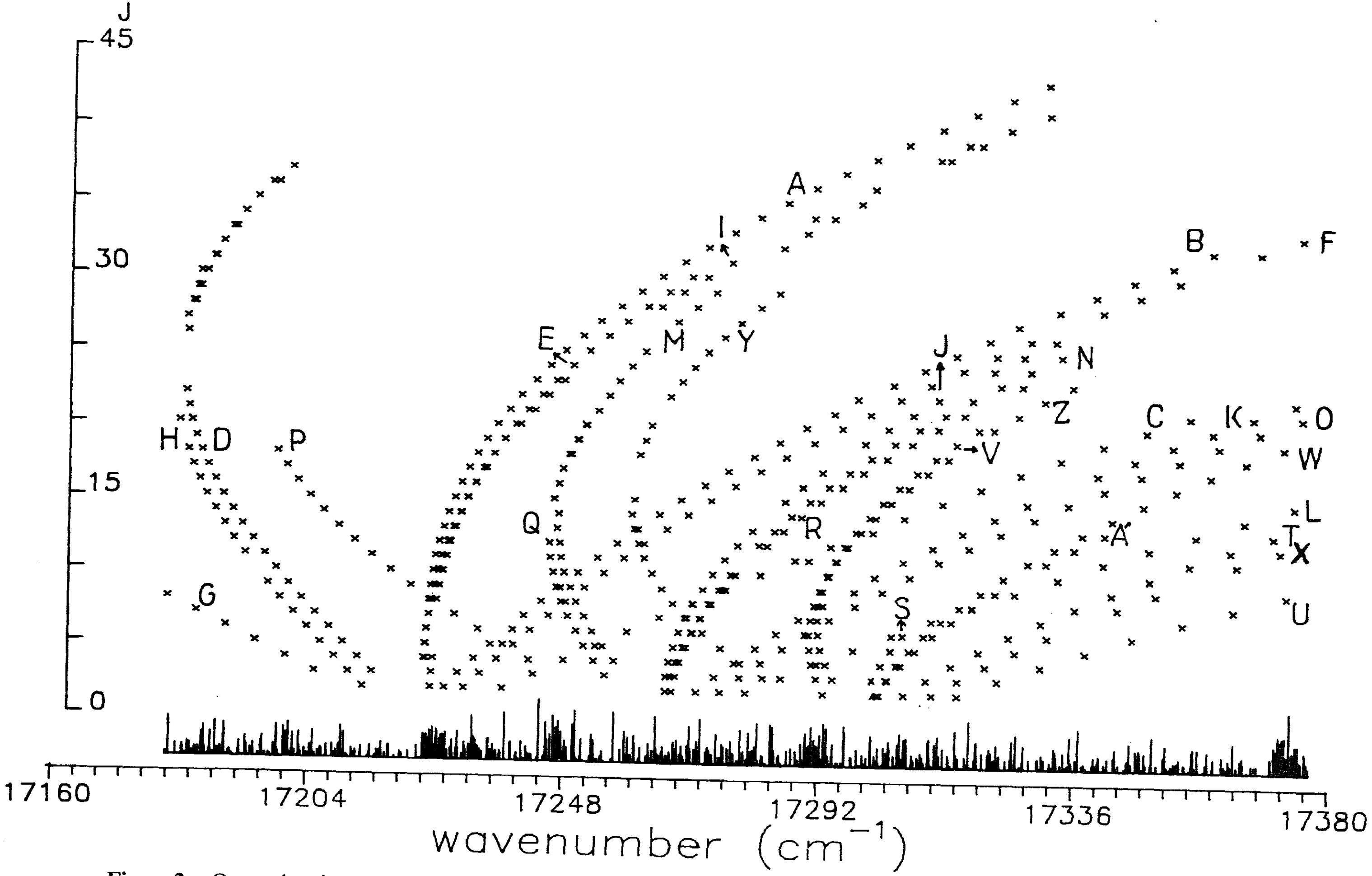

Figure 2. Optogalvanic spectrum along with Fortrat diagram of the (11, 7) band in the $B^3\Pi_g - A^3\Sigma_u^+$ transition of N_2 from 17179 to 17376 cm^{-1}.
(27 branches namely $P_{11}, Q_{11}, \ldots Q_{33}$ and R_{33} are indicated as by A, B, … Z and A′ respectively.)

Table 1. Identification of the OG resonances with the rotational transitions of the (11, 7) band of N_2: $B^3\Pi_g$–$A^3\Sigma_u^+$ system.

J	P_{11}	Q_{11}	R_{11}
2		17227·64	17237·57
3		17229·97	17242·95
4	17224·25	17232·65	17248·07
5	17224·32	17235·50	17253·48
6	17224·47	17239·29	17258·96
7		17241·17	17264·50
8	17224·86	17244·18	17270·15
9	17225·14	17247·34	17275·85
10	17225·59	17250·40	17281·72
11	17225·89	17253·66	17287·63
12	17226·52	17257·06	17293·72
13	17227·32	17260·56	17299·96
14	17228·09	17264·27	17306·33
15	17229·20	17267·98	17312·89
16	17230·24	17271·98	17319·50
17	17231·51	17276·03	17326·32
18	17232·90	17280·31	17333·26
19	17234·48	17284·72	17340·44
20	17236·31	17289·32	17347·84
21	17238·27	17294·02	17355·24
22	17240·35	17298·02	
23	17242·74	17304·11	
24	17245·19	17309·48	
25	17247·78	17314·93	
26	17250·71	17320·58	
27	17253·66	17325·53	
28	17257·06	17332·47	
29	17260·56	17338·72	
30	17264·10	17345·16	
31	17267·93	17351·77	
32	17271·98	17358·62	
33	17276·40		
34	17280·76		
35	17285·38		
36	17290·18		
37	17295·25		
38	17300·49		
39	17305·99		
40	17311·77		
41	17317·62		
42	17323·82		
43	17330·05		

J	P_{12}	Q_{12}	R_{12}
2		17225·24	17230·98
3	17215·13	17225·38	17233·72
4	17212·63	17225·59	17236·59
5	17210·08		17239·41
6	17207·66		17242·27
7	17205·24		17245·38
8	17202·94	17226·19	17248·36
9	17200·67	17226·62	17251·49
10	17198·55	17227·19	17254·86
11	17196·52	17227·78	17258·24
12	17194·58	17228·39	17261·70
13	17192·60	17229·25	17265·57
14	17191·00	17230·24	17269·21
15	17189·34	17231·36	17273·13
16	17187·92	17232·65	17277·31
17	17186·64	17234·10	17281·51
18	17185·49	17235·74	17285·91
19	17184·53	17237·50	17290·66
20	17183·76	17239·41	17295·45
21	17183·19	17241·51	17300·23
22	17182·74	17243·93	17305·41
23		17246·29	17310·60
24		17249·07	17316·13
25		17251·85	17321·88
26	17182·85	17255·08	17327·68
27		17258·24	
28	17184·04	17261·70	17339·96
29	17185·00	17265·38	17346·25
30	17186·08	17269·21	17352·97
31	17187·33		
32	17188·86		17366·89
33	17190·47		17374·03
34	17192·49		
35	17194·58		
36	17197·09		
37	17200·42		

J	P_{13}	Q_{13}	R_{13}
2		17213·55	
3	17205·24	17211·08	
4	17200·21	17208·60	17224·01
5	17195·05	17206·20	17224·25

J	P_{21}	Q_{21}	R_{21}
2		17271·00	17279·47
3	17265·78	17274·08	17285·51
4	17266·16	17277·41	17291·55
5	17266·95	17281·00	17297·90

Continued

Table 1. *Continued*

J	P_{13}	Q_{13}	R_{13}
6	17189·92	17203·83	17224·47
7	17184·83	17201·52	17224·86
8	17179·85	17199·23	17225·24
9		17197·09	17225·89
10			17226·52
11		17193·13	17227·09
12		17191·22	17228·09
13		17189·59	17229·02
14		17187·99	17230·18
15		17186·48	17231·36
16		17185·20	17232·65
17		17184·12	17234·48
18		17183·19	
19			
20		17181·65	17240·22
21			17242·58
22			17244·99
23			17247·57
24			
25			
26			
27		17182·74	
28		17183·70	17264·05
29		17184·53	17267·79
30		17185·00	17271·88
31		17187·47	17276·03
32			
33		17191·00	
34			17290·01
35			
36		17198·14	17300·39
37			
38			17311·49
39			17316·45
40			17323·56

J	P_{21}	Q_{21}	R_{21}
6	17267·79	17284·59	17304·46
7	17268·88	17288·43	17311·27
8	17270·30	17292·55	17318·26
9	17271·88	17297·90	17325·53
10	17273·58	17301·40	17332·97
11	17275·59	17306·23	17340·69
12	17277·76	17311·27	17348·54
13	17280·23	17316·45	17356·63
14		17321·88	17364·98
15	17285·82	17327·55	17373·52
16	17288·79		
17	17292·17	17339·56	
18		17345·91	
19	17299·43	17352·42	
20	17303·39	17359·20	
21	17307·58	17366·17	
22	17311·97	17373·39	
23			
24	17321·50		
25	17326·59		
26	17331·98		

J	P_{22}	Q_{22}	R_{22}
2		17266·75	17275·06
3		17267·31	17278·41
4	17256·74	17267·98	17281·89
5	17254·73	17269·08	17285·68
6	17252·95	17270·15	17289·52
7	17251·49	17271·46	17293·68
8	17250·13	17272·96	17298·09
9	17249·07	17274·73	17302·67
10	17248·03	17276·74	17307·42
11	17247·39		17312·41
12	17247·19	17281·40	17317·58

J	P_{23}	Q_{23}	R_{23}
2			17265·68
3		17255·22	17266·54
4	17242·05	17253·24	17267·41
5	17237·57	17251·49	17268·59
6	17233·31	17250·13	17270·01
7	17229·25	17248·68	17271·60
8	17225·38	17247·57	17273·41
9	17221·71	17246·69	17275·30
10	17218·23	17246·10	17277·57
11	17214·93	17245·54	17279·99
12	17211·99	17245·38	17282·80

Continued

Table 1. *Continued*

J	P_{22}	Q_{22}	R_{22}
13	17246·69	17284·08	17323·06
14	17246·89	17286·92	17328·73
15		17290·11	17334·62
16		17293·30	17340·73
17		17296·83	17347·07
18	17248·99	17300·59	17353·61
19	17250·01	17304·56	17360·34
20	17251·43	17308·75	17367·37
21		17313·17	17374·56
22		17317·80	
23	17256·98	17322·65	
24	17259·14	17327·75	
25	17261·50	17333·05	
26			
27	17266·95		
28	17270·15		
29	17273·41		
30			
31			
32	17284·83		
33	17288·79		
34	17293·40		
35	17298·02		
36			
37			
38	17313·17		
39	17318·66		
40			
41	17330·29		

J	P_{23}	Q_{23}	R_{23}
13	17209·22		17285·59
14	17206·59		17288·61
15	17204·26	17246·10	17291·98
16	17202·11	17246·89	17295·62
17	17200·21	17247·57	17299·21
18	17198·55	17248·68	17303·21
19		17250·13	17307·49
20		17251·49	17311·97
21		17253·48	17316·45
22		17255·35	
23			17326·38

J	P_{31}	Q_{31}	R_{31}
2		17306·67	17315·91
3	17301·31	17310·51	17322·77
4	17302·58	17314·72	17330·10
5	17304·25	17319·50	17337·82
6	17306·33	17324·66	17345·93
7		17330·10	17354·43
8		17335·98	17363·23
9		17342·16	17372·35
10		17348·71	
11		17355·52	
12		17362·59	
13		17369·98	

J	P_{32}	Q_{32}	R_{32}
2		17302·31	17311·49
3	17294·39	17303·60	17315·91
4	17293·08	17305·32	17320·62
5	17292·17	17307·49	17325·74
6	17291·81	17309·99	17331·28
7	17291·69	17312·89	
8	17291·81	17316·13	17343·28
9	17292·45	17319·67	17349·80
10	17293·50	17323·56	
11	17294·64	17327·75	17363·75
12	17296·22	17332·27	17371·17
13	17298·09	17337·10	
14	17300·39	17342·16	
15	17302·67	17347·50	
16	17305·41	17353·12	
17	17308·47	17359·01	
18	17311·71	17365·11	
19	17315·19	17371·56	
20	17318·99		

Table 1. *Continued*

J	P_{33}	Q_{33}	R_{33}
2		17292·76	17301·99
3	17282·33	17291·55	17303·79
4	17278·41	17290·66	17305·97
5	17275·06	17290·35	17308·47
6	17271·88	17290·18	17311·49
7	17269·21	17290·45	17314·72
8	17266·82	17291·08	17318·26
9	17264·82	17291·98	17322·15
10	17263·13	17293·30	
11	17261·70	17294·80	17330·89
12	17260·73	17296·71	17335·69
13	17260·00	17298·93	17340·90
14	17259·50	17301·40	
15	17260·00	17304·04	
16		17307·07	
17		17310·31	
18	17260·73	17313·85	
19	17261·70		
20	17262·74	17321·59	
21		17325·80	
22	17265·88	17330·29	
23	17267·79	17335·03	
24	17269·93		
25	17272·23		
26	17274·97		
27	17277·76		
28	17281·00		
29	17284·22		

Acknowledgement

Authors are thankful to the Department of Science and Technology (India), for financial assistance. One of the authors (PRS), is grateful to University Grants Commission for research fellowship.

References

[1] R B Green, R A Keller, G G Luther, P K Schenck and J C Travis, *Appl. Phys. Lett.* **29**, 727 (1976)
[2] D Feldman, *Opt. Commun.* **29**, 67 (1979)
[3] A Lofthus and P H Krupenie, *J. Phys. Chem. Ref. Data* **6**, 113 (1977)
[4] F Roux, F Michaud and J Verges, *J. Mol. Spectrosc.* **97**, 253 (1983)
[5] G Ullas and S B Rai, *Pramana – J. Phys.* **36**, 647 (1991)
[6] P R Sasi Kumar, B Ambadi, V P N Nampoori and C P G Vallabhan *Pramana – J. Phys.* **40**, 113 (1993)
[7] T Suzuki and M Kakimoto, *J. Mol. Spectrosc.* **93**, 423 (1982)
[8] K Miyazaki, H Scheingraber and C R Vidal, *Phys. Rev. Lett.* **50**, 1046 (1983)
[9] G Herzberg, *Spectra of diatomic molecules* (D Van Nostrand, New York, 1961)

PRAMANA
— journal of
physics

© Printed in India

Vol. 42, No. 3,
March 1994
pp. 239–243

New band system of YbI molecule

K N UTTAM and M M JOSHI
Saha's Spectroscopy Laboratory, Physics Department, University of Allahabad, Allahabad 211 002, India

MS received 19 October 1993; revised 5 February 1994

Abstract. Thermal emission spectrum of YbI molecule has been photographed for the first time in the spectral region $\lambda\lambda$ 6100–6400 Å using Saha's high temperature furnace at a reciprocal linear dispersion of 7·3 Å/mm. A total of 52 single-headed and violet degraded bands have been recorded and are classified into a single system. Vibrational analysis has been carried out and it has been suggested that system arises from the ground state with the vibrational constant $\omega_e'' = 153{\cdot}0\,\mathrm{cm}^{-1}$.

Keywords. Thermal emission spectra; spectra of YbI molecule; vibrational analysis.

PACS No. 33·20

1. Introduction

Electronic spectrum of ytterbium monoiodide was first studied by Kramer [1] in the spectral region $\lambda\lambda$ 4500–6000 Å. He classified the observed single headed and violet degraded bands into two subsystems viz. $A^2\Pi_{1/2}$ and $A^2\Pi_{3/2}$ and reported two values of vibrational frequencies for the ground state ($^2\Sigma$). Lee and Zare [2] identified the presence of a new system in red region of YbF and YbCl molecule. However because of the highly perturbed upper state in both the cases (YbF and YbCl molecules) they could not present any data and vibrational analysis. Since YbF, YbCl and YbI molecules are isovalent molecules, similar band system for the YbI molecule can be reasonably expected. Therefore we examine the spectrum of YbI molecule in red region.

In the present paper we report the first observation of the thermal emission spectrum of YbI molecule in the region $\lambda\lambda$ 6100–6400 Å.

2. Experimental

The complete experimental set-up is described elsewhere [3] but a brief description is given here. A small quantity of spec-pure ytterbium metal (Johnson Matthey, 99·9%) and iodine (Sarabhai, 99·9%) was kept inside the experimental tube of Saha's high temperature furnace [4]. After making necessary routine adjustment and evacuation of the furnace chamber, argon gas was filled at a pressure of about 50 cm of mercury to prevent rapid effusion of molecular vapours from the open ends of the experimental tube. The spectrum has been photographed at 2000°C using first order of 2 meter plane grating spectrograph with a reciprocal linear dispersion 7·3 Å/mm. An exposure time of about three minutes was found sufficient to record the spectra on ORWO/INDU 125 ASA black and white film. Iron d.c. arc spectrum was used for the comparison standard. The measurements were performed using CZ Abbe Comparator with the least count of 0·0001 cm.

3. Results and discussion

Thermal emission spectrum, attributed to $A'-X$ system of YbI molecule has been photographed for the first time in the spectral region $\lambda\lambda$ 6100–6400 Å and is shown in figure 1. The spectrum is free from atomic lines. A total of 52 single-headed and violet degraded bands have been recorded and classified into a single system viz. $A'-X$. The (0,0) of the system lies at 6309·6 Å. The observed band head data, their estimated relative intensities and classifications are given in table 1.

The equation given below [5] represents the wave numbers for the various observed band heads:

$$\nu = T_e + \omega'_e(v' + 1/2) - \omega'_e x'_e(v' + 1/2)^2 - \omega''_e(v'' + 1/2) + \omega''_e x''_e(v'' + 1/2)^2$$

with

$$T_e = 15836{\cdot}9 \quad \omega'_e = 168{\cdot}0, \quad \omega'_e x'_e = 1{\cdot}20\,\mathrm{cm}^{-1}$$

$$\omega''_e = 153{\cdot}0, \quad \omega''_e x''_e = 0{\cdot}85\,\mathrm{cm}^{-1}$$

where ν is the wave number of the band head for a given vibrational transition between two electronic states; T_e is the electronic term value or the difference in electronic energy between the emitting and ground or terminal states; ω_e is the vibrational frequency; $\omega_e x_e$ is the anharmonicity; and v is the vibrational quantum number. The single prime denotes the upper state and the double prime denotes the lower state.

The proposed analysis of $A'-X$ system has certain intensity anomalies. This is due to the fact that graphite tube emits strong continuous radiations in red region which is difficult to remove. This gives rise to a different estimate of intensity rather than the actual one.

The earlier work on the YbI molecule by Kramer [1] has established the ground state vibrational frequency for this molecule to be 152·1 cm^{-1}. The proposed analysis of the system $A'-X$ recognized in the thermal emission from YbI molecule reveals the vibrational frequency of the lower state as 153·0 cm^{-1}. Thus the emitter of the new bands can be identified to be diatomic YbI. In addition no bands of Yb_2 and I_2 molecules are known in thermal emission in this region. All these considerations, therefore, confirm that bands can be rightly attributed to the YbI molecule.

The vibrational constants for the ground state of YbI molecule by us and those by Kramer [1] are compared in the following:

Kramer		Present authors	
$\omega''_e = 157{\cdot}9 \pm 3{\cdot}6$,	$\omega''_e x''_e = 1{\cdot}36 \pm 1{\cdot}24$,	$\omega''_e = 153{\cdot}0$	$\omega''_e x''_e = 0{\cdot}85\,\mathrm{cm}^{-1}$
$\omega''_e = 152{\cdot}1 \pm 0{\cdot}7$,	$\omega''_e x''_e = 0{\cdot}34 \pm 0{\cdot}04$.		

The difference in the molecular constants is because Kramer [1] has reported two values of vibrational frequencies for the ground state $^2\Sigma$ while a $^2\Sigma$ should have single vibrational frequency. The value obtained by us for $\omega''_e = 153{\cdot}0\,\mathrm{cm}^{-1}$ is very near to one of the values of $\omega''_e = 152{\cdot}1\,\mathrm{cm}^{-1}$ reported by Kramer [1].

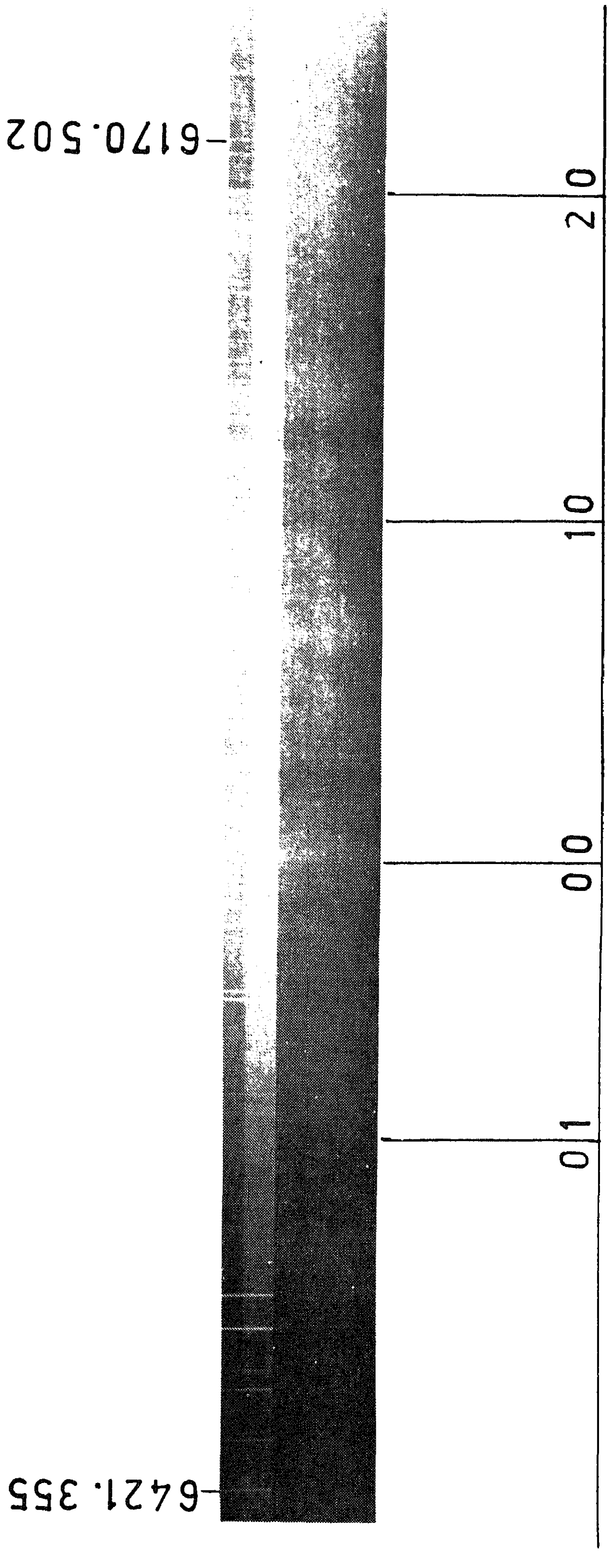

Figure 1. Thermal emission spectrum of YbI molecule at a reciprocal linear dispersion of 7·3 Å/mm.

Table 1. Band head data of YbI molecule: A'–X system.

ν_{obs} (cm^{-1})	$\Delta\nu$ (cm^{-1})	Int	Analysis (v', v'')	ν_{obs} (cm^{-1})	$\Delta\nu$ (cm^{-1})	Int.	Analysis (v', v'')
15693·9	0·9	3	(0, 1)	15980·4	−0·4	2	(14, 14)
15710·5	1·5	3	(1, 2)	15984·7	−0·6	2	(15, 15)
15724·6	0·3	2	(2, 3)	16010·6	0·7	3	(1, 0)
15737·1	−1·1	2	(3, 4)	16021·7	−0·1	3	(2, 1)
15753·1	0·3	3	(4, 5)	16032·8	−0·2	3	(3, 2)
15765·0	−1·0	2	(5, 6)	16045·3	1·8	4	(4, 3)
15778·5	0	2	(6, 7)	16052·8	−0·5	2	(5, 4)
15790·0	−0·3	4	(7, 8)	16062·2	−0·2	5	(6, 5)
15802·7	1·3	4	(8, 9)	16069·9	−0·9	4	(7, 6)
15810·8	−1·1	4	(9, 10)	16077·8	−0·7	3	(8, 7)
15822·1	0·6	5	(10, 11)	16086·8	1·3	3	(9, 8)
15831·8	1·3	5	(11, 12)	16092·2	0·4	2	(10,9)
15844·3	0	6	(0, 0)	16096·5	−0·9	2	(11, 10)
15858·4	−0·2	4	(1, 1)	16101·7	−0·6	2	(12, 11)
15871·6	−0·6	4	(2, 2)	16105·3	−1·2	2	(13, 12)
15884·2	−0·9	4	(3, 3)	16109·8	−0·2	2	(14, 13)
15896·2	−1·1	4	(4, 4)	16113·9	1·1	2	(15, 14)
15909·3	0·5	3	(5, 5)	16174·4	1·3	2	(2, 0)
15918·9	−0·7	3	(6, 6)	16181·3	−1·3	2	(3, 1)
15928·9	−0·8	3	(7, 7)	16192·3	0·9	2	(4, 2)
15939·5	0·4	3	(8, 8)	16201·2	1·7	2	(5, 3)
15948·0	0·2	3	(9, 9)	16207·2	0·3	2	(6, 4)
15954·9	−0·9	3	(10, 10)	16213·3	−0·3	2	(7, 5)
15962·1	−1·0	3	(11, 11)	16218·1	−1·5	1	(8, 6)
15970·3	0·6	3	(12, 12)	16225·1	0·2	1	(9, 7)
15977·1	1·5	2	(13, 13)	16228·3	−1·2	1	(10,8)

$\Delta\nu = \nu_{\text{obs}} - \nu_{\text{cal}}$

The electronic configuration of ytterbium and iodine atoms are:

$$_{70}\mathrm{Yb} = 1s^2, 2s^2 2p^6, 3s^2 3p^6 3d^{10}, 4s^2 4p^6 4d^{10} 4f^{14}, 5s^2 5p^6, 6s^2 \text{—} {}^1S$$

$$_{53}\mathrm{I} = 1s^2, 2s^2 2p^6, 3s^2 3p^6 3d^{10}, 4s^2 4p^6 4d^{10}, 5s^2 5p^5 \text{—} {}^2P.$$

Consider the separated atom model, we have Yb with ^1S and chlorine with ^2P as their ground states. Combination of these two atomic states gives rise to $^2\Pi$ and $^2\Sigma$ electronic states. It is well established [2,3] that ground state for YbF and YbCl molecule is to be $^2\Sigma$. Since YbF, YbCl and YbI molecules are isoelectronic molecule, we expect YbI to have the same ground state as YbF and YbCl molecules. If $^2\Sigma$ is the ground state of YbI molecule, the optically accessible transitions are $^2\Sigma$–$^2\Sigma$ and $^2\Pi$–$^2\Sigma$. Further the observed bands of the A'–X system are single headed therefore this system involves $^2\Sigma$–$^2\Sigma$ transition.

Acknowledgement

One of the authors (KNU) is thankful to CSIR, New Delhi for the financial assistance.

References

[1] J Kramer, *J. Chem. Phys.* **68**, 5370 (1978)

[2] H U Lee and R N Zare, *J. Mol. Spectrosc.* **64**, 233 (1977)

[3] K N Uttam, *Investigations of spectra of the diatomic molecules in thermal emission*, D. Phil thesis, University of Allahabad, Allahabad, India, (1993)

[4] M N Saha, N K Sur and K Majumdar, *Z. Phys.* **40**, 648 (1927)

[5] G Herzberg, *Spectra of diatomic molecules* (Van Nostrand, Company, New York, 1950) pp 151, Vol. I

PRAMANA
— journal of
physics

© Printed in India

Vol. 42, No. 3,
March 1994
pp. 245–250

CH local mode overtone excitations in benzyl chloride—A conformational study

T M A RASHEED and V P N NAMPOORI
Department of Physics, Cochin University of Science and Technology, Cochin 682 022, India

MS received 28 September 1993; revised 13 January 1994

Abstract. The CH local mode overtone spectrum of benzyl chloride in the visible and NIR regions studied by laser induced thermal lens and conventional NIR absorption is presented. The analysis shows that the $-CH_2Cl$ group is symmetrically oriented with respect to the benzene ring, thus finalizing one of the two possible conformational models predicted by electron diffraction studies. The aryl CH bonds have a slightly larger force constant than that in benzene.

Keywords. Overtone spectroscopy; conformation; thermal lens technique.

PACS No. 33·20

1. Introduction

Vibrational overtone spectroscopy of molecules containing X–H oscillators ($X = \mathrm{C, N, O}$) is an area of recent interest [1–3]. The local mode (LM) model in which the X–H oscillators are considered to be loosely coupled anharmonic Morse oscillators, has been widely used for interpretation of overtone spectra. The overtone transition energies obey the relation

$$\Delta E_{V \leftarrow 0} = \mathrm{A}V + \mathrm{B}V^2$$

where V is the quantum level of excitation, $\mathrm{A} - \mathrm{B} = X_1$ is the mechanical frequency and $\mathrm{B} = X_2$ is the anharmonicity of the X–H bond. A plot of $\Delta E/V$ vs V yields the local mode parameters, X_1 and X_2. In a molecule containing non-equivalent X–H bonds, different overtone progressions are formed due to their differing mechanical frequency and/or anharmonicity values. Thus overtone spectroscopy has become an effective tool for structural studies of organic molecules pertaining to nonequivalent CH bonds; the nonequivalence may arise due to factors like structural difference, conformational difference, anisotropic environments created by lone pair and/or π electron interactions etc. [4–13]. Overtone spectroscopy has also been used to study the influence of various substituents on benzene ring CH bonds [8, 9, 14–19].

In the present paper we report the CH overtone spectrum of liquid phase benzyl chloride recorded by the dual beam thermal lens ($\Delta V = 6$) and conventional NIR absorption ($\Delta V = 2$–4) techniques. The analysis of the structure of chloromethyl CH overtones leads to the conclusion that the $-CH_2Cl$ group is oriented symmetrically with respect to the benzene ring, thus finalizing one of the two structures compatible with electron diffraction data. The aryl CH bonds in this molecule are found to have a slightly larger force constant than that in benzene.

2. Experimental

High purity (99%) benzyl chloride (E Merck India) is used for the present experiments. The dual beam thermal lens technique [20] uses a rhodamine 6 G dye laser (Spectra Physics 380 A) pumped by an argon laser (Spectra Physics 171–17) as the pump source. The chopped dye laser beam (50–100 mW) creates a pulsating thermal lens in the sample (path length 1 cm). The intensity modulations on a probe He–Ne laser beam (2 mW) passing through the sample are synchronously detected and normalized for pump laser power variation. The details of our thermal lens experimentation are given elsewhere [13]. The near infrared absorption spectrum is recorded in a Hitachi 3410 spectrophotometer from pure liquid with air as reference and path length 1 cm. All spectra are recorded at 25 ± 2°C.

3. Results

The thermal lens and near infrared absorption spectra are shown in figures 1–4. The thermal lens absorption spectrum (figure 1) shows only the fifth overtone of the aryl

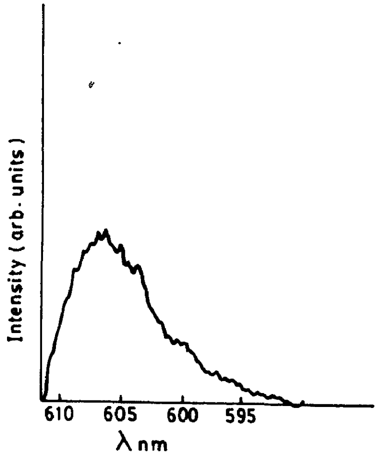

Figure 1. Fifth overtone absorption spectrum of aryl CH bonds in benzyl chloride recorded from pure liquid by dual beam thermal lens technique.

Table 1. Observed overtone energies (cm^{-1}) their assignments, mechanical frequencies $X_1(cm^{-1})$ and anharmonicities $X_2(\mathrm{cm}^{-1})$ of aryl and chloromethyl CH local modes in benzyl chloride. Data for benzene [23] is also given for a comparison.

Molecule	$\Delta V=2$	$\Delta V=3$	$\Delta V=4$	$\Delta V=5$	$\Delta V=6$	X_1	X_2
Benzene	5983	8760	11442	14015	16467	3148·1	− 57·6
Benzyl chloride							
Aryl CH	5988	8775	11464	···	16475	3175·4 ± 7	− 61·6 ± 2
Chloro-methyl CH	5806	8553	11191	···	···	3062·7 ± 2	− 53·0 ± 0·5

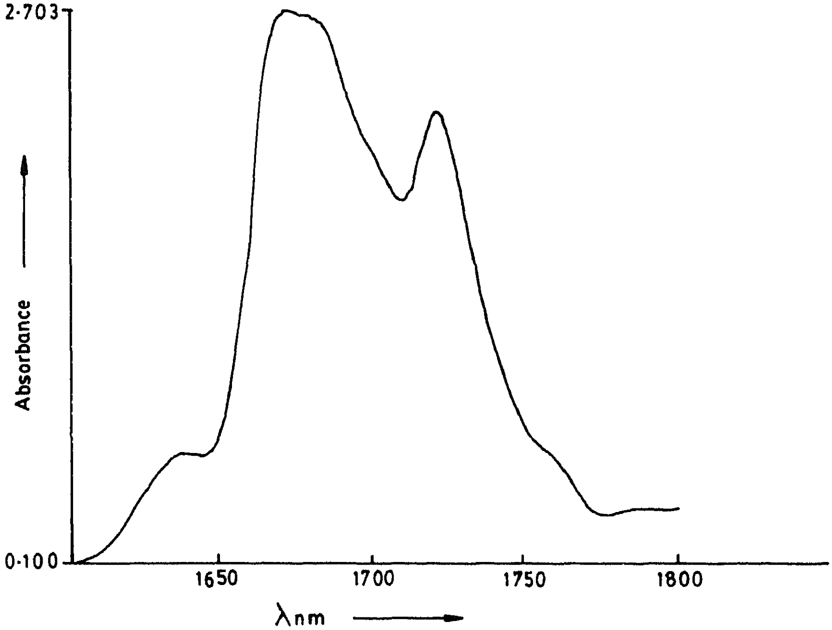

Figure 2. First overtone spectrum of benzyl chloride recorded from pure liquid. Reference-air.

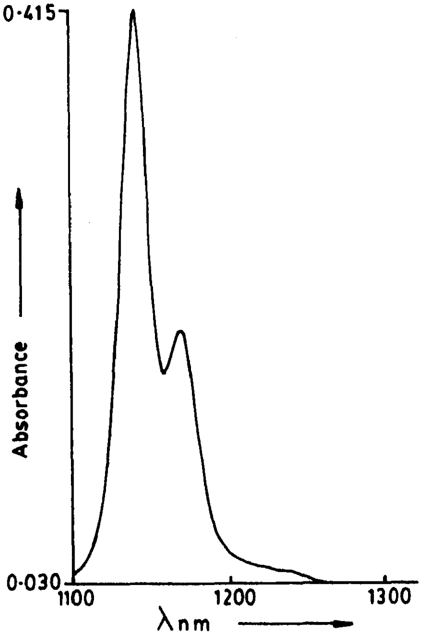

Figure 3. Second overtone spectrum of benzyl chloride recorded from pure liquid. Reference-air.

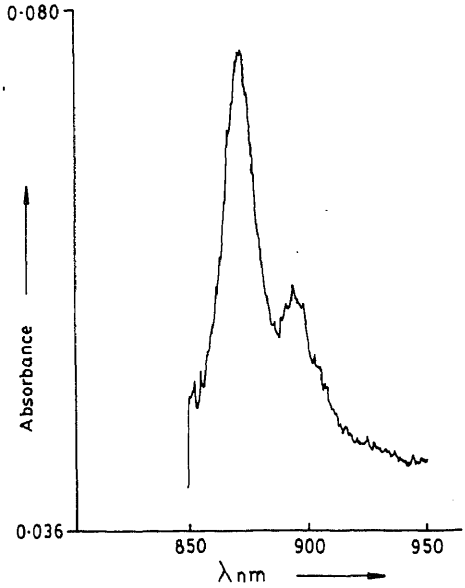

Figure 4. Third overtone spectrum of benzyl chloride recorded from pure liquid. Reference-air.

CH bond due to the limited tuning range of the dye laser. The first through third overtone spectra show bands due to aryl and alkyl local mode excitations. The fourth overtone spectrum is not presented due to the poor signal to noise ratio of the spectrophotometer in that region. The peak positions, their assignments and the local mode parameters obtained from Birge–Sponer plot are given in table 1.

4. Discussion

4.1 *Chloromethyl CH overtones*

The overtone spectrum in the region $\Delta V = 2$–4 (figures 2–4) shows the chloromethyl CH overtone peaks occurring on the low energy side of the aryl CH overtones. The chloromethyl CH overtones in all these regions give rise to sharp peaks. As explained below the occurrence of these sharp peaks lead to important conclusions regarding the conformation of the $-CH_2Cl$ group with respect to the benzene ring.

The electron diffraction studies on benzyl chloride was carried out by Sadova *et al* [21]. The results of their studies are compatible with two possible structures. In one structure, the angle of rotation (as seen in Newman projection) of the $-CH_2Cl$ group around the C–C bond is $\phi = 67{\cdot}5°$ ($\phi = 0$ when the C–Cl bond is the plane of the benzene ring), with relatively large torsional amplitudes (hereafter referred to as structure I). In the other possible structure, the potential for internal rotation is given by $V(\phi) = (V_2/2)[1 - \cos 2(\phi - \phi_0)]$ with $V_2 = 6{\cdot}3\,\mathrm{kJ\,mol^{-1}}$ with a minimum at $\phi = \phi_0 = 90°$ and relatively smaller torsional amplitudes (hereafter referred to as structure II). The overtone spectral structure shows that the structure II is the one which is acceptable (see below).

Before discussing the chloromethyl CH overtones in benzyl chloride it is necessary to consider the alkyl CH overtones reported in related compounds like toluene, *p*-xylene, *m*-xylene and *o*-xylene. The liquid phase overtone study of these compounds by Nakagaki and Hanazaki [22] shows that the methyl CH overtones of toluene, *p*-xylene and *m*-xylene are broad flat peaks whereas those of *o*-xylene are resolved doublets. Later the gas phase overtone spectral studies carried out by Gough and Henry [8] have shown that the methyl CH overtone regions of toluene, *p*-xylene and *m*-xylene consist of three peaks corresponding to in-plane CH, out of plane CH and free rotor states above the torsional potential barrier. The gas phase *o*-xylene overtone spectra again shows only two peaks which correspond to the in-plane and out-of plane CH bonds of the methyl group. The difference occurs for *o*-xylene compared to toluene, *p*-xylene and *m*-xylene due to the fact that the methyl groups in the latter molecules are almost free rotors whereas it is not so in *o*-xylene (barrier-6·3–9·2 kJ mol^{-1}).

The present case of benzyl chloride is similar to *o*-xylene since the $-CH_2Cl$ group is not at all a free rotor in both the possible structures [21]. For *o*-xylene, the non-equivalent methyl CH overtones have frequency separations of 100 cm^{-1}($\Delta V = 3$) and 150 cm^{-1}($\Delta V = 4$) and are well resolved in liquid and gas phase spectra. The stable conformation of this molecule is such that one of the three CH bonds is in the plane of the benzene ring while the other two are out of plane, i.e., they are at 60° to the ring. Thus we have a frequency shift of 100 cm^{-1}($\Delta V = 3$) and 150 cm^{-1} ($\Delta V = 4$) for an orientation angle variation of 60° for the CH bonds. In benzyl chloride, if structure I is valid then one of the CH bonds will be at 7·5° while the other CH bond will be at 52·5° with respect to the benzene ring. Thus we have an orientation angle variation of 45° and hence we expect two peaks in the chloromethyl CH overtone region of the spectrum. But the overtone spectrum shows only one sharp peak at all the quantum levels. This shows that the two CH bonds in the $-CH_2Cl$ group of benzyl chloride are equivalent. This result is in perfect agreement with structure II in which the C–Cl bond is at 90° and the two CH bonds are at 30° with respect to the ring (as seen in Newman projection). We thus conclude that structure II is the one which is acceptable.

4.2 *Aryl CH overtones*

The major peaks observed in the overtone spectra are due to the aromatic CH bonds in the benzene ring. The peak positions and the local mode parameters obtained from Birge–Sponer plot are given in table 1. Mizugai and Katayama [14] have reported the fifth overtone peak position of aryl CH in benzyl chloride to be 16490 cm^{-1}. We believe that our value 16475 cm^{-1} is more accurate than the data obtained from point-by-point thermal lens measurement of these authors. The most reliable overtone data of liquid benzene reported [23] is also given in table 1 for a comparison. The aryl CH overtone peak positions of benzyl chloride are slightly blue shifted with respect to those of benzene. It can be seen from table 1 that this blue shift in overtone energy is due to an increased mechanical frequency of the ring CH bonds compared to that in benzene. It is well established from extensive overtone studies of substituted benzenes [8, 9, 14–19], that an electron withdrawing group causes shortening of the ring CH bonds (thereby increasing overtone frequency) and an electron donating group causes lengthening of the ring CH bonds thereby decreasing overtone frequency. Correlation between shift in overtone energy and inductive part of Hammet $\sigma(\sigma_I)$ and correlation between overtone energy and bond length are also established from these earlier studies.

The small blue shift with respect to benzene overtone positions resulting from increased mechanical frequency is in line with the small electron withdrawing power of the $-CH_2Cl$ group $\sigma_I = 0{\cdot}11$ [14]. As is true in many other molecules [14–18] the electron withdrawing group reduces the electron density at the ring carbon atoms. This results in a net positive charge on them thus increasing the force constant of the ring CH bonds.

5. Conclusions

The analysis of the CH overtone spectrum of benzyl chloride has shown that, out of the two different conformational models compatible with electron diffraction data, the one symmetric conformation in which C–Cl bond is perpendicular to the benzene ring plane (as seen in Newman projection) is acceptable. Also the aryl CH bonds in benzyl chloride is found to have slightly larger force constant than that in benzene.

Acknowledgements

The authors gratefully acknowledge the financial assistance from Department of Science and Technology and University Grants Commission. They are also thankful to Dr K P B Moosad, Dr M K Jayaraj and Mr George James for their assistance in recording the spectra.

References

[1] B R Henry, in *Vibrational spectra and structure* edited by J R Durig (Elsevier, Amsterdam, 1981) Vol. 10, p. 269
[2] M S Child and L Halonen, *Adv. Chem. Phys.* **57**, 1 (1984)
[3] B R Henry, *Acc. Chem. Res.* **20**, 429 (1987)
[4] W R A Greenlay and B R Henry, *J. Chem. Phys.* **69**, 82 (1978)
[5] M S Burberry, J A Morrel, A C Albrecht and R L Swofford, *J. Chem. Phys.* **70**, 5522 (1979)
[6] B R Henry and W R A Greenlay, *J. Chem. Phys.* **72**, 5516 (1980)
[7] J S Wong and C B Moore, *J. Chem. Phys.* **77**, 603 (1982)
[8] K M Gough and B R Henry, *J. Phys. Chem.* **88**, 1298 (1984)
[9] M K Ahmed and B R Henry, *J. Phys. Chem.* **90**, 1737 (1986)
[10] H L Fang and R L Swofford, *Appl. Opt.* **21**, 55 (1982)
[11] H L Fang, D M Meister and R L Swofford, *J. Phys. Chem.* **88**, 405 (1984)
[12] H L Fang, D M Meister and R L Swofford, *J. Phys. Chem.* **88**, 410 (1984)
[13] T M A Rasheed, K P B Moosad, V P N Nampoori and K Sathianandan, *J. Phys. Chem.* **91**, 4228 (1987)
[14] Y Mizugai and M Katayama, *J. Am. Chem. Soc.* **102**, 6424 (1980)
[15] Y Mizugai, M Katayama and N Nakagawa, *J. Am. Chem. Soc.* **103**, 5061 (1981)
[16] K M Gough and B R Henry, *J. Phys. Chem.* **87**, 3433 (1983)
[17] R Nakagaki and I Hanazaki, *Spectrochim. Acta* **A40**, 57 (1984)
[18] M K Ahmed, D J Swanton and B R Henry, *J. Phys. Chem.* **91**, 293 (1987)
[19] T M A Rasheed, K P B Moosad, V P N Nampoori and K Sathianandan, *Pramana – J. Phys.* **33**, 391 (1989)
[20] H L Fang and R L Swofford, 1983 in *Ultrasensitive laser spectroscopy* edited by D S Kliger (Academic Press, New York, 1983) p. 275
[21] N I Sadova, L V Vilkov, I Hargittai and J Brunvoll, *J. Mol. Struct.* **31**, 131 (1976)
[22] R Nakagaki and I Hanazaki, *Chem. Phys. Lett.* **83**, 512 (1981)
[23] C K N Patel, A C Tam and R J Kerl, *J. Chem. Phys.* **71**, 1470 (1979)

PRAMANA
— journal of
physics

© Printed in India

Vol. 42, No. 3,
March 1994
pp. 251–260

A calorimeter for operation in the temperature range 2–150 K

I DAS and E V SAMPATHKUMARAN
Tata Institute of Fundamental Research, Homi Bhabha Road, Bombay 400005, India

MS received 5 September 1993; revised 23 December 1993

Abstract. The description of a calorimeter for measurement of heat-capacity in the temperature range, 2–150 K, by semi-adiabatic heat-pulse method is presented. The data collection is computerized and various parameters monitored through the software ensure high quality of the data. The performance of the calorimeter was verified with the well-known standard materials. Results on the alloys, $PrCu_2Si_2$ and $GdCu_2Si_2$, are also presented.

Keywords. Heat-capacity; calorimeter.

PACS No. 7·20

1. Introduction

It is well-known that the measurement of heat-capacity (C) as a function of temperature is valuable in obtaining information about the Debye temperature, the density of states at Fermi level (E_F) and phase transitions in materials [1–3]. There are different ways of measuring C, for instance, semi-adiabatic, thermal relaxation, continuous heating and AC calorimetric methods. The complexities of the calorimeter design, designed by solid state physicists in different laboratories around the world vary, even for the same method of measurement (see the references cited in [1, 3–8]), suiting to the specific need of the user, for instance, the temperature range of interest. One has to take special care to design a calorimeter, which can be employed over a wide temperature range; particularly, at temperatures above 20 K, the heat transfer by radiation varying as T^4, becomes significant and maintaining the adiabatic conditions becomes very crucial. As brought out by Gmelin [3], the temperature range 2– 120 K offers most calorimetric problems and hence the total number of successfully operating calorimeters in this temperature range around the world is rather limited in spite of tremendous importance for thermoanalysis data.

In this article, we describe a simple calorimeter designed by us to measure C by semi-adiabatic heat-pulse method with the following salient features: (i) It is a top-loading type; therefore, the method of isolation of the sample chamber by indium wire or woods alloy for the vacuum purpose as is the case with most of the designs is avoided and hence this design reduces the vacuum problems due to cold leaks; the interchange of samples is very quick and easy; (ii) there is no mechanical switch for cooling the sample; (iii) it can be operated in the temperature range 5–150 K with a very good accuracy (less than 2%); by letting in traces of helium gas in the sample chamber when the helium bath is pumped to 1·5 K, the sample could be cooled to 2 K and the data collected in the temperature interval 2–6 K are fairly reliable at least to look for qualitative features. The measurement is automated by using a PC/XT and the software ensures minimum scatter in the data; the temperature-time curve can be seen on the monitor and the program facilitates the change of parameters intermittently to improve the quality of the data. Reliable data could be obtained even for smaller amount, for instance, 400 mg of the sample and the amount required is still smaller for materials with a large low temperature heat-capacity.

2. Experimental details

2.1 *Calorimeter*

Schematic illustration of our heat-capacity measuring set-up is shown in figure 1. The cryostat employed is a superinsulated fibre-glass dewar, D, of about 3 litres capacity supplied by Precision Cryogenics (USA) and, in this way, liquid nitrogen

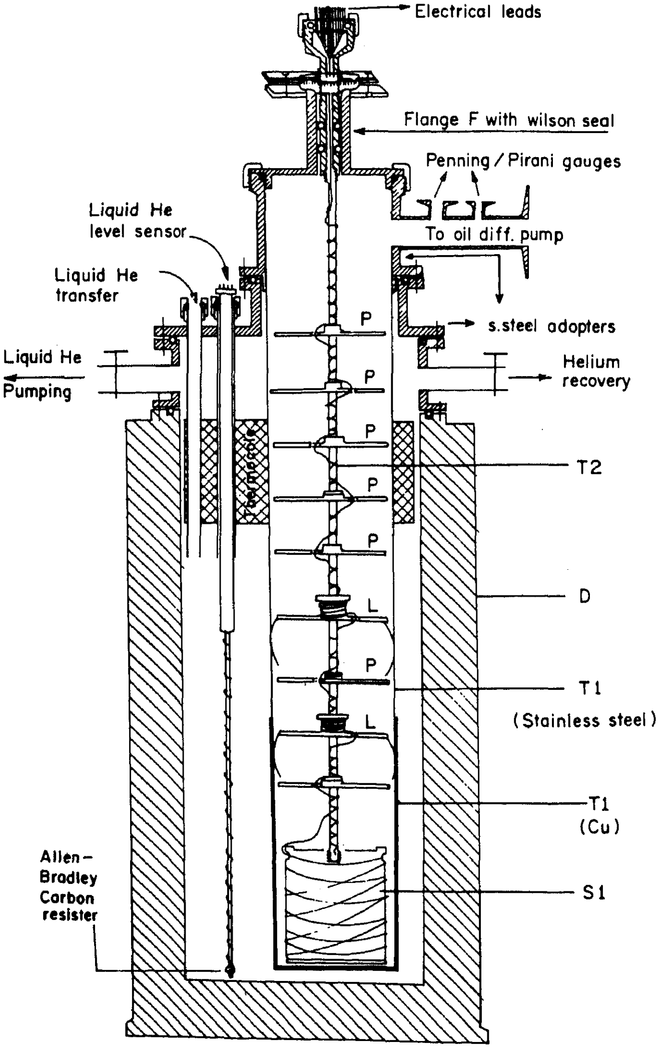

Figure 1. Schematic of the complete set-up of the calorimeter.

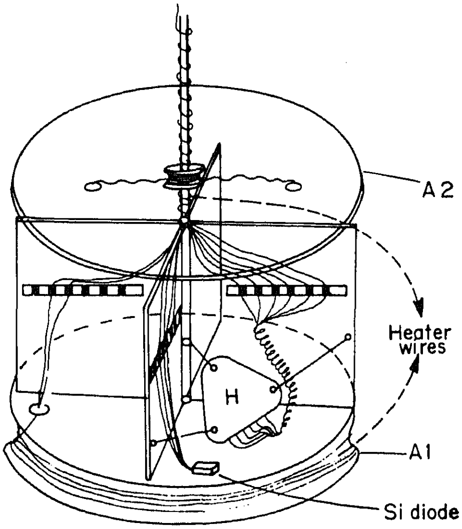

Figure 2. The assembly A surrounding the sample holder is shown separately. The specifications marked in the figure are described in the text.

jacket is made redundant. T1 is a 1 m long tube; the bottom portion (about 1 foot long) is made up of Cu tube (wall thickness 1 mm) and the top portion is made up of a thin walled (0·25 mm thick; 50 cm dia) stainless steel tube; the Cu tube facilitates thermal homogeneity in the region of interest. The calorimeter-insert essentially consists of a (gold-plated) Cu shield (S1), a Cu assembly, A, (figure 2) made up of gold plated Cu, the sample holder (H) and a 1 metre long stainless steel tube (T2) of 6 mm diameter.

The assembly A (figure 2) consists of two circular Cu plates, A1 (5 mm thick) and A2 (1 mm thick), joined together by about 6 cm long Cu rod (4 mm dia). The dimensions of S1 are chosen such that it can rest on A1 thereby making very good thermal contact and S1 needs to be lifted up whenever a sample is to be mounted. The bottom portion of the region between A1 and A2 is divided vertically into four segments by 1 mm thick Cu plates (this division is not necessary for measuring C of only one sample; this provision is made to try out the measurement of C for 4 samples simultaneously at a later stage). Heater wires are wound around the groove provided on A1, the top portion of the 4 mm diameter Cu rod (between A1 and A2) and also at the outer surface of the Cu cylinder S1. The terminals provided on one of the four quarters are used to connect these heaters in series; the corresponding heater wire resistances are 25 Ω, 6 Ω, and 12 Ω respectively. A silicon diode temperature sensor fixed on the Cu plate A1 is used to control the temperature of the shield and the Cu assembly. The sample holder (H) is made up of a high purity oxygen free copper sheet (0·25 mm thick and about 10 mm dia); one side of this Cu plate contains a Ge thermometer (Lakeshore, Model GR-200B–1500) and two thin film strain gauges (Tokyo Sokkai Kenkyujo Co., CFLA–1–1350 Ω) as a sample heater glued with GE7031 varnish. The sample holder is suspended by three nylon strings at one of the four segments. Electric lead wires from the thermometer and the heater (fixed on H) are connected to the terminal provided on the Cu plates via some springs made out of Cu wire (ϕ 0·03 mm × 60 cm), as shown in the figure; the utility of these thin long Cu wires to maintain semi-adiabatic conditions during the course of the measurements was also verified (*vide infra*).

The assembly described above is connected to an approximately 1 m long stainless steel tube of 6 mm diameter, T2, and the other end of this tube is coupled to a stainless steel flange F (which in turn is provided with a O-ring seal so as to be able to mount on the stainless adopters at the top of T1). The movement of this stainless steel tube by a few cm, if necessary, is made possible via the use of a wilson sealing arrangement provided on the flange. Two lotus-shaped Cu assemblies, L, are provided on T2 and the dimensions are chosen in such a way that they are in good thermal contact with T1; this arrangement serves as a sink for the heat-flow from the top. Additional radiation shields made out of Cu plates, P (about 2 mm thickness) are also fixed at various places on T2.

The electronic instruments employed in the set-up are commonly available general purpose type, like Keithley Programmable Constant Current source (Model 220), Keithley nanovoltmeter (Model 181) and Lakeshore temperature controller (Model DRC93C). These instruments are interfaced to a PC/XT via GPIB and the program for controlling the parameter and automatic data collection was developed using quickbasic language.

2.2 *Thermometer calibration and data acquisition*

We have first calibrated the Ge thermometer mounted on the sample holder. The calibration is performed in the presence of small traces of helium exchange gas (about 1 torr) against a calibrated Ge thermometer up to 100 K and a calibrated silicon-diode sensor in the temperature range 100–160 K using a four-wire DC technique. The calibrated sensors were mounted on the other side of the Cu plate H. We have employed Keithley constant current source and Keithley nanovoltmeter (resolution 10 nV) in the above calibration. In Ge sensors, the current values were chosen in such a way that the voltage (as measured by the nanovoltmeter) falls in the range 1 to 2 mV to avoid self-heating error. After stabilizing the temperature of the assembly A at a desired value with the help of the Lakeshore temperature controller and silicon diode sensor (mounted on Al), the resistance/voltage values of the thermometers on the sample holder are collected; in the case of resistance thermometers, the voltage values for both positive and negative current directions were recorded to correct for thermal EMF's. This calibration process above 1·6 K is computer controlled and the calibration data were collected automatically for every 0·1 K below 4 K, 0·2 K interval in the temperature range 4 to 10 K and 0·5 K interval above 10 K. The data points do not always correspond to integer temperatures and a polynomial equation (Chebychev polynomials as prescribed by Lakeshore Cryotronics) was employed to fit the curves of temperature versus resistance/voltage.

The preparation for the data collection is performed by the usual procedure. The weighed amount of the sample, which can be of any shape and polished on one side is fixed to the Cu sample holder with a thin layer of Apiezon N grease (about 5 mg) for good thermal contact. We normally keep track of the amount of the grease used, so that the contribution to C from this grease can be taken into account while obtaining the C of the sample. After mounting the sample, the insert is sealed with a viton O-ring to the tube T1 at the top. The calorimeter chamber is pumped down to 2×10^{-6} torr. Now, helium exchange gas of about 1 torr is let inside the calorimeter and liquid nitrogen is transferred in the fibreglass dewar. After waiting for a minimum period of about 2 h, the exchange gas is pumped out. Liquid nitrogen is then removed and liquid helium (about 3 litres including precooling) is transferred in the dewar. We wait for a few hours for the sample holder to reach around 8 K and the wilson seal provided at the top enables us to move the insert down so as to make the contact with the Cu plate at the bottom of the tube T1 which is at the temperature of the helium bath. The liquid helium bath is pumped down to about 1·5 K. After a waiting period of about 1 h at this stage, the sample holder reaches a temperature of about 5 K. We start data collection at this stage. If the measurements are required down to 2 K, we let 1 torr of helium gas inside the sample chamber as a result of which the entire region surrounding sample reaches the temperature of the bath immediately. Due to cryopumping, the measured vacuum in the sample space is better than 1×10^{-5} torr. In order to maintain adiabatic conditions during the course of measurement, this adsorbed gas should be completely removed. This requires an efficient pumping system [2] and, to achieve this, the inner diameter of the pumping line leading to the oil diffusion pump (not shown in the figure) from the top of the tube T_1 should be sufficiently large (in our case 2″). This continuous pumping with this arrangement results in a vacuum of about 4×10^{-6} in half an hour. If necessary, one can wait for a sufficiently long time to make sure that there is no further degassing in the sample chamber. We subsequently start the collection of the data. Since the exchange gas absorbed on the walls of T1 and A is not released till 6 K, the data collected in this way are found to be reliable.

The sequence of operations in a pulse calorimeter is well-known and is illustrated in terms of a temperature-time graph in figure 3. During the period AB, the temperature is recorded every 2 s by measuring the resistance of the germanium resistance thermometer by a four-probe method. Then a known quantity of heat, ΔQ (decided by the current applied through the strain gauge heaters for a fixed duration t) so as to cause an increment (ΔT) in the temperature of the sample, is fed, simultaneously measuring the temperature. The increase in the temperature at low temperatures after the heat-pulse is typically 1 to 4%, which is about two to three orders of magnitude larger than the temperature resolution at a given temperature.

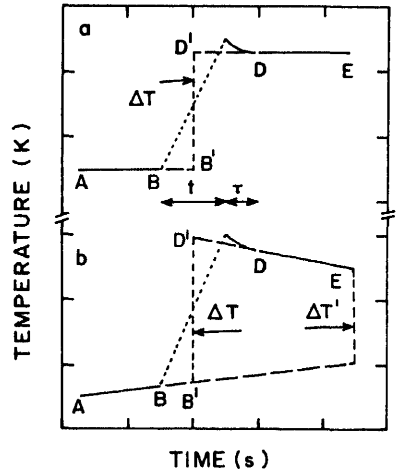

Figure 3. (**a**) Temperature-time curve (heat-pulse curve) when there is no heat-leak; (**b**) Heat-pulse curve when there is a heat-leak. Other details are described in the text.

After the heat pulse is terminated, the temperature is recorded in the drift period. Before the heat-pulse is applied, the temperature of the surrounding is made equal (within desired accuracy) to that of the sample with the help of the heater coils provided on the Cu assembly, A, and this temperature is made to follow the heating curve shown in figure 3; that is achieved with the help of Si diode sensor mounted on A1 and the Lakeshore temperature controller. This ensures that there is no heat-leak to and from the sample holder and that AB and DE are not only parallel to each other, but also to the X-axis (figure 3a). Therefore, the increment in the temperature (ΔT) due to the heat-pulse (ΔQ) is straightaway given by B′D′; the heat-capacity, C, of the sample (+ the sample holder) is given by $\Delta Q/\Delta T$. At this juncture, we like to mention that even if the temperature of the surrounding is intentionally kept different (say, much more than 10% of that of the sample), the time taken (external relaxation time) for the sample holder to reach the initial temperature (that is, at B on the line AB) is found to be extremely large compared to the duration of a heating-cycle, thereby confirming the fulfillment of semi-adiabatic conditions by the use of Cu springs. In the event of such a slow heat leak, AB cannot be perfectly parallel to DE (figure 3b) and the C values obtained as above will not be accurate. To have an estimate of such an error, we calculate C values from two different values of ΔT(i) ΔT given by B′D′, that is, by the usual extrapolation procedure and (ii) N temperature values (N is typically 10 along the line DE) taken as a function of time in 2 s interval after the delay period (internal relaxation time), τ, which is typically a few seconds below about 30 K and a few tenths for higher temperatures, are least square fit to a straight line and the temperature corresponding to the time of the Nth point on this fitted line is assumed to be the final temperatures; the temperature corresponding to the time of the Nth point on the line AB, obtained by extrapolation of the line AB, is assumed to be the initial temperature. From this procedure, the change in the temperature due to the heat pulse is obtained as $\Delta T'$ and the corresponding heat-capacity as C1. Since the heating-curve is displayed on the computer monitor, we can control various parameters, like τ, pulse duration, temperature of the surrounding, (approximately required) percentage increase in temperature etc, so as to keep the difference, C–C1, within 1%. The care taken to ensure that the lines AB and DE are parallel to X-axis results in good quality data with minimum scatter. The entire measurement in the temperature range 2–150 K can be performed within 10 h. One has to be careful while taking data in the temperature range 2–5 K, particularly for materials with very low heat-capacity values, to make sure that the liberation of the exchange gas above 5 K does not falsify the data, in case the measurement is started from 2 K. The procedure we normally follow is to take the data in the temperature interval 6–50 K after removing the exchange gas (at 77 K) and then let very little exchange gas in when liquid helium bath is at 1·5 K so as to enable us to take the data below 5 K. Then the sample chamber is pumped by an oil diffusion pump. (A liquid nitrogen trap is provided between the calorimeter and the diffusion pump). We continue to pump the sample chamber throughout the course of measurement. We constantly monitor the pressure in the sample chamber and if the pressure is worse than 1×10^{-5} torr, the data collection is disrupted for some time till the vacuum improves.

Needless to point out that the heat-capacity of the addenda without the sample was obtained in order to take into account the contributions from Cu sample holder, the thermometer, the strain gauge heaters, varnishes etc. We have also measured the heat-capacity of the Apiezon-N grease employed for mounting the sample. These heat-capacity values were fit to some functional forms and incorporated in the software for data collection.

3. Illustrations

We have measured the temperature dependent heat-capacity behavior in Cu and single crystalline Pb (purity 99·99%) above 5 K and also looked for various phase transitions in some standard materials. The measured heat capacity values of Cu are plotted in figure 4 and selected temperatures are also shown in table 1. In order to compare our values with those reported in the literature, we reproduce alongwith, the data reported by two different groups [9, 10]. It is to be noted that the heat-capacity of Cu below 10 K is extremely small and the low temperature values reported by different groups often differ at least by 1% (see, for instance, Gmelin and Rodhammer [11]). The data on Cu are found to be reproducible within 1% below

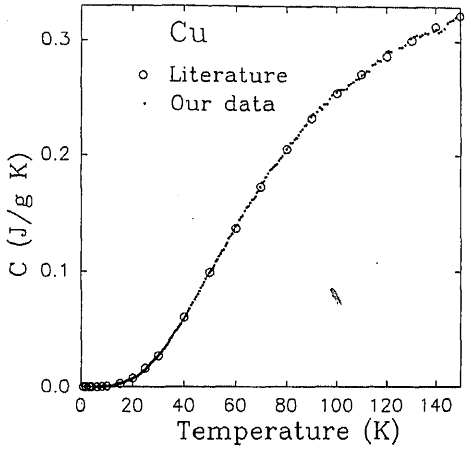

Figure 4. The heat-capacity of Cu in a wide temperature range. The literature data points are taken from a table in Weast [9].

Table 1. The heat-capacity (J/gK) of Cu at selected temperatures. Our data are given in the second column and two representative literature data are shown in the next two columns.

T(K)	Our data	Weast [9]	Martin [10]
6	0·00023	0·00023	—
10	0·00090	0·00086	—
20	0·00757	0·0077	0·00724
40	0·0591	0·060	0·0586
60	0·138	0·137	0·136
80	0·205	0·205	0·203
100	0·256	0·254	0·252
120	0·291	—	0·287
140	0·311	—	0·312
150	0·318	—	0·321

80 K and within 2% at higher temperatures from one measurement to the other. Considering all these factors, it can be stated that our values agree with those reported in the literature within a few per cent in the temperature range 5–150 K, and that the present design can be successfully used for heat-capacity measurements in this temperature range. In fact, we have extended the measurements to 2 K for some of the rare-earth intermetallic compounds [12–14], the C data for some of which were obtained in other laboratories abroad and such experiments prove that our set-up could be employed even below 5 K without losing much accuracy, particularly to look for qualitative features in the materials with heat-capacity values much larger than those of Cu. The features due to various phase transitions (figure 5) are found

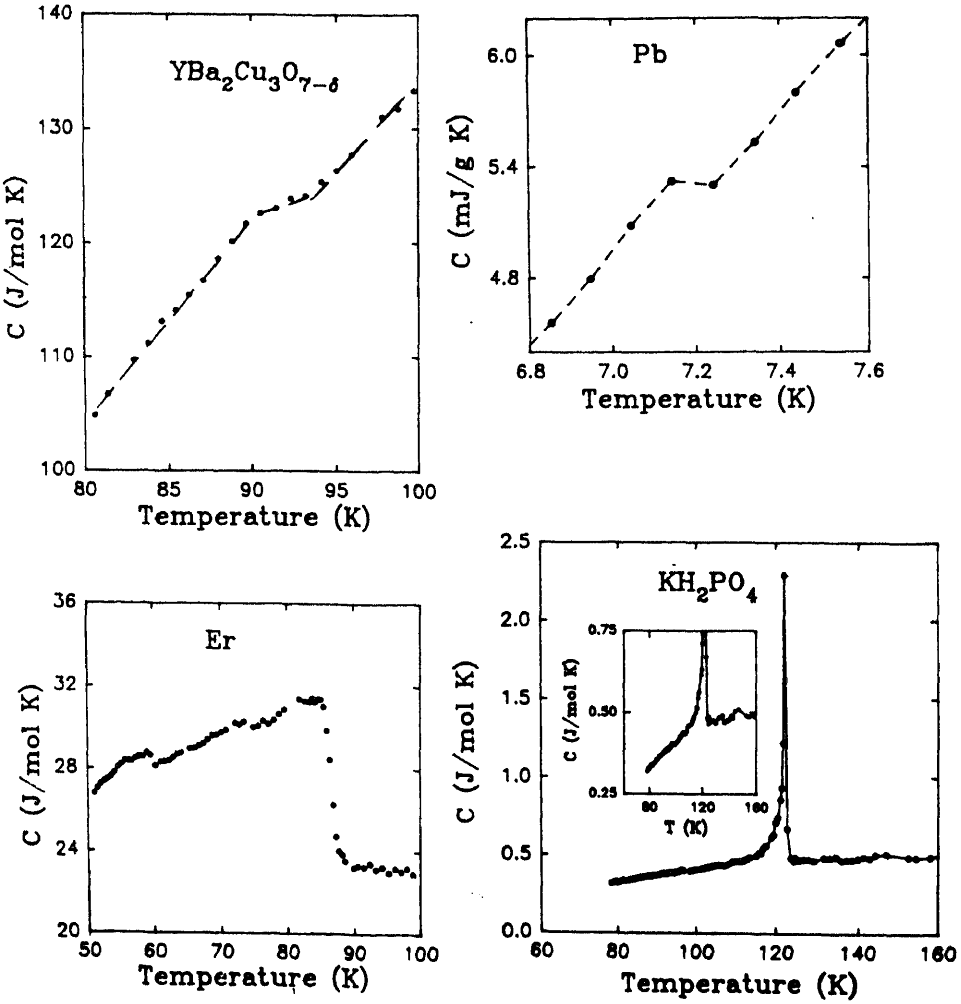

Figure 5. The temperature dependence of heat-capacity across superconducting transitions in Pb and $YBa_2Cu_3O_{7-\delta}$, magnetic transition in Er and ferroelectric transition in KH_2PO_4. In order to highlight the fact that the variation of C with T in the near vicinity of ferroelectric transition in KH_2PO_4 is in agreement with that known in literature [1], the plot is shown in an expanded form in the inset. A feature for Er at 60 K [1] is also reproducible in our data. The lines drawn through the data points are the guides to the eyes.

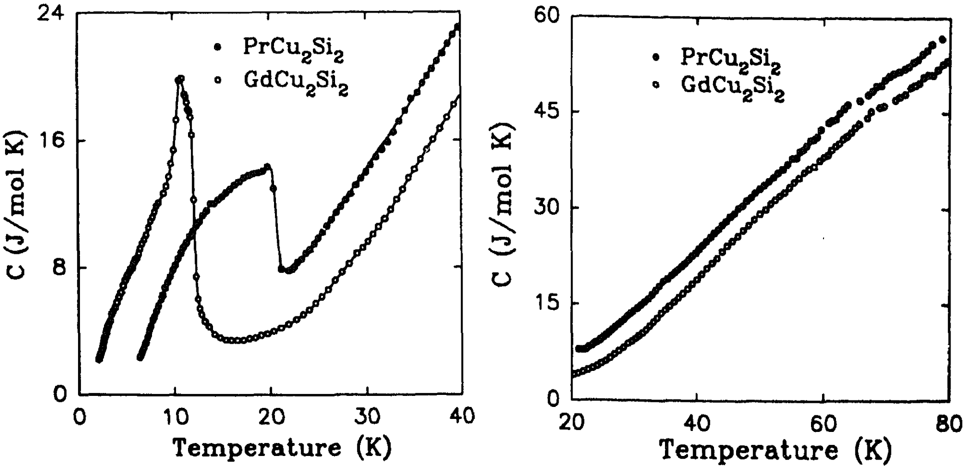

Figure 6. The heat-capacity as a function of temperature in $PrCu_2Si_2$ and $GdCu_2Si_2$. The lines drawn through the data points are the guides to the eyes. The C values in the temperature interval 20–80 K are plotted separately in order to show that these plots are parallel in the temperature interval 30–80 K.

to be in excellent agreement with the literature data, for instance, superconducting transition in Pb ($T_c = 7{\cdot}2$ K) and $YBa_2Cu_3O_{7-\delta}$ ($T_c = 90$ K) magnetic ordering in Er at 84·5 K and ferroelectric transition in KH_2PO_4 ($T_c = 122$ K) (see [1]).

We also measured the heat-capacity of the two alloys of interest to us, viz., $PrCu_2Si_2$ and $GdCu_2Si_2$ in the temperature range 2–120 K. The results are shown in figure 6. These alloys are known to undergo antiferromagnetic phase transitions at 21 K and 13 K respectively [15]. The data shown in figure 6 are in agreement with this. It may be remarked that the heat-capacity data reported earlier [16] were restricted to 40 K. The C values of the Pr alloy was found to be higher than that of Gd alloy by about 3·5 to 4 J/mol K in the temperature range 25–40 K; the origin of this excess heat-capacity was speculated to arise from the heavy-fermion-like character of Pr ions, a phenomenon unexplored in Pr-based intermetallics. In order to place this speculation on firm grounds, there is a need to exclude possible interference from the Schottky peaks (due to crystal-field effects) in the temperature range of interest (viz., above 20 K in $PrCu_2Si_2$). If the Schottky anomalies interfere, then the C versus T plots for Pr and Gd are not expected to be parallel. The data shown in figure 6 clearly suggest that the plots are practically parallel in a wide temperature range, thereby suggesting that the contribution due to Schottky peaks in the temperature interval 30–80 K for the Pr sample is presumably insignificant. Above 80 K, there is a marginal deviation from this behavior (not shown in the figure), which can also arise from different Debye temperature values. It may be remarked that Boulier *et al* [17] have shown that short range order effects persist up to 30 K in $GdCu_2Si_2$, and hence the two curves in figure 6 below 30 K are not expected to be parallel. We would like to avoid further discussion of these results, as it is not the main aim of this article.

4. Conclusion

We have described a simple and unconventional design of a calorimeter to measure heat-capacity in a wide temperature range employing semi-adiabatic heat-pulse method.

The results shown in figures 4–6 convince that the statistics and the quality of the data are satisfactory. We believe that the same calorimeter can be used to measure heat-capacity at much higher temperatures by making the following provisions: (i) replacement of the Ge sensor by Pt sensor and (ii) another stainless steel tube can be provided surrounding the tube T1 and the temperature of the Cu tube in T1 can be controlled (to that of sample) after evacuation of the annular space. We hope that the design described here can be employed to make thermopower and thermal conductivity measuring instruments of top-loading type with necessary modifications of the sample holder.

Acknowledgement

We thank R Vijayaraghavan for his support.

References

[1] E S R Gopal, *Specific heats at low temperatures* (Plenum Press, New York, 1966) and references therein

[2] E Gmelin, *Thermochimica Acta* **29**, 1 (1979)

[3] E Gmelin, *Thermochimica Acta* **110**, 183 (1987)

[4] O Joseph, D E Moody and J P Whitehead, *J. Phys.* **E9**, 595 (1976)

[5] N Sankar, V Sankaranarayanan and G Rangarajan, *Indian. J. Pure Appl. Phys.* **27**, 408 (1989)

[6] T Ashworth and H Steeple, *Cryogenics* **8**, 225 (1968)

[7] S Banerjee, M W J Prins, K P Rajeev and A K Raychaudhuri, *Pramana – J. Phys.* **39**, 391 (1992)

[8] Y Nakazawa, Ph. D thesis, The University of Tokyo, Tokyo (1990)

[9] R C Weast, *Handbook of chemistry and physics* (CRC Press, Ohio, 1976) p. D167 and references therein

[10] D L Martin, *Rev. Sci. Instrum.* **58**, 639

[11] E Gmelin and P Rodhammer, *J. Phys.* **E14**, 223 and references therein

[12] I Das, E V Sampathkumaran and R Vijayaraghavan, *Physica* **B**, (1993) (in press)

[13] I Das, E V Sampathkumaran, K Hirota and M Ishikawa, *Phys. Rev.* **B49**, 3586 (1994)

[14] E V Sampathkumaran, I Das and R Vijayaraghavan, *J. Phys.* **6**, L11 (1994)

[15] E V Sampathkumaran and I Das, *Physica* **B186–188**, 328 (1993)

[16] E V Sampathkumaran, I Das, R Vijayaraghavan, K Hirota and M Ishikawa, *J. Magn. Magn. Mater.*, **108**, 85 (1992)

[17] M Boulier, P Lethuillier and D Schmitt, *Phys. Rev.* **B43**, 13137 (1991)

PRAMANA
— journal of
physics

© Printed in India

Vol. 42, No. 3,
March 1994
pp. 261–270

Losses in pendular suspensions due to centrifugal coupling

SANGITA N PITRE, S V DHURANDHAR, D G BLAIR* and JU LI*
Inter University Centre for Astronomy and Astrophysics, Post Bag 4, Ganeshkhind, Pune 411 007, India
* Department of Physics, University of Western Australia, Nedlands, WA 6009, Australia

MS received 21 June 1993; revised 2 November 1993

Abstract. We present an analysis of the centrifugal coupling of a simple pendulum to a dissipative support. We show that such a coupling leads to an amplitude dependent quality factor. For amplitudes which could be present in laser interferometer gravitational wave detector suspensions, this mechanism could limit the quality factor of the test mass suspension significantly to 10^{10} and should be considered in the design of advanced LIGO type detectors.

Keywords. Gravitational wave detectors; seismic isolation; Q-factor.

PACS Nos 04·30; 46·30

1. Introduction

Large scale laser interferometric gravitational wave detectors are being planned [1–5] and constructed [6]. Such detectors require extremely low amplitudes of vibrational noise in their mirror suspensions. The chief sources of noise are seismic vibrations and thermal noise. The former can, in principle, be reduced to arbitrarily low levels by suitable filter design. Thermal noise however, is generated internally by the acoustic losses in the mirror and by the losses in the mirror suspension. Internal mirror losses generally give rise to a thermal noise peak in the kHz range (assuming a suitable shape for the mirror). Pendulum losses give rise to a noise amplitude which, in the frequency range ~ 1–100 Hz, is generally expected to dominate the noise of a large scale detector.

In figure 1 we show the predicted thermal noise of a 100 kg, 1 Hz pendulum for a range of Q-factors. There would clearly be a great advantage in using pendula with Q-factors $> 10^{10}$ (see [7]). Losses in such pendula are normally considered to arise from elastic losses in the flexure or hinge from which the pendulum is supported. The elastic losses can be substantially reduced, due to the fact that the majority of the *elastic* stored energy is in the gravitational potential energy. Practical pendulum designs can use thin foil flexures in which typically only one part in 10^4 of the elastic stored energy is in the lossy foil. It has been shown by Saulson [8] that under these circumstances the pendulum Q-factor is given by,

$$Q = Q_0 \frac{K_g}{K_s}, \tag{1.1}$$

where K_g/K_s is the ratio of the elastic spring constants and Q_0 is the intrinsic Q of the foil. Since materials such as niobium have an intrinsic $Q \sim 10^6$ at room temperature,

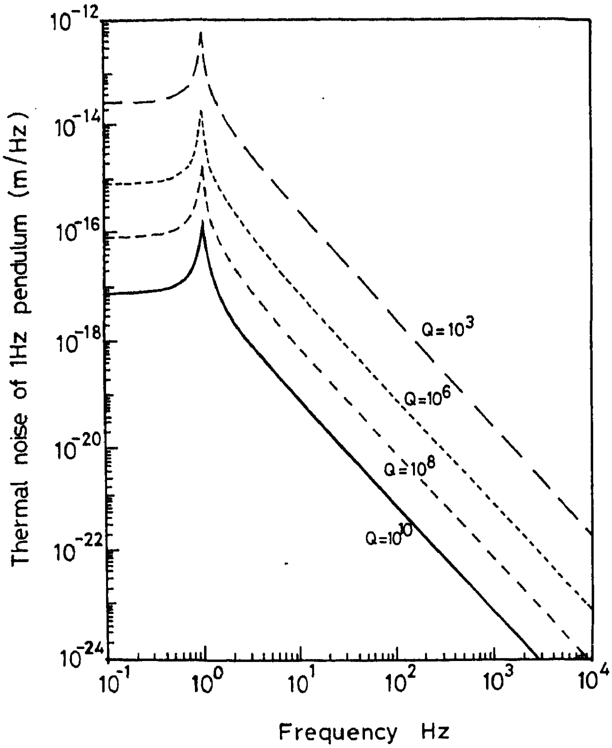

Figure 1. The frequency dependence of the thermal noise predicted for a 1 Hz pendulum for various Q-factors. A pendulum with $Q = 10^{10}$ would allow a strain sensitivity of about $10^{-23}/\sqrt{\mathrm{Hz}}$ at 35 Hz in a 1 km laser interferometer gravitational wave detector.

pendulum Q-factors limited by linear losses in the suspension exceeding 10^{10} are possible [9].

However, even if the elastic loss was reduced to nearly zero using suitable materials and configurations, losses in practice can remain due to the coupling of the pendulum to its support structure. There are two ways in which this coupling can arise:

(a) One is a simple linear horizontal coupling of the suspension point to its support structure. This can be modelled by conventional linear analysis and is accounted for in most isolation system designs. These recoil losses are difficult to overcome. However, Hough *et al* [10] and Braginsky [11] have demonstrated Q factors $\sim 10^7$ and 10^8 respectively. The thermal noise associated with recoil losses is filtered by the suspension. Thus a significant level of recoil losses is tolerable as shown by Saulson [8].
(b) The second is a loss which arises from the centrifugal (vertical) coupling of the pendulum to vertical losses in the support structure. This is a non-linear problem, surprisingly difficult to solve. Here we present the solution to this problem, and give examples of the limiting Q-factor in various situations.

The dominant and relevant effect of a high quality factor is to reduce the thermal noise of the pendulum suspension. The dependence of the thermal noise spectral density on the quality factor has been derived earlier [1]. The thermal noise is given in terms of the quantity $\tilde{h}^2$ where the *tilde* denotes the Fourier transform of the quantity below it. The quantity h is the metric perturbation of the gravitational wave one is trying to detect. The thermal noise is given in terms of this metric perturbation. Thus,

$$\tilde{h}^2_{\text{thermal}} \sim \frac{16kT\omega_p}{mQ_{\text{eff}}\omega^4 l^2}. \tag{1.2}$$

Here k is the Boltzmann constant, T the absolute temperature, l the length of the arm of the laser interferometric detector, Q_{eff} the effective quality factor, ω_p the pendulum frequency and ω the frequency of the thermal noise. The $\tilde{h}$ falls off as $Q_{\text{eff}}^{-(1/2)}$ and therefore a higher Q_{eff} has the effect of reducing the thermal noise. If we observe the noise profiles for burst or continuous wave sources [1] of laser interferometric gravitational wave detectors, the thermal noise is present at the lower end of the band of detectable frequencies. Increasing the Q_{eff} will push this thermal curve 'downwards' reducing the noise at lower frequencies near the seismic cut-off. This will have the effect of increasing the signal to noise ratios for sources which emit gravitational waves predominantly at lower frequencies. For example coalescing binaries which radiate more power at lower frequencies will have their signal to noise enhanced if the quality factor is boosted.

2. The equations of motion

We consider here a simple model of a seismic isolator which consists of a pendulum attached to a spring. The spring motion has a dissipative element in it while the dissipation in the pendular motion is neglected. We set up the classical equations for the system which turn out to be non-linearly coupled. We then solve this system of equations numerically and find that under the assumption that the amplitudes of the motion are small, analytic approximations are possible and an analytic but approximate solution can be derived. We finally compute an effective quality factor for the pendular motion which now depends on amplitude (or time) because the motion is not damped according to the usual exponential law.

Consider the system as shown in figure 2. In terms of the two dynamical variables, x the extension of the spring beyond its normal length and θ the angular displacement of the pendulum, the Lagrangian $\mathscr{L}$ for the system is given by,

$$\mathscr{L} = \frac{1}{2}M(\dot{x}^2 - \omega_s^2 x^2 + l^2\dot{\theta}^2) - Ml\sin\theta\dot{x}\dot{\theta} + Mg(x + l\cos\theta), \tag{2.1}$$

where M is the mass of the bob of the pendulum, l the length of the pendulum, ω_s the natural frequency of the spring and g the acceleration due to gravity. We assume that the damping of the spring is proportional to the velocity which means that the damping force Q_x is of the form,

$$Q_x = -2\frac{M}{\tau}\dot{x}, \tag{2.2}$$

where τ is the damping time constant. We assume that the damping for the θ motion can be neglected ($Q_\theta = 0$). In terms of the dimensionless variables,

$$\alpha = \frac{\omega_p}{\omega_s}, \quad z = \frac{x}{l} - \alpha^2, \quad Q = \frac{1}{2}\omega_s\tau, \quad T = \omega_s t, \tag{2.3}$$

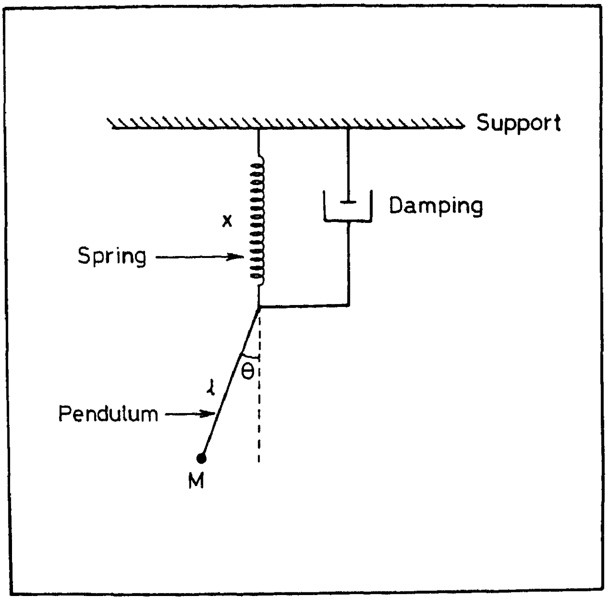

Figure 2. A schematic diagram of a simple model for a seismic isolator is shown which consists of a pendulum attached to a spring. The spring motion is damped with the damping force proportional to the velocity.

where, $\omega_p = (g/l)^{1/2}$, the Euler–Lagrange equations can be reduced to the following equations of motion, for the two dynamical variables z and θ:

$$\ddot{z} + \frac{1}{Q}\dot{z} + z = \theta\ddot{\theta} + \dot{\theta}^2, \tag{2.4a}$$

$$\ddot{\theta} + \alpha^2\theta = \theta\ddot{z}, \tag{2.4b}$$

where the dot is the time derivative with respect to the dimensionless time T. *The aim is to compute the quality factor Q_{eff} of the θ motion.*

The equations are too complex to solve in full generality. They are nonlinearly coupled and do not possess any exact solutions. There are basically only two parameters, namely, α and Q. All the other quantities have been thrown into the background by resorting to dimensionless units. However, if the actual values are known for these parameters it is possible to obtain approximate analytic solutions. We may guess approximate analytic solutions by first solving the equations numerically.

3. The solutions

3.1 *General features*

Many of the qualitative features of the solutions can be seen by examining the nature of the equations themselves, but in order to get a quantitative idea of the timescales of oscillations and damping we resorted to numerical computations. Although the parameters used in the numerical solutions did not correspond to actual situations, they had the advantage of providing us with useful guidelines in assuming the form of the analytic solution. We experimented with several values for the initial parameters (for instance, $z_0 = \dot{z}_0 = \dot{\theta}_0 = 0, \theta_0 = 0{\cdot}05$, where the subscript '0' denotes the values of the variables at the initial time t_0) and came up with the following salient features:

(i) The θ motion is oscillatory with period α and the amplitude of the oscillations is damped over a much larger timescale (this is for a sensible choice of the parameters). We have taken the computation far enough up to $T = 10^4$ so that the damping is appreciable.
(ii) For lower values of α and θ_0 the damping is milder and is not easily seen. For such values we have taken the computation till $T \sim 10^6$. However the results are not qualitatively different.
(iii) The z-motion consists of two superimposed oscillations:

(a) The cycles are at a frequency 2α. This is due to the quadratic nonlinearity, namely, θ^2 forcing the z motion.
(b) On these oscillations is superimposed a transient of about unit frequency which is damped at the rate $e^{-T/2Q}$. At late times the transients die out and the spring oscillates with the frequency 2α.

At late times both the θ and z oscillations are slowly damped. The damping is not exponential but slower and is quantified in the next section. It is remarkable that in the regime of interest, analytic solutions to this system of equations are possible. The above mentioned features are observed in the analytic solution.

3.2 *The transients and the particular solution*

Since the θ displacement is small, we start with a trial solution

$$\theta(T) = \theta_1 \cos(\alpha T), \tag{3.1}$$

so that at $T = 0$ the θ displacement is maximum, namely, $\theta_1 = \theta_0$. θ_1 here is assumed to be constant although it happens to be a slowly varying function of time on the time scale of the damping rate. For a few cycles this assumption is alright during which little decay in the amplitude occurs. The oscillation time scale is of course of the order of α^{-1}. This solution assumes that $\theta\ddot{z} \sim 0$ which is justified later. We further proceed to compute the right hand side of the z equation from equation (3.1). Thus,

$$\ddot{z} + \frac{1}{Q}\dot{z} + z = -\alpha^2\theta_1^2\cos 2\alpha T, \tag{3.2}$$

which means that the z motion is forced at twice the frequency of the θ oscillation, which is at the second harmonic of the θ oscillation. The total solution for $z(t)$ is obtained as a superposition of the transient solution and the forced solution. Thus,

$$z(t) = z_{\text{transient}}(t) + z_{\text{forced}}(t), \tag{3.3}$$

where,

$$z_{\text{transient}} = e^{-T/2Q}(A_1 \cos\beta T + A_2 \sin\beta T), \tag{3.4}$$

where, $\beta = (1 - (1/4Q^2))^{1/2}$, and A_1 and A_2 are to be determined from initial conditions imposed on the full solution. The forced solution is,

$$z_{\text{forced}} = z_1 \cos(2\alpha T + \Phi_1), \tag{3.5}$$

where,

$$z_1 = -\alpha^2\theta_1^2/A, \quad \tan\Phi_1 = \frac{2\alpha}{Q(1-4\alpha^2)}, \quad A = [(1-4\alpha^2)^2 + 4\alpha^2/Q^2]^{1/2}. \tag{3.6}$$

Again here the behaviour of z_1 is analogous to θ_1. The transient solution dies out in the timescale Q^{-1} so that at late times ($T \gg Q^{-1}$) only the forced solution survives.

The trial solution for $\theta(T)$ as given in equation (3.1) can be justified in the following way. We observe that if we choose $\alpha \sim 1$ or less and $Q \sim 1$ to 100 then $z \sim \alpha^2\theta_1^2$. Since the z motion is also sinusoidal with frequency $2\alpha, \ddot{z} \sim \alpha^4\theta_0^2$. Thus, the term $\theta\ddot{z}$ is of the order of $\alpha^4\theta_0^3$ which is very small. Therefore the assumption of neglecting this term in our trial solution for θ is not unjustified.

3.3 *Damped motion*

The motion is damped since the system loses energy because of the dissipation in the spring. We analyse the damping from energy considerations. We need to evaluate first the total average energy of the system and then relate it to the rate of loss of average energy. Since the dissipative element is in the spring, the system loses energy *only* through the z-motion. However, the θ-motion will also be damped because of the coupling. The instantaneous energy is the Hamiltonian of the system and is given in dimensionless units by,

$$E = \frac{1}{2}\dot{z}^2 + \frac{1}{2}\dot{\theta}^2 - \theta\dot{\theta}\dot{z} + \frac{1}{2}z^2 + \frac{1}{2}\alpha^2\theta^2. \tag{3.7}$$

We now substitute the late time solutions,

$$z = z_1(T)\cos(2\alpha T + \Phi_1), \quad \theta = \theta_1(T)\cos\alpha T, \tag{3.8}$$

where θ_1 and z_1 are 'slowly' varying functions on the timescale of α^{-1} in equation (3.7) and compute the average energy per cycle $\langle E\rangle$ of the oscillations. The calculation leads to,

$$\langle E\rangle = \left(\alpha^6\theta_1^4 - \frac{1}{4}\alpha^4\theta_1^4 + 2\alpha^6\theta_1^4\right)A^{-2} + \frac{1}{2}\alpha^2\theta_1^2. \tag{3.9}$$

Since θ_1 has been assumed to be small, the higher order terms in θ_1 may be neglected and to the lowest order in θ_1, we have, $\langle E\rangle \sim \frac{1}{2}\alpha^2\theta_1^2$. The rate of loss of energy is computed by first differentiating the expression for the Hamiltonian and then using the equations of motion. We then have,

$$\frac{\mathrm{d}}{\mathrm{d}T}E = -\frac{1}{Q}\dot{z}^2. \tag{3.10}$$

The average loss of energy per unit time can then be computed from equations (3.6) and (3.8) and averaging the trigonometric functions over unit time. Thus,

$$\frac{\mathrm{d}}{\mathrm{d}T}\langle E\rangle = -\frac{2\alpha^6\theta_1^4}{A^2Q}. \tag{3.11}$$

The milder damping rate, i.e. milder than the exponential rate, is evident from the above analysis and can be seen in the following way:

The dominant contribution to the energy comes from the θ motion and is quadratic in θ_1. On the other hand, the rate of energy loss is quadratic in z_1 since the damping, which is proportional to the velocity, is in this vertical mode. But since the θ mode is coupled quadratically to the z mode the rate of energy decay depends on the *fourth* power of θ_1. This is a much milder decay rate than the one compared to the exponential case, where the energy of the system as well as the energy decay rate, scale quadratically in the amplitude. Also since the rate of the decay of energy is governed by the amplitude of the oscillations in the above manner, the damping is less for lower amplitudes. This was one of our observations in subsection 3.1.

From (3.9) and (3.11) we get a differential equation for the decay of the average energy, or equivalently for the amplitude θ_1:

$$\frac{\mathrm{d}}{\mathrm{d}T}\theta_1^2 = -\frac{4\alpha^4\theta_1^4}{A^2 Q}. \tag{3.12}$$

Solving this equation with the initial conditions $T=0$, $\theta=\theta_0$, we have,

$$\theta_1(T) = \frac{\theta_0}{B(T)}, \tag{3.13a}$$

where,

$$B(T) = (1+\varepsilon T)^{1/2}, \quad \varepsilon = \frac{4\alpha^4\theta_0^2}{A^2 Q}.$$

The decay of the z-motion is obtained from equation (3.6). Thus,

$$z_1(T) = -\frac{\alpha^2\theta_0^2}{AB^2(T)}. \tag{3.13b}$$

Therefore we notice that the z motion is damped at a faster rate than the θ motion. This behaviour remains true for various values of α, Q and θ_0 as has been verified on the computer and cross checked with the above formulae. But if α and θ are very small then enormous amount of time is required on the computer to produce appreciable damping as can be seen from the foregoing discussion. The analytic solution then is useful in predicting the damping profile.

4. The effective Q for the pendular motion

Consider a damped simple harmonic oscillator with natural frequency ω_0 and damping time constant τ. Then the time dependence of the amplitude is $\sim e^{-t/\tau \pm i\omega_0 t}$. The quality factor Q is then given by the formula: $Q = \frac{1}{2}\omega_0\tau$. In terms of the dimensionless time T the effective quality factor Q_{eff} for general damped motion, which is not necessarily an exponential decay, is given by,

$$Q_{\mathrm{eff}} = \frac{1}{2}\alpha\left[-\frac{\mathrm{d}}{\mathrm{d}T}(\ln\theta_1(T))\right]^{-1}. \tag{4.1}$$

Using equation (3.13a), the above expression leads to the result,

$$Q_{\mathrm{eff}} = \alpha\frac{(1+\varepsilon T)}{\varepsilon}. \tag{4.2}$$

Therefore in this case the quality factor is a function of time which is to be expected since the damping is not exponential. We observe that, the Q_{eff} increases with time. At early times, i.e. when $\varepsilon T \ll 1$ the Q_{eff} is given by,

$$Q_{\mathrm{eff}} \sim \frac{\alpha}{\varepsilon} = \frac{A^2 Q}{4\alpha^3 \theta_0^2}. \tag{4.3}$$

We observe that at early times Q_{eff} is a constant and hence in this regime the system behaves like a normal damped harmonic oscillator i.e. the amplitude θ_1 decays exponentially with time $\theta_1(T) \sim e^{-\alpha T/2Q_{\mathrm{eff}}}$. However when $T \sim \varepsilon^{-1}$ the decay of the amplitude is slower than the exponential rate. Figure 3 compares the decay of the amplitudes of the two oscillators:

(a) exponentially damped,
(b) pendular, which corresponds to the system under consideration.

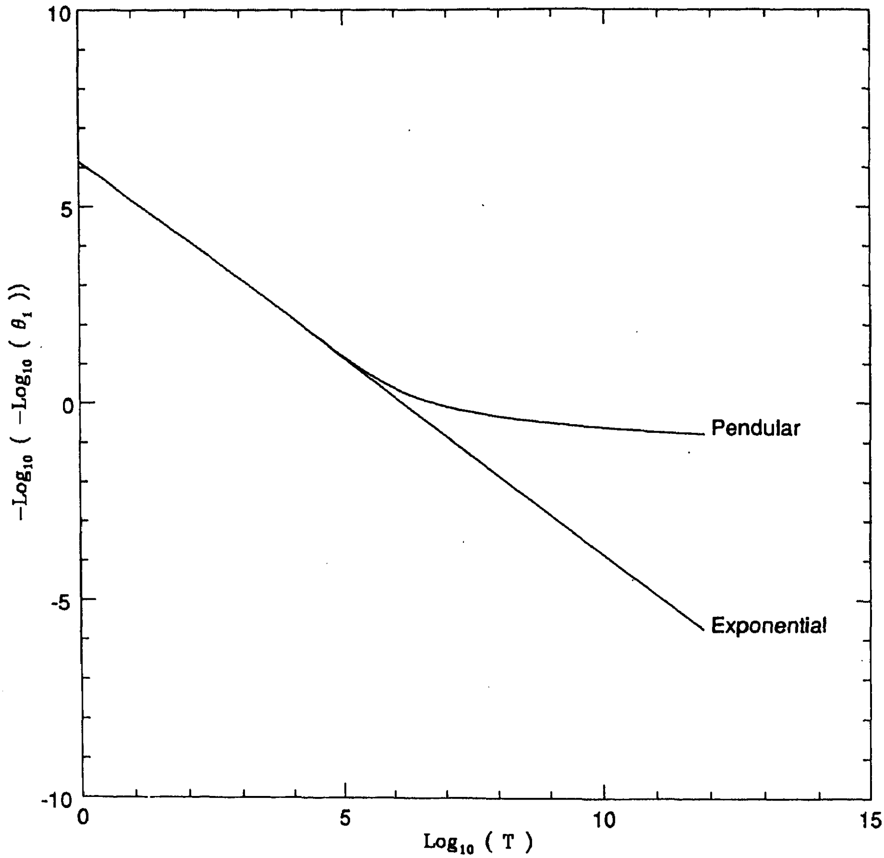

Figure 3. The figure depicts the decay of the amplitudes with time for the standard exponential case and for the model considered here (pendular). The parameters have the following values $\alpha = 0{\cdot}3$, $Q = 2$ and $\theta_0 = 0{\cdot}01$. (a) *exponential*: The amplitude is damped exponentially with time. This appears as a straight line with slope $= -1$ in the logarithmic scale. (b) *pendular*: In the model considered the amplitude decays slower than in the standard case (a).

In figure, $\alpha = 0{\cdot}3$, $Q = 2$ and $\theta_0 = 0{\cdot}01$ which corresponds to $\varepsilon \sim 10^{-6}$. It is convenient to use logarithmic scales for depicting the behaviour. We plot $-\log_{10}(-\log_{10}\theta_1)$ verses $\log_{10} T$. The usual case of the exponentially damped oscillator appears as a straight line with slope $= -1$. This curve is labelled as *exponential*. The intercept on the vertical axis turns out to be $\log_{10} Q_{\text{eff}} - \log_{10}(\frac{1}{2}\alpha \log_{10} e) - \log_{10}(-\log_{10}\theta_0)$ which increases with Q_{eff}. We observe that when $T \sim \varepsilon^{-1} \sim 10^6$ the pendular curve departs from the exponential and the decay is slower. Although the parameters used here are not realised in actual situations, they have the advantage of bringing out the difference in the behaviours of the two types of damping.

For the case of the spring constant $k \sim 10^7\,\text{kg}\cdot\text{s}^{-2}$, $M \sim 10^3\,\text{kg}$, $l \sim 1$ m and Q say 10, we have the following values for the relevant parameters: $\omega_s \sim 100$, $\omega_p \sim 3$, $\alpha \sim 0{\cdot}03$ and $A \sim 1$. From the equations (3.13) and (4.2) we get an amplitude dependent quality factor for the pendular motion. Thus,

$$Q_{\text{eff}} = \frac{A^2 Q}{4\alpha^3} \times \frac{1}{\theta_1^2}. \tag{4.4}$$

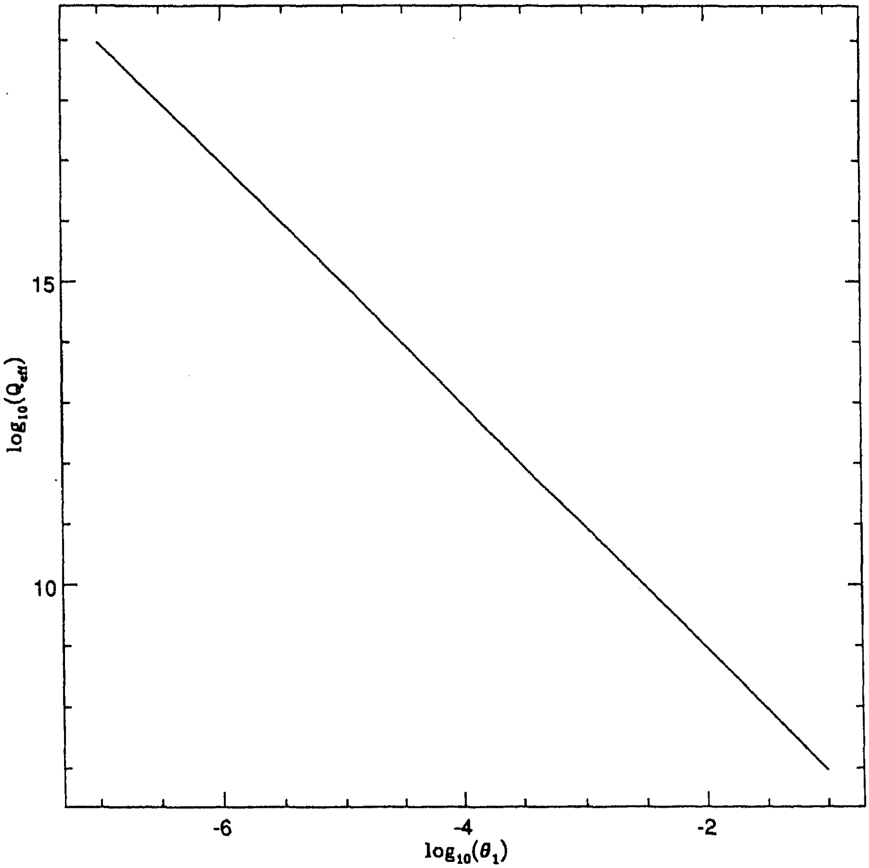

Figure 4. The figure shows that the quality factor Q_{eff} is amplitude dependent for the model considered here. The Q_{eff} is plotted versus the amplitude θ_1 in a logarithmic scale. We find that the Q_{eff} increases as the inverse square of the amplitude. In this figure the relevant parameters have the values $Q = 10$, $\alpha = 0{\cdot}03$ and hence the constant $A^2Q/4\alpha^3 \sim 10^5$.

Figure 4 displays this behaviour in which $\log_{10} Q_{\text{eff}}$ is plotted against $\log_{10} \theta_1$. For the values of the parameters mentioned above, the constant $A^2 Q/4\alpha^3 \sim 10^5$. The tendency is for the Q_{eff} to increase with the decrease of amplitude. Therefore a value of $Q_{\text{eff}} \sim 10^{10}$ is not impossible under the circumstances.

5. Conclusions

We have shown that the coupling of a pendulum to a lossy support structure can create an amplitude dependent Q-factor and this can significantly degrade the Q of an intrinsically high Q pendulum if care is not taken in the design. Since metal and rubber vibration isolator elements have intrinsically low Q, these can contribute particularly large amplitude dependent losses. The coupling of noise into such a suspension will occur through *parametric amplification* type processes more familiar in optical and radio frequency parametric amplifiers. Some interferometer designs have proposed a suspension point servo which uses a secondary interferometer to lock together the pendulum suspension points. Such a suspension does not eliminate seismic noise, but forces it into common mode so that there is no differential motion. In such a situation residual seismic amplitudes could be large enough to degrade the suspension Q through the mechanism discussed here.

Acknowledgement

One of us (SNP) thanks C-DAC for research assistantship.

References

[1] J Hough *et al*, Proposal for a Joint German–British Interferometric Gravitational Wave Detector, *MPQ* 147, (1989)

[2] A Brillet and A Giazotto *et al*, VIRGO Final Conceptual Design, INFN, Pisa, (1992)

[3] Australian International Gravitational Research Centre Proposal, The University of Western Australia, (1990)

[4] D G Blair, D McClelland and H Bachor, Gravitational Waves and the AIGO proposal, *Australian and New Zealand Physicist*, **29**, 4, (1992)

[5] H Bachor, D G Blair, J Ferreirinho, D McClelland, R J Sandeman, P Veitch and A Wrightson; Should Australia have a gravity telescope? *Asia-Pacific Physics News*, **5**, (1990)

[6] A Abramovici, W E Althouse, R W P Drever, Y Gürsel, S Kawamura, F J Raab, D Shoemaker, L Sievers, R E Spero, K S Thorne, R E Vogt, R Weiss, S E Whitcomb and M E Zucker. LIGO: The laser interferometer gravitational wave observatory, *Science*, **256**, 325 (1992)

[7] Ju Li, D G Blair and M Notcutt, Ultra high Q pendulum suspensions for gravitational wave detectors. (To be published 1992)

[8] P Saulson, *Phys. Rev.* **D42**, 2437 (1990)

[9] D G Blair, L Ju and M Notcutt, *Rev. Sci. Instrum.* **64**, 1899 (1993)

[10] W Martin, Ph. D. thesis, University of Glasgow, U.K., (1978)

[11] V B Braginsky, V F Mitrofanof and O A Oklirimenko, *Phys. Lett.* **A175**, 82 (1993)

PRAMANA
— journal of
physics

© Printed in India

Vol. 42, No. 3,
March 1994
pp. 271–282

High pressure measurement with simple piston gauge in static condition

J K N SHARMA, KAMLESH K JAIN and H N P PODDAR
National Physical Laboratory, K S Krishnan Road, New Delhi 110012, India

MS received 15 November 1993; revised 18 February 1994

Abstract. This paper describes the characterization of the newly developed piston gauge pressure standard at the National Physical Laboratory (NPL), with particular reference to its fall rate, engagement length of the piston and the deceleration rate for the measurement of hydraulic hydrostatic pressure up to 60 MPa. The low pressure effective area of the gauge derived from its dimensional measurements when compared with the value obtained by its direct calibration against NPL transfer pressure standard agrees within 0·025%. The pressure gauge is quite stable, reproducible and has a sensitivity of 3 ppm. Though the theoretically calculated value of the pressure coefficient is low as compared to the experimentally observed one in its absolute terms, the pressure dependent effective area agrees within ± 0·025% over whole of the pressure range which is well within the uncertainty statement of the two independent techniques used.

Keywords. Piston gauge; pressure measurement; pressure standard.

PACS Nos 47·80; 07·10

1. Introduction

With the advancement of scientific and technological research and rapid industrialisation in the developing countries a need is felt to have a reliable, reproducible secondary pressure standard with long-term stability. The pressure can be measured by simple Bourdon gauges or the liquid column manometer. The use of the former is limited due to the large uncertainty in the pressure measured whereas the use of the latter is not common due to requirement of large column height. However, the pressure balance/piston gauges are widely used as primary pressure standard [1–3] over a wide range of pressure, from a few kilo pascals to several hundred mega pascal, with a relatively low uncertainty of the order of a few ppm in the measured pressure.

In piston gauges a cylindrical piston rotates in a closely fitted circular cylinder. The pressure at the base of the piston is defined as the ratio of the total downward force on the piston to the effective area (A_e) of the gauge when floating at its operating level. The accuracy of measuring pressure using these gauges depends on the accuracy of both force and pressure dependent effective area measurement. The pressure dependent effective area is most often attributed to the elastic distortion of the piston-cylinder assembly. At low pressures (barometric pressure region) the changes in the effective area caused by the elastic deformation of piston-cylinder assembly are very small and are usually negligible [3]. The effective area of simple geometry large diameter piston gauges can be calculated analytically by the dimensional measurement and thermo-mechanical properties of the piston-cylinder assembly [1, 4, 5]. At higher pressure besides the dimensional uncertainty there is an additional uncertainty in determining the effective area of a piston gauge due to the relatively large elastic distortion of the piston-cylinder assembly. As the high pressure pistons and cylinders, in general have relatively small diameters, a given dimensional uncertainty results in larger uncertainty in both the low pressure effective area and the elastic distortion coefficient of the gauge. The estimated accuracy of the pressure measured by the gauge is mainly limited by how precisely the pressure distortion coefficient of the piston gauge can be determined at least for gauges of the simple design in which the pressurising fluid acts only on the inside (and sometimes end) surface of the cylinder. In gauges of the re-entrant design the pressurising fluid acts over some or all of the outer surface of the cylinder as well. In such cases the ability to measure or predict the overall distortion coefficient of the piston and cylinder becomes quite complicated [2].

Different ways of dealing with the pressure coefficient and hence the pressure dependent effective area have led to various piston gauge designs, various materials from which the piston cylinders are made and various pressure ranges for which they are to be used. More recently, we [6] have shown an agreement of 5 ppm in the effective area values of the piston gauge of 28 MPa full scale pressure, obtained from the standard gauge used either in the primary controlled clearance, or simple mode. The use of the controlled clearance piston gauge is quite complicated, time consuming and it is an expensive piece of equipment compared to the simple piston gauge. Simple piston gauge is easy to use and one needs only a few operating parameters to calculate pressure which minimises errors. It is a much preferred method to measure pressure up to about 500 MPa.

With this aim in view a piston gauge to be used as transfer pressure standard/master standard in industrial organisations up to 60 MPa in hydraulic hydrostatic pressure region was designed and fabricated at NPL. The systematic study of its metrological characterisation, in particular, the parameters like the best piston position, fall rates, and rotation speed etc. have been made and the results of these studies are reported here. Though the results presented here relate to one of the four such gauges developed at NPL, they are representative of all the four gauges.

2. Theory

The pressure generated at the reference level of a piston gauge is given by Heydemann and Welch [1]

$$P = \left[\sum_{i=1}^{n} M_i(1 - \rho_{\text{air}}/\rho_i)g + \gamma c \right] \Big/ (A_e(\rho)) \tag{1}$$

where M_i is mass of the ith weight, ρ_{air} is the density of air in the vicinity of the piston, ρ_i is the density of the ith weight, g is the local acceleration due to gravity, γ is the surface tension of the operating fluid, c is the circumference of the piston and A_e is the effective area of the gauge.

The effective area A_e of a controlled clearance piston gauge is typically expressed as [7].

$$A_e = \pi r_P^2(1 + b_P P)[1 + d(P_z - P_j)][1 + (\alpha_P + \alpha_c)(T - T_r)] \tag{2}$$

where r_P is the piston radius for zero applied pressure, b_P is the pressure distortion coefficient of the piston, P is the pressure at the reference level of the piston, alpha p, c are the thermal expansion coefficients of the piston (p) and cylinder (c). T is the absolute temperature of the piston and the cylinder, T_r is the absolute reference temperature, d is the jacket pressure coefficient, P_z is the zero clearance jacket pressure, P_j is the operating jacket pressure when dealing with the controlled clearance primary pressure standard. These parameters can either be measured or determined from the knowledge of the mechanical properties of the material which the piston and cylinder are made of. In practice r_{P}, t, d, P_z and P_j are usually measured, b_{P} is calculated, alpha p, c are usually obtained from the manufacturer without the need of any other more accurate pressure standard.

If the same controlled clearance piston gauge is used in the simple mode then the applied jacket pressure P_j in eq. (2) becomes zero. It is also possible to derive an independent expression for the effective area of the simple piston gauge

$$A_e = \pi r_{\mathrm{p}}^2(1 + H/r_{\mathrm{p}})(1 + b_{\mathrm{p/c}}P) \times [1 + (\alpha_{\mathrm{p}} + \alpha_{\mathrm{c}})(T - T_r)] \tag{3}$$

where H is the gap within the piston and cylinder for low applied pressure. In practice it is very difficult to measure H dimensionally. The simplest way is to determine the area of the piston and cylinder to an accuracy of 1 ppm by dimensional metrology, whereas b_{P}/c, the pressure distortion coefficient of the piston-cylinder combination, can either be determined on the basis of elastic theory or experimentally by cross-floating the test gauge against another piston gauge the pressure dependent effective area of which is known to a fairly high accuracy. The theoretical determination of b_{P}/c based on elastic theory requires the measurement of outer and inner diameters of the cylinder with a fairly high accuracy which is difficult to obtain as discussed above. Moreover, the value of b_{P}/c calculated theoretically from elastic theory is based on a few approximations and these along with the larger uncertainty in the diameter measurement add a large amount of uncertainty in the estimation of b_{P}/c value theoretically. It would not be out of place to mention that generally the small diameter piston and cylinder are used to measure pressure beyond 10 MPa. In the case of small diameter piston-cylinder, experimental methods are generally used to obtain the pressure distortion coefficient.

However, in these studies the value of b_{P}/c has been determined by both these methods. The effective area of a piston gauge under test can be expressed [5] as

$$\begin{aligned} A_e &= \{A_0(1 + b_{\mathrm{P}})[1 + (\alpha_{\mathrm{P}} + \alpha_{\mathrm{c}})(T - T_r)]\}_T \\ &= \sum_{i=1}^{n} \frac{\left[M_i\left(1 - \frac{\rho_{\mathrm{air}}}{\rho_{\mathrm{mi}}}\right)_g\right]_T}{P_s + \Delta P} \end{aligned} \tag{4}$$

P_s is the pressure at the reference level of the standard gauge, Δp is the head correction $(\rho_f - \rho_{\mathrm{air}})\, gh$, where h is the height difference between the reference levels of the two gauges and ρf is the density of the pressure transmitting fluid, Δp can be positive or negative depending on whether the reference level of the standard is lower or higher than that of the test gauge.

3. Experiment

The schematic representation of the NPL-designed piston gauge pressure standard used in these studies, designated as NPL-60, is equipped with a piston-cylinder device of a simple geometry and capable of measuring/generating full scale pressure up to 60 MPa, (see figure 1). The pressure measurement range can be extended upto 100 MPa by using different piston-cylinder assembly. The piston is rotated manually to relieve friction. The piston of die steel and the cylinder of special steel are hardened to Rockwell C 60. The nominal area of the piston is 1·64 E-5 meter square. Two NPL transfer and secondary pressure standards i.e. NPL-100 and NPL-140 used during these studies have the total estimated uncertainty of 74 ppm at 3 sigma level to the full scale'pressure of 100 and 140 MPa, respectively. The characteristics of these standards are well documented during the international intercomparison exercise carried out by the high pressure working group of BIPM in hydraulic hydrostatic pressure region up to 100 MPa [8]. The metrological characteristics of these two standards are given in table 1 alongwith the parameters associated with the new NPL-60 standard as derived during these studies.

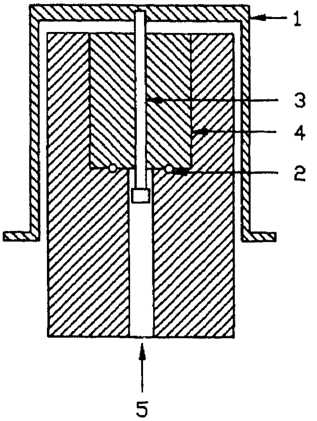

Figure 1. Schematic cross-sectional view of the piston and cylinder assembly for the pressure standard (NPL-60).
(1) Weight loading table; (2) "O" ring: (3) piston (4) cylinder; (5) pressure input.

Table 1. Description of the piston gauges used.

Parameter	NPL-140	NPL-100	NPL-60 (Test)
Range (MPa)	0·24 – 240	0·2 – 100	5 – 60
Material of piston and cylinder	cemented tungsten carbide	tungsten carbide	Steel
Effective area at zero applied pressure and at ref. temperature (E-5 m^2)	1·680244	9·80487	1·646127
Coefficient of thermal expansion of piston and cylinder (E-6 c^{-1})	9·1	9·0	23·0
Distortion coefficient (E-12 Pa^{-1})	2·76	0·3	4·3
Estimated total uncertainty of the effective area (3 sigma) ppm.	73	74	110

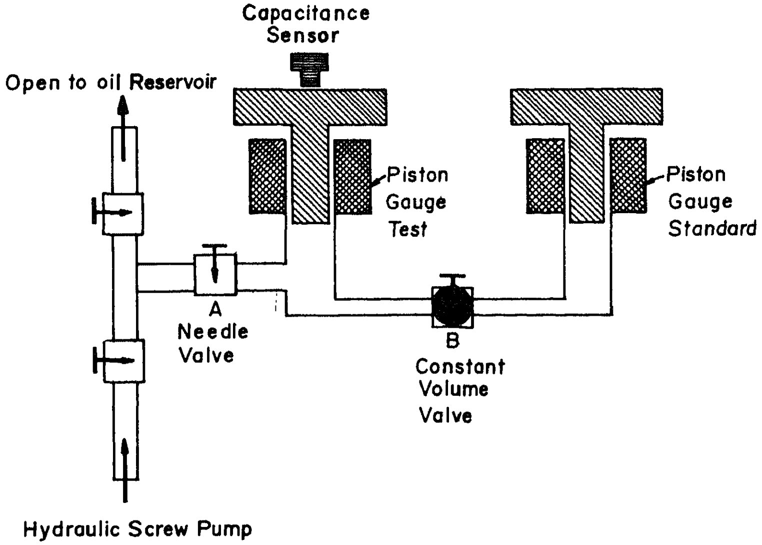

Figure 2. Experimental crossfloat arrangement between the test gauge and the standard piston gauge.

The piston gauges used during these studies were kept on heavy nonmagnetic stainless steel base in order to minimise vibrations and magnetic effects. The effective area of the NPL-60 piston gauge, hereafter designated as test gauge, was determined by direct calibration using the well-known crossfloat technique [1, 2, 7]. A schematic experimental arrangement for the crossfloat of the piston gauges is shown in figure 2. It comprises a manually operated needle valve and the hydraulic screw pump to generate the desired pressure and a constant volume valve B to isolate the piston gauges from one another. The bare minimum length of all the connecting pressure lines is used to have a better crossfloat sensitivity. Before the crossfloat both piston gauges were levelled to ensure the verticality of the axis and the system was checked for leaks to the full scale pressure of 60 MPa. The piston gauges were loaded with the weights calculated to generate the desired pressure and then pressurised to float at the reference level. They were then isolated from rest of the pressurising system by closing valve A and subsequently from each other by closing valve B.

The fall rate of the test gauge, the area of which was being evaluated was measured using a capacitance type linear voltage displacement transducer to avoid any extraneous force on the piston. The output of the transducer was directly recorded on a X-T chart recorder moving at a constant speed of 6 cm/min which monitored both the position and the fall rate of the piston. The change in piston position is known with a resolution better than 5×10^{-3} mm and the time interval is determined better than 0·2 s.

All the measurements were made in an environment which provided stable temperature conditions of 23 ± 1 c. The temperature of the NPL-140 pressure standard was measured within 0·1 c by a mercury-in-glass thermometer placed near the pressure column. The temperature of the NPL-100 pressure standard was measured with a PRT attached just near the piston and its output was read with an auto ranging digital multimeter having a resolution of 2 mΩ corresponding to a temperature resolution of 0·005 c. The temperature of the test gauge was measured with a PRT attached to the pressure column and the output of the PRT is read on the digital display having a resolution corresponding to 0·01 c.

By adjusting fractional weights on the test gauge which was generating comparatively lower pressure, crossfloat equilibrium was achieved as determined when the test gauge had the same fall rate irrespective of whether the valve B was closed or opened. The pressure was then raised and the same procedure was repeated, up to the full scale pressure of 60 MPa. A period of 30 min between the two successive observations was found adequate to allow the system to return to equilibrium and about 10 min was required to repeat observations at each pressure point.

As it was not possible to bring the reference level of individual piston gauges to the same operating level during crossfloat, a pressure head correction term was applied to compensate for the difference in the operating levels. The reference level of NPL-60 was lower by 0·050 m against NPL-100 whereas it was 0·105 m against NPL-140 standard.

Throughout these studies, the piston of the NPL-60 was manually rotated clockwise so as to maintain the piston rotational speed of 25 ± 10 rpm. The NPL-100 and NPL-140 pressure standards were rotated anti-clockwise with a rotational speed of 25 ± 5 rpm by a pulley system coupled to a dc motor.

4. Results and discussion

The performance of the gauge is evaluated by measuring its deceleration rate and sink rate at different applied pressures. It is desirable to have small sink rate to get high accuracy during the crossfloat equilibrium of the two gauges. Moreover, it helps to trace out the leakage in the system, if any, and also the deterioration of the piston and cylinder surfaces over a period of time. During these studies the manually rotated piston has sufficiently large deceleration rate (figure 3) owing to large diameter masses used. Typically, the sink rate of 4·6 E-4 m/min at 5 MPa is observed during

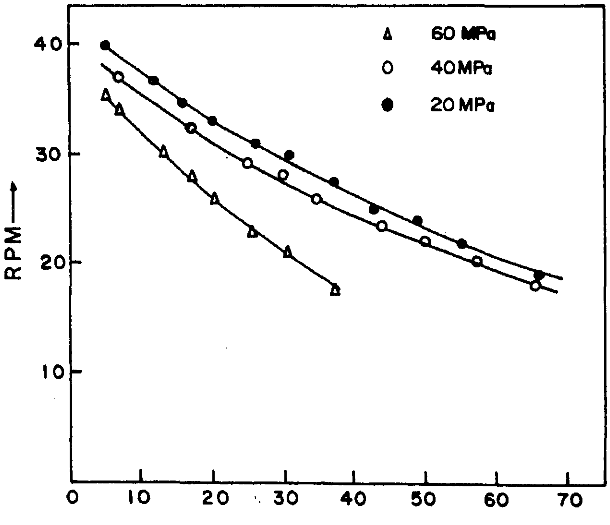

Figure 3. Deceleration rate of the piston with time operating at different applied pressures.

these studies which increases to 9·2 E-4 m/min at its full scale pressure value of 60 MPa which is sufficiently high for pressure measurements. The sink rates of the gauge were also measured at different engagement length of the piston and at different applied pressure. In all the cases the sink rates were well within the measurement uncertainty i.e. 2·5%.

Dimensional metrology has been used to characterise the test gauge (NPL-60). For calculating its effective area the model of Meyers and Jessup [9] has been used which assumes the piston cylinder as merely straight and free from taper, and there is no dependence of viscous drag on fluid viscosity. In practice, since the piston cylinder never posseses perfect geometry one could follow the method developed by Dadson *et al* [10] to derive the effective area of the gauge by simply averaging the diameter measurements. In these studies, the effective area was calculated by simply averaging the dimensional measurements taken at different points in a plane perpendicular to the piston-cylinder axis and in different plane along the axis. All the measurements were made on CMM machine (Model UPMC 850 CARAT, Carl Zeiss) having an uncertainty of 1 μm in the range used here. The diameter was measured at approximately five locations along the length of piston and cylinder. The measurements were repeated after the piston and cylinder had been rotated by 90 degrees. The straightness measurements of the piston as shown in figure 4 were taken in auto mode whereas the same could not be done for the inner diameter of the cylinder due to the limitations of the probe size. These measurements were made along the entire length of piston and cylinder at four different positions along the circumference and were repeated at least twice. The straightness and roundness measurements of both the pieces were made throughout its length of 40 mm and were within two micron. The diameter measurements of the piston and the cylinder were made and averaged. These values were then used as discussed above to calculate the effective area and the elastic distortion coefficient [1, 7] of the piston-cylinder assembly. Combining the elastic distortion 3·47 E-12/Pa, with the low pressure effective area 1·646863 E-5 sq meter as calculated, and taking into account the uncertainty due to roundness and straightness, the pressure dependent effective area of NPL-60 has an uncertainty of 200 ppm at its full scale pressure value of 60 MPa.

Alternatively, the effective area of the test gauge was determined by calibrating it against NPL standard gauges NPL-100 and NPL-140 using a well-known crossfloat

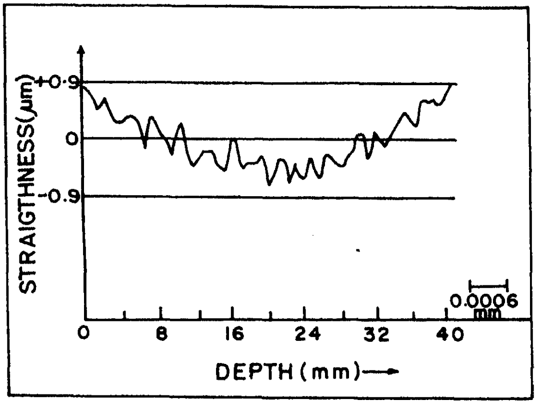

Figure 4. Dimensional measurement of straightness of the piston along its length of 40 mm. (Magnification 16300).

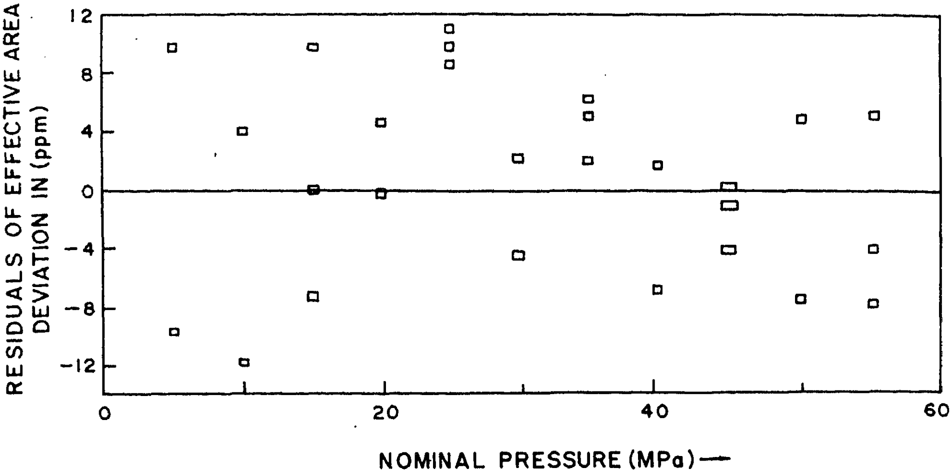

Figure 5. Deviation of measured values of the effective area of NPL-60 from the best linear fit $A_e = 1{\cdot}647127$ E-5 (1 + 4·3 E-12 P) when calibrated by NPL-100.

technique. A computer programme [11] that determines the effective area and the pressure coefficient of the test gauge based upon those of the standard was used to analyse the data. This program is based upon equations (1–4) above and also provides the standard deviation of the residuals of the area and the standard deviation of the coefficients.

In all the calibrations of the test gauge against the NPL-100 pressure standards, three test cycles were carried out. In one cycle the pressure was increased to 55 MPa and then decreased from 55 to 5 MPa and in the other two cycles the measurement proceeded from the highest pressure to the lowest and back to the highest. In one test cycle 11 observations were taken leading to a total of 33 observations for complete calibration.

Figure 5 shows a plot of residuals in the effective area of NPL-60 as a function of nominal applied pressure, when NPL-60 is crossfloated against NPL-100. This figure gives the deviation of the measured values of the effective area, in ppm, for the individual measured pressures, from the best low order fit equation $A_e = A_0(1 + b_p)$ where $A_0 = 1{\cdot}647127$ E-5 and $b = 4{\cdot}3$ E-12 and P is in Pa. The residuals of the effective area of the NPL-60 pressure standard are randomly distributed within ± 12 ppm. It may be concluded that the effective area of NPL-60 gauge has an uncertainty of 110 ppm (3 sigma) over the full scale pressure of 60 MPa. These uncertainties represent the combined systematic uncertainty of NPL-100 (74 ppm 3 sigma) with the random uncertainty of the individual calibrations.

Due to the relatively large difference in the values of b of NPL-60 obtained experimentally and by calculation from elastic theory, it is desirable to check the consistency of the effective area of NPL-60 obtained by these two independent methods. The NPL-60 was again calibrated against other NPL secondary standard which in turn has the tracability to NPL primary standard and has also been used in BIPM international intercomparison exercise up to 100 MPa [8]. This would show the existence of a relative systematic error if any, which would in turn increase the confidence in the estimated uncertainties of the test gauge.

NPL-60 was compared with NPL-140 secondary transfer pressure standard at 11 different standard pressures for a total of 33 observations. The deviations in the

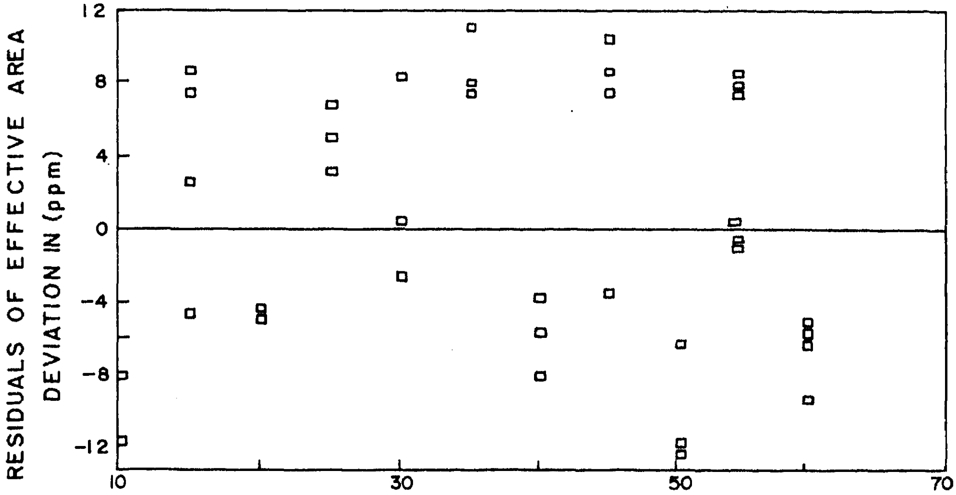

Figure 6. Deviation of measured values of the effective area of NPL-60 from the best linear fit $A_e = 1{\cdot}647188$ E-5 (1 + 4·4 E-12 P) when calibrated by NPL-140.

effective area, in ppm, for the individual measured pressures, from the linear best fit equation, $A_e = 1{\cdot}647188$ E-5 (1 + 4·43 E-12) where A_e is in m^2 and P is in pascal, are shown in figure 6. Similar scatter within ± 12 ppm in the residuals (observed minus calculated) of the effective area of NPL-60 is observed when it was calibrated against NPL-100 (figure 5) except in the low pressure region. The values of low pressure effective area (A_e) of NPL-60 as obtained by crossfloating against NPL-100 differ by 37 ppm from the values obtained against its calibration by NPL-140. Though the 37 ppm difference is outside the 3 sigma standard deviation of A_0 coefficient but considering the uncertainty associated with individual standards (table 1), this is well within the uncertainty statement of the standards. Further, b value of NPL-60 obtained from NPL-100 as compared to that obtained during the crossfloat against NPL-140 differ by 0·13 E-12/Pa, in absolute term, considering the 3 sigma standard deviation of these measured values i.e., 0·23 E-12/Pa and 0·24 E-12/Pa, respectively, the difference is not unreasonable. Additionally, this observed difference in b causes a relative difference in the effective area value by less than 1 ppm at a measured pressure of 5 MPa which increases to 7 ppm at its full scale pressure of 60 MPa (figure 7). The overall difference in A_e value of NPL-60 obtained by two independent calibrations against NPL-100 and NPL-140 is 37 ppm at 5 MPa increased to 43 ppm at 60 MPa is mainly dominated due to the basic difference of 37 ppm observed in its low pressure effective area value obtained by two independent calibrations. These results are hence within the measurement uncertainties associated with the individual transfer standard (table 1).

To have a check on the consistency in the value of the effective area of NPL-60, the crossfloat data have also been evaluated with reference to pressure generated by the two gauges (NPL-60 and NPL-140). Using (4) the pressure measured simultaneously by these two gauges at a specified reference level were calculated from 33 direct crossfloat intercomparison discussed earlier. The fractional pressure difference is

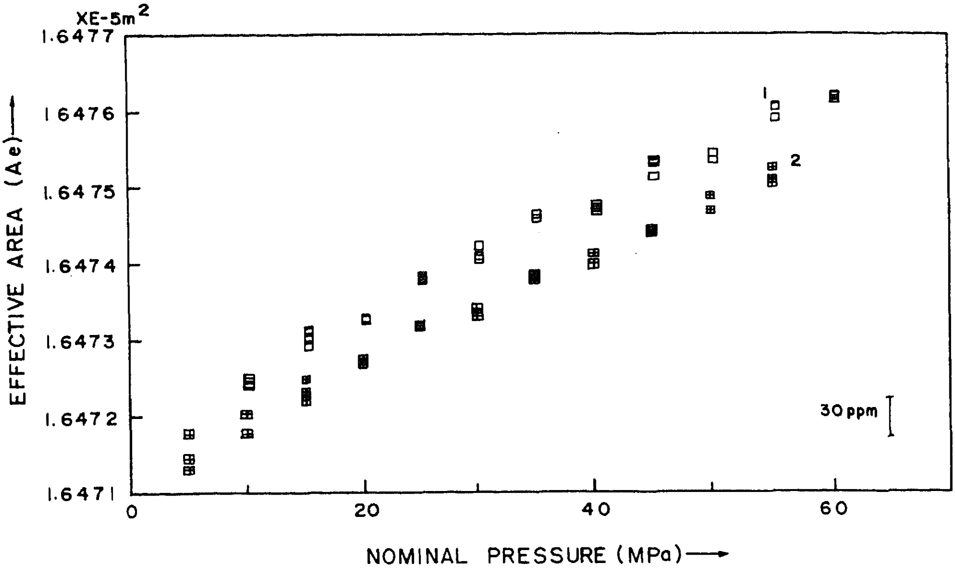

Figure 7. Effective area A_e of NPL-60 obtained by direct crossfloating against NPL-140 (1) and by crossfloating against NPL-100(2).

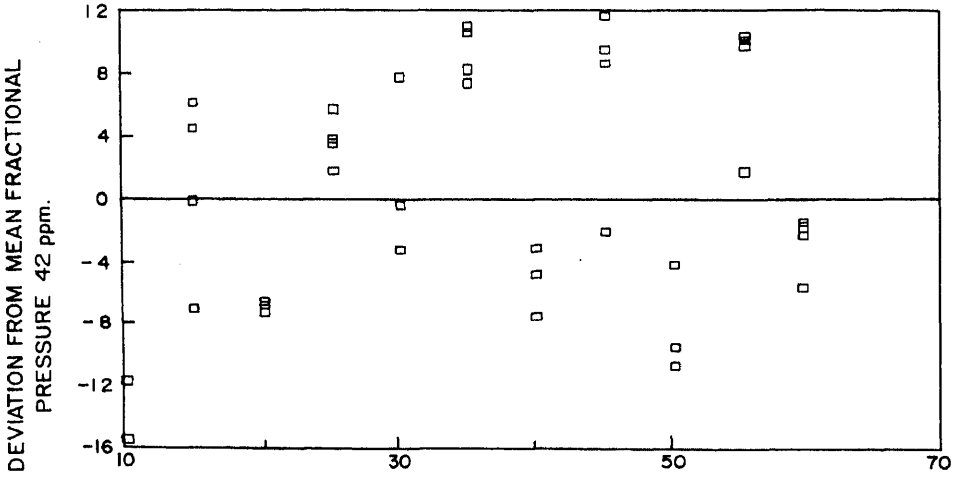

Figure 8. Fractional pressure differences from the mean value of 42 ppm between pressure measurements with the NPL-60 and NPL-140 pressure standard as a function of nominal applied pressure.

defined as

$$\frac{\Delta P}{P}=\frac{P_{P60}-P_{P140}}{P_{P140}}$$

where $P60$ is the applied pressure as measured by NPL-60 and $P140$ by NPL-140 transfer pressure standard. Figure 8 shows the deviation from the mean value of

42 ppm of the fractional pressure difference $\Delta P/P$ as a function of the nominal applied pressure. The distribution of the fractional pressure difference along its mean value is random and the overall behavior of the fractional pressure difference as expected is almost the same as that of the residuals of the effective area of the NPL-60 obtained during its calibration either against NPL-100 or NPL-140. So it is considered here that there is no significant discrepancy in the estimation of the pressure distortion of NPL-60 as determined by two different ways i.e. calibration against NPL standard and from elastic theory as discussed earlier. Though the systematic difference of 42 ppm exists throughout the pressure range: it is relatively small compared to the estimated uncertainty in the effective area of the standards used (table 1). The uncertainty in the measurement of pressure using a piston gauge arises from two main sources: (1) inherent uncertainties associated with the gauge itself and (2) other uncertainties associated with the local experimental conditions. The former is mainly attributed to the determination of the effective area of the piston-cylinder assembly and uncertainties in the mass of the load and/or piston. However the latter arises from the experimental procedures including (i) uncertainty associated with the measurement of temperature, (ii) correction due to any difference of reference levels and (iii) the resolution of the balancing criteria when the two systems are in equilibrium.

During the crossfloat of NPL-60 either against NPL-100 or NPL-140 fractional masses were so adjusted as not to contribute more than 1·2 ppm uncertainty at the minimum pressure of 5 MPa, which reduces to less than 1 ppm at the full scale pressure of 60 MPa. As the reference levels were measured to an estimated accuracy of 5 E–4 m and temperature was read with an estimated accuracy of ± 0·1°C, the contribution to the total estimated uncertainties in effective area due to temperature and difference in reference level is not significant compared to the total uncertainties associated with the standards.

5. Conclusion

1. Both methods of expressing the results of the measurements namely the comparison of simultaneous pressure measurement to a common reference level and the comparison of the effective area of NPL-60 as obtained by NPL-100 and NPL-140 standards show an agreement which is significantly better than that of the estimated total uncertainty of the two standards.
2. The NPL-60 standard can be used as a pressure standard with confidence where the accuracy requirement in pressure measurement is not more than 0·03%.
3. The larger uncertainty in the effective area of NPL-60 determined on the basis of the dimensional measurements is due to the fact that diameter measurements could not be performed with better accuracy than that used here.
4. These uncertainty values can further be improved by reducing the uncertainty in the effective area of NPL-100 and/or NPL-140 pressure standards or by making the dimensional measurements of NPL-60 with better accuracy.

Acknowledgement

The authors are thankful to Yash Pal for his help during the course of investigation.

References

[1] P L M Heydemann and B E Welch, *Experimental thermodynamics* edited by B LeNeindre and B Vodar (Guildford: Butterworth 1975) vol. II 147

[2] J K N Sharma and K K Jain, *Pramana – J. Phys.* **27**, 417 (1986)

[3] J K N Sharma, K K Jain and A K Bandyopadhyay, *Rev. Sci. Instrum.* **59**, 2063 (1988)

[4] R S Dadson, S L Lewis and G N Peggs, *The pressure balance: theory and practice* (National Physical Laboratory, Teddington, England HMSO) (1982)

[5] J K N Sharma, K K Jain, C D Ehrlich, J C Houck and D B Ward, *J. Res. Natl. Bur. Stand.* (1993) (to be published)

[6] K Jain, C Ehrlich and J Houck, *Rev. Sci. Instrum.* **63**, 3127 (1992)

[7] K Jain, C Ehrlich, J Houck and J K N Sharma, *Meas. Sci. Technol.* **4**, 249 (1993)

[8] J C Legras, G F Molinar, K Schmalhofer, J K N Sharma, M Thrane and D B Walker, *BIPM Internal Report* 90/10 (1990)

[9] C H Meyers and R S Jessup, *J. Res. Natl. Bur. Stand.* **6**, 1061 (1931)

[10] R S Dadson, R G P Greig and A Horner, *Metrologia* **1**, 55 (1965)

[11] J C Houck, G F Molinar and R Menghenzani, *J. Res. Natl. Bur. Stand.* **88**, 253 (1983)

ERRATA

Pramana – J. Phys., Vol. **41**, No. 4, October 1993, pp. 345–362

Ab-initio Hartree-Fock self-consistent-field calculations— An indigenous development of computer programs

by SAMBHU N DATTA

Eq. (18), p. 351

$\frac{2\pi^2}{\gamma_1 + \gamma_2}$ should be replaced by $\frac{2\pi^2}{\gamma_1 \gamma_2}$.

Eq. (A9), p. 361

$\frac{2\pi^2}{\gamma_1 + \gamma_2}$ should be replaced by $\frac{2\pi^2}{\gamma_1 \gamma_2}$.

Pramana – J. Phys., Vol. **42**, No. 1, January 1994, pp. 23–31

The white line in L absorption spectra of rare earth oxides

by N V MOGHE, V S PAI, G G SAHASRABUDHE and V B SAPRE

The x-axis in both figures 1(a) and 1(b) should be read as

Stepper motor steps
(Energy in eV = Stepper motor steps × dispersion)

PRAMANA
— journal of
physics

© Printed in India

Vol. 42, No. 4,
April 1994
pp. 285–297

Non perturbative effective potentials of quantum oscillators

ROSE P IGNATIUS and K BABU JOSEPH
Department of Physics, Cochin University of Science and Technology, Kochi 682 022, India

MS received 23 July 1993

Abstract. Non perturbative analogues of the Gaussian effective potential (GEP) are defined for quantum oscillators obeying q—or (q, p)—deformed commutation relations. These are called the non perturbative q-effective potential ($\mathrm{NP}_q\mathrm{EP}$) and the non perturbative qp effective potential ($\mathrm{NP}_{qp}\mathrm{EP}$), in the respective cases. A system-specific effective potential (SSEP) is also introduced by means of an additional minimization with respect to the q or q and p parameters. The method is applied to q and (q, p) oscillators of the quartic and sextic types. The SSEP in the case of ground states of the q-oscillators corresponds to $q = 1$, which is the ordinary bosonic limit. A potential shape transition that involves the conversion of a double well to a single well or vice versa, is seen to exist in the case of quantum oscillators sitting in a double well potential.

Keywords. Quantum groups; q-oscillator; non-perturbative effective potential; anharmonic oscillators.

PACS Nos 02·20; 03·65; 11·10; 12·40

1. Introduction

Quantum groups and quantum algebras have been receiving considerable attention in recent years [1–6]. Some of these investigations focus on quantum group modified quantum mechanics. In reference 6, for example, the spectrum of a q-anharmonic oscillator with quartic interaction has been studied using first order perturbation theory. There is a logical need to apply the non perturbative approach to such systems that are generically known as quantum oscillators.

It is clear by now that the Gaussian effective potential (GEP) provides a powerful method for accounting the effect of quantum fluctuations on the classical potential [7]. A non perturbative technique enables one to perform systematic approximations in quantum mechanics as well as quantum field theory [7–9]. In this work we formulate a non perturbative q—or (q, p)—analogue of GEP with the help of appropriate quantum oscillator commutation relations that depend on a single parameter q, or two parameters q, p. The resulting quantity is called the non perturbative q-effective potential ($\mathrm{NP}_q\mathrm{EP}$) or the non perturbative (q, p)—effective potential ($\mathrm{NP}_{qp}\mathrm{EP}$), as the case may be. In the original version of GEP there is a positive mass parameter Ω with respect to which the potential is minimized. When a quantum oscillator algebra is employed, the quantum parameters such as q, p can serve as additional parameters in the potential, suggesting a more elaborate scheme of minimization. The end product of the minimization procedure is termed the system-specific effective potential (SSEP). Following Barnes and Ghandour [10] the renormalized mass m_{R}^2 and coupling constant λ_{R} are calculated directly from the $\mathrm{NP}_q\mathrm{EP}$.

We study three kinds of quantum oscillator systems: quartic coupled quantum oscillators in a single well and in a double well, and sextic coupled quantum oscillators. Several interesting aspects emerge from these analyses. For example, for the ground state of a quartic or sextic anharmonic q-oscillator, the $\mathrm{NP}_q\mathrm{EP}$ is a minimum corresponding to $q = 1$ and a maximum corresponding to $q = -1$. The renormalized mass m_R turns out to be a maximum at $q = 1$. Since m_R has the physical significance of being the first excitation energy, these observations seem to cast ordinary ($q = 1$) quantum mechanics in a new perspective. For the X^4-anharmonic (q,p)-oscillator, $\mathrm{NP}_{qp}\mathrm{EP}$ yields a minimum only if λ or $\hbar$ vanishes. In the case of quartic q or (q,p)-oscillator in a double well potential, critical values exist for q or q as well as p, for which the double well degenerates into a single well. Results for quantum oscillators with sextic interaction also exhibit some interesting features.

This paper is organized into five sections. In § 2 the concept of $\mathrm{NP}_q\mathrm{EP}$, $\mathrm{NP}_{qp}\mathrm{EP}$ and SSEP are introduced. Quartic quantum oscillators in single and double well are discussed in § 3. Sextic quantum oscillators constitute the theme of § 4 and concluding remarks comprise § 5.

2. Non perturbative effective potentials

It is well-known that quantum fluctuations modify the classical potential energy, the zero point energy being the prime example. To discuss these effects in the framework of q-deformed quantum mechanics, we seek generalizations of position and momentum operators, X and P, in the form

$$X = X_0 + \left(\frac{\hbar}{2\Omega}\right)^{1/2}(a_\xi + a_\xi^+) \tag{1}$$

$$P = \frac{-i}{2}(2\hbar\Omega)^{1/2}(a_\xi - a_\xi^+) \tag{2}$$

where X_0 is a classical c-number and a_ξ and a_ξ^+ are annihilation and creation operators, respectively, with the set $\xi = [\Omega, q]$. Here Ω denotes a variational parameter having the dimension of mass or frequency that appears in the original $q = 1$ formulation of the GEP [7], and q is a quantum deformation parameter. For $q = 1$ the standard definitions of X and P are recovered.

We impose the q-commutation relation:

$$a_\xi a_\xi^+ - q a_\xi^+ a_\xi = q^{-N_\xi} \tag{3}$$

where N_ξ is the number operator which is not assumed to be the same as $a_\xi^+ a_\xi$. In terms of X and P the q-commutation relation reads

$$[X, P] = i\hbar[q^{-N_\xi} + (q-1)a_\xi^+ a_\xi]. \tag{4}$$

Although, in principle, q could be real or complex, consistency of (4) with the assumption that X and P are simultaneously hermitian, constrains q to be a real parameter. The number operator N_ξ is required to satisfy the commutation relations:

$$[a_\xi, N_\xi] = a_\xi, \tag{5}$$

$$[a_\xi^+, N_\xi] = -a_\xi^+. \tag{6}$$

The number eigenstates $|n\rangle_\xi$ are defined by the relation

$$N_\xi|n\rangle_\xi = n|n\rangle_\xi \tag{7}$$

where $n = 0, 1, 2\ldots$ The ground state $|0\rangle_\xi$ is assumed to be annihilated by a_ξ:

$$a_\xi|0\rangle_\xi = 0. \tag{8}$$

The nth excited state $|n\rangle_\xi$ is obtained from $|0\rangle_\xi$ by operating a_ξ^+, n times:

$$|n\rangle_\xi = \frac{(a_\xi^+)^n}{([n]!)^{1/2}}|0\rangle_\xi \tag{9}$$

where the q-factorial $[n]!$ is

$$[n]! = [n][n-1]\ldots\quad[1]$$

with

$$[\mathrm{A}] = \frac{q^A - q^{-A}}{q - q^{-1}}.$$

The action of a_ξ and a_ξ^+ on the eigenkets $|n\rangle_\xi$ is postulated as follows:

$$a_\xi|n\rangle_\xi = [n]^{1/2}|n-1\rangle_\xi, \tag{10}$$

$$a_\xi^+|n\rangle_\xi = [n+1]^{1/2}|n+1\rangle_\xi. \tag{11}$$

The GEP is customarily defined [7] in the following fashion:

$$\begin{aligned} V_G(X_0) &= \min_\Omega V_G(X_0, \Omega), \\ &\equiv \min_\Omega \langle\psi|H|\psi\rangle, \end{aligned} \tag{12}$$

where $X_0 = \langle\psi|X|\psi\rangle$ and the lowest variational state $|\psi\rangle$ is a Gaussian,

$$|\psi\rangle = \left(\frac{\Omega}{\pi\hbar}\right)^{1/4}\exp\left[\frac{-\Omega}{2\hbar}(X - X_0)^2\right], \qquad \Omega > 0. \tag{13}$$

When q is real and $q > 1$, a q-analogue of the Gaussian function has been defined, [11] but its explicit form is not required here. We merely assume that the lowest variational trial state $|\psi\rangle_\xi$ depends on Ω as well as q, and the excited states can be generated therefrom by applying a_ξ^+ as many times as necessary. The NP$_q$EP, with respect to any state $|\psi\rangle_\xi$ is defined as follows:

$$\begin{aligned} V_q(X_0) &= \min_\Omega V_q(X_0, \Omega) \\ &\equiv \min_\Omega {}_\xi\langle\psi|H|\psi\rangle_\xi. \end{aligned} \tag{14}$$

Studies in quantum group phenomenology [12] indicate the possibility of a given system being associated with a particular q value. This motivates one to define the

$SS_q EP$ as follows:

$$V(X_0) = \min_{\xi} V(X_0, \xi), \tag{15}$$

$$\equiv \min_{\Omega, q} {}_{\xi}\langle \psi | H | \psi \rangle_{\xi}.$$

If the two-parameter quantum algebra characterising a (q, p)-oscillator is used [13] then the relevant commutation relations are

$$a_\eta a_\eta^+ - q a_\eta^+ a_\eta = p^{-N_\eta}, \tag{16}$$

$$a_\eta a_\eta^+ - p^{-1} a_\eta^+ a_\eta = q^{N_\eta}, \tag{17}$$

where the set $\eta = [\Omega, q, p]$. A (q, p)-deformed number $[A]_{q,p}$ is defined by the relation

$$[A]_{q,p} = \frac{q^A - p^{-A}}{q - p^{-1}}.$$

It is clear that the q-oscillator corresponds to the particular case where $q = p$. By analogy with the $NP_q EP$, one defines the $NP_{qp} EP$ by the relation,

$$V_{q,p}(X_0) = \min_{\Omega} V_{q,p}(X_0, \Omega), \tag{18}$$

$$\equiv \min_{\Omega} {}_{\eta}\langle \psi | H | \psi \rangle_{\eta}.$$

The system-specific $V(X_0)$, denoted $SS_{qp} EP$, is defined as

$$V(X_0) = \min_{\eta} V(X_0, \eta), \tag{19}$$

$$= \min_{\Omega, q, p} {}_{\eta}\langle \psi | H | \psi \rangle_{\eta}.$$

The renormalized mass m_R and renormalized coupling constant λ_R (in the quartic case) are obtained by differentiating the effective potential:

$$m_R^2 = \left(\frac{d^2 V}{dX_0^2} \right)_{X_0 = 0}, \tag{20}$$

$$\lambda_R = \frac{1}{4!} \left(\frac{d^4 V}{dX_0^4} \right)_{X_0 = 0}. \tag{21}$$

It is clear that both m_R^2 and λ_R depend on the quantum parameter(s). m_R can be interpreted as the difference between the first excited state and ground state energies while λ_R denotes the amplitude for a transition from the state $|1\rangle$ to $|3\rangle$ under the action of coupling λX^4 [10].

3. Quartic quantum oscillators

3.1 *Single well*

The Hamiltonian representing a quartic quantum (single well) oscillator is

$$H = \tfrac{1}{2}P^2 + \tfrac{1}{2}m^2X^2 + \lambda X^4. \tag{22}$$

If the system is a q-oscillator, then its NP$_q$EP can be evaluated using the method developed in the preceding section. The expectation value of H for the nth eigenstate is written as

$$\langle n|H|n\rangle = \sum_{l=0,2,4} K_l X_0^l \tag{23}$$

where

$$\begin{aligned}
K_0 &= \frac{\hbar\Omega}{4}([n]+[n+1]) \\
&\quad + \frac{\hbar m^2}{4\,\Omega}([n]+[n+1]) \\
&\quad + \lambda\left(\frac{\hbar}{2\Omega}\right)^2([n+1][n+2]+[n+1]^2+2[n][n+1] \\
&\qquad + [n]^2+[n][n-1]) \\
K_2 &= \tfrac{1}{2}m^2 + 3\lambda([n]+[n+1]) \\
K_4 &= \lambda.
\end{aligned}$$

The condition for the potential to be a minimum with respect to Ω is the cubic equation

$$A\bar{\Omega}^3 + B\bar{\Omega} + C = 0, \tag{24}$$

where

$$\begin{aligned}
A &= [n]+[n+1], \\
B &= -(m^2+12\lambda X_0^2), \\
C &= -2\hbar\lambda([n+1][n+2]+[n+1]^2 \\
&\qquad + 2[n+1][n]+[n]^2+[n][n-1]).
\end{aligned}$$

Of the three roots of (24), the largest positive one, designated as $\bar{\Omega}$, is to be employed for setting up the effective potential. This procedure is an extrapolation from the usual $q = 1$ bosonic theory [7].

The NP$_q$EP for the ground state is obtained as

$$\begin{aligned}
V_q(X_0)_g &= \tfrac{1}{4}\hbar\bar{\Omega} + \tfrac{1}{2}m^2\left(X_0^2 + \frac{\hbar}{2}\bar{\Omega}\right) \\
&\quad + \lambda\left\{X_0^4 + \frac{6X_0^2\hbar}{2\bar{\Omega}} + \frac{\hbar^2}{(2\bar{\Omega})^2}([1]+[2])\right\}
\end{aligned} \tag{25}$$

where $\bar{\Omega}$ is the largest root of the equation

$$\bar{\Omega}^3 - (m^2 + 12\lambda X_0^2)\bar{\Omega} - 2\hbar\lambda([1] + [2]) = 0. \tag{26}$$

Assuming $\bar{\Omega} \neq 0$, (25) may be rewritten in the form

$$V_q(X_0)_g = \frac{\hbar}{2}\bar{\Omega} + \tfrac{1}{2}m^2 X_0^2 + \lambda X_0^4 - \frac{\hbar}{(2\bar{\Omega})^2}([1] + [2]). \tag{27}$$

The renormalized mass m_R which is equal to the first exitation energy $E_1 - E_0$, is obtained from $V_q(X_0)_g$:

$$m_R^2 = m^2 + \frac{6\hbar\lambda}{\bar{\Omega}_0}, \tag{28}$$

where

$$\bar{\Omega}_0 = \bar{\Omega}|_{X_0 = 0}.$$

The renormalized coupling constant is

$$\lambda_R = \left(1 - \frac{12\lambda\hbar}{3\bar{\Omega}_0^3 - m_R^2\bar{\Omega}_0}\right)\Bigg/\left(1 + \frac{6\hbar\lambda}{3\bar{\Omega}_0^3 - m_R^2\bar{\Omega}_0}\right). \tag{29}$$

In order to evaluate the ground state SSEP, we extremise the ground state potential (25) with respect to q:

$$\frac{\hbar^2\lambda}{(2\bar{\Omega})^2}(1 - q^{-2}) = 0. \tag{30}$$

Since $\lambda \neq 0$, $\bar{\Omega} \neq \infty$, it follows that the extrema correspond to $q = \pm 1$. One readily checks that, for positive λ, the ground state potential is a minimum for $q = 1$ (giving $SS_q EP = GEP$) and a maximum for $q = -1$. However, the extremal condition for the potential for the nth excited state, when written out fully, is a complicated algebraic equation of the $2(2n + 1)$ degree in q. Some of its roots may represent minima, while others, maxima, corresponding to $q \neq \pm 1$.

We have studied the variation of m_R^2 given by (28) as a function of q (figure 1) and found that for $q > 0$, $m_R^2 > 0$ and that m_R^2 has a maximum at $q = 1$, the ordinary bosonic limit. If m^2 is not very much larger than λ, for all negative q values $\bar{\Omega}_0$ becomes negative. Recalling that in the ordinary bosonic theory the mass parameter Ω for the ground state GEP, is kept positive for convergence reasons [7], we are prompted to retain this proviso in the q-boson/(q,p)-boson theory, as well. Equally important is the positivity of m_R^2. However, for very small positive λ (compared to m^2), we obtain positive $\bar{\Omega}_0$ and positive m_R^2.

The effective potential for a quartic (single well) (q,p)-oscillator may be evaluated using the procedure sketched in the preceding section. Assuming the same Hamiltonian as given by (22), but invoking the (q,p)-commutation relations (16) and (17), one obtains the $NP_{qp}EP$ for any state $|n\rangle_{q,p}$. The potential is formally the same as $NP_q EP$ with all the q-deformed brackets [ ] replaced by the corresponding (q,p)-deformed ones $[\ ]_{q,p}$. The $NP_{qp}EP$ is finally derived by minimization with respect to Ω.

In the case of q-oscillators, it has been mentioned above that the $SS_q EP$ for the ground state is same as the GEP. For a (q,p) oscillator the ground state effective

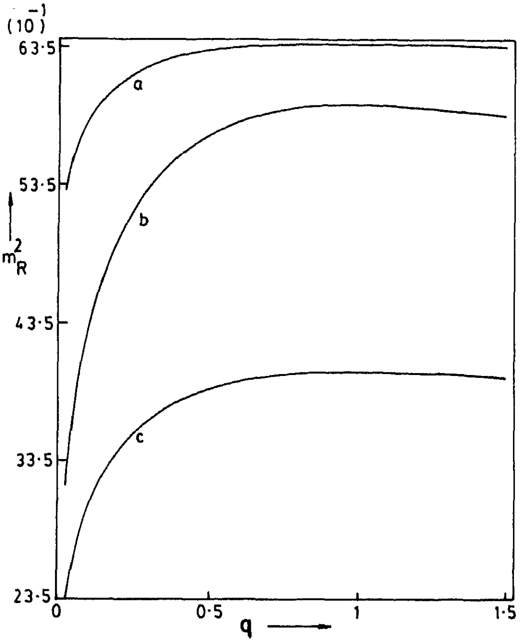

Figure 1. Variation of the renormalized mass m_{R}^2 with the q parameter for a q-oscillator moving in a quartic potential well.
a) $m = 2$ $\lambda = 1$; b) $m = 1$ $\lambda = 2$; c) $m = 1$ $\lambda = 1$.

potential is a minimum only if

$$\frac{\lambda\hbar^2}{(2\bar{\Omega})^2} = 0 \tag{31}$$

and

$$\frac{\lambda\hbar^2}{(2\Omega p)^2} = 0. \tag{32}$$

These relations imply that either $\lambda = 0$ or $\hbar = 0$. Since the latter condition can be easily ruled out, one is confronted with the possibility of a trivial, non-interacting (q, p)-oscillator theory. The message is clear: the ground state SS_{qp}EP for a quartic (q, p)-oscillator cannot be found by the variational method herein presented. These remarks, however, need not apply to the excited states.

3.2 *Double well*

The Hamiltonian for a double well quartic potential is chosen in the form

$$H = \tfrac{1}{2}P^2 + \tfrac{1}{2}m^2X^2 + \lambda X^4 + \frac{m^4}{16\lambda} \tag{33}$$

where $m^2 < 0$, $\lambda > 0$. As this differs from the single well Hamiltonian only by the presence of the constant term, the evaluation of the nonperturbative effective potential is not a novel exercise.

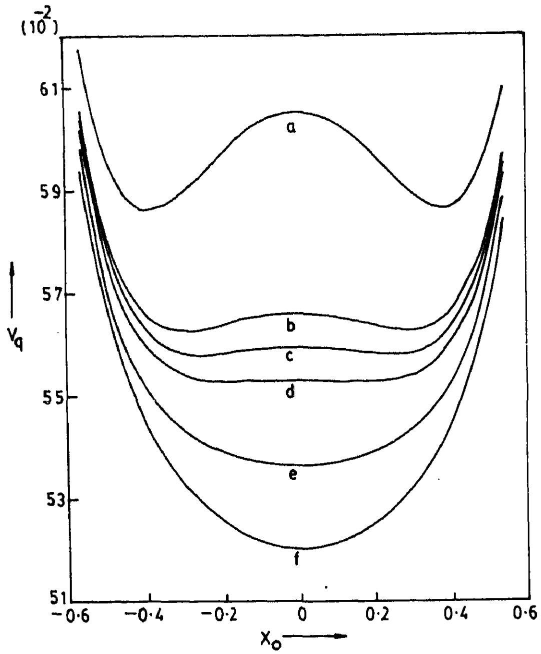

Figure 2. Variation of V_q of a q-oscillator moving in a double well potential, with position X.
a) $q = 0{\cdot}2$; b) $q = 4$; c) $q = 0{\cdot}26$; d) $q = 3{\cdot}7$; e) $q = 0{\cdot}3$; f) $q = 3$.

The only interesting point that crops up is the existence of critical parameter values that separate the double well region from the single well region. This becomes evident from a numerical study. Fixing $\lambda = 1$ and $(m^2/\lambda) = -2$ it is seen that, for a q oscillator, there is a critical value for q, denoted by $q_{\text{crit}\,1}$, above which the double well shape degenerates into a single well shape and another critical value $q_{\text{crit}\,2}$ at which the double well shape is regained. In the present case, $q_{\text{crit}\,1} \approx 0{\cdot}16$ and $q_{\text{crit}\,2} \approx 6{\cdot}27$. Again with $\lambda = 2$, $q_{\text{crit}\,1} \approx 0{\cdot}26$ and the second critical value $q_{\text{crit}\,2} \approx 3{\cdot}66$ at which the double well shape is recovered. The variation of V_q vs X for various values of q parameter, showing the details of the potential shape transitions, is sketched in figure 2.

Critical behaviour is exhibited also by (q, p)-oscillators moving in a double well potential. In this case, one varies both q and p. For instance, taking $\lambda = 2$, $m^2/\lambda = -2$, $q = 0{\cdot}2$, we have obtained double well behaviour in the domain $-0{\cdot}83 \lesssim p \lesssim 0{\cdot}26$. However, for $-0{\cdot}83 \lesssim p < 0$, $\bar{\Omega}_0$ is negative and for $0 < p \lesssim 0{\cdot}25$. $\bar{\Omega}_0$ is positive. In the single well region corresponding to $p \lesssim -0{\cdot}83$, $\bar{\Omega}$ is positive. Similar critical behaviour may be monitored, alternatively, by keeping p fixed and tuning q.

4. Sextic quantum oscillators

A general sextic anharmonic oscillator is modelled by the Hamiltonian

$$H = \tfrac{1}{2}P^2 + \sum_{j=1}^{6} C_j X^j. \tag{34}$$

Assuming q-commutation relations, the expectation value of the Hamiltonian for the

nth state is obtained:

$$\langle n|H|n\rangle = \sum_{l=0}^{6} C_l g_l \tag{35}$$

where C_0 is a constant that depends only on Ω and q parameters:

$$C_0 = \frac{\hbar\Omega}{4}([n] + [n+1]).$$

The remaining coefficients $C_1 (l \neq 0)$ have the same significance as in (34). The functions g_1 are given by the following set of relations:

$$\begin{aligned}
g_0 &= 1 \\
g_1 &= X_0 \\
g_2 &= X_0^2 + \frac{\hbar}{2\Omega}([n] + [n+1]) \\
g_3 &= X_0^3 + \frac{3\hbar}{2\Omega} X_0([n] + [n+1]) \\
g_4 &= X_0^4 + \frac{\hbar}{2\Omega} X_0^2 6([n] + [n+1]) + \left(\frac{\hbar}{2\Omega}\right)^2 ([n+2][n+1] + [n+1]^2 \\
&\quad + 2[n+1][n] + [n]^2 + [n][n-1]) \\
g_5 &= X_0^5 + \frac{10X_0^3\hbar}{2\Omega}([n] + [n+1]) + \frac{5X_0\hbar^2}{(2\Omega)^2}([n+2][n+1] + [n+1]^2 \\
&\quad + 2[n+1][n] + [n]^2 + [n][n-1]) \\
g_6 &= X_0^6 + \frac{15X_0^4\hbar}{2\Omega}([n] + [n+1]) + 15X_0^2\left(\frac{\hbar}{2\Omega}\right)^2 ([n+2][n+1] \\
&\quad + [n+1]^2 + 2[n+1][n] + [n]^2 + [n][n-1]) + \left(\frac{\hbar}{2\Omega}\right)^3 ([n+3][n+2] \\
&\quad + [n+1] + [n+2]^2[n+1] + 2[n+2][n+1]^2 \\
&\quad + 2[n+2][n+1][n] + [n+1]^3 + 2[n+1][n-1][n] \\
&\quad + 3[n+1]^2[n] + 3[n+1][n]^2 + [n]^3 \\
&\quad + 2[n]^2[n-1] + [n][n-1]^2 + [n][n-1][n-2]).
\end{aligned}$$

The condition for the optimum $\Omega(\bar{\Omega})$ is expressed as

$$\bar{\Omega}^4 + D\bar{\Omega}^2 + \hbar E\bar{\Omega} + \hbar^2 F = 0, \tag{36}$$

where the coefficients are

$$\begin{aligned}
D &= -(2C_2 + 6C_3X_0 + 12C_4X_0^2 + 20C_5X_0^3 + 30C_6X_0^4) \\
E &= -(C_4 + 5C_5X_0 + 15C_6X_0^2)([n+2][n+1] \\
&\quad + [n+1]^2 + 2[n+1][n] + [n]^2 + [n][n-1])/([n] + [n+1])
\end{aligned}$$

$$\begin{aligned} F = \frac{-3}{2} C_6 (& [n+3][n+2][n+1] + [n+2]^2[n+1] \\ & + 2[n+2][n+1]^2 + 2[n+2][n+1][n] + [n+1]^3 \\ & + 2[n+1][n-1][n] + 3[n+1]^2[n] \\ & + 3[n+1][n]^2 + [n]^3 + 2[n]^2[n-1] \\ & + [n][n-1]^2 + [n][n-1][n-2]). \end{aligned}$$

The ground state expectation value of the Hamiltonian is

$$\langle 0|H|0\rangle = f_0 + \sum_{k=1}^{6} C_k f_k \tag{37}$$

where

$$f_0 = \frac{\hbar\Omega}{4} + \left(\frac{\hbar}{2\Omega}\right)^3 C_6([1] + 2[2] + [2]^2 + [2][3])$$

$$f_1 = X_0,$$

$$f_2 = X_0^2 + \frac{\hbar}{2\Omega},$$

$$f_3 = X_0^3 + \frac{3\hbar}{2\Omega} X_0,$$

$$f_4 = X_0^4 + \frac{6\hbar}{2\Omega} X_0^2 + \left(\frac{\hbar}{2\Omega}\right)^2 ([1] + [2]),$$

$$f_5 = X_0^5 + \frac{10\hbar}{2\Omega} X_0^3 + 5X_0 \left(\frac{\hbar}{2\Omega}\right)^2 ([2] + [1]),$$

$$f_6 = X_0^6 + \frac{15}{2\Omega} \hbar X_0^4 + 15 \left(\frac{\hbar}{2\Omega}\right)^2 ([1] + [2]) X_0^2.$$

The optimization condition is

$$\bar{\Omega}^4 + G\bar{\Omega}^2 + X\bar{\Omega} + I = 0, \tag{38}$$

with the symbols standing for the following:

$$G = -(2C_2 + 6C_3X_0 + 12C_4X_0^2 + 20C_5X_0^3 + 30C_6X_0^4)$$

$$H = -\hbar(2C_4 + 10C_5X_0 + 30C_6X_0^2)([1] + [2]).$$

$$I = \frac{-3}{2} C_6 \hbar^2 ([1] + 2[2] + [2]^2 + [2][3]).$$

Denoting the largest positive root of (38) at $X_0 = 0$ by $\bar{\Omega}_0$, one writes an expression for the renormalized mass:

$$\begin{aligned} m_R^2 = {} & 2C_2 + 12C_4 \left(\frac{\hbar}{2\bar{\Omega}_0}\right) + 30C_6([1] + [2]) \left(\frac{\hbar}{2\bar{\Omega}_0}\right)^2 \\ & - \left\{ 3C_3 \frac{\hbar}{2\bar{\Omega}_0} + 5C_5 \frac{\hbar^2}{2\bar{\Omega}_0^2} ([2] + [1]) \right\} \frac{d\bar{\Omega}}{dX_0}\bigg|_{X_0 = 0} \end{aligned} \tag{39}$$

where

$$\left.\frac{\mathrm{d}\bar{\Omega}}{\mathrm{d}X_0}\right|_{X_0=0} = \frac{6C_3\bar{\Omega}_0 + 5C_5\hbar([2]+[1])}{4\bar{\Omega}_0^3 - 4C_2\bar{\Omega}_0 - C_4\hbar([2]+[1])}.$$

Numerical computations show that when q is negative, for positive coefficients $C_1, \ldots C_6$, and C_6 not very much smaller than C_2, all the roots of the quartic equation (38) are imaginary. Under the same conditions, and for positive q values, two real roots exists, of which one is positive and the other negative.

Setting the odd order coefficients equal to zero, we obtain a sextic oscillator with only even powers of X in the potential. In this case the renormalized mass is

$$m_{\mathrm{R}}^2 = 2C_2 + \frac{6\hbar C_4}{\bar{\Omega}_0} + 30C_6\left(\frac{\hbar}{2\bar{\Omega}_0}\right)^2([1]+[2]). \tag{40}$$

A plot of m_{R}^2 vs positive q values, is quite similar to that for the X^4 theory. Taking only even order coefficients as positive, and C_6 not very much smaller than C_2, for negative q values the theory is not defined, because all the roots of the $\bar{\Omega}$ equation (38) become imaginary. This shows that the quantum sextic model possesses physical significance only in selected parameter domains.

One can define renormalized quartic ($C_{4\mathrm{R}}$) and renormalized sextic ($C_{6\mathrm{R}}$) coupling constants in respect of the even power sextic q-oscillator model. Thus

$$\begin{aligned} C_{4\mathrm{R}} &= \left.\frac{1}{4!}\frac{\mathrm{d}^4 V_q}{\mathrm{d}X_0^4}\right|_{X_0=0} \\ &= C_4 - \left.\frac{3C_4}{24}\frac{\hbar}{\bar{\Omega}_0^2}\frac{\mathrm{d}^2\bar{\Omega}}{\mathrm{d}X_0^2}\right|_{X_0=0} + 15C_6\frac{\hbar}{2\bar{\Omega}_0} \\ &\quad - \left.\frac{15}{8}C_6\frac{\hbar^2}{\bar{\Omega}_0^3}([1]+[2])\frac{\mathrm{d}^2\bar{\Omega}}{\mathrm{d}X_0^2}\right|_{X_0=0} \end{aligned} \tag{41}$$

and

$$\left.\frac{\mathrm{d}^2\bar{\Omega}}{\mathrm{d}X_0^2}\right|_{X_0=0} = \frac{24\bar{\Omega}_0^2 C_4 + 60C_6\hbar\bar{\Omega}_0([1]+[2])}{4\bar{\Omega}_0^3 - 4C_2\bar{\Omega}_0 - 2C_4\hbar([1]+[2])}.$$

Expressing the fourth derivative of $\bar{\Omega}$ at $X_0 = 0$, in the form

$$\begin{aligned} \left.\frac{\mathrm{d}^4\bar{\Omega}}{\mathrm{d}X_0^4}\right|_{X_0=0} &= \left\{ -720C_6\bar{\Omega}_0^2 - 2[144C_4\bar{\Omega}_0 + 180C_6([1]+[2])\left.\frac{\mathrm{d}^2\bar{\Omega}}{\mathrm{d}X_0^2}\right|_{X_0=0} \right. \\ &\quad \left. + (36\bar{\Omega}_0^2 - 12C_2)\left(\frac{\mathrm{d}^2\bar{\Omega}}{\mathrm{d}X_0^2}\right)_{X_0=0} \right\} \Big/ (4\bar{\Omega}_0^3 - 4\bar{\Omega}_0 C_2 - 2C_4\hbar([1]+[2])) \end{aligned}$$

$$\begin{aligned} C_{6\mathrm{R}} &= \left.\frac{1}{6!}\frac{\mathrm{d}^6 V_g}{\mathrm{d}X_0^6}\right|_{X_0=0} \\ &= C_6\frac{-5C_6\hbar}{2\bar{\Omega}_0^2} - \frac{\hbar}{2\bar{\Omega}_0^2}\left[\frac{1}{12}C_4 + \frac{\hbar}{2\bar{\Omega}_0}([1]+[2])\frac{10C_6}{24}\right]\left(\frac{\mathrm{d}^4\bar{\Omega}}{\mathrm{d}X_0^4}\right)_{X_0=0} \\ &\quad + \frac{\hbar}{2\bar{\Omega}_0^3}\left[\frac{C_4}{2} + \frac{\hbar}{2\bar{\Omega}_0}\frac{15C_6}{4}([1]+[2])\right]\left(\frac{\mathrm{d}^2\bar{\Omega}}{\mathrm{d}X_0^2}\right)_{X_0=0}. \end{aligned} \tag{42}$$

To get the system-specific q effective potential (SS_qEP), one has to determine the optimization condition for q also.

Differentiating $\langle 0|H|0\rangle$ given by (37) with respect to q, we have

$$(1-q^{-2})\left(\frac{\hbar}{2\bar{\Omega}}\right)^2\left\{C_4+5C_5X_0+C_6\left(15X_0^2+\frac{\hbar}{2\bar{\Omega}}(q^{-2}-q^{-1}+1)\right.\right.$$
$$\left.\left.(1+q^2+q^{-2}+2)\right)\right\}=0. \qquad (43)$$

This equation has the roots $q=\pm 1$.
But

$$\frac{d^2V_q}{dq^2}=(1+2q^{-3})\left(\frac{\hbar}{2\bar{\Omega}}\right)^2\left\{C_4+5C_5X_0\right.$$
$$\left.+C_6\left(15X_0^2+\frac{\hbar}{2\bar{\Omega}}(q^{-4}-q^{-3}+2q^{-2}-q^{-1}+q^2-q+2)\right)\right\}.$$

For posivive coefficients, this equation becomes positive at $q=1$, showing that it is a minimum of the potential. If $q=-1$ it becomes negative, and hence corresponds to the maximum of the effective potential. q can have another set of six values corresponding to the roots of the factored out expression, which depend on the coefficients C_k. The possibility of some of them representing true minima, cannot be ruled out.

As for the (q,p) analogue of the sextic oscillator, we have equations (35), (36), (37) and (38) with $[A]$ replaced by $[A]_{q,p}$. In order to get the $SS_{qp}EP$ for the ground state, the conditions are

$$\frac{\partial V_{q,p}}{\partial p}=\left(\frac{\hbar}{2\bar{\Omega}}\right)^2(-p^{-2})\left[C_4+5C_5X_0+15C_6X_0^2+\frac{C_6\hbar}{2\bar{\Omega}}(3p^{-2}+2q^2\right.$$
$$\left.+4qp^{-1}+2q+2p^{-1}+2)\right]=0 \qquad (44)$$

$$\frac{\partial V_{q,p}}{\partial q}=\left(\frac{\hbar}{2\bar{\Omega}}\right)^2\left[C_4+5C_5X_0+15X_0^2C_6+C_6\frac{\hbar}{2\bar{\Omega}}(3q^2+2p^{-2}\right.$$
$$\left.+4qp^{-1}+2q+2p^{-1}+2)\right]=0 \qquad (45)$$

besides equation (38).

If $p=\infty$ then the conditions (44) and (45) imply $q=0$. Non-trivial solutions of (44) and (45) correspond to $p^{-2}\neq 0$. The $SS_{qp}EP$ corresponds to $q=p^{-1}$ subject to the condition that the second derivatives of $V_{q,p}$ are greater than or equal to zero.

5. Concluding remarks

In this paper we have addressed the question of formulating q and (q,p) analogues of the GEP. A direct generalization of GEP gives the non perturbative effective potentials, namely NP_qEP and $NP_{qp}EP$, applicable to q-oscillators and (q,p)-oscillators, respectively. The SS_qEP is seen to correspond to $q = 1$, at least in the ground state of q oscillators, showing that the ordinary bosonic theory appears to have a natural significance in the variational approach. Such uniqueness is not necessarily shared by the excited states of the system.

The potential shape transitions exhibited by double well oscillators at critical values of the parameter(s), is a novel phenomenon which may have implications in the study of spontaneous symmetry breaking in q and (q, p)-quantum field theories.

Acknowledgements

One of the authors (RPI) wishes to thank Drs V C Kuriakose, M P Joy, K M Valsamma and Lalaja Varughese for discussions and help with the computations.

References

[1] V G Drinfeld, Quantum groups, *Proc. Int. Cong. Math*, (Berkeley: California USA, 1986)
[2] M Jimbo, *Int. J. Mod. Phys.* **A4**, 3759 (1989)
[3] S Majid, *Int. J. Mod. Phys.* **A5**, (1990) 1
[4] Quantum groups edited by T Curtright, D Fairlie and C Zachos (World Scientific, Singapore, 1990)
[5] O W Greenberg, *Phys. Rev.* **D43**, 4111 (1991)
[6] V C Kuriakose, K K Leelamma and K Babu Joseph, *Pramana – J. Phys.* **39**, 521 (1992)
[7] P M Stevenson, *Phys. Rev.* **D30**, 1712 (1984)
[8] P M Stevenson, *Phys. Rev.* **D32**, 1389 (1985)
[9] R P Ignatius, V C Kuriakose and K Babu Joseph, *Phys. Lett.* **B220**, 181 (1989)
[10] T Barnes and G I Ghandour, *Phys. Rev.* **D22**, 924 (1980)
[11] J A Minahan, *Mod. Phys. Lett.* **A5**, 2625 (1990)
[12] D Bonatsos, E N Argyres and P P Raychev, *J. Phys.* **A24**, L403 (1991)
[13] R Chakrabarti and R Jagannathan, *J. Phys.* **A24**, L711 (1991)

PRAMANA
— journal of
physics

© Printed in India

Vol. 42, No. 4,
April 1994
pp. 299–309

Coherent states and squeezed states of real q-deformed quantum oscillators

G VINOD, K BABU JOSEPH and V C KURIAKOSE
Department of Physics, Cochin University of Science and Technology, Kochi 682 022, India

MS received 24 August 1993; revised 20 November 1993

Abstract. A detailed physical characterisation of the coherent states and squeezed states of a real q-deformed oscillator is attempted. The squeezing and q-squeezing behaviours are illustrated by three different model Hamiltonians, namely i) Batemann Hamiltonian ii) harmonic oscillator with time dependent mass and frequency and iii) a system with constant mass and time-dependent frequency.

Keywords. Quantum groups; quantum oscillators; q-coherent states; q-squeezed states.

PACS Nos 02·20; 03·65; 42·50

1. Introduction

Quantum groups and quantum oscillators have been widely studied recently. Biedenharn [1] and Macfarlane [2] discussed q-oscillators and realized the quantum algebra $\mathrm{su}_q(2)$ in terms of these oscillators. Many other versions of q-oscillator have appeared [3, 4]. Quantum oscillators have already found applications in diverse fields such as molecular spectroscopy [5], condensed matter physics [6], quantum optics [4, 7] and many-body theory [8]. An anharmonic version of q-oscillator with quartic interaction has been discussed recently [9].

Coherent states and squeezed states of the electromagnetic field have been the subject of several investigations. Schrodinger [10] introduced a system of wavefunctions to describe the nonspreading wave packets for the quantum harmonic oscillator. Later Glauber [11] called these states coherent states (CS) and applied them to the radiation field. Squeezed states were first introduced by Yuen [12] and are of great importance in quantum optics. Coherent states and squeezed states can be defined for the q-oscillators also and are of current interest [4, 7]. Chaturvedi *et al* [4] have constructed the coherent states and squeezed states corresponding to the commutation relation $aa^+ - qa^+a = 1$. In this paper we compute the variances associated with the coherent and squeezed states and attempt to distinguish between squeezing and q-squeezing for real q-deformed oscillators.

Section 2 is a brief review of the spectrum of a real q-deformed oscillator. In § 3 a general treatment of the coherent states and squeezed states is given, emphasising the physical aspects. Section 4 deals with these model Hamiltonians that illustrate the ideas and formalism of squeezing and q-squeezing under the SU(1, 1) pattern. The results of numerical computations of the probability for observing a definite number of quanta in q-squeezed states are presented and some concluding remarks are offered in § 5.

2. Spectrum of a q-deformed oscillator

Here we recapitulate the basic facts about real q-deformed oscillators [4]. Let us consider the q-commutation relation (q-CR)

$$aa^+ - qa^+a = 1 \tag{1}$$

where q is real. We demand that

$$\begin{aligned}[][N, a^+] &= a^+,\\ [N, a] &= -a.\end{aligned} \tag{2}$$

If we take

$$\begin{aligned} aa^+ &= [N+1]_q\\ a^+a &= [N]_q\end{aligned} \tag{3}$$

with $[X]_q = (q^X - 1)/(q-1)$, (1) is readily satisfied. With the help of (3), (1) can be rewritten as

$$[a, a^+] = q^N. \tag{4}$$

The operators a^+, a and N can be thought of as creation, annihilation and number operators respectively for a q-deformed H.O. with the Hamiltonian

$$H_q = P_q^2/2m + \tfrac{1}{2}m\omega^2 X_q^2 \tag{5}$$

where

$$\begin{aligned} X_q &= \sqrt{\hbar/2m\omega}(a + a^+),\\ P_q &= -i\sqrt{\frac{m\hbar\omega}{2}}(a - a^+),\end{aligned} \tag{6}$$

X_q and P_q are hermitian operators satisfying the CR

$$[X_q, P_q] = i\hbar q^N. \tag{7}$$

The uncertainty relation corresponding to this is

$$\Delta X_q \Delta P_q \geqslant \frac{\hbar}{2}\langle q^N\rangle.$$

As $q \to 1$, one recovers the corresponding operators of ordinary quantum mechanics namely X and P.

The q-oscillator Hamiltonian can be written as

$$\begin{aligned} H_q &= \frac{\hbar\omega}{2}(aa^+ + a^+a),\\ &= \frac{\hbar\omega}{2}([N]_q + [N+1]_q).\end{aligned} \tag{8}$$

The energy eigenvalues are

$$E_n = \tfrac{1}{2}\hbar\omega([n]_q + [n+1]_q) \tag{9}$$

where n is an eigenvalue of the operator N:

$$N|n\rangle_q = n|n\rangle_q. \tag{10}$$

In general, any state $|n\rangle_q$ can be built up from the q-vacuum

$$|n\rangle_q = \frac{(a^+)^n}{\sqrt{[n]!}}|0\rangle_q \tag{11}$$

where $[n]! = [n]\,[n-1]\cdots[2][1]$ and the q-vacuum $|0\rangle_q$ is identified with ordinary vacuum $|0\rangle$.

3. Coherent states and squeezed states

A normalized q-coherent state (q-CS) is defined as

$$a|\alpha\rangle_q = \alpha|\alpha\rangle_q \tag{12}$$

$$|\alpha\rangle_q = [\exp_q(|\alpha|^2)]^{-1/2}\sum_{n=0}^{\infty}\frac{\alpha^n}{\sqrt{[n]!}}|n\rangle_q \tag{13}$$

where

$$\exp_q\chi = \sum_{n=0}^{\infty}\frac{\chi^n}{[n]!}$$

The q-CS can be obtained from the q-vacuum by the action of a q-displacement operator $D_q(\alpha)$:

$$|\alpha\rangle_q = D_q(\alpha)|0\rangle_q \tag{14}$$

where

$$D_q(\alpha) = [\exp_q|\alpha|^2]^{-1/2}\exp_q(\alpha a^+).$$

Note that the displacement operator that generates a q-CS from the vacuum is not equal to $\exp_q(\alpha a^+ - \alpha^* a)$, which is the q analogue of $\exp(\alpha a^+ - \alpha^* a)$, the displacement operator in the $q = 1$ theory.

The probability of measuring n quanta in the q-CS is

$$\begin{aligned} P_n &= [\exp_q(|\alpha|^2)]^{-1}\left(\frac{|\alpha|^{2n}}{[n]!}\right) \\ &= [\exp_q(\langle[n]\rangle)]^{-1}\left(\frac{\langle[n]\rangle^n}{[n]!}\right) \end{aligned} \tag{15}$$

where we have made use of the fact that

$$|\alpha|^2 = \langle[n]\rangle. \tag{16}$$

Equation (15) represents a q-Poisson distribution. Variances of X_q and P_q defined by (7) are calculated:

$$\mathrm{Var}\,X_q = \frac{\hbar}{2m\omega}\,(|\alpha|^2(q-1)+1),$$

$$\mathrm{Var}\,P_q = \frac{m\hbar\omega}{2}\,(|\alpha|^2(q-1)+1). \tag{17}$$

Equation (17) fixes an upper limit for α i.e. $|\alpha| \leqslant 1/(1-q)$.

The uncertainty product for a q-CS$|\alpha\rangle_q$ is expressed in the form

$$(\Delta X_q)(\Delta P_q) = \hbar/2(|\alpha|^2(q-1)+1) \tag{18}$$

while the corresponding relation for the state $|n\rangle_q$ is

$$(\Delta X_q)_n(\Delta P_q)_n = (\hbar/2)([n]+[n+1]). \tag{19}$$

The q-vacuum state satisfies the relation

$$(\Delta X_q)_0(\Delta P_q)_0 = \hbar/2 \tag{20}$$

which coincides with the position-momentum uncertainty relation for the ordinary vacuum state $|0\rangle$. Thus the uncertainty product for q-CS is different from that of the q-vacuum state, which is $\hbar/2$. Also the uncertainty product depends on the parameter α.

Let us introduce two self-adjoint operators A_1 and A_2, called the quadrature components, such that

$$a = A_1 + iA_2$$

$$a^+ = A_1 - iA_2 \tag{21}$$

then it can be seen that

$$\mathrm{Var}\,A_1 = (\tfrac{1}{4})((q-1)|\alpha|^2+1),$$

$$\mathrm{Var}\,A_2 = (\tfrac{1}{4})((q-1)|\alpha|^2+1),$$

$$(\Delta A_1)(\Delta A_2) = \tfrac{1}{4}((q-1)|\alpha|^2+1). \tag{22}$$

The quantum noise energy [12] is zero for q-CS also:

$$\langle\alpha|(\Delta a)^+(\Delta a)|\alpha\rangle_q = 0. \tag{23}$$

Let us now define two new operators b and b^+:

$$\begin{pmatrix} b \\ b^+ \end{pmatrix} = \begin{pmatrix} \mu & \nu \\ \nu^* & \mu^* \end{pmatrix}\begin{pmatrix} a \\ a^+ \end{pmatrix}. \tag{24}$$

With

$$|\mu|^2 - |\nu|^2 = 1 \tag{25}$$

it follows that

$$bb^+ - b^+b = q^N. \tag{26}$$

The SU(1, 1) squeezed states of the q-oscillator are defined as follows:

$$b|\beta\rangle_q = \beta|\beta\rangle_q. \tag{27}$$

We can express $|\beta\rangle_q$ as a linear combination of the number states $|n\rangle_q$ [13]:

$$|\beta\rangle_q = \sum_{n=0}^{\infty} C_n|n\rangle_q, \tag{28}$$

$$\begin{aligned} b|\beta\rangle_q &= (\mu a + \nu a^+) \sum_{n=0}^{\infty} C_n|n\rangle_q, \\ &= \beta \sum_{n=0}^{\infty} C_n|n\rangle_q. \end{aligned} \tag{29}$$

It follows that

$$C_1 = \beta C_0/\mu$$

$$C_2 = (\beta C_1 - \nu C_0)/\sqrt{([2])}\mu$$

or in general,

$$C_n = \frac{\beta C_{n-1} - \nu\sqrt{([n-1])}C_{n-2}}{\mu\sqrt{[n]}}. \tag{30}$$

Although, in general μ and ν are arbitrary, here we consider the evolution of a state which is initially a q-coherent state (i.e. $\mu(0) = 1$, $\nu(0) = 0$) into a q-squeezed state $|\beta\rangle_q$ at t. This procedure is motivated by similar considerations made in references [14] and [15] in the context of ordinary coherent states and squeezed states. Inverting (24), we have

$$a = \mu^* b - \nu b^+$$

$$a^+ = \nu^* b + \mu b^+$$

so that the Hamiltonian (8) becomes

$$H = \frac{\hbar\omega}{2}(2\mu^*\nu^* b^2 - 2\mu\nu b^{+2} + bb^+ + b^+ b). \tag{31}$$

It can easily be shown that

$$\langle A_1\rangle_\beta = 1/2(\beta(\mu^* - \nu^*) + \beta^*(\mu - \nu)), \tag{32}$$

$$\langle A_2\rangle_\beta = 1/2(\beta^*(\mu + \nu) + \beta(\mu^* + \nu^*)),$$

$$\mathrm{Var}\,A_1 = \tfrac{1}{4}|\mu - \nu|^2\sigma(t),$$

$$\mathrm{Var}\,A_2 = \tfrac{1}{4}|\mu + \nu|^2\sigma(t). \tag{33}$$

Also $(\Delta A_1)\,(\Delta A_2) = \frac{1}{4}|\mu^2 - \nu^2|\sigma(t)$ (34)
where

$$\sigma(t) = \sum_{n=0}^{\infty} q^n|C_n|^2. \tag{35}$$

In the present work we restrict q to the domain $0 \leqslant q \leqslant 1$, and assume the normalization

$$\sum_{n=0}^{\infty} |C_n|^2 = 1. \tag{36}$$

This yields the inequality $\sigma(t) \leqslant 1$.

At this point we wish to draw a distinction between squeezing and q-squeezing. By squeezing we mean that the variance goes below the value of the uncertainty product in the q-vacuum state, which is same as that for the ordinary state. On the other hand, q-squeezing implies that the variance is less than the uncertainty product for the q-CS state. For an undeformed oscillator the uncertainty product is the same for vacuum as well as for CS. But when $q \neq 1$, the uncertainty product has different values corresponding to q-vacuum and q-CS.

From (35),

$$\sigma(0) = \frac{\exp_q(q|\beta|^2)}{\exp_q(|\beta|^2)}. \tag{37}$$

We assume that $|\beta\rangle_q$ is prepared initially as a q-CS. Hence it follows from (22), (34) and (37) that

$$(q-1)|\alpha|^2 + 1 = \frac{\exp_q(q|\beta|^2)}{\exp_q(|\beta|^2)} \tag{38}$$

Thus in the $q \neq 1$ theory, α and β are interrelated. Squeezing means (ΔA_1) or $(\Delta A_2) \leqslant \frac{1}{4}$ and q-squeezing means (ΔA_1) or $(\Delta A_2) \leqslant \sigma(0)/4$. We may define the degree of squeezing and the degree of q-squeezing respectively as

$$S^{(A)} = \frac{2\langle(\Delta A)^2\rangle - \frac{1}{4}}{\frac{1}{4}}, \tag{39}$$

$$S_q^{(A)} = \frac{2\langle(\Delta A)^2\rangle - (\frac{1}{4})\sigma(0)}{\frac{1}{4}\sigma(0)}. \tag{40}$$

Squeezing corresponds to $S^{A_1} < 0$, or $S^{A_2} < 0$, while q-squeezing implies $S_q^{A_1} < 0$ or $S_q^{A_2} < 0$.

4. SU(1, 1) squeezed states of real q-deformed Hamiltonians

4.1 *Batemann Hamiltonian*

Baseia *et al* [14] studied the appearance of squeezed states for the Batemann Hamiltonian where the mass of the oscillator changes suddenly. In this section we discuss the squeezing and q-squeezing properties associated with SU(1, 1) squeezed states of a real q-deformed Batemann Hamiltonian, defined by the relation

$$H(t) = \frac{P^2}{2M(t)} + \frac{1}{2}M(t)\omega^2 X^2 \tag{41}$$

where

$$M(t) = M_0 e^{\lambda t}.$$

We take the corresponding q-deformed Hamiltonian in ~~the~~ form:

$$H_q(t) = \frac{P_q^2}{2M(t)} + \frac{1}{2}M(t)\omega^2 X_q^2 \tag{42}$$

Setting

$$\mu(t) = \cosh(\lambda t/2) = \frac{1}{2}\left(\sqrt{\frac{M(t)}{M_0}} + \sqrt{\frac{M_0}{M(t)}}\right)$$

$$\nu(t) = \sinh(\lambda t/2) = \frac{1}{2}\left(\sqrt{\frac{M(t)}{M_0}} - \sqrt{\frac{M_0}{M(t)}}\right), \tag{43}$$

the condition $|\mu|^2 - |\nu|^2 = 1$ is easily satisfied. Now consider the case where mass changes suddenly as

$$M_0 \to M_1 \text{ at } t = t_1:$$

$$M(t) = M_0\theta(t - t) + M_1\theta(t - t_1), \tag{44}$$

where θ is the Heaviside step-function.

The quadrature components A_1 and A_2 have equal variances:

$$(\Delta A_1)_\beta^2 = (\Delta A_2)_\beta^2 = \tfrac{1}{4}\sigma(t) = (\Delta A_1)_\beta(\Delta A_2)_\beta. \tag{45}$$

Thus $|\beta\rangle_q$ behaves as a q-CS.

For $t > t_1$,

$$M(t) = M_0 + \Delta M = M_0(1 + \delta)$$

where

$$\delta = \frac{\Delta M}{M_0}, \quad \Delta M = M_1 - M_0$$

Then

$$(\Delta A_1)^2 = \frac{\sigma(t)}{4(1 + \delta)},$$

$$(\Delta A_2)^2 = \left(\frac{1 + \delta}{4}\right)\sigma(t),$$

$$(\Delta A_1) = (\Delta A_2) = \frac{\sigma(t)}{4}. \tag{46}$$

This implies that the uncertainty product can go below $\frac{1}{4}$. For $(\sigma(t) - 1) < \delta < (1/[\sigma(t)] - 1)$, both $(\Delta A_1)^2$ and $(\Delta A_2)^2$ fall below this value. In this region one can in principle measure both A_1 and A_2 with uncertainties less than that predicted by Heisenberg's uncertainty principle. Also in the region $([\sigma(t)]/[\sigma(0)] - 1) < \delta < ([\sigma(0)]/[\sigma(t)] - 1)$, both A_1 and A_2 have variances below that in q-CS. The squeezing pattern is as follows:

$$A_1 \text{ is squeezed if } \delta > (\sigma(t) - 1),$$

$$A_1 \text{ is } q\text{-squeezed if } \delta > (\sigma(t)/\sigma(0) - 1). \tag{47}$$

Similar remarks apply to squeezing and q-squeezing of the A_2 component.

4.2 *Harmonic oscillator with time dependent mass and frequency*

Consider the Hamiltonian

$$H = P^2/2M(t) + (1/2)M(t)\omega^2(t)X^2$$

where

$$M(t) = M_0 e^{\lambda t}, \quad \omega(t) = \omega_0 e^{-\rho t}. \tag{48}$$

Squeezing properties of this Hamiltonian have been studied earlier [15]. We can q-deform it as

$$H_q = \frac{P_q^2}{2M(t)} + (1/2)M(t)\omega^2(t)X_q^2. \tag{49}$$

The coefficients $\mu(t)$ and $\nu(t)$ are expressed as

$$\mu(t) = \cosh\left(\frac{\lambda-\rho}{2}\right)t,$$

$$\nu(t) = \sinh\left(\frac{\lambda-\rho}{2}\right)t. \tag{50}$$

The variances of the quadrature components are calculated as:

$$(\Delta A_1)^2 = \tfrac{1}{4}e^{-(\lambda-\rho)t}\sigma(t),$$

$$(\Delta A_2)^2 = \tfrac{1}{4}e^{(\lambda-\rho)t}\sigma(t),$$

$$(\Delta A_1)(\Delta A_2) = \tfrac{1}{4}\sigma(t). \tag{51}$$

Here also the uncertainty product may decrease below $\frac{1}{4}$.

A_1 is squeezed if $(\lambda-\rho) < \frac{-1}{t}\ln(\sigma(t))$ and q squeezed if $(\lambda-\rho) < \frac{1}{t}\ln\left(\frac{\sigma(0)}{\sigma(1)}\right)$. Similar conditions can be obtained for A_2 also.

4.3 *System with constant mass and time dependent frequency*

Consider the q-deformed Hamiltonian

$$H_q = \frac{P_q^2}{2M} + \tfrac{1}{2}M\omega_0^2[1+\chi\cos(2\omega_0+\varepsilon)t]X_q^2. \tag{52}$$

The squeezing properties of the corresponding $q = 1$ Hamiltonians have been studied by Geethakumari *et al* [unpublished].

We put

$$\mu(t) = \tfrac{1}{2}\left[\left(\frac{1+\cos(2\omega_0+\varepsilon)t}{1+\chi}\right)^{1/2} + \left(\frac{1+\chi}{1+\cos(2\omega_0+\varepsilon)t}\right)^{1/2}\right],$$

$$\nu(t) = \tfrac{1}{2}\left[\left(\frac{1+\cos(2\omega_0+\varepsilon)t}{1+\chi}\right)^{1/2} - \left(\frac{1+\chi}{1+\cos(2\omega_0+\varepsilon)t}\right)^{1/2}\right]. \tag{53}$$

Then

$$(\Delta A_1)^2 = \tfrac{1}{4}\left[\frac{1+\chi}{1+\cos(\omega_0+\varepsilon)t}\right]\sigma(t),$$
$$(\Delta A_2)^2 = \tfrac{1}{4}\left[\frac{1+\chi}{1+\cos(2\omega_0+\varepsilon)t}\right]\sigma(t),$$
$$(\Delta A_1)(\Delta A_2) = \tfrac{1}{4}\sigma(t). \tag{54}$$

A_1 is squeezed if $\dfrac{1+\chi}{1+\cos(2\omega_0+\varepsilon)t} < \dfrac{1}{\sigma(t)}$ and

q-squeezed if $\dfrac{1+\chi}{1+\cos(2\omega_0+\varepsilon)t} < \dfrac{\sigma(0)}{\sigma(t)}$.

5. Results and discussion

We have calculated the probability distribution P_n for various values of q keeping α fixed. In figure 1, $\log_{10}P_n(q)$ is plotted against n for four different values of q, namely 1, 0·9, 0·8 and 0 for $\alpha = 0{\cdot}5$. Figure 2 gives the corresponding graph for $\alpha = 0{\cdot}9$. It is clear from these that the graphs for a given q value for different α values are similar.

In figure 3, $\log_{10}P_0(q)/P_0(1)$ is plotted against q where $P_0(q)$ is the probability of the ground state corresponding to $q \neq 1$ and P_0 that corresponding to $q = 1$. These graphs plotted for the values, namely, $\alpha = 0{\cdot}5$ and 0·9, show marked variation in their behaviour except near the standard value, namely, $q = 1$, where they converge.

Starting from a commutation relation for the q oscillator, coherent states of the oscillator have been constructed and the variances of the quadrature components calculated. The q analogues of bosonic squeezed states have been defined in two ways and are illustrated using three model Hamiltonians. It has been found that if we could achieve a condition which pushes q below unity, we could measure X_q or P_q (or both) with uncertainties smaller than $\hbar/2$. But ultimately, it is experiment that ought to determine the physical realizability of such states.

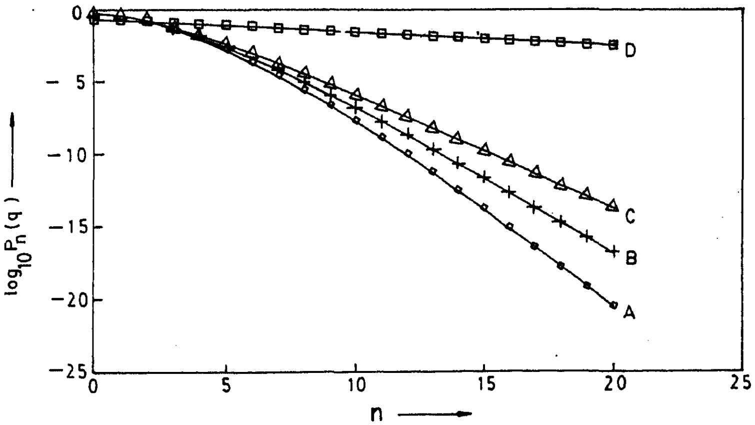

Figure 1. Variation of $\log_{10}P_n(q)$ with n, for $\alpha = 0{\cdot}5$: A) $q = 1$; B) $q = 0{\cdot}9$; C) $q = 0{\cdot}8$; D) $q = 0$.

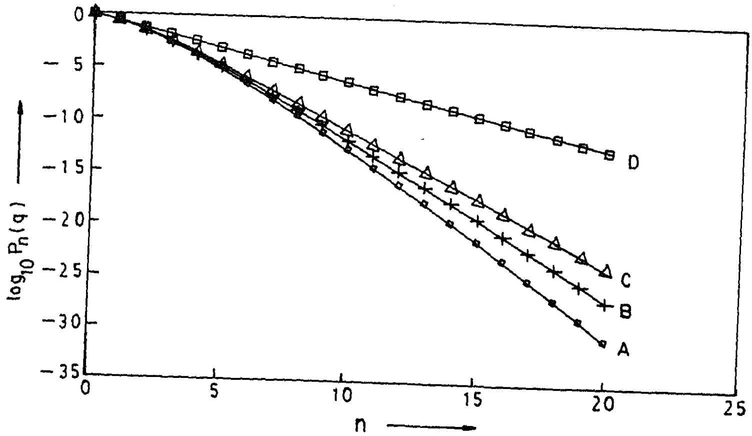

Figure 2, Variation of $\log_{10}P_n(q)$ with n, for $\alpha = 0{\cdot}9$: A) $q = 1$; B) $q = 0{\cdot}9$; C) $q = 0{\cdot}8$; D) $q = 0$.

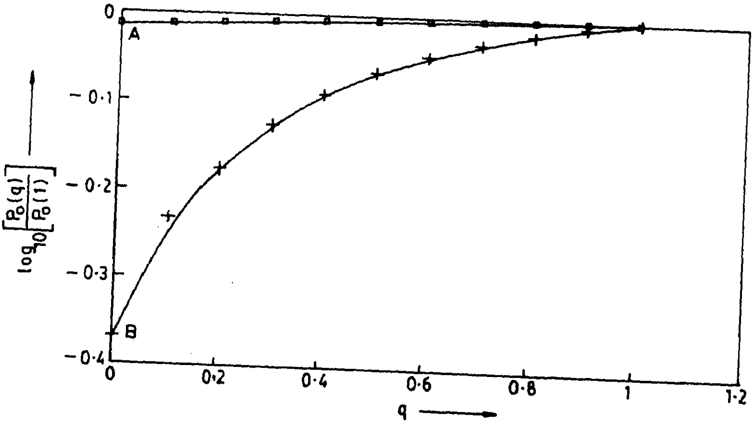

Figure 3. Variation of $\log_{10}[P_0(q)/P_0(1)]$ with q: A) $\alpha = 0{\cdot}5$; B) $\alpha = 0{\cdot}9$.

Acknowledgements

The authors are grateful to Prof. S Chaturvedi, School of Physics, Central University of Hyderabad for a careful reading of the manuscript and useful suggestions. One of us (GV) thanks UGC for the award of a junior research fellowship.

References

[1] L C Biedenharn, *J. Phys.* **A22**, L873 (1989)
[2] A J Macfarlane, *J. Phys.* **A22**, 4581 (1989)
[3] D Ellinas, *Phys. Rev.* **A45**, 595 (1992)
P P Kulish and E V Damaskinski, *J. Phys.* **A23**, L415 (1989)
M Chaichan and P P Kulish, *Phys. Lett.* **B234**, 72 (1990)
[4] S Chaturvedi, A K Kapoor, R Sandhya, V Srinivasan and R Simon, *Phys. Rev.* **A43**, 4555 (1991)
[5] Zhe Chang and Hong Yan, *Phys. Lett.* **A154**, 254 (1991)
Zhe Chang and Hong Yan, *Phys. Lett.* **A156**, 242 (1991)
Zhe Chang and Hong Yan, *Phys. Lett.* **A158**, 242 (1991)

[6] K K Leelamma, V C Kuriakose and K Babu Joseph, *Int. J. Mod. Phys.* **B7**, 2697 (1993)

[7] A I Solomon and J Katriel, *J. Phys.* **A23**, L1209 (1990)
J Katriel and A I Solomon, *J. Phys.* **A23**, 2093 (1990)
V Buzek, *J. Mod. Opt.* **38**, 801 (1991)
Zhe Chang, *J. Phys.* **A25**, L707 (1992)
E Caleghini, M Rasetti and G Vitiello, *Phys. Rev. Lett.* **66**, 2056 (1991)
S H Chiu, R W Gray and C A Nelson, *Phys. Lett.* **A164**, 237 (1992)
Zusong Yu, *High Energy Phys. Nucl. Phys.* **16**, 461 (1992)
A K R Gopal and V Gupta, *Mod. Phys. Lett.* **A7**, 3759 (1992)
C Quesne, *Phys. Lett.* **A153**, 303 (1991)
B Jurco, *Lett. Math. Phys.* **21**, 51 (1991)

[8] E G Floratos, *J. Phys.* **A24**, 4723 (1991)

[9] V C Kuriakose, K K Leelamma and K Babu Joseph, *Pramana – J. Phys.* **39**, 521 (1992)

[10] E Schrödinger, *Naturwissenschaften* **14**, 664 (1926)

[11] R Glauber, *Phys. Rev.* **131**, 2769 (1963)

[12] H P Yuen, *Phys. Rev.* **A13**, 2226 (1976)

[13] R W Henry and S C Glotzer, *Am. J. Phys.* **56**, 4 (1988)

[14] B Baseia, A L De Brito and V S Bagnato, *Phys. Rev.* **A45**, 5308 (1992)

PRAMANA
— journal of
physics

© Printed in India

Vol. 42, No. 4,
April 1994
pp. 311–314

Squeezed vacuum as an eigenstate of two-photon annihilation operator

C L MEHTA, ANIL K ROY* and G M SAXENA**
Department of Physics, Indian Institute of Technology, New Delhi 110 016, India
*Centre for Theoretical Studies, Indian Institute of Science, Bangalore 560 012, India
**Time and Frequency Section, National Physical Laboratory, New Delhi 110 012, India

MS received 22 November 1993

Abstract. We introduce the inverse annihilation and creation operators $\hat{a}^{-1}$ and $\hat{a}^{\dagger -1}$ by their actions on the number states. We show that the squeezed vacuum $\exp(\frac{1}{2}\xi\hat{a}^{\dagger 2}]|0\rangle$ and squeezed first number state $\exp[\frac{1}{2}\xi\hat{a}^{\dagger 2}]|n=1\rangle$ are respectively the eigenstates of the operators $(\hat{a}^{\dagger -1}\hat{a})$ and $(\hat{a}\hat{a}^{\dagger -1})$ with the eigenvalue ξ.

Keywords. Coherent states; squeezed states; squeezed vacuum; two-photon annihilation operators.

PACS No. 42·50

1. Introduction

There are several representations of the harmonic oscillator states. The extensively studied states are the number states, the coherent states [1] and the squeezed states [2–6]. The squeezed states are particularly important due to their potential application in noise reduction.

The number states are the eigenstates of the number operator $\hat{a}^\dagger\hat{a}$:

$$\hat{a}^\dagger\hat{a}|n\rangle = n|n\rangle, \qquad n = 0, 1, 2, \ldots, \tag{1.1}$$

whereas the coherent states are the eigenstates of the annihilation operator $\hat{a}$:

$$\hat{a}|\alpha\rangle = \alpha|\alpha\rangle. \tag{1.2}$$

Here $\hat{a}$ and $\hat{a}^\dagger$ are the boson annihilation and creation operators satisfying the commutation relation $[\hat{a}, \hat{a}^\dagger] = 1$ and α is an arbitrary complex number.

It is interesting to note that the ground state $|0\rangle$ corresponding to $n = 0$ is also a coherent state with $\alpha = 0$. This state, also called the vacuum state, is an eigenstate of the annihilation operator $\hat{a}$ with eigenvalue zero. A unitarily transformed vacuum $\hat{U}|0\rangle$ will then be an eigenstate of the unitarily transformed operator $\hat{U}\hat{a}\hat{U}^\dagger$ with zero eigenvalue:

$$\hat{U}\hat{a}\hat{U}^\dagger(\hat{U}|0\rangle) = 0. \tag{1.3}$$

Here we have used the unitarity relation of the operator $\hat{U}$:

$$\hat{U}^\dagger\hat{U} = \hat{U}\hat{U}^\dagger = I. \tag{1.4}$$

If we choose $\hat{U}$ to be the displacement operator

$$\hat{D}(\alpha)=\exp(\alpha\hat{a}^{\dagger}-\alpha^{*}\hat{a}), \tag{1.5}$$

we get the coherent state eigenvalue equation

$$(\hat{a}-\alpha)|\alpha\rangle=0. \tag{1.6}$$

Similarly, if we choose $\hat{U}$ to be the squeeze operator

$$\hat{S}(\sigma)=\exp[\tfrac{1}{2}(\sigma\hat{a}^{\dagger 2}-\sigma^{*}\hat{a}^{2})], \tag{1.7}$$

we obtain

$$(\hat{a}\cosh r-\hat{a}^{\dagger}e^{i\phi}\sinh r)|\sigma,0\rangle=0, \tag{1.8}$$

where we have written $|\sigma,0\rangle$ for squeezed vacuum, i.e.,

$$|\sigma,0\rangle=\hat{S}(\sigma)|0\rangle \tag{1.9}$$

and

$$\sigma=re^{i\phi}. \tag{1.10}$$

While (1.6) can be expressed as the eigenvalue equation $\hat{a}|\alpha\rangle=\alpha|\alpha\rangle$, we note that such a separation is not possible for (1.8), where the operator could be made independent of the parameter σ.

In this paper we aim to obtain a new eigenvalue equation for the squeezed vacuum which does not have the above mentioned limitation. Our motivation is, therefore, to look for an operator independent of σ of which the state $|\sigma,0\rangle$ is an eigenstate. In fact, we consider a slight generalization: In place of the usual squeeze operator (1.7) we let the exponential of a general quadratic $[\frac{1}{2}(\sigma\hat{a}^{\dagger 2}-\sigma^{*}\hat{a}^{2})+i\beta(\hat{a}^{\dagger}\hat{a}+\hat{a}\hat{a}^{\dagger})]$ act on to the vacuum. By making use of the normal ordered form of this exponential operator, we may express the state

$$\exp[\tfrac{1}{2}(\sigma\hat{a}^{\dagger 2}-\sigma^{*}\hat{a}^{2})+i\beta(\hat{a}^{\dagger}\hat{a}+\hat{a}\hat{a}^{\dagger})]|0\rangle \tag{1.11}$$

in the form [7]

$$(1-|\xi|^{2})^{1/4}\exp(\tfrac{1}{2}\xi\hat{a}^{\dagger 2})|0\rangle, \tag{1.12}$$

with

$$\xi=\frac{\sigma}{(\lambda\coth\lambda-2i\beta)}, \tag{1.13}$$

where $\lambda^{2}=(|\sigma|^{2}-4\beta^{2})$ and β is real.

In §2 we introduce the inverse operators $\hat{a}^{-1}$ and $\hat{a}^{\dagger^{-1}}$ and discuss some of the commutation relations obeyed by them. In §3 the desired eigenvalue equation is derived and we show that the state (1.12) is an eigenstate of the operator $(\hat{a}^{\dagger^{-1}}\hat{a})$. Also, we show that the squeezed first number state $\exp(\frac{1}{2}\xi\hat{a}^{\dagger 2})|n=1\rangle$ is the eigenstate of another operator $(\hat{a}\hat{a}^{\dagger^{-1}})$.

2. Inverse operators

We introduce inverse of the operators $\hat{a}$ and $\hat{a}^{\dagger}$ by their actions on the number states $|n\rangle$. These operators $\hat{a}^{-1}$ and $\hat{a}^{\dagger^{-1}}$ are defined as [8]

$$\hat{a}^{-1}|n\rangle=\frac{1}{(n+1)^{1/2}}|n+1\rangle, \qquad n=0,1,2,\ldots, \tag{2.1a}$$

$$\hat{a}^{\dagger^{-1}}|n\rangle = \frac{1}{\sqrt{n}}|n-1\rangle, \qquad n=1,2,\ldots, \tag{2.1b}$$

$$= 0, \qquad\qquad n = 0. \tag{2.1c}$$

From (2.1) one can see that $\hat{a}^{-1}$ behaves as a creation operator, while $\hat{a}^{\dagger^{-1}}$ behaves as an annihilation operator. The matrix elements of these operators are given by the following relations:

$$\langle m|\hat{a}^{-1}|n\rangle = \frac{1}{(n+1)^{1/2}}\delta_{m,n+1}, \tag{2.2a}$$

$$\langle m|\hat{a}^{\dagger^{-1}}|n\rangle = \frac{1}{\sqrt{n}}(1-\delta_{n,0})\delta_{m,n-1}. \tag{2.2b}$$

It is readily seen that $\hat{a}^{-1}$ is the right inverse of $\hat{a}$ and $\hat{a}^{\dagger^{-1}}$ is the left inverse of $\hat{a}^{\dagger}$, i.e.

$$\hat{a}\hat{a}^{-1} = \hat{a}^{\dagger^{-1}}\hat{a}^{\dagger} = I, \tag{2.3}$$

whereas

$$\hat{a}^{-1}\hat{a} = \hat{a}^{\dagger}\hat{a}^{\dagger^{-1}} = I - |0\rangle\langle 0|. \tag{2.4}$$

Here $|0\rangle\langle 0|$ is the projection operator on to the vacuum. We find that these operators satisfy the following commutation relations:

$$[\hat{a},\hat{a}^{-1}] = [\hat{a}^{\dagger^{-1}},\hat{a}^{\dagger}] = |0\rangle\langle 0|, \tag{2.5}$$

$$[\hat{a},\hat{a}^{\dagger k}] = k\hat{a}^{\dagger(k-1)}, \tag{2.6}$$

$$[\hat{a}^{\dagger},\hat{a}^{k}] = -k\hat{a}^{(k-1)}, \tag{2.7}$$

where k is any positive or negative integer.

3. The eigenvalue equation

As mentioned earlier, the squeezed vacuum [eq. (1.11)] may be expressed in the form:

$$|\xi,0\rangle = (1-|\xi|^2)^{1/4}\exp(\tfrac{1}{2}\xi\hat{a}^{\dagger^2})|0\rangle. \tag{3.1}$$

We are, therefore, looking for an operator of which the state (3.1) is an eigenstate. Since the generation of a squeezed vacuum is essentially a two photon process, we consider the two photon annihilation operator $(\hat{a}^{\dagger^{-1}}\hat{a})$. From eq. (2.3) and the relation

$$[\hat{a},\exp(\tfrac{1}{2}\xi\hat{a}^{\dagger^2})] = \xi\hat{a}^{\dagger}\exp(\tfrac{1}{2}\xi\hat{a}^{\dagger^2}), \tag{3.2}$$

we find that

$$[\hat{a}^{\dagger^{-1}}\hat{a},\exp(\tfrac{1}{2}\xi\hat{a}^{\dagger^2})] = \xi\exp(\tfrac{1}{2}\xi\hat{a}^{\dagger^2}) + [\hat{a}^{\dagger^{-1}},\exp(\tfrac{1}{2}\xi\hat{a}^{\dagger^2})]\hat{a}. \tag{3.3}$$

If we let (3.3) act on the vacuum, we obtain

$$[\hat{a}^{\dagger^{-1}}\hat{a},\exp(\tfrac{1}{2}\xi\hat{a}^{\dagger^2})]|0\rangle = \xi\exp(\tfrac{1}{2}\xi\hat{a}^{\dagger^2})|0\rangle. \tag{3.4}$$

Equation (3.4) is of interest since it can be expressed in the form

$$\hat{a}^{\dagger^{-1}}\hat{a}[\exp(\tfrac{1}{2}\xi\hat{a}^{\dagger^2})|0\rangle] = \xi[\exp(\tfrac{1}{2}\xi\hat{a}^{\dagger^2})|0\rangle], \tag{3.5}$$

which is an eigenvalue equation. Hence, we conclude that the squeezed vaccum (3.1), i.e., $\exp[\frac{1}{2}\xi\hat{a}^{\dagger 2}]|0\rangle$ is an eigenstate of the operator $(\hat{a}^{\dagger^{-1}}\hat{a})$ with an eigenvalue ξ.

If we consider another two photon annihilation operator $(\hat{a}\hat{a}^{\dagger^{-1}})$, we find that

$$[\hat{a}\hat{a}^{\dagger^{-1}}, \exp(\tfrac{1}{2}\xi\hat{a}^{\dagger 2})] = \xi\exp(\tfrac{1}{2}\xi\hat{a}^{\dagger 2})\hat{a}^{\dagger}\hat{a}^{\dagger^{-1}} + \hat{a}[\hat{a}^{\dagger^{-1}}, \exp(\tfrac{1}{2}\xi\hat{a}^{\dagger 2})]. \tag{3.6}$$

On letting (3.6) operate on the first number state $|n=1\rangle$ we find that

$$[\hat{a}\hat{a}^{\dagger^{-1}}, \exp(\tfrac{1}{2}\xi\hat{a}^{\dagger 2})]|n=1\rangle = \xi\exp(\tfrac{1}{2}\xi\hat{a}^{\dagger 2})|n=1\rangle. \tag{3.7}$$

One can write immediately from this equation that

$$\hat{a}\hat{a}^{\dagger^{-1}}[\exp(\tfrac{1}{2}\xi\hat{a}^{\dagger 2})|n=1\rangle] = \xi[\exp(\tfrac{1}{2}\xi\hat{a}^{\dagger 2})|n=1\rangle]. \tag{3.8}$$

Hence, we conclude that the squeezed first number state, i.e., $\exp[\frac{1}{2}\xi\hat{a}^{\dagger 2}]|n=1\rangle$, is an eigenstate of the operator $(\hat{a}\hat{a}^{\dagger^{-1}})$ with an eigenvalue ξ.

References

[1] R J Glauber, *Phys. Rev.*, **131**, 2766 (1963)
[2] D F Walls, *Nature (London)* **306**, 141 (1983) and references therein
[3] R E Slusher, L W Hollberg, B Yurke, J C Mertz and J F Valley, *Phys. Rev. Lett.*, **55**, 2409 (1985)
[4] R M Shelby, M D Levenson, S H Perlmutter, R G Devoe and D F Walls, *Phys. Rev. Lett.*, **57**, 691 (1986)
[5] L A Wu, H J Kimble, J L Hall and H Wu, *Phys. Rev. Lett.*, **57**, 2520 (1986)
[6] R M Shelby, M D Levenson, D F Walls, A Aspect and G J Milburn, *Phys. Rev.* **A33**, 4008 (1986)
[7] Anil K Roy and C L Mehta, *J. Mod. Opt.*, **39**, 1619 (1992)
[8] C L Mehta, Anil K Roy and G M Saxena, *Phys. Rev.* **A46**, 1565 (1992)

PRAMANA
— journal of
physics

© Printed in India

Vol. 42, No. 4,
April 1994
pp. 315–318

A note on the harmonic plus inverse-harmonic potential in quantum mechanics

R S KAUSHAL
Department of Physics and Astrophysics, University of Delhi, Delhi 110 007, India

MS received 15 October 1993; revised 17 January 1994

Abstract. The ground state of a class of potentials described by $V(x) = a_{20}x^2 + a_1/x^2$ is investigated. This potential possesses some distinct features like that of a symmetric double-well potential, and can be used in modelling the fusion process of two identical nuclei as well.

Keywords. Schrödinger equation; eigenfunction; square integrability.

PACS No. 3·65

It is well-known [1] that as a result of the separation of the Schrödinger equation in radial and angular coordinates, a central potential $v(r)$ attains an effective form $\mathscr{V}(r) = v(r) + l(l+1)\hbar^2/(2\mu r^2)$ when appears in the reduced Schrödinger equation. Here the integer values of l (called the orbital quantum number) correspond to the orbital excitations of the system described by $v(r)$. In this note we study the one-dimensional system described by the potential

$$V(x) = a_{20}x^2 + a_1/x^2. \tag{1}$$

It is noticed that the square integrability as well as the single-valued nature of the eigenfunctions for (1) in the region $x \in (-\infty, \infty)$ demand some discrete values of a_1 (namely, $a_1 = m(m-1)\hbar^2/2\mu$, where m is an integer which is allowed to take the values $m = 2, 3, 4, \ldots$, and it should not be confused with the standard magnetic quantum number). As a result there appears a striking similarity between the three-dimensional central potential $\mathscr{V}(r)$ for the harmonic form of $v(r)$ and the one-dimensional potential (1). While it may be interesting to note this type of similarity, a difference worth mentioning is that the discrete values of l describe the excitations of the same system whereas the discrete values of a_1, correspond altogether to different systems. Moreover, the origins of $l(l+1)$-term in $\mathscr{V}(r)$ and that of $m(m-1)$-term in $V(x)$ are different. The study of such distinct features for the potential (1) is new.

The Schrödinger equation for the potential (1) can be written as

$$\left(-\frac{\mathrm{d}^2}{\mathrm{d}x^2} + b_{20}x^2 + \frac{b_1}{x^2}\right)\psi(x) = \lambda\psi(x), \tag{2}$$

where $b_{20} = 2\mu a_{20}/\hbar^2$, $b_1 = 2\mu a_1/\hbar^2$ and $\lambda = 2\mu E/\hbar^2$. In order to solve (2) we make use [2] of an ansatz for the eigenfunction, namely $\psi(x) = N\exp((g(x))$, with $g(x) = \beta_{20}x^2 + \beta_1 \ln x$. Using this form in (2) and subsequently rationalizing the resultant equation, one obtains the unknown constants β_{20} and β_1 in terms of b_{20} and b_1 as

$$\beta_{20} = \pm\sqrt{b_{20}}/2; \quad \beta_1 = [1 \pm (1+4b_1)^{1/2}]/2.$$

However, for the well behaved nature of the solution $\psi(x)$ at $x = \pm\infty$, one should choose the negative sign in β_{20} and the positive sign in β_1. This will yield the expressions for the eigenvalue λ and the eigenfunction $\psi(x)$ as

$$\lambda = [2 + (1+4b_1)^{1/2}]\sqrt{b_{20}}, \tag{3a}$$

$$\psi(x) = Nx^{1/2\{1+(1+4b_1)^{1/2}\}}\exp(-\sqrt{b_{20}}x^2/2), \tag{3b}$$

where the normalization constant, N, can be determined from

$$\int_{-\infty}^{\infty} |\psi(x)|^2 \mathrm{d}x = 1. \tag{4}$$

It may be noted that for the existence of integral (4) the exponent of x in (3b) should be a positive integer including zero (say m) i.e.

$$1 + (1+4b_1)^{1/2} = 2m, \quad (m = 0, 1, 2, \ldots)$$

implying

$$b_1 = m(m-1). \tag{5}$$

In fact for $m = 0$ and 1, b_1 becomes zero and thus reducing the problem to the pure harmonic case. Further, for any nonzero contribution from the inverse-harmonic term in (1) one should have $m \geqslant 2$. Finally, λ and $\psi(x)$ for the potentials

$$V(x) = a_{20}x^2 + \frac{m(m-1)\hbar^2}{2\mu x^2}, \quad (m = 2, 3, 4, \ldots) \tag{6}$$

turn out to be

$$\lambda = (2m+1)\sqrt{b_{20}}, \tag{7a}$$

$$\psi(x) = Nx^m \cdot \exp(-\sqrt{b_{20}}x^2/2), \tag{7b}$$

with the normalization constant given by

$$N = \left[\frac{2^m b_{20}^{1/2(m+1/2)}}{\sqrt{\pi}(2m-1)!!}\right]^{1/2}.$$

For a typical value of b_{20} (say $b_{20} = 2{\cdot}5$) the behaviour of the potential (6) and that of the corresponding eigenfunctions is shown in figures 1 and 2, respectively for $m = 2$, 4 and 7. Here we have set $\hbar = 2\mu = 1$. For $m \geqslant 2$, figure 1 clearly shows the features of a symmetric double-well potential however with an infinite barrier between the two wells. Further, a uniformly shifting tendency of the minima with respect to the increasing values of m can be noticed alongwith the fact that the energy levels are identical in both the wells. While for even values of m, $\psi(x)$ has two maxima (cf. figure 2) lying symmetrically on either side at $x = \pm[m(m-1)/b_{20}]^{1/4}$, there exists a node at $x = 0$ in $\psi(x)$ for odd values of m.

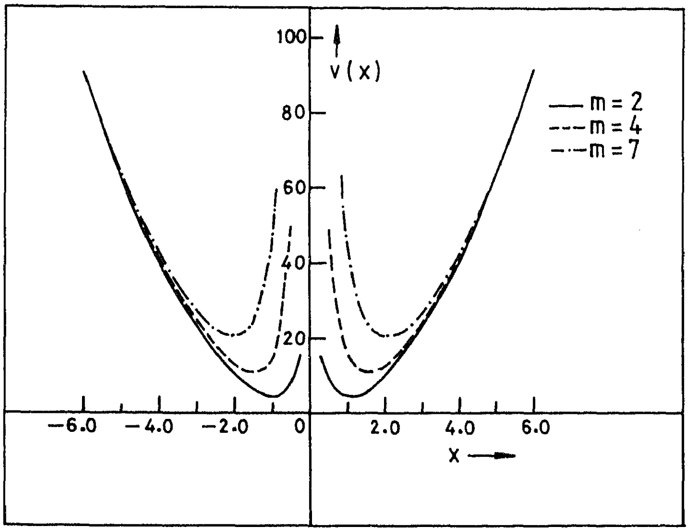

Figure 1. Plot of potential (6) for different values of m and for $\hbar = 2\mu = 1$; $b_{20} = 2{\cdot}5$.

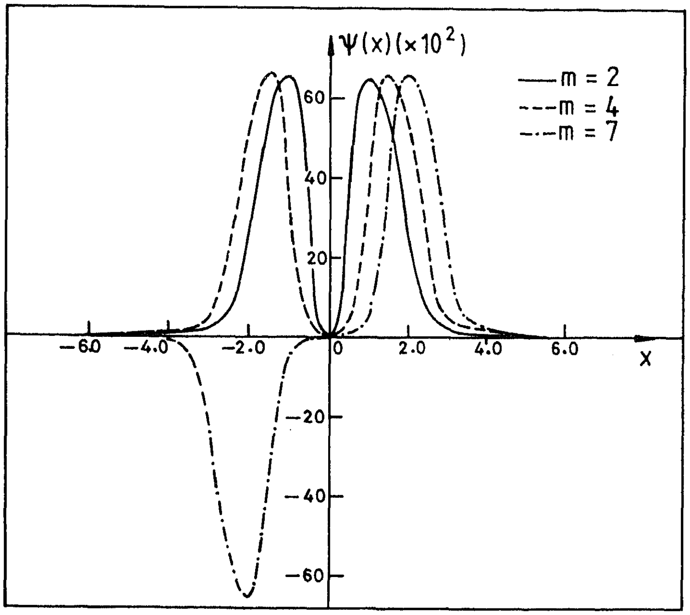

Figure 2. Plot of the ground state normalized wave functions for parameter values defined for figure 1.

From the point of view of applications of the potential (1) a few remarks are in order: (i) Here we have considered only the ground state of (1). For the excited states, however, one can as well start with the ansatz $\psi(x) = Nf(x)\cdot\exp(g(x))$, where $f(x)$ is a polynomial and $g(x)$ can be chosen as before, and obtain [3] the solution of (2); or else one can look for the solutions of (2) directly in terms of the Laguerre polynomials. (ii) Generalization of (1) to the noncentral case in two-dimensions is also possible [2] in a straightforward manner, e.g. the cases (a) and (b) of § 2 (cf. [2]) are worth investigating in this context. (iii) Potential (1) can offer a model-description for the fusion of two identical nuclei, particularly when each nucleus is capable of being described in terms of a harmonic potential. In fact, by reducing successively the values of b_1 (or that of m) and finally choosing $b_1 = 0$, the two nuclei can be put together in the same harmonic well. In other words, the integer values of m accounts for the relative separation between the two wells (cf. figure 1) which are expected to have the identical energy levels. As a matter of fact such an idealised description will overcome some of the difficulties which already arise in the conventional two-centre model for nuclei. For example, the problem of eliminating the barrier between the two wells or that of the corrections needed [4] for the quantum numbers of the one well in the presence of the other, is automatically resolved in the present description. This description, however, remains more of an illustrative type than the realistic one in the sense that the problem is solved only in one dimension. (iv) Potential (1) can also be useful in the description of those field theories or the structural phase transitions (see, for example, Khare and Behera [5]) in which the role of tunnelling is either of least importance or not at all important. It is also possible to study the phenomenon of tunnelling by introducing some perturbation in the potential (1) and consequently by generating an asymmetry between the two wells. In this case, however, the ground state (7b) can be used to develop the higher order perturbation solutions for different values of m.

Acknowledgement

The author wishes to thank Dr D Parashar for several discussions.

References

[1] See, for example, L I Schiff, *Quantum mechanics* (McGraw Hill Book Co. Inc. 1955) p. 74; or S Gasiorowicz, *Quantum physics* (John Wiley and Sons, 1974) p. 179

[2] R S Kaushal, *Ann. Phys.* **206**, 90 (1991)

[3] R S Kaushal and D Parashar, *Phys. Lett.* **A170** 335 (1992)
D R Taylor and P G L Leach, *J. Math. Phys.* **30**, 1525 (1989)

[4] P -T Ong and W Scheid, *Z. Naturforsch.* **30a**, 406 (1975)

[5] A Khare and S N Behera, *Pramana – J. Phys.* **14**, 327 (1980)

PRAMANA
— journal of
physics

© Printed in India

Vol. 42, No. 4,
April 1994
pp. 319–332

WKB approximation in complex time II

S BISWAS, J GUHA and N G SARKAR
Department of Physics, University of Kalyani, Kalyani 741 235, India

MS received 4 October 1993; revised 18 January 1994

Abstract. The non-perturbative method, developed recently, of WKB approximation in complex time is applied to some known curved space time. Three cases namely (1) static in and out region, (2) non-static in and out region, (3) static in and non static out region are considered here. We find non-trivial particle production corresponding to the quantum vacuum definition of Castagnino and Mazzitelli.

Keywords. Multiple reflection; particle production; curved space time.

PACS No. 98·80

1. Introduction

The particle production by a time dependent field is an active area of research both in quantum electrodynamics and quantum cosmology. The primary work in this direction dates back to Schwinger [1] who calculated Im L_{eff} (needed in defining probability of particle production) for particles moving in electric and magnetic fields, and the field of a plane electromagnetic wave. Subsequently many authors [2–8] have considered the particle production in various frameworks. In quantum cosmology the particle production plays an important role in the inflationary model of the universe. In this model though the universe classically turns back from a finite radius to an expanding mode, quantum corrections that occur at Planck length do not lead to bounce off at finite radius and re-expand to infinity. The universe may not reexpand at all or if it expands it does not settle down to Friedman solution, rather it explodes with a de Sitter mode with

$$ds^2 = dt^2 - a^2(t)[dx^2 + dy^2 + dz^2], \tag{1}$$

where $a(t) = \exp(At)$; $A > 0$. To have an exit from the inflationary scenario, one requires damping so that $a(t)$ settles down to steady Friedman mode. It is suggested that in isotropic cosmologies damping comes from particle production and it is due to time dependent change in curvature or matter fields in the model. This in turn is related to the cosmological constant problem. In all standard models of inflationary universe, it is impossible to demand zero vacuum energy in both the symmetric and asymmetric phase. Practically vacuum energy is large enough i.e., we have a large cosmological constant whereas the present limit of cosmological constant fixed by Hubble's measurement is $|\Lambda|/m_{\text{p}}^2 < 10^{-120}$, where m_{p} is the Planck mass. It is hoped that in expanding universe particle production might cause a large Λ_{initial} to arrive at the value $\Lambda_{\text{obs}}/m_{\text{p}}^2 < 10^{-120}$ satisfactorily. This idea is as follows. In curved space time when one deals with motion of particles in a gravitational background, one requires to define 'in' and 'out' vacuua corresponding to given gravitational background. In such a situation particle production might occur as the particle evolves from 'in' vacuum to 'out' vacuum due to a change in vacuum energy. This is turn, can be regarded as a change in the effective cosmological constant as the particle production proceeds. In view of the importance of particle production as mentioned above, it is necessary to look at its scenario in expanding space time. The present paper is an attempt in this direction.

In this paper we will concentrate mainly on the particle production in some models of expanding universe i.e., $\dot{a}/a > 0$ within the framework of recently proposed WKB approximation in complex time [9: referred to as I] to settle the role of vacuua, a delicate object in curved space time. The standard procedure in dealing with particle production is to evaluate the Bogolubov mixing transformation and classify the vacuum. The energy momentum of the created particle is evaluated by computing the energy differences corresponding to the two sets of vacuua, namely adiabatic and conformal vacuua. In curved space time the appropriate definition of vacuum is still not well resolved. Moreover one is not able to calculate $\langle T_{\mu\nu} \rangle$ more than one loop approximation satisfactorily. In Bogolubov transformation technique, out of the many possible solutions only two particular sets are chosen to fix the vacuua and hence the Bobolubov coefficients α_k and β_k are fixed. A non-zero β_k implies particle production with a mixing of positive and negative energy states. The procedure does not elucidate clearly the role of paths especially the complex paths of scattering states as well as the origin of thermal spectrum. More specifically the role of tunnelling paths i.e., paths in imaginary time is not exemplified by Bogolubov transformation technique. The complex paths are necessary to explain the particle production in curved space time.

To bypass this difficulty, we take recourse to a non perturbative method of WKB approximation in complex time, recently developed by us [9, 10]. In most problems e.g., problems dealing with motion of particles in strong time varying electromagnetic field, the Wheeler–DeWitt equation in quantum cosmology [11], transport equation in quark gluon plasma based on Wigner representation [12], the temporal equation takes the form of one dimensional Schrödinger equation, not in space but in time, viz.,

$$\frac{d^2\psi}{dt^2} + [w^2 - V(t)]\psi = 0, \tag{2}$$

where w plays the role of energy and $V(t)$ is a time dependent potential.

Knoll and Schaeffer [13, 14] and Schrempp and Schrempp [15] developed the method of complex reflection using semiclassical paths in space. We extend the method to the time variable in the form of the complex multiple reflection in time [9, 10] treating $V(t)$ as a function of complex time t.

The WKB approximation for complex trajectories accounts for contribution of the order of $\exp(-c/\hbar)$ to the usual WKB wave which would vanish in the classical limit. The WKB approximation generalised to complex time turns out to reproduce quantitatively all quantum mechanical effects and remain accurate in cases when the potential $V(t)$ varies rapidly over a distance of wavelength or less.

In some problems particle production takes place by non-local barrier penetration. In WKB approximation this non-local behaviour is well described by non-local functional $\int [w^2 - V(t)]^{1/2} dt$. Moreover, the complex path approach takes into account the behaviour of tunnelling path (mainly in Euclidean space) that is barely needed for mixing of positive and negative energy states. One loop correction, basically an order $\hbar$ approximation, breaks down when the quantum correction is large enough compared to classical contribution. Therefore it is necessary to look at the particle production through semiclassical WKB approximation, and if it is unimportant in WKB approximation it is unlikely to be important in an improved approximation [2]. In wavefunction or classical path approaches it is found by many authors that the region near the turning points (bounces in the problem considered) is important, whereas the WKB approximation (real paths) is needed to show that the region away from the points is negligible.

In § 2 we briefly outline the method of complex multiple reflection in time. The role of vacuum has been discussed in § 3. In § 4 we apply our method to calculate pair production amplitude in some known space times. We discuss three cases viz., the static in and out region; non static in and out region and finally static in and non-static out region. The consequences of the results are then discussed. Concluding remarks are given in § 5.

2. WKB approximation in complex time

Let us start with the one dimensional Schrödinger equation in time i.e., equation (2) and generalize the result of Schrempp and Schrempp [14] in complex t-plane where $V(t)$ is treated as a function of complex t. In this approach one starts at a real point and ends at another real point, but is complex in between. In our work we consider two cases with

$$\Omega(t) = [w^2 - V(t)]^{1/2}, \tag{3}$$

having one and two turning points, real or complex. The standard WKB approximation with real t is written as [15]

$$\psi = \frac{C_1}{[\Omega(t)]^{1/2}} \exp \int i\Omega(t)\mathrm{d}t + \frac{C_2}{[\Omega(t)]^{1/2}} \exp \int (-i)\Omega(t)\mathrm{d}t. \tag{4}$$

To proceed with WKB approximation in complex time we define

$$S(t, t') = \int_{t'}^{t} \Omega(t)\mathrm{d}t = S(t) - S(t'). \tag{5}$$

In (5), $S(t)$ refers to the value of the integral evaluated at the limit t i.e.,

$$S(t) = \left[\int \Omega(t)\mathrm{d}t \right]_t. \tag{6}$$

Treating $\Omega(t)$ as a function of complex t the turning points are determined from

$$\Omega(t) = [w^2 - V(t)]^{1/2} = 0. \tag{7}$$

The boundary conditions are chosen such that

$$\begin{aligned} &\psi \sim \exp[iS(t\,t_1)] && ; \quad t \to -\infty \\ &\psi \sim \exp[iS(t\,t_1)] + iR\exp[-iS(t\,t_1)]; && \quad t \to \infty \end{aligned} \tag{8}$$

where R is called reflection amplitude. In (8) t is real but the turning points t_1 and t_2 are complex. When we consider the pair production as a consequence of reflection in time, the reflection coefficient is identified as pair production amplitude. The basis of our method rests on Feynmann prescription [9] of negative energy particle solution propagating backward in time as being equivalent to positive energy antiparticle solution moving forward in time. The idea of considering particle production as a process of reflection in time was also pursued by Cornwall and Ticktopoulos [17], albeit in a different context. They view pair production as Klein paradox like situation, not in space but in time. Our approach is a generalization of the Klein paradox like situation, not in space but in time, proposed by Cornwall and Ticktopoulos [17]. In I we have established connection between reflection in time and pair production namely

$$|\text{pair production amplitude}|^2 = |\text{reflection amplitude}|^2. \tag{9}$$

In other words, the particle production amplitude, using complex semiclassical method yields wavefunction identical to that obtained by generalized WKB approximation.

Case A: One turning point

For one complex turning point t_1, the complex semiclassical approximation leads to the wavefunction [9]

$$\psi(t) \underset{t\to\infty}{\sim} \exp[iS(t\,t_0)] + (-i)\exp[iS(t_1\,t_0)]\exp[-iS(t\,t_1)] \tag{10}$$

where we have dropped the WKB pre-exponential factor for convenience. In (10) the complex turning point is determined from (7) and $S(t\,t')$ is defined as in (5). Equation (10) is interpreted as follows. A wave starting from $t = t_0$ and ending at t can be considered to be composed of (i) a wave starting at $t = t_0$, moving left reaches t and (ii) a wave starting at $t = t_0$ reaches the complex reflection point t_1 and turns back towards t. The factor $(-i)$ in (10) has been introduced to ensure reflection at t_1.

Equation (10) leads to the pair production amplitude [9]

$$R = -\exp[2iS(t_1)]. \tag{11}$$

Case B: Two turning points

For two turning points t_1 and t_2 in the complex t plane the resulting multiple reflection series is given by [9, 10]

$$\psi(t) \underset{t\to\infty}{\sim} \exp[iS(t\,t_0)] + (-i)\exp[iS(t\,t_0) - iS(t\,t_1)] \sum_{\mu=0}^{\infty} [-i\exp\{iS(t_1\,t_2)\}]^{2\mu} \tag{12}$$

The interpretation of (12) is as follows. The classical trajectories building up the quantum mechanical waves are (i) the direct (real) trajectory from t_0 to t represented by the first term in (12) and (ii) the trajectory from t_0 returning to t after complex reflections between t_1 and t_2 leading to geometrical series $\Sigma_{\mu=0}^{\infty}$ in (12). In the usual WKB approximation with real semiclassical path we have only the first term $\exp[iS(t\,t_0)]$ in (12). But in the case under discussion a second term makes its presence due to contribution from reflection. Equation (12) leads to the reflection coefficient [9]

$$R = -\frac{\exp[2iS(t_1)]}{1+\exp[2iS(t_1 t_2)]}. \tag{13}$$

In the expressions for pair production amplitude R in (11) and (13) we have overlooked contribution from t_0 limit. This is justified in view of the following. In our early works [9, 10] we have established the equivalence between this method and the Bogolubov transformation technique [18, 19] that is generally used in cosmological particle creation problems. One may recall that while calculating the pair production amplitude through Bogolubov technique we form two sets of normalized modes $\{\bar{u}_p, \bar{u}_p^*\}$ and $\{u_p, u_p^*\}$ related by

$$\bar{u}_p = \alpha_p u_p + \beta_p u_p^*. \tag{14}$$

Our R is related to the Bogolubov coefficients α_p and β_p as $|R| \sim \left|\frac{\beta_p}{\alpha_p}\right|$. Since the same contributions from the t_0 limit occurs in both α_p and β_p they cancel out and hence do not occur in R.

The method we are advocating has many attractive features. In this new method the exact solution of the field equation is not required explicitly and also propagators that make the situation very complicated. Our method requires calculation of simple integrals (involving branch points) like (5) and (6) at the turning points. In spite of the extreme simplicity of our method we get results [9, 10, 20, 21] which coincide with the standard results suggesting that the complex multiple reflection technique in time is a valid description for calculating the pair production amplitude. A very important aspect of our method is that while evaluating the reflection amplitude the behaviour of the solution near the turning point is not required, and we take the contributions of classical paths and tunnelling paths (i.e., imaginary paths in time) correctly which will be justified through calculations that follow. The appropriateness of our method will be clarified from the work of Neville [2]. However they were unable to tackle the contributions of tunnelling paths correctly, though they mentioned the usefulness of complex paths.

Another significant aspect of our method is that the pair production amplitude depends on the bounce points (i.e., turning points) which lie in the complex plane. Basically we get contributions from disconnected region i.e., from the euclidean space.

We have employed our technique to the case of pair production in time dependent electromagnetic field [10, 20] and obtained results which coincide with that of Barut and Duru [22]. We have shown elsewhere [10, 20] that our technique leads exactly to the result of Cornwall and Ticktopoulos [17]. We have further applied the method of complex multiple reflection in time to the pair production scenario in two dimensional Milne universe and reproduced standard results [9, 21]. In quantum cosmology we have calculated the wavefunction of the universe identifying the pair production wavefunction as wormhole solutions in Euclidean space. We in this paper, test how our method works when we consider different space times to find pair production amplitude.

3. Role of vacuua

Before we pass on to the calculation of pair production amplitude in curved space time it is necessary to specify the choice of vacuum in the calculation. In curved space time the correct choice of vacuum is still an open question. It has been shown that a reasonable quantum vacuum can be defined in Bianchi type I universes, at the cosmological singularity and at the asymptotic far future region provided the initial expansion is not violent. The reader is referred to the works of Castagnino and others [23–26] for the vacuum definition in curved space time. These authors prescribe a vacuum choice as

$$\psi_k^{\text{in}} = \begin{cases} \dfrac{1}{(2k)^{1/2}}\exp(-ik\eta)\ ; & \eta \leqslant 0 \\ \alpha_k \phi_k^{\text{out}} + \beta_k \phi_k^{*\,\text{out}}\ ; & \eta > 0 \end{cases} \tag{15}$$

where the Bogolubov coefficient $|\beta_k|^2$ measures the pair production between $t=0$ and $t=\infty$; ϕ_k^{out} is given by the WKB approximation solution of the field equation and η is a conformal time defined in (17).

Our definition is basically equivalent to the above definition of vacuum. However we extend the idea of Cornwall and Ticktopoulos [9, 17] as follows. At $t=-\infty$ there is no particle but at $t=+\infty (t>t_a)$ due to reflection in time there is a particle moving forward in time and an antiparticle moving backward in time; where t_a is the reflection point. As the particle-antiparticle definition in Minkowski time is not valid in curved space time we adopt Parker's definition [27] so that particle-antiparticle solution are now replaced by $\exp(\pm iS)$ where S is obtained through WKB solution. With this definition our reflection coefficient will be equivalent to $|\beta_k/\alpha_k|$ of Castagnino and others [23–26]. The equivalence of the two approaches is quite convincing for the following facts. In our calculation we always convert the metric (1) as

$$\mathrm{d}s^2 = C^2(\eta)[\mathrm{d}\eta^2 - (\mathrm{d}x^2 + \mathrm{d}y^2 + \mathrm{d}z^2)], \tag{16}$$

where we have introduced the conformal time coordinate η given by

$$\eta = \int^t \frac{\mathrm{d}t}{a(t)}. \tag{17}$$

We then write the equation in η and look for the turning points. To our surprise we find that the turning points occur at $\eta = \pm i\beta$ which is an indication of the fact that this defines the cosmological singularity as in the work of Castagnino and others. This allows us to define the vacuum $t=0$ i.e., $\eta = -\infty$. The definition of vacuum at $\eta=\infty$ is not a problem. Here the WKB solution exactly coincides with the exact solution of the problem. So the vacuum defined with the WKB solution will be an adiabatic vacuum. It has been shown by Castagnino and others that this type of definition takes into account Hadamard renormalisation [23–26] properly i.e., the Green function shows Hadamard singularity. This discussion allows us to identify the turning points in the complex plane (in most cases Re $t=0$) as the cosmological singularity though we did not analytically continue the scale factor $a(t)$ for complex t. But in the solution the effect of complex t (paths in imaginary time $\equiv$ paths in euclidean space) is properly taken into account. We now proceed to the calculation of R for various space times.

4. Applications to different space times

We now apply our technique to some known space times to find the pair production amplitude by our method. We consider the motion of a scalar or a Dirac particle in the space time given by (16). For a scalar particle the temporal equation is [18]

$$\ddot{f}_k(\eta) + [k^2 + m^2 C^2(\eta)] f_k(\eta) = 0, \tag{18}$$

and for Dirac particle we have [28, 30]

$$\ddot{f}^{\pm}_{\lambda} + [\lambda^2 + m^2 C^2(\eta) \pm imC(\eta)] f^{\pm}_{\lambda} = 0. \tag{19}$$

where λ is a separation constant. This separation constant arises when one tries to solve the Dirac equation by the method of separation of variables [29] with the substitution

$$\psi_{\lambda jlm} = \exp(-3/2\eta) B_{\lambda}(\eta) M_{\lambda jl}(r) S(\theta, \phi) Z_{jlm}(\theta, \phi) \tag{20}$$

where

$$0 \leqslant \lambda < \infty, \quad j = \tfrac{1}{2}, \tfrac{3}{2}, \ldots, \quad l = j \pm \tfrac{1}{2}, \quad -j \leqslant m \leqslant j \tag{21}$$

$$B_{\lambda}(\eta) = \begin{pmatrix} f^{+}_{\lambda}(\eta) I & 0 \\ 0 & f^{-}_{\lambda}(\eta) I \end{pmatrix}; \quad I = \begin{pmatrix} 1 & 0 \\ 0 & 1 \end{pmatrix} \tag{22}$$

and $M_{\lambda jl}(r)$, $S(\theta, \phi)$, $Z_{jlm}(\theta, \phi)$ are defined as in [29]. Substituting (20) and (22) in the Dirac equation one gets two first order equations for $f^{\pm}_{\lambda}$. Equation (19) is obtained from the first order equations (see reference [29]). For a Dirac particle the relation

$$f^{+}_{\lambda}(m) = f^{-}_{\lambda}(-m), \tag{23}$$

is satisfied. So we consider the solution with one sign only.

We mentioned earlier that the nature of vacuum plays a crucial role in all particle production situations in curved space times. We thus consider two types of problems where in and out regions are static and where either of these two or both are non static.

Case 1. Static in and out regions

We first consider a case where both in and out regions are static. For this purpose we choose a scale factor

$$C^2(\eta) = A + B \tanh \rho\eta. \tag{24}$$

Now we have

$$\begin{aligned} C^2_{\text{in}} &= C^2(\eta \to -\infty) = A - B, \\ C^2_{\text{out}} &= C^2(\eta \to +\infty) = A + B, \end{aligned} \tag{25}$$

so that from (18) we can write

$$\begin{aligned} w^2_{\text{in}} &= k^2 + m^2(A - B) \\ w^2_{\text{out}} &= k^2 + m^2(A + B). \end{aligned} \tag{26}$$

This implies that for both the in and out regions $\partial/\partial\eta$ is the killing vector. As $w_{\text{in}} \neq w_{\text{out}}$ we expect particle production in such a space time.

Equation (18) with (24) is of the form of (2) with

$$\Omega(\eta) = [k^2 + m^2(A + B\tanh\rho\eta)]^{1/2}. \tag{27}$$

The indefinite integral

$$I = \int \Omega(\eta)\mathrm{d}\eta, \tag{28}$$

with the substitution

$$\tau = \exp(\rho\eta) \tag{29}$$

becomes

$$I = \frac{1}{\rho}\int\left(\frac{w_{\mathrm{out}}^2\tau^2 + w_{\mathrm{in}}^2}{\tau^2 + 1}\right)^{1/2}\frac{\mathrm{d}\tau}{\tau}. \tag{30}$$

Evaluation of (30) gives

$$\begin{aligned} I &= \frac{w_{\mathrm{out}}}{\rho}\ln[(\tau^2+1)^{1/2} + (\tau^2+\gamma^2)^{1/2}] \\ &\quad + \frac{w_{\mathrm{out}}\gamma}{2\rho}\ln\left[\frac{(\tau^2+\gamma^2)^{1/2} - \gamma(\tau^2+1)^{1/2}}{(\tau^2+\gamma^2)^{1/2} + \gamma(\tau^2+1)^{1/2}}\right], \end{aligned} \tag{31}$$

where we have introduced

$$\gamma = w_{\mathrm{in}}/w_{\mathrm{out}}. \tag{32}$$

With the help of (7) the turning points are determined to be

$$\begin{aligned} \tau_1 &= i\gamma, \\ \tau_2 &= -i\gamma. \end{aligned} \tag{33}$$

Using (5) we evaluate $S(\tau_1\tau_2)$ to be

$$S(\tau_1\tau_2) = 0. \tag{34}$$

We find $S(\tau_1)$ from (6) to be

$$S(\tau_1) = \frac{w_{\mathrm{out}}}{\rho}\ln(1-\gamma^2)^{1/2} + \frac{i}{2\rho}w_{\mathrm{out}}\gamma\pi. \tag{35}$$

From (13), (34) and (35) we evaluate the pair production amplitude to be

$$R = -i\exp\left[\frac{2i}{\rho}w_{\mathrm{out}}\ln(1-\gamma^2)^{1/2}\right]\exp\left(-\frac{\gamma\pi w_{\mathrm{out}}}{\rho}\right), \tag{36}$$

so that we have

$$|R|^2 = \exp\left(-\frac{2\pi w_{\mathrm{in}}}{\rho}\right). \tag{37}$$

The expression (37) has also been calculated using Bogolubov transformation technique [18]. The result is

$$|R|^2 = \frac{|\beta_k|^2}{|\alpha_k|^2} = \frac{\sinh^2 \frac{\pi}{2\rho}(w_{\text{out}} - w_{\text{in}})}{\sinh^2 \frac{\pi}{2\rho}(w_{\text{out}} + w_{\text{in}})} \sim \exp\left(-\frac{2\pi w_{\text{in}}}{\rho}\right), \tag{38}$$

for $w_{\text{in}} < w_{\text{out}}$. This result (38) exactly coincides with (37).

Case 2. Non static in and out region

We now consider space times where the explicit role of conformal and adiabatic vacua has been clarified. We consider two types of universe in 4 dimensions namely the Chitre-Hartle universe

$$\mathrm{d}s^2 = \mathrm{d}t^2 - t^2(\mathrm{d}x^2 + \mathrm{d}y^2 + \mathrm{d}z^2), \tag{39}$$

and the Milne universe

$$\mathrm{d}s^2 = \mathrm{d}t^2 - t^2[\mathrm{d}r^2 + \sinh^2 r(\mathrm{d}\theta^2 + \sin^2\theta \mathrm{d}\phi^2)] \tag{40}$$

and discuss pair production of spinor particle. For both the cases the metric is given by [29]

$$\mathrm{d}s^2 = C^2(\eta)[\mathrm{d}\eta^2 - \mathrm{d}r^2 - f^2(r)(\mathrm{d}\theta^2 + \sin^2\theta\,\mathrm{d}\phi^2)], \tag{41}$$

where

$$f(r) = r, \sinh r \text{ for } k = 0;\ -1; \quad C(\eta) = \exp\eta. \tag{42}$$

The vacuum expectation value of the regularised energy momentum tensor for spinor fields has been evaluated [29] in the background of the Chitre-Hartle and Milne metric in the framework of the one-loop approximation to quantum gravity. As in the case of scalar particles, it has been shown that

$$\langle T_{ik}^{(1/2)} \rangle_{\text{reg}}^{\text{Milne}} = \langle T_{ik}^{(1/2)} \rangle_{\text{reg}}^{\text{Chitre}} = 0. \tag{43}$$

Another method to foresee particle production is the non perturbative technique of complex multiple reflection in time. We verify with our method whether or not there is particle production in adiabatic vacuum. The one loop correction is basically an approximation where $O(\hbar)$ correction is taken into account. But in our method we have taken corrections non perturbatively as $O(\hbar) + O(\hbar)^2 + \ldots$ In this sense our method will be checked in the light of the correctness of one loop approximation as well as renormalization procedure.

Equation (19) with (42) reads

$$\ddot{f}_\lambda + [\lambda^2 + m^2\exp(2\eta) + im\exp(\eta)]f_\lambda = 0 \tag{44}$$

Equation (44) is of the form of (2) with

$$\Omega(\tau) = (\lambda^2 + i\tau + \tau^2)^{1/2}, \tag{45}$$

where we have substituted

$$\tau = m\exp(\eta). \tag{46}$$

The turning points are determined from (7) to be

$$\begin{aligned}\tau_1 &= -i/2 + i(\lambda^2 + \tfrac{1}{4})^{1/2},\\ \tau_2 &= -i/2 - i(\lambda^2 + \tfrac{1}{4})^{1/2}.\end{aligned} \tag{47}$$

Using (5) we calculate $S(\tau_1 \tau_2)$ to be

$$S(\tau_1 \tau_2) = \pi/2 + i\pi\lambda. \tag{48}$$

Using (6) we find $S(\tau_1)$ to be

$$S(\tau_1) = -\pi/4 + i[\ln(\lambda^2 + \tfrac{1}{4}) + \pi\lambda/2]. \tag{49}$$

The pair production amplitude can now be obtained from (13), (48) and (49) to be

$$R = -i\frac{1}{(\lambda^2 + \frac{1}{4})^{1/2}} \cdot \frac{\exp(-i\pi/2)\exp(-\pi\lambda)}{1 - \exp(-2\pi\lambda)}, \tag{50}$$

so that we have

$$|R|^2 = \frac{1}{(\lambda^2 + \frac{1}{4})} \cdot \frac{\exp(-2\pi\lambda)}{[1 - \exp(-2\pi\lambda)]^2}. \tag{51}$$

The consequence of this result will be discussed shortly.

Case 3. Static in and non-static out region

We consider now the scale factor with the past statically bounded expansion,

$$C(\eta) = C_{\text{in}} + \exp(2b\eta), \tag{52}$$

where $b = \text{constant} > 0$ is the expansion parameter. The expansion starts at $\eta \to -\infty$ with the constant scale factor $C_{\text{in}} = \text{constant}$ which we assume to be always $C_{\text{in}} \neq 0$; thus the in region is Minkowskian.

Equation (19) with (52) becomes

$$\ddot{f}_\lambda + [w_{\text{in}}^2 + 2m(mC_{\text{in}} + ib)\exp(2b\eta) + m^2\exp(4b\eta)]f_\lambda = 0 \tag{53}$$

where we have put

$$w_{\text{in}}^2 = \lambda^2 + m^2 C_{\text{in}}^2. \tag{54}$$

Equation (53) is of the form of (2) with

$$\Omega(\tau) = [\tau^2 + (2\mu + i)\tau + \nu^2]^{1/2}, \tag{55}$$

where we have introduced

$$\tau = \frac{m}{2b}\exp(2b\eta), \tag{56}$$

$$\nu = w_{\text{in}}/2b, \tag{57}$$

$$\mu = mC_{\text{in}}/2b. \tag{58}$$

The turning points are determined from (7) to be

$$\tau_1 = -(\mu + i/2) + [(\mu + i/2)^2 - \nu^2]^{1/2},$$
$$\tau_2 = -(\mu + i/2) - [(\mu + i/2)^2 - \nu^2]^{1/2}. \tag{59}$$

Using (5) we calculate $S(\tau_1 \tau_2)$ to be

$$S(\tau_1 \tau_2) = \pi/2 + i(\nu - \mu)\pi. \tag{60}$$

Using (6) we have for $S(\tau_1)$

$$S(\tau_1) = \mathrm{Re} + i\Big[\ln\{(\mu^2 - \tfrac{1}{4} - \nu^2)^2 + \mu^2\}^{1/8} + \tfrac{1}{2}\mu \tan^{-1}\frac{\mu}{\mu^2 - \frac{1}{4} - \nu^2} + \frac{\nu\pi}{2}\Big] \tag{61}$$

where 'Re' refers to the real part of $S(\tau_1)$. From (13), (60) and (61) we have for the pair production amplitude

$$R = -i[(\mu^2 - \tfrac{1}{4} - \nu^2)^2 + \mu^2]^{1/4} \times \frac{\exp(2i\,\mathrm{Re})\exp\left(-\mu\tan^{-1}\frac{\mu}{\mu^2 - \frac{1}{4} - \nu^2}\right)\exp(-\nu\pi)}{1 - \exp[-i(\nu - \mu)\pi]} \tag{62}$$

so that we have

$$|R|^2 = \frac{1}{[(\mu^2 - \frac{1}{4} - \nu^2)^2 + \mu^2]^{1/2}} \frac{\exp\left[-\mu\tan^{-1}\frac{\mu}{\mu^2 - \frac{1}{4} - \nu^2}\right]\exp(-2\nu\pi)}{[1 - \exp\{-2(\nu - \mu)\pi\}]^2} \tag{63}$$

In case $C_{\text{in}} = 0$ we have $\mu = 0$ and (63) reduces to

$$|R|^2 = \frac{1}{(\nu^2 + \frac{1}{4})} \cdot \frac{\exp(-2\nu\pi)}{[1 - \exp(-2\nu\pi)]^2}, \tag{64}$$

which is the same result (51) we obtained from Chitre-Hartle and Milne metric.

We now discuss the results we have so far obtained. For the static in and out regions [case 1] our results exactly reproduce the result of Birrel and Davies [18].

In the case of Chitre-Hartle and Milne universe [case 2] our result needs a careful analysis. It has been mentioned that there will be no particle production in Chitre-Hartle or Milne case in adiabatic vacuum though we see pair production in conformal vacuum. But in our analysis through WKB approximation the vacuum chosen is definitely adiabatic vacuum. If we translate our results to two dimensions, we find particle production even in adiabatic vacuum though this is not actually the case as demanded by Sahni [29]. Our suggestion is that this type of reduction should not be done directly from the results of $|R|^2$ in 4 dimensions. The reason is as follows. Elsewhere [9, 21] we calculated $|R|^2$ in degenerate Kasner's space time, namely

$$ds^2 = dt^2 - dx^2 - t^2 dy^2 - dz^2. \tag{65}$$

We found a non-zero $|R|^2$ for such a space time. Using $x=0$, $z=0$, thereby setting $k_1=k_3=0$ in the expression for $|R|^2_{\text{kasner's space time}}$, we found $|R|^2 \longrightarrow 0$ i.e., $|R|^2_{\text{Milne universe}} \longrightarrow 0$. This is quite an usual result. The reason is that the 2 dimensional Milne universe can be reduced to a flat space time under the substitution [18]

$$\begin{aligned} y^0 &= \exp\eta \cosh x \\ y^1 &= \exp\eta \sinh x \end{aligned} \tag{66}$$

with $0<y^0<\infty$ and $-\infty<y^1<\infty$. Hence we do not expect particle production in 2 dimensional Milne universe. But the 4 dimensional Milne universe is not 'merely flat space time in disguise'. Naturally in our calculation [9] we find that $|R|^2_{\text{Milne in 4 dimension}} \neq 0$. As λ in (51) does not explicitly contain k_1, k_2, k_3 it is difficult to set any two of the three variables to be equal to zero. In other words, a direct reduction of λ(4 dimension) to λ(2 dimension) is not readily possible. Hence passage from 4 dimensions to 2 dimensions is not justified. A definite conclusion can be obtained by considering the Dirac equation in 2 dimensional Milne universe and investigating particle production aspect in such a space time. But Milne universe in 4 dimension is not directly related to the Minkowski covering space to give a special significance to adiabatic vacuum. In this respect non-zero $|R|^2$ in adiabatic vacuum for Milne universe in 4 dimension is not unusual. However, the standard result that there will be no particle production in adiabatic vacuum follows from our expression of $|R|^2$. If the ψ_{WKB} is to be identified with the adiabatic vacuum then in the expression (13) we should put m or λ large in $\exp[\pm iS(t)]$. For large λ the vacuum defined by (19) will then reproduce the results of adiabatic vacuum. In that case from (51) we have $|R|^2 \longrightarrow 0$, because of the exponential factor. The surprising fact is that (51) is independent of m indicating that the vacuum in question does not depend upon m. It should be noted that adiabatic vacuum is a result of large mass approximation whereas the conformal vacuum exploits the conformal symmetry of the massless case. Our non-perturbative calculation takes the contribution from disconnected region and origin of the thermal spectrum [denominator of (51)] is inherent in our approach. In (51) term $\sim 1/\lambda^2$ generally arises in standard calculations but the rest is due to the contribution of tunnelling behaviour in complex treatment. The origin of the thermal spectrum is basically due to the contribution from the bounce points which depends on the topology of the space time chosen. It is evident that if we consider the adiabatic vacuum we must take $\lambda \longrightarrow$ large in the expression for $|R|^2$ but if the vacuum is not adiabatic (of course our vacuum is not conformal) then the approximation λ large is not necessary and the origin of thermal spectrum is definitely related to the topology of the spacetime. This requires further investigation.

Lotze [19] has also investigated the statically bounded expansion cases [case 3]. However our result is slightly different from his result. Let us suppose that the expansion is rapid. By this we mean that the expansion parameter b is so large that at Compton time $t_c = 1/m$, C_{in} may be omitted in $C(\eta)$. In that case we have $a(t_c)$ [see (1)] approximately equal to $2bt_c > C_{\text{in}}$ and hence $\mu_{\text{in}} \ll 1$, a condition of rapid expansion. In expanding universe λ/a is the momentum where λ is a separation constant in (19). So the non-relativistic particles satisfy the condition $\lambda/am \ll 1$, i.e., $\lambda/(2bt_c m) \ll 1$, which means $\lambda/2b \ll 1$ (since $mt_c = 1$). Thus even in the expanding universe the particles can be non-relativistic so long as b is large i.e., expansion is rapid. We finally conclude that the vacuum defined in Chitre-Hartle or Milne case is not exactly the adiabatic vacuum though it behaves as adiabatic vacuum only in large λ approximation. This is an interesting result. However it is a matter of investigation to judge this vacuum with respect to strong and weak vacuum as defined by Castagnino and others [23–26]. At least we can say that the vacuum chosen to WKB approximation in complex time is not adiabatic vacuum for λ, m not large, even if the conditions (15) are satisfied.

5. Conclusion

Let us summarize the essential features and the conclusions that follow therefrom. (1) We employ WKB approximation in complex time to find out pair production amplitude. Real path corresponds to the standard WKB approximation but complex semiclassical paths in time takes into account the tunnelling behaviour. (2) It is a non-perturbative approach, at least a step further from the one-loop approximation. (3) The use of WKB method in this type of problem is quite justified. (4) Thermal spectrum arises from the tunnelling path. Classically, the particle is at rest at the turning points but the quantum behaviour makes the particle to tunnel into complex plane to come back as if it spends most of the time at the turning points. (5) The method is applied to various cases almost reproducing the exact result obtained through Bogolubov transformation technique. (6) It is a noticeable result that the turning points in most cases studied lies at $t = 0 \pm i\varepsilon$. This suggests that particle production takes place at very early stage of the universe. Behaviour of the particle in the euclidean space determines the nature of production. This aspect is very important in the light of quantum cosmology particularly in evaluating quantum wavefunction. (7) We have chosen our vacuum such that the scale factor satisfies the criteria laid down by Castagnino and others [23–26] i.e., we are dealing with adiabatic vacuum. (8) We have also evaluated the amount of particle production in a de-Sitter space time with $a(t) = \exp(2bt)$ and found a pair production $\alpha \dfrac{\exp(-m\pi/b)}{1+\exp(-m\pi/b)}$. This is due to the fact that the adiabatic vacuum reduces to conformal vacuum. The particle production in de-Sitter space time, stability of de-Sitter vacuum and evolution of cosmological constant will be dealt with in future.

References

[1] J F Schwinger, *Phys. Rev.* **82**, 664 (1951)
[2] D E Neville, *Phys. Rev.* **D8**, 1695 (1984)
[3] A H Najmi and A C Ottewill, *Phys. Rev.* **D8**, (1984)
[4] G Samenoff and N Weiss, *Phys. Rev.* **D31**, (1985)
[5] E Mottla, *Phys. Rev.* **D31**, 754 (1985)
[6] W R Walker, *Phys. Rev.* **D31**, 767 (1985)
[7] L H Ford, *Phys. Rev.* **D31**, 710 (1985)
[8] L Parker, *Phys. Rev. Lett.* **21**, 582 (1968)
[9] S Biswas and J Guha, *Pramana – J. Phys.* **40**, 467 (1993)
[10] S Biswas and L Das, *Int. J. Theor. Phys.* **30**, 789 (1991)
[11] A Vilenkin, *Phys. Rev.* **D37**, 888 (1988)
[12] J M Eisberg and G Kalbermann, *Phys. Rev.* **D37**, 1197 (1988)
[13] J Knoll and R Schaeffer, *Ann. Phys.* **97**, 307 (1976)
[14] J Knoll and R Schaeffer, *Phys. Rep.* **31**, 159 (1977)
[15] F Schrempp and B Schrempp, *Nucl. Phys.* **B163**, 397 (1980)

[16] A K Ghatak and S Loknathan, *Quantum mechanics, theory and applications* (Macmillan India Ltd, New Delhi, 1984) Ch 13

[17] J M Cornwall and G Ticktopoulos, *Phys. Rev.* **D39**, 334 (1989)

[18] N D Birrel and P C W Davies, *Quantum field in curved space time* (University Press, Cambridge, 1982)

[19] K H Lotze, *Simultaneous creation of* e^+e^- *pairs and photons in RW universe*, IC/89/115

[20] S Biswas, J Guha and P Dasgupta, *Int. J. Mod. Phys.* (submitted)

[21] S Biswas, B Modak and J Guha, *Pramana – J. Phys.* (submitted)

[22] A O Barut and I H Duru, ICTP preprint, *Pair production in electric field in a time dependent gauge*, IC/89/179 (1989)

[23] M A Castagnino and F D Mazitelli, *Phys. Rev.* **D31**, 742 (1985)

[24] M A Castagnino and L Chimento, *Phys. Rev.* **D34**, 3676 (1986)

[25] M A Castagnino, E Gunzig, P Nardone and J P Paz, *Phys. Rev.* **D34**, 3698 (1986)

[26] F D Mazzitelli, J P Paz and M A Castagnino, *Phys. Rev.* **D36**, 2994 (1987)

[27] L Parker, *Fundam. Cosmic Phys.* 7, 201 (1982)

[28] A O Barut and L P Singh, *Exact solution of the Dirac equation in spatially non-flat RW space time II*, ICTP (1990) IC/90/205

[29] V Sahni, *Class. Quantum. Gravitation* **1**, 579 (1984)

[30] S Biswas, *Pramana – J. Phys.* **36**, 519 (1991)

PRAMANA
— journal of
physics

© Printed in India

Vol. 42, No. 4,
April 1994
pp. 333–340

An application of hypervirial perturbation theory to calculate energy eigenvalues of the Morse potential for various diatomic molecules

M R M WITWIT
Department of Applied Mathematics, University of Hull, Hull, HU6 7RX, UK

MS received 23 June 1993; revised 16 September 1993

Abstract. The Schrödinger equation with the potential $V(r) = D[\exp(-2\beta(r-r_e)) - 2\exp(-\beta(r-r_e))]$ is treated in the framework of the hypervirial-renormalization parameter scheme. The energy eigenvalues of various eigenstates for different molecules are calculated.

Keywords. Schrödinger equation; Morse potential; eigenvalues.

PACS No. 3·65

1. Introduction

The Schrödinger equation with the potential

$$V(r) = D[\exp(-2\beta(r-r_e)) - 2\exp(-\beta(r-r_e))] \tag{1}$$

has frequently been used to describe vibrating molecules. In quantum mechanics textbooks, the energy levels of potential (1) are often derived to the second order of the approximation within the framework of the Rayleigh-Schrödinger perturbation theory [1–3]. On the other hand, the Schrödinger equation with potential (1) has been studied by Hajj *et al* [4] using the Numerov finite difference approach to calculate the eigenvalues for the first five states. Also, Adam *et al* [5] have used a perturbative numerical technique to compute the energy levels for various eigenstates. Johnson [6] applied the Numerov–Cooley integration method to the Morse potential and obtained good results for the energy eigenvalues. Fernandez and Castro [7] applied diagonal and off-diagonal hypervirial relationships in order to obtain recursion formulae for matrix elements related to the perturbed Morse oscillator model. Their results simplify the variational and perturbative calculation of the energy eigenvalues for the Morse potential. Fernandez and Ogilvie [8] developed an approach to calculate analytic perturbation corrections of large order to the vibrational-rotational energies; their approach is based on a combination of perturbation theory and the hypervirial and Hellmann–Feynman theorems. Bonatsos *et al* [9] have shown that the quantum algebra $SU_q(1,1)$ can be used for the description of the vibrational spectra of diatomic molecules, in the same way as the quantum algebra $SU_q(2)$ can be used for the description of the rotational spectra of molecules.

In this paper we outline the formalism for the hypervirial calculation and obtain recurrence relations involving the energy perturbation coefficients. The renormalization parameter K plays an important role in ensuring the convergence of our calculations. We list the results of the calculated energy eigenvalues for many molecules for various eigenstates in tables (1–3) and compare our results with those available in the literature. Our calculation intends to test HVPT for a case where the $V(x)$ is an infinite series (not polynomial of low order) and where the numerical accuracy can be tested against an exact formula. K gives convergence- exact formula checks that the converged results is indeed the desired energy value.

2. The Schrödinger equation with the Morse potential

In connection with the description of the vibrational bound states of diatomic molecules, Morse [10] defined the following Schrödinger equation problem.

$$-\frac{d^2\psi(x)}{dx^2}+D[\exp(-2\beta x)-2\exp(-\beta x)]\quad\psi(x)=E\psi(x) \tag{2}$$

where

$$x=r-r_e \tag{3}$$

The notation for the constants in (2) in the one customarily employed in spectroscopic works, D is the dissociation energy in Å^{-2} referred to the minimum of the potential, r is the internuclear separation in Å, r_e the equilibrium value of r, and β is an adjustable parameter. The vibrations of various diatomic molecules are reasonably well described by the Morse potential. To study small vibrations we can expand $V(x)$ in a series of powers of $x=r-r_e$, where r_e is the value of r for which $V(r)$ has a minimum. The potential in (1) can be rewritten in the form

$$\begin{aligned}V(x)&=D[\exp(-2\beta x)-2\exp(-\beta x)]\\&=4D\exp(-\beta x)\left[\frac{\exp(-\beta x/2)-\exp(\beta x/2)}{2}\right]^2-D\\&\equiv 2D\exp(-\beta x)[\cosh(\beta x)-1]-D\end{aligned} \tag{4}$$

to facilitate its expansion as Taylor series. Truncating this expansion at the x^2 term produces the familiar harmonic oscillator potential. Taking terms up to (say) x^{15} provides an improved fit close to the bottom of the well, but at higher distances the fit becomes unrealistic. We find

$$V(x)=D[-1+\beta^2x^2-\beta^3x^3+V_4\beta^4x^4+\cdots+V_{14}\beta^{14}x^{14}+V_{15}\beta^{15}x^{15}] \tag{5}$$

with

$$V_0=-1,\quad V_1=0,\quad V_2=1,\quad V_3=-1,\quad V_4=\frac{7}{12},\quad V_5=-\frac{1}{4},\quad V_6=\frac{31}{360},\quad V_7=-\frac{1}{40},$$

$$V_8=\frac{127}{20160},\quad V_9=-\frac{17}{12096},\quad V_{10}=\frac{73}{259200},\quad V_{11}=-\frac{31}{604800},\quad V_{12}=\frac{2047}{239500800},$$

$$V_{13}=-\frac{1}{760320},\quad V_{14}=\frac{8191}{43589145600},\quad V_{15}=\frac{5461}{217945728000}$$

The coefficients given by (5) alternate in sign; even coefficients take (+ sign) and odd coefficients take (−) sign. We have expanded the potential (5) to a limit in which any term beyond that limit makes no difference to our eigenvalues. For our calculations this limit was reached for (15).

In this way the Hamiltonian for this potential can be written in a form which has the unperturbed part

$$H_0 = -\frac{d^2}{dx^2} - D + D\beta^2 x^2. \tag{6}$$

The total Hamiltonian takes the form

$$H = H_0 + D[-\beta^3 x^3 + V_4\beta^4 x^4 + V_5\beta^5 x^5 + \cdots + V_{14}\beta^{14}x^{14} + V_{15}\beta^{15}x^{15}] \tag{7}$$

The central idea of this work is to expand the potential $V(r)$ in a Taylor series about its minimum value, and solve the resulting approximate problem by hypervirial perturbation theory physically, as the potential well is very deep, the classical turning points for the lowest bound states are very close to the minimum of the well; therefore the particle, even quantum mechanically, can in the main see only the region of the potential near the minimum. We thus expect that the eigenvalues obtained in this way will certainly be accurate only for the first few states. For higher bound states, with their classical turning points further from the minimum, we expect that the accuracy of the approximation will decrease progressively relative to that for the lowest bound states. This is indeed confirmed by the explicit results obtained.

3. Formulation of the problem

The Hamiltonian for the potential described by (1) is

$$H = -\frac{d^2}{dx^2} + V(x) \tag{8}$$

where the potential $V(x)$ can be rewritten in terms of the single perturbation parameter

$$V(x) = \sum_{I=0}^{J} \lambda V(I) x^I \quad (J = 15) \tag{9}$$

The coefficients $\beta^J V_J D$ given by (7) are replaced by $\lambda V(I)$ in (9). From the hamiltonian given by (8) and using the basic relations for the commutator,

$$\left[\frac{d}{dx}, H\right] = \frac{dV}{dx} \tag{10}$$

$$[x^N, H] = \frac{N}{2}(N-1)x^{N-2} + Nx^{N-1}\frac{d}{dx} \tag{11}$$

we obtain the result

$$\left[x^N\frac{d}{dx}, H\right] = x^N\frac{dV}{dx} + \frac{N}{2}(N-1)x^{N-2}\frac{d}{dx} + 2Nx^{N-1}(V-H). \tag{12}$$

The diagonal hypervirial requirement that $\left\langle\left[x^N\frac{d}{dx}, H\right]\right\rangle$ shall vanish for the bound states of (7) leads to the result

$$2E(N+1)\langle x^N\rangle = \sum_{I=0}^{J} \lambda V(I)(2N+2+I)\langle x^{N+I}\rangle - \frac{N}{2}(N^2-1)\langle x^{N-2}\rangle \tag{13}$$

The Hellmann–Feynman theorem and the virial theorem provide relationships between the energy E and the expectation values $\langle x^N\rangle$. Let us assume that the energy E and the expectation values $\langle x^N\rangle$ can be expanded in power series of the perturbation parameter λ as

$$E = \sum E(I)\lambda^I, \tag{14}$$

$$\langle x^N\rangle = \sum A(N,M)\lambda^M. \tag{15}$$

In order to improve the convergence properties of the perturbation series we used a rearrangement of terms in the potential as given by (8). To illustrate this technique it is necessary to write the potential appearing in (5) in a renormalized form involving a parameter K

$$V(x) = V(0) + [\mu - \lambda K]x^2 + \sum_{I=3}^{J} V(I)\lambda \tag{16}$$

where

$$\mu = V(2) + \lambda K. \tag{17}$$

The use of the renormalization parameter K is helpful in improving convergence. If we use the perturbation expansions (14 and 15) in the hypervirial relation given by (13), we obtain recurrence relations corresponding to the $V(x)$ given by (16) as follows:

$$\begin{aligned}(2N+2)\sum_{0}^{M} E(I)A(N,M-I) &= -\frac{N}{2}[N^2-1]A(N-2,M)\\ &\quad -(2N+4)[\mu A(N+2,M) - KA(N+2,M-1)]\\ &\quad + \sum_{I=3}^{J} V(I)(2N+2+I)A(N+I,M-1)\end{aligned} \tag{18}$$

Applying the Hellmann–Feynman theorem in the form

$$\frac{\partial E}{\partial \lambda} = \left\langle \frac{\partial H}{\partial \lambda}\right\rangle = \left\langle \frac{\partial V}{\partial \lambda}\right\rangle \tag{19}$$

we obtain a recurrence relation for the energy coefficients in the form

$$(M+1)E(M+1) = \sum_{I=0}^{J} V(I)A(I,M) - KA(2,M). \tag{20}$$

The unperturbed energy corresponding to the Morse potential can be expressed as

$$E = V(0) + (2n+1)\sqrt{\mu} \quad (n = 0,1,2,\ldots) \tag{21}$$

The analytic eigenvalues for the Morse potential for bound states are given by Landau (19)

$$E = -D\left[1 - \frac{\beta}{\sqrt{D}}\left(n + \frac{1}{2}\right)\right]^2. \tag{22}$$

The pure vibrational spectrum (22) is very simple. The spacing between vibrational levels decreases with increasing vibrational quantum number n, and goes to zero when $E = 0$. The number of vibrational levels, however, is finite and can easily be seen to be equal to

$$N = \frac{\sqrt{D}}{\beta} - \frac{1}{2} \tag{23}$$

According to the results (23) there are 19 bound states for the diatomic molecule H_2^+, and this is confirmed by Adam *et al* [5]. Our method is adequate to calculate the first six bound states, with some convergence problems for higher states. From the recurrence relations (18 and 20) together with the unperturbed energy (21) and initial coefficient $A(0,0) = 1$, we can calculate the perturbation series for the energy.

4. Discussion and conclusion

We have used the hypervirial-renormalization method to calculate the eigenvalues of the Morse potential for different molecules and for various vibrational quantum numbers n. We diminish convergence problems by using the adjustable renormalization parameter K; this parameter has been used widely by Witwit [11, 12]. Both the convergence and the accuracy of the results can be controlled by varying the values of K.

We list our results in tables 1–3. We present the eigenvalues for various molecules, as described by the appropriate values of D and β. In tables 1 and 2 we list the energy eigenvalues for the diatomic molecules H_2^+ and HCl; the potential parameters corresponding to these molecules are ($D = 188{\cdot}4355\ \text{Å}^{-2}$, $\beta = 0{\cdot}711248\ \text{Å}^{-1}$, $r_e = 1{\cdot}3$ Å) and ($D = 2000\ \text{Å}^{-2}$, $\beta = 1{\cdot}7\ \text{Å}^{-1}$ $r_e = 1{\cdot}3$ Å), respectively. Our results are given for the first seven energy levels. The results for H_2^+ are compared with the results of Hajj *et al* [4] and Adam *et al* [5]. It is clear from the listed results in table 1 that there is agreement between our results and their results. For higher states it was found that the renormalized series method faced increasing convergence difficulties, and in general the results decreased in accuracy. We list in table 2 the results for HCl. The results can be compared with corresponding results calculated from the exact formula (22) for the bound states.

We used two different ranges of Taylor series coefficients $\sum_{I=0}^{J=7,15} V(I)$ in order to check the effect on the calculated eigenvalues. The best accuracy was obviously achieved with $J = 15$, with accuracy being reduced with other values of ($J = 7$), this situation was more noticable at high state numbers such as $n = 5, 6$; We should note that the present technique works equally well for the two forms $V(x) = \sum_{I=0}^{J} \lambda V(I) x^I$, $\lambda = 1$ and $V(x) = \sum_{I=0}^{J} \lambda^I V(I) x^I$; $\lambda = \beta$. We used both forms in numerical calculations but for the Morse potential we found that use of the form with various powers of λ did not improve the numerical accuracy.

Table 1. Eigenvalues of Morse potential for H_2^+. First line represents the present result, second line Adam *et al* [5], third line Hajj *et al* [4]. Our calculations carry out for two different terms number of perturbation expansion. The empty spaces mean these are not reported.

n	$-E_n(n_0 = 15)$	N	K	$-E_n(n_0 = 6)$	N	K
0	178·79853835103	198	400	178·7986447313	155	400
	178·79853835			178·79853835		
	178·79853			178·79853		
1	160·283425629	240	400	160·278522266	220	400
	160·28342563			160·28342563		
	160·28342			160·28342		
2	142·7800603	260	400	142·7947516	230	400
	142·780060347			142·78060347		
	142·78004			142·78004		
3	126·2884425	264	450	126·36845	230	450
	126·28844249			126·28844249		
	126·28840			126·28840		
4	110·80857	220	460	111·260	230	460
	110·80857207			110·80857207		
	110·80849			110·80849		
5	96·3404	240	500	97·78	166	450
	96·340449093			96·340449093		
6	82·884	280	550	80·785	220	600
	82·884073546			82·884073546		

Table 2. First eleven eigenvalues of Schrödinger equation with Morse potential for HCl, first line represents the present calculations, the second line calculations computed from analytic solution given by equation (22).

n	$-E_n$	N	K	$-E_{\text{analytic}}$
0	1924·696198876	42	6500	1924·696198876
1	1778·423566295	166	12550	1778·423566295
2	1637·930943825	167	12500	1637·930943825
3	1503·2183213	170	13000	1503·218321355
4	1374·285698	224	18000	1374·285698885
5	1251·13307	240	19000	1251·133076415
6	1133·7604	270	23000	1133·760453945
7	1022·167	270	26000	1022·167831475
8	916·355	272	26000	916·3552090051
9	816·32	275	25000	816·3225865351
10	722·06	300	27000	722·0699640651

The results in table 3 are calculated for the H_2, HCl, I_2 molecules (for various vibrational quantum numbers ($n = 0$ to 6)); the energy is given in cm^{-1}. Again, our results can be compared with those produced by the exact formula, equation (22). We note that the energy levels calculated by the exact equation (22) agree formally

Table 3. The eigenvalues of Schrödinger equation with Morse Potential for various molecules, the numerical results yielded by renormalized series, and analytic results computed from equation (22). The potential parameters are given by Siegfried [1]. The empty spaces mean the results cannot be calculated by the renormalized series method.

n	molecules	Numerical (cm^{-1})	N	K	Analytic (cm^{-1})
0	HCl	−35764·09225012	81	12000	−35764·09225012
	H_2	−36125·80569054	195	2500	−36125·80569054
	I_2	−12442·90131346	32	8000	−12442·90131346
1	HCl	−32894·28123766	122	13000	−32894·28123766
	H_2	−31982·62147534	210	2200	−31982·62147534
	I_2	−12230·08075308	48	8000	−12230·08075308
2	HCl	−30144·47620872	187	16000	−30144·47620827
	H_2	−28091·709799	233	2400	−28091·709798
	I_2	−12019·09594289	77	9000	−12019·09594298
3	HCl	−27514·67716145	199	17000	−27514·67716195
	H_2	−24453·0706587	216	2200	−24453·0706597
	I_2	−11809·94688324	185	12000	−11809·94688314
4	HCl	−25004·88409880	225	20000	−25004·88409870
	H_2	−21066·70405955	229	2200	−21066·70405942
	I_2	−11602·63357346	96	60000	−11602·63357356
5	HCl	−22615·09701356	221	21000	−22615·09701851
	H_2	−17932·60988	228	2200	−17932·60999
	I_2	−11397·15601446	132	8000	−11397·15601426
6	HCl	−20345·31592249	210	22000	−20345·31592139
	H_2	−15050·7866	238	2500	−15050·7854
	I_2	−11193·5142062	166	1000000	−11193·51420522

with the second order of approximation within the framework of standard Rayleigh–Schrödinger perturbation theory. Our results for the renormalized series use different potential and perturbation expansions and this leads to a slight difference in the numerical results.

Our calculated values of the energy levels at low values of n are excellent as compared with the results of Adam *et al* [5] and Hajj *et al* [4]. From our results it can be seen that the hypervirial method with a renormalization parameter K is sufficient to calculate the energy eigenvalue of the first few states without using Padé approximants to overcome the convergence problem. We illustrated the effect of use the of renormalization parameter K on the convergence rate in the following table

K	E_0
0	178·79
10	178·798
50	178·79853
100	178·798538
150	178·7985384
200	178·79853809
400	178·798538103

It is clear from the above table how the renormalization parameter K can be used to give perturbation series with a better convergence.

Although the renormalized series method has calculational elegance at low values of n, it suffers from a drawback that the numerical accuracy and the rate of convergence falls off very rapidly with increasing value of the vibrational quantum number n.

It is interesting to note that the renormalized series method has not been used before to treat Morse potential for various diatomic molecules.

Acknowledgement

The author is grateful to the referee for valuable comments and suggestions.

References

[1] Flügge Siegfried, *Practical quantum mechanics* (Springer-Verlag, 1971) **Vol. 1**, 182
[2] L D Landau and M E Lifshitz, *Quantum mechanics* (pergamon, 1963) p. 111
[3] John C Slater, *Quantum theory of matter* (McGraw Hill, 1968) **Vol. 1**, p. 368
[4] F Y Hajj, H Kobeisse and N R Nassif, *J. Comput. Phys.* **16**, 150 (1974)
[5] G Adam, L G Ixaru and Corciovei, *J. Comput. Phys.* **22**, 1 (1976)
[6] B R Johnson, *J. Chem. Phys.* **67**, 4086 (1977)
[7] F M Fernandez and E A Castro, *J. Mol. Spectrosc.* **94**, 28 (1982)
[8] F M Fernandez and J F Ogilvie, *Phys. Rev.* **A42**, 4001 (1990)
[9] Bonatsos Dennis, E N Argyres and P P Raychev, *J. Phys.* **A24**, L403 (1991)
[10] P Morse, *Phys. Rev.* **34**, 98 (1929)
[11] M R M Witwit, *J. Phys.* **A24**, 3041 (1991)
[12] M R M Witwit, *J. Phys.* **A24**, 3053 (1991)
[13] J P Killingbeck, *J. Phys.* **A21**, 3399 (1988)

PRAMANA
— journal of
physics

© Printed in India

Vol. 42, No. 4,
April 1994
pp. 341–348

Ensemble interpretation of the EPR-Bell correlations

RAVI K MENON and V K THANKAPPAN
Department of Physics, University of Calicut, Calicut 673 635, India

MS received 19 August 1993; revised 28 January 1994

Abstract. The EPR-Bell correlations between the spins of a pair of particles originally in a singlet state are discussed both on the basis of the mathematical formalism of quantum mechanics and the ensemble interpretation. It is shown that the correlations predicted by the mathematical formalism are in agreement with those expected on the basis of the ensemble interpretation, if the electrons are treated as distinguishable particles after they separate and undergo observation. In this case, the correlations are only in partial agreement with a *gedanken* experiment of Mermin on the subject. It is pointed out, however, that agreement with Mermin's conclusions is possible if one treats the electrons as indistinguishable even when they are subjected to observation after separation, though there is no obvious theoretical justification for doing so.

Keywords. Ensemble; locality; singlet; triplet; wavefunction.

PACS No. 3·65

1. Introduction

The paper entitled "Can quantum mechanical description of physical reality be considered complete?" by Einstein *et al* (EPR) [1] has become a classic in the annals of the epistemological foundation of quantum mechanics. The paper brought in sharp focus for the first time the basic problem afflicting quantum mechanics from an interpretational point of view, namely, the fact that the laws of quantum mechanics appear to be either incompatible with local realism [which is a basic tenet of classical physics and which, as defined by Einstein [2], is the premise that "the real states of spatially-separated non-interacting objects are independent"] or incomplete with regard to an individual system.

The heart of the EPR paper is a thought-experiment which, in its Bohm version [3], consists of a pair of spin-half particles in a singlet (spin-zero) state. The pair decays through angular momentum-conserving interactions and the component particles move away in opposite directions. After the interaction between the particles have ceased, the spin of one of the particles in a specified direction **n** is measured. It is argued then that the spin of the other particle along **n** can be deduced from this measurement (without disturbing that particle) because of the perfect correlation that exists between the spins of two particles in the singlet state. Since the choice of **n** is at our disposal and since measurement on particle 1 can in no way affect particle 2 which is spatially separated from particle 1, it follows that all components of the spin of particle 2 have definite values, contrary to the principles of quantum mechanics which permits only one of the components of the spin to have a definite value. One is, therefore, constrained to conclude that either the quantum mechanical wave function, which stipulates perfect correlation between the spins of the two particles, does not provide a complete description of an individual pair or that the assumption of locality is not valid in this case.

The debate that followed the publication of the EPR paper gave rise to the formulation of two schools of interpretation. The Copenhagen or individual system interpretation propounded by Neils Bohr maintains that quantum mechanics is a complete theory in the sense that the wave function provides an exhaustive description of an individual system (in this case, the pair) but demands modification in the Einstein definition of local realism. On the other hand, the ensemble interpretation advocated by Einstein affirms the validity of locality but insists that the wave function refers to an ensemble (of pairs in the singlet state, in the EPR case) and not to an individual system. Vindication of the ensemble interpretation is therefore an indirect validation of locality in quantum mechanics, and vice versa.

2. The EPR-Bell correlations

The EPR thought-experiment is, obviously, beyond the realm of actual experiments. So it cannot be used to settle experimentally the dispute between the advocates and opponents of locality in quantum mechanics. Bell [4] has suggested a modified version of the EPR experiment which at once raises the dispute to the realm of actual experiments. The modifications suggested by Bell consist in:

(i) replacing the single pair of the EPR experiment with an ensemble of pairs.
(ii) replacing the single Stern-Gerlach magnet with one for each particle of the pair.

Thus in the EPR-Bell experiment, we have a pair of Stern-Gerlach magnets D1 and D2 (whose axes can be varied) arranged on the opposite sides of an ensemble of pairs of spin-half particles in the singlet state. D1 measures the spin along a direction specified by the unit vector $\mathbf{a}$ of particles emerging on one side while D2 measures the spin along $\mathbf{b}$ of particles emerging from the other side. The experiment is run until a large number of pairs undergo decay. The recordings of D1 an D2 provide a statistical correlation between the spins of the two particles.

Now according to the quantum theory of angular momentum, the recordings at D1 and D2 can be only either spin-up or spin-down. Therefore, there are four possibilities: spin up–spin up (that is, spin up at D1 and spin up at D2), spin up–spin down, spin down–spin up and spin down–spin down. We denote these respectively by uu, ud, du and dd.

Mermin [5] has described a gedanken experiment which is claimed to demonstrate the results of actual EPR-Bell experiments on the EPR correlations carried out by Alain Aspect and his group [6, 7] at the University of Paris. According to this, the observed correlations are as follows:

(C1) Each of the four cases occur with equal probability and constitutes one-fourth of the total. [In Mermin's demonstration, the proportion of the four cases varies from 22% to 27·7% in an ensemble consisting of 585 individual pairs. For the enormously large number involved in a typical quantum process, the deviation from 25% would be practically nil.]
(C2) However, when $\mathbf{a} = \mathbf{b}$ ($\mathbf{a}$ and $\mathbf{b}$ parallel), a spin up (spin-down) recording at D1 is invariably accompanied by a spin-down (spin-up) recording at D2. That is, there is a perfect correlation between the spins of the two particles.

Mermin contends that these results are in conformity with the mathematical formalism of quantum mechanics and asserts that (C2) constitutes a rebuttal of Einstein's concept of locality. We propose to examine these assertions.

3. Quantum mechanical analysis

Mermin's justification of (C2) is based on the quantum mechanical wavefunction of a pair of spin-half particles in the singlet state, namely

$$|\psi_0\rangle = (2)^{-1/2}[|1-1\rangle - |-11\rangle] \tag{1}$$

where, in $|m_1 m_2\rangle$, m_1 is the value of $\boldsymbol{\sigma}_1$ along the quantization axis while m_2 is that of $\boldsymbol{\sigma}_2$, $\boldsymbol{\sigma}_1$ and $\boldsymbol{\sigma}_2$ being the Pauli spin vectors of the two particles constituting the pair. However, this explanation ignores an important feature of the quantum formalism which is repeatedly emphasized by Bohr and which is a key element in his principle of complementarity. This is the fact that observations could seriously affect the state of a quantum system. That is, as remarked by Jordan [8], whereas in classical mechanics measurements merely reveal what exists before the measurement is made, in quantum mechanics "observations not only disturb what has to be measured, they produce it." Consequently, it is necessary to make a distinction between the properites of a system contained in its wavefunction (when the system is closed) and the properties that will be revealed in an experiment (when the system is open). We can illustrate this point using the simple example of a spin-half particle:

Consider the particle in a spin-up state quantized along the z-axis. We will denote the state by the ket $|z{:}1\rangle$. This state has the property

$$\sigma_z|z{:}1\rangle = |z{:}1\rangle, \tag{2}$$

$$\langle z{:}1|\sigma_x|z{:}1\rangle = 0. \tag{3}$$

These equations signify that the state $|z{:}1\rangle$ is characterized by a definite value for σ_z namely $+1$, which can be measured, and an average value of zero for σ_x which, however, cannot be measured (i.e., σ_x has no definite value in $|z{:}1\rangle$). In fact, any experimental arrangement designed to measure σ_x will change the state of the particle from $|z{:}1\rangle$ to $|x{:}\pm 1\rangle$. This is the meaning of the remark quoted above as due to Jordan. Observation of σ_x not only disturbs the state $|z{:}1\rangle$ in which σ_x has no definite value, but produces the state $|x{:}1\rangle$ or $|x{:}-1\rangle$ in which it has a definite value. Here we see another peculiarity of the quantum formalism: it cannot say for certain which of the two states, $|x{:}1\rangle$ or $|x{:}-1\rangle$, will be produced in any particular observation. In order to see what exactly would be the result of the experiment, we should adopt the following procedure:

Choose a basis to construct the matrix of σ_x. Then diagonalize this matrix to obtain the eigenvalues and eigenvectors of σ_x. Since $|z{:}1\rangle$ alone does not form a basis, we have to include the vector $|z{:}-1\rangle$ also. Then, the matrix of σ_x is $\left(\begin{smallmatrix}0&1\\1&0\end{smallmatrix}\right)$ and the eigenvalues are ± 1 with corresponding eigenvectors given by

$$|x{:}1\rangle = (2)^{-1/2}[|z{:}1\rangle + |z{:}-1\rangle], \tag{4a}$$

$$|x{:}-1\rangle = (2)^{-1/2}[|z{:}1\rangle - |z{:}-1\rangle]. \tag{4b}$$

We could invert (4a, 4b) to obtain

$$|z{:}1\rangle = (2)^{-1/2}[|x{:}1\rangle + |x{:}-1\rangle], \tag{5a}$$

$$|z{:}-1\rangle = (2)^{-1/2}[|x{:}1\rangle - |x{:}-1\rangle]. \tag{5b}$$

These equations imply that, if we prepare a large number of spin-half particles in the state $|z{:}1\rangle$ and then make a measurement of σ_x, we will get the value $+1$ for about half the cases and -1 for the other half. But we note that the same will be the case if the particles are prepared in the $|z{:}-1\rangle$ state instead of the $|z{:}1\rangle$ state. Therefore, the measured values of σ_x do not reflect any specific (or, exclusive) property of either $|z{:}1\rangle$ or $|z{:}-1\rangle$, but represents merely the property of an ensemble of spin-half particles. This conclusion is further confirmed by the fact that there would be no change in the observed values of σ_x if we replace the initial states (quantized along the z-axis) with those quantized along the y-axis; and that the same proportion of spin-up and spin-down states are obtained if we observe σ_y instead of σ_x. The conclusions of the foregoing considerations may be summarized as follows:

(a) Equation (2) represents a specific property of the state $|z{:}1\rangle$. This property can be verified by measuring σ_z. That is, measurement of σ_z will not change the state of the system.
(b) Equation (3) may be interpreted in two ways:

(i) It represents a (non-exclusive) property of $|z{:}1\rangle$. The equation is exact in this sense (that is, the average value of σ_x is exactly zero in the state $|z{:}1\rangle$) but cannot be verified by observing σ_x.
(ii) It represents the property of an ensemble of spin-half particles and tells that in a measurement of σ_x (or any other component of $\boldsymbol{\sigma}$) $+1$ and -1 values will each be realised half of the time, provided the number of particles involved is large enough. The latter condition emphasizes that the property is a statistical one.

The first one of the above interpretations refer to the property of the wavefunction $|z{:}1\rangle$ (closed system), and the second one to the property of a spin-half (open) system that will be revealed in an experiment. Bohr has been emphasizing the first interpretation and Einstein insisting on the second. But it is obvious that we need both (in their distinct domains) if quantum mechanics is to be regarded not only as a self-consistent physical theory, but also as one that can account for actual observations.

In short, there are two types of properties implicit in the wavefunction of an individual quantum system. Those which can be directly observed (without affecting the wavefunction) and those which cannot be so observed but are nevertheless required by the quantum mechanical formalism. An observational realisation of the latter is, however, possible in relation to an ensemble.

Let us look at (1) in the light of the above considerations. To be more specific, let us rewrite the equation in the form,

$$|\psi_0\rangle = (2)^{-1/2}[|z{:}1-1\rangle - |z{:}-11\rangle]. \tag{1a}$$

The quantum mechanical properties of this state are contained in the equations,

$$\{(\boldsymbol{\sigma}_1 + \boldsymbol{\sigma}_2)\cdot\mathbf{n}\}|\psi_0\rangle = 0 \tag{6}$$

$$(\boldsymbol{\sigma}_1\cdot\mathbf{n})(\boldsymbol{\sigma}_2\cdot\mathbf{n})|\psi_0\rangle = -\mathbf{n}^2|\psi_0\rangle = -|\psi_0\rangle \tag{7}$$

where **n** is a unit vector. These follow from the relationships,

$$(\boldsymbol{\sigma}_1\cdot\mathbf{n})|\psi_0\rangle = n_z|\psi_{10}\rangle + (2)^{-1/2}\{n_+|\psi_{1-1}\rangle - n_-|\psi_{11}\rangle\} \tag{8a}$$

$$(\boldsymbol{\sigma}_2\cdot\mathbf{n})|\psi_0\rangle = -n_z|\psi_{10}\rangle + (2)^{-1/2}\{n_-|\psi_{11}\rangle - n_+|\psi_{1-1}\rangle\} \tag{8b}$$

with

$$|\psi_{10}\rangle = (2)^{-1/2}[|z:1-1\rangle + |z:-11\rangle] \tag{9a}$$

$$|\psi_{1-1}\rangle = |z:-1-1\rangle \tag{9b}$$

$$|\psi_{11}\rangle = |z:11\rangle \tag{9c}$$

and

$$n_\pm = (n_x \pm i n_y). \tag{10}$$

The singlet state of the pair is thus characterised by (i) a total spin equal to zero [eq. (6)] and (ii) a perfect correlation between the spins of the two particles comprising the pair [eq. (7)]. The second characteristic means that a spin-up (spin-down) state of one particle is accompanied by a spin-down (spin-up) state for the other particle. However, (8a, b) show that these characteristics of the singlet state cannot be verified by measuring the spins of the individual (component) particles just as characteristic (3) of the state $|z:1\rangle$ cannot be verified by measuring σ_x. The reason in both cases is the same, the concerned observables have no definite values in the state under consideration (that is, the states are not eigenvectors of these observables).

4. Experiment to measure individual spins

In spite of the conclusions arrived at above, if one sets up an experiment to observe the spins of the individual particles, Jordan's dictum (quoted in the previous section) will rule the results. In other words, the results of the experiment would reflect only the general properties of an ensemble of pairs of spin-half particles, and not an exclusive property of the singlet system. In order to deduce the results of the experiment, we can adopt the same procedure as the one followed in the measurement of σ_x. That is, construct the matrix of $[(\boldsymbol{\sigma}_1\cdot\mathbf{a})(\boldsymbol{\sigma}_2\cdot\mathbf{b})]$ in a basis corresponding to the pair, and diagonalise the matrix to get the eigenvalues and eigenvectors.

We choose as basis states the vectors (in the notation of § 3) $|z:1-1\rangle$, $|z:11\rangle$, $|z:-11\rangle$ and $|z:-1-1\rangle$, which are the eigenvectors of the observables corresponding to the components of the spins of the individual particles. The matrix can be calculated by writing

$$(\boldsymbol{\sigma}_1\cdot\mathbf{a}) = \sigma_{1z}a_z + (1/2)[\sigma_{1+}a_- + \sigma_{1-}a_+] \tag{11}$$

and similarly $(\boldsymbol{\sigma}_2\cdot\mathbf{b})$, and using the relationships,

$$\langle z:m_3m_4|\sigma_{1z}\sigma_{2z}|z:m_1m_2\rangle = m_1m_2\delta_{m_1m_3}\delta_{m_2m_4}, \tag{12a}$$

$$\langle z:m_3m_4|\sigma_{1z}\sigma_{2\pm}|z:m_1m_2\rangle = m_1\{(1\mp m_2)(3\pm m_2)\}^{1/2}\delta_{m_1m_3}\delta_{m_2\pm 2,m_4}, \tag{12b}$$

$$\langle z:m_3m_4|\sigma_{1\pm}\sigma_{2z}|z:m_1m_2\rangle = m_2\{(1\mp m_1)(3\pm m_1)\}^{1/2}\delta_{m_1\pm 2,m_3}\delta_{m_2m_4}, \tag{12c}$$

$$\langle z:m_3m_4|\sigma_{1\pm}\sigma_{2\pm}|z:m_1m_2\rangle = \{(1\mp m_1)(1\mp m_2)(3\pm m_1)(3\pm m_2)\}^{1/2}\delta_{m_1\pm 2,m_3}\delta_{m_2\pm 2,m_4} \tag{12d}$$

and

$$\langle z{:}m_3 m_4|\sigma_{1\pm}\sigma_{2\mp}|z{:}m_1 m_2\rangle = \{(1\mp m_1)(1\pm m_2)(3\pm m_1)(3\mp m_2)\}^{1/2}\delta_{m_1\pm 2,m_3}\delta_{m_2\mp 2,m_4} \tag{12e}$$

We consider three different cases: $\mathbf{a}//\mathbf{b}//\mathbf{z}, \mathbf{a}//\mathbf{b}\perp\mathbf{z}$ and $\mathbf{a}\perp\mathbf{b}//\mathbf{z}$. In all these cases the eigenvalues are $+1$ and -1, each of degeneracy 2 (This could, of course, be deduced without diagonalising the matrix, but the matrix diagonalization confirms these values). The wavefunctions are listed in Appendix A.

These wavefunctions have been obtained subject to the constraint that they be also eigenvectors of $(\sigma_1\cdot\mathbf{a})$ and $(\sigma_2\cdot\mathbf{b})$. We feel that, the conditions of the experiment require this. So the wavefunctions are labelled by the eigenvalues of both $(\boldsymbol{\sigma}_1\cdot\mathbf{a})(\boldsymbol{\sigma}_2\cdot\mathbf{b})$ and $(\boldsymbol{\sigma}_1\cdot\mathbf{a})$. Thus $|+\,-\rangle$ is an eigenvector belonging to eigenvalue $+1$ of $(\boldsymbol{\sigma}_1\cdot\mathbf{a})(\boldsymbol{\sigma}_2\cdot\mathbf{b})$ and eigenvalue -1 of $(\boldsymbol{\sigma}_1\cdot\mathbf{a})$.

Since the initial (singlet) state itself does not occur as one of the eigenvectors, it may be concluded that all the four eigenvectors, $|+\,+\rangle$, $|+\,-\rangle$, $|-\,+\rangle$ and $|-\,-\rangle$, would be realized in the experiment with equal probability. Thus, Mermin's conclusion (C1) is justified. For the same reason, conclusion (C2) would not be consistent with the results.

Let us elaborate this point:

Mermin's conclusion (C2) is that whenever **a** is parallel to **b**, a spin-up recording at D1 must be accompanied by a spin-down recording at D2 and vice versa. In our formalism, this requires that either the singlet state ψ_0 [eq. (1a)] should continue to be an eigenvector or else only the eigenvectors $|-\,+\rangle$ and $|-\,-\rangle$ listed in Appendix A should be realized [remember that, in the states $|-\,+\rangle$ and $|-\,-\rangle$, $(\boldsymbol{\sigma}_1\cdot\mathbf{a})$ and $(\boldsymbol{\sigma}_2\cdot\mathbf{b})$ have eigenvalues differing in sign, whereas in the states $|+\,+\rangle$ and $|+\,-\rangle$ these operators have the same eigenvalue]. Neither of these conditions are satisfied, for, we have no reason to rule out the other two eigenvectors $|+\,+\rangle$ and $|+\,-\rangle$.

5. The ensemble interpretation

It is easy to see that the result of the above quantum mechanical analysis of the outcome of measurements on the spins of the individual particles are in agreement with the ensemble interpretation of the wavefunction $|\psi_0\rangle$ [eq. (1a)] of the singlet pair. For, according to this interpretation, (1a) does not represent an individual pair, but an ensemble of pairs of spin-half particles in the singlet state such that the number of pairs with particle 1 in the spin-up state and particle 2 in the spin-down state is the same as the number with particle 1 in the spin-down state and particle 2 in the spin-up state. Thus, in the experiment, the number with spin-up recording at D1 accompanied by spin-down recording at D2 will be the same as the number with spin-down recording at D1 accompanied by spin-up recording at D2. But it is essential for the validity of this ensemble interpretation that every recording of spin-up (spin-down) at D1 should not be associated with spin-down (spin-up) recording at D2. For, if it were so, then the spin-correlation represented by (1a) would be applicable to every single observation, rendering thereby the ensemble interpretation redundant. Hence there should be spin-up (spin-down) recording at D1 accompanied by spin-up (spin-down) recording at D2.

However, as we explained in §3, the predicted results of observation on the individual spins do not invalidate the individual system interpretation of the wavefunction. The two interpretations merely refer to two different aspects of the quantum system. Thus, it appears that Mermin's conclusion (C2), if true, will not only invalidate locality but also certain basic mathematical aspects of the quantum formalism as they relate to the wavefunction of a quantum system.

6. An explanation of (C2)

It should be emphasized that in the foregoing analysis we have treated the two electrons of the pair after separation and on being subjected to observation as distinguishable particles. The logic of the experimental set up demands this: the electrons are far apart; we can tell if the electron registering at a particular detector is spin up or down. However, if (C2) is really an experimental fact (as claimed by Mermin—though we would like it to be confirmed by two or three indeoendent experimental groups), then the theory has to account for it.

It is possible to get agreement with (C2) if we treat the electrons as indistinguishable. This means that we should use properly symmetrised wavefunctions of the pair [that is, singlet and triplet combinations—(1a) and (9a–c)] as basis states in place of the unsymmetrized ones. The matrix of $(\boldsymbol{\sigma}_1 \cdot \mathbf{a})(\boldsymbol{\sigma}_2 \cdot \mathbf{b})$ in this case is given in Appendix B. It is obvious that a pair initially in the singlet state will continue to be in that state if **a** is parallel to **b**. So (C2) is accounted for. But here the problem is how to theoretically justify treating the two electrons as indistinguishable in the given situation.

7. Conclusion

We have discussed, in this paper, the EPR-Bell correlations from the point of view of the ensemble interpretation as well as on the basis of the mathematical formalism of quantum mechanics. We have shown that the correlations predicted by the mathematical formalism are in agreement with those expected on the basis of the ensemble interpretation if we treat the electrons of the pair as distinguishable particles after the decay. In this case the correlations are only in partial agreement with the conclusions of Mermin represented in a thought-experiment. In particular, the conclusion that the spins of the two electrons would be correlated as in the singlet state whenever the axes of the two detectors are set parallel, is not borne out. Agreement with Mermin's conclusions is, however, possible if we treat the electrons as indistinguishable even after they are subjected to observation on separation; though there appears to be no theoretical justification for doing so.

Acknowledgements

The authors are thankful to N D Mermin for critical comments on certain points which helped to elucidate the significance of the results. One of the authors (RKM) is also indebted to the Council of Scientific and Industrial Research, Government of India, for financial support in the form of a senior research fellowship.

Appendix A

Listed here are the common eigenvectors of $(\boldsymbol{\sigma}_1 \cdot \mathbf{a})$ $(\boldsymbol{\sigma}_2 \cdot \mathbf{b})$, $(\boldsymbol{\sigma}_1 \cdot \mathbf{a})$ and $(\boldsymbol{\sigma}_2 \cdot \mathbf{b})$ for three cases. The eigenvectors are identified by the eigenvalues of $(\boldsymbol{\sigma}_1 \cdot \mathbf{a})$ $(\boldsymbol{\sigma}_2 \cdot \mathbf{b})$ and $(\boldsymbol{\sigma}_1 \cdot \mathbf{a})$.

Thus $|-+\rangle$ denotes an eigenvector belonging to eigenvalue -1 of $(\boldsymbol{\sigma}_1\cdot\mathbf{a})(\boldsymbol{\sigma}_2\cdot\mathbf{b})$ and eigenvalue $+1$ of $(\boldsymbol{\sigma}_1\cdot\mathbf{a})$.

case 1. $\mathbf{a}/\!/\,\mathbf{b}/\!/\,\mathbf{z}$ $(a_z=b_z;\ a_-=a_+=0)$

$$\begin{aligned}|++\rangle&=|11\rangle,\\ |+-\rangle&=|-1-1\rangle,\\ |-+\rangle&=|1-1\rangle,\\ |--\rangle&=|-11\rangle.\end{aligned}\tag{A1}$$

case 2. $\mathbf{a}/\!/\,\mathbf{b}\perp\mathbf{z}$ $(a_z=b_z=0;\ a_-a_+=1)$

$$\begin{aligned}|++\rangle&=(1/2)[a_-|11\rangle+|1-1\rangle+|-11\rangle+a_+|-1-1\rangle],\\ |+-\rangle&=(1/2)[-a_-|11\rangle+|1-1\rangle+|-11\rangle-a_+|-1-1\rangle],\\ |-+\rangle&=(1/2)[-a_-|11\rangle+|1-1\rangle-|-11\rangle+a_+|-1-1\rangle],\\ |--\rangle&=(1/2)[a_-|11\rangle+|1-1\rangle-|-11\rangle-a_+|-1-1\rangle].\end{aligned}\tag{A2}$$

case 3. $\mathbf{a}\perp\mathbf{b}/\!/\,\mathbf{z}$ $(a_z=0;\ b_z=1;\ a_-a_+=1;\ b_-b_+=0)$

$$\begin{aligned}|++\rangle&=(1/2)^{1/2}[|11\rangle+a_+|-11\rangle],\\ |+-\rangle&=(1/2)^{1/2}[|1-1\rangle-a_+|-1-1\rangle],\\ |-+\rangle&=(1/2)^{1/2}[|11\rangle-a_+|-11\rangle],\\ |--\rangle&=(1/2)^{1/2}[|1-1\rangle+a_+|-1-1\rangle].\end{aligned}\tag{A3}$$

Appendix B

Here we give the matrix of $(\boldsymbol{\sigma}_1\cdot\mathbf{a})(\boldsymbol{\sigma}_2\cdot\mathbf{b})$ for $\mathbf{a}/\!/\,\mathbf{b}$ when the basis states are ψ_{00}, ψ_{11}, ψ_{10} and ψ_{1-1}. The rows and columns of the matrix are labelled in this order.

$$\begin{pmatrix}-1 & 0 & 0 & 0\\ 0 & (1-a_+a_-) & \sqrt{2}a_-a_z & a_-{}^2\\ 0 & \sqrt{2}a_+a_z & (2a_+a_--1) & -\sqrt{2}a_za_-\\ 0 & a_+{}^2 & -\sqrt{2}a_za_+ & (1-a_+a_-)\end{pmatrix}$$

References

[1] A Einstein, B Podolsky and N Rosen, *Phys. Rev.* **47**, 777 (1935)
[2] A Einstein, in *Albert Einstein: Philosopher-scientist*, edited by P A Schilpp (Library of Living Philosophers, Evanston, Ill. 1949), p. 682
[3] D Bohm, *Quantum theory* (Prentice-Hall, New Jersey, 1951), p. 614
[4] J S Bell, *Physics* **1**, 195 (1964)
[5] N D Mermin, *Phys. Today* **36**, 38 (April 1985)
[6] A Aspect, P Grangier and G Roger, *Phys. Rev. Lett.* **47**, 460 (1981); **49**, 91 (1982)
[7] A Aspect, J Dalibard and G Roger, *Phys. Rev. Lett.* **49**, 1804 (1982)
[8] M Jammer, *The Philosophy of quantum mechanics* (John Wiley, New York 1974) p. 151

PRAMANA
— journal of
physics

© Printed in India

Vol. 42, No. 4,
April 1994
pp. 349–363

Analysis of the excitation functions of (α, *xnyp*) reactions on natural copper

N L SINGH, B J PATEL, D R S SOMAYAJULU and S N CHINTALAPUDI*
Physics Department, Faculty of Science, M. S. University, Baroda 390 002, India
*IUC-DAEF, Calcutta Centre, 3/LB-8, Bidhan Nagar, Calcutta 700 091, India

MS received 17 August 1993; revised 3 January 1994

Abstract. Excitation functions of the reactions $^{63}\mathrm{Cu}[(\alpha,n), (\alpha,2n)+(\alpha,pn)]$ and $^{65}\mathrm{Cu}[(\alpha,n), (\alpha,2n), (\alpha,3n), (\alpha,4n)+(\alpha,p3n)]$ were investigated up to 50 MeV using stacked foil activation technique and Ge(Li) gamma ray spectroscopy method. Since natural copper used as the target has two odd-mass stable isotopes of abundance, ^{63}Cu(69·17%) and ^{65}Cu(30·83%), their activation in some cases, gives the same residual nucleus through different reaction channels but with very different threshold energies. In such cases, the individual reaction cross sections are separated with the ratio of theoretical cross sections. The experimental results were compared with the predictions of preequilibrium hybrid model of Blann. A general agreement was found in all reactions using initial exciton number $n_0 = 4(4p0h)$ and also preequilibrium fraction depends on the incident particle energy.

Keywords. Nuclear reactions; $^{63,65}\mathrm{Cu}(\alpha, xnyp)$; stacked foil activation technique; $E \leqslant 50$ MeV preequilibrium emission.

PACS No. 25·60

1. Introduction

The preequilibrium reaction mechanism is being used since the last two decades to explain high energy continuum of the ejectile spectrum. The mechanism takes into account the emission of particles during the relaxation process of the target plus projectile composite nucleus towards the statistically equilibrated compound nucleus. The relaxation is assumed to take place through a cascade of two body interactions and ejectile emitted at any stage of the binary cascade constitute the preequilibrium spectra. The preequilibrium process has been extensively studied since the exciton model was proposed by Griffin [1]. The exciton model has been extended and refined through analysis of many experimental data, and several models have been developed within the framework of semiclassical or phenomenological approaches [2–10]. On the other hand fully quantum mechanical theories of preequilibrium processes have been developed by several groups [11–16], which so far been confined to nucleon interactions with not more than two emergent particles. Due to the complexity of computation, for the interaction of complex-particle like an α-particle the quantum mechanical picture is yet to come.

Indeed rather extensive experimental data are available in literature [17–27] for α-induced reactions on copper, mostly using poor resolution detectors i.e. GM counter, scintillation detector and proportional counters. Because of the poor resolution of the detectors there were many inconsistencies in the data. Recently Graf *et al* [24], Rizvi *et al* [25] Bhardwaj *et al* [26] and Mohan Rao *et al* [27] have also studied α-induced reactions on copper using Ge(Li) detector. In view of the large uncertainties and mutual discrepancies, a reinvestigation of the above reactions was undertaken with the two-fold aim of (i) improving the quality of experimental data and (ii) to test the preequilibrium models with systematic data obtained in the present work.

2. Experimental procedure

The excitation functions of the α-induced nuclear reactions on natural copper were determined by the stacked-foil technique and Ge(Li) gamma ray spectroscopy method. The excitation functions were measured in three steps namely 50–20 MeV, 40–10 MeV and 30–10 MeV, using copper foils of thicknesses 23 mg/cm^2, 8·9 mg/cm^2 and 12 mg/cm^2 respectively together with several aluminium degraders of varying thicknesses to reduce the beam energy to desired levels. These three independent measurements have large overlapping energy regions which enabled us to check the consistency of the measurements. The beam spot on the foil stack was always restricted to 5 mm by a central hole in a 6 mm thick tantalum collimator placed in front of each stack. No catcher foil is used since recoil distribution is small at this energy and falls within experimental errors. The α-beam is totally stopped in the electrically insulated foil stack which is itself serving as a Faraday cup. The total α-particle flux was measured using current integrator. Beam current of the order of 250 nA was maintained for about 1 h in each irradiation. After accounting for the energy degradation in Al-foils, the energy of the alpha beam at half the thickness of the

Table 1. Nuclear data used for identification of residual nuclei [29].

Reaction	Q-value (MeV)	Half-life ($T_{1/2}$)	Gamma ray energy E_r(keV)	% Abundance (θ_r)
${}^{63}_{29}\mathrm{Cu}(\alpha,n)^{66}_{31}\mathrm{Ga}$	−7·5	9·45 h	834 1039	6·06 38 ± 2
${}^{63}_{29}\mathrm{Cu}(\alpha,2n)^{65}_{31}\mathrm{Ga}$	−16·64	15·2 m	153 752	5·98 5·49
${}^{63}_{29}\mathrm{Cu}(\alpha,pn)^{65}_{30}\mathrm{Zn}$	−12·59	244 d ± 0·2	1115·5	50·75 ± 0·10
${}^{65}_{29}\mathrm{Cu}(\alpha,n)^{68}_{31}\mathrm{Ga}$	−5·85	68 m	1077 1261	3·0 ± 0·3 0·09
${}^{65}_{29}\mathrm{Cu}(\alpha,2n)^{67}_{31}\mathrm{Ga}$	−14·1	78·26 h + 0·07	184·5 300·2	23·56 19·00 ± 1·39
${}^{65}_{29}\mathrm{Cu}(\alpha,3n)^{66}_{31}\mathrm{Ga}$	−25·3	9·45 h	835 1039	6·06 38 ± 2
${}^{65}\mathrm{Cu}(\alpha,4n)^{65}\mathrm{Ga}$	−34·37	15·2 m	153 752	5·98 5·49
${}^{65}_{29}\mathrm{Cu}(\alpha,p3n)^{65}_{30}\mathrm{Zn}$	−30·42	244 d ± 0·2	1115·5	50·75 ± 0·10

Error is shown only for those characteristic γ-rays which is used for the evaluation of cross-section.

experimental foil was calculated from range-energy tables of Williamson *et al* [28]. After the irradiation the induced gamma activities in each foil were observed with a high resolution 95 cc Ge(Li) detector (FWHM 2 keV at 1332 keV) coupled with a pre-calibrated 4 k channel Canberra 88 analyser. The residual nuclei were identified using their characteristic γ-rays as mentioned in table 1 [29]. Several spectra were taken at suitable intervals to enable the identification of the half-lives of residual nuclei. The efficiency calibrations of the detector were performed with a calibrated ^{152}Eu source obtained from the Radio-Chemistry division at VECC. The extended source geometry correction has been applied.

2.1 *Cross-section determination*

The formula used in the cross-section calculation was reported in our earlier papers [30, 31].

$$\sigma = \frac{A_r A_{gm} \lambda}{\Phi \theta_r P_r w_i P_i N_{av} (1 - e^{-\lambda t_i}) e^{-\lambda t_w} (1 - e^{-\lambda t_c})} \tag{1}$$

where σ is the cross section for the reaction (mb), A_r is the photopeak area of the characteristic gamma ray of the residual nucleus, A_{gm} is the gram atomic weight of the target element, λ is the disintegration constant of the residual nucleus (s^{-1}), Φ is the flux of the incident particle (No. of particle/cm^2 s), w_i is the weight per unit area of the target foil (g/cm^2), P_i is the fractional abundance by weight of the target isotope of interest, θ_r is the fractional abundance of characteristic gamma ray emitted per decay of the residual nucleus, P_r is the photopeak efficiency of the gamma ray, N_{av} is the Avogadro's number, t_i, t_w and t_c are the periods (s) of irradiation, waiting and counting respectively.

The measured cross-sections for the reactions ^{63}Cu(α, n), ^{63}Cu(α, 2n) + ^{63}Cu(α, pn), ^{65}Cu(α, n), ^{65}Cu(α, 2n) and ^{63}Cu[(α, 2n) + (α, pn)] + ^{65}Cu[(α, 4n) + (α, p3n)] have been listed in table 2. The total error in the experimental cross-section is contributed by photopeak area (1–5%), photopeak efficiency (4–5%), uniformity of the foil thickness (1–2%) spectroscopic data (0·08–8%), the beam current (2–3%). The overall projected error of our measurement is thus between 8–13% for various reactions. The excitation functions for the above reactions are shown in figures 1–4. The horizontal bars show the estimated total energy loss in the actual thickness of the foils, while the vertical flags shown on the cross-sections show the overall error in the measurement.

3. Results and discussion

Consequent on the use of natural copper target which has two odd-mass isotopes of abundances ^{63}Cu(69·17%) and ^{65}Cu(30·83%), the isotopic contributions arise in the production of a given final nucleus through different reaction channels, for example ^{66}Ga is formed in ^{63}Cu(α, n) and ^{65}Cu(α, 3n) reactions and ^{65}Zn is formed in ^{63}Cu(α, pn) and ^{65}Cu(α, p3n) reactions respectively. However, more often than not, it turns out that at a given energy only one of the two reaction channels is predominant and the other is a small contribution. One of the two vanishes, if the energy happens to be less than the threshold energy for that reaction. On this basis the experimentally measured weighted average cross sections can be easily interpreted using the formula

$$\langle\sigma\rangle = \bar{A}\left(\frac{P_1\sigma_1}{A_1} + \frac{P_2\sigma_2}{A_2}\right) \tag{2}$$

Table 2. Cross sections of the α-induced reactions on ^{63,65}Cu.

E_α(MeV)	(mb)	(mb)	(mb)	(mb)	(mb)	(mb)
Target nucleus reaction	^{65}Cu (α, n)	^{65}Cu $(\alpha, 2n)$	^{63}Cu (α, n)	^{63}Cu + ^{65}Cu $(\alpha, n) + (\alpha, 3n)$	^{63}Cu $(\alpha, pn) + (\alpha, 2n)$	^{63}Cu + ^{65}Cu $[(\alpha, pn) + (\alpha, 2n)]$ $+ [(\alpha, p3n) + (\alpha, 4n)]$
Product nucleus	^{68}Ga	^{67}Ga	^{66}Ga	^{66}Ga	^{65}Zn + ^{65}Ga	^{65}Zn + ^{65}Ga
Threshold Energy (MeV)	6·2	15·0	8·0	8·0, 26·9	13·4, 17·7	13·4, 17·7, 32·3, 36·6
11·6 ± 1·6			45·4 ± 3·8			
12·1 ± 1·1	315·0 ± 38·2					
14·3 ± 1·0	615·0 ± 74·5		197·0 ± 16·4			
16·4 ± 1·2	760·0 ± 92·4		417·0 ± 34·6			
17·3 ± 2·3	790·0 ± 95·8	72·0 ± 7·8	490·0 ± 40·7		64·0 ± 5·2	
20·2 ± 1·1	580·0 ± 70·3	475·0 ± 47·5	510·0 ± 42·3		260·0 ± 20·8	
21·5 ± 2·0		542·0 ± 54·2			530·0 ± 42·4	
22·6 ± 0·7	337·0 ± 40·9		327·0 ± 27·2		653·0 ± 52·3	
23·5 ± 0·9		860·0 ± 86·0			789·0 ± 63·2	
25·1 ± 1·7	206·0 ± 25·0	930·0 ± 93·0	181·0 ± 15·1		905·0 ± 72·4	
26·5 ± 0·9		1032·0 ± 10·3	126·0 ± 10·5		1013·0 ± 81·0	
28·4 ± 1·6	60·0 ± 7·8	943·0 ± 94·3			1040·0 ± 83·2	
29·0 ± 0·6					1085·0 ± 86·8	
31·6 ± 1·5	31·0 ± 4·1	762·0 ± 76·2		110·0 ± 9·2	960·0 ± 76·8	
34·5 ± 0·5	18·0 ± 2·4	560·0 ± 56·0		276·0 ± 22·9	780·0 ± 62·4	
37·1 ± 1·3	8·0 ± 1·1	380·0 ± 38·0		360·0 ± 30·0	554·0 ± 44·3	
39·6 ± 1·2	6·2 ± 0·8	254·0 ± 25·4		390·0 ± 32·4	437·0 ± 35·0	
42·1 ± 1·3	4·8 ± 0·6	183·0 ± 18·3		350·0 ± 29·0		
44·5 ± 1·1	3·2 ± 0·4	140·0 ± 14·0		292·0 ± 24·2		390·0 ± 31·2
46·7 ± 1·2	2·4 ± 0·3	108·0 ± 11·6		266·0 ± 22·0		452·0 ± 36·2
49·0 ± 1·0	2·0 ± 0·3	83·0 ± 8·9		216·0 ± 17·9		530·0 ± 42·4

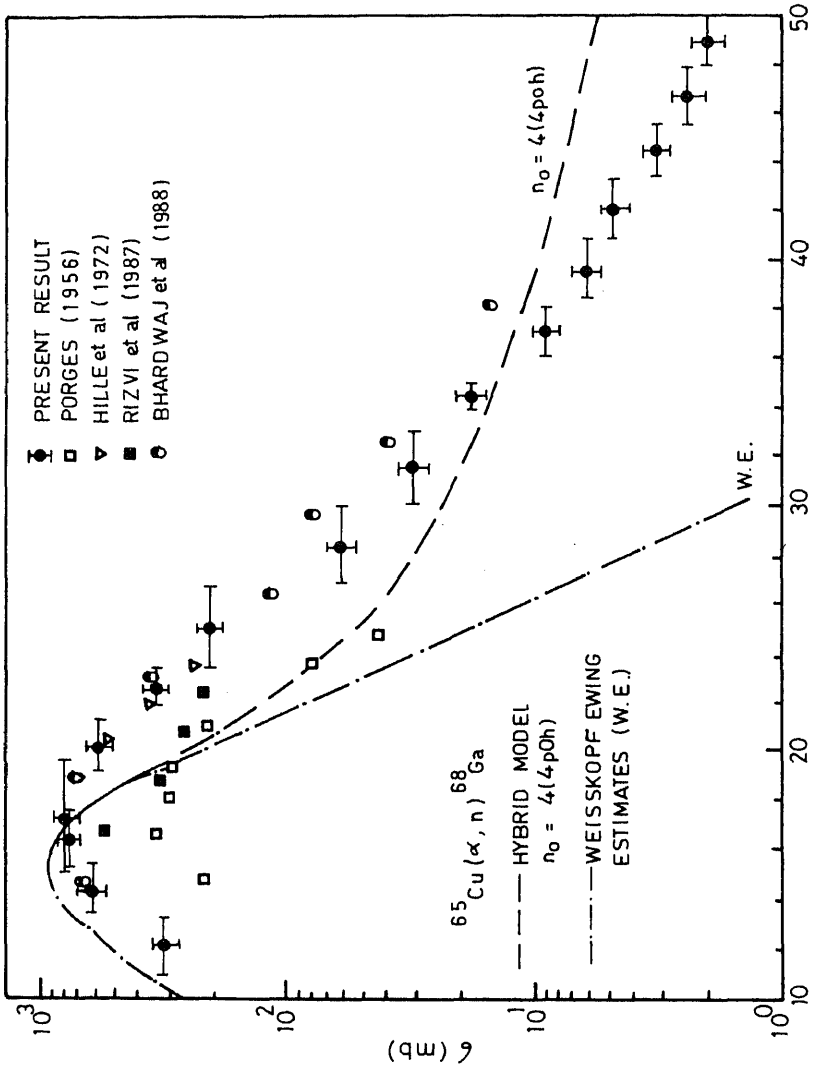

Figure 1. Excitation function of ^{65}Cu(α, n) reaction.

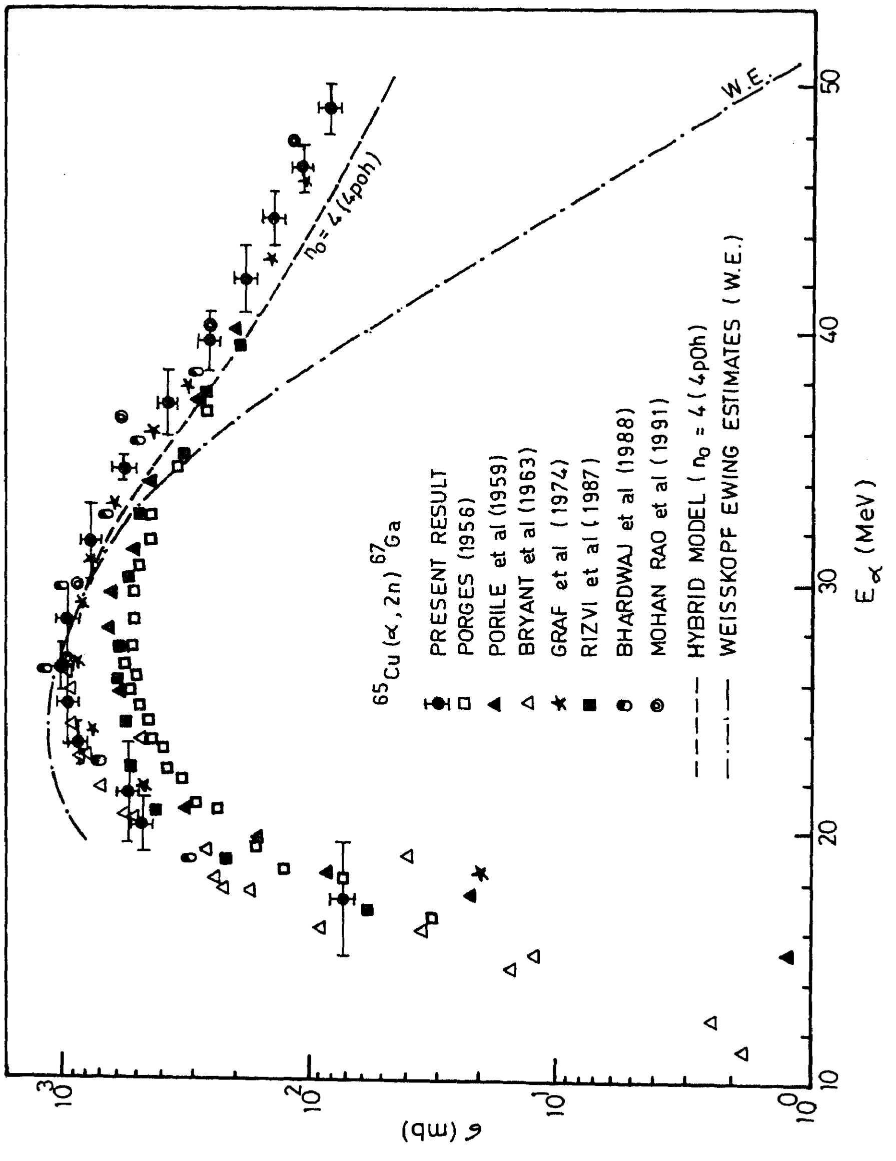

Figure 2. Excitation function of ^{65}Cu(α, 2n) reaction.

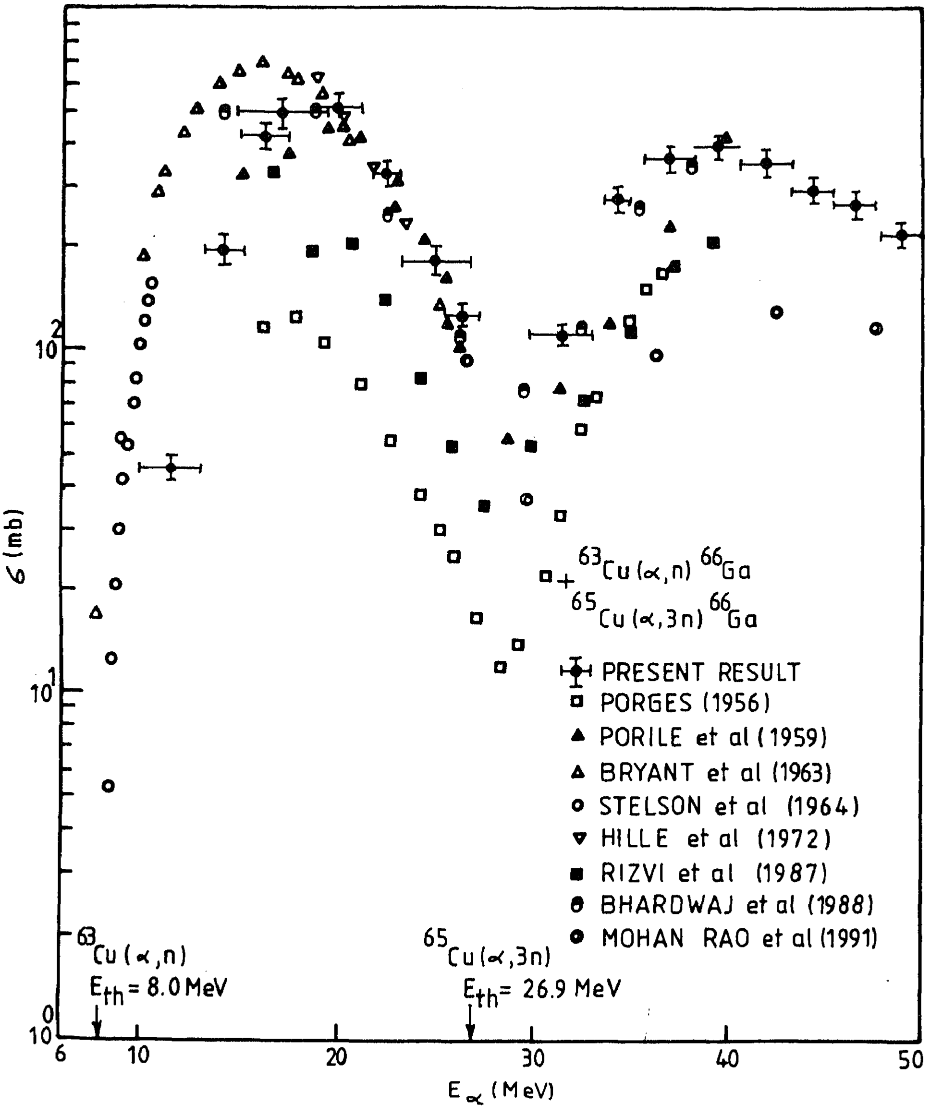

Figure 3. Excitation function of $^{63}Cu(\alpha, n) + {}^{65}Cu(\alpha, 3n)$ reactions.

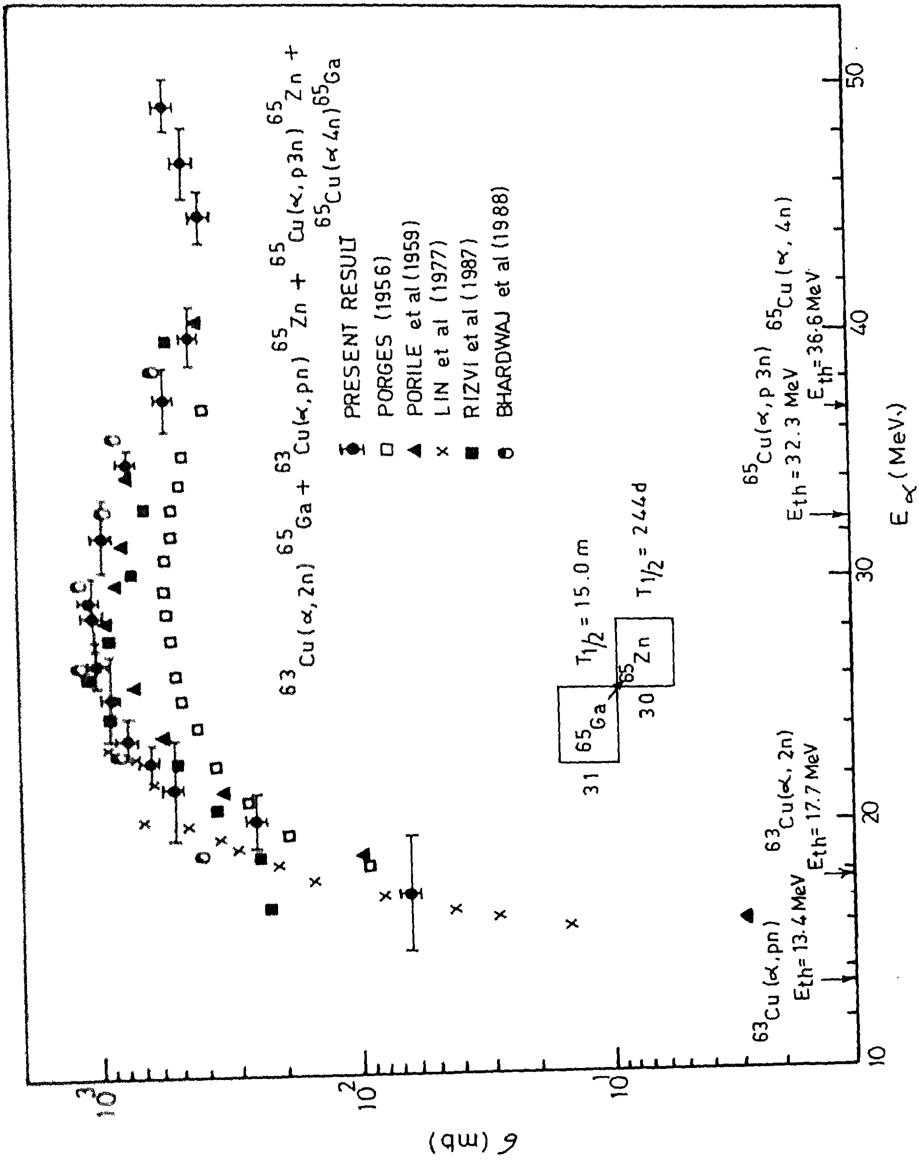

Figure 4. Excitation function of ^{63}Cu(α, 2n) + ^{63}Cu(α, pn) + ^{65}Cu(α, 4n) + ^{65}Cu(α, p3n) reactions.

where $\bar{A}$ is the average atomic weight of copper, P_1, A_1, and P_2, A_2 are the percentage abundances and mass numbers of the two isotopes of copper in respective order and σ_1, σ_2 are the individual cross-sections for ^{63}Cu(α, n) and ^{65}Cu($\alpha, 3n$) reactions respectively. The two contributions can be separated out accurately using either the known ratio of cross-sections from theory [26, 32, 33] or by subtracting out the contribution with enriched isotopes [34].

We have separated the individual contributions of the reactions employing the first method and using the theoretical ratio of cross-sections in formulae [32].

$$\sigma_1 = \sigma^{63}_{(\alpha,n)}$$

$$= \frac{A_r \lambda}{\left[\dfrac{P_i^{63}}{A_i^{63}} + \dfrac{P_i^{65}(\sigma^{65}_{(\alpha,3n)}/\sigma^{63}_{(\alpha,n)})_{\text{theo.}}}{A_i^{65}}\right] \Phi \theta_r P_r w_i N_{av}(1 - e^{-\lambda t_i}) e^{-\lambda t_w}(1 - e^{-\lambda t_c})} \tag{3a}$$

$$\sigma_2 = \sigma^{65}_{(\alpha,3n)}$$

$$= \frac{A_r \lambda}{\left[\dfrac{P_i^{65}}{A_i^{65}} + \dfrac{P_i^{63}(\sigma^{63}_{(\alpha,n)}/\sigma^{65}_{(\alpha,3n)})_{\text{theo.}}}{A_i^{63}}\right] \Phi \theta_r P_r w_i N_{av}(1 - e^{-\lambda t_i}) e^{-\lambda t_w}(1 - e^{-\lambda t_c})} \tag{3b}$$

where the cross-section ratio $(\sigma^{65}_{(\alpha,3n)}/\sigma^{63}_{(\alpha,n)})_{\text{theo.}}$ and its inverse are taken from the theoretical calculations based on pre-equilibrium model prediction, which predicts shape and absolute value of the excitation functions.

Below the threshold energy of ^{65}Cu($\alpha, 3n$) reaction, the value of $\sigma^{65}_{(\alpha,3n)}$ will be zero and hence the second factor in the square bracket will be zero, therefore (3a) reduces to formula (1), (i.e. original formula).

Consequent on the use of natural copper as the target, two reactions are involved, in the production of the residual nucleus ^{66}Ga. Therefore, the experimental cross-section $\langle \sigma \rangle$ in this case gives the weighted average cross-section, for the two reactions ^{63}Cu(α, n) and ^{65}Cu($\alpha, 3n$). Below the threshold of ^{65}Cu($\alpha, 3n$) reaction (i.e. 26·9 MeV), the measured excitation function is due to ^{63}Cu(α, n) reaction only. The contribution of ^{63}Cu(α, n) and ^{65}Cu($\alpha, 3n$) reactions, beyond 26·9 MeV, was separated at each energy using formulae (3a) and (3b). This method for separating the two activities is justified, since the excitation function, for the reaction ^{63}Cu(α, n) and for ^{65}Cu($\alpha, 3n$) (figure 5), so resolved, are reproduced individually by theoretical calculation using the same set of parameters.

More often than not, nuclear reactions in which two genetically related product nuclei (e.g. isobars or isomers) are formed with comparable half-lives and one of them, the daughter nucleus being continuously fed by the parent for example, ^{65}Zn is produced by (i) ^{63}Cu(α, pn)^{65}Zn and (ii) ^{63}Cu($\alpha, 2n$)^{65}Ga $\xrightarrow{\beta^+}$ ^{65}Zn. This is because ^{65}Ga decay with a relatively small half-life (15 min) into ^{65}Zn which in turn decays with a half-life of 244 days. In the present measurements a comparatively longer time was allowed between the end of the irradiation and the beginning of the counting and therefore the short-lived activity of ^{65}Ga was not observed separately.

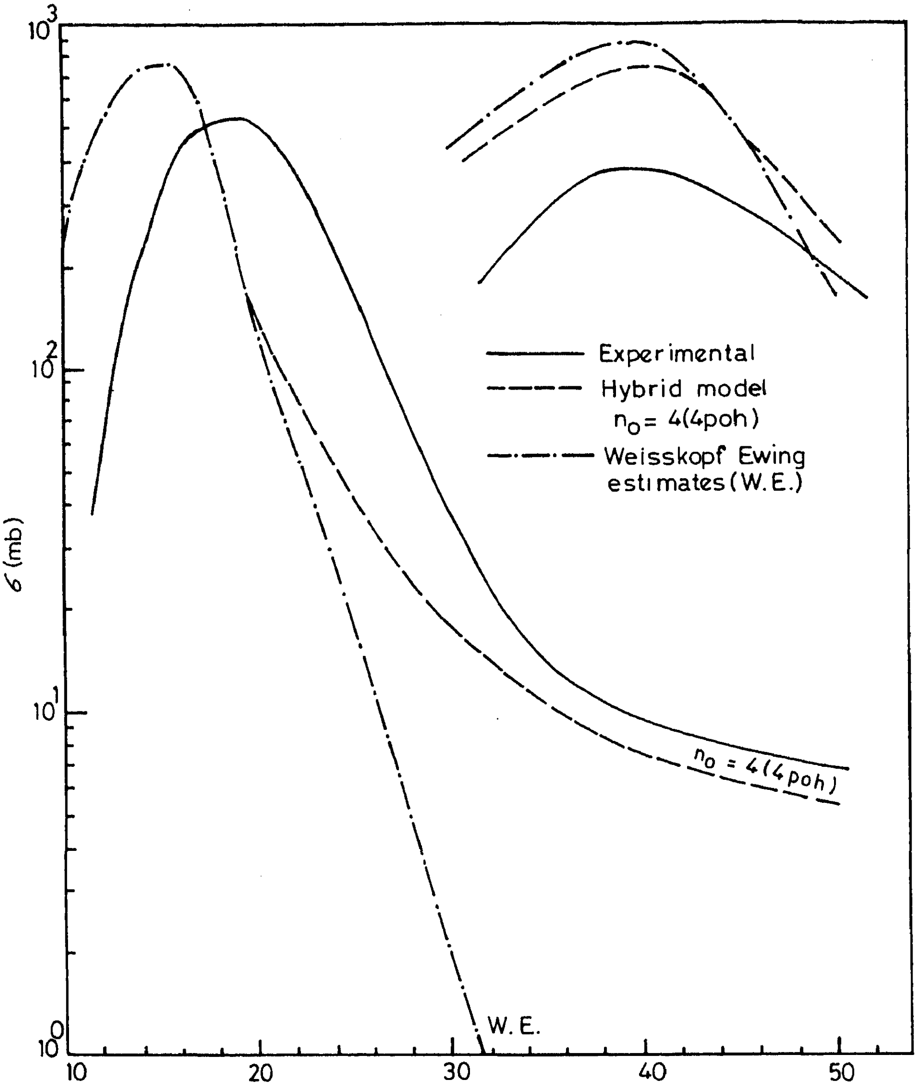

Figure 5. Experimental and theoretical excitation function of ^{63}Cu(α, n) and ^{65}Cu($\alpha, 3n$) reactions.

3.1 *Comparison of present and previous experimental results*

Figures 1–4 show the present experimental results together with the previous measurements. Most of the work on this element performed during 1956–1975, was carried out employing GM counter, scintillation detector, proportional counter as well as 4π flat energy response graphite sphere detector.

During the past twenty years, semiconductor radiation detector has become one of the principal tools in studies requiring high resolution measurements of gamma rays. There have been several Ge(Li) measurements of cross-sections but in limited energy regions [24–27]. It may be observed in figures 1–4 that while there is a fair agreement between the present measurement and those of Graf *et al*, Bhardwaj *et al* and Mohan Rao *et al*, there are some disagreements between the present results and those of Rizvi *et al.*

It is appropriate to mention that the present experimental study adds nine new energy-point cross-sections in ^{65}Cu(α, n), four new energy-point cross-sections in ^{63}Cu(α, n) + ^{65}Cu($\alpha, 3n$) and three new energy-point cross-sections in ^{63}Cu[($\alpha, 2n$) + (α, pn)] + ^{65}Cu[($\alpha, 4n$) + ($\alpha, p3n$)] reactions in the high energy region.

3.2 *Comparison with pre-equilibrium model predictions*

The excitation functions have been calculated theoretically using the statistical model with and without the inclusion of preequilibrium emisson of particles using code ALICE/85/300 [35]. The forerunner for this model is the idea of Griffin [1] called as the statistical model of intermediate structure, to qualitatively explain the observed non-Maxwellian structure of continuous particle spectra. This model has been later quantified by deriving the unknown value of the matrix element for binary collision through various means. There are versions called exciton models in which the matrix element obtained semi-empirically [36] or through a picture of particle-hole interactions in a Fermi sea [5] or by simply treating it as a fit parameter [37]. An attempt to derive it from free nucleon–nucleon scattering cross-sections or from the imaginary part of the optical potential [4] resulted in what are popularly known as the hybrid model versions.

A short description of the option chosen is given below:

The nuclear masses were calculated from the Mayers and Swiatecki [38] mass formula considering the liquid drop without shell and pair corrections i.e. the level density pairing shift absorbed in binding energies. The inverse cross-sections were calculated by an optical model subroutine included into the code which uses the Becchetti and Greenless [39] optical model parameters. The equilibrium part was calculated using standard Weisskopf and Ewing [40] formalism. The mean-free-path was kept constant (i.e. $K = 1{\cdot}0$). The mean free path, which is a kind of free parameter, was introduced by Blann [3] to account for the transparency of nuclear matter in the lower density nuclear periphery. A level density parameter of A/8 MeV^{-1} was used.

A crucial parameter in the model is the initial exciton number n_0, defined as $n_0 = p_0 + h_0$ with $p_0 = p_\pi + p_\nu$, where p_0 and h_0 are initially excited particles above and holes below the Fermi sea, and p_π and p_ν are the number of protons and neutrons among the excited particles. It is customary to use the initial exciton number $n_0(p_0 h_0)$ as a fit parameter to match the theoretical predictions with the experimentally observed shape of spectra and excitation function. The initial exciton number governs the entire cascading process of binary collisions and thereby influences the shape of the hard component in the particle spectra. A good guess would be the number of nucleons in the projectile or an additional particle/hole or both. For the incident α-particle used in the present work a reasonable choice for the initial exciton number is $n_0 = 4$, 5 and 6 using different initial exciton configurations such as ($4p0h$), ($5p0h$) and ($5p1h$) respectively [3, 41, 42]. We performed the calculations using the above exciton configurations and it was found that $n_0 = 4(4p0h)$ gives by far the best results than the other two configurations. The prediction of the $n_0 = 5(5p0h)$ and $n_0 = 6(5p1h)$ configurations were lower than those obtained with $n_0 = 4(4p0h)$. Figures 1, 2 and 5 show the comparison of experimental results with $n_0 = 4(4p0h)$ and Weisskopf–Ewing estimates.

Figures 1, 2 and 5 show the (α, xn) type of reactions on ^{63}Cu and ^{65}Cu; the experimental excitation functions of ^{65}Cu(α, n), ^{65}Cu$(\alpha, 2n)$, ^{63}Cu(α, n) and ^{65}Cu$(\alpha, 3n)$ reactions with the theoretical calculations based on the Weisskopf–Ewing estimates giving compound nucleus contributions as well as pre-equilibrium hybrid model prediction using $n_0 = 4(4p0h)$. The agreement between the experimental and the theoretical excitation functions can be judged from their peak positions and widths. It is observed that Weisskopf–Ewing estimates accounted fairly well for the lower energy compound nucleus dominated part of the excitation functions, but failed to account for the observed cross-sections at high energies where non-equilibrium effects predominate beyond a few tens of MeV of bombarding energy.

As can be seen from figures 1, 2 and 5 there is a slight shift in the energy of the compound nucleus peaks between the theoretical and experimental values. Generally such shifts are prescribed due to the complete neglect of angular momentum effects in the Weisskopf–Ewing theoretical calculations of the compound nucleus contribution. Compound systems attained with incident particles of different masses have appreciably different angular momenta when excited to the same excitation energy. This, in principle, can lead to differences in the excitation function. If, in the last stages of nucleon de-excitation, high angular momentum inhibits particle emission more than it does gamma ray emission, then the peak of the excitation function, corresponding to the particle emitting mode, will be shifted to the higher energy side. Such a shift could also be produced if the mean energy of the evaporated particles increases with increasing nucleon spin. The order of magnitude of this shift can be obtained from nuclear-rotational energy [43, 44]. More elaborate computations, using Hauser–Feshbach theory may bring about a better agreement. However, since the calculated inverse cross-sections depend critically on the optical model parameters and since there is no unique set of such parameters, a certain amount of uncertainty is inherent in the theoretical cross-sections.

In the case of (α, pxn) type of reactions, there are more complications due to isotopic contributions for a natural copper target. For example the long-lived ^{65}Zn$(T_{1/2} = 244$d) is formed not only in ^{63}Cu(α, pn) and ^{65}Cu$(\alpha, p3n)$ reactions but also by the β^+ decay of the 15 min ^{65}Ga. Which, in turn, is formed in ^{63}Cu$(\alpha, 2n)$ and ^{65}Cu$(\alpha, 4n)$ reactions. No attempt has been made in this case to separate out the isotopic contributions and to compare them with theory.

4. Fraction of pre-equilibrium particle emission

The present studies clearly show considerable pre-equilibrium contribution in α-induced reactions (figure 6). Pre-equilibrium fraction (f_{PE}) is a measure of the relative weights of the pre-equilibrium and equilibrium components needed to reproduce an experimental excitation function. It is defined as the integral pre-equilibrium neutron cross-section plus the pre-equilibrium proton cross-section divided by the total compound nucleus cross-section. This quantity is designated by f_{PE}. The calculated f_{PE} for ^{63,65}Cu are shown in figure 6 as a function of bombarding energy (E_α). It was found that f_{PE} increases very fast as the energy of the α-particle increases. Furthermore, the threshold for pre-equilibrium emission is higher for the lower mass number and f_{PE} is higher for the system of higher mass number at a given α-particle energy [45].

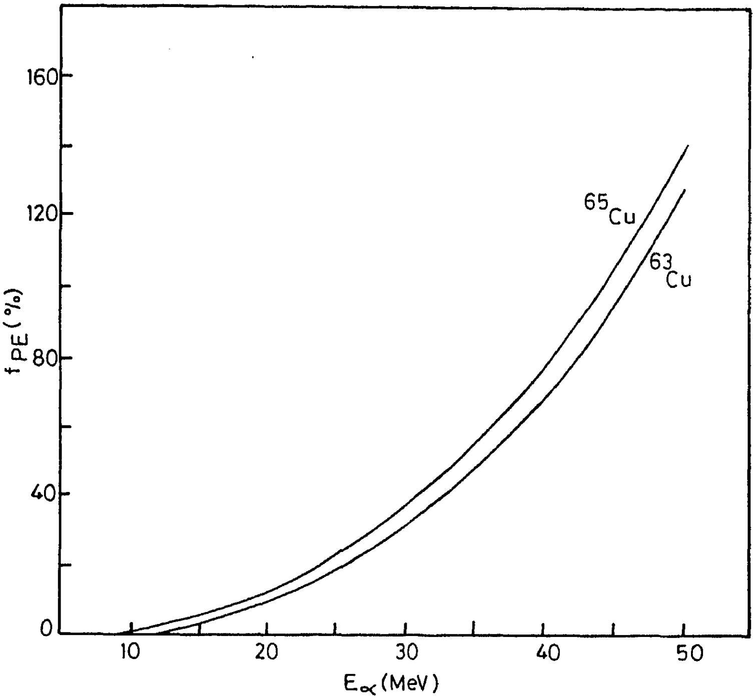

Figure 6. Pre-equilibrium fraction (f_{PE}) as a function of incident energy of alpha particle.

5. Conclusions

From an overall comparison of the experimental results and theoretical predictions based on compound nucleus Weisskopf–Ewing estimates as well as hybrid model, one can infer as in other works that the Weisskopf–Ewing estimate accounted well for the low energy compound nucleus dominated part of the excitation functions but failed to account for the observed cross-sections at higher energies, where non-equilibrium effects predominate beyond a few tens of MeV of bombarding energy. The basic tenet that only a small number of degrees of freedom is excited in pre-equilibrium reactions is amply borne out by the consistently good agreement observed between the experimental results and the pre-equilibrium predictions for an initial exciton number $n_0 = 4(4p0h)$. The physical interpretation of $n_0 = 4(4p0h)$ is that, only four excitons initially share the excitation energy and that these are particles above a completely filled Fermi-sea (i.e. pure particle state). The pre-equilibrium fraction (f_{PE}) for ^{63}Cu and ^{65}Cu has also been calculated. It is found that the pre-equilibrium reaction increases fast with the increase of incident α-particle energy. The threshold for pre-equilibrium emission is higher for lower mass number. It is also observed that the value of f_{PE} is higher for the system of higher mass number at a given α-particle energy.

Acknowledgements

We wish to express our sincere thanks to Prof. J Rama Rao and Dr S Mukherjee for stimulating discussions and help during the course of this work. We also thank the members of the cyclotron group for their cooperation. This work was supported by University Grants Commission (UGC), New Delhi.

References

[1] J J Griffin, *Phys. Rev. Lett.* **17**, 478 (1966)
[2] G D Harp, J M Miller and B J Berne, *Phys. Rev.* **165**, 1166 (1968)
[3] M Blann, *Phys. Rev. Lett.* **27**, 337; 700 E; 1550 E; (1971)
M Blann, *Ann. Rev. Nucl. Sci.* **25**, 123 (1975)
[4] M Blann and H K Vonach, *Phys. Rev.* **C28**, 1475 (1983)
[5] E Gadioli, E Gadioli-Erba and P G Sona, *Nucl. Phys.* **A217**, 589 (1973)
[6] J Ernst and J Rama Rao, *Z. Phys.* **A281**, 129 (1977)
[7] G Mantzouranis, D Agassi and H A Weidenmueller, *Z. Phys.* **A27**, 145 (1976)
[8] H Machner, *Phys. Lett.* **B86**, 129 (1979)
[9] J M Akkermans, H Gruppelaar and G Reffo, *Phys. Rev.* **C22**, 73 (1980)
[10] J Ernst, W Friedland and H Stoekhorst, *Z. Phys.* **A328**, 333 (1987); **A333**, 45 (1989)
[11] D Agassi, H A Weidenmueller and G Mantzouranis, *Phys. Rev.* **22**, 145 (1975)
[12] T Tamura, T Udagawa, D H Feng and K K Kan, *Phys. Lett.* **B68**, 109 (1977)
[13] L Avaldi, R Bonetti and L Colli Milazzo, *Phys. Lett.* **B94**, 463 (1980)
[14] H Feshbach, A Kerman and S Koonin, *Ann. Phys.* **125**, 429 (1980)
[15] G M Field, R Bonetti and P E Hodgson, *J. Phys.* **G12**, 93 (1986)
[16] P E Hodgson, Workshop on Applied Nuclear Theory and Nuclear Model Calculations for Nuclear Technology Applications, ICTP Report SMR/284-5 (1988)
[17] K G Porges, *Phys. Rev.* **101**, 225 (1956)
[18] N T Porile and D L Morrison, *Phys. Rev.* **116**, 1193 (1959)
[19] E A Bryant, D F Cochran and J D Knight, *Phys. Rev.* **130**, 1512 (1963)
[20] P H Stelson and F R McGrown, *Phys. Rev.* **B133**, 911 (1964)
[21] E Lebowitz and M W Greens, *Int. J. Appl. Radiat. Isot.* **21**, 625 (1970)
[22] M Hille, P Hille, M Uhl and W Weisz, *Nucl. Phys.* **A198**, 625 (1972)
[23] S Y Lin and I M Alexander, *Phys. Rev.* **C16**, 688 (1977)
[24] H P Graf and H Muenzel, *J. Inorg. Nucl. Chem.* **36**, 3647 (1974)
[25] I A Rizvi, M A Ansari, R P Gautam, R K Y Singh and A K Chaubey, *J. Phys. Soc. Jpn.* **56**, 3135 (1987)
[26] H D Bhardwaj, A K Gautam and R Prasad, *Pramana – J. Phys.* **31**, 109 (1988)
[27] A V Mohan Rao, S Mukherjee and J Rama Rao, *Pramana – J. Phys.* **36**, 115 (1991)
[28] C E Williamson, J P Boujot and J Picard, CENS Report, CEA-R 3042 (1966)
[29] C M Lederer and V S Shirley, *Table of isotopes* 7th edn. (John Wiley, New York, 1978)
[30] J Rama Rao, A V Mohan Rao, S Mukherjee, R Upadhyay, N L Singh, S Agarwal, L Chaturvedi and P P Singh, *J. Phys.* **G13**, 535 (1987)
[31] N L Singh, S Agarwal and J Rama Rao, *Can. J. Phys.* **71**, 115 (1993)
[32] N L Singh, S Agarwal, L Chaturvedi and J Rama Rao, *Nucl. Instrum. Methods* **B24/25**, 480 (1987)
[33] I A Rizvi, M K Bhardwaj, M A Ansari and A K Chaubey, *Can. J. Phys.* **67**, 870 (1989)
[34] P Misaelides and H Muenzel, J. Inorg. Nucl. Chem. **42**, 937 (1980)
[35] M Blann, Code ALICE/85/300 UCID-2069 (1984)
[36] C K Cline and M Blann, *Nucl. Phys.* **A172**, 225 (1971)
[37] H Stockhorst, W Friedland and J Ernst, *Proc. of the 3rd Int. Conf. on Nuclear reaction mechanism*, Verenna, June 14–19, Edited by E Gadioli (1982) pp. 119
[38] W D Mayers and W J Swiatecki, *Nucl. Phys.* **81**, 1 (1966)
[39] F D Becchetti and F W Greenless, *Phys. Rev.* **182**, 1190 (1969)

[40] V F Weisskopf and D H Ewing, *Phys. Rev.* **57**, 472 (1940)
[41] E Gadioli, E Gadioli-Erba, L Sajo-Bahus and G Tagliaferri, *Riv. Nuovo Cimenta.* **6**, 1 (1976)
[42] N L Singh, S Agarwal and J Rama Rao, *J. Phys. Soc. Jpn.* **59**, 3916 (1990)
[43] D Bodansky, *Ann. Rev. Nucl. Sci.* **12**, 79 (1962)
[44] M Blann and G Merkel, *Phys. Rev.* **B137**, 367 (1965)
[45] B P Singh, H D Bhardwaj, A K Gautam and R Prasad, *DAE Symp. Nucl. Phys.* **B35**, 232 (1992)

PRAMANA
— journal of
physics

© Printed in India

Vol. 42, No. 4,
April 1994
pp. 365–374

Multiple scattering of gamma rays in water, concrete and sand

G S BHANDAL, VIJAY KUMAR, RAMA RANI, KAWALDEEP and K SINGH*
Radiation Physics Lab., Department of Physics, Guru Nanak Dev University, Amritsar 143 005, India
*Author for correspondence

MS received 20 September 1993; revised 29 January 1994

Abstract. The transmitted photon spectra of ^{133}Ba, ^{22}Na, ^{137}Cs, ^{54}Mn and ^{60}Co point sources are measured through different thicknesses of water, concrete and sand. The multiple-scatter peaks observed in these materials at 60, 90 and 100 keV energies respectively are found to be independent of incident photon energy and thickness of the medium.

Keywords. Multiple-scatter peak; transmitted photon spectra; radioisotopes

PACS No. **32·80**

1. Introduction

The investigation of the transmitted photon spectra through a medium has led to better understanding of the process of transport and energy degradation of a primary photon. Swarup and Peshori [1] showed that, in energy degradation of a gamma ray photon in a medium of low effective atomic number, a multiple-scatter peak, irrespective of the energy of primary photon entering the medium, is observed at an energy between 100 keV, at which Compton interactions are not very effective in energy degradation of the photon, and a lower energy above which the photoelectric cross-section for the medium is negligible.

The multiple-scatter peak has been studied in nuclear graphite, water and air by Swarup and Peshori [1, 2] and Swarup [3]. They reported this peak at 50, 60 and 72 keV respectively. Smith and Scofield [4] also reported similar peak in aluminium at 92 keV. Swarup and Peshori [2] concluded that a higher energy primary photon produces a greater number of multiple scattered photons for the same thickness of the medium that does a lower energy primary photon. Singh [5] has also studied the transmitted photons spectra of ^{133}Ba, ^{137}Cs and ^{60}Co through different thicknesses of a soil medium and a multiple-scatter peak was observed at an energy of 100 keV. Thye also observed a linear relationship between the effective atomic number and the multiple-scatter peak energy. Brust [6] has shown that for media of different atomic numbers, the multiple scatter peak is at different energies in the soft part of the spectrum and Mintato [7] has concluded that, as a first approximation its energy varies directly with the atomic number of the medium.

We extend the study here to transmitted photon spectra of ^{133}Ba, ^{22}Na, ^{137}Cs, ^{54}Mn and ^{60}Co gamma ray sources through different thicknesses of water, concrete and sand.

2. Experimental set-up

The experimental system (figure 1) consists of a aluminium drum (90 cm high, 60 cm diameter and 0·2 cm wall thickness) kept on a plywood stand with a circular hole of 8 cm diameter in its centre below which a detector assembly is placed. A NaI(Tl) (2″∗2″) detector is housed in a cylindrical lead shield which is lined on the inside with brass and aluminium sheets. The axis of the drum is placed co-linear with the extended axis of the crystal. The pulse height spectra were recorded with PC/XT AC–4 K plug in card multichannel analyzer.

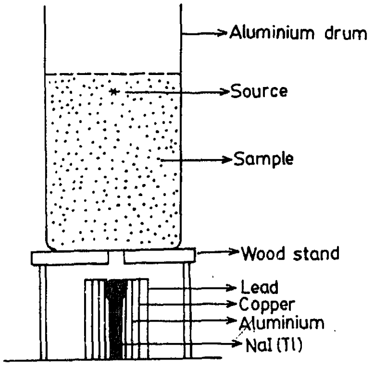

Figure 1. Experimental set-up.

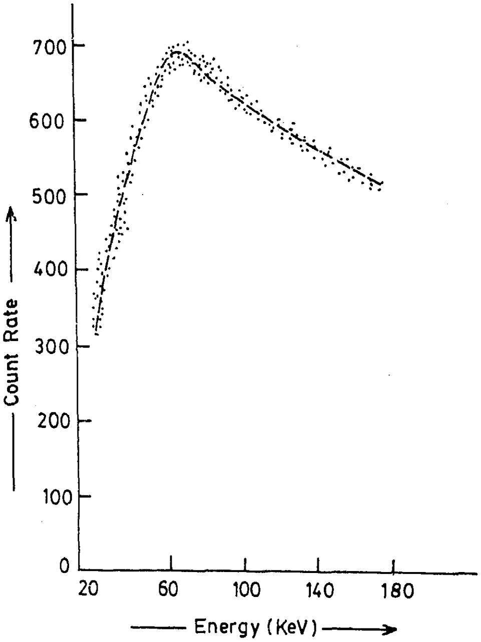

Figure 2. Transmitted photon spectra of ^{137}Cs through water medium.

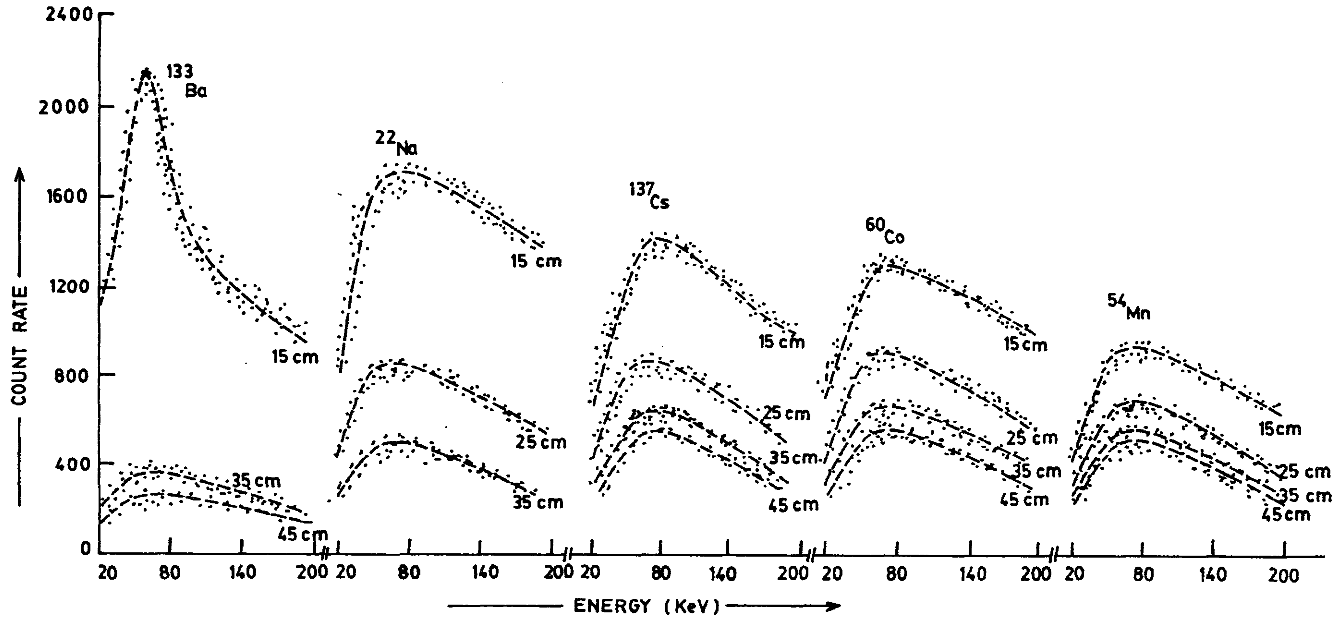

Figure 3. Transmitted photon spectra of different sources through different thicknesses of water.

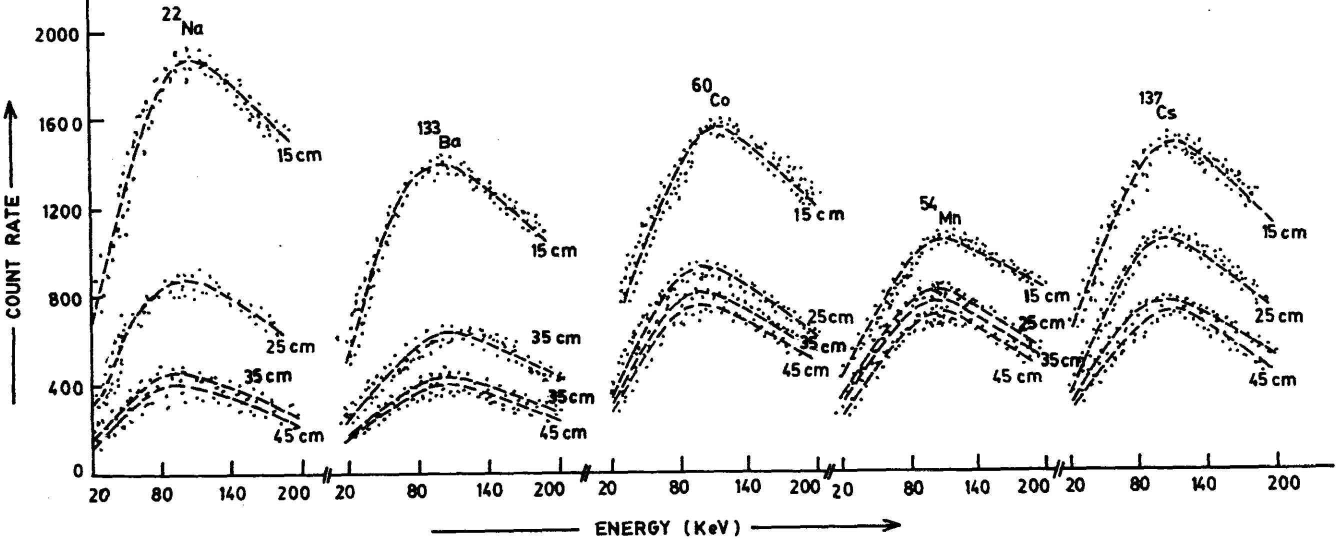

Figure 4. Transmitted photon spectra of different sources through different thicknesses of sand.

3. Measurements

After calibration of the spectrometer in the low energy region with X-rays and gamma ray photons from ^{57}Co, ^{241}Am and ^{133}Ba, the following five sets of observations were recorded.

i) In the first set, experimental set-up was checked with incident energy of 662 keV from ^{137}Cs through water where a multiple scatter peak of 60 keV (figure 2) was observed. This value is in good agreement with the value reported in [2].
ii) In the second set, the sources were placed in a thin plastic cup glued on a thermocole float (2 cm thick) and the level of water in the drum was changed from 15 cm to 45 cm in four steps. The recorded spectrum is shown in figure 3.
iii) In the third set, the sealed sources were placed 3 cm below the sand medium at the axis of the drum. Different transmitted photon spectra were recorded for four different thicknesses of the sand medium. The spectra are shown in figure 4.
iv) In the fourth set, to determine the effect of backscattering due to different thicknesses of the sand on the transmitted spectra, the distance of the ^{137}Cs source was fixed at 10 cm in sand medium and spectra were recorded for different thicknesses of sand above the source. The spectra are shown in figure 5.
v) In the last set, the sand medium was replaced by concrete and observations were recorded with different sources as in step (iii). The spectra are shown in figure 6.

4. Results and discussion

In all the transmitted photon spectra shown in figures 2–4 and 6 and for all the thicknesses of the media, broad peaks at 60, 90 and 100 keV are observed in water, concrete and sand respectively. These peaks are the properties of the scattering media through which primary gamma rays pass to the detector. These peaks are due to multiple scattering in the media. It was checked that the multiple-scatter peaks are not due to electronic artifacts. Minato [7] with his Monte Carlo calculations has concluded that in different media shapes of multiple-scatter peaks in transmission

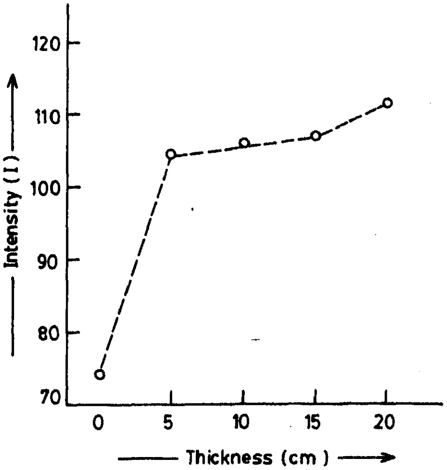

Figure 5. Variation in intensity of multiple scatter peak with thickness of sand above source (10 cm).

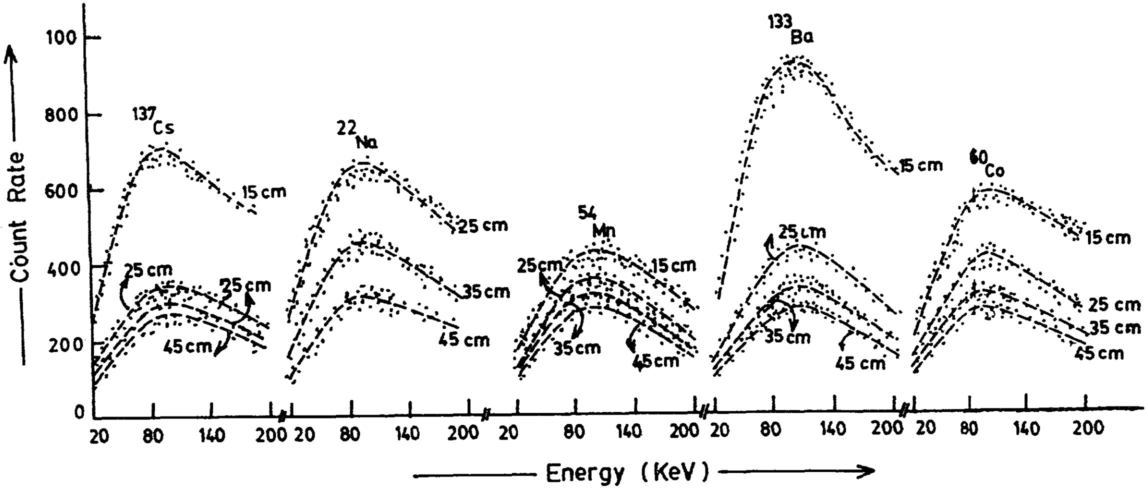

Figure 6. Transmitted photon spectra of different sources through different thicknesses of concrete.

spectra are quite similar to each other. According to him multiple-scatter energy is a characteristic constant of the medium. From these figures it is clear that multiple-scatter peak is independent of primary incident photon energy and thickness of the medium. Similar results are reported in [1,2].

In the experimental setting (iv) above, it is found that the intensity of scattered peak changes with the thickness of the medium beyond 10 cm behind the source. Above a certain thickness the change in intensity is very small (figure 5). Transmitted flux increases with increase in thickness above the medium due to backscattering. It is also evident from figure 7 that energy of multiple-scatter peak is independent of the thickness of a medium above the source.

From figure 8, it is clear that transmitted intensity of multiple-scatter peak decreases exponentially with increase in thickness of medium whereas the multiple-scatter peak energy is independent of thickness of medium. The log of normalized counts of the multiple-scatter peaks is plotted against thickness of the medium (figure 9). It is to be noted that energy spectra in figures 8 and 9 are corrected for detector efficiency and transmission through aluminium drum wall and detector window. From this it is seen that the logarithm of the intensity decreases linearly with increase in thickness of the medium. This shows that the intensity I of the multiple-scattered photons can be expressed by

$$I = I_0 e^{-ax} \tag{1}$$

where a, the slope, is called the multiple-scatter coefficient and x is the thickness of the medium. It is observed that a values decrease with increase in incident photon

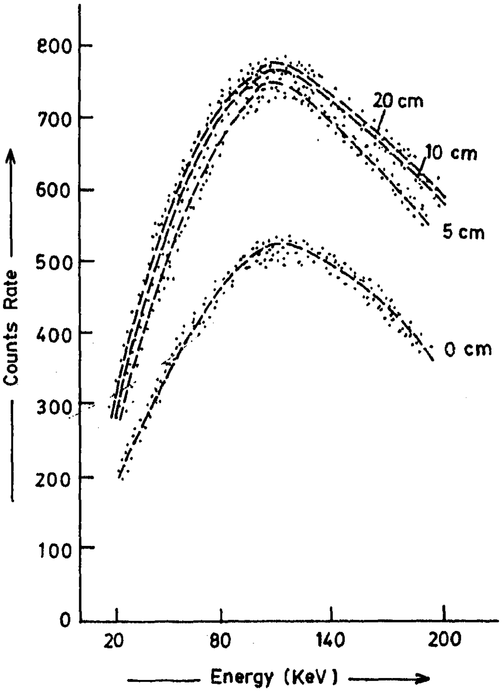

Figure 7. Plot of energy of multiple scatter peak for different thicknesses of sand above source at 662 keV.

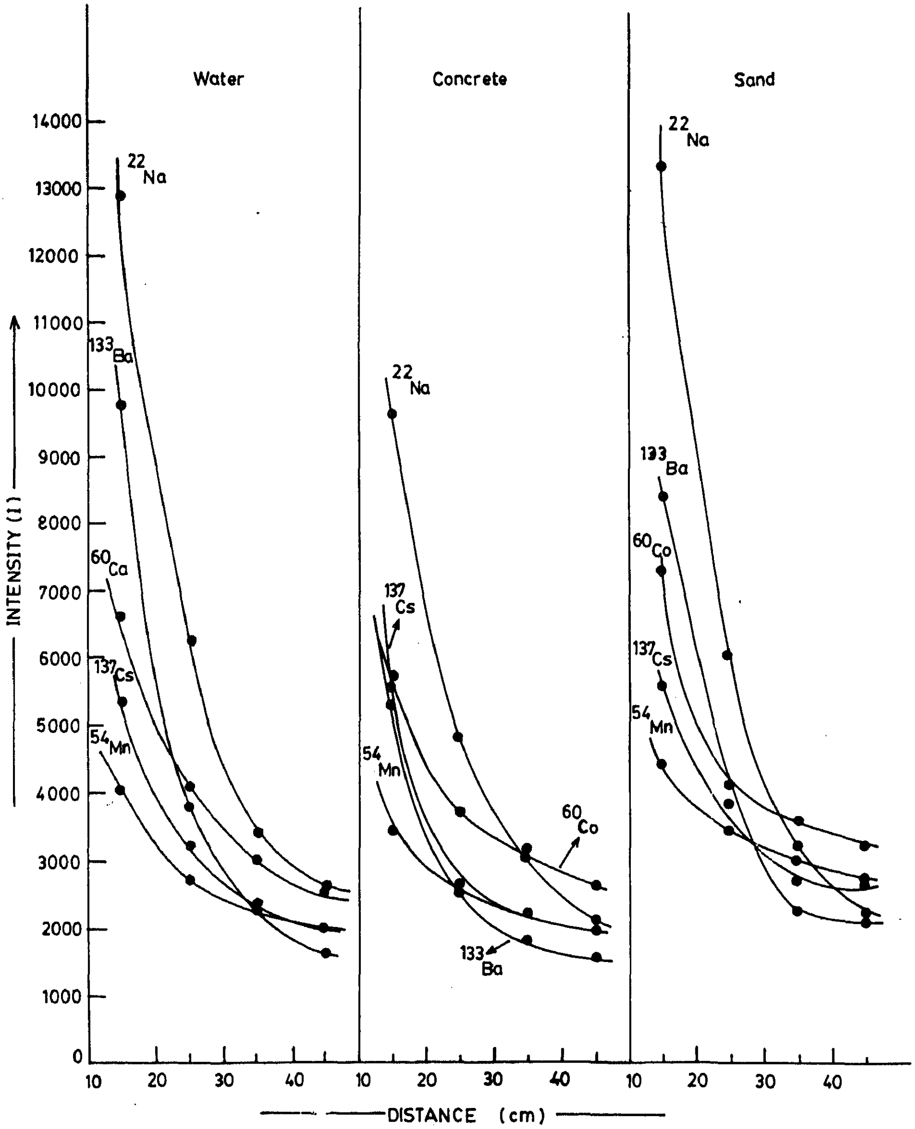

Figure 8. Variation in intensity of multiple scatter peak with thickness in different media.

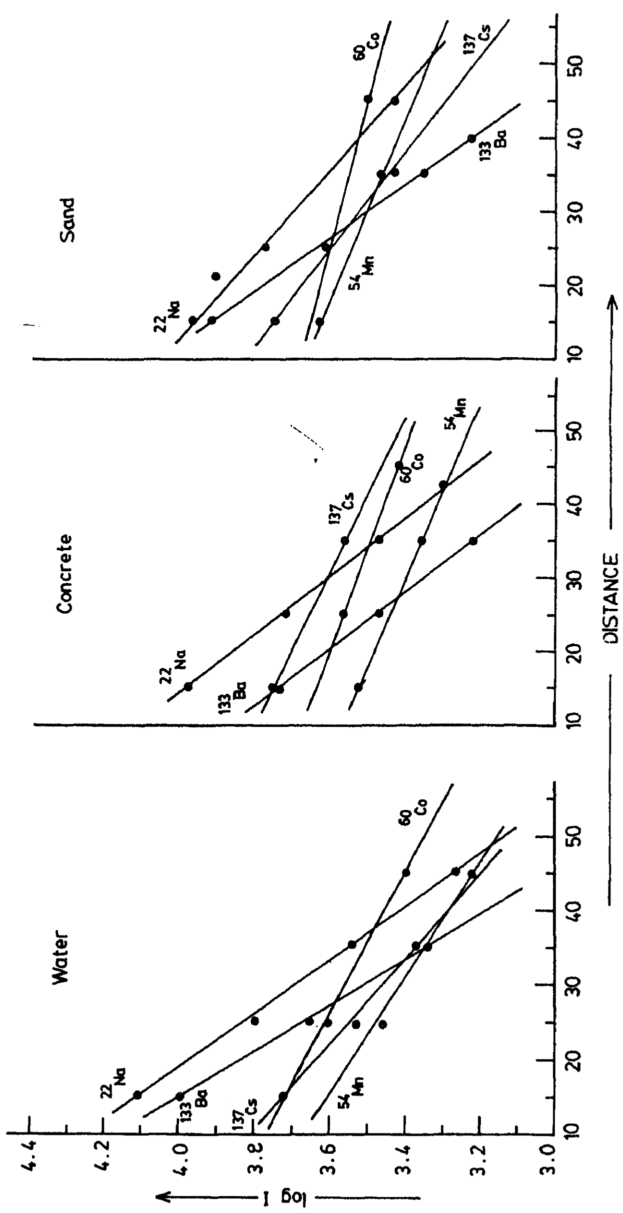

Figure 9. Logarithm of normalized peak counts compared with the thickness of different media.

Table 1. The values of multiple-scatter coefficient *a* in water, concrete and sand.

Sample	Values of *a* 356 keV	511 keV	662 keV	835 keV	1280 keV
Water	0·0330	0·0285	0·0175	0·0130	0·0105
Concrete	0·026	0·025	0·0095	0·0085	0·0075
Sand	0·028	0·017	0·015	0·0085	0·005

energy. The coefficient *a* is a characteristic constant of the medium which depends on incident energy, like linear attenuation coefficient. The multiple scatter coefficients obtained from figure 9 are shown in table 1.

References

[1] J Swarup and L H Peshori, *Int. J. Appl. Radiat. Isot.* **36**, 531 (1985)
[2] J Swarup and L H Peshori, *Int. J. Appl. Radiat. Isot.* **37**, 13 (1986)
[3] J Swarup, *Nucl. Instrum. Methods* **172**, 559 (1980)
[4] C V Smith and N E Scofield, *Nucl. Sci. Eng.* **47**, 1 (1972)
[5] Makhan Singh, Ph.D. Thesis, Punjabi University, Patiala (Unpublished) (1993)
[6] P Brust, *Kernenergie* **15**, 193 (1972)
[7] S Minato, *Nucl. Sci. Eng.* **51**, 32 (1973)

PRAMANA
— journal of
physics

© Printed in India

Vol. 42, No. 5,
May 1994
pp. 375–385

Structure and vibrational properties of carbon tubules

N CHANDRABHAS[1], A K SOOD[1,4], D SUNDARARAMAN[2], S RAJU[2], V S RAGHUNATHAN[2], G V N RAO[3], V S SASTRY[3], T S RADHAKRISHNAN[3], Y HARIHARAN[3], A BHARATHI[3] and C S SUNDAR[3]
[1] Department of Physics, Indian Institute of Science, Bangalore 560 012, India
[2] Metallurgy Division, [3] Materials Science Division, Indira Gandhi Centre for Atomic Research, Kalpakkam 603 102, India
[4] Also at Jawaharlal Nehru Centre for Advanced Scientific Research, IISc Campus, Bangalore 560 012, India

MS received 11 February 1994; revised 6 April 1994

Abstract. The structure of multilayered carbon tubules has been investigated by electron microscopy and X-ray diffraction. The structure of tubules is characterized by disorder in the stacking of cylindrical graphene sheets. Raman scattering measurements have been carried out in tubules and compared with graphite. The observed features in the Raman spectra in tubules can be understood in terms of the influence of disorder. The additional Raman modes predicted for single layer carbon tubules have not been observed.

Keywords. Nanoparticles; tubule; graphite; Raman spectroscopy.

PACS Nos 78·30; 61·46

1. Introduction

Since the first observation of carbon tubules by Iijima [1] there has been a tremendous excitement with respect to their novel structure, and physical properties and their potential for applications in nanotechnology [2]. The tubular morphology usually consists of several concentric folded graphitic sheets, capped at ends. Theoretical calculations [3, 4] of single tubules have predicted exotic electronic properties ranging from metallic to semiconductor behaviour depending on the chirality and diameter of the tubule. The vibrational properties have been extensively investigated theoretically by Dresselhaus and co-workers [5, 6] with specific reference to Raman and infra-red active modes. The number of Raman and infrared active modes are only dependent on the symmetry, but the phonon frequencies are seen to depend on the tubule diameter. While most of the theoretical interest has been on a single tubule, and recently some experimental methods for the preparation of predominantly single tubules have been obtained [7], the experiments so far have been only in multi-layered tubules.

In the present work, studies on the structure and vibrational properties of multilayered tubules are reported. The structural studies have been carried out using electron microscopy and X-ray diffraction. The vibrational properties have been investigated using Raman spectroscopy. During the course of this study, we became aware of the work of Hiura *et al* [8] on these systems. These results will be compared with our present study. In addition, new results especially in low-frequency range of Raman scattering will be presented.

2. Experimental details

Following the prescription of Ebessen and Ajayan [9] for the large scale synthesis of carbon nanotubes, arcing between graphite electrodes (5N5 pure from Johnson and Mathey, USA) was carried out under 500 torr He atmosphere using a Kratscmer–Huffman type apparatus described in detail elsewhere [10]. When the arcing was carried out at 20 V AC, 125 A, the smaller graphite electrode of 6 mm diameter was consumed and a carbonaceous deposit gets formed on the larger 10 mm diameter graphite electrode. The central core of the deposit, rich in tubules [9] was scooped out, crushed, suspended in ethanol, and ultrasonically agitated for about an hour and then allowed to settle down. A drop or two of the supernatant was transferred to holey carbon film for electron microscopy observations, which were carried out using Philips EM 400 T and JEOL EXII microscopes. The extracted powder was used for X-ray and Raman scattering experiments. X-ray diffraction measurements were carried out with Cu-K_α radiation, using Siemens D-500 diffractometer, operating in the $\theta - 2\theta$ Bragg–Brentano arrangement. Raman measurements were done in the back scattering geometry using 5145 Å line of argon-ion laser (laser power ~ 30 mW) and DILOR-XY spectrometer equipped with liquid nitrogen cooled CCD detector. The low frequency (less than 200 cm^{-1}) spectra were recorded from the sample kept in vacuum to avoid interference with the Raman lines of nitrogen gas. In addition, experiments were also done on the powder obtained from the outer shell of the carbonaceous deposit and on the starting graphite sample.

3. Results and discussion

3.1 *Electron microscope studies*

Electron microscope observations indicated a preponderance of multi layered carbon tubules along with occasional presence of polyhedral particles having spherical shell structure. Figure 1(a) shows a typical transmission electron micrograph of a nested carbon tubule in which the diameter varies from 15 nm to 50 nm. As has been discussed earlier [11] such a change in diameter is associated with the presence of pentagons and heptagons in the hexagonal graphitic sheet. Figure 1(b) shows the selected area diffraction pattern taken with the electron beam perpendicular to the tubule axis. As discussed by Iijima [9], the sharp (001) spots arise from the parallel graphitic sheets and point to the co-axial arrangement of graphitic sheets in the tubule. The ring-like spots which are a superposition of the (*hk*0) reflections (the (100) and (110) can be seen in figure 1(b)) arise because the successive hexagonal sheets are not under exact superposition.

The high resolution microscope image of the (002) lattice fringes is shown in figure 1(c). The tubule pictured in figure 1(c) shows one half of the tubule containing about 46 layers and has a core of about 2 nm. One of the important features seen in this figure is the presence of localized region with significant faulting in the stacking of graphene sheets. It is well-known [9] that for tubular arrangement of graphitic sheets, the ABABAB... stacking present in ideal graphite structure is not possible and a turbostatic arrangement is expected. The present high resolution picture indicates the presence of stacking faults which are shown in detail in figure 1(d), which also shows in some regions considerable puckering from true planarity. A schematic illustrating the possible stacking of graphene layers from ABAB... type to ABCABC...

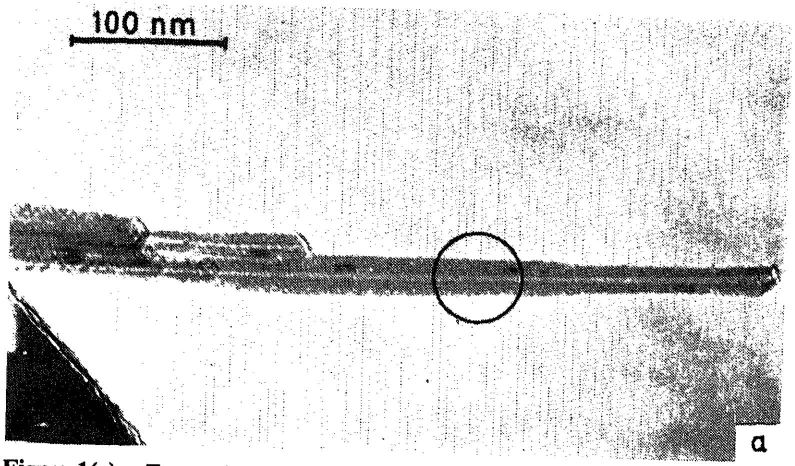

Figure 1(a). Transmission electron micrograph of multi-layered carbon tubule showing the nested arrangement. The diameter in the ringed region of tubule is 25 nm and in the thinner region is 15 nm.

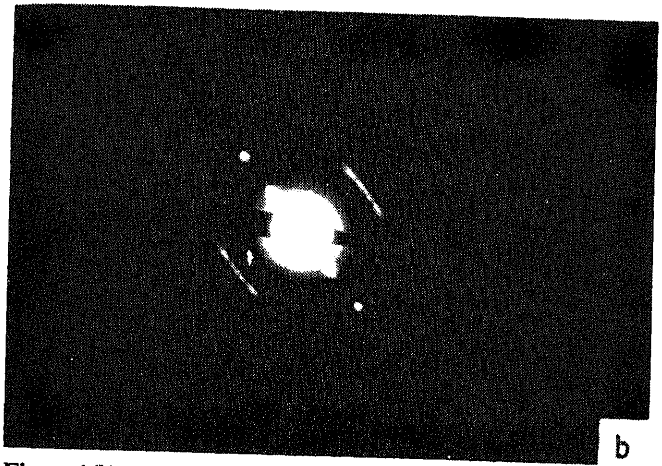

Figure 1(b). Selected area diffraction from the circled portion of tubule.

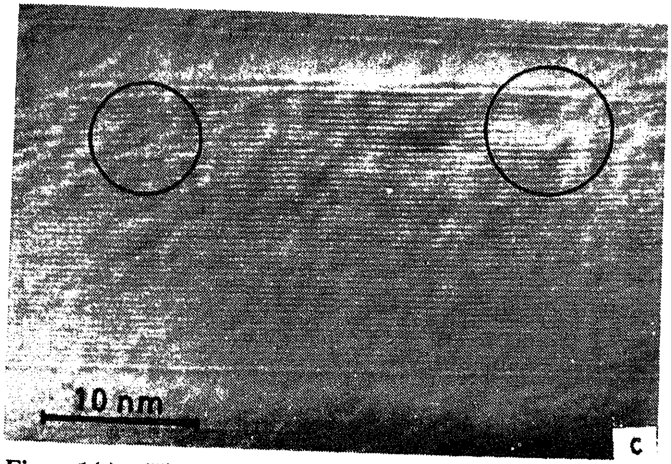

Figure 1(c). High resolution electron micrograph of tubule. Note the significant local deviations of (002) fringes from planarity. Dislocation type defects are also observable.

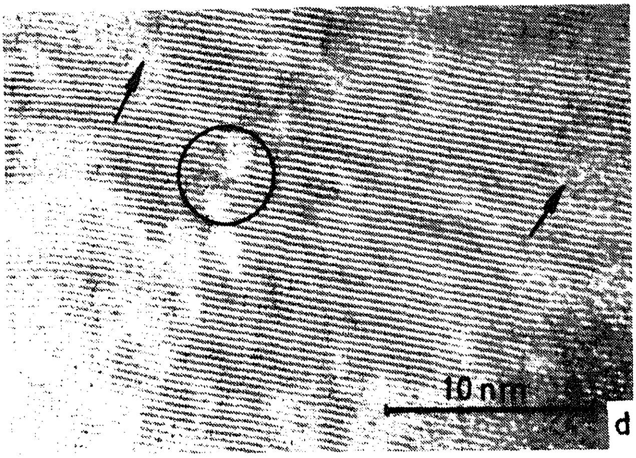

Figure 1 (d). A region similar to that shown in (c), but is slightly enlarged showing clearly the puckering of planes and dislocation type defects.

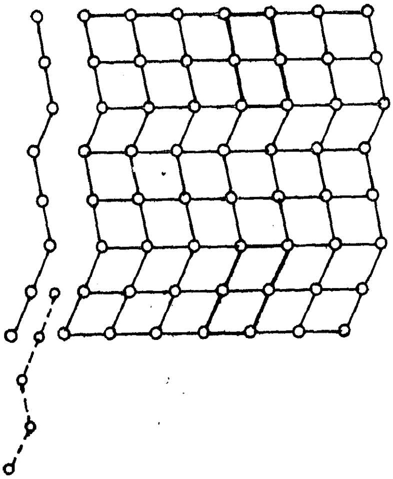

Figure 2. Schematic illustrating the stacking of graphene layers giving rise to defects as shown in figures 1(c) and (d). The illustrated sequence corresponds to a *fcc* stacking with a twin boundary in between. A dislocation like arrangement is also illustrated through dotted lines. A unit cell like configuration is outlined by strong lines.

(rhombohedral type) is shown in figure 2. The restoration of a particular stacking sequence could be interpreted in a multitude of ways by allowing for planar defects: this stacking fault defects are mandatory for larger diameter tubes and may even serve as potent nucleating site for another tubular variant. Further, in view of the considerable influence that these defects may have on the electronic and vibrational properties, detailed studies of defects in multi layered tubules are called for.

3.2 *X-ray diffraction*

The X-ray diffraction pattern of the starting graphite powder and that of the tubule powder are shown in figures 3(a) and 3(b), respectively. The diffraction pattern of graphite can be indexed to a hexagonal cell with lattice parameters $a = 2{\cdot}46$ Å and $c = 6{\cdot}72$ Å in accordance with the results reported in literature [12]. In the diffraction pattern of the tubule, the (002) and (004) lines can be clearly seen to be shifted to lower angles indicating an increase in the 'c' lattice parameter to 6·85 Å. The reflections indexed as (10) and (11) (i.e., diffraction from a two dimensional lattice) are broad and asymmetric and are similar to that seen in turbostatic graphite [13]. From the positions of the (10) and (11) reflections, the 'a' lattice parameter can be evaluated to be 2·46 Å. Thus in the tubule structure, while the intra-layer distance between the carbon atoms is unaffected that between the layers is larger than in graphite [14]. The diffraction pattern from the outer shell is shown in figure 3(c). It is interesting to note that the diffraction pattern is similar to that of tubules (figure 3(b)) though no tubules have been observed by electron microscopy. It is also worth pointing out that the diffraction pattern of the outer shell does not correspond to that of amorphous carbon.

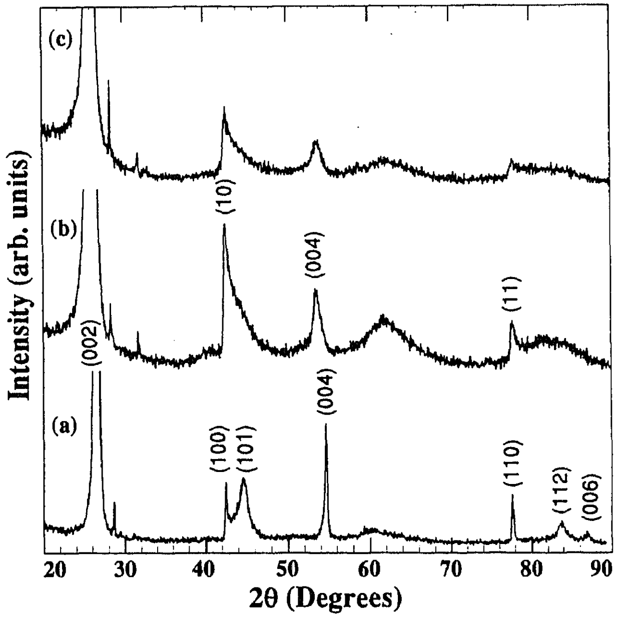

Figure 3. X-ray diffraction pattern in (a) graphite, (b) tubules from the inner core and (c) outer shell of the carbonaceous deposit.

3.3 *Raman spectroscopy*

Raman spectroscopy has proven to be a powerful technique for the study of graphite, its intercalation compounds [15] and fullerenes [16]. Apart from providing information on the zone centre Raman active phonons, the Raman spectra (RS), in the case of disordered solids, contains information on the phonon density of states (PDOS). Further, the degree of sp^2—sp^3 bonding also leaves characteristic Raman finger prints.

Pristine graphite crystallises according to the D^4_{6h} and has nine vibrational optic modes: $2E_{2g}(R) + 2B_{1g} + A_{2u}(IR) + E_u(IR)$, where R and IR denote Raman active and infra-red active modes respectively. The two Raman active modes are (a) E^2_{2g} at $\omega = 1582\,\mathrm{cm}^{-1}$ which involves out of phase intra-layer displacements and (b) E^1_{2g} at $\omega = 42\,\mathrm{cm}^{-1}$ which involves in phase inter-layer displacements resulting in rigid shearing motion between graphite layers [15]. Jishi *et al* [6] have calculated the allowed Raman modes of a tubule using a zone-folding technique for two-dimensional dispersion curves from a graphene layer, which indicate that there are 15 allowed Raman modes for each diameter tube: Whereas the frequency of the allowed modes depend on the tube diameter and the chiral angle, the number of modes is independent of diameter.

Figure 4 shows the RS in the region of the E^2_{2g} mode (1250–$1750\,\mathrm{cm}^{-1}$) of (a) high purity graphite (b) inner core of the carbonaceous deposit containing tubules and (c) the outer shell of the deposit. The PDOS calculated in terms of an axially symmetric Born–von Karman force-constant model [17] is shown in figure 4(d) which shows peaks at about 1335, 1425 and $1610\,\mathrm{cm}^{-1}$. In the case of graphite, the sharp Raman

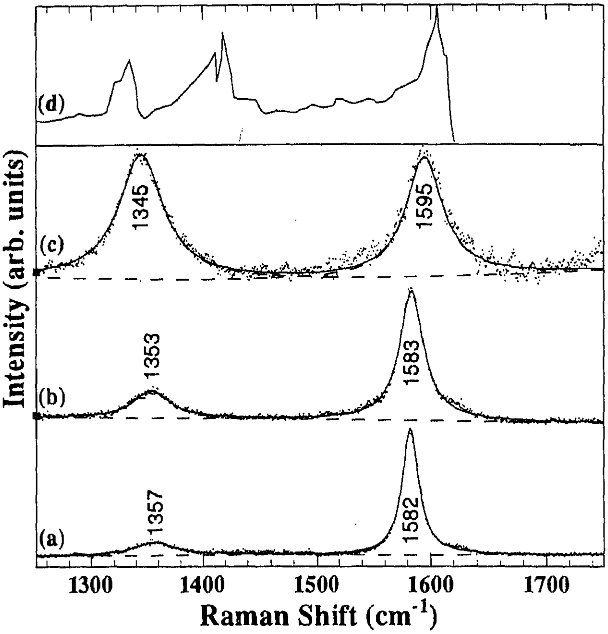

Figure 4. Raman spectra in the range $1250\,\mathrm{cm}^{-1}$ to $1750\,\mathrm{cm}^{-1}$ in (a) graphite, (b) tubules in the inner core and (c) the outer shell of the carbonaceous deposit. The calculated PDOS (Ref. 17) is shown in (d).

line at 1582 cm^{-1} is seen. The broad hump centered at 1357 cm^{-1} is related to the presence of disorder/finite-size effects leading to break down in the wave vector selection rules and a peak in the RS occurs near the maxima in the PDOS [18]. The corresponding Raman line of the inner core (figure 4(b)) is at 1353 cm^{-1}. The peak positions are (i) 1582 and 1357 cm^{-1} for graphite (figure 4(a)) (ii) 1583 and 1353 cm^{-1} for the inner core (figure 4(b)) and (iii) 1595 and 1345 cm^{-1} for the outer deposit (figure 4(c)). As we go progressively from graphite to the inner core and the outer shell (figure 4(a) to figure 4(c)), the following features in the RS are observed: (1) The Raman line associated with the E_{2g}^{2} mode broadens and shifts to higher wave number, (2) The 1357 cm^{-1} line associated with the disorder increases in relative intensity and shifts towards lower wave number.

As already remarked the intensity of Raman lines in a disordered material reflects the dominant features in the PDOS [15, 18]. Theoretical calculations of the PDOS of graphite by Leung *et al* [19] using the phonon dispersion relations calculated by Maeda *et al* [20] and by Niclow *et al* [17] indicate that the largest peak in the PDOS occurs at $\sim 1610\,\mathrm{cm}^{-1}$, upshifted from the zone-centre Raman active phonon at 1582 cm^{-1}. In the case of tubules in the inner core and the outer shell, having considerable disorder, this feature in the PDOS is probed, resulting in a up-shift of the Raman line. This can be clearly seen as the small shoulder at 1620 cm^{-1} seen even in graphite (figure 4(a)) merges with the 1582 cm^{-1} line leading to a broad peak at 1595 cm^{-1} in the outer deposit (figure 4(c)). The next dominant feature in the PDOS is [17–20] at 1355 cm^{-1} which accounts for the small peak in graphite shown figure 4(a). As we go from figure 4(a) to figure 4(c), this peak is seen to increase in

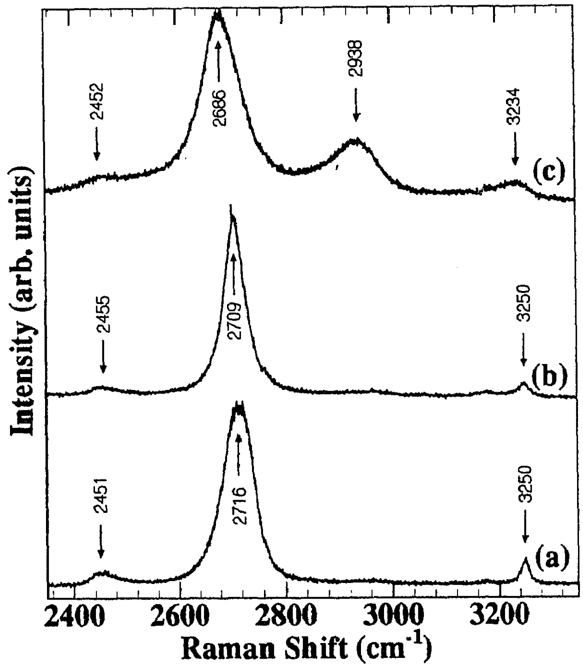

Figure 5. Second-order RS in the range 2400 cm^{-1} to 3200 cm^{-1} in three samples as in figure 4.

relative intensity and shift to lower wave number. This softening of phonons can be related to the larger *c*-axis lattice parameter in tubule and outer shell as compared to graphite (cf. § 3.2). Thus it is seen that the progressive changes of both the line positions and intensity of the Raman lines seen in figure 4 can be qualitatively understood in terms of the increase in disorder as we go from figure 4(a) to figure 4(c).

The second-order RS are associated with the phonons of wave vector $\mathbf{q}$ and $-\mathbf{q}$ and hence are sensitive to PDOS [15, 18]. Figure 5 shows the second-order RS in the range $2400\,\mathrm{cm}^{-1}$ to $3200\,\mathrm{cm}^{-1}$. The progressive downshift of the $2716\,\mathrm{cm}^{-1}$ line (overtone corresponding $1357\,\mathrm{cm}^{-1}$ mode) can be seen from figure 5(a) to figure 5(c) and this is consistent with the downshift seen in the first-order spectra (cf. figure 4). The other two lines at $2451\,\mathrm{cm}^{-1}$ and $3250\,\mathrm{cm}^{-1}$ can be accounted in terms of combination of the peak at $1620\,\mathrm{cm}^{-1}$ and $860\,\mathrm{cm}^{-1}$ phonon and of the two $1620\,\mathrm{cm}^{-1}$ modes. The line at $2938\,\mathrm{cm}^{-1}$ seen only in the case of outer shell (figure 5(c)) can be a combination of the phonons of frequency $1595\,\mathrm{cm}^{-1}$ and $1345\,\mathrm{cm}^{-1}$ peaks. This band also occurs in the RS of the glassy carbon reported by Hiura *et al* [8]. This is interesting because even though the outer deposit is not X-ray amorphous (figure 3(c)), the RS resembles that of the glassy carbon.

The results of Raman experiments in the range of $200\,\mathrm{cm}^{-1}$ to $1250\,\mathrm{cm}^{-1}$ were characterized by poor signal to noise (S/N) ratio. In order to improve the S/N ratio, these measured spectra were subjected to discrete wavelet transform filtering [21] and the results are shown in figure 6 for graphite (curve (a)), inner deposit (curve (b)) and the outer deposit (curve (c)). The features in the RS appear due to relaxation of Raman selection rules due to disorder and hence should map the PDOS which is shown from the known calculations [17] in figure 6(d). The peaks in PDOS occur at 468 and $\sim 770\,\mathrm{cm}^{-1}$. Following Nemanich and Solin [18], the $\sim 770\,\mathrm{cm}^{-1}$ peak is associated with the M-point zone boundary phonon modes with 'out-of-plane' and 'in-plane' displacements whereas the $468\,\mathrm{cm}^{-1}$ mode arises solely from the M-point mode with 'out-of-plane' displacement. The RS in figure 6(a–c) do show bands near $470\,\mathrm{cm}^{-1}$. The bands near $700\,\mathrm{cm}^{-1}$ in the tubule and outer deposit perhaps correspond to the $770\,\mathrm{cm}^{-1}$ band in the PDOS. The downward shift of the band can arise due to larger *c*-axis lattice parameter in comparison to graphite, as also reflected in figure 4. The spectrum in figure 6(c) also shows peaks at ~ 860 and $1120\,\mathrm{cm}^{-1}$ which are not prominent in the PDOS. The $860\,\mathrm{cm}^{-1}$ band is seen to contribute to the combination mode at $2451\,\mathrm{cm}^{-1}$ (figure 5). The additional Raman modes predicted in this spectral range by Jishi *et al* [6] for single tubules have not been observed.

Figure 7 shows the RS of tubules in the low frequency range of 30 to $150\,\mathrm{cm}^{-1}$. The E_{2g}^{1} mode of graphite corresponding to the intra layer shear mode has been identified at $42\,\mathrm{cm}^{-1}$ and $45\,\mathrm{cm}^{-1}$ based on Raman scattering [22] and neutron diffraction [17] experiments. In the case of tubules Raman peak at $49\,\mathrm{cm}^{-1}$ can be seen clearly in addition to the lines at 66 and $77\,\mathrm{cm}^{-1}$ which are the laser plasma lines. It is a moot question whether the Raman line in the tubule is slightly upshifted from the intra-layer shear mode in graphite. First we note that in going from graphite to tubules, the intra-layer carbon distance is not affected (cf. § 3.2). In addition, the three carbon–carbon bond angles are also not very different [23] from 120 degrees due to the cylindrical curvature of graphene sheets (unlike in the case of C_{60}). Further, as to whether the small upshift can be related to the features in the PDOS (cf. figure 4), it may be pointed out that theoretical calculations [17, 19] do not indicate any peaks in the PDOS in this spectral range. Thus the Raman line at $49\,\mathrm{cm}^{-1}$ can be taken to be similar to that in graphite with no special significance with respect to either

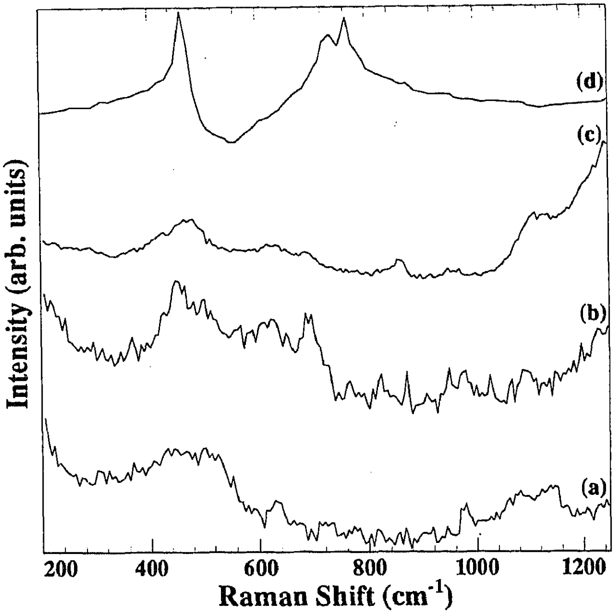

Figure 6. Raman spectra in the range 200 cm^{-1} to 1250 cm^{-1} in (a) graphite, (b) tubules and (c) outer shell. These spectra have been subjected to discrete wavelet transform filtering. The calculated PDOS (ref. 17) is shown in (d).

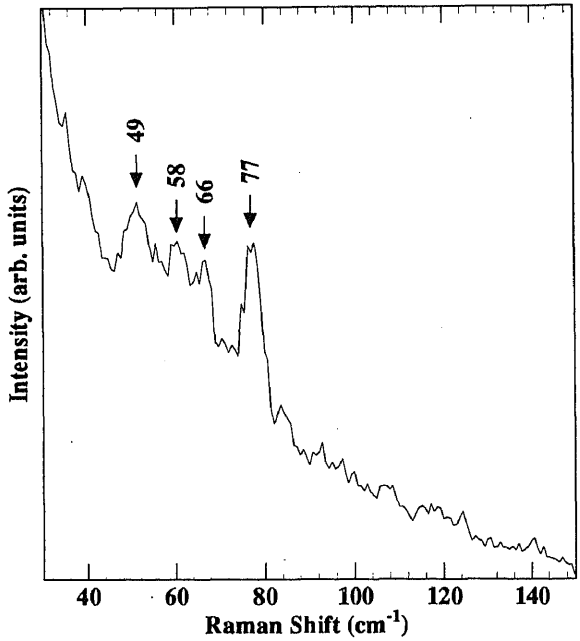

Figure 7. RS of the inner core of the deposit in the range 30 cm^{-1} to 150 cm^{-1}.

the tubular structure or disorder in graphitic structure. In figure 7, a small feature at 58 cm^{-1} can be discerned. It is tempting to associate this with defects in the graphene layer, such as the pentagons and heptagons [11] which will lead to altering of bond distances and angles and thus hardening of tangential modes.

4. Summary

The structural studies on multi-layered tubules point to the existence of considerable disorder in the stacking of graphene sheets. The influence of disorder is reflected in the changes in RS with respect to graphite. Additional Raman lines characteristic of single-layered tubules [6] have not been observed in the present experiments. With the recent methods for the synthesis of predominantly single-layered tubules [7], Raman experiments on these may become feasible. In addition to studies on the Raman active tangential modes, infra-red studies of the radial modes will be also of interest.

Acknowledgements

The authors would like to thank Shri M C Valsakumar for graciously carrying out the discrete wavelet transform filtering of the spectra shown in figure 6. One of the authors (AKS) thanks the Department of Science and Technology for financial assistance.

References

[1] S Iijima, *Nature* (*London*), **358**, 220 (1992)
[2] See *Materials Science and Engineering* **B19**, (1993)
[3] R Saito, M Fujita, G Dresselhaus and M S Dresselhaus, *Appl. Phys. Lett.* **60**, 2204 (1992)
[4] N Hamada, S Sawada and A Oshiyama, *Phys. Rev. Lett.* **68**, 631 (1992)
[5] M S Dresselhaus, G Dresselhaus and R Saito, *Phys. Rev.* **B45**, 6234 (1992)
[6] R A Jishi, L Venkataraman, M S Dresselhaus and G Dresselhaus, *Chem. Phys. Lett.* **209**, 77 (1993)
R A Jishi, M S Dresselhaus and G Dresselhaus, *Phys. Rev.* **B47**, 16671 (1993)
[7] S Iijima, *Proc. of MRS meeting* (Boston, Dec., 1993);
S C Tsang, P J F Harris and M L H Green, *Nature* **362**, 520 (1993)
[8] H Hiura, T W Ebbesen, K Tanigaki and H Takahashi, *Chem. Phys. Lett.* **202**, 509 (1993)
[9] T W Ebessen and P M Ajyan, *Nature* (*London*), **358**, 220 (1992)
[10] Y Hariharan, A Bharathi, C S Sundar, V S Sastry, M Yousuf, T S Radhakrishnan, G V N Rao, T Geetha Kumary, N Subramanian, P Ch Sahu, V S Raghunathan and M C Valsakumar, *Curr. Sci.* **63**, 25 (1992)
[11] S Iijama, T Ichihashi and Y Ando, *Nature* (*London*), **356**, 776 (1992)
B I Dunlap, *Phys. Rev.* **B46**, 1933 (1992)
[12] P Trucano and R Chen, *Nature* (*London*), **258**, 136 (1975)
[13] B T Kelley, *Physics of graphite* (Applied Science Publishers, London, 1981)
[14] Y Saito, T Yoshikawa, S Bandow, M Tomita and T Hayashi, *Phys. Rev.* **B48**, 1907 (1993)
[15] M S Dresselhaus and G Dresselhaus, in *Light scattering in solids III, Recent results*, edited by M Cardona and G Guntherodt (Springer Verlag, Berlin, 1983), p3
[16] P C Eklund, P Zhou, K A Wang, G Dresselhaus and M S Dresselhaus, *J. Phys. Chem. Solids* **53**, 1391 (1992)
N Chandrabhas, K Jayaram, D V S Muthu, A K Sood, R Seshadri and C N R Rao, *Phys. Rev.* **B47**, 10963 (1993)
[17] R Niclow, N Wakabayashi and H G Smith, *Phys. Rev.* **B5**, 4951 (1972)

[18] R J Nemanich and S A Solin, *Phys. Rev.* **B20**, 392 (1979)
[19] S Y Leung, M S Dresselhaus and G Dresselhaus, *Physica* **B105**, 375 (1981)
[20] M Maeda, Y Kuramoto and C Horie, *J. Phys. Soc. Jpn.* **47**, 337 (1979)
[21] I Daubachies, *Wavelets* (SIAM, Philadelphia, 1992)
[22] R J Nemanich, G Lucovsky and S A Solin, in *Proc. Int. Conf. on Lattice Dynamics*, edited by M Balkanski (Flammarion Press, Paris, 1977) p. 619
[23] R A Jishi and M S Dresselhaus, *Phys. Rev.* **B45**, 11305 (1992)

PRAMANA
— journal of
physics

© Printed in India

Vol. 42, No. 5,
May 1994
pp. 387–394

The elastic moduli, the volume contribution and the Cauchy ratio for *d* and *f* shell metals

N SINGH and B S YADAV
Department of Physics, M.D. University, Rohtak 124001, India

MS received 15 September 1993; revised 11 March 1994

Abstract. The elastic constants of nine transition metals and four rare-earths and actinides are calculated using the ion–ion interaction defined by us recently. The volume contribution to elastic moduli is calculated by exploiting the density dependence of the screening function. The calculated volume contribution to bulk modulus is found to vary between 17·1% and 62·4% for a number of metals, which is quite significant and play an important role for describing quantitatively the violation of the Cauchy ratio for these metals.

Keywords. Elastic constants; Cauchy ratio; bulk modulus.

PACS No. 62·20

1. Introduction

In the past there have been many attempts to obtain different analytical forms of the pair interaction $V(r)$ between ions in solids based on pseudopotentials, linear screening theory and second-order perturbation in the energy. Previous attempts to obtain such analytical forms have met with partial success [1–3]. Pettifor and Ward [4, 5] have shown that fitting a rational function to the Lindhard [6] susceptibility $\chi(\mathbf{q})$ leads to an analytical form for $V(r)$. The ion–ion interaction obtained by them is fast converging and can be used to get quick calculations. Inspired by Pettifor and Ward's work, Hafner and Heine [7] obtained a simple form of the pair potential by solving the integral appearing in band-structure part of it. Their form of $V(r)$ exhibits the Friedel [8] oscillations through the oscillatory terms. The Friedel oscillations are found to be necessary for the physical stability of the solids.

The pair potentials have been popular in describing metallic bonding because of their computational simplicity. But they do not describe properly the violation of the Cauchy ratio. This problem can be overcome by including a volume dependent energy term [9], introducing many-body interactions. Finnis [10] has shown that for simple metals violation of the Cauchy ratio can be obtained by calculating the derivatives of the density dependent total energy. Walker and Taylor [11] have obtained density dependent pair potential following the approach of Pettifor and Ward [4]. They have used the non-local pseudopotential instead of the local pseudopotential and have made energy-wave-number characteristic function rational rather than the logarithmic term of the Lindhard [6] dielectric function.

The problem of the Cauchy ratio violation can also be overcome by introducing many-body interaction in the pair potential. Daw and Baskes [12] and Foiles *et al* [13] have developed the model pair potential known as the embedded-atom model

(EAM), which is based on the density functional and the effective-medium theory [14–16]. Finnis and Sinclair [17] developed independently a model which is mathematically equivalent to the EAM, using the second-moment approximation to the density of states in the tight-binding method [18]. Ercolessi *et al* [19] have used the same approach forgetting N-body potential. In non-centrosymmetric lattices the elastic constants are composed of a homogeneous and an inhomogeneous contribution [20]. The elastic constants of hcp solids have been calculated by van Midden and Sasse [21] using embedded-atom potential. Wallace [22] and Martin [23] showed that influence of sublattice relations for hcp and diamond crystals does not cancel out when we use many-body potentials.

The rare earths and actinides have comparatively complex electronic structure. In these solids some of the *d* and *f* electrons are itinerant and some of them are tightly bound. Therefore, not many attempts have been made to obtain the simple analytical form of the ion–ion interaction for these metals. Wills and Harrison [24] and Harrison [25] in their classic work, have obtained the attractive and overlap contributions due to *d* and *f* electrons considering the following approximations: (i) the non-interacting band model scheme for *s*, *d* and *f* electrons, (ii) Friedel model of density of states and (iii) Andersen model of muffin-tin orbital theory for *d* and *f* orbitals. Following the approach of Wills and Harrison [24], Walzer [26] has written the total energy for transition metals as a function of volume and calculated the elastic and bulk properties of a number of transition and rare earth metals. The first principle method based on density functional idea has been used by Per Soderlind *et al* [27, 28] to calculate the elastic constants of transition metals and rare earths. The work of Hafner and Heine [7] has inspired us [29] to obtain the pair potential for simple metals, using two-parameter Heine–Abarenkov [30] model potential instead of Asheroft [31] model potential. Combining this interaction with ion–ion interaction obtained by Wills and Harrison [24] and Harrison [25], we define the pair potential for rare earth metals. This ion–ion interaction is then used to calculate the elastic constants and binding energy of transition metals, rare-earths and actinides in fcc and bcc phase. The volume dependent contribution to elastic moduli is calculated by taking the derivatives of the density dependent part of the total energy. As has been suggested by Hafner and Heine [7], the local-field corrections due to Ichimaru and Utsumi [32] are considered to normalize the screening function.

2. Theory

The total energy of a solid in second-order perturbation theory combined with local pseudopotential can be written as [22, 33] and [34]:

$$E = E_{\mathrm{eg}}(n_0) + \tfrac{1}{2} V_{\mathrm{bs}}(r=0) + \tfrac{1}{2} \sum_{i \neq 0} V(\mathbf{r}_i). \tag{1}$$

$E_{\mathrm{eg}}(n_0)$ is the energy of all electrons in a homogeneous electron gas of density $n_0 = Z_s/V_0$, where V_0 is the atomic volume and Z_s is the valence of the ion. The exchange-correlation corrections appropriate to the metallic densities [35] have been included in $E_{\mathrm{eg}}(n_0)$. All the structure dependence has been included in the sum over pairwise interaction between atoms, $V(\mathbf{r}_i)$, $\mathbf{r}_i$ being the position of the *i*th ion. The volume dependence in this term is included through the dielectric screening function $\varepsilon(\mathbf{q})$, where $\mathbf{q}$ is the phonon wave vector. The volume dependent energy $V_{\mathrm{bs}}(r=0)$ is really a multi-ion interaction of sufficiently long range and sufficiently weak structure; so that it does not contribute to the volume dependent part of bulk modulus.

Considering the non-interacting band model for s, d and f electrons, the ion–ion interaction for rare earths is written as the sum of $s-s$ contribution, $d-d$ and $f-f$ attractive and repulsive contributions as follows:

$$V(r) = [V_{FE}(r) + V_d(r) + V_{dd}(r) + V_f(r) + V_{ff}(r)] \exp(-\pi K_B \mathrm{Tr}/\hbar v_F). \tag{2}$$

The free electron part of pair interaction $V_{FE}(r)$ is obtained in second-order perturbation theory using two-parameter Heine–Abarenhov [30] model potential. The integral appearing in the band structure term can be solved following the procedure devised by Hafner and Heine [7]. After a lengthy but straightforward algebra, we arrive at the following results [29]:

$$\begin{aligned} V_{FE}(r) = \frac{Z_s^2}{r}[&H_1(r-2r_c) + \tfrac{1}{4}H_3(r-2r_c) + \tfrac{1}{2}H_2(r) \\ &+ \tfrac{1}{4}H_1(r+2r_c) - \tfrac{1}{4}H_3(r+2r_c)]. \end{aligned} \tag{3}$$

H_1, H_2 and H_3 are represented as the sum of the repulsive and the oscillatory contributions. The analytical expressions for these functions are given in [29]. The coupling between the local nonoverlapping d states and orthogonalized plane waves is obtained by Wills and Harrison [24] in second-moment approximation and using Friedel model of density of states. The $s-d$ hybridization in $V_d(r)$ is included through the factor $Z_d\left(1 - \frac{Z_d}{10}\right)$ which represents the continuous filling of bonding levels, where Z_d is the occupation number of d states. The overlapping contribution due to different d orbitals $V_{dd}(r)$ is obtained using Andersen's model of muffin-tin orbital theory. In rare earth metals the f bands play the same role as the d bands play in transition metals. Therefore, Harrison [25], in his subsequent paper, has obtained the attractive $V_f(r)$ and overlapping $V_{ff}(r)$ contributions by treating f electrons just like d electrons. The analytical expressions for $V_d(r)$, $V_{dd}(r)$, $V_f(r)$ and $V_{ff}(r)$ are given in [36]. The temperature dependence in the pair potential is included through the damping factor [37], $\exp(-\pi K_B Tr/\hbar v_F)$. Here $v_F = \hbar K_F/m$ is the Fermi velocity and K_B is the Boltzmann constant. The band structure energy $V_{\mathrm{bs}}(r=0)$ can be obtained from the band structure part of $V_{FE}(r)$ by putting $r = 0$ and then solving the integrals following the procedure of Hafner and Heine [7].

The pressure required to hold a solid can be evaluated by differentiating (1) with respect to its volume V. Differentiating (1) once more, we get the bulk modulus [22, 33]:

$$B = V\frac{\partial^2}{\partial V^2}\left(\frac{1}{2}\sum_{i\neq 0} V(\mathbf{r}_i)\right) + \Delta_{\mathrm{bs}}. \tag{4}$$

The first term in (4) is identical to the contribution obtained using dynamical longwave method. Δ_{bs} is the additional contribution to B arising from the volume dependence of the band structure part of the energy $\sum_q' V_{\mathrm{bs}}(\mathbf{q})$, i.e.,

$$\Delta_{\mathrm{bs}} = V\left(2\frac{\partial^2}{\partial V_0 \partial V_{\mathrm{osc}}} + \frac{\partial^2}{\partial V_{\mathrm{osc}}^2}\right)\sum_q{}' V_{\mathrm{bs}}(\mathbf{q}). \tag{5}$$

$\partial/\partial V_0$ operates on explicit volume term while $\partial/\partial V_{\rm osc}$ operates on volume dependence of the dielectric function $\varepsilon(\mathbf{q})$ only.

If we now choose to differentiate $V_{\rm bs}(\mathbf{q})$ with respect to $\mathbf{q}$ rather than V and K_F rather than $V_{\rm osc}$, eq. (5) may be written as [22]:

$$\Delta_{\rm bs}=\frac{1}{9V_0}\sum_q{}'\left(10K_F\frac{\partial}{\partial K_F}+K_F^2\frac{\partial^2}{\partial K_F^2}+2qK_F\frac{\partial^2}{\partial q\partial K_F}\right)V_{\rm bs}(\mathbf{q}). \tag{6}$$

The elastic constants for cubic crystals in longwave length limit [20] C_{11}, C_{12} and C_{44} can be calculated easily once the force constants are known. Including the volume-dependent contribution obtained using (6), we can get the elastic moduli using the following relations:

$$C_{11}=C_{11}+\Delta_{\rm bs}, \tag{7a}$$

$$C_{12}=C_{12}+\Delta_{\rm bs}, \tag{7b}$$

$$C_{44}=C_{44}, \tag{7c}$$

It is to be noted that C_{44} remains unaffected by volume forces because it only involves homogeneous strain at constant volume [22, 34]. The bulk modulus defined by eq. (4) can now be written as:

$$B=\tilde{B}+\Delta_{\rm bs}. \tag{8}$$

3. Calculation and results

The atomic radius r_0 is taken corresponding to the observed [38] volume for all metals. The number of s electrons per atom [24] Z_s for each Cu, Ag, Ni, Pd and Pt is taken as 1·5. Z_s is taken equal to 2 for Au. The number of electrons in s and d shells are taken to be 2 and 4, respectively, for all the three metals Cr, Mo and W. The number of electrons in d and f shells are taken from [24] and [25]. The d and f shell radii r_d and r_f are calculated from the respective d and f band widths, as has been suggested in [24] and [25]. The calculations for La, Ce, Yb and Th are done for the configuration $5d^1 6s^2$, $5d^{0\cdot5}4f^1 6s^{2\cdot5}$, $5d^{0\cdot5}4f^{14}6s^{1\cdot5}$ and $6d^0 5f^1 7s^3$, respectively, because these configurations have been found to yield overall better results of phonon frequencies in [36]. The potential parameters D and r_c for a metal are determined by matching the calculated values of the binding energy E_{BI} and the elastic constant C_{44}. The damping parameter $\delta=2$ is found to yield overall better results. It is to be noted that the value of C_{44} remains unaffected by the volume forces. The values of D and r_c so obtained are given in table 1. The contributions up to 7th shell have been found sufficient to achieve convergence. The theoretical values of the binding energy are presented in table 1 alongwith its estimated [39], [40] results from the cohesive energy and the ionization energies. The calculated and estimated values of the binding energy for fcc transition metals, bcc transition metals and rare earths and actinides to within 10–20% except for Pb, Pt and W. The maximum discrepancy between calculated and experimental values of binding energy is found to be 36·2% for Pt. The calculated results of elastic constants are presented in table 2 alongwith the observed [41–46] values. It is found that the radial force constants play a dominant role in yielding the elastic constants.

The volume contribution to bulk modulus is found to vary between 17·1% and

Table 1. r_0 is the observed [38] atomic radius. D and r_c are the fitted values of the potential parameters. E_{BI} represents the binding energy. The estimated values of the binding energy $E_{BI} = E_{\text{coh}} + E_I + E_Z$ are obtained from the experimental values of the cohesive energy, E_{coh} [39] and using the first, second and third ionization energies [39–40], E_I, E_{II} and E_{III}, respectively. E_Z represents $\frac{1}{4}(E_I + E_{II})$, E_{II}, $E_{II} + \frac{1}{4}(E_{II} + E_{III})$ and $E_{II} + E_{III}$ for $Z_s = 1{\cdot}5$, $2{\cdot}0$, $2{\cdot}5$ and $3{\cdot}0$, respectively. The values in the parantheses represent the difference (in per cent) between the theoretical and estimated values.

Element	r_0 (a.u.)	D (a.u.)	r_c (a.u.)	$-E_{BI}$(eV/atom) Theor.	$-E_{BI}$(eV/atom) Expt.
Cu	2·664	0·98	2·0	14·99 (− 17·6)	18·19
Ag	3·005	1·14	2·4	14·95 (− 15·7)	17·73
Au	3·005	1·20	2·4	27·00 (− 19·4)	33·51
Ni	2·608	0·275	1·447	14·61 (− 21·1)	18·51
Pd	2·872	0·99	2·749	13·94 (− 27·2)	19·15
Pt	2·891	1·0	2·80	13·84 (− 36·2)	21·68
Cr	2·684	0·60	2·132	24·66 (− 9·9)	27·36
Mo	2·930	0·40	2·30	24·90 (− 17·2)	30·07
W	2·949	0·37	2·345	24·89 (− 28·0)	34·58
La	3·961	0·70	2·44	19·17 (− 9·2)	21·11
Ce	3·819	0·95	2·76	32·18 (+ 13·3)	28·40
Yb	3·762	0·80	2·72	12·50 (+ 0)	12·45
Th	3·762	0·80	2·635	41·48 (+ 7·0)	44·60

Table 2. Values of the elastic moduli (C_{ij}), Bulk modulus (B), volume contribution (Δ_{bs}) (in 10^{12} dyn/cm^2) at 300 K and the volume contribution to B in per cent ($\%\Delta_{\text{bs}}$). (a) and (b) represent the theoretical results obtained without including Δ_{bs} and by including Δ_{bs}, respectively. (c) represents the observed values of the elastic constants and are taken from [41–46], *represents that the value of C_{12} is estimated from the experimental values of C_{11} and bulk modulus B of Cr.**

Element		C_{11}	C_{12}	C_{44}	B	Δ_{bs}	$\%\Delta_{\text{bs}}$	C_{12}/C_{44}
Cu	(a)	1·579	1·412	0·628	1·468	—	—	2·25
	(b)	1·537	1·370	0·628	1·426	− 0·042	− 2·9	2·18
[41]	(c)	1·684	1·214	0·754	1·371	—	—	1·61
	(d)	1·93	1·51	0·82	1·65	—	—	1·84
	(e)	1·67	1·24	0·76	1·38	—	—	1·63
Ag	(a)	1·107	0·929	0·442	0·989	—	—	2·10
	(b)	1·128	0·950	0·442	1·010	+ 0·021	+ 2·1	2·15
[41]	(c)	1·240	0·937	0·461	1·010	—	—	2·03
	(d)	1·28	0·86	0·61	1·00	—	—	1·41
	(e)	1·29	0·91	0·57	1·04	—	—	1·60
Au	(a)	1·520	1·147	0·598	1·271	—	—	1·92
	(b)	1·570	1·197	0·598	1·321	+ 0·050	+ 3·8	2·00
[41]	(c)	1·94	1·61	0·47	1·72	—	—	3·40
	(d)	2·09	1·75	0·31	1·86	—	—	5·64
	(e)	1·83	1·59	0·45	1·67	—	—	3·53

(Continued)

Table 2. (*Continued*)

Element	C_{11}	C_{12}	C_{44}	B	Δ_{bs}	$\%\Delta_{bs}$	C_{12}/C_{44}
Ni (a)	2·393	2·081	1·442	2·185	—	—	1·44
(b)	2·044	1·732	1·442	1·836	−0·349	−19·0	1·20
[41] (c)	2·508	1·500	1·235	1·86	—	—	1·21
(d)	3·33	1·54	1·28	1·80	—	—	1·20
Pd (a)	1·823	1·747	0·719	1·772	—	—	2·43
(b)	1·723	1·648	0·719	1·673	−0·100	−6·0	2·29
[41] (c)	2·271	1·760	0·717	1·810	—	—	2·45
(d)	1·95	1·76	0·73	1·82	—	—	2·41
(e)	2·18	1·84	0·65	1·95	—	—	2·83
Pt (a)	2·811	2·528	1·118	2·622	—	—	2·26
(b)	2·714	2·431	1·118	2·525	−0·097	−3·8	2·17
[41] (c)	3·467	2·507	0·765	2·78	—	—	3·28
(d)	3·72	2·53	0·85	2·93	—	—	2·98
(e)	3·03	2·73	0·68	2·83	—	—	4·01
Cr (a)	3·205	1·599	1·094	2·134	—	—	1·46
(b)	2·727	1·122	1·094	1·657	−0·477	−28·8	1·03
[41] (c)	3·47	1·12*	1·00	1·90	—	—	1·12
Mo (a)	4·289	2·227	1·570	2·914	—	—	1·42
(b)	3·742	1·681	1·570	2·368	−0·546	−23·0	1·07
[42] (c)	4·75	1·67	1·08	2·73	—	—	1·55
(d)	4·06	1·50	1·07	2·35	—	—	1·40
W (a)	4·720	2·543	1·657	3·269	—	—	1·53
(b)	4·242	2·065	1·657	2·790	−0·478	−17·1	1·25
[42] (c)	5·13	2·06	1·53	3·23	—	—	1·35
(d)	5·53	2·07	1·78	3·22	—	—	1·16
La (a)	0·320	0·230	0·184	0·260	—	—	1·25
(b)	0·310	0·210	0·184	0·243	−0·019	−7·9	1·14
[43] (c)	0·285	0·204	0·165	0·24	—	—	1·24
(d)	0·29	0·17	0·16	0·21	—	—	1·06
Ce (a)	0·294	0·102	0·168	0·166	—	—	0·61
(b)	0·249	0·057	0·168	0·121	−0·045	−37·2	0·34
[44] (c)	0·241	0·102	0·194	0·148	—	—	0·53
Yb (a)	0·226	0·172	0·192	0·190	—	—	0·90
(b)	0·152	0·099	0·192	0·117	−0·073	−62·4	0·52
[45] (c)	0·186	0·104	0·177	0·131	—	—	0·59
Th (a)	0·907	0·582	0·467	0·690	—	—	1·25
(b)	0·766	0·442	0·467	0·550	−0·141	−25·6	0·95
[45] (c)	0·753	0·489	0·478	0·577	—	—	1·02

**(d) and (e) represent the theoretical results of elastic constants taken from [27] and [13] respectively.

62·4% for Ni, Cr, Mo, W, Ce, Yb and Th, which is quite significant and important for describing quantitatively the Cauchy ratio for these metals. The volume contribution for Au and Pt metals is found to be +3·8% to −3·8%, respectively, which is quite negligible. Even though the discrepancy between calculated and experimental values of the elastic constants and the Cauchy ratio for these two metals are found comparatively large. The large discrepancy found between the calculated and experimental results of binding energy for Pt and W is also reflected in our calculated results of elastic constants for these metals. This is because of the limitation of the central pair potential. The angular forces [47] and many-body contributions [48] play a significant role in yielding good results of elastic constants. Recently, Per Soderlind *et al* [27] and Foiles *et al* [13] have calculated the elastic constants of transition metals including many-body contributions. In table 2, we have compared our calculated results of elastic constants with those obtained in [27] and [13]. It is found that many-body contributions improve the results of elastic constants in Au, Pt, Mo and W to a great extent. However, the central potential yield equally good results of elastic constants for rest of the metals considered so far.

4. Conclusions

The interionic potential is determined by assuming simple forms for s, d for f electron contributions. We have endeavoured here to use the simplest parametrized forms possible with the lowest number of parameters. The validity of the ionic interaction has been tested by calculating the bulk properties for as many as 13 cubic metals. Δ_{bs} makes up typically 62·4% of the bulk modulus in Yb. It is therefore significant to include Δ_{bs} to describe the Cauchy ratio and the elastic constants properly. Δ_{bs} is found to be positive or negative and depends markedly on the pseudopotential and the screening considered. The present treatment can be extended easily to study the bulk properties of metallic alloys.

Acknowledgements

This work is supported by the University Grants Commission, New Delhi. The computer facility provided by the Computer Centre, M.D. University, Rohtak is greatly appreciated.

References

[1] G Jaccuci and R Taylor, *J. Phys.* **F11**, 787 (1981)
[2] M S Duesbery and R Taylor, *J. Phys.* **F7**, 47 (1977)
[3] M S Duesbery, G Jaccuci and R Taylor, *J. Phys.* **F9**, 413 (1979)
[4] D G Pettifor and M A Ward, *Solid State Commun.* **49**, 291 (1984);
M A Ward, *Ph.D. Thesis*, Imperial College, London, England, (1985)
[5] D G Pettifor, *Phys. Scr.* **11**, 26 (1982)
[6] J Lindhard, *Kgl. Danske Mat. Fys. Medd.* (Denmark) **28**, 8 (1954)
[7] J Hafner and V Heine, *J. Phys.* **F16**, 1429 (1986)
[8] J Friedel, *Philos. Mag.* **43**, 153 (1952)
[9] R A Johnson, *Phys. Rev.* **B6**, 2094 (1972)
[10] M Finnis, *J. Phys.* **F4**, 1645 (1974)
[11] A B Walker and R Taylor, *J. Phys.* **F2**, 9481 (1990); **2**, 9501 (1990)
[12] M S Daw and M I Baskes, *Phys. Rev.* **B29**, 6443 (1984)
[13] S M Foiles, M I Baskes and M S Daw, *Phys. Rev.* **B33**, 7983 (1986)
[14] J K Norskov and N D Lang, *Phys. Rev.* **B22**, 2131 (1980)
[15] K W Jacobsen, J K Norskov and M J Puska, *Phys. Rev.* **B35**, 7423 (1987)
[16] M S Daw, in *Atomistic simulation of materials: Beyond pair potentials* Edited by V Vitek and D J Srolovitz (Plenum, New York, 1989) p. 181
[17] M W Finnis and J E Sinclair, *Philos. Mag.* **A50**, 45 (1984)
[18] G J Ackland, M W Finnis and V Vitek, *J. Phys.* **F18**, L153 (1988)
[19] F Ercolessi, S Tosatti and M Parrinello, *Phys. Rev. Lett.* **57**, 719 (1986)

[20] M Born and K Huang, *Dynamical theory of crystal lattices* (Clarendon, Oxford, 1954)
[21] H J P van Midden and A G B M Sasse, *Phys. Rev.* **B46**, 6020 (1992)
[22] D C Wallace, *Thermodynamics of Crystals* (Wiley, New York, 1972)
[23] J M Martin, *J. Phys.* **C8**, 2837 (1975); **C8**, 2858 (1975)
[24] J M Wills and W A Harrison, *Phys. Rev.* **B28**, 4363 (1983)
[25] W A Harrison, *Phys. Rev.* **B28**, 550 (1983)
[26] U Walzer, *Phys. Status Solidi* **B125**, 55 (1984)
[27] Per Soderlind, Olle Erikssen, J M Wills and A M Boring, *Phys. Rev.* **B48**, 5844 (1993)
[28] Per Soderlind, Olle Eriksson, J M Wills and A M Boring, *Phys. Rev.* **B48**, 9306 (1993)
[29] N Singh and B S Yadav, *Physica* **B192**, 205 (1993)
[30] V Heine and I V Abarenkov, *Philos. Mag.* **9**, 451 (1964)
[31] N W Ashcroft, *Phys. Lett.* **23**, 48 (1966)
[32] S Ichimaru and K Utsumi, *Phys. Rev.* **B24**, 7385 (1981)
[33] S H Taole and H R Glyde, *Can. J. Phys.* **57**, 1870 (1979)
[34] R Evans, in *Electrons in disordered metals and metallic surfaces* Edited by P Phariseau, B L Györffy and L Scheire (Plenum, New York, 1979)
[35] D Pines, *Elementary excitations in solids* (Benjamin, Amsterdam, 1963)
[36] N Singh and S P Singh, *Phys. Rev.* **B42**, 1652 (1990)
[37] K Takanaka and R Yamamoto, *Phys. Status. Solidi* **B84**, 813 (1977)
[38] W B Pearson, *A Handbook of lattice spacings and structure of metals and alloys* (Pergamon, New York, 1958)
[39] C Kittel, *Introduction to solid state physics*, 5th ed. (Wiley, New York, 1976)
[40] *C R C Handbook of chemistry and physics* Edited by R C Weast and M J Astle, 61st ed. (Chemical Rubber Company, Florida, 1980)
[41] G Simmons and H Wang, *Single crystal elastic constants and calculated aggregate properties: A Handbook* (MIT, Press, Cambridge, 1971)
[42] D I Bolef and J de Klerk, *Phys. Rev.* **129**, 1063 (1963)
[43] H B Huntigton, in *Solid State Physics* Edited by F Seitz and D Turnbull (Academic, New York, 1958) Vol. 7
[44] C Stassis, C K Loong and J Zarestky, *Phys. Rev.* **B26**, 5426 (1982)
[45] C Stassis, T Gould, O D Macmasters, K A Gschneider Jr and R M Nicklow, *Phys. Rev.* **B19**, 5746 (1979)
[46] C Stassis, C K Loong, C Theisen and R M Nicklow, *Phys. Rev.* **B26**, 4106 (1982)
[47] G D Barrera and A Batana, *Phys. Rev.* **B47**, 8588 (1993)
[48] R F Wallis, A A Maradudin, V Bortolani, A G Equiluz, A A Quong, A Franchini and G Santoro, *Phys. Rev.* **B48**, 6043 (1993)

PRAMANA
— journal of
physics

© Printed in India

Vol. 42, No. 5,
May 1994
pp. 395–404

Temperature dependence of low angle structure factors of liquid alkali metals using electron-ion plasma model

A BARI, P PAL and R N JOARDER
Department of Physics, Jadavpur University, Calcutta 700 032, India

MS received 20 October 1993; revised 28 February 1994

Abstract. The analytic solution of EIP model in the MSA via the OCP criterion yields temperature dependent results in RPA quite satisfactorily at high temperatures. The same set of parameters produces low and high angle structural properties. The model can work almost near to the critical point if the ion-core radius is allowed to vary systematically in the region $\rho < 2\rho_c$, ρ_c being the critical density. The model can also accommodate the general scaling behaviour observed for the structure factors of liquid alkali metals.

Keywords. Temperature; structure; liquid metals.

PACS No. **61·25**

1. Introduction

In recent years there has been considerable development in the structure and thermodynamics of liquid metals through the electron-ion plasma (EIP) model where one takes the EIP to have the same density, temperature and ionic mass as those of the real system [1–5]. There is however, some unsolved problem of consistent description of structure and thermodynamics, long wave and high angle structure factors with single set of parameters for various classical one component plasma (OCP) model available in the literature [6–8]. The clear reason being that all the liquid state theories are approximate in nature and they suffer from thermodynamic inconsistencies. There have been attempts earlier [9] to evolve criterion that could at least partially restore desired consistency.

The aim of the present communication is to present some temperature dependent results based on the analytic solution of EIP in the mean spherical approximation (MSA) [10]. The model enjoys the advantage that it has accommodated within it the analytic and soft sphere nature not found together in hard sphere (HS) and pure OCP models. The two characterizing parameters, packing density, η and plasma parameter, Γ are related via some suitable criterion [11]. The electronic screening necessary to describe low angle structure and thermodynamics, can be included through random phase approximation (RPA), optimized random phase approximation (ORPA) [5, 12] or the mean density approximation (MDA) [13]. The ORPA calculation [12] has shown that the long wave behaviour is not significantly different from RPA results provided considerable reductions in the effective charge (i.e. Γ values) and ion-core radius are allowed. This is also consistent with Gibbs–Bogoliubov (GB) variational calculation [14]. The WCA-ORPA calculation [15] for liquid Rb shows that for moderately high temperature the method works well but for temperatures beyond 1400 K, the calculated structure factors in general and long wave length values in particular fail to agree with experiment. The failure was attributed to the fact that the density dependence of the interatomic potential was underestimated. The electron mean free path becomes comparable with interatomic separation and the linear screening theory fails. It is now quite well established that in the long wavelength region RPA is a good approximation for quite high temperatures. Henderson and Ashcroft showed that the difference between the long wavelength RPA and experimental structure factors is related to the density derivative of the reference structure factor, the so-called MDA approximation. Young showed that the inconsistencies in Γ values for GB and isothermal compressibility calculations could be reconciled by introducing the idea of MDA term. Ono and Yokoyama [4] however, found that the MDA term is, at least near the melting point not as important as Young's analysis suggested. The recent OCP calculation of Iwamatsu [16] using MDA is relevant. The author uses the GB variational prescription to define the reduced plasma parameter Γ. But since these values were considerably smaller the author used $\Gamma = 155$ [2, 3] and MDA was shown to be consistent with the long wavelength structure factors of Rb at very high temperature and so shown to work better than RPA. But at melting and moderately high temperature MDA and RPA results are comparable. The MDA result at very high temperature too shoots up like RPA though this occurs at a higher temperature.

In view of the calculations mentioned above we find it important to review the RPA calculation for alkali metals at high temperatures. We have also done the MDA calculation to check the relative merits. The present calculation confirms Ono and Yokoyama's and Iwamatsu's observations. In fact, for alkali metals at least, MDA results progressively deviate from experiment as we go to thermodynamic states away from melting pont. RPA presents somewhat better description even at very high temperature provided one considers a systematic change in the ion core radius in the region $\rho < 2\rho_c$, where ρ_c is the critical density. Similar variation of r_c was first proposed by McLaughlin and Young [17]. It is also to be noted that the same set of parameters give in RPA, both the long wave and high angle structure factors quite well.

2. Calculation procedure

From the RPA expression of free energy the expression for liquid structure factor, $S(q)$ is given by

$$S(q) = \frac{S_0(q)}{1 + \beta\rho V(q) S_0(q)} \tag{1}$$

where, $S_0(q)$ is the reference structure factor, $V(q)$ is the indirect electron mediated ion–ion interaction expressible in terms of suitable pseudopotential and dielectric screening function [4] (in the present case Ashcroft model and Geldart–Vosko (GV) respectively), ρ is the number density and β, the inverse temperature, $(k_B T)^{-1}$. From (1) the long wave expression for structure factor is given by

$$S^{-1}(0) = k_d^2 [k_i^{-2} + k_e^{-2} + r_c^2] \tag{2}$$

where, in au

$$k_d = \frac{\sqrt{3}}{a} \Gamma^{1/2} \tag{3a}$$

$$k_i = k_d/(1-\alpha)^{1/2} \tag{3b}$$

$$k_e = \left[\frac{\pi}{4k_f} - \frac{1}{4\pi k_f^3}\quad(\pi k_f + 0{\cdot}153)\right]^{-1/2} \tag{3c}$$

are respectively the Debye–Hückel, CHS plasma (in the present case) and the electron gas inverse screening lengths, k_f, the Fermi wave vector, a, the interparticle distance and α is a term related to η and Γ of the CHS system and expression for which is available elsewhere [18].

Again note that

$$\underset{q\to 0}{\mathrm{Lt}}\; S_0(q) = \frac{q^2}{k_d^2}\left(1 - \frac{q^2}{k_i^2}\right) \tag{4a}$$

and

$$\underset{q\to 0}{\mathrm{Lt}}\; \varepsilon(q) = 1 + \frac{k_e^2}{q^2}. \tag{4b}$$

So we have the very low q convenient expression for $S(q)$ given by

$$S(q) \cong S(0)\Big/\left[1 + q^2 S(0) k_d^2 \left\{\frac{1}{k_i^2(k_i^2 - q^2)} - \left(\frac{1}{k_e^4} + \frac{r_c^4}{3} + \frac{r_c^2}{k_e^2}\right)\right\}\right.$$
$$\left. + q^4 S(0) k_d^2 r_c^2 \left\{\frac{1}{k_e^4} + \frac{r_c^2}{3k_e^2} + \frac{r_c^4}{24}\right\}\right]. \tag{5}$$

The MDA expression [13] corresponding to eq. (2) is

$$S^{-1}(0) = S_0^{-1}(0) + \beta\rho V(0) + 2\beta\rho\left(\frac{\partial I}{\partial\rho} + 1/2\,\rho\,\frac{\partial^2 I}{\partial\rho^2}\right) \tag{6}$$

with

$$I = \frac{1}{4\pi^2}\int_0^\infty \mathrm{d}q\, q^2 V(q)(S_0(q) - 1). \tag{7}$$

The MDA approximation is thought to be essentially exact for $0 \leqslant q \leqslant 0{\cdot}4k_f$ [13].

For high q calculations via RPA one requires to truncate the screened potential $V(q)$ beyond the first node which occurs near $q \simeq 2k_f$ and the justification is available elsewhere [18, 19] and essentially the ORPA results of [12] could be reproduced for all alkalis at different temperatures.

The CHS plasma is extremely good representation of OCP for $\Gamma \geqslant 10$ if η and Γ satisfy the following criterion [20].

$$C_0(r=0) \simeq -1{\cdot}33\Gamma \tag{8}$$

$C_0(r=0)$ being the CHS direct correlation function at $r=0$. Γ as a function of η is shown in figure 1(b). It is quite well-known that the GB method approximates the true structure factor of the system by reference one with optimum $\Gamma \simeq 155$ [2, 3]. This value of Γ is considerably reduced compared to one from the observed density and temperature using valency, $z=1$ (the bare ionic charge number) for most of the alkalis at melting point ($\Gamma \sim 163 - 210$). Such a reduced Γ represents considerable reduced valency ($z<1$) and this is also qualitatively in accord with entropy analysis

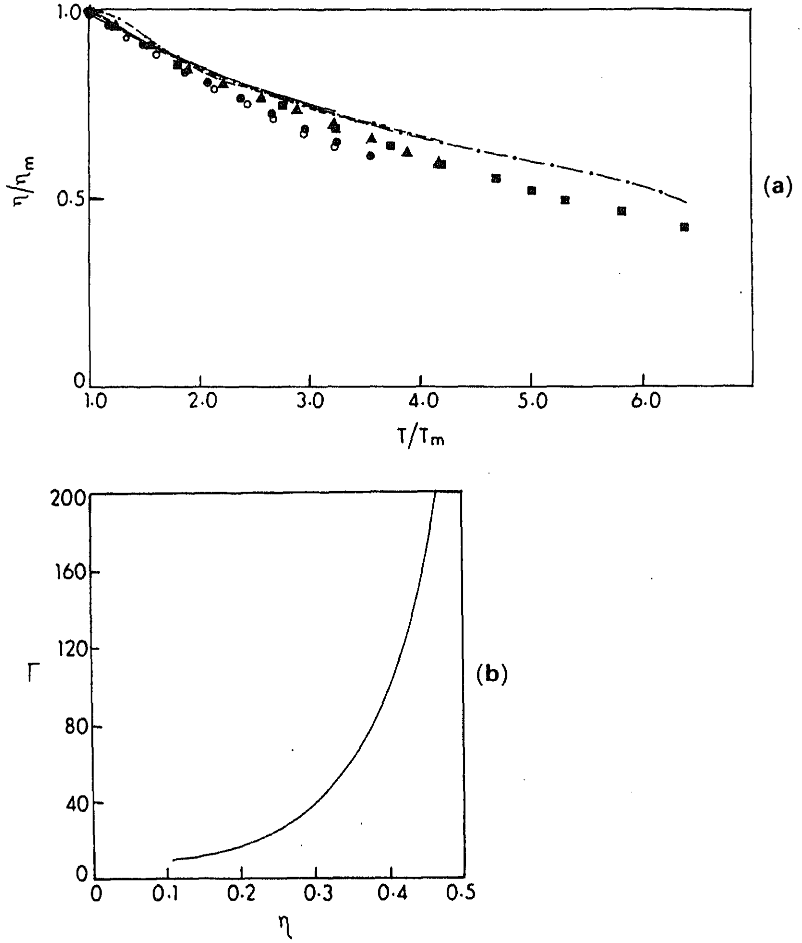

Figure 1(a). η/η_m as a function of T/T_m ——— (Na); – – – (k); –·–·–(Rb); – –·– –·– – (Cs) From eq. (8). ○○○ (Na); ●●● (k); ■■■ (Rb); ▲▲▲ (Cs) with Hs model [23], **(b)** Γ as a function of η (eq. (8)).

[6]. The isothermal compressibility by the method of long wave, on the other hand, is well described by using $z = 1$ [21]. The OCP is known to freeze at $\Gamma \sim 178$ [22]. We have chosen Γ via (8) by taking η's from the CHS calculation of [18]. These η's are well in accord with the value 0·455 obtained from (8) using $\Gamma = 178$. The Γ's at higher temperature are obtained using the relation

$$\frac{\Gamma}{\Gamma_m} = \frac{T_m}{T}\left(\frac{\rho}{\rho_m}\right)^{1/3} \tag{9}$$

where m refers to melting point and corresponding η's are obtained from (8). η's obtained this way agree well with that for HS model [23] (figure 1(a)) and this is expected. r_c's given in [18] reproduce the isothermal compressibility at melting point quite well and so used in our calculations for $S(0)$ values at melting point (table 1). These r_c's are used for calculations at thermodynamic states away from the m.p. The

Table 1. $S(0)$ values at or near melting points.

Liquid metal	T(K)	ρ (a.u.$^{-3}$)	η	Γ	r_c (a.u.)	$S(0)$ present RPA	$S(0)$ present MDA	$S(0)$ Expt.[23]
Na	371·0	0·0035834	0·449	167·0	1·821	0·0240	0·0228	0·0240
K	337·0	0·0018846	0·457	182·0	2·358	0·0228	0·0211	0·0224
Rb	313·0	0·0015368	0·452	172·5	2·526	0·0257	0·0241	0·0220
Cs	301·6	0·0012340	0·457	182·0	2·790	0·0227	0·0203	0·0237

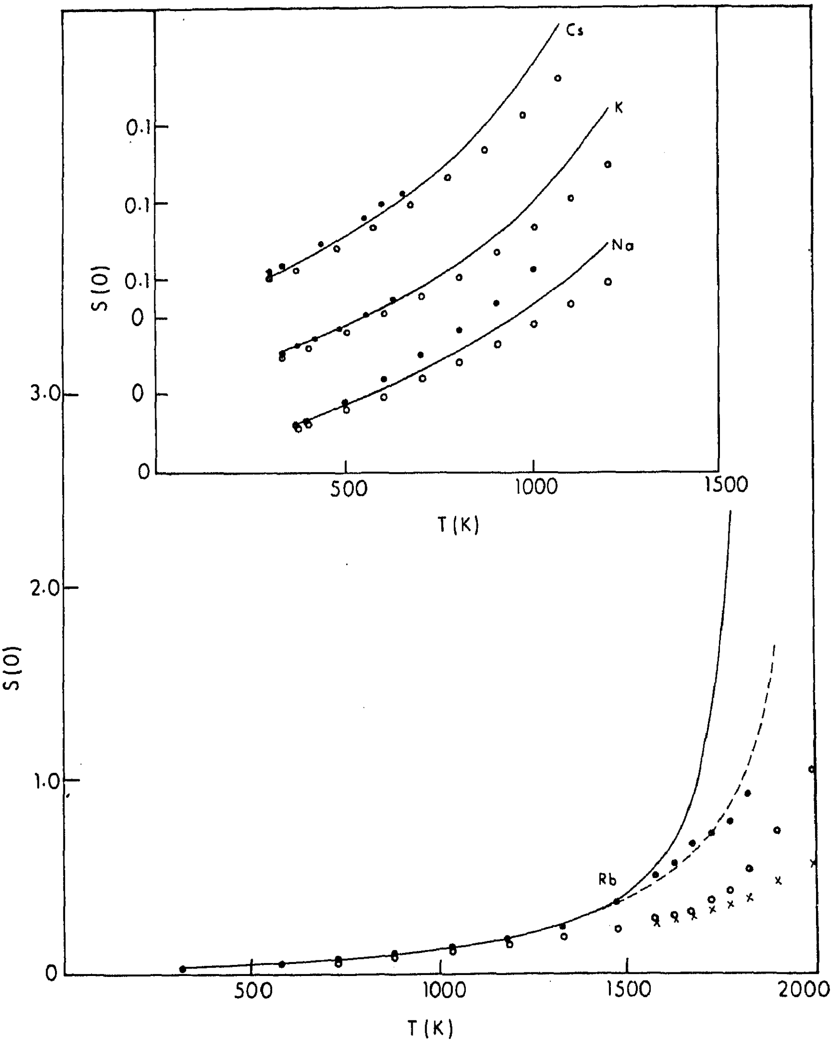

Figure 2. $S(0)$ as a function of temperature ——— RPA calc. (fixed r_c); – – – RPA calc. (variable r_c); ○ ○ ○ MDA calc. (fixed r_c); × × × MDA calc. (variable r_c); ● ● ● experimental [29].

$S(0)$ values are expected to shoot up as the critical point is approached. In RPA however, the result shoots up quite earlier and this behaviour is attributed to possible breakdown of nearly free electron approximation in the region $\rho < 2\rho_c$ since the electron–electron correlation effects would become more important and the electron-ion interaction becomes less amenable to a pseudopotential description [21]. However, a variable r_c, as McLaughlin and Young [17] have observed, could reconcile this discrepancy of the theory and description almost near to the critical point is possible. In the spirit of McLaughlin and Young we have therefore used a variable r_c in the region $\rho < 2\rho_c$, to describe the structural behaviour of liquid Rb for $T > 1500\,\mathrm{K}$ using the relation, $r_c = 1{\cdot}35 + 0{\cdot}19 r_s$ in au with $r_s = az^{-1/3}$, a being the interparticle separation. The argument concerning the volume dependent r_c at low density ($\rho < 2\rho_c$) may be the following. The breakdown of nearly free electron approximation results as the electron mean free path becomes of the order of interatomic distance. It is well-known that the Friedel oscillation arises from the Fourier transform of the logarithmic term in the dielectric function and it is directly related to the assumption that the Fermi surface is sharply defined. At high temperature, the increased blurring of Fermi surface decreases the oscillation and makes the potential more like that of non-metallic liquids. As the volume increases the term due to overlap repulsion should be added, the coulomb repulsion being now relatively small [24]. For metallic potential, the variation of r_c changes the

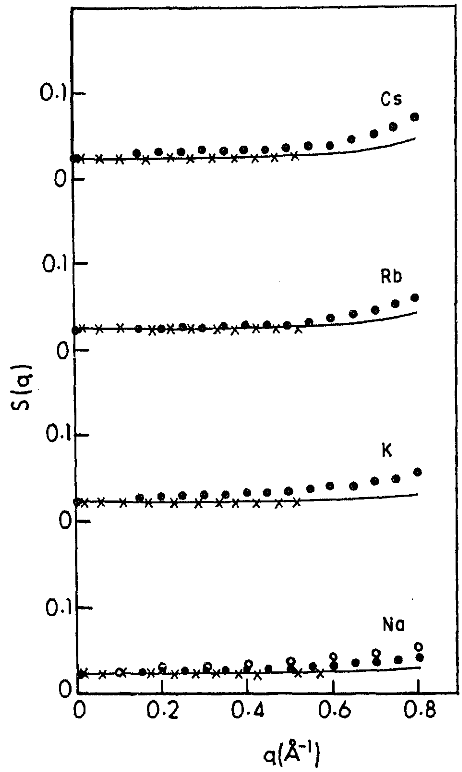

Figure 3. Low angle $S(q)$ as a function of q ——— calc. with eq. (1); × × × calc. with eq. (5); ○○○ MDA calc. by McLaughlin *et al* [13]; ●●● experimental [23].

electron mediated term, the position and depth of the attractive well and also the Friedel oscillation changes significantly. The results of our calculations are shown in fiugures 2–4.

3. Results and discussion

The calculations shown clearly indicate that RPA describes the temperature variation of $S(0)$ over a wide range quite well. For Rb, above 1500 K where $\rho < 2\rho_c$, a variable r_c is used. For thermodynamic states approaching the critical region, RPA result with constant r_c shoots up at a quite lower temperature (figure 2). It is important to note that the addition of MDA term considerably lowers the values at high temperature

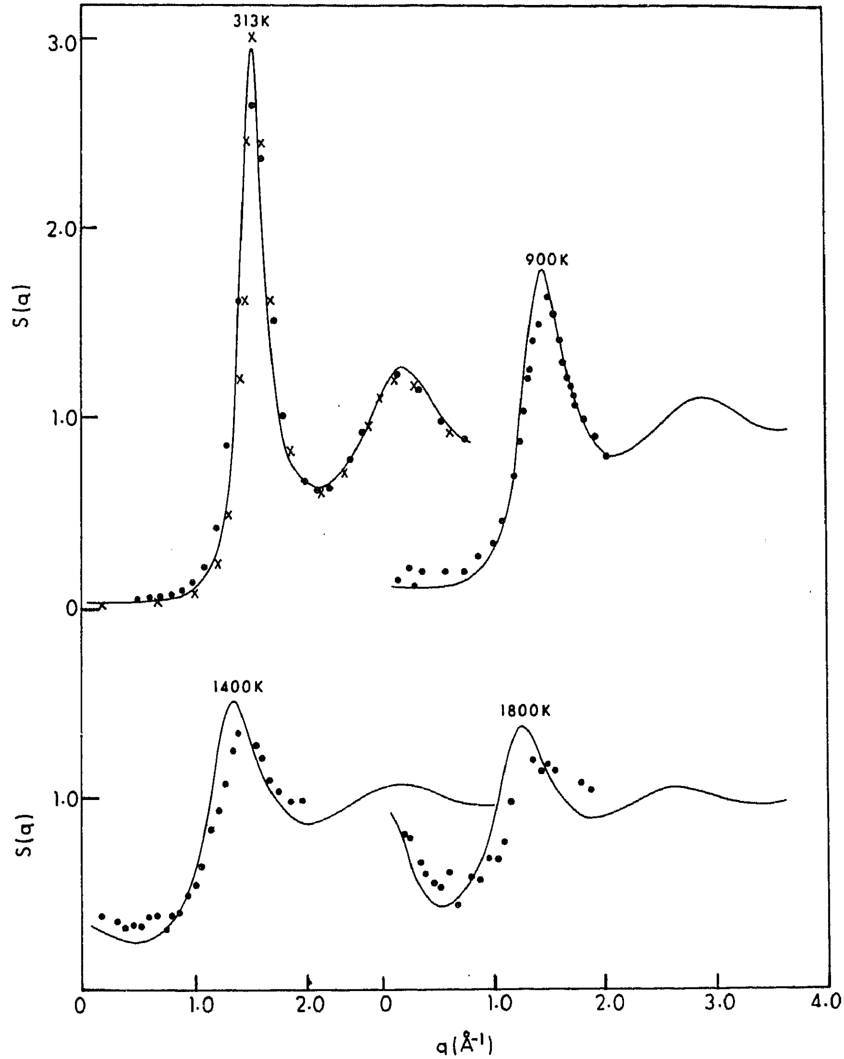

Figure 4. $S(q)$ as a function of q for Rb at different temperatures. ——— Calc.; × × × MD data [30]; ● ● ● experimental [29].

and in fact the result progressively deviates from the experimental result. This is compatible with observations in [4] and [16]. Of course, originally MDA was developed for hard cores [13] and it provided satisfactory description of the region near the critical point with variable r_c [17]. RPA with variable r_c also works reasonably near the critical region probably because the increase in r_c reduces the long range oscillations of the effective interionic potential and makes it more like that of a nonmetallic system, almost L–J type. The CHS plasma model based on the OCP criterion (eq. (8)) also describes well the low and high angle structure factors with same set of parameters (figures 3 and 4). It is to be noted that MDA with hard core is more successful for polyvalent metals than alkali metals so far as the high angle structure factor values are concerned [13]. The RPA low q results are satisfactory (figure 3). The very low q behaviour given by (5) reproduces the $S(q)$ values quite well. The low q expression closely resembles the one of Evans and Sluckin [21] and the results are consistent with the Ornstein–Zernike (OZ) behaviour ([25] i.e. $S(q) = S(0)/(1 + \xi^2 q^2)$, ξ being the long range correlation length. The O–Z behaviour suggests that at high temperature the low $q\,S(q)$ values will shoot up. Evans and Sluckin estimated this transition temperature to be quite low (~ 500 K) in their OCP model. The present model gives this temperature to be ~ 1000 K, much better in agreement with observation. The very low q expression is similar to one observed in liquid argon [26] and does not contain a linear term as has been suggested [27] empirically by the low q experimental data near the melting point. The very low q expression however yields results in good agreement with values from full expression (1) and experimental data. Remembering that there is large uncertainty in the experimental data in this low q region we believe that the expression (5) would describe the system quite well particularly at high temperature where the nearly free electron model progressively fails. It is now quite well-known [28] that for densities $\rho \sim 2\rho_c$ and conditions near the saturation curve, characteristic changes have been observed for both the electrical and magnetic properties which mark the onset of a transition from metallic to nonmetallic states and the effective interaction potential changes to one very similar to that for Kr described by L–J potential. In order to explore this point we have computed full structure factor curves of liquid Rb at different temperatures for this model through (1). The screened potential $V(q)$ has been truncated beyond its first node. The results at high temperature are reasonable and OZ behaviour is well produced. The high temperature results are compared with the experimental data of Hensel *et al* [29]. The model first peak height decreases less and position shifts to the left more relative to the experimental data as the high temperature is approached. This deviation is attributed to the approximate nature of the OCP criterion (8) which somewhat under reduces the η parameter at high temperature (figure 1(a)). In spite of these discrepancies we feel that the overall behaviour described by the present model at states near the critical point is quite satisfactory. The critical temperature T_c, estimated is ~ 2010 K and this is in excellent agreement with experiment.

Further, it has been recently found that the structure factors of liquid alkali metals scale if they are plotted against q/q_m where q_m refers to the position of the first peak of structure factor for each system [31]. We have therefore plotted our $S(q)$ against q/q_m to see whether this scaling behaviour follows. The results shown in figure 5 clearly exhibit that the present model can satisfactorily accommodate the scaling behaviour. The scaling property associated with $S(0)$ is also shown to be reasonably justified in this model.

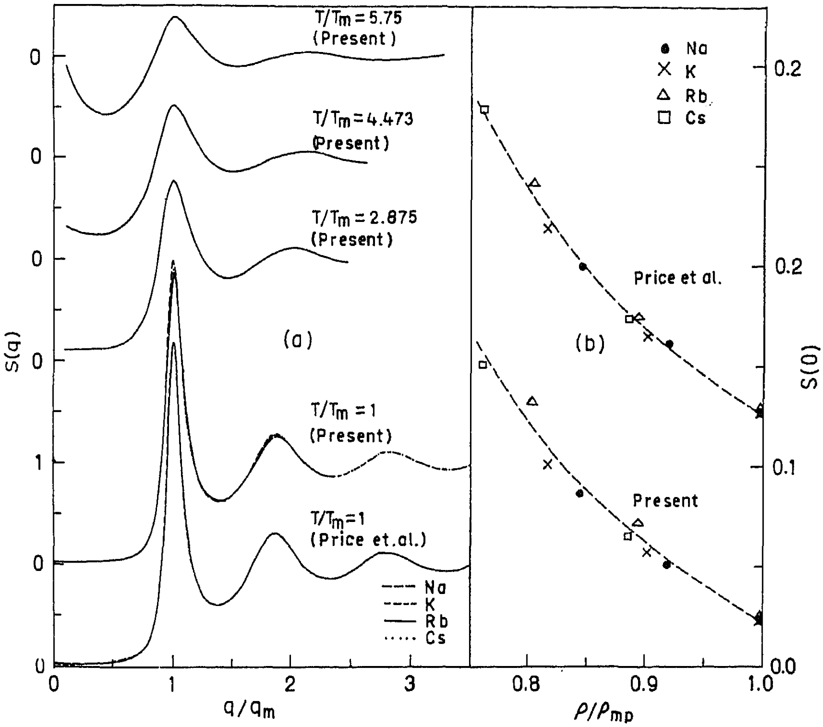

Figure 5. (**a**) $S(q)$ vs q/q_m for Na, K, Rb and Cs. (**b**) $S(0)$ vs $\rho/\rho_{\mathrm{m.p.}}$ for Na, K, Rb and Cs.

It is to be noted that we have used GV screening throughout and this screening is known to describe the liquid alkali metals at melting point, quite well. The long wave results depend on screening function to some extent but the use of other screening functions will not change the general behaviour reported here significantly. In fact a slightly different interactomic potential due to Price *et al* [32] (Ashcroft pseudopotential with self consistent screening) is known to yield the Monte Carlo (MC) and molecular dynamics (MD) structure factors [31] in good agreement with experiments. Like Price *et al* potential, the present potential too scales with proper units. To compare the present model results with those due to Price *et al* potential, we have calculated in RPA with length and energy parameters of Price *et al* potential [31] and tested the scaling behaviour. It is clear that the scaling behaviour with Price *et al* potential is only slightly better (figure 5).

Thus in this communication, we have reviewed the RPA calculation for EIP model of liquid alkali metals and shown that with parameters provided by OCP criterion various structural aspects including long wave behaviour are very reasonably described over a wide range of temperature.

Acknowledgement

RNJ gratefully acknowledges the financial support by DST, New Delhi.

References

[1] M Baus and J P Hansen, *Phys. Rep.* **59**, 1 (1980)
[2] D K Chaturbedi, G Senatore and M P Tosi, *Lett, Nuovo Cimento* **30**, 47 (1981)
[3] K K Mon, R Gawn and D Stroud, *Phys. Rev.* **A24**, 2145 (1981)
[4] S Ono and I Yokoyama, *J. Phys.* **F14**, 2909 (1984)
[5] G Pastore and M P Tosi, *Physica* **B124**, 383 (1984)
[6] W H Young, *J. Phys.* **F12**, L19 (1982)
[7] M Iwamatsu, R A Moore and S Wang, *Phys. Lett.* **A101**, 97 (1984)
[8] J L Bretonnet and K N Khanna, *Phys. Lett.* **A110**, 420 (1985)
[9] J S Hoye and G Stell, *J. Chem. Phys.* **67**, 439 (1977)
D MacGowan, *J. Phys.* **C16**, 59 (1983)
D MacGowan, *J. Stat. Phys.* **32**, 123 (1983)
[10] R G Palmer and J D Weeks, *J. Chem. Phys.* **58**, 4171 (1973)
[11] M J Gillan, *J. Phys.* **C1**, L1 (1974)
[12] T Das and R N Joarder, *Phys. Lett.* **A131**, 111 (1988)
[13] R L Henderson and N W Ashcroft, *Phys. Rev.* **A13**, 859 (1976)
I L McLaughlin and W H Young, *J. Phys.* **F12**, 245 (1982)
[14] R N Joarder and T Das, *Phys. Scr.* **37**, 762 (1988)
[15] G Kahl and and J Hafner, *Phys. Rev.* **A29**, 3310 (1984)
[16] M Iwamatsu, *J. Phys. Cond. Matt.* **2**, 3053 (1990)
[17] I L McLaughlin and W H Young, *J. Phys.* **C15**, 1121 (1982)
[18] H B Singh and A Holz, *Phys. Rev.* **A28**, 1108 (1983)
[19] G Senatore and M P Tosi, *Phys. Chem. Liq.* **11**, 365 (1982)
[20] H B Singh, *J. Stat. Phys.* **33**, 371 (1983)
H B Singh and A Holz, *Phys. Rev.* **A29**, 1554 (1984)
[21] R Evans and T J Sluckin, *J. Phys.* **C14**, 3137 (1981)
[22] W L Slattery, G D Doolen and H E Dewitt, *Phys. Rev.* **A26**, 2255 (1982)
[23] Y Waseda, *The Structure of non-Crystalline materials* (McGraw Hill, New York, 1980)
[24] P A Egelstaff, *The Introduction to liquid state* (Academic, London, 1967)
[25] L S Ornstein and F Zernike, *Proc. K. Ned Acad. Wet. Ser.* **17**, 793 (1914)
[26] P G Mikolaj and C J Pings, *J. Chem. Phys.* **46**, 1401, 1412 (1967)
[27] C C Mathai and N H March, *Phys. Chem. Liq.* **11**, 207 (1982)
[28] G Franz, W Freyland and F Hensel, *J. Phys. Coll.* **41**, C8-70 (1980)
[29] C J Foust, *Na-Nak Engineering handbook* (Gordon and Breach, New York, 1972), Vol. 1
J Jarzynski and T A Litovitz, *J. Chem. Phys.* **41**, 1290 (1964)
J P Chan, *Phys. Chem. Liq.* **3**, 55 (1972)
M S Zei, *Phys. Rev.* **B24**, 4509 (1981)
G Franz, W Freyland, W Glazer, F Hensel and E Schneider, *J. Phys. Coll.* **41**, C8-194 (1980)
[30] A Rahman, *Phys. Rev.* **A9**, 1667 (1974)
[31] M J Huijben and W van der Lugt, *Acta Crystallogr.* **A35**, 431 (1979)
N Matsuda, H Mori, K Hoshino and M Watabe, *J. Phys. Cond. Matt.* **3**, 827 (1991)
U Balucani, A Torcini and R Vallauri, *Phys. Rev.* **A46**, 2159 (1992)
[32] D L Price, K S Singwi and M P Tosi, *Phys. Rev.* **B2**, 2983 (1970)

PRAMANA
— journal of
physics

© Printed in India

Vol. 42, No. 5,
May 1994
pp. 405–420

Electronic structure of non-magnetic impurities in dilute alloys of Al

P SINGH and S PRAKASH
Department of Physics, Panjab University, Chandigarh 160014, India

MS received 4 December 1993

Abstract. The electronic structure of substitutional non-magnetic impurities Cu, Ag, Cd, Mg, Zn, Ga, In, Ge, Si and Sn in Al is studied using density functional theory. A simple physical model is proposed to calculate the effective charges on impurities in trivalent metal Al. A linear relation is found between the effective charges on impurities and impurity vacancy capture radii. The spherical solid model (SSM) is used to account for discrete nature of the host. The impurity-induced change in charge density, scattering phase shifts, host-impurity potential, residual resistivity and impurity self-energy are calculated. Higher order scattering phase shifts are found significant and the host-impurity potential is found proportional to effective charge on impurity in its vicinity. The self-consistently calculated potential is used to calculate the electric field gradients (EFGs) at the first and second nearest neighbours (1NNs, 2NNs) of impurity. The calculated values are in agreement with the experimental results.

Keywords. EFG; defects; resistivity.

PACS Nos 71·50; 71·55

1. Introduction

The electronic structure of dilute alloys has been studied using jellium model of the metal and density functional theory [1,2]. Manninen and Nieminen [3] replaced jellium model by SSM to include the discrete nature of lattice and investigated the magnetic structure of 3*d* impurities in Al [4]. Mahajan and Prakash [2] have included the size effect and Friedel criterion for bound states to determine the effective charges on impurities [2,5] and the size effect was found significant in the calculation of impurity-induced charge density and host-impurity potential.

Prakash [6] used the model wavefunction transformation to study the impurity-induced charge density $\delta n_i(\mathbf{r})$ in a *d*-band metal. $\delta n_i(\mathbf{r})$ is separated into two parts: one due to non-nodal character of the wavefunction and other due to depletion hole around the host ions. Raj *et al* [7] used this $\delta n_i(\mathbf{r})$ to calculate the EFGs. Ponnambalam and Jena [8] used the asymptotic form of $\delta n_i(\mathbf{r})$ to calculate EFGs in Al alloys. However the size effect was ignored.

In all the above calculations either the SSM or the size effect was ignored. Recently we studied the electronic structure of non-magnetic impurities in dilute alloys of Cu [9] and hydrogen and muon in Al, Mg and Cu [10] including both the discrete nature of lattice and size effect. The host-impurity potentials are found proportional to the impurity charge in the vicinity of the impurity and Friedel oscillations are found at large distances. The virtual bound states of proton and muon are favoured in Al, Mg and Cu. The experimental results of residual resistivity and Knight shift are explained. Therefore we found it interesting to extend the calculations for dilute alloys of Al for which lots of experimental data exist.

In the following we present the physical model for determining the impurity valencies, explanation of vacancy-impurity, capture radii of impurities, host-impurity potentials, induced charge densities, charge transfers, residual resistivities and EFGs in dilute alloys of Al.

2. Physical model

In a monovalent metal if the zero of the energy is taken as the energy of an electron at rest outside the metal, the bottom of the conduction band has the energy $-E_0$, which is given as

$$E_0 = E_s + E_1 + \tfrac{3}{5}E_F + E_{xc}. \tag{1}$$

Here sublimation energy E_s is the sum of molecular dissociation energy and work function, E_1 is the first ionization energy, $(3/5E_F)$ is the average kinetic energy and E_{xc} is the exchange-correlation energy of conduction electrons per electron. The energy required to dissociate the ith electron of the impurity atom in the lattice is

$$E_I \simeq E_i + E_{xc}, \tag{2}$$

where E_i is ith ionization potential of impurity atom and E_{xc} is the same as in (1). If $E_i \gg E(E = E_0 - E_{xc})$, the bound state will exist and the ith electron will not be dissociated in the lattice. If $E_i < E$, the ith electron of impurity atom will be added in the conduction band and the band structure of the host metal will be changed. This criterion has been found applicable to the monovalent metal Cu [9, 11].

In general it is assumed that Al is a trivalent metal. The E_0 given in (1) consists of only first ionization energy E_1, therefore E_0 does not represent the bottom of the conduction band in Al metal. Johnson and Martensson [12] calculated the core level binding energy shifts in the metal relative to the atom. The energy of different ionic configurations is about half of the corresponding ionization energy. Therefore replacement of E_1 by third ionization potential E_3 in (1) does not seem justified.

The detailed calculations of [12] suggest that the zero of energy should be renormalized to determine the realistic valencies of impurities in Al. This is essential as at least first ionization is needed to get the impurity dissolved. Therefore we choose E_0 as given in (1) as the reference energy. We further assume that ionization potentials, other than E_1, of the impurity atoms and Al atom are reduced in the same ratio in the solid solution. Thus we compare the ionization potentials E_2, E_3, E_4 of the impurity atoms with the corresponding potentials of Al atom [12]. If E_i of the impurity atom is less than E_i of Al atom, the ith electron of impurity atom is dissociated, otherwise the ith electron is the bound electron. According to this criterion Al atom in Al host is a trivalent interstitial which is required. These realistic valencies Z_I of impurities in Al host are given in table 1. The size effect is included in the same way as discussed earlier [9, 10]. The impurity valency Z_I is modified as

$$Z' = Z_I - \left(\frac{\Delta V}{V}\right) Z_H, \tag{3}$$

and the net charge on the impurity becomes

$$\Delta Z = Z' - Z_H. \tag{4}$$

Here $(\Delta V/V)$ is local dilation around impurity and Z_H is the host ionicity. The second term in (3) is due to lattice dilation. Equation (4) suggests that the net charge on self-interstitial atom is only due to lattice dilation.

We notice that Ag and Cu are monovalent and Mg and Zn are divalent impurities in Al. Since E_2 for Zn is just close to E_2 for Al, Zn may also be monovalent. However the polyvalent impurities In, Si, Ge, Sn and Cd are divalent except Ga which is monovalent. For the same reason as discussed for Zn, In and Si may also be monovalent. There are uncertainties about the ionization potentials of transition metal (TM) atoms. We have taken averaged values of ionization potentials [13]. Ti is trivalent while V and Cr are divalent. These impurities also consist of partially localized *d*-electrons. This effect is included implicitly in the determination of the bound state. We have taken the averaged value of available data for dilation and estimated $(\Delta V/V)$ [14]. The size effect $(\Delta V/V)Z_H$ is significant except for Zn and In. The calculated values of ΔZ show that all the simple metal (SM) impurities are negatively charged while TM impurities are positively charged.

3. Capture radii of impurities

The impurity vacancy capture radii r_t/r_v for various impurities are tabulated in the last column of table 1. The caputre radii of Ag and Mg impurities are adopted from the measurements of Rizk *et al* [15]. The starred value of capture radius for Mg impurity and capture radii for Ga and Si impurities are taken from Dworschak *et al*

Table 1. The physical parameters for Al alloys. Z_I are realistic valencies of impurities, Z_H is host ion valency, $(\Delta V/V)$ is lattice dilation, ΔZ are the effective charges on impurities and (r_t/r_v) are the relative capture radii of impurities.

Impurity	Z_I	$(\Delta V/V)Z_H$	ΔZ	(r_t/r_v)
Ag	1	0·14	−2·14	0·60 ± 0·05[a]
Cu	1	−0·56	−1·44	
Mg	2	0·60	−1·60	0·33 ± 0·05[a] 0·43 ± 0·05*[b] (0·2)
Zn	2	−0·08	−1·92	(0·57 ± 0·05)[d] (0·75 ± 0·05)
Ga	1	0·27	−2·27	0·65 ± 0·05[b]
In	2	0·0	−1·0	
Si	2	−0·26	−0·74	0·50[b]
Ge	2	0·27	−1·27	(0·43 ± 0·05)[d]
Sn	2	0·86	−1·86	
Cd	2	−0·55	−0·45	
Ti	3	−0·82	0·82	0·40 ± 0·10[c]
V	2	−0·83	0·17	0·15 ± 0·05[c]
Cr	2	−1·59	0·59	0·35 ± 0·05[c]

[a] Rizk *et al* [15]; [b] Dworschak *et al* [16]; [c] Maury *et al* [17]; [d] Normalized values of [16]

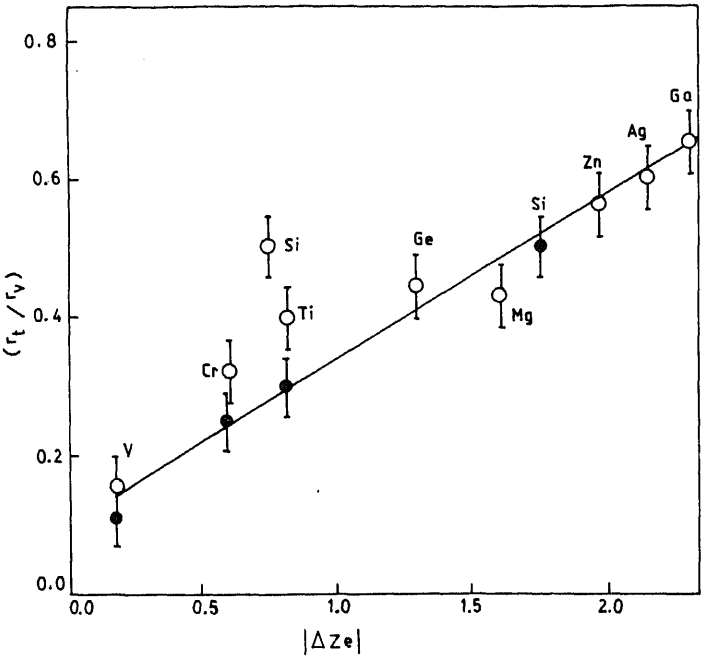

Figure 1. (r_t/r_v) vs $|\Delta Ze|$ for dilute alloys of Al.

[16]. Maury *et al* [17] pointed out that the results of Dworschak *et al* [16] for TM impurities need a further analysis. Maury [18] found that the capture radii for Cr, V and Ti impurities are $0{\cdot}35 \pm 0{\cdot}05$, $0{\cdot}15 \pm 0{\cdot}05$ and $0{\cdot}40 \pm 0{\cdot}10$ respectively. These values are adopted in table 1. Dworschak *et al* [16] evaluated the capture radii for Ag, Ge, Mg and Zn impurities as 2·2, 1·6, 0·74 and (2·8, 2·1) respectively at 540 K. These values are consistently higher for reasons discussed by Prakash and Lucasson [11], than those obtained by Rizk *et al* [15]. Therefore we normalized these values with respect to capture radius of Ag impurity obtained by Rizk *et al* [14]. These normalized capture radii are tabulated in table 1 in brackets.

The results for capture radii for different impurities versus the magnitude of effective charges $|\Delta Ze|$ on impurities are plotted in figure 1. The corresponding error bars are also shown there. An acceptable correlation is found between the capture radii and $|\Delta Ze|$ for all SM impurities except Si. However if Si is taken as monovalent, the correlation is almost perfect. This justifies the renormalization of capture radii of Zn and Ge impurities. The capture radii of TM impurities also show a linear correlation with $|\Delta Ze|$ although the slope is different from that for SM impurities. If the capture radii of TM impurities are reduced uniformly say by 25%, a reasonable linear correlation is established. This suggests that the capture radii of impurities are proportional to the magnitude of total perturbation caused by both the valence and size effects and not only the valence or size effect as discussed earlier [16].

4. Spherical solid model and non-linear screening

The Kohn-Sham density-functional formalism is used to calculate the screening of impurity atom by the conduction electrons. A set of wave functions ψ_i with energy eigenvalues ε_i is generated by solving the Schrödinger equation

$$[-\tfrac{1}{2}\nabla^2 + V(\mathbf{r})]\psi_i(\mathbf{r}) = \varepsilon_i \psi_i(\mathbf{r}), \tag{5}$$

where

$$V(\mathbf{r}) = \phi(\mathbf{r}) + V_{ss}(\mathbf{r}) + \mu_{xc}(n, r). \tag{6}$$

$\phi(\mathbf{r})$ is the electrostatic potential due to induced charge density defined as

$$\phi(\mathbf{r}) = \int \frac{\mathrm{d}\mathbf{r}'[n(\mathbf{r}') - n_+(\mathbf{r}')]}{|\mathbf{r} - \mathbf{r}'|}, \tag{7}$$

where

$$n(\mathbf{r}) = \Sigma |\psi_i(\mathbf{r})|^2, \tag{8}$$

and for the substitutional impurity

$$n_+(\mathbf{r}) = n_0 \theta(\mathbf{r} - \mathbf{R}_{ws}) + Z'\delta(\mathbf{r}). \tag{9}$$

Here $n_0 (= 3/(4\pi r_s^3))$ is the uniform electronic charge density, r_s is interelectronic distance, R_{ws} is Wigner-Seitz cell radius and $\theta(r)$ is the unit step function.

The spherical solid potential $V_{ss}(r)$ is given as

$$V_{ss}(\mathbf{r}) = -\frac{1}{4}\int \mathrm{d}\Omega \sum_n{}' w(\mathbf{r} - \mathbf{R}_n^0) + \int \frac{\mathrm{d}\mathbf{r}' n_0 \theta(\mathbf{r} - \mathbf{R}_{ws})}{|\mathbf{r} - \mathbf{r}'|}. \tag{10}$$

In (10) the first term in the spherical average of bare ion pseudopotential at $\mathbf{r}$ and the second term is the potential due to uniform positive charge background. The last term on rhs of (6) is the exchange-correlation potential. In the local density approximation it is given as

$$\mu_{xc}(n, \mathbf{r}) \simeq \frac{\mathrm{d}}{\mathrm{d}n}[n\varepsilon_{xc}(n) - \mu_{xc}(n)] - \mu_{xc}(n_0), \tag{11}$$

where ε_{xc} is the exchange-correlation energy per electron of electron gas of density $n(r)$ and $\mu_{xc}(n_0)$ is the exchange-correlation potential for density n_0. We used the following parametrized form of ε_{xc} in our calculations [18]

$$\varepsilon_{xc}(R_s) = -\frac{0{\cdot}9163}{R_s} - 0{\cdot}112 + 0{\cdot}0335 \ln R_s - \frac{0{\cdot}02}{0{\cdot}1 + R_s}, \tag{12}$$

where $R_s = (3/(4\pi n(r))^{1/3}$ and $\mu_{xc}(n_0)$ is subtracted to get convergence of $\mu_{xc}(n, r)$ at large r.

We used the Ashcroft model potential for the host ions and calculated $V_{ss}(r)$ for substitutional impurity in the same manner as discussed in [9]. The final expression is given as

$$V_{ss}(r) = V_{ss}(0) - \frac{2\pi n_0}{3}\left(r^2 + \frac{2R_{ws}^3}{r}\right)\theta(r - R_{ws}) - \left[\begin{array}{ll} \displaystyle\sum_n{}' \frac{Z_H}{R_n^0}\left(\frac{r + R_n^0 - r_c}{2r} - 1\right); & |\mathbf{R}_n^0 - \mathbf{r}_c| \leqslant r \leqslant |\mathbf{R}_n^0 + \mathbf{r}_c| \\ \displaystyle\sum_n{}' \left(\frac{Z_H}{|\mathbf{r}|} - \frac{Z_H}{|\mathbf{R}_n^0|}\right); & r > |\mathbf{R}_n^0 + \mathbf{r}_c| \end{array}\right. \tag{13}$$

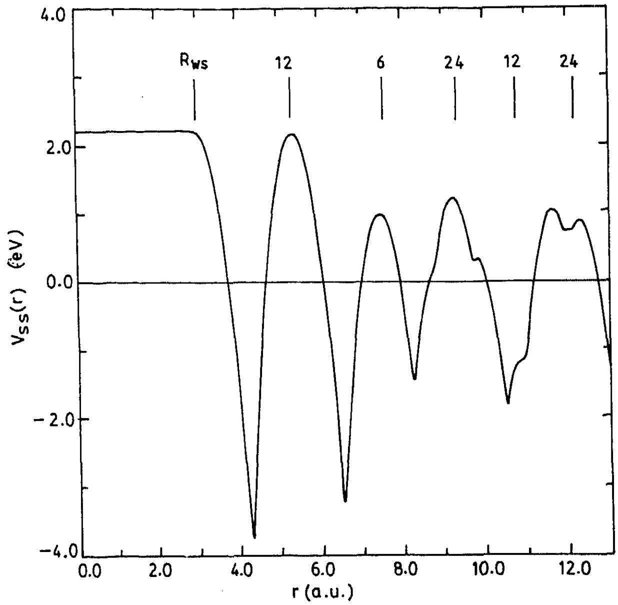

Figure 2. Spherical solid potential $V_{ss}(r)$ versus r for Al around substitutional site. The positions and number of NNs are indicated. R_{ws} is Wigner-Seitz radius.

where

$$V_{ss}(0) = \frac{Z_H \alpha_{EW}}{R_{WS}} - 2\pi n_0 R_{ws}^2 \theta(R_{ws} - r). \tag{14}$$

and r_c is potential parameter. Here $\alpha_{EW} = 1{\cdot}79172$ is used for fcc structure. For convergence purpose a constant potential $V_{ss}(r \to \infty) = 3r_c^2/2r_s^3$ is subtracted from (13). The results for Al are shown in figure (2). $V_{ss}(r)$ is found constant for $r < R_{ws}$ as given in (14). $V_{ss}(r)$ has the maxima at the lattice sites and minima between two sites and consists of both attractive as well as repulsive characteristics.

Equation (5) for spherically symmetric potential can be written as

$$\left(-\frac{1}{2}\frac{\partial^2}{\partial r^2} + V(r) + \frac{l(l+1)}{2r^2}\right) rR_{lk}(r) = \varepsilon_k rR_{lk}(r) \tag{15}$$

where $rR_{lk}(r)$ is the radial wavefunction, $\varepsilon_k = k^2/2$, $\mathbf{k}$ is the electron wavevector and l is the angular momentum (atomic units are used). At large distances

$$rR_{lk}(r) \simeq j_l(kr)\cos\delta_l - n_l(kr)\sin\delta_l \tag{16}$$

where j_l and n_l are the spherical Bessel and Neumann functions of order l respectively and δ_l are the scattering phase shifts. For a bound state the energy $\varepsilon_b < 0$ and the asymptotic form of radial wavefunction is

$$rR_b(r) \sim e^{-k_0 r} \tag{17}$$

where

$$k_0 = (-2\varepsilon_b)^{1/2}.$$

we calculate the change in charge density for convergence purpose as

$$\delta n(r) = n(r) - n_0 = \frac{1}{\pi^2}\int_0^{k_F} \mathrm{d}k\,k^2 \sum_{l=0}^{\infty}(2l+1)[R_{lk}^2(r) - j_l^2(kr)] + 2|R_b|^2. \quad (18)$$

The sum over l in (18) converges as the effective potential is localized. Equations (15–18) are solved self-consistently following the procedure suggested by Manninen *et al* [20]. The electrostatic potential $\phi(r)$ obtained by solving the Poisson equation is given as

$$\phi^i(r) = -\frac{1}{4\pi}\int \frac{\mathrm{d}\mathbf{r}'\,e^{-k_{TF}|\mathbf{r}-\mathbf{r}'|}}{|\mathbf{r}-\mathbf{r}'|}(4\pi[Z\delta(\mathbf{r}') - n^{i-1}(\mathbf{r}') + n_0] - k_{TF}^2\phi^{i-1}(\mathbf{r}'))$$
$$+\begin{cases} \dfrac{4\pi n_0}{k_{TF}^3 r}[k_{TF}r - \sinh(k_{TF}r)(1 + k_{TF}R_{ws})e^{-k_{TF}R_{ws}}]; & r < R_{ws} \\ \dfrac{4\pi n_0 e^{-k_{TF}r}}{k_{TF}^3 r}[k_{TF}R_{ws}\cosh(k_{TF}R_{ws}) - \sinh(k_{TF}R_{ws})]; & r > R_{ws}. \end{cases} \quad (19)$$

Here i and $(i-1)$ correspond to the number of iterations in the self-consistent solution and $(1/k_{TF})$ is Thomas-Fermi screening length. Equation (19) is mathematically correct when $\phi^i(\mathbf{r}) = \phi^{(i-1)}(\mathbf{r})$. In this procedure the Coulombic tail, if persists, gets truncated due to exponential term. The self-consistency is achieved within about 0·1 % in charge density. The radial integration of (18) is carried out by Fox and Goodwin method in the steps of 0·1 a.u. up to 19·5 a.u. The phase shifts sum is performed up to $l = 14$. It is found that the charge density and hence the potential remains converged within the limits of accuracy if $V_{ss}(r)$ is included up to $r = 8$ a.u.

The calculations are carried out in two steps. In the first step the calculations are performed for the perfect crystal by putting $n(r) = n_H(r)$, $Z' = Z_H$, $\delta n(r) = \delta n_H(r) = n_H(r) - n_0$, in eqs (5–10) and (15–19). The self-consistently calculated $V_H(r)$ and $\delta n_H(r)$ are retained. In the second step the calculations are performed for the defect crystal with an impurity at the origin. $n(r) = n_I(r)$, $Z' = Z'$ and $\delta n_I(r) = n_I(r) - n_0$ are used in eqs (5–10) and (15–19). The self-consistently calculated $V_I(r)$ and $\delta n_I(r)$ are obtained. However the Friedel sum rule

$$\Delta Z = \frac{2}{\pi}\sum_l (2l+1)\delta_l(k_F) \quad (20)$$

has to be satisfied for the defect crystal with the help of calculated phase shifts. The differences

$$\delta V_i(r) = V_I(r) - V_H(r) \quad (21)$$

and

$$\delta n_i(r) = n_I(r) - n_H(r) \quad (22)$$

give the host-impurity potential and the impurity induced charge density respectively.

5. Host-impurity potential

The self-consistently calculated host-impurity potentials given by (21) are shown in figure 3 for *Al*Cd, *Al*Si, *Al*In and *Al*Ge alloys. The inset shows the potentials on the

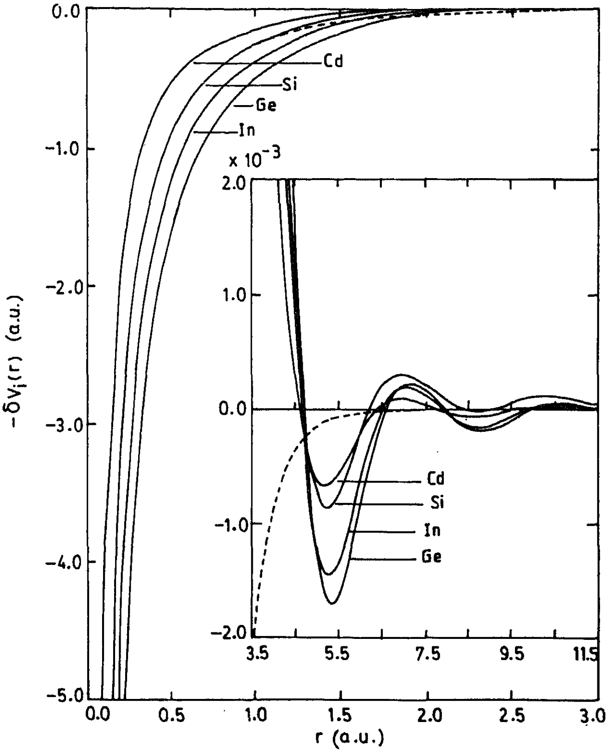

Figure 3. The host-impurity potential $\delta V_i(r)$ versus r for Al(Cd, Si, In, Ge) alloys. The inset shows Friedel oscillations. The dashed line represents the potential obtained from Eq. (23) for *Al*Si.

enhanced scale at larger distances from the impurity. The magnitude of potentials for *Al*(Cd, Si, In, Ge) are in the decreasing order.

The $\delta V_i(r)$ are repulsive for $r < 2{\cdot}5$ a.u. for *Al*Cd, *Al*Si, *Al*In and *Al*Ge alloys and oscillatory afterwards. The relative comparison shows that $\delta V_i(r)$ are proportional to effective charges of impurities at smaller r while at larger r these have Friedel oscillations. It is found that $V_{ss}(r)$ reduces the amplitude of oscillations and shifts the position of first minimum of $\delta V_i(r)$ at the 1NN site of impurity. The ranges of attractive and repulsive potentials are also altered.

We express these potentials in the analytical form [21]

$$\delta V_i(r) = -\Delta Z\left(1 + \frac{\beta r}{2}\right)\exp(-\beta r)/r. \tag{23}$$

The parameter β is determined by the method of least square fit for each alloy. These values of β are given in table 2. The potential obtained from (23) is shown by dashed line for *Al*Si in figure 3. For $r < 1{\cdot}5$ a.u. eq. (23) coincides with the calculated $\delta V_i(r)$. At larger distances the potential obtained by (23) decays exponentially and there are no oscillations. Equation (23) is quite useful in determining the physical properties where the interactions from the first few neighbors of impurity are dominant.

Table 2. The calculated and experimental results for Al alloys. $\Delta\rho$ is residual resistivity, Δn_s is the excess charge in the impurity Wigner-Seitz cell, E_{se} is self-energy and β is the potential parameter. The lattice parameter $a = 7{\cdot}64$ a.u. and Ashcroft potential parameter $r_c = 1{\cdot}12$ a.u. are used.

	$\Delta\rho$ ($\mu\Omega$cm/at%)				
Impurities	Cal.	Exp.	Δn_s	β	E_{se}(eV)
Cu	1·25	0·89	0·70	0·52	−0·14
Ag	0·32	1·08	1·85	1·00	−0·79
Cd	1·08	0·51	0·64	1·82	−0·03
Mg	1·22	0·36	1·44	0·64	−0·15
Zn	0·73	0·24	1·47	0·88	−0·30
Ga	0·24	0·22	1·15	1·05	−0·51
In	0·92	—	1·40	1·60	−0·15
Ge	0·92	0·79	1·43	1·51	−0·23
Si	0·98	0·60	0·85	1·70	−0·09
Sn	0·85	—	1·42	0·84	−0·27

6. Electron charge density and charge transfer

The impurity-induced electron charge densities $\delta n_i(r)/n_0$, given in (22), are shown in figure 4 for *Al*Cd, *Al*Si, *Al*In, *Cu*Ge, and *Al*Ga alloys. The Friedel oscillations are exhibited in the inset for *Al*Cd, *Al*In and *Al*Ga. The results for *Al*Ge and *Al*Si are close to *Al*In and *Al*Cd respectively. $[\delta n_i(r)/n_0]$ decreases rapidly with increase of r and shows oscillatory behavior for $r > 3{\cdot}0$ a.u. for Al(Cd, In, Ge, Si) and for $r > 4{\cdot}0$ a.u. for *Al*Ga. Thus Ga impurity is screened up to larger r. The $V_{ss}(r)$ has reduced the amplitude of Friedel oscillations and displaced the positions of the minima and maxima due to shell periodic character.

The solution of Poisson equation for $\delta V_i(r)$ given in (23) gives

$$\delta n_i(r) = (\Delta Z \beta^3/8\pi)\exp(-\beta r). \tag{24}$$

Equation (24) underestimates $\delta n_i(r)$ at the impurity site. The impurity self-energy $E_{se} = [-3(\Delta Z)^2 \beta/32]$ is also calculated [10] for all the impurities and these results are tabulated in table 2. The self-energy is minimum for *Al*Cd and hence the stable solid solution and the minimum for *Al*Ag and hence the least stable solid solution.

We also calculated the net electronic charge in the impurity Wigner-Seitz cell by integrating $\delta n_i(r)$ from 0 to R_{ws}. These values are also tabulated in table 2 as Δn_s. The charge transfer is estimated by comparing Δn_s with Z_I. It is found the Cu, Cd, Mg, Zn, In, Ge, Si and Sn impurities transfer the charge to Al host while Ag and Ga impurities gain the charge from host. The calculations of Deutz *et al* [22] suggest that these impurities gain the charge of order of 2–4%. This difference is due to consideration of bound states and inclusion of size effect. The size effect is not included in the calculations of Deutz *et al* [22].

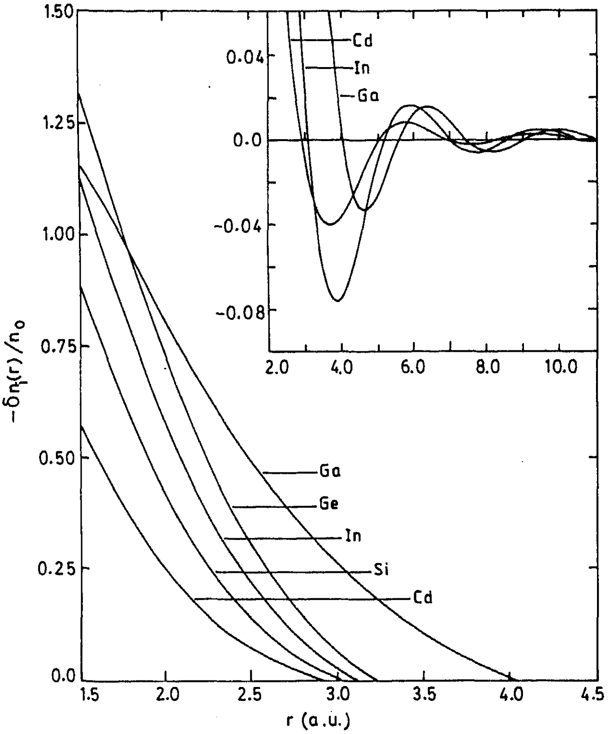

Figure 4. The impurity-induced normalized charge density ($\delta n_i(r)/n_0$) versus r for *Al*(Cd, Si, In, Ge, Ga) alloys. The inset shows Friedel oscillations.

7. Scattering phase shifts and residual resistivity

The scattering phase shifts obtained in the self-consistent calculations of $V_I(r)$ and $n_I(r)$ by satisfying the Friedel sum rule are tabulated in table 3 up to $l = 9$. The higher order phase shifts are found negligibly small. The magnitude of the phase shifts is oscillatory. This is due to the inclusion of $V_{ss}(r)$ [2]. The p, d and f scattering phase shifts are mainly due to lattice effects through $V_{ss}(r)$. Using these phase shifts the residual resistivity is estimated with the help of following expression [10].

$$\Delta\rho = \frac{2{\cdot}732}{k_F Z_H}\left[\sum_{l=0}^{14}(l+1)\sin^2(\delta_l - \delta_{l+1})\right] \tag{25}$$

The calculated values of $\Delta\rho$ are given in table 2. The agreement with the experimental results is just qualitative. A relative comparison with the results of Mahajan and Prakash [2] shows that the introduction of $V_{ss}(r)$ enhances $\Delta\rho$. In fact $\Delta\rho$ involves a careful calculation of electron-phonon matrix element and anisotropy of Fermi surface [23]. These effects are not included in (25).

8. Electric field gradient

The total change in crystal potential due to insertion of a substitutional impurity is [24]

Table 3. The phase shifts evaluated at the Fermi surface ($E = E_F$) for Al alloys.

Phase shifts	Impurities									
	Cu	Ag	Cd	Mg	Zn	Ga	In	Ge	Si	Sn
δ_0	1·0548	−0·2287	2·3302	0·8291	0·2343	−0·4873	2·0062	1·8466	2·1610	0·3567
δ_1	−0·5343	−0·5063	0·2883	−0·5384	−0·5235	−0·4973	0·0756	−0·0212	0·1796	−0·5280
δ_2	−0·2268	−0·2168	−0·0965	−0·2292	−0·2237	−0·2113	−0·0798	−0·0776	−0·0827	−0·2256
δ_3	−0·0762	−0·0740	−0·0485	−0·7666	−0·0751	−0·0723	−0·0443	−0·0425	−0·0440	−0·0756
δ_4	0·0054	0·0055	0·0117	0·0055	0·0061	0·0062	0·0116	0·0115	0·0132	0·0059
δ_5	0·0040	0·0034	0·0046	0·0042	0·0042	0·0039	0·0042	0·0040	0·0057	0·0042
δ_6	−0·0049	−0·0054	−0·0052	−0·0048	−0·0048	−0·0050	−0·0055	−0·0057	−0·0044	−0·0048
δ_7	−0·0025	−0·0028	−0·0026	−0·0025	−0·0024	−0·0025	−0·0028	−0·0030	−0·0022	−0·0025
δ_8	−0·0003	−0·0003	−0·0002	−0·0002	−0·0002	−0·0002	−0·0003	−0·0004	−0·0001	−0·0002
δ_9	0·0001	0·0001	0·0002	0·0001	0·0001	0·0002	0·0001	0·0001	0·0002	0·0001

$$\Delta\Phi_H(\mathbf{r}) = \Delta\phi_I(\mathbf{r}) + \Delta\phi_H(\mathbf{r}) \tag{27}$$

where

$$\Delta\phi_I(r) = \phi_I(r) - \phi_H(r) \tag{28}$$

and

$$\Delta\phi_H(\mathbf{r}) = \sum_n{}' [\phi_H(\mathbf{r} - \mathbf{R}_n) - \phi_H(\mathbf{r} - \mathbf{R}_n^0)]. \tag{29}$$

Here $\phi_H(r)$ and $\phi_I(r)$ are self-consistent interatomic potentials for host and impurity atoms respectively. $\mathbf{R}_n^0$ and $\mathbf{R}_n$ are the undisplaced and displaced positions of the host atom respectively. $\Delta\phi_I(\mathbf{r})$ involves only one host and one impurity atom and arises from the valence difference. $\Delta\phi_H(\mathbf{r})$ arises from the strain field and involves the entire lattice.

The EFG tensor **V** at $\mathbf{r} = \mathbf{R}_m$, the mNN of impurity, is obtained by computing the second derivative of $\Delta\Phi_H(\mathbf{r})$ which is given as

$$\underset{\sim}{V}(\mathbf{R}_m) = \underset{\sim}{V}^v(\mathbf{R}_m) + \underset{\sim}{V}^s(\mathbf{R}_m) \tag{30}$$

where the valence EFG

$$\mathbf{V}^v(\mathbf{R}_m) = (1 - \gamma_\infty)[\nabla\cdot\nabla\{\Delta\phi_I(\mathbf{r})\}]_{\mathbf{r}=\mathbf{R}_m} \tag{31}$$

and the size EFG

$$\mathbf{V}^s(\mathbf{R}_m) = (1 - \gamma_\infty)[\nabla\cdot\nabla\{\Delta\phi_H(\mathbf{r})\}]_{\mathbf{r}=\mathbf{R}_m}. \tag{32}$$

$(1 - \gamma_\infty)$ is Sternheimier antishielding factor [25].

The displaced positions of host atoms are calculated in the continuum model of the lattice and these are given as [9]

$$\mathbf{R}_m = \sqrt{m}R_1^0 + \frac{(1+\sigma)}{4\pi(1-\sigma)} \frac{\Omega_0}{(\sqrt{m}R_1^0)^2} \left(\frac{1}{a}\frac{\mathrm{d}a}{\mathrm{d}c}\right) \tag{33}$$

where Ω_0 is the atomic volume of the host lattice. σ is Poisson ratio and $(1/a)$ $(\mathrm{d}a/\mathrm{d}c)$ is the fractional change in lattice parameter 'a' per unit concentration. The total EFG is obtained by adding the corresponding Cartesian components of the valence and size EFGs i.e.

$$V_{\alpha\beta}(\mathbf{R}_m) = V_{\alpha\beta}^v(\mathbf{R}_m) + V_{\alpha\beta}^s(\mathbf{R}_m). \tag{34}$$

The components of traceless EFG tensor **q** are given as

$$q_{\alpha\beta} = V_{\alpha\beta} - (1/3)\sum_\alpha V_{\alpha\alpha}. \tag{35}$$

The (3×3) matrix of $q_{\alpha\beta}$ is diagonalized to obtain the eigenvalues and eigenvectors. The eigenvalue corresponding to eigenvector parallel to the line joining the impurity and host atom is taken as

$$q_{ZZ} = q_\parallel. \tag{36}$$

Other two components are written as

$$q_{YY} = q_\perp \text{ and } q_{XX} = q_{xx}. \tag{37}$$

In general $|q_{ZZ}| \geqslant |q_{YY}| \geqslant |q_{XX}|$ and the asymmetry parameter η is defined as

$$\eta = |q_{XX} - q_{YY}|/|q_{ZZ}|. \tag{38}$$

In the fcc lattice $\mathbf{V}^{\mathrm{v}}$ and $\mathbf{V}^{\mathrm{s}}$ are similar matrices at the 1NN and 2NN sites. Therefore these can be diagonalized separately and eigenvalues of the same eigenvectors can be added.

To calculate the valence EFGs $\Delta\phi_{\mathrm{l}}(\mathbf{r}) = (1/e)\delta V_{\mathrm{i}}(\mathbf{r})$ is calculated from (21) and it is used in (31). The differentiation is carried out numerically at the displaced positions of 1NNs and 2NNs of impurities. These values are used in (35) to get the traceless EFG components $q^{\mathrm{v}}_{\alpha\beta}$. $\gamma_{\infty} = -2{\cdot}59$ is used [8].

To evaluate the size EFGs, we have adopted the continuum model of the lattice. In this model size EFG is given as [26]

$$q^{\mathrm{s}}_{\alpha\beta} = (1/e)\left[(F_{11} - F_{12})\delta_{\alpha\beta}\left\{\varepsilon_{\alpha\alpha} - \frac{1}{3}\sum_{\gamma}\varepsilon_{\gamma\gamma}\right\} + 2F_{44}(1 - \delta_{\alpha\beta})\varepsilon_{\alpha\beta}\right] \tag{39}$$

where $\varepsilon_{\alpha\beta}$ are the components of a symmetric strain tensor and $F_{\alpha'\beta'}$ are the components of a fourth order tensor, $\alpha', \beta' = 1, 2 \ldots 6$. For a cubic crystal $F_{11} = -2F_{22} = -2F_{44}$. F_{11} is taken from the calculations of Pal *et al* [27]. The following components are at the 1NN site

$$q^{\mathrm{s}}_{XX} = -2q^{\mathrm{s}}_{YY} = -2q^{\mathrm{s}}_{ZZ} = \frac{1}{3e}(3D_2/R_1^3)(F_{11} - F_{12})$$

$$q^{\mathrm{s}}_{YZ} = -\frac{1}{2e}(3D_2/R_1^3)F_{44};$$

and

$$q^{\mathrm{s}}_{XY} = q^{\mathrm{s}}_{ZX} = 0. \tag{40}$$

Here

$$D_2 = \frac{a^3}{16\pi}\left(\frac{1}{a}\frac{\mathrm{d}a}{\mathrm{d}c}\right)\left(\frac{1+\sigma}{1-\sigma}\right). \tag{41}$$

Similarly at the 2NN site

$$q^{\mathrm{s}}_{XX} = q^{\mathrm{s}}_{YY} = -\frac{1}{2}q^{\mathrm{s}}_{ZZ} = \frac{1}{3e}(3D_2/R_2^3)(F_{11} - F_{22})$$

and

$$q^{\mathrm{s}}_{XY} = q^{\mathrm{s}}_{YZ} = q^{\mathrm{s}}_{ZX} = 0. \tag{42}$$

The calculated values of q^{v}_{XX}, $q^{\mathrm{v}}_{\perp}$, $q^{\mathrm{v}}_{\parallel}$ and q^{s}_{XX}, $q^{\mathrm{s}}_{\perp}$, $q^{\mathrm{s}}_{\parallel}$ at the 1NN and 2NN sites of impurity are tabulated in tables 4 and 5 respectively. The size strength parameter D_2 is increased by a factor of 7·50 for an over all agreement of EFG with the experimental value of *Al*Cu at 1NN site. The same enhancement is used for other alloys also. Such an enhancement is not introduced for the 2NN site EFG calculations. The respective components are added and the magnitude of the largest sum is taken as EFG for that particular alloy. The calculated values of η are also tabulated in table 4. η vanishes at the 2NN site. The results are compared with the experimental values. The following observations are made:

(i) At the 1NN site the valence EFG components have cylindrical symmetry while

Table 4. Calculated and experimental values of EFG $q(\text{Å}^{-3})$ and asymmetry parameter η at the 1NN site in Al alloys. v, s, t denote valence, size and total EFGs. Underlined values are the principal components of net EFG (q_{cal}).

Impurities	EFG Components	q_{xx}	$q_{\perp}$	q	$\lvert q_{\mathrm{cal}}\rvert$ [exp]	η_{cal} [exp]
Cu	v	0·025	0·025	−0·051	0·244	0·68
	s	0·179	−0·269	0·090	[0·297]	[0·23]
	t	0·204	$\underline{0{\cdot}244}$	0·039		
Ag	v	0·024	0·024	−0·048	0·067	0·85
	s	−0·029	0·043	−0·014	[0·218]	[0·31]
	t	−0·005	$\underline{0{\cdot}067}$	−0·062		
Cd	v	0·017	0·017	−0·033	0·243	0·56
	s	0·174	−0·260	0·087	[0·182]	[0·03]
	t	0·191	$\underline{-0{\cdot}243}$	0·054		
Mg	v	0·029	0·029	−0·059	0·273	0·03
	s	−0·162	0·244	−0·081	[0·195]	[0·07]
	t	−0·133	$\underline{0{\cdot}273}$	−0·140		
Zn	v	0·015	0·015	−0·031	0·033	0·39
	s	0·018	−0·028	0·009	[0·180]	[0·27]
	t	$\underline{0{\cdot}033}$	−0·013	−0·022		
Ga	v	0·024	0·024	−0·048	0·103	0·44
	s	−0·053	0·079	−0·026	[0·228]	[0·03]
	t	−0·029	$\underline{0{\cdot}103}$	−0·074		
Si	v	0·029	0·029	−0·059	0·095	0·47
	s	0·066	−0·100	0·033	[0·282]	[0·03]
	t	$\underline{0{\cdot}095}$	0·071	−0·026		
Sn	v	0·023	0·023	−0·046	0·317	0·02
	s	−0·196	0·294	−0·098	[0·266]	[0·37]
	t	−0·173	$\underline{0{\cdot}317}$	−0·144		

the size EFG components have cubic symmetry. This is due to the fact that $\Delta\phi_i(r)$ is spherically symmetric while crystal symmetry is considered in the determination of F_{11}. At the 2NN site both the valence and size EFGs are cylindrically symmetric.

(ii) At the 1NN site $q^{\mathrm{v}}_{\perp}$ is consistently smaller than $q^{\mathrm{s}}_{\perp}$. The maximum components are along the perpendicular direction. The calculated values of EFGs at 1NN are in agreement with the experimental values except for *Al*Ag, *Al*Zn and *Al*Si where the calculated values are smaller than the experimental values. This is due to the fact that size effect is overestimated. The size strength parameter D_2 is not varied for each alloy to get an agreement between the calculated and experimental values of EFGs. The agreement between the calculated and experimental values of η is rather uneven. This is because η depends on the cancellation of two small quantities and also divided by a small quantity.

(iii) At the 2NN site the magnitudes of EFGs are small. The maximum components are along the parallel direction. The calculated values are in agreement with the

Table 5. Calculated and experimental values of EFG q(Å^{-3}) at the 2NN site in Al alloys. The description is the same as that of table 4.

Impurities	EFG Components	q_{xx}	$q_{\perp}$	q	$\lvert q_{\text{cal}} \rvert$ [exp]
Cu	v	−0·011	−0·011	0·022	0·005
	s	0·008	0·008	−0·017	[< 0·020]
	t	−0·003	−0·003	0·005	
Ag	v	−0·008	−0·008	0·016	0·019
	s	−0·002	−0·002	0·003	[0·032]
	t	−0·010	−0·010	0·019	
Cd	v	0·0	0·0	0·001	0·015
	s	0·080	0·080	−0·016	[−]
	t	0·080	0·080	−0·015	
Mg	v	−0·011	−0·011	0·022	0·038
	s	−0·008	−0·008	0·016	[< 0·020]
	t	−0·019	−0·019	0·038	
Zn	v	−0·010	−0·010	0·019	0·017
	s	0·001	0·001	−0·002	[< 0·020]
	t	−0·009	−0·009	0·017	
Ga	v	−0·008	−0·008	0·016	0·021
	s	−0·002	−0·002	0·005	[< 0·020]
	t	−0·010	−0·010	0·021	
Si	v	0·0	0·0	−0·001	0·007
	s	0·003	0·003	−0·006	[< 0·020]
	t	0·003	0·003	0·007	
Sn	v	−0·010	−0·010	0·020	0·039
	s	−0·009	−0·009	0·019	[0·049]
	t	−0·019	−0·019	0·039	

experimental values except for *Al*Ag and *Al*Sn. The calculated values of EFGs for these alloys are lower than experimental values.

In the present calculations the valence EFG does not involve any core enhancement factor and there are no restrictions of asymptotic and preasymptotic limits of charge distributions. In the earlier calculations [28] the valence EFG was evaluated with the help of asymptotic charge distribution involving core enhancement factor. In the present calculations valence EFG is evaluated directly from $\Delta V_i(r)$ without introducing any parameter. The size EFG at the 1NN sites involves a unified size strength parameter and no size strength parameter is introduced at the 2NN sites. The general agreement of the calculated EFGs and η with the experimental values is as good as found in earlier calculations [28]. Thus we conclude that our simplified model does explain the local electronic structure of dilute alloys of Al.

9. Discussion

Our calculations are based on a simple but realistic physical model for dilute alloys. The effective valency is determined considering bound states and rigid ion model.

The lattice effects are included through SSM and the lattice distortion through Blatt correction. In a dilute alloy the host ion configuration may also alter, however this effect is not included here. The results may further be improved by including more realistic periodic potential. However this leads to intractable non-linear screening calculations [28]. The host-impurity potentials and impurity-induced charge densities are taken spherically symmetric in these calculations. The consideration of anisotropy of charge density may improve the results [29]. But these effects may be quite small in SM Al alloys of close packed cubic symmetry.

Acknowledgements

The authors are thankful to Dr J Singh for fruitful discussion. The financial support from Department of Atomic Energy, Bombay is also acknowledged.

References

[1] P Hohenberg and W Kohn, *Phys. Rev.* **B136**, 864 (1964)
W Kohn and L J Sham, *Phys. Rev.* **A140**, 1133 (1965)
[2] S Mahajan and S Prakash, *Phys. Status. Solidi* **B119**, 381 (1983)
[3] M Manninen and R M Nieminen, *J. Phys.* **F9**, 1333 (1979)
[4] R M Nieminen and M Pushka, *J. Phys.* **F10**, L123 (1980)
[5] S Mahajan, *Energetics of interstitial and substitutional impurities in metals* Thesis, Panjab University, Chandigarh (India) 1984
[6] S Prakash, *J. Phys.* **F8**, 2497 (1978)
[7] S D Raj, J Singh and S Prakash, *J. Phys.* **F12**, 1941 (1982)
[8] M J Ponnambalam and P Jena, *Hyperfine Int.* **20**, 65 (1984)
[9] P Singh, J Singh, S K Rattan and S Prakash, *Phys. Rev.* **B49**, 2335 (1994)
[10] P Singh and S Prakash, *Pramana – J. Phys.* **41**, 239 (1993)
[11] S Prakash and P Lucasson, *J. Phys.* **F11**, 2515 (1981)
[12] B Johnsson and N Martensson, *Phys. Rev.* **B21**, 4427 (1980)
[13] Handbook of Chemistry and Physics, The Chemical Rubber Publications, E-76 (1962)
[14] W B Pearson, *Handbook of lattice spacings and structures of metals and alloys* (Pergamon, New York, 1978)
[15] R Rizk, P Vajda, F Maury, A Lucasson, P Lucasson, C Dimitrov and O Dimitrov, *J. Appl. Phys.* **47**, 4740 (1976)
[16] F Dworschak, C Dimitrov and O Dimitrov, *J. Phys.* **F8**, L153 (1978)
[17] F Maury, A Lucasson, P Lucasson J Le Herichy, P Vajda, C Dimitrov and O Dimitrov, *Radiat Eff.* **51**, 57 (1980)
[18] F Maury, *J. Phys.* **F14**, 1395 (1984) and references therein
[19] P Vashistha and K S Singwi, *Phys. Rev.* **B6**, 8756 (1972)
[20] M Manninen, R Nieminen, P Haützarvi and J M Arpponen, *Phys. Rev.* **B12**, 4012 (1975)
[21] C A Sholl and P V Smith, *J. Phys.* **F8**, 775 (1978)
[22] J Deutz, P H Dederichs and R Zeller, *J. Phys.* **F11**, 1787 (1981)
[23] N Singh, J Singh and S Prakash, *Phys. Status Solidi* **B79**, 787 (1977) and the references therein
[24] S Prakash, J Singh and S K Rattan, *Phys. Rev.* **B48**, 6927 (1993)
[25] M H Cohen and F Reif, *Solid State Phys.* **5**, 321 (New York, Academic Press, 1957)
[26] P L Sagalyn and M N Alexander, *Phys. Rev.* **B15**, 5581 (1977)
[27] B Pal, S Mahajan, S D Raj, J Singh and S Prakash, *Phys. Rev.* **B30**, 3191 (1984)
[28] S Mahajan, B Pal and S Prakash, *Physica* **B132**, 61 (1985)
[29] J Singh, S K Rattan and S Prakash, *Phys. Rev.* **B38**, 10440 (1988)

PRAMANA
— journal of
physics

© Printed in India

Vol. 42, No. 5,
May 1994
pp. 421–425

Transport phenomena of $SmSe_{1-x}As_x$

S ARIPONNAMMAL and S NATARAJAN
Department of Physics, Anna University, Madras 600025, India

MS received 18 October 1993; revised 16 February 1994

Abstract. Results are presented on the measurements of unit cell parameter and electrical resistivity under pressure on $SmSe_{1-x}As_x$ for $x = 0.1$, 0·2, 0·3 and 0·4. The electrical resistivity values are found to be decreasing with increase of pressure and also with increase of arsenic concentration. The semiconductor to metallic transition is induced by chemical alloying of SmSe with SmAs similar to that observed under pressure. The electrical resistivity values are also calculated which are in good agreement with the experimental values. In this calculation, the carrier mobility is of negative sign and so the sample $SmSe_{1-x}As_x$ is found to be *n*-type semiconductor.

Keywords. $SmSe_{1-x}As_x$; lattice parameter; electrical resistivity; semiconductor to metal transition; high pressure.

PACS Nos 62·50; 72·20

1. Introduction

Monochalcogenides of divalent Sm, Eu and Yb crystallize in the NaCl structure and are found to be semiconductors [1]. Because of the smaller atomic volume in the trivalent state, pressure in general induce a transition from the divalent semiconducting state to trivalent metallic state [2], which can also be induced at room temperature and pressure by chemical alloying. To study the effect of alloying SmAs with SmSe [3], we have already reported [4] the electrical conductivity measurements and the results of X-ray diffraction studies on $SmSe_{1-x}As_x$ for $x = 0·1$ and 0·4. The present study has been undertaken to closely examine the behaviour of electrical resistivity under pressure and lattice parameter variation between these two concentrations.

2. Experimental methods

X-ray powder diffraction studies on $SmSe_{1-x}As_x$ for $x = 0·2$ and 0·3 have been carried out using Cukα radiation produced by a rotating anode X-ray generator. The sample had expected NaCl structure. Lattice parameters (table 1) obtained from six *d*-values by least square method are in good agreement with the reported values [5].

Electrical resistivity measurements has been carried out by using four-probe method [6] in Bridgemann anvil set-up, with anvils made of EN24 (AISI4340) alloy steel (Composition: C 0·04%, Mn 0·60%, Ni 1·55%, Cr 1·1%) hardened to RC60. The anvil face was 10 mm in diameter and had a tapering angle 10°. The pressure medium was steatite of 0·2 mm dia. The gaskets were pyrophyllite discs of 10 mm dia. A hydraulic press was used to apply the force.

From the electrical resistivity measurements, impurity activation energy [3, 7] ΔE

Table 1. Experimental and theoretical results of $SmSe_{1-x}As_x$.

x	a in Å: Present study	a in Å: Reported	ΔE in eV	ρ experimental Ω-metre	ρ calculated Ω-metre
0·0	—	6·20	0·440	30[Ref. 7]	14·3
0·1	$6{\cdot}18 \pm 0{\cdot}02$	6·15	0·120	$1{\cdot}2528 \times 10^{-2}$ $\pm 0{\cdot}00010$	$1{\cdot}333 \times 10^{-2}$
0·2	$6{\cdot}03 \pm 0{\cdot}02$	6·05	0·074	$1{\cdot}3265 \times 10^{-3}$ $\pm 0{\cdot}00009$	$7{\cdot}351 \times 10^{-3}$
0·3	$5{\cdot}99 \pm 0{\cdot}01$	5·98	—	$2{\cdot}2510 \times 10^{-4}$ $\pm 0{\cdot}00001$	—
0·4	$5{\cdot}94 \pm 0{\cdot}02$	5·94	—	$1{\cdot}2005 \times 10^{-4}$ $\pm 0{\cdot}00001$	—

x	Calculated parameters: m^* in kg	n	ε	u in $m^2V^{-1}s^{-1}$
0·0	$4{\cdot}794 \times 10^{-31}$	$1{\cdot}804 \times 10^{21}$	4·023	$-2{\cdot}417 \times 10^{-4}$
0·1	$2{\cdot}108 \times 10^{-31}$	$2{\cdot}671 \times 10^{23}$	5·108	$-1{\cdot}753 \times 10^{-3}$
0·2	$1{\cdot}370 \times 10^{-31}$	$3{\cdot}428 \times 10^{23}$	5·244	$-2{\cdot}477 \times 10^{-3}$

which is equal to αp_0 can be deduced. Here, α is the rate of closing of energy gap with pressure given by

$$\alpha = \frac{d\Delta Eg}{dp} = kT\left[\frac{d\ln\rho}{dp}\right] \tag{1}$$

and p_0 is the minimum pressure needed for the complete conversion of Sm^{2+} into Sm^{3+}, characterized in a sharp bending over and saturation effect conductivity in the $\ln\rho$-P plot [3].

3. Estimated electrical resistivity

The electrical resistivity has been theoretically calculated using the lattice constant and impurity activation energy. The Drude's model [8] defines the electrical conductivity σ which is the reciprocal of the electrical resistivity as

$$\sigma = 1/\rho = neu \tag{2}$$

where n is the carrier density, e the electron charge and u is the carrier mobility. The carrier density [9] n can be calculated by the formula

$$n = \frac{2(2\pi m^* kT)^{3/2}}{h^3}\exp\left[-\frac{\Delta E}{2kT}\right] \tag{3}$$

here m^* is the effective mass, ΔE impurity activation energy, k Boltzmann constant,

h the Plancks constant and T the temperature. The effective mass [10] can be given in terms of lattice parameter a and impurity activation energy ΔE as

$$\frac{m_0}{m^*} = 1 + \frac{2h^2}{m_0 a^2 \Delta E}. \tag{4}$$

Where m_0 is the electron rest mass. Then, the carrier mobility u can be determined [9] from the expression

$$u = \frac{3\varepsilon^2}{16\pi^2 m^* [\ln(1+x) - x/(1+x)]} \left[\frac{h}{e}\right]^3. \tag{5}$$

Here ε is the dielectric constant [9] which is given by

$$\varepsilon = \left[\frac{13{\cdot}53}{\Delta E} \frac{m^*}{m_0}\right]^{1/2} \tag{6}$$

and

$$x = \left[\frac{h}{e}\right]^2 \left[\frac{e}{m^*}\right] \left[\frac{3N}{8\pi}\right]^{1/3} \tag{7}$$

Where N is the impurity concentration given by

$$N = \frac{n^2}{2\left[\frac{2\pi m^* kT}{h^2}\right]^{3/4} \exp\left[-\frac{\Delta E}{2kT}\right]}. \tag{8}$$

Thus, the value of electrical resistivity at room temperature and pressure has been calculated by substituting n and u in eq. (3) for various values of x. The results are given in table 1. SmSe is characterized as [11] n type semiconductor. In this calculation the calculated mobility is of negative sign and therefore $SmSe_{1-x}As_x$ must be of n type semiconductors.

4. Conclusion

X-ray diffraction study on $SmSe_{1-x}As_x$ for $x = 0{\cdot}1$, $0{\cdot}2$, $0{\cdot}3$ and $0{\cdot}4$ shows that the sample is having expected NaCl type structure. The lattice parameters obtained for the samples are in good agreement with the reported values. The arsenic substitution in SmSe for Se causes the valence transition from Sm^{2+} to Sm^{3+}. The transition starts at $x = 0{\cdot}1$ and is nearly completed at about $x = 0{\cdot}4$. The behaviour of electrical resistivity of the samples as a function of pressure is shown in figure 1. The electrical resistivity decreases continuously with increase of pressure. From the resistivity measurements, impurity activation energy has been determined. The resistivity decreases continuously with increase of arsenic concentration similar to the behaviour observed under pressure. These lead to a conclusion that the semiconductor to metallic transition can be induced by chemical alloying SmSe with SmAs similar to that induced under pressure. The sample is in divalent semiconducting state at ambient pressure and temperature, and goes to trivalent metallic state under pressure at room temperature. As a function of arsenic concentration, $SmSe_{1-x}As_x$ is in semiconducting state at lower values of x and metallic state at about $x = 0{\cdot}4$. Then the electrical

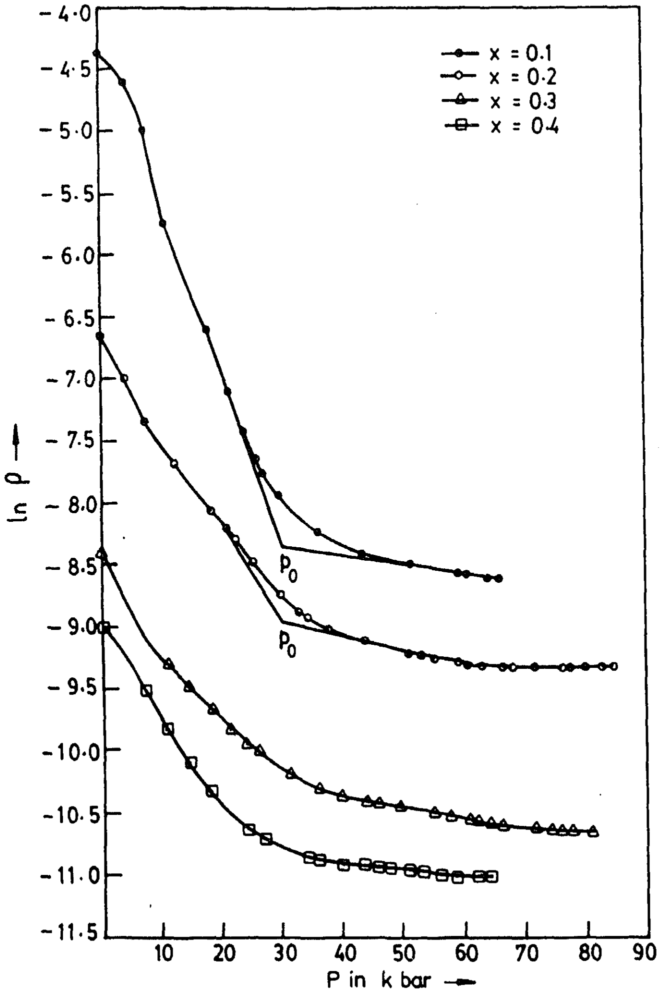

Figure 1. The behaviour of electrical resistivity of $SmSe_{1-x}As_x$ as a function of pressure.

resistivity values at ambient temperature and pressure are calculated using Drude's model for $x = 0{\cdot}0$, 0·1 and 0·2 which are in agreement with the experimental values. This method is applicable only to semiconductors and not to metals because of the dependence of the energy gap. Since the ρ values are approaching nearer to metallic state for $x = 0{\cdot}3$ and 0·4, this method is not applicable. The calculated effective mass, carrier density, carrier mobility and dielectric constant are given in table 1. It is notable that the calculated carrier mobility is of negative sign which leads to a conclusion that the sample is of *n* type semiconductor. The values of lattice constant, impurity activation energy and experimental as well as calculated electrical resistivity values are given in table 1. They are fairly in good agreement.

Acknowledgements

Authors are thankful to Prof. K B Garg for providing the samples for this study and CSIR, Government of India for financial support.

References

[1] A Jayaraman, V Narayanamurti, E Bucher and R G Maines, *Phys. Rev. Lett.* **25**, 368 (1970)

[2] E Bucher and R G Maines, *Solid State Commun.* **11**, 1441 (1972)

[3] E Bucher, V Narayanamurti and A Jayaraman, *J. Appl. Phys.* **42**, 1741 (1971)

[4] S Ariponnammal, S Ezhilvalavan and S Natarajan, *Pramana – J. Phys.* **37**, 141 (1991)

[5] R B Beeken and J W Schweitzer, *Phys. Rev.* **B23**, 3620 (1981)

[6] N Victor Jaya, *High pressure studies of quasi crystals and superconducting compounds* Ph.D. Thesis, Anna University (1988)

[7] A Jayaraman, V Narayanamurti, E Bucher and R G Maines, *Phys. Rev. Lett.* **25**, 1430 (1970)

[8] J S Blakemore, in *Solid state physics* Second edition (W B Saunders Company, Cambridge, 1985) p. 330

[9] A F Ioffe, in *Physics of semiconductors* edited by H J Goldsmid (Publishing House of USSR Academy of Sciences, Moscow-Leningrad, 1960) p. 334, 333, 362, 176

[10] Walter A Harrison, in *Solid state physics* edited by Bradford Bayne, Alice S Goehring and Stuart A Kenter (McGraw Hill, USA, 1970) p. 142

[11] F J Reid, L K Matson, J F Miller and R C Himes, *J. Phys. Chem. Solids* **25**, 969 (1964)

PRAMANA
— journal of
physics

© Printed in India

Vol. 42, No. 5,
May 1994
pp. 427–433

Modification of spectral characteristics and optogalvanic response in neon hollow cathode under laser excitation

P R SASI KUMAR, V P N NAMPOORI and C P G VALLABHAN
Laser Division, Department of Physics, Cochin University of Science and Technology, Cochin 682 022, India

MS received 18 October 1993; revised 28 March 1994

Abstract. The changes in emission characteristics of a neon hollow cathode discharge by resonant laser excitation of $1s_5 \rightarrow 2p_2$ and $1s_5 \rightarrow 2p_4$ transition have been studied by simultaneously monitoring the optogalvanic effect and the laser induced fluorescence. It has been observed that resonant excitation causes substantial variation in the relative intensities of lines in the emission spectrum of neon discharge.

Keywords. Optogalvanic spectroscopy; hollow cathode discharge.

PACS Nos **82·80; 52·25**

1. Introduction

The selective perturbation of the energy level population using lasers of high spectral brightness, produces some noticeable modifications in the discharge characteristics. Laser optogalvanic (OG) effect [1], which is the change in impedance of a discharge, and laser induced fluorescence are the consequences of this perturbation. Investigations on simultaneous monitoring of OG effect and fluorescence phenomena in a neon discharge have been reported by a few workers [2–4]. Such studies give information regarding population of various levels, electron density in the discharge and the details of ionization processes that generate the OG effects. In this work, we present the changes in emission characteristics which occur simultaneously with the OG effect as a result of laser excitation of $1s_5 \rightarrow 2p_2$ and $1s_5 \rightarrow 2p_4$ transition in a neon hollow cathode discharge (hcd).

2. Experimental

A frequency stabilized ring dye laser (Spectra Physic-380D) pumped by argon ion laser (Spectra Physic-171) was used as the excitation source. Wavelength of the laser was exactly tuned on the line centre of the neon transition ($1s_5 \rightarrow 2p_2$, $1s_5 \rightarrow 2p_4$) where the OG signal amplitude is a maximum. The wavelength was measured with an accuracy of $0{\cdot}01\,\mathrm{cm}^{-1}$ using a wavemeter (Burliegh WA-20 VI). A commercial Ne/Mo hollow cathode lamp with a gas pressure of 13·3 mBar (Cathodean UK) was used as the discharge source and the laser beam was focused into it. A 0·5 m monochromator (Jarrell–Ash) was used for recording emission spectrum with and without laser excitation up to a discharge current of 5 mA. The PMT output was processed by a lock-in amplifier and a computer was used for the data acquisition. Since the

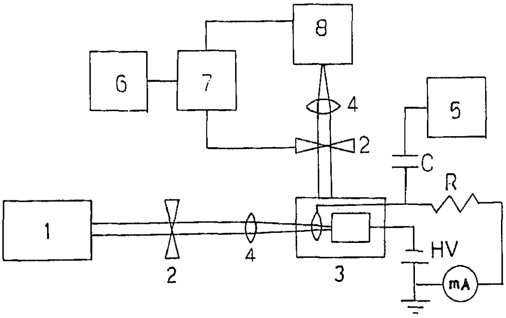

Figure 1. Experimental set-up (1. single mode ring dye laser, 2. chopper, 3. Ne–Mo hollow cathode, 4. lens, 5. CRO, 6. computer, 7. lock-in amplifier, 8. monochromator, $R = 45\,\mathrm{K}\Omega$, $C = 0{\cdot}1\,\mu F$).

range of current used for the operation of the discharge was very low, Mo atomic lines were not observed in the emission spectrum. The neon transitions within the scanning range of the monochromator were identified in all cases. The OG signal which corresponds to an increase in the discharge impedance during laser excitation, was measured using an oscilloscope. A schematic of the experimental set up is shown in figure 1.

3. Results and discussion

a) *Energy level diagram of neon*

The first excited state of neon ($2p^5 3s$) has four components designated as $1s_i (i = 2$, 3, 4 and 5) two of which ($1s_3$ and $1s_5$) are metastables with a long life time. The next excited state configuration is $2p^5 3p$ giving rise to ten states represented as $2p_j$ ($j = 1$ to 10) which are coupled radiatively to the $1s_i$ states [5].

b) *Laser-induced fluorescence spectrum*

Laser excitation of $1s_5 \rightarrow 2p_2$ *transition* (*588·2 nm*)

The emission and the laser induced fluorescence spectrum of the neon hollow cathode at a discharge current of 5 mA by laser excitation of $1s_5 \rightarrow 2p_2$ transition in neon are shown in figure 2. This shows that laser absorption produces a noticeable change in the emission characteristics of the discharge (table 1). These changes are mainly due to non-radiative decay from $2p_2$ state to $2p_j$ ($j \neq 2$) state and also due to the coupling of these levels to the ground state. Measurements of variation in emission intensity of $2p_2 \rightarrow 1s_i$ ($i = 2, 3, 4$ and 5) transitions as a function of the discharge current (figure 3) show that in the presence of laser beam, the emission intensities are non-linear functions of current while in the absence of laser excitation they have a linear dependence. The enhancement in the intensity of these transitions during laser excitation indicates that the population of the $2p_2$ state increases considerably. The emission intensity of $2p_1 \rightarrow 1s_2$ also shows slight increase under laser irradiation due to collisional excitation of atoms from $2p_2$ to $2p_1$ level. It has been established that such collisional excitation or de-excitation cross-section between two levels with energy difference ΔE varies as $\exp(-\Delta E/kT)$. This implies that atoms in $2p_2$ level

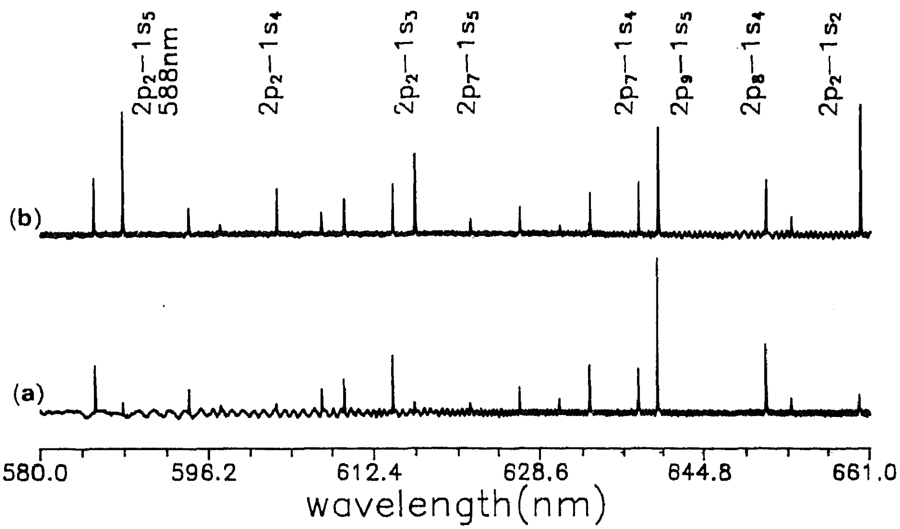

Figure 2. a) Emission spectrum of neon discharge at 5 mA and b) the same under laser irradiation at 588·2 nm.

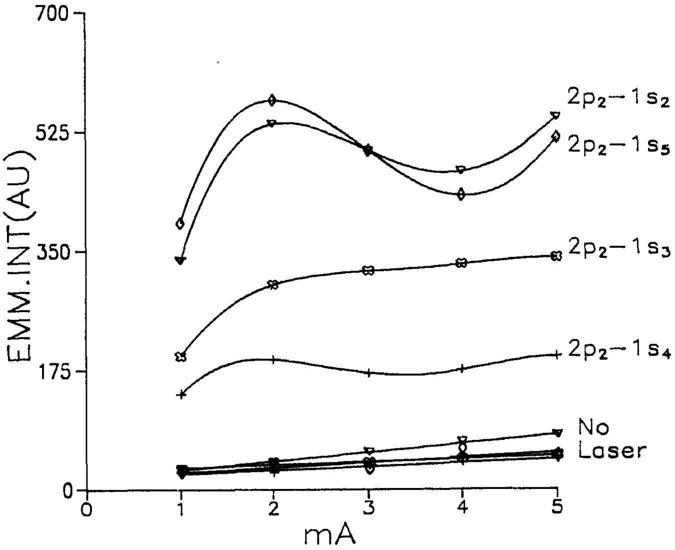

Figure 3. Dependence of the emission intensity for $2p_2 \rightarrow 1s_i$ $(i = 2, 3, 4, 5)$ transitions on discharge current.

can de-excite to nearby sub levels $(j = 3, 4, 5)$ while such collisional de-excitations to $2p_j$ levels with $j = 6, 7, 8, 9, 10$ will be less probable. It should be noted that population of $1s_5$ level will decrease due to absorption of laser light and hence the $2p_j$ manifolds arising through electron collision from $1s_5$ level viz,

$$Ne(1s_5) + e^- \rightarrow Ne(2p_j) + e^-$$

Table 1. Change in emission intensities under laser excitation at 588·2 nm and 594·5 nm with a discharge current of 5 mA.

Wavelength (nm)	Transition	$(I_L - I)/I$[a]	
		$1s_5 \to 2p_2$[b]	$^1s_5 \to 2p_4$[c]
585·2	$2p_1 \to 1s_2$	0·17	~0
588·2	$2p_2 \to 1s_5$	9·23[d]	0·23
594·5	$2p_4 \to 1s_5$	0·09	22·0[d]
597·5	$2p_5 \to 1s_5$	0·12	0·17
603·0	$2p_2 \to 1s_4$	3·33	~0
607·4	$2p_3 \to 1s_4$	−0·03	1·50
609·6	$2p_4 \to 1s_4$	0·03	5·06
614·3	$2p_6 \to 1s_5$	−0·12	0·07
616·3	$2p_2 \to 1s_3$	5·79	~0
621·7	$2p_7 \to 1s_5$	0·55	0·02
626·6	$2p_5 \to 1s_3$	0·04	1·09
630·4	$2p_6 \to 1s_4$	−0·30	−0·16
633·4	$2p_8 \to 1s_5$	−0·10	0·06
638·3	$2p_7 \to 1s_4$	0·18	0·21
640·2	$2p_9 \to 1s_5$	−0·29	−0·53
650·6	$2p_8 \to 1s_4$	−0·18	−0·39
653·2	$2p_7 \to 1s_3$	0·14	−0·04
659·9	$2p_2 \to 1s_2$	5·85	~0
667·8	$2p_4 \to 1s_2$		6·12

[a] I_L and I are emission intensities with and without laser irradiation.

[b] 10 μm and [c] 5 μm—slit width of the monochromator used for recording the spectrum.

[d] Intensity includes scattered radiation from the exciting laser at these wavelengths.

will diminish. In presence of laser irradiation for $2p_6 \to 1s_5$, $2p_6 \to 1s_4$, $2p_8 \to 1s_5$, $2p_8 \to 1s_4$ and $2p_9 \to 1s_5$ transitions decrease in intensity is observed, where a reduction in the population of $2p_j$ manifolds due to above process is large as compared to collisional de-excitation from $2p_2$ to these states. This decrease in intensity under laser excitation is predominant in the case of $2p_8 \to 1s_4$ and $2p_9 \to 1s_5$ transitions as shown in figure 2. However such decrease in population density in $2p_j$ levels ($j = 1, 3, 4, 5$) will be compensated by non-radiative transitions from $2p_2$ state. This fact is in support of the observations that the emission intensity for transitions from $2p_j$ levels ($j = 1, 3, 4, 5$) do not have any decrease under laser excitation. An exception is observed in the case of $2p_7 \to 1s_5$ transition where there is an enhancement in intensity at higher current.

Laser excitation of $1s_5 \to 2p_4$ transition (594·5 nm)

The emission and the laser-induced fluorescence spectrum of the neon discharge in the wavelength range from 580 nm to 670 nm at a discharge current of 5 mA are shown in figure 4. The emission intensity for both conditions varies linearly with the discharge current for all the observed transitions within this spectral region. The

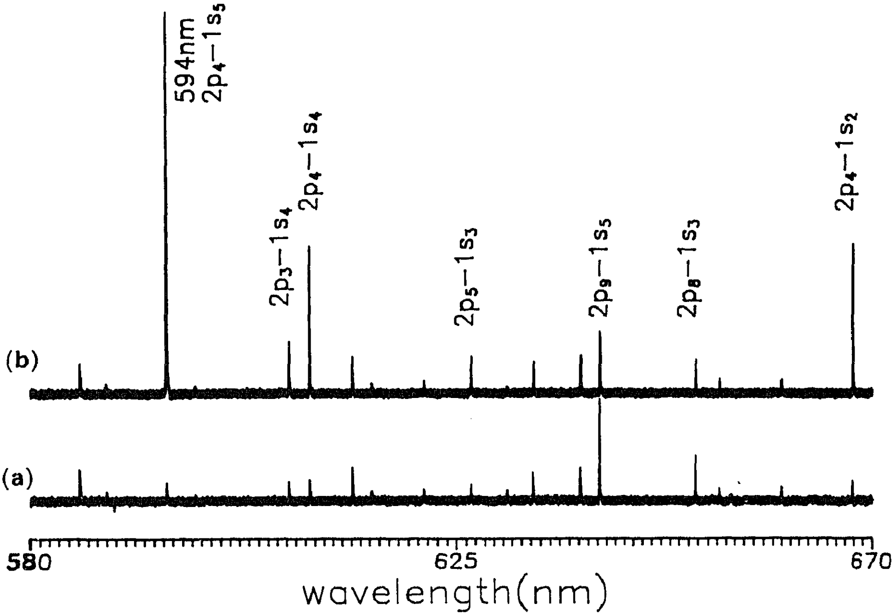

Figure 4. a) Emission spectrum of neon discharge at 5 mA and b) the same under laser irradiation at 594·5 nm.

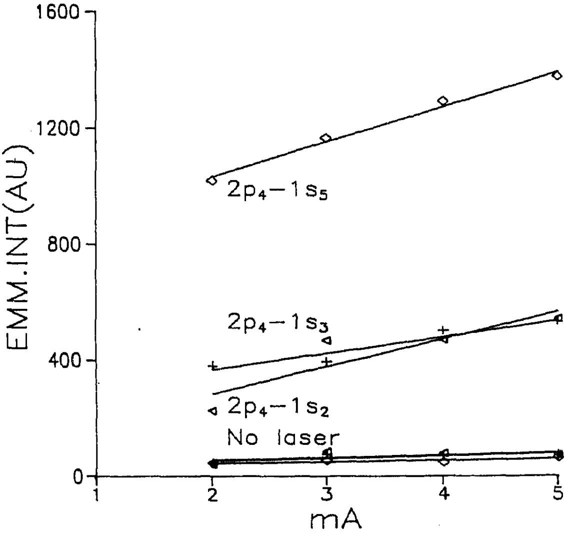

Figure 5. Dependence of the emission intensity for $2p_4 \rightarrow 1s_i$ ($i = 2, 4, 5$) transitions on discharge current.

transitions having considerable change in emission intensities during laser-on and laser-off conditions are shown in the figure 5. Laser excitation at 594·5 nm ($1s_5 \rightarrow 2p_4$) modifies the emission characteristics of transitions from $2p_4 \rightarrow 1s_i$ ($i = 2, 4$ and 5) which is obviously due to a large increase in the population of $2p_4$. For $2p_3 \rightarrow 1s_4$ and $2p_5 \rightarrow 1s_3$ transitions also the same behavior is observed while for $2p_8 \rightarrow 1s_3$, and

$2p_9 \rightarrow 1s_5$ the emission intensity during laser excitation is less than that of the unperturbed discharge. For all other transitions intensities under both conditions are more or less the same. In this case also as it is clear from table 1 that for states close to $2p_4$ the population density increases.

c) *Optogalvanic signal*

The observed OG signal for these transitions as a function of the discharge current is shown in figure 6. It is to be noted that the OG signal was measured at the line centre of these transitions by tuning the laser with an accuracy of 0·01 cm^{-1}. It is well-known that the nature of OG signal is determined mainly by the metastable concentrations. In general, the impedance of a neon discharge increases with resonant excitation of transitions starting from the $1s_3$ and $1s_5$ levels due to the depletion in these metastables and consequently in electron density and the impedance decreases in the case of transitions from $1s_2$ and $1s_4$ states which may decay radiatively to the ground state [4, 6]. Excitation at 588·2 nm and 594·5 nm corresponds to $1s_5 \rightarrow 2p_2$ and $1s_5 \rightarrow 2p_4$ transition respectively where the lower state is metastable and hence the OG signals of these transitions will be an increase in the discharge impedance or will be an equivalent decrease in current in the circuit.

These observations indicate that the major factor which influences the generation of the OG signal is the modifications in the ionization processes as a result of the perturbations in the populations of states. The laser excitation at the above wavelengths result in an increase in the population of $2p_2$ (or $2p_4$), $2s_2$ and $1s_4$ while it decreases in the case of $1s_5$ density. Thus the contributions of $1s_2$, $1s_4$ and the upper state ($2p_2$ or $2p_4$) states, which have strong radiative coupling to the lower states, are negligible whereas the role of $1s_3$ and $1s_5$ metastables are prominent in generating the OG effect. As shown in figure 6, the current dependence of OG signal corresponding to 588·2 nm and 594·5 nm differ widely. This indicates that apart from the metastable nature of the lower level, there exists other processes which will affect magnitude of the OG signal. One such process is due to the change in ionization rate as a result of collisional mixing between $2p_j$ states followed by laser irradiation which is different for these two transitions.

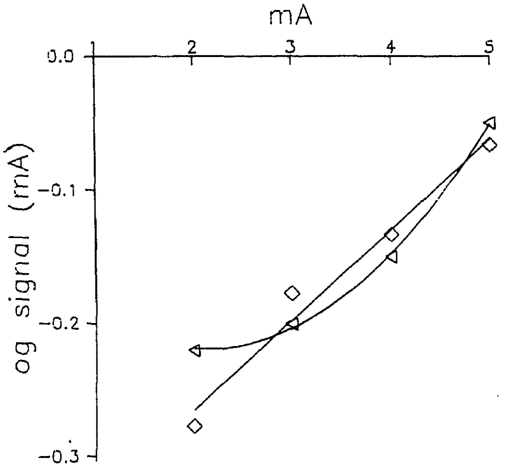

Figure 6. OG signal for $1s_5 \rightarrow 2p_2$ (□) and $1s_5 \rightarrow 2p_4$ (Δ) transition.

4. Conclusions

Modifications in the emission characteristics of a neon hollow cathode discharge due to the perturbation caused by resonant absorption of $1s_5 \rightarrow 2p_2$ and $1s_5 \rightarrow 2p_4$ transition are investigated. In both cases the emission properties are found to be altered significantly due to the changes in the population of $2p$ state by radiative and non-radiative processes. The population of metastable lower state ($1s_5$) and the nature of excitation/de-excitation path ways play an important role in generating the OG signal.

Acknowledgements

Financial assistances from MHRD and DST (India) are gratefully acknowledged. PRS is thankful to University Grants Commission (India) for research fellowship.

References

[1] R B Green, R A Keller, G G Luther, P K Schenck and J C Travis, *Appl. Phys. Lett.* **29**, 727 (1976)
[2] E F Zalewski, R A Keller and R Engleman Jr., *J. Chem. Phys.* **70**, 1015 (1979)
[3] E De Marinis and A Sasso, *J. Appl. Phys.* **63**, 649 (1988)
[4] D M Kane, *J. Appl. Phys.* **56**, 1267 (1984)
[5] A Sasso, M Ciocca and E Arimondo, *J. Opt. Soc. Am.* **B5**, 1484 (1988)
[6] G Erez, S Lavi and E Miron, *IEEE J. Quantum Electron.* **QE-15**, 1328 (1979)

PRAMANA
— journal of
physics

© Printed in India

Vol. 42, No. 5,
May 1994
pp. 435–446

Plasma-maser interaction of Langmuir wave with kinetic Alfvén wave turbulence

BIPULJYOTI SAIKIA, B K SAIKIA, S BUJARBARUA and M NAMBU*
Centre of Plasma Physics, Saptaswahid Path, Dispur, Guwahati 781 006, India
*College of General Education, Kyushu University, Ropponmatsu, Fukuoka 810, Japan

MS received 26 October 1993; revised 10 March 1994

Abstract. A theoretical study is made on the generation mechanism of Langmuir mode wave in the presence of kinetic Alfvén wave turbulence in a magnetized plasma on the basis of plasma-maser interaction. It is shown that a test high frequency Langmuir mode wave is unstable in the presence of low frequency kinetic Alfvén wave turbulence. The growth of the Langmuir wave occurs due to direct and polarization coupling terms. Because of the universal existence of the kinetic Alfvén waves in large scale plasmas, the results have potential importance in space and astrophysical radiation processes.

Keywords. Weak turbulence theory; wave particle interaction; resonant and nonresonant waves; growth rate.

PACS No. 52·35

1. Introduction

According to the recent weak turbulence theory [1], the lowest order mode–mode coupling processes are composed of three parts. The first two processes are the three waves resonance and the nonlinear scattering resonance; the conditions for which are $\mathbf{K}-\mathbf{k}=\mathbf{K}'$, $\Omega-\omega=\Omega'$ and $\Omega-\omega-(K_\parallel-k_\parallel)v_\parallel+a\Omega_e=0$ respectively. These processes are extensively studied by many authors [2]. The third process which we consider here is the plasma-maser. The plasma-maser effect occurs when nonresonant as well as resonant plasma oscillations are present. The resonant waves are those for which the Cherenkov resonance condition $\omega-k_\parallel v_\parallel=0$ is satisfied, while the nonresonant waves are those for which both the Cherenkov and scattering conditions are not satisfied: $\Omega-K_\parallel v_\parallel\neq 0$ and $\Omega-\omega-(K_\parallel-k_\parallel)v_\parallel+a\Omega_e\neq 0$. It corresponds to vortex correction, and is effective without electron population inversion which differs it markedly from other maser effects (e.g., inverse nonlinear Landau interaction). The most important characteristics of plasma-maser is the energy up-conversion from the resonant low frequency mode to the non-resonant high frequency mode in open plasma system where energy and particle sources are available [3] (in the form of continuous beam injection, external magnetic field etc.). For closed system without magnetic field, the plasma-maser invariably cancels out with the reverse absorption process due to quasilinear process.

In recent years, there has been an increasing interest in theoretical, experimental and observational studies in plasma-maser [4, 5, 6]. This new mode coupling process has been applied to auroral kilometric radiation, type III radio emission, chorus related electrostatic bursts, Jovian kilometric radiation and Saturnian kilometric radiation. The nature of plasma-maser based on quantum electrodynamical methods is investigated [7]. The nonlinear effect of the resonant and non-resonant modes simultaneously on the evolution of electron distribution function, known as the inverse plasma-maser, has also been studied [8]. Recently, the basic physics involved in the process, i.e., the energy and momentum conservation relations among the waves and the electrons is also investigated [4, 9]. In [9], it has been shown that the energy and momentum conservation relations between particle kinetic energy and wave energy is satisfied for the plasma-maser process, while the Manley–Rowe relation for plasma waves is violated and as a result an efficient energy up-conversion from the low frequency resonant mode to high frequency nonresonant mode becomes possible. The violation of Manley–Rowe relation for open system is already mentioned by Krlin [10].

Almost all the previous studies in plasma-maser, except [6], electrostatic turbulences are considered. But, due to its small scale length (on the order of Debye length), electrostatic wave is not dominant turbulent fluctuations in cosmic plasmas. On the other hand, magnetohydrodynamic waves have a large scale size because the parallel wavelength is comparable to the system size. MHD turbulence occurs in laboratory settings such as fusion confinement systems (e.g., reverse-field pinch) and astrophysical systems (e.g., solar corona, earth's magnetosheath etc.). Here, we show that nonlinear interaction of kinetic Alfvén wave turbulence with a test high frequency electrostatic (Langmuir) wave can lead to amplification of the high frequency wave through the plasma-maser interaction.

We study the interaction between stationary kinetic Alfven wave and electrons in an open system. Electrons that have velocities close to the phase velocity of kinetic Alfvén wave experience mixed mode perturbations between kinetic Alfvén wave and electrostatic waves. As a result, the growth of the test electrostatic wave occur through the plasma-maser process.

The organization of the paper is as follows. In §2, the formulation and basic assumptions of the plasma-maser process are given and the nonlinear dielectric constant of the Langmuir mode in presence of the kinetic Alfvén wave turbulence is derived. The nonlinear dielectric constant is composed of two parts: direct and polarization mode coupling terms. The growth rate of the Langmuir mode through the form of the Landau resonance is obtained for direct and polarization terms respectively in §3. Finally, §4 contains a discussion on the study and its potential importance and applicability.

2. Formulations

We derive the dispersion relation of the Langmuir mode in the presence of stationary kinetic Alfvén wave turbulence propagating in the $x-z$ plane with wave vector $\mathbf{k}(=k_\perp, 0, k_\parallel)$. The wave fields are $\mathbf{E}_l(=E_{l\perp}, 0, E_{l\parallel})$ and $\mathbf{B}_l(=0, B_{ly}, 0)$. The kinetic Alfvén wave turbulence is assumed to be driven by electron beam. The electron distribution function is

$$f_{oe}(v)=\left(\frac{m}{2\pi T_e}\right)^{3/2}\exp\left(-\frac{mv_\perp^2}{2T_e}\right)\exp\left(-\frac{m(v_\parallel-v_0)^2}{2T_e}\right), \tag{1}$$

where the symbols have their usual meaning. We assume that the electron beam is injected continuously from system outside to keep the distribution function stationary.

Thus, in spite of the quasilinear interaction between kinetic Alfvén wave and electrons, the electron distribution function remains stationary. This is the main reason why the Manley–Rowe relation is violated for open plasma system.

The basic equations are the Vlasov-Poisson equations

$$\left[\frac{\partial}{\partial t} + \mathbf{v}\cdot\frac{\partial}{\partial \mathbf{r}} - \frac{e}{m}\left(\mathbf{E}(\mathbf{r},t) + \frac{\mathbf{v}\times\mathbf{B}(\mathbf{r},t)}{c}\right)\cdot\frac{\partial}{\partial \mathbf{v}}\right] f_e(\mathbf{r},\mathbf{v},t) = 0, \tag{2}$$

$$\nabla\cdot\mathbf{E}(\mathbf{r},t) = -4\pi e\int f_e(\mathbf{r},\mathbf{v},t)\,\mathrm{d}\mathbf{v}, \tag{3}$$

where the notations are standard. According to the linear response theory of turbulent plasma, the unperturbed electron distribution function and fields are,

$$\begin{aligned} F_{oe} &= f_{oe} + \varepsilon f_{1e} + \varepsilon^2 f_{2e}, \\ \mathbf{E}_{oe} &= \varepsilon \mathbf{E}_l, \quad \mathbf{B}_{oe} = \mathbf{B}_0 + \varepsilon \mathbf{B}_l, \end{aligned} \tag{4}$$

where ε ($\ll 1$) is a small parameter associated with the turbulence fields and $\mathbf{B}_0 (= 0, 0, B_0)$ is the external magnetic field.

We assume that the system is open. Further, the fluctuation level of the kinetic Alfvén wave is assumed to be a given quantity and the interaction between the low frequency Alfvén wave turbulence and the high frequency Langmuir mode is considered through resonant electrons. With the assumption that the density gradient be negligibly small, the linear response of the electron distribution function (f_{1e}) due to the kinetic Alfvén wave reduces to,

$$f_{1e}(\mathbf{k},\omega) = \frac{ie}{m}\frac{1}{\omega - k_\parallel v_\parallel + i0}\,\mathrm{E}_{l\parallel}(\mathbf{k},\omega)\frac{\partial}{\partial v_\parallel} f_{oe}, \tag{5}$$

where $i0$ is the small imaginary part.

We now perturb the quasi-steady state by a high frequency test Langmuir mode wave field $\mu\delta\mathbf{E}_h$ with a propagation vector $\mathbf{K}(=0,0,K)$ and a frequency Ω, here $\mu \ll \varepsilon$. Thus the total perturbed electric and magnetic fields and the electron distribution functions are,

$$\begin{aligned} \delta\mathbf{E} &= \mu\delta\mathbf{E}_h + \mu\varepsilon\delta\mathbf{E}_{lh}, \\ \delta\mathbf{B} &= 0 + \mu\varepsilon\delta\mathbf{B}_{lh}, \\ \delta f &= \mu\delta f_h + \mu\varepsilon\delta f_{lh} + \mu\varepsilon^2\Delta f. \end{aligned} \tag{6}$$

Linearizing the Vlasov equation (2) to the orders μ, $\mu\varepsilon$ $\mu\varepsilon^2$ we obtain,

$$P\delta f_h - \frac{e}{m}\delta\mathbf{E}_h\cdot\frac{\partial}{\partial \mathbf{v}} f_{oe} = 0 \tag{7}$$

$$\begin{aligned} P\delta f_{lh} - \frac{e}{m}\left(\mathbf{E}_l + \frac{\mathbf{v}\times\mathbf{B}_l}{c}\right)\cdot\frac{\partial}{\partial \mathbf{v}}\delta f_h - \frac{e}{m}\delta\mathbf{E}_h\cdot\frac{\partial}{\partial \mathbf{v}} f_{1e} \\ - \frac{e}{m}\left(\delta\mathbf{E}_{lh} + \frac{\mathbf{V}\times\delta\mathbf{E}_{lh}}{c}\right)\cdot\frac{\partial}{\partial \mathbf{v}} f_{oe} = 0 \end{aligned} \tag{8}$$

$$P\Delta f - \frac{e}{m}\left\langle\left(\mathbf{E}_l + \frac{\mathbf{v}\times\mathbf{B}_l}{c}\right)\cdot\frac{\partial}{\partial\mathbf{v}}\delta f_{lh}\right\rangle - \frac{e}{m}\left\langle\left(\delta\mathbf{E}_{lh} + \frac{\mathbf{v}\times\delta\mathbf{B}_{lh}}{\mathbf{c}}\right)\cdot\frac{\partial}{\partial\mathbf{v}}f_{1e}\right\rangle$$
$$= 0 \tag{9}$$

where $\langle\cdots\rangle$ means average over the kinetic Alfvén waves and P is the operator,

$$P \equiv \frac{\partial}{\partial t} + \mathbf{v}\cdot\frac{\partial}{\partial\mathbf{r}} - \frac{e}{m}\mathbf{v}\times\mathbf{B}_0\cdot\frac{\partial}{\partial\mathbf{v}}$$

In (4), (6) and (9), we omitted the second-order field quantities, which can be justified under random phase approximations.

Taking Fourier transform in space and time for the various quantities, we obtain from (3) the non-linear dielectric constant of the Langmuir mode in the presence of the kinetic Alfvén wave turbulence as (see Appendix),

$$\varepsilon_h(\mathbf{K},\Omega) = \varepsilon_0(\mathbf{K},\Omega) + \varepsilon_d(\mathbf{K},\Omega) + \varepsilon_p(\mathbf{K},\Omega), \tag{10}$$

where $\varepsilon_0(\mathbf{K},\Omega)$ is the linear part given by

$$\varepsilon_0(\mathbf{K},\Omega) = 1 + \frac{\omega_{pe}^2}{K}\int 2\pi v_\perp\,\mathrm{d}v_\perp\,\mathrm{d}v_\parallel\frac{1}{\Omega - Kv_\parallel}\frac{\partial}{\partial v_\parallel}f_{oe}, \tag{11}$$

$\varepsilon_d(\mathbf{K},\Omega)$ is the direct mode coupling term given by

$$\begin{aligned}\varepsilon_d(\mathbf{K},\Omega) = {} & -\frac{\omega_{pe}^2}{K}\left(\frac{e}{m}\right)^2\sum_{\mathbf{k}}|E_{l\parallel}(\mathbf{k})|^2\sum_{a=-\infty}^{\infty}\int 2\pi v_\perp\,\mathrm{d}v_\perp\,\mathrm{d}v_\parallel\frac{1}{\Omega - Kv_\parallel}\\ & \times\left[\frac{\partial}{\partial v_\parallel} + \frac{a\Omega_e}{v_\perp\omega}\left(v_\parallel\frac{\partial}{\partial v_\perp} - v_\perp\frac{\partial}{\partial v_\parallel}\right)\right]\frac{J_a^2(k_\perp v_\perp/\Omega_e)}{\Omega - \omega - (K - k_\parallel)v_\parallel + a\Omega_e}\\ & \times\frac{\partial}{\partial v_\parallel}\frac{1}{k_\parallel v_\parallel - \omega + i0}\frac{\partial}{\partial v_\parallel}f_{oe} - \frac{\omega_{pe}^2}{K}\left(\frac{e}{m}\right)^2\sum_{\mathbf{k}}[E_{l\perp}(\mathbf{k})\mathbf{E}_{l\parallel}(-\mathbf{k})]\\ & \times\sum_{a=-\infty}^{+\infty}\int 2\pi v_\perp\,\mathrm{d}v_\perp\,\mathrm{d}v_\parallel\frac{1}{\Omega - Kv_\parallel}\left[\left(1 - \frac{k_\parallel v_\parallel}{\omega}\right)\frac{\partial}{\partial v_\perp} + \frac{k_\parallel v_\perp}{\omega}\frac{\partial}{\partial v_\parallel}\right]\\ & \times\frac{J_a^2(k_\perp v_\perp/\Omega_e)}{\Omega - \omega - (K - k_\parallel)v_\parallel + a\Omega_e}\frac{a\Omega_e}{k_\perp v_\perp}\frac{\partial}{\partial v_\parallel}\frac{1}{k_\parallel v_\parallel - \omega + i0}\frac{\partial}{\partial v_\parallel}f_{oe}\end{aligned} \tag{12}$$

and $\varepsilon_p(\mathbf{K},\Omega)$ is the polarization mode coupling term given by

$$\begin{aligned}\varepsilon_p(\mathbf{K},\Omega) = {} & \frac{\omega_{pe}^2}{K}\left(\frac{e}{m}\right)^2\sum_{\mathbf{k}}\frac{\omega_{pe}^2(\Omega - \omega)}{R(\mathbf{K} - \mathbf{k})[(\Omega - \omega)^2 - c^2k_\perp^2]}[|E_{l\perp}(\mathbf{k})|^2(A\times B)\\ & + |E_{l\parallel}(\mathbf{k})|^2[(C + D)\times(F + G)] + [E_{l\perp}(\mathbf{k})E_{l\parallel}(-\mathbf{k})][A\times(F + G)]\\ & + [E_{l\parallel}(\mathbf{k})E_{l\perp}(-\mathbf{k})][(C + D)\times B]]\end{aligned} \tag{13}$$

where,

$$A = \int 2\pi v_\perp\,\mathrm{d}v_\perp\,\mathrm{d}v_\parallel\frac{1}{\Omega - Kv_\parallel}\left[\left(1 - \frac{k_\parallel v_\parallel}{\omega}\right)\frac{\partial}{\partial v_\perp} - \frac{k_\parallel v_\perp}{\omega}\frac{\partial}{\partial v_\parallel}\right]$$

$$\times \frac{J_a^2}{\Omega-\omega-(K-k_\|)v_\| + a\Omega_e} \frac{a\Omega_e}{k_\perp v_\perp}\left[\frac{\partial}{\partial v_\|} - \frac{a\Omega_e}{v_\perp(\Omega-\omega)} \times \left(v_\| \frac{\partial}{\partial v_\perp} - v_\perp \frac{\partial}{\partial v_\|}\right)\right] f_{oe}$$

$$B = \int 2\pi v_\perp v_\| \mathrm{d}v_\perp \mathrm{d}v_\| \frac{J_a^2}{\Omega-\omega-(K-k_\|)v_\| + a\Omega_e} \frac{a\Omega_e}{k_\perp v_\perp} \times \left[\left(1-\frac{k_\| v_\|}{\omega}\right)\frac{\partial}{\partial v_\perp} - \frac{k_\| v_\perp}{\omega}\frac{\partial}{\partial v_\|}\right]\frac{1}{\Omega-Kv_\|}\frac{\partial}{\partial v_\|} f_{oe}$$

$$C = \int 2\pi v_\perp \mathrm{d}v_\perp \mathrm{d}v_\| \frac{1}{\Omega-Kv_\|}\left[\frac{\partial}{\partial v_\|} + \frac{a\Omega_e}{v_\perp \omega}\left(v_\| \frac{\partial}{\partial v_\perp} - v_\perp \frac{\partial}{\partial v_\|}\right)\right] \times \frac{J_a^2(k_\perp v_\perp/\Omega_e)}{\Omega-\omega-(K-k_\|)v_\| + a\Omega_e}\left[\frac{\partial}{\partial v_\|} - \frac{a\Omega_e}{v_\perp(\Omega-\omega)}\left(v_\| \frac{\partial}{\partial v_\perp} - v_\perp \frac{\partial}{\partial v_\|}\right)\right] f_{oe}$$

$$D = \int 2\pi v_\perp \mathrm{d}v_\perp \mathrm{d}v_\| \frac{1}{\Omega-Kv_\|}\frac{\partial}{\partial v_\|}\frac{1}{\omega-k_\| v_\| + i0}\frac{\partial}{\partial v_\|} f_{oe}$$

$$F = \int 2\pi v_\perp v_\| \mathrm{d}v_\perp \mathrm{d}v_\| \frac{J_a^2(k_\perp v_\perp/\Omega_e)}{\Omega-\omega-(K-k_\|)v_\| + a\Omega_e}\left[\frac{\partial}{\partial v_\|} + \frac{a\Omega_e}{v_\perp \omega} \times \left(v_\| \frac{\partial}{\partial v_\perp} - v_\perp \frac{\partial}{\partial v_\|}\right)\right]\frac{1}{\Omega-Kv_\|}\frac{\partial}{\partial v_\|} f_{oe}$$

$$G = \int 2\pi v_\perp v_\| \mathrm{d}v_\perp \mathrm{d}v_\| \frac{J_a^2(k_\perp v_\perp/\Omega_e)}{\Omega-\omega-(K-k_\|)v_\| + a\Omega_e}\frac{\partial}{\partial v_\|}\frac{1}{k_\| v_\| - \omega + i0}\frac{\partial}{\partial v_\|} f_{oe} \tag{14}$$

$$R(\mathbf{K}-\mathbf{k}) = 1 + \frac{\omega_{pe}^2(\Omega-\omega)}{(\Omega-\omega)^2 - c^2 k_\perp^2}\int 2\pi v_\perp v_\| \mathrm{d}v_\perp \mathrm{d}v_\| \frac{J_a^2(k_\perp v_\perp/\Omega_e)}{\Omega-\omega-(K-k_\|)v_\| + a\Omega_e} \times \left[\frac{\partial}{\partial v_\|} + \frac{a\Omega_e}{k_\perp v_\perp}\left(v_\| \frac{\partial}{\partial v_\perp} - v_\perp \frac{\partial}{\partial v_\|}\right)\right] f_{oe}. \tag{15}$$

In evaluating (10), according to the linear response theory of a turbulent plasma, we keep linear terms with respect to μ up to $\mu\varepsilon^2$. The terms of order ε^2 and higher order give nonlinear frequency shift for kinetic Alfvén wave which can be neglected because $\Omega \gg \omega$.

3. Plasma-maser interaction

We consider the plasma-maser interaction between electron and kinetic Alfvén turbulence. The condition for the plasma-maser is $\omega = k_\| v_\|$, $\Omega > Kv_\|$. We first estimate the linear part of the dielectric constant of Langmuir mode (11). This can be expressed as,

$$\varepsilon_0(\mathbf{K},\Omega) \simeq 1 - \left(\frac{\omega_{pe}}{\Omega}\right)^2. \tag{16}$$

With $\varepsilon_0(\mathbf{K},\Omega)=0$, we get the linear dispersion relation for Langmuir mode. The growth rate of Langmuir mode is given by

$$\gamma(\mathbf{K},\Omega) = -\left.\frac{\operatorname{Im}\varepsilon_h(\mathbf{K},\Omega)}{\dfrac{\partial}{\partial\Omega}\varepsilon_0(\mathbf{K},\Omega)}\right|_{\Omega=\Omega_r}, \tag{17}$$

where Im shows that imaginary part of the dielectric constant and Ω_r is the real frequency of the Langmuir mode. We obtain from (16),

$$\frac{\partial}{\partial\Omega}\varepsilon_0(\mathbf{K},\Omega) \simeq 2\frac{\omega_{pe}^2}{\Omega^3} \simeq \frac{2}{\omega_{pe}}. \tag{18}$$

3.1 *Growth rate due to the direct coupling term*

As is well-known, the plasma-maser effect is particularly important for strongly magnetised plasma, $\Omega_e > \omega_{pe}$. Here we estimate the imaginary part of the direct mode coupling term, (12). In estimating (12) [and (13) as well] we keep contributions only for $a=0$, because for kinetic Alfvén wave, the finite Larmor radius effect for electrons is neglected [11], i.e., $k_\perp \rho_e \ll 1$. Furthermore, for strongly magnetized plasma considered here ($\Omega_e > \omega_{pe}$), the dominant contribution comes from $a=0$. The terms which are neglected in estimating (12) and (13) can be shown to be smaller by a factor of the order of $(\omega_{pe}/\Omega_e)^2$. Thus (12) reduces to,

$$\begin{aligned}\varepsilon_d(\mathbf{K},\Omega) = -\frac{\omega_{pe}^2}{K}\left(\frac{e}{m}\right)^2 \sum_{\mathbf{k}} |E_{l\parallel}(\mathbf{k})|^2 \int 2\pi v_\perp \,\mathrm{d}v_\perp \,\mathrm{d}v_\parallel \frac{1}{\Omega - K v_\parallel} \\ \times \frac{\partial}{\partial v_\parallel}\frac{J_0^2}{\Omega - \omega - (K - k_\parallel)v_\parallel}\frac{\partial}{\partial v_\parallel}\frac{1}{k_\parallel v_\parallel - \omega + i0}\frac{\partial}{\partial v_\parallel} f_{oe}.\end{aligned} \tag{19}$$

From (19) we evaluate the imaginary part as,

$$\operatorname{Im}\varepsilon_d(\mathbf{K},\Omega) = -b\sqrt{\pi}\sum_{\mathbf{k}} \frac{|E_{l\parallel}(\mathbf{k})|^2}{4\pi N T_e}\frac{3K}{|k_\parallel|}\frac{v_A^* - v_0}{v_e}\exp\left[-\left(\frac{v_A^* - v_0}{v_e}\right)^2\right]. \tag{20}$$

Here,

$$b = \int 2\pi v_\perp J_0^2 f_{oe}(v_\perp)\,\mathrm{d}v_\perp \tag{21}$$

Inserting (20) in (17), we obtain,

$$\frac{\gamma_d}{\omega_{pe}} = \frac{3}{2}b\sqrt{\pi}\sum_{\mathbf{k}} \frac{|E_{l\parallel}(\mathbf{k})|^2}{4\pi N T_e}\frac{K}{|k_\parallel|}\frac{v_A^* - v_0}{v_e}\exp\left[-\left(\frac{v_A^* - v_0}{v_0}\right)^2\right]. \tag{22}$$

The normalized turbulence energy of Alfvén wave (W_T) is given by

$$W_T = \sum_{\mathbf{k}} \frac{|B_{ly}|^2}{16\pi N T_e}, \tag{23}$$

where B_{ly} is the magnetic field of the kinetic Alfvén wave. Inserting the relation between B_{ly} and $E_{l\|}$, we obtain,

$$W_T = \sum_{\mathbf{k}} \frac{|E_{l\|}(\mathbf{k})|^2}{16\pi N T_e} \left(\frac{k_\perp}{k_\|}\right)^2 \left(\frac{c}{v_A^{\neq}}\right)^2 (Q+1)^2. \tag{24}$$

Here Q is related to the amplitude ratio of the electric field components of the kinetic Alfvén wave:

$$\frac{E_{l\|}(\mathbf{k})}{E_{l\perp}(\mathbf{k})} = -\frac{k_\|}{k_\perp}\frac{T_e}{T_i}[1 - I_0(\beta_i)\exp(-\beta_i)] \equiv \frac{k_\|}{k_\perp} Q^{-1}. \tag{25}$$

Here, T_e, T_i and I_0 are electron, ion temperatures and modified Bessel function respectively; $\beta_i = (k_\perp \rho_i)^2/2$ and ρ_i is ion gyroradius.

Thus in terms of normalized turbulence energy of the kinetic Alfvén wave, (22) reduces to,

$$\frac{\gamma_d}{\omega_{pe}} = 6b\sqrt{\pi}\sum_{\mathbf{k}} W_T \left(\frac{k_\|}{k_\perp}\right)^2 \left(\frac{v_A^*}{c}\right)^2 (Q+1)^{-2} \frac{K}{|k_\||} \times \frac{v_A^* - v_0}{v_e} \exp\left[-\left(\frac{v_A^* - v_0}{v_e}\right)^2\right] \tag{26}$$

Thus, growth occurs $\gamma_d > 0$ for $\Omega/K < 0$ under the condition $v_0 > v_A^*$, in presence of kinetic Alfvén wave turbulence.

3.2 *Growth rate due to polarization coupling term*

Next, we estimate the growth rate from the polarization mode coupling term (13). This contribution to the growth rate vanishes only for unmagnetized system. For an open system, such as a magnetized plasma, the polarization mode coupling gives the dominant contribution in plasma-maser instability. After a lengthy, but straightforward calculations, we find that the dominant imaginary part contribution of (13) comes from $|E_{l\|}(\mathbf{k})|^2 \operatorname{Im}[(C+D)\times(F+G)]$. With $a = 0$, C, D, F and G reduces to [from (14)]

$$C = \int 2\pi v_\perp \,\mathrm{d}v_\perp \,\mathrm{d}v_\| \frac{1}{\Omega - Kv_\|}\frac{\partial}{\partial v_\|}\frac{J_0^2}{\Omega - \omega - (K - k_\|)v_\|}\frac{\partial}{\partial v_\|} f_{oe}$$

$$D = \int 2\pi v_\perp \,\mathrm{d}v_\perp \,\mathrm{d}v_\| \frac{1}{\Omega - Kv_\|}\frac{\partial}{\partial v_\|}\frac{1}{\omega - k_\| v_\| + i0}\frac{\partial}{\partial v_\|} f_{oe}$$

$$F = \int 2\pi v_\perp v_\| \,\mathrm{d}v_\perp \,\mathrm{d}v_\| \frac{J_0^2}{\Omega - \omega - (K - k_\|)v_\|}\frac{\partial}{\partial v_\|}\frac{1}{\Omega - Kv_\|}\frac{\partial}{\partial v_\|} f_{oe}$$

$$G = \int 2\pi v_\perp v_\| \,\mathrm{d}v_\perp \,\mathrm{d}v_\| \frac{J_0^2}{\Omega - \omega - (K - k_\|)v_\|}\frac{\partial}{\partial v_\|}\frac{1}{k_\| v_\| - \omega + i0}\frac{\partial}{\partial v_\|} f_{oe}. \tag{27}$$

It is easy to show that,

$$\operatorname{Im}(C+D)\times(F+G)] = \frac{3(\Omega-\omega)}{\Omega^5}(1-b^2)\frac{m\sqrt{\pi}}{T_e}\frac{K^2}{|k_\||}\frac{v_A^* - v_0}{v_e} \times \exp\left[-\left(\frac{v_A^* - v_0}{v_e}\right)^2\right]. \tag{28}$$

Next, we estimate $R(\mathbf{K}-\mathbf{k})$. For $\Omega > \omega$, (15) gives to the lowest order,

$$\frac{1}{R(\mathbf{K}-\mathbf{k})[(\Omega-\omega)^2 - c^2 k_\perp^2]} \approx \frac{1}{c^2 k_\perp^2}. \tag{29}$$

From (17), (28) and (29) we obtain the growth rate due to the polarization term as,

$$\frac{\gamma_p}{\omega_{pe}} = 12\sqrt{\pi}(1-b^2)\sum_{\mathbf{k}} W_T (Q+1)^{-2} \frac{K}{|k_\parallel|}\left(\frac{k_\parallel}{k_\perp}\right)^2 \left(\frac{k_e}{k_\perp}\right)^2 \left(\frac{v_e}{c}\right)^2 \times \left(\frac{v_A^*}{c}\right)^2 \left(\frac{v_A^* - v_0}{v_e}\right) \exp\left[-\left(\frac{v_A^* - v_0}{v_e}\right)^2\right] \tag{30}$$

for strongly magnetized plasma. Here W_T is the normalized turbulence energy of the kinetic Alfvén wave [eq. (24)], and k_e is the electron Debye wave number. Since $b \ll 1$, for $k_\perp \rho_e \ll 1$, $1-b^2$ is always a positive quantity. Accordingly, a Langmuir wave with negative phase velocity ($\Omega/K < 0$) always grows in the presence of kinetic Alfvén wave turbulence with $v_0 > v_A^*$. Equations (26) and (30) are the main results of our investigation.

It is straightforward to compare the magnitudes of the two growth rates, equations (26) and (30):

$$R = \frac{\gamma_p}{\gamma_d} = 2\frac{1-b^2}{b}\left(\frac{k_e}{k_\perp}\right)^2 \left(\frac{v_e}{c}\right)^2.$$

For typical plasma parameters $k_\perp \rho_e = 0{\cdot}5$, $k_e/k_\perp = 10^3$, $v_e/c = 0{\cdot}1$, we find that $R \gg 1$, and therefore, we conclude that the polarization term gives the main destabilizing effect in the plasma-maser interaction. As an illustration of our process, we estimate the dominant contribution to the growth rate. Taking typical plasma parameters and MHD data [6], $k_\perp/k_\parallel = 10$, $v_A^{\neq}/c = 0{\cdot}01$, $K/k_\parallel = 10^2$ and $Q = 1{\cdot}5$, we obtain $\gamma_p/\omega_{pe} \approx 10^{-1} W_T$.

4. Discussion

The stability of stationary kinetic Alfvén wave turbulence driven by a weak electron beam in an open plasma system against a test high frequency nonresonant wave is studied. It is shown that the growth of the high frequency wave occurs through the plasma-maser interaction between beam electrons and the kinetic Alfvén wave. The growth originates from two processes, viz., direct and polarization mode coupling. In contrast to the ion acoustic turbulence case [1], where $\gamma/\omega_{pe} \approx (m/M)^{1/2}(kK/k_e^2) W_T \ll W_T$, the growth rate with MHD wave turbulence is large, because here $\gamma/\omega_{pe} \approx 10^{-1} W_T$. Accordingly, the plasma-maser interaction of Langmuir wave with kinetic Alfvén wave turbulence considered in this paper has a large growth rate in contrast to earlier results based on electrostatic turbulence.

The plasma-maser is one of the three mode–mode coupling processes in plasmas, the other two being the three-wave resonant interaction and the nonlinear Landau interaction. These belong to the lowest order mode-coupling processes, and potentially give same order contribution to the growth rate. Following the prediction of the plasma-maser effect, the reverse absorption process was sought for some time.

Recently, it has been pointed out that plasma-maser emission, which comes from the imaginary part of the nonlinear dielectric constant, $\mathrm{Im}\,\varepsilon_h(\mathbf{K},\Omega)$, is accompanied by absorption due to the quasilinear effect, $\partial^2\varepsilon_0(\mathbf{K},\Omega,f_{oe}(t))/2\partial\Omega\partial t$. For closed system there is exact cancellation between the above two effects [3]. In contrast, plasma-maser is effective in open system where energy and momentum sources and sinks are available. Furthermore, for a magnetized plasma with an external magnetic field, cancellation between emission and absorption processes does not occur, since the presence of the magnetic field is equivalent to externally driven rotation. From this point of view the magnetized plasma is an open system.

Here we comment on the direct and polarization term contributions to the growth rate in the plasma-maser process in unmagnetized and magnetized plasmas. It was expected that plasma-maser process depends on the nature of polarization of the interacting waves in addition to the external environment of the system, and the polarization term was shown to contribute to the process even for unmagnetized plasma [12]. But the mistake was clarified in a recent communication [13]. This paper shows that for unmagnetized plasma ($b = 1$), polarization contribution to the growth rate vanishes [see (30)]. In other words, irrespective of the fact that whether the interacting waves are longitudinal or transverse, only the direct coupling term contributes to the growth rate for unmagnetized plasma. Accordingly, the energy (momentum) source of the process lies in the external environment only. Recently, Nambu *et al* [4] examined the transition from magnetized to unmagnetized plasma and showed that for pure nonresonant test wave $(\mathbf{K},\Omega)$ the polarization coupling term due to plasma-maser vanishes for unmagnetized plasma.

The kinetic Alfvén wave was introduced by Hasegawa and Chen in relation to plasma heating [14]. It can be excited by a MHD surface wave through a resonant mode conversion process and is shown to cause electron acceleration which may be applicable to aurora formation [15]. The kinetic Alfvén wave can also be generated by the drift wave instability in a plasma with β larger than the electron to ion mass ratio. Further, the kinetic Alfvén wave has a scale length of MHD waves in the direction parallel to the magnetic field and a scale length of ion gyroradius in the perpendicular direction. Hence the scale size of a plasma volume affected by the kinetic Alfvén wave is much larger than the scale sizes of plasma volumes affected by either electrostatic turbulence or cyclotron wave turbulence. Due to these reasons, the existence of such wave is considered to be an universal property of large scale plasmas [16].

In this work, we have considered the plasma-maser process including a test electrostatic wave for an open plasma system with a magnetic field. It is shown that kinetic Alfvén wave turbulence can radiate unstable Langmuir mode. The growth rate of the unstable Langmuir mode is given by (26) [direct coupling term] and (30) [polarization coupling term]. Our results and mechanism have potential importance in explaining electrostatic turbulences occurring in the magnetosheath, the generation of plasma wave in the earth's bowshock and numerous other astrophysical radiation processes. This point may be appreciated from the following observation. It is well known that for nonlinear scattering resonance with $a = 0$ $(\Omega - \omega - (K - k_\parallel)v_\parallel = 0)$, $\Omega \sim \omega_{pe} \gg \omega$ and $K \ll k_\parallel$, one finds $k_\parallel \lambda_{De} \approx 1$ and $\beta \approx m_e/m_i$. On the other hand, for plasma-maser, one gets $k_\parallel \sim \omega/v_A \ll \Omega_i/v_A = \omega_{pi}/c$. Since $\omega_{pi}/c \ll 1/\lambda_{De}$, the parallel wavelength which satisfies the plasma-maser is much larger than that of the nonlinear scattering resonance. This is the reason why plasma-maser including the kinetic Alfvén wave is important for cosmic plasmas. The primary condition necessary for this mechanism is the presence of a turbulence field from which energy can be transferred to the radiation field via resonant electrons.

Acknowledgement

One of the authors (BS) acknowledges the financial support from the CSIR, India, in performing this work.

Appendix

Here we show a brief derivation of (10). The unperturbed orbits for electrons are,

$$\begin{aligned} x' &= x - \frac{v_\perp}{\Omega_e}\sin(\phi - \Omega_e\tau) + \frac{v_\perp}{\Omega_e}\sin\phi \\ y' &= y + \frac{v_\perp}{\Omega_e}\cos(\phi - \Omega_e\tau) - \frac{v_\perp}{\Omega_e}\cos\phi \\ z' &= z + v_\parallel \tau. \end{aligned} \tag{A1}$$

The Fourier component of the high frequency electron number density modification from (7) is,

$$\delta f_h(\mathbf{K},\Omega) = \frac{ie}{m}\frac{1}{\Omega - Kv_\parallel}\,\delta E_h(\mathbf{K},\Omega)\frac{\partial}{\partial v_\parallel} f_{oe} \tag{A2}$$

In a similar manner, we get from (8) and (9),

$$\begin{aligned} \delta f_{lh}(\mathbf{K}-\mathbf{k},\Omega-\omega) = {} & \frac{ie}{m}\sum_{a,b}\frac{J_b(k_\perp v_\perp/\Omega_e)\exp[i(a-b)\phi]}{(\Omega-\omega)-(K-k_\parallel)v_\parallel + a\Omega_e} \\ & \times \Bigg\{ E_{l\perp}(\mathbf{k}')\frac{(J_{a+1}+J_{a-1})}{2}\left[\frac{\partial}{\partial v_\perp} - \frac{k'_\parallel}{\omega'}\left(v_\parallel\frac{\partial}{\partial v_\perp} - v_\perp\frac{\partial}{\partial v_\parallel}\right)\right]\delta f_h(\mathbf{K}-\mathbf{k}-\mathbf{k}') \\ & + E_{l\parallel}(\mathbf{k}')\left[J_a\frac{\partial}{\partial v_\parallel} + \frac{(J_{a+1}+J_{a-1})}{2}\frac{k'_\perp}{\omega'}\left(v_\parallel\frac{\partial}{\partial v_\perp} - v_\perp\frac{\partial}{\partial v_\parallel}\right)\right]\delta f_h(\mathbf{K}-\mathbf{k}-\mathbf{k}') \\ & + \delta E_{lh}(\mathbf{K}-\mathbf{k})\left[J_a\frac{\partial}{\partial v_\parallel} - \frac{(J_{a+1}+J_{a-1})}{2}\frac{k_\perp}{\Omega-\omega}\left(v_\parallel\frac{\partial}{\partial v_\perp} - v_\perp\frac{\partial}{\partial v_\parallel}\right)\right] f_{oe} \\ & + J_a\,\delta E_h(\mathbf{K}-\mathbf{k}-\mathbf{k}')\frac{\partial}{\partial v_\parallel} f_{1e}(\mathbf{k}')\Bigg\} \end{aligned} \tag{A3}$$

$$\begin{aligned} \Delta f(\mathbf{K},\Omega) = {} & \left(\frac{ie}{m}\right)^2 \sum_{a,b}\frac{1}{\Omega - Kv_\parallel}\left\langle \Bigg\{ E_{l\perp}(\mathbf{k})\frac{(J_{b+1}+J_{b-1})}{2}\right. \\ & \times \left[\frac{\partial}{\partial v_\perp} - \frac{k_\parallel}{\omega}\left(v_\parallel\frac{\partial}{\partial v_\perp} - v_\perp\frac{\partial}{\partial v_\parallel}\right)\right] + E_{l\parallel}(\mathbf{k})\Bigg[J_b\frac{\partial}{\partial v_\parallel} \\ & + \frac{(J_{b+1}+J_{b-1})}{2}\frac{k_\perp}{\omega}\left(v_\parallel\frac{\partial}{\partial v_\perp} - v_\perp\frac{\partial}{\partial v_\parallel}\right)\Bigg]\Bigg\}\frac{\exp[i(a-b)\phi]}{(\Omega-\omega)-(K-k_\parallel)v_\parallel + a\Omega_e} \end{aligned}$$

$$\times \left\{ E_{l\perp}(\mathbf{k}') \frac{(J_{a+1}+J_{a-1})}{2} \left[\frac{\partial}{\partial v_\perp} - \frac{k'_\perp}{\omega'} \left(v_\parallel \frac{\partial}{\partial v_\perp} - v_\perp \frac{\partial}{\partial v_\parallel} \right) \right] \delta f_h(\mathbf{K}-\mathbf{k}-\mathbf{k}') \right.$$

$$+ E_{l\parallel}(\mathbf{k}') \left[J_a \frac{\partial}{\partial v_\parallel} - \frac{(J_{a+1}+J_{a-1})}{2} \frac{k'_\perp}{\omega'} \left(v_\parallel \frac{\partial}{\partial v_\perp} - v_\perp \frac{\partial}{\partial v_\parallel} \right) \right] \delta f_h(\mathbf{K}-\mathbf{k}-\mathbf{k}')$$

$$+ \delta E_{lh}(\mathbf{K}-\mathbf{k}) \left[J_a \frac{\partial}{\partial v_\parallel} - \frac{(J_{a+1}+J_{a-1})}{2} \frac{k_\perp}{\Omega-\omega} \left(v_\parallel \frac{\partial}{\partial v_\perp} - v_\perp \frac{\partial}{\partial v_\parallel} \right) \right] f_{oe}$$

$$\left. + J_a \delta E_h(\mathbf{K}-\mathbf{k}-\mathbf{k}') \frac{\partial}{\partial v_\parallel} f_{1e}(\mathbf{k}') \right\} + \delta E_{lh}(\mathbf{K}-\mathbf{k}) \left[\frac{\partial}{\partial v_\parallel} - \cos\phi \frac{k_\perp}{\Omega-\omega} \right.$$

$$\left. \times \left(v_\parallel \frac{\partial}{\partial v_\perp} - v_\perp \frac{\partial}{\partial v_\parallel} \right) \right] f_{1e}(\mathbf{k}) \Big\rangle \tag{A4}$$

where $f_{1e}(\mathbf{k})$ is given by (5).

The Maxwell equation for mixed mode field can be written as,

$$\nabla \times \delta \mathbf{B}_{lh}(\mathbf{K}-\mathbf{k}) = \frac{1}{c} \frac{\partial}{\partial t} \delta \mathbf{E}_{lh}(\mathbf{K}-\mathbf{k}) - \frac{4\pi e}{c} \int \mathbf{v} \delta f_{lh}(\mathbf{K}-\mathbf{k}) \mathrm{d}\mathbf{v}. \tag{A5}$$

Accordingly, the Fourier component of the mixed mode electric field is given by,

$$\delta E_{lh}(\mathbf{K}-\mathbf{k}) = \frac{4\pi i e(\Omega-\omega)}{(\Omega-\omega)^2 - c^2 k_\perp^2} \int v_\parallel \delta f_{lh}(\mathbf{K}-\mathbf{k}) \mathrm{d}\mathbf{v} \tag{A6}$$

Substituting (A3) into (A6), we get,

$$\delta E_{lh}(\mathbf{K}-\mathbf{k}) =$$

$$- \frac{4\pi e^2(\Omega-\omega)}{mR(\mathbf{K}-\mathbf{k})[(\Omega-\omega)^2 - c^2 k_\perp^2]} \sum_{a,b} \int v_\parallel \frac{J_a(k_\perp v_\perp/\Omega_e) \exp[i(a-b)\phi]}{(\Omega-\omega) - (K-k_\parallel)v_\parallel + a\Omega_e}$$

$$\times \left\{ E_{l\perp}(\mathbf{k}') \frac{(J_{a+1}+J_{a-1})}{2} \left[\frac{\partial}{\partial v_\perp} - \frac{k'_\parallel}{\omega'} \left(v_\parallel \frac{\partial}{\partial v_\perp} - v_\perp \frac{\partial}{\partial v_\parallel} \right) \right] \delta f_h(\mathbf{K}-\mathbf{k}-\mathbf{k}') \right.$$

$$+ E_{l\parallel}(\mathbf{k}') \left[J_a \frac{\partial}{\partial v_\parallel} + \frac{(J_{a+1}+J_{a-1})}{2} \frac{k'_\perp}{\omega'} \left(v_\parallel \frac{\partial}{\partial v_\perp} - v_\perp \frac{\partial}{\partial v_\parallel} \right) \right] \delta f_h(\mathbf{K}-\mathbf{k}-\mathbf{k}')$$

$$\left. + J_a \delta E_h(\mathbf{K}-\mathbf{k}-\mathbf{k}') \frac{\partial}{\partial v_\parallel} f_{1e}(\mathbf{k}') \right\} \mathrm{d}\mathbf{v} \tag{A7}$$

where $R(\mathbf{K}-\mathbf{k})$ is given by (15).

Finally, from (3), the Fourier component of the electric field of the Langmuir mode can be written as,

$$\delta E_h(\mathbf{K},\Omega) = -\frac{4\pi e}{K} \int [\delta f_h(\mathbf{K},\Omega) + \Delta f(\mathbf{K},\Omega)] \mathrm{d}\mathbf{v} \tag{A8}$$

Substituting (A2), (A3), (A4) and (A7) into the rhs of (A8) and assuming random phase approximation for the kinetic Alfvén wave, and performing the integration with respect to ϕ (only $a=b$ terms do survive), we obtain (10).

References

[1] M Nambu, *Laser and particle beams* **1**, 427 (1983)
[2] See, for example, K Akimoto, *Phys. Fluids* **B1**, 1998 (1989)
K Akimoto, *Phys. Fluids* **31**, 538 (1988)
[3] S B Isakov, V S Krivitskii and V N Tsytovich, *Sov. Phys. JETP* **63**, 545 (1986)
[4] M Nambu, S V Vladimirov and H Schamel, *Phys. Lett.* **A178**, 400 (1993)
[5] K S Goswami, B K Saikia, S Bujarbarua and M Nambu, *Contrib. Plasma Phys.* **33**, 235 (1993)
[6] M Nambu, T Hada, T Terasawa, K S Goswami and S Bujarbarua, *Phys. Scr.* **47**, 419 (1993)
[7] V S Krivitskii, *Sov. Phys. JETP* **71**, 888 (1990)
[8] V S Krivitskii and S V Vladimirov, *Comments Plasma Phys. Controlled Fusion* **13**, 219 (1990)
[9] M Nambu and T Hada, *Phys. Fluids* **B5**, 742 (1993)
[10] L Krlin, *J. Plasma Phys.* **12**, 365 (1974)
[11] A Hasegawa and C Uberoi, in *The Alfvén wave* (Technical Information Centre, US Department of Energy, 1982) p. 19
[12] M Nambu, S N Sarma and S Bujarbarua, *Phys. Fluids* **B2**, 302 (1990)
[13] Erratum to Ref. [12], *Phys. Fluids* **B5**, 1371 (1993)
[14] A Hasegawa and L Chen, *Phys. Rev. Lett.* **36**, 370 (1975)
[15] A Hasegawa, *J. Geophys. Res.* **81**, 5083 (1976)
[16] A Hasegawa and K Mima, *J. Geophys. Res.* **83**, 1117 (1978)

PRAMANA
— journal of
physics

© Printed in India

Vol. 42, No. 6,
June 1994
pp. 447–453

Universality in the length spectrum of integrable systems

DEBABRATA BISWAS
Theoretical Physics Division, Bhabha Atomic Research Centre, Bombay 400085, India

MS received 14 October 1993; revised 10 February 1994

Abstract. The length spectrum of periodic orbits in integrable hamiltonian systems can be expressed in terms of the set of winding numbers $\{M_1, \ldots, M_f\}$ on the f-tori. Using the Poisson summation formula, one can thus express the density, $\Sigma\delta(T - T_{\mathrm{M}})$, as a sum of a smooth average part and fluctuations about it. Working with homogeneous separable potentials, we explicitly show that the fluctuations are due to quantal energies. Further, their statistical properties are universal and typical of a Poisson process as in the corresponding quantal energy eigenvalues. It is interesting to note however that even though long periodic orbits in chaotic billiards have similar statistical properties, the form of the fluctuations are indeed very different.

Keywords. Length spectrum; periodic orbits; integrable systems; fluctuations; Poisson summation formula.

PACS Nos 05·45; 03·65

The quantal spectra of time-independent Hamiltonian systems exhibit fluctuations that can be classified on the basis of certain broad features of the underlying classical dynamics [1–3]. Typical measures used in these studies are the nearest neighbour level spacing distribution, $P(s)$ and the spectral rigidity, Δ_3. Their behaviour is quite distinct for the two extreme cases of classical flow. In the integrable case, the motion is regular and the quantal spectrum exhibits fluctuations typical of a Poisson process. On the other hand, the fluctuation measures of chaotic systems are adequately modelled by random matrices chosen from ensembles reflecting the presence or absence of anti-unitary symmetries.

Recently, there has been some interest in the statistical properties of the length spectrum of classical periodic orbits as well [4–7]. Clearly, the integrated density of lengths [8] $\Sigma\Theta(T - T_i)$ has a smooth average part superposed with fluctuations which determine the exact staircase. While the mean proliferation of periodic orbits in both integrable and chaotic systems is well established [2], the form of the fluctuations has been investigated only recently [7, 9, 10]. For pseudointegrable billiards [10] as well as for a system comprising of a particle moving on a compact surface of constant negative curvature [9], the analysis is based on a direct inversion of the Gutzwiller trace formula [2]. For chaotic billiards [7], where Maslov indices are orbit dependent, the inversion technique needs to be suitably modified to remove the information of phases altogether. In all three cases however, the average density arises from the zero energy contribution similar to the zero length orbits which give rise to the average density of quantal states. The fluctuations here arise from quantal energies as oscillatory contributions thus establishing the dual relationship between classical periodic orbit lengths and quantal energies.

In the present article, we shall confine ourselves to integrable systems and use a different approach to extract information about the density of lengths. We first show that the length spectrum can be treated on the same footing as the quantal energies for integrable systems since a single expression for the lengths can be obtained in terms of the winding numbers on the tori. We thus obtain the average density as well as the fluctuations using the Poisson summation formula. We also study the statistical properties of these fluctuations and find that the nearest neighbour spacings distribution, $P(s)$ and the spectral rigidity, $\Delta_3(L)$ are universal (for generic integrable systems) and typical of a Poisson process [11].

An f-dimensional integrable system is characterized by the existence of invariant f-tori foliating the entire phase space. Thus there exists a canonical transformation to a set of conjugate variables $(\mathbf{I}, \boldsymbol{\theta})$ such that the hamiltonian is cyclic in the f angles, $\boldsymbol{\theta}$. The time periods (of the periodic orbits) can thus be obtained by solving the set of f equations,

$$\boldsymbol{\omega}(\mathbf{I}) = 2\pi\mathbf{M}/T_{\mathbf{M}}, \tag{1}$$

where $\omega_i = \partial H/\partial I_i$ and $\mathbf{M} = (M_1, M_2, \ldots, M_f)$ denotes the number of windings around the f irreducible circuits. The f-actions, $(I_1, I_2, \ldots, I_f)$ can be eliminated to obtain $T_{\mathbf{M}}$ as a function of the energy, E and $\mathbf{M}$. The procedure is similar to the Böhr–Sommerfeld quantization scheme where $(f-1)$ parameters are eliminated from the f quantization conditions to obtain the energy eigenvalues, $E_{\mathbf{m}}$, in terms of the quantum numbers $\mathbf{m} = \{m_1, m_2, \ldots, m_f)$.

We illustrate this for 2-dimensional separable systems, with potentials of the form, $V(x_1, x_2) = c_1 x_1^{2n} + c_2 x_2^{2n}$. The Hamiltonian in action co-ordinates can be written as $H = \gamma_1 (I_1)^p + \gamma_2 (I_2)^p$ where $p = 2n/(n+1)$ and γ_i are constants which depend on c_i and n. The semiclassical eigenvalues are thus

$$E_{\mathbf{m}} = \hbar^p [\gamma_1 (m_1)^p + \gamma_2 (m_2)^p], \tag{2}$$

while the corresponding time periods obtained using the above prescription are

$$T_{\mathbf{M}} = 2\pi [(M_1/\gamma_1^{1/p})^{p/(p-1)} + (M_2/\gamma_2^{1/p})^{p/(p-1)}]^{(p-1)/p} / pE^{(p-1)/p}. \tag{3}$$

The time periods, $T_{\mathbf{M}}$ (also written as $T(\mathbf{M})$ subsequently) are thus functions of f integer variables like the corresponding quantal eigen-energies. Clearly they can be treated on the same footing. The density of time periods, $\mathrm{d}(T) = \Sigma\delta(T - T_{\mathbf{M}})$, can thus be recast in a set of conjugate integer variables $\{m_1, \ldots, m_f\}$ using the Poisson summation formula [12, 11].

$$\mathrm{d}(T) = \sum_{\mathbf{m}} \int \mathrm{d}^f M \exp(2\pi i \mathbf{M}\cdot\mathbf{m}) \delta(T - T(\mathbf{M})). \tag{4}$$

For large time periods, T (analogous to the semiclassical limit for the energy eigenvalues) the analysis is identical to that of Berry and Tabor (12). The $\mathbf{m} = \mathbf{0}$ term gives rise to the average density, $d_{\mathrm{av}}(T)$ and is equal to

$$d_{\mathrm{av}}(T) = \int \mathrm{d}^f M \, \delta(T - T(\mathbf{M})), \tag{5}$$

an expression that is analogous to the Thomas–Fermi term for the mean density of quantal energies. Similarly, terms with $m_i = 0$ provide the perimeter corrections as discussed by Seligman and Verbaarschot [13]. The rest of the terms in the sum of (4) provides oscillatory corrections and constitute the fluctuating part of the density.

Since part of this work seeks to identify the origin of these fluctuations in non-billiard systems (specifically we wish to investigate the role of quantal energies, if any), we shall deal with systems where both the time periods and quantal energies can be evaluated analytically. To this end, we consider the separable homogeneous potential discussed above for which (2) and (3) give the quantal energies and time periods respectively. Since the system is homogeneous, we shall for simplicity choose $E = (2\pi/p)^{p/(p-1)}$ in the expression for time periods. Using (3) in (5), we thus have

$$d_{\mathrm{av}}(T) = \frac{T}{q(\alpha_1\alpha_2)^{1/q}} B(1/q, 1/q), \tag{6}$$

where $q = p/(p-1)$, $\alpha_i = (\gamma_i)^{-1/(p-1)}$ and $B(x, y)$ is the beta function. Thus the mean density of time periods is linear in T, irrespective of the value of n in the potential, $V(x_1, x_2)$.

Let us now look at the form of the fluctuations. A transformation to polar co-ordinates, $\alpha_1 I_1^q = r^q \cos^2\phi$, $\alpha_2 I_2^q = r^q \sin^2\phi$ is helpful in evaluating the integral in (4) with $m_1, m_2 \neq 0$. The Jacobian of this transformation is $2(\alpha_1\alpha_2)^{-1/q} r(\sin\phi\cos\phi)^{(2-q)/q}/q$. For a given $\mathbf{m}$, the integral thus reduces to

$$F_{\mathbf{m}} = \frac{2T}{q(\alpha_1\alpha_2)^{1/q}} \int_0^{\pi/2} \mathrm{d}\phi (\sin\phi\cos\phi)^{(2-q)/q} \exp[i2\pi T\{m_1\alpha_1^{-1/q}\cos^{2/q}\phi + m_2\alpha_2^{-1/q}\sin^{2/q}\phi\}], \tag{7}$$

where we have carried out the r integration. For large T, we can now evaluate the ϕ integration by the method of stationary phases. The stationary point occurs at $m_1\alpha_1^{-1/q}\cos^{(2-2q)/q}\phi = m_2\alpha_2^{-1/q}\sin^{(2-2q)/q}\phi$ and the second derivative of the argument in the exponential is

$$i2\pi T \frac{4(1-q)}{q^2}[(m_1\alpha_1^{-1})^{q/(q-1)} + (m_2\alpha_2^{-1/q})^{q/(q-1)}]^{(q-1)/q}.$$

The density of lengths can thus be expressed as

$$\mathrm{d}(T) = d_{\mathrm{av}}(T) + \sum_{\mathbf{m}} A_{\mathbf{m}} \exp(iS_{\mathbf{m}}), \tag{8}$$

where $d_{\mathrm{av}}(T)$ is given by (6),

$$A_{\mathbf{m}} = \frac{\left(\dfrac{T}{q-1}\right)^{1/2} \{(\gamma_1\gamma_2)^{q-1}(m_1 m_2)^{2-q}\}^{1/2(q-1)}}{[(m_1/\alpha_1^{1/q})^{q/(q-1)} + (m_2/\alpha_2^{1/q})^{q/(q-1)}]^{(3-q)/2q}} \tag{9}$$

and

$$S_{\mathbf{m}} = 2\pi T[(m_1/\alpha_1^{1/q})^{q/(q-1)} + (m_2/\alpha_2^{1/q})^{q/(q-1)}]^{(q-1)/q} - \frac{\pi}{4}. \tag{10}$$

Replacing α_i by $\gamma_i^{-1/(p-1)}$ and q by $p/(p-1)$, it is easy to see that the quantity in the square bracket in (9) and (10) is the quantal eigen-energy of (2) with $\hbar = 1$. Thus fluctuations are indeed due to contributions from (scaled) quantal energies as in pseudointegrable [10] and chaotic [7, 9] systems. Moreover, the average density is due to the zero energy contribution, a fact that is transparent in this derivation for integrable systems.

The statistical properties of these fluctuations form the subject of subsequent discussions. As mentioned earlier, the measures commonly used on the spectrum are the nearest neighbour spacings distribution, $P(s)$ and the special rigidity, $\Delta_3(L)$. The spacings distributions $P(s)$ is defined such that $P(s)\mathrm{d}s$ is the probability of finding adjacent levels (lengths) with spacing between s and $s + \mathrm{d}s$ while the spectral rigidity measures the average mean square deviation of the integrated density of levels (lengths) from the best fitting straight line

$$\Delta(L) = \left\langle \min_{a,b} \frac{d_{\mathrm{av}}}{L} \int_{-L/2d_{\mathrm{av}}}^{L/2d_{\mathrm{av}}} \mathrm{d}\tau [N(T+\tau) - a - b\tau]^2 \right\rangle.$$

For the quantal energies of integrable systems, both $P(s)$ and $\Delta_3(L)$ can be evaluated analytically [1, 3]. Clearly a similar analysis can be carried over for the periodic orbits as well once the relevant scales are defined. The inner scale in the length spectrum is the mean spacing $1/d_{\mathrm{av}}(T)$ while the outer scale $(= L_{\mathrm{max}}/d_{\mathrm{av}}(T))$ is determined by the period of the slowest oscillation (as a function of T) in (8) and is given by $1/(E_0)^{(q-1)/q}$ where E_0 is the ground state energy. We quote here only the final expressions for $P(s)$ [1] and $\Delta_3(L)$ [3] applicable for long periodic orbits

$$P(s) = g(s)\exp\left(-\int_0^s g(u)\mathrm{d}u\right), \tag{11}$$

where

$$g(u) = 1 + \int_{-\infty}^{+\infty} \mathrm{d}k\, e^{iku}\{\phi_D(k) - d_{\mathrm{av}}/2\pi\}$$

and

$$\Delta(L) = \frac{L}{d_{\mathrm{av}}}\int_0^\infty \frac{\mathrm{d}y}{y^2}\,\phi_D(2d_{\mathrm{av}}y/L)G(y), \tag{12}$$

where, $G(y) = 1 - F^2(y) - 3F'^2(y)$, and $F(y) = \sin(y)/y$. Note that (12) holds when $L \ll L_{\mathrm{max}}$ [3]. The function $\phi_D(\varepsilon)$ in both cases is equal to $\langle \Sigma A_{\mathbf{m}}^2\,\delta(\varepsilon - \varepsilon_{\mathbf{m}})\rangle$ where $A_{\mathbf{m}}$ and $S_{\mathbf{m}}$ are the amplitude and action defined in (9) and (10) and $\varepsilon_{\mathbf{m}} = 2\pi(E_{\mathbf{m}})^{(q-1)/q}$. The averaging here is over an interval larger than the outer scale and the summation runs over all $\mathbf{m}$. The function $G(y)$ in (12) picks those quantal energies which contribute substantially at a given L. It is almost zero for $y \leqslant \pi/4$ where after it rises monotonically and saturates at a value close to unity for $y > \pi$ [3].

The integrations in (11) and (12) can be carried out once ϕ_D is evaluated. This can be achieved by computing the quantity $\mathscr{F}(\varepsilon) = \int_0^\varepsilon \phi_D(\varepsilon')\mathrm{d}\varepsilon' = \Sigma A_{\mathbf{m}}^2$ where the sum now runs over all energies, E_m for which $\varepsilon_m \leqslant \varepsilon$. The summation over m_1 and m_2 in $\mathscr{F}(\varepsilon)$ can be converted to an integral and evaluated quite easily using polar co-ordinates. The limit of r integration is now from 0 to ε while ϕ goes from 0 to $\pi/2$. Using (6) we thus have $\mathscr{F}(\varepsilon) = d_{\mathrm{av}}(T)\varepsilon/2\pi$ and hence $\phi_D(\varepsilon) = d_{\mathrm{av}}(T)/2\pi$ [14] which is identical to the case of quantal energies. Equations (11) and (12) therefore yield $P(s) = e^{-s}$ and $\Delta_3(L) = L/15$ for $L \ll L_{\mathrm{max}}$.

Note that long orbits in chaotic billiards also have identical universal statistical

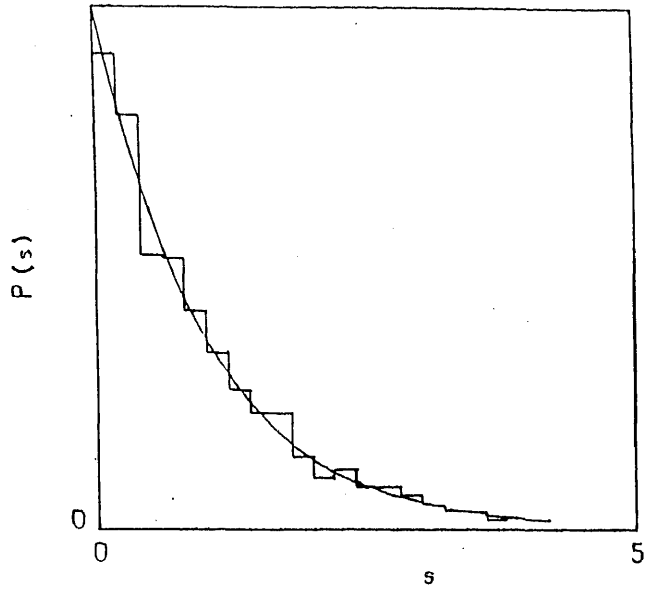

Figure 1. Nearest neighbour spacings distribution, $P(s)$ for the classical time periods. The continuous curve is the Poisson distribution, e^{-s}. For details of the system, see text.

properties [7] even though there are differences in the form of the amplitude of oscillation (see (8) above and ref. [7]).

As pointed out by Biswas *et al* [15] for the energy spectrum, deviations from these universalities do occur when the periodic orbit actions are degenerate. Similar deviations are thus expected here if the actions S_{m} in (10) are degenerate.

A further consequence of (8) for the density of lengths is the saturation of the spectral rigidity for $L > L_{\max}$. This is evident when $\Delta_3(L)$ is expressed as the sum $2\Sigma \frac{A_{\mathrm{m}}^2}{\varepsilon_{\mathrm{m}}^2} G(L\varepsilon_{\mathrm{m}}/2d_{\mathrm{av}}(T))$ for integrable systems [3]. For $L > L_{\max}$, the function G and hence the spectral rigidity saturates. Note that this is at variance with the observation of Harayama and Shudo (5).

In order to demonstrate our results numerically, we shall consider here a system with $n = 4$, $\gamma_1 = 1{\cdot}21393$ and $\gamma_2 = 0{\cdot}75025$. The time periods have been unfolded in order to compare and characterize the fluctuations. The new sequence thus obtained is used to evaluate the measures, $P(s)$ and Δ_3.

For the nearest neighbour spacings distribution, a sequence of 3000 lengths have been used after eliminating the shortest 3000 orbits. The result is displayed in figure 1. The histogram closely approximates the Poisson distribution, e^{-s}.

Figure 2 shows our result for the spectral rigidity evaluated at the 3500th length and averaged in a stretch containing 1000 lengths. The agreement with the continuous line ($L/15$) is excellent for $L \leqslant 6$.

Finally, figure 3 shows a plot of the spectral rigidity for the same system evaluated at the 1000th length and averaged in an interval containing 800 lengths. The saturation for $L > 70$ is evident.

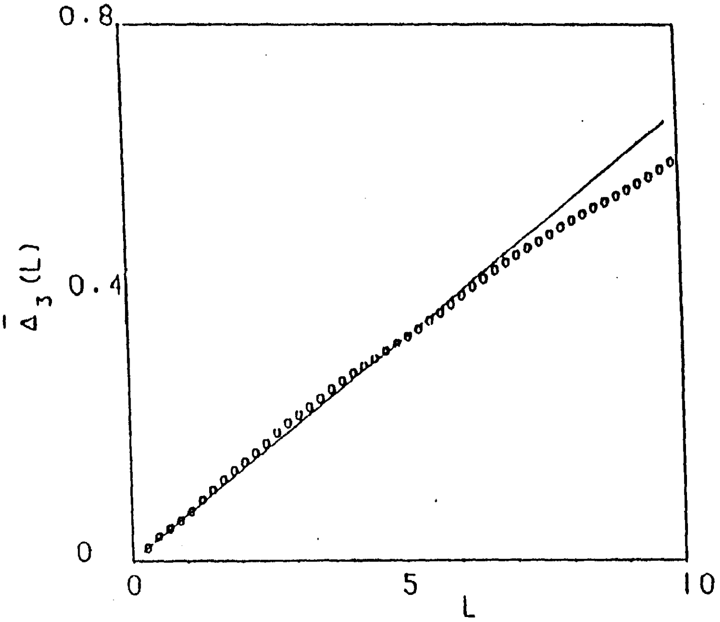

Figure 2. The spectral rigidity, $\bar{\Delta}_3$ for the classical time periods. The continuous line is $L/15$. The agreement is excellent for $L < 6$.

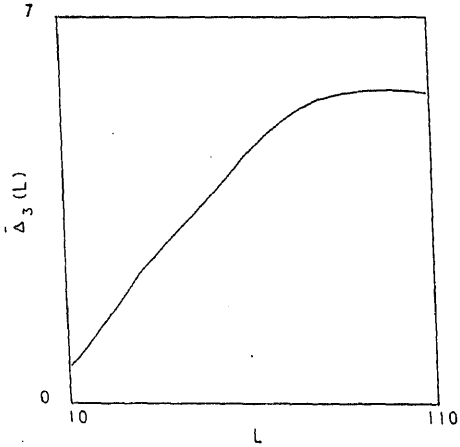

Figure 3. The spectral rigidity for the time periods clearly shows saturation for $L > 70$.

Our studies on other separable potentials confirm the above universalities in the nearest neighbour spacing distribution and the spectral rigidity.

In summary, we have shown that for integrable systems where the length spectrum can be expressed in terms of the winding numbers on the torus, the Poisson summation formula can be used to separate out the average and the fluctuating parts in the density of lengths. Working with separable homogeneous potentials, we explicitly show that the fluctuations are a sum of contributions from quantal energies. Further their statistical properties are typical of a Poisson process as in the case of quantal energy eigenvalues. It is important to note however that while long orbits in chaotic billiards seem to exhibit Poisson fluctuations as well, the form of the amplitude indeed differs from the integrable case.

References

[1] M V Berry and M Tabor, *Proc. R. Soc. London* **A356**, 275 (1977)

[2] M C Gutzwiller, *Chaos in classical and quantum mechanics* (Springer–Verlag, Interdisciplinary Applied Mathematics, 1991)
A M Ozorio de Almeida, *Hamiltonian systems chaos and quantization*, (Cambridge University Press, 1989)

[3] M V Berry, *Proc. R. Soc. London* **A400**, 229 (1985)

[4] M Seiber and F Steiner, *Physica* **D44**, 248 (1990)

[5] T Harayama and A Shudo, *J. Phys.* **A25**, 4595 (1992)

[6] D Biswas and S Sinha, *Phys. Lett.* **A173**, 392 (1993)

[7] D Biswas, *Phys. Rev. Lett.* **71**, 2714 (1993)

[8] The words lengths and time-periods are used in the same sense throughout the text. They are trivially related in homogeneous systems

[9] R Aurich and F Steiner, *Phys. Rev.* **A45**, 583 (1992)

[10] D Biswas and S Sinha, *Phys. Rev. Lett.* **70**, 916 (1993)

[11] D Biswas, BARC/ThPD/DB/Jan'92 (unpublished)

[12] M V Berry and M Tabor, *Proc. R. Soc. London* **A349**, 101 (1976)
M V Berry and M Tabor, *J. Phys.* **A10**, 371 (1977)

[13] T H Seligman and J J M Verbaarschot, *J. Phys.* **A20**, 1433 (1987)

[14] This result has been obtained for billiard systems earlier in [6]

[15] D Biswas, M Azam and S V Lawande, *Phys. Rev.* **A43**, 5674 (1991)

PRAMANA
— journal of
physics

© Printed in India

Vol. 42, No. 6,
June 1994
pp. 455–465

On phases and length of curves in a cyclic quantum evolution

ARUN KUMAR PATI
Theoretical Physics Division, Bhabha Atomic Research Centre, Bombay 400085, India

MS received 3 January 1994; revised 24 February 1994

Abstract. The concept of a curve traced by a state vector in the Hilbert space is introduced into the general context of quantum evolutions and its length defined. Three important curves are identified and their relation to the dynamical phase, the geometric phase and the total phase are studied. These phases are reformulated in terms of the dynamical curve, the geometric curve and the natural curve. For any arbitrary cyclic evolution of a quantum system, it is shown that the dynamical phase, the geometric phase and their sums and/or differences can be expressed as the integral of the contracted length of some suitably-defined curves. With this, the phases of the quantum mechanical wave function attain new meaning. Also, new inequalities concerning the phases are presented.

Keywords. Geometric phase; distance function; length of the curves.

PACS No. 03·65

1. Introduction

The phase change of the quantum mechanical wave function is of vital importance as it gives information about the dynamical changes in the system as well as the geometry of the path of the evolution. This paper aims at giving a new meaning towards all phase changes in general. When we are dealing with the cyclic evolution of a physical system, the possible natural questions that concern us are: (i) what is the phase factor that is associated with the final state (ii) how much distance the quantum state has travelled during the period of evolution in the projective Hilbert space $\mathscr{P}$ as measured by the Fubini–Study metric and (iii) what is the total length of the curve traced by the state vector (or other curves traced by the phase-transformed vectors)? The answer to (i) is well-known: the total phase factor contains two parts. One is the usual dynamical phase that gives the information about the duration of the evolution of the system and the second phase factor is the geometric phase (Berry phase [1, 2]) that gives the information about the geometry of the path of the evolution in $\mathscr{P}$ [3, 4]. The answer to the question (ii), though not widely-studied, has drawn some attention in connection with the introduction of geometric structures into quantum mechanics [5–14] and in relating the geometric phase to the geometric distance function [11–13]. The total distance travelled by the quantum states along a given curve $\hat{C}$ in $\mathscr{P}$, as measured by the Fubini–Study metric [7–13] is the time integral of the uncertainty in the energy of the system. Anandan and Aharonov [7] have remarked that it is also a geometric quantity analogous to the geometric phase, in the sense that it does not depend on the particular Hamiltonian used to move the quantum system along a given curve $\hat{C}$ in $\mathscr{P}$. In fact these are not just analogies but are related quantities. Recently, the author [11] has shown that the geometric phase could be derived from metric considerations. It appears as a result of the principle of minimization of the speed of transportation in $\mathscr{P}$. However the question (iii) has not drawn much attention. Recently we [11, 13] have asked such a question in connection with the geometric phase. For any cyclic evolution, when we say the geometric phase depends only on the closed curve $\hat{\mathrm{C}}$ in $\mathscr{P}$ it is not transparent in what way the phase depends on the curve (unless we define the curve and its length).

In this paper, we introduce the concept of a curve traced by a normalized vector in the Hilbert space $\mathscr{H}$ and give a general definition of the length of a curve during an arbitrary cyclic quantum evolution. Next, we elucidate the properties of the length of a curve. In the sequel, we define three important curves and their lengths. We study their relation to the dynamical phase and the geometric phase for cyclic evolutions of the quantum system. Any phase (we mean dynamical, geometric and/or their sums and differences) can be expressed as an integral of the contracted length of (some suitably-defined) curves. With these curves, the phases of the quantum mechanical wave function attain new meanings. For all cyclic evolutions of the quantum system we show that the value of the phases cannot be arbitrarily large, but are limited by the total length of their corresponding curves. Furthermore each curve is characterized by a number called energy associated with the curve. We point out the importance of the energy of the curve by carrying out a variational calculation leading to the equation of geodesic. We obtain some new inequalities among phases, lengths and energies for various kinds of curves in the Hilbert space. Lastly, we study a simple example to illustrate the concepts that are introduced here.

2. Concept of various curves and their lengths

To be concrete we start this section by defining a curve traced by any arbitrary vector in the Hilbert space $\mathscr{H}$ and its length. Let $|\chi(t)\rangle$ be a unit-norm vector belonging to $\mathscr{H}$. When $|\chi(t)\rangle$ evolves in time it traces a curve in $\mathscr{H}$, i.e. $t \to |\chi(t)\rangle$, $0 \leqslant t \leqslant T$ is a curve on the unit ball $\mathbb{B}$ of the Hilbert space $\mathscr{H}$. Since $\mathscr{H}$ is Riemannian this curve has a length. This curve projects to either a closed or an open curve in the projective Hilbert space $\mathscr{P} = \mathscr{B}/U(1) = \mathscr{H} - \{0\}/\mathbb{C}^*$ depending on the type of evolution, named cyclic or non-cyclic. The projected curve $\hat{\mathrm{C}} = \pi(\mathrm{C})$ also has a length, given by the Fubini–Study metric on $\mathscr{P}$. Thus if $|\chi(t)\rangle$ is a quantum state then we say that the state of the system at any instant of time is represented by a point and the evolution of the state is by a curve in $\mathscr{P}$. Since the inner product in $\mathscr{H}$ induces a metric in $\mathscr{P}$, we can define the length of the curve precisely.

Definition Let $t \in [0, T] \subset \mathbb{R}$ and let $\mathrm{C}: t \to \chi(t)$ be a piecewise C^1 curve on the unit ball $\mathscr{B} \subset \mathscr{H}$. Its length is defined to be

$$l(\chi(t))|_0^T = \int_0^T \langle \dot{\chi}(t) | \dot{\chi}(t) \rangle^{1/2} \mathrm{d}t, \tag{1}$$

where $|\dot{\chi}(t)\rangle$ is the velocity vector in the Hilbert space $\mathscr{H}$ of the curve $|\chi(t)\rangle$ at point t along the path of evolution of the state vector.

Some of the properties of the length of a curve can be spelled out. First of all the integral (1) exists since the integrand is continuous due to the map: $t \to \|\dot{\chi}\|$ being continuous. The length of a broken C-curve is defined as the (finite) sum of the length of its C-pieces. This means that the broken curve $t \to \chi(t)$ is a broken C^∞-curve in

$\mathscr{H}$ and it is a continuous mapping $C:[0,T]\rightarrow\mathscr{H}$ together with a subdivision $0\leqslant t_1<t_2<\cdots<t_n\leqslant T$ on whose closed subinterval $t\rightarrow\chi(t)$ is a C^∞-curve. The length of the curve has an important property of reparametrization invariance. Given a smooth curve C and two fixed points $\chi(0)$ and $\chi(T)$ corresponding to the parameter values $t=0$ and $t=T$, if we change the parameter t by τ that is an arbitrary smooth transformation and a smooth monotonically increasing function of time (i.e. $\mathrm{d}t/\mathrm{d}\tau>0$), then the length of the curve $l(\chi)|_0^T$ remains unchanged. The curve C can be viewed as a continuous set of points in $\mathscr{H}$ along with a parametrization. Thus length is a geometric property of the whole curve C in $\mathscr{H}$, defined by the equivalence classes of parametrized paths. Hence the length of the curve defined from the inner product of the tangent vectors is an important concept in studying the geometry of quantum evolution.

It is now convenient to define the infinitesimal length of the curve during an infinitesimal time, dt, for an arbitrary time evolution of the quantum system as follows:

$$\mathrm{d}l(\chi(t))=\langle\dot{\chi}(t)|\dot{\chi}(t)\rangle^{1/2}\mathrm{d}t. \tag{2}$$

This will help us in studying the infinitesimal properties of a curve on a manifold of quantum states. If the parameter t is such that $\langle\dot{\chi}|\dot{\chi}\rangle^{1/2}$ is constant along C, then we say the length of the curve is parametrically proportional to the arc length. The quantity $u_{\mathscr{H}}(\chi)=\mathrm{d}l(\chi)/\mathrm{d}t$ is called the magnitude of the rate of change of arc length of the curve C in $\mathscr{H}$. This can be seen by changing the parameter from t to τ, the curve $\tau\rightarrow|\chi(\tau)\rangle$ will then be the locus of the same points in $\mathscr{H}$ as for the curve $t\rightarrow|\chi(t)\rangle$, nevertheless, the state traverses along the curve at a different rate because $u_{\mathscr{H}}(\chi)$ is not reparmeterization invariant.

We now introduce various curves such as the dynamical curve, the geometric curve and the natural curve and define their lengths. These lengths share all the properties elucidated in the general discussion.

Dynamical curve: Let $|\psi(t)\rangle$ be the quantum state that evolves according to the Schrödinger equation $i\hbar|\psi(t)\rangle=H(t)|\psi(t)\rangle$. The curve $t\rightarrow|\psi(t)\rangle$ traced by the vector $|\psi(t)\rangle$ is called as the dynamical curve C_d. This satisfies $|\psi(T)\rangle=\exp(i\phi)|\psi(0)\rangle$, $\phi\in\mathbb{R}$ (phase ϕ is called as the total phase). It begins and ends on the same ray but at different points.

The length of the dynamical curve C_d can be defined through (1) by taking $|\chi(t)\rangle$ to be $|\psi(t)\rangle$. Since it depends on the Hamiltonian of the system (in view of $|\psi(t)\rangle$ satisfies the Schrödinger equation corresponding to a given Hamiltonian) and consequently on the detailed dynamics, hence the name dynamical curve.

Geometric curve: The curve $t\rightarrow|\tilde{\psi}(t)\rangle$ traced by the single valued vector $|\tilde{\psi}(t)\rangle$ is called as the geometric curve C_g. It is a phase-transformed solution curve of $|\psi(t)\rangle$ (because $|\tilde{\psi}(t)\rangle=\exp(-if(t))|\psi(t)\rangle$ with $f(T)-f(0)=\phi$) such that $|\tilde{\psi}(T)\rangle=|\tilde{\psi}(0)\rangle$. It starts and ends on the same ray at same point, i.e. C_g is a closed curve in $\mathscr{H}$ with $\pi(C_\mathrm{g})=\pi(C_\mathrm{d})=\hat{C}$.

The length of the geometric curve can be defined through (1) by taking $|\chi(t)$ to be $|\tilde{\psi}(t)\rangle$. It is independent of the particular Hamiltonian used to transport the quantum system. This is true to the extent that an addition of a scalar E to the Hamiltonian, ensues a different total phase factor to the evolving state keeping the single valued state unchanged. That is why we call the curve traced by the single-valued vector

$|\tilde{\psi}(t)\rangle$ as a geometric curve. Since the single valued vector only depends on the image of the evolution of $|\psi(t)\rangle$ on the projective Hilbert space $\mathscr{P}$, it further consolidates the geometric nature of the curve $\mathrm{C_g}$.

Natural curve: The curve $t \rightarrow |\bar{\psi}(t)\rangle$ traced by the parallel-transported vector $|\bar{\psi}(t)\rangle$ is called as the natural curve $\mathrm{C_n}$. This is also a phase-transformed solution curve of $|\psi(t)\rangle$ (because $|\bar{\psi}(t)\rangle = \exp(i/\hbar \int_0^t \langle\psi(t')|H(t')|(t')\rangle \mathrm{d}t')|\psi(t)\rangle$, with the parallel transport rule $\langle\bar{\psi}(t)|\bar{\psi}(t)\rangle = 0$) such that $|\bar{\psi}(T)\rangle = \exp(i\beta)|\bar{\psi}(0)\rangle$, where β is the geometric phase acquired by the system during a cyclic evolution. This curve starts and ends on the same ray but at different points.

The length of the natural curve can be defined in the same way by taking $|\chi(t)\rangle$ to be $|\bar{\psi}(t)$ in the definition (1). Like the length of the geometric curve it is also $H(t)$- and t-invariant quantity.

For further clarification, we can see that the length of the natural curve is exactly equal to the total distance travelled by the state vector $|\psi(t)\rangle$ along a given curve $\hat{\mathrm{C}}$ in the projective Hilbert space $\mathscr{P}$. More precisely, the projective Hilbert space $\mathscr{P}$ admits a natural metric structure and that the distance as measured by the metric topology coincides with the length of the natural curve. Thus $l(\bar{\psi})|_0^T = D$, where $D = \int_0^T \Delta E(t)\mathrm{d}t/\hbar$ and $\Delta E(t) = [\langle\psi(t)|H^2(t)|\psi(t)\rangle - \langle\psi(t)|H(t)|\psi(t)\rangle^2]^{1/2}$. Therefore, the total length of the natural curve is equal to the time integral of the uncertainty of the energy during the period of the evolution.

3. Concept of energy of the curve

After studying different curves traced by the equivalence classes of state vectors, we now introduce the energy of the various curves. With this, any arbitrary evolution can be classified by the length and energy of the curve [15].

Proposition To each curve, there is associated an energy, which is distinct from the length of the curve.

The number defined through

$$E(\chi(t))|_0^T = \hbar \int_0^T \langle\dot{\chi}(t)|\dot{\chi}(t)\rangle \mathrm{d}t \tag{3}$$

is called the energy associated with the curve $t \rightarrow |\chi(t)\rangle$. If we allow $|\chi(t)\rangle$ to be $|\psi(t)\rangle$, $|\tilde{\psi}(t)\rangle$ and $|\bar{\psi}(t)\rangle$ we will get the quantum mechanical energies of the dynamical, geometric and natural curves respectively. We denote these energies by $E(\psi)$, $E(\tilde{\psi})$ and $E(\bar{\psi})$ respectively.

To avoid confusion among the readers we would like to remark that the energy of the curve $E(\chi)$ has nothing to do with the true quantum mechanical energy of the system, in general. The energy of a curve is a property that is attributed to a particular curve during an evolution of a quantum system. The true quantum mechanical energy E_s of a system is given by the expectation value of the hamiltonian in the state $|\psi(t)\rangle$ and is a property of the system at a given instant of time. So these two energies are different altogether. However, the energy of the dynamical curve and the true quantum mechanical energy of the system obey a simple inequality. Since the infinitesimal change in the energy of the dynamical curve is given by $\mathrm{d}E(\psi) = \hbar \langle\dot{\psi}(t)|\dot{\psi}(t)\rangle \mathrm{d}t$, we have $E_s^2 \leqslant \hbar \mathrm{d}E(\psi)/\mathrm{d}t$. Here, we have used the fact that the variance in the energy of the system is a non-negative quantity. Thus the (squared) energy of the system is limited by the rate of change of energy of the dynamical curve.

Next, we make a comparison between the length and the energy of the curve. We state a theorem which elicits the important fact that the length and the energy of the curve are distinct objects in the Hilbert space $\mathscr{H}$.

Theorem 1. The (squared) length of the curve during a cyclic evolution of the quantum system is limited by the energy of the curve, i.e. the length and the associated energy of the curve are related by the inequality

$$l^2(\chi(t))|_0^T \leqslant E(\chi(t))|_0^T(T/\hbar). \tag{4}$$

The equality holds good for a curve which is parametrically proportional to the arc length of the curve, i.e., when $\langle\dot{\chi}(t)|\dot{\chi}(t)\rangle$ is constant. We have three such inequalities for each of the curves mentioned above.

4. Variation of the energy of the curve and geodesic equation

In this section we outline as to how the concept of energy of the curves can be used to define geodesics by studying their extremal properties under smooth variations. Among all other curves and energies, the natural curve and its associated energy deserve a separate status in studying the geometry of quantum evolution. On a Riemannian manifold of quantum states a geodesic can be defined as a curve traced by the parallel transported vector $|\bar{\psi}(t)\rangle$ along which the translation preserves the velocity vector of the curve $\mathrm{C_n}$. Alternatively, geodesics in $\mathscr{P}$ can be defined as those curves for which the energy of the natural curve is stationary. We now present a variational argument to arrive at a geodesic equation.

Using the definition of the energy of the natural curve we write the energy of the varied curve as

$$\delta E(\bar{\psi})|_0^T = \hbar\int_0^T \mathrm{d}t\left[\mathrm{Re}\left(\left\langle\frac{\partial\dot{\psi}}{\partial u}\middle|\dot{\psi}\right\rangle - \left\langle\frac{\partial\dot{\psi}}{\partial u}\middle|\psi\right\rangle\langle\psi|\dot{\psi}\rangle - \langle\dot{\psi}|\psi\rangle\left\langle\frac{\partial\psi}{\partial u}\middle|\dot{\psi}\right\rangle\right)\right]\mathrm{d}u. \tag{5}$$

On using

$$\left\langle\frac{\partial\dot{\psi}}{\partial u}\middle|\frac{\delta\psi}{\mathrm{d}t}\right\rangle = \left\langle\frac{\partial\dot{\psi}}{\partial u}\right|(|\dot{\psi}\rangle - \langle\psi|\dot{\psi}\rangle|\psi\rangle),$$

we have

$$\delta E(\bar{\psi})|_0^T = \hbar\int_0^T \mathrm{d}t\left[\mathrm{Re}\left(\left\langle\frac{\partial\dot{\psi}}{\partial u}\middle|\frac{\delta\psi}{\mathrm{d}t}\right\rangle - \left\langle\frac{\partial\psi}{\partial u}\middle|\dot{\psi}\right\rangle\langle\dot{\psi}|\psi\rangle\right)\mathrm{d}u\right], \tag{6}$$

where

$$\left|\frac{\delta\psi}{\mathrm{d}t}\right\rangle = |\dot{\psi}\rangle - \langle\psi|\dot{\psi}\rangle|\psi\rangle.$$

Notice that $\langle\psi|\dot{\psi}\rangle$ and $\left\langle\psi\middle|\frac{\partial\psi}{\partial u}\right\rangle$ are purely imaginary. Facilitating the usage of the identity $\mathrm{Re}\left[\mathrm{d}u\left\langle\frac{\partial\psi}{\partial u}\middle|\frac{\delta\psi}{\mathrm{d}t}\right\rangle\langle\psi|\dot{\psi}\rangle\right] = -\mathrm{Re}\left[\mathrm{d}u\left\langle\frac{\partial\psi}{\partial u}\middle|\dot{\psi}\right\rangle\langle\dot{\psi}|\psi\rangle\right]$, we have

$$\delta E(\bar{\psi})|_0^T = \hbar \int_0^T \mathrm{d}t \left[\mathrm{Re}\left(\left\langle \frac{\partial \dot{\psi}}{\partial u} \middle| \frac{\delta \psi}{\mathrm{d}t} \right\rangle + \left\langle \frac{\partial \psi}{\partial u} \middle| \frac{\delta \psi}{\mathrm{d}t} \right\rangle \langle \psi | \dot{\psi} \rangle \right) \mathrm{d}u \right]. \tag{7}$$

On integrating the first term by parts and allowing the variation of $|\psi(u,t)\rangle$ at end points to vanish, we obtain

$$\delta E(\bar{\psi})|_0^T = \hbar \int_0^T \mathrm{d}t \left[\mathrm{Re}\left(\left\langle \frac{\partial \psi}{\partial u} \middle| \left(-\frac{\mathrm{d}}{\mathrm{d}t} + \langle \psi | \dot{\psi} \rangle \right) \middle| \frac{\delta \psi}{\mathrm{d}t} \right\rangle \right) \mathrm{d}u \right]. \tag{8}$$

The equation for the geodesic comes naturally, if one observes that $\left\langle \psi \middle| \frac{\partial \psi}{\partial u} \right\rangle$ is purely imaginary and the integrand vanishes for arbitrary variations. This amounts to saying that [16]

$$\left(\frac{\mathrm{d}}{\mathrm{d}t} - \langle \psi | \dot{\psi} \rangle \right) \left| \frac{\delta \psi}{\mathrm{d}t} \right\rangle = g(t) |\psi(t)\rangle, \tag{9}$$

for any real, smooth function $g(t)$. This is the geodesic equation of motion for the system. Evolutions of the quantum system for which the energy of the natural curve is stationary satisfies (9). In terms of the parallel-transported vector the geodesic equation is simple and is given by

$$\frac{\mathrm{d}^2}{\mathrm{d}t^2} \left| \bar{\psi}(t) \right\rangle + v_{\mathscr{H}}^2(t) |\bar{\psi}(t)\rangle = 0, \tag{10}$$

where the function $g(t)$ is eliminated by using the parallel-transport rule $\langle \bar{\psi} | \dot{\bar{\psi}} \rangle = 0$, and is found to be $v_{\mathscr{H}}$, where $v_{\mathscr{H}} = \mathrm{d}l(\bar{\psi})/\mathrm{d}t$.

Since the geodesics are special paths, it would be interesting to know the phase information of a quantum system when it passes through a geodesic. Especially, we would like to know what is the geometric phase acquired by a quantum system when it passes through a geodesic. The following theorem answers this question.

Theorem 2. For a time independent Hamiltonian, if the system passes through geodesic (meaning, (10) is satisfied by the parallel-transported vector) and further, the tangent vector is proportional to the vector itself at time $t = 0$, i.e. $|\dot{\bar{\psi}}(0)\rangle = i v_{\mathscr{H}} |\bar{\psi}(0)\rangle$, then the geometric phase acquired by the system in one cycle is just equal to the total length of the natural curve during the evolution.

Proof. The general solution to (10) is

$$|\bar{\psi}(t)\rangle = (\cos v_{\mathscr{H}} t) |\bar{\psi}(0)\rangle + (\sin v_{\mathscr{H}} t)/v_{\mathscr{H}} |\dot{\bar{\psi}}(0)\rangle. \tag{11}$$

Imposing the condition $|\dot{\bar{\psi}}(0)\rangle = i v_{\mathscr{H}} |\bar{\psi}(0)\rangle$ we can write $|\bar{\psi}(t)\rangle = \exp(i v_{\mathscr{H}} t) |\bar{\psi}(0)\rangle$. In one cycle, $|\bar{\psi}(T)\rangle$ is related to $|\bar{\psi}(0)\rangle$ through $|\bar{\psi}(T)\rangle = \exp(i v_{\mathscr{H}} T) |\bar{\psi}(0)\rangle = \exp(i l(\bar{\psi})|_0^T) |\bar{\psi}(0)\rangle$. But $|\bar{\psi}(T)\rangle$ is again equal to $\exp(i\beta(\mathrm{C}))\, |\bar{\psi}(0)\rangle$ where $\exp(i\beta(\mathrm{C}))$ is the holonomy transformation in parallel-transporting the vector $|\bar{\psi}(t)\rangle$ arround a closed curve in the projective Hilbert space $\mathscr{P}$ and $\beta(\mathrm{C})$ is the geometric phase acquired by the system during a cyclic evolution, hence the proof.

5. Relating phases and length of the curves

In this section we relate the phases and length of the curves during any cyclic quantum evolution. Before doing so, we state the following theorem which is of paramount importance in proving the central result of the paper.

Theorem 3. The length of the curves traced by any equivalence classes of states is greater than the total length of the natural curve during an arbitrary cyclic evolution of the quantum system. (Here, equivalence classes we mean vectors differing only in phases. The equivalence relation is $|\psi\rangle \sim |\psi'\rangle$ if $|\psi'\rangle = c|\psi\rangle$ where $0 \neq c \in \mathbb{C}^*$ and $\mathbb{C}^* = \mathbb{C} - \{0\}$ is a multiplicative group of non-zero complex numbers.)

This is reminiscent of a theorem that is known in differential geometry [17]. From theorem 3, it immediately follows that the total length of the dynamical and geometric curves is greater than the total length of the natural curve during an arbitrary cyclic evolution. Also, it is easy to show that the total energy of the dynamical and geometric curves is greater than the total energy of the natural curve.

Theorem 4. For an arbitrary cyclic evolution of the quantum system, (if the frequencies (change of phases over unit time interval) do not change sign during the evolution) then the dynamical phase, the geometric phase, their sums (called total phase) and their differences can be expressed as an integral of the contracted length of some (suitably-defined) curves.

Proof. For a cyclic quantum evolution, the dynamical phase is the time integral of the expectation value of the Hamiltonian $H(t)$, i.e. $\delta = -1/\hbar \int_0^T \langle\psi|H(t)|\psi\rangle \mathrm{d}t$. This can be expressed as

$$\delta = \int_0^T (1 - v^2_{\mathscr{H}}(\bar{\psi})/u^2_{\mathscr{H}}(\psi))^{1/2} \mathrm{d}l(\psi). \tag{12}$$

From the above theorem, we know that $u_{\mathscr{H}}(\psi) > v_{\mathscr{H}}(\bar{\psi})$, where $u_{\mathscr{H}}(\psi)$ is the rate of change of arc length of the dynamical curve and $v_{\mathscr{H}}(\bar{\psi})$ is the rate of change of arc length of the natural curve (also called as the speed of transportation of the state vector in the projective Hilbert space $\mathscr{P}$). We call the quantity $[(1 - v^2_{\mathscr{H}}(\bar{\psi})/u^2_{\mathscr{H}}(\psi)]^{1/2}$ as the contraction factor (CF) for the dynamical curve. Hence the magnitude of the dynamical phase is the integral of the contracted length of the dynamical curve.

The geometric phase for a cyclic quantum evolution is given by $\beta(\mathrm{C}) = i\int_0^T \langle\tilde{\psi}|\dot{\tilde{\psi}}\rangle \mathrm{d}t$, which can be expressed as

$$\beta(c) = \int_0^T [1 - v^2_{\mathscr{H}}(\bar{\psi})/u^2_{\mathscr{H}}(\tilde{\psi})]^{1/2} \mathrm{d}l(\tilde{\psi}). \tag{13}$$

Since $u_{\mathscr{H}}(\tilde{\psi}) > v_{\mathscr{H}}(\bar{\psi})$, where $u_{\mathscr{H}}(\tilde{\psi})$ is the rate of change of arc length of the geometric curve, we call the quantity $[(1 - v^2_{\mathscr{H}}(\bar{\psi})/u^2_{\mathscr{H}}(\tilde{\psi}))]^{1/2}$ as the CF for the geometric curve. Hence the magnitude of the geometric phase is the integral of the contracted length of the geometric curve.

The total phase (difference phase) is just $\phi_+ = \phi = \delta + \beta(\phi_- = \delta - \beta)$. To express this in terms of some suitably defined length of the curve let us define a vector $|\psi_+(t)\rangle$

($|\psi_-(t)\rangle$) as follows:

$$|\psi_\pm(t)\rangle = \exp\left(\pm i\int_0^t i\langle\tilde{\psi}(t')|\dot{\tilde{\psi}}(t')\rangle \mathrm{d}t'\right)|\psi(t)\rangle. \tag{14}$$

One can see that the phases ϕ_+ and ϕ_- can be expressed as

$$\phi_\pm = \mp i\int_0^T \langle\psi_\pm(t)|\dot{\psi}_\pm(t)\rangle \mathrm{d}t. \tag{15}$$

Correspondingly, the total length of the curve traced by the vector $|\psi_\pm(t)\rangle$ is given by

$$l(\psi_\pm(t))|_0^T = \int_0^T \langle\dot{\psi}_\pm(t)|\dot{\psi}_\pm(t)\rangle^{1/2}\mathrm{d}t. \tag{16}$$

On evaluating the infinitesimal length of the curve $dl(\psi_\pm)$ we get

$$\mathrm{d}l^2(\psi_\pm) - \mathrm{d}l^2(\tilde{\psi}) = (\mp i\langle\psi_\pm(t)|\dot{\psi}_\pm(t)\rangle \mathrm{d}t)^2. \tag{17}$$

Therefore $\phi_\pm$ is given by

$$\phi_\pm = \int_0^T [1 - v_{\mathcal{H}}^2(\tilde{\psi})/u_{\mathcal{H}}^2(\psi_\pm)]^{1/2}\mathrm{d}l(\psi_\pm), \tag{18}$$

which is nothing but integral of the contracted length of the curve $t \to |\psi_\pm(t)\rangle$ during the period of evolution. This proves theorem 4.

This is one of the main results of our paper. It provides expressions for any given phases in terms of the integral of the contracted length of some (suitably-defined) curves. Moreover, it establishes an equivalence between the lengths and phases in quantum theory. It can be seen as follows. If the rate of change of the length of the natural curve $v_{\mathcal{H}}(\tilde{\psi})$ is much smaller than the rate of change of the length of the other curves, then to the lowest order in $(v_{\mathcal{H}}^2/u_{\mathcal{H}}^2)$ the phases are equal to the total length of their respective curves. Thus a new interpretation of the phases is that they are all of some form or the other of the length of the curves. A necessary and sufficient condition for acquiring a phase is that the corresponding CF should not vanish during a cyclic evolution of the quantum system. Since the CF varies from zero to unity, it sets a limit on the respective phases. During such evolutions of the quantum systems the maximum attainable value of the phases are therefore equal to the total length of the respective curves (of course mod 2π). For constant CF's the phases are proportional to the total length of the corresponding curves. This statement is parallel to the well-known fact that the dynamical phase gives the duration of the period of evolution (since it is proportional to the time period for a constant energy). Here it is transparently seen that the phases also give information about the total length of the curves.

Reformulation of phases in terms of the length of the curves leads us to present some inequalities among the phases and the energies.

$$\delta \leqslant [E(\psi)\,T/\hbar]^{1/2}, \quad \beta \leqslant [E(\tilde{\psi})\,T/\hbar]^{1/2} \text{ and } \phi_\pm \leqslant [E(\psi_\pm)\,T/\hbar]^{1/2}. \tag{19}$$

This is true, because the phases are limited by the length of the respective curves and the lengths are limited by their energies. The physical relevance of these inequalities are as follows. In an experiment if one measures the phase change of a wave function during a cyclic quantum evolution and obtains some value then he may not be sure whether the phase is of dynamical or geometric origin. However, if he compares the measured value of the phase with the (calculated) length or energy of the corresponding curve and finds that the value of the phase satisfies any one of the inequality then he will be sure about the nature of the phase. Hence, these inequalities can be used to discern the phases in a cyclic quantum evolution.

Apart from all this, we now raise the fundamental question on the origin of the phases in general. Indeed, our result holds the clue providing a novel way towards an answer. At each instant of time, t, the length of the curves is greater than the "distance" or the length of the natural curve. Because of these fundamental inequalities among these curves, the phases appear in the final state of the system. Thus, during a cyclic quantum evolution, we may regard the excess length of curves over the length of the natural curve go on accumulating, so that their integrated squared difference finally appear as the phases associated with the final state vector. This shows that during a cyclic evolution, the nature of the phase that appears depends squarely on the particular length of the curve. An important question that we wish to answer is that whether the concept of length of a curve provides the means of realising the accumulation of a surplus geometric phase over and above the dynamical phase. This is, in fact, achieved by adjusting the Hamiltonian of the system for the following reason. Since length of the natural curve $l(\bar{\psi})$ is independent of the Hamiltonian H, by changing H we can only change the length of the dynamical curve. Therefore by varying the Hamiltonian we can allow the length of the dynamical curve to be as close as to the length of the natural curve, and thereby, making the dynamical phase vanishingly small. In the process of adjusting the Hamiltonian the length of the geometric curve remains unchanged and hence the geometric phase, too. So whatever geometric phase the system will acquire upon a cyclic excursion, can be kept intact with a very small contribution from the dynamical phase. Making the dynamical phase vanishingly small amounts to saying that the state vector of the quantum system undergoes parallel-transport arround a closed curve approximately. What kind of Hamiltonian will lead to such a situation is work of a separate paper.

6. An example

The above ideas can be clarified in the following simple example. We consider a two-level quantum system which has an analogous description of a spin-1/2 particle. The quantum system is a single, two level atom driven by an intense, classical laser field, for which the Hamiltonian in the rotating wave approximation [18] can be written as $H = 1/2\hbar\Delta\sigma_3 + \hbar\lambda[\sigma_+ \exp(-i\varphi) + \sigma_- \exp(i\varphi)]$ where σ_3 is the Pauli spin matrix, Δ is the laser frequency, λ is the coupling strength and φ is the constant phase of laser field; σ_+ and σ_- being the Pauli raising and lowering operators. In this case, the Hilbert space is spanned by the basis vectors $|e\rangle$ and $|g\rangle$; therefore $\mathscr{H} = \mathrm{C}^2$ and the projective space $\mathscr{P} = \mathscr{P}_1(\mathrm{C})$ is a sphere. If the initial state $|\psi(0)\rangle$ is chosen to be $|e\rangle$, where

$$|e\rangle = \sin\theta/2 e^{i\varphi}|+\rangle + \cos\theta/2|-\rangle, \tag{20}$$

then, at any other time the state vector $|\psi(t)\rangle$ can be written as

$$|\psi(t)\rangle = \sin\theta/2 e^{i\varphi} e^{-i\omega t}|+\rangle + \cos\theta/2 e^{i\omega t}|-\rangle, \tag{21}$$

where $|+\rangle$ and $|-\rangle$ are the new basis vectors constructed from the linear superposition of the basis vectors $|e\rangle$ and $|g\rangle$, i.e.

$$|+\rangle = \cos\theta/2|g\rangle + \sin\theta/2 e^{-i\varphi}|e\rangle$$
$$|-\rangle = \cos\theta/2|e\rangle - \sin\theta/2 e^{i\varphi}|g\rangle.$$

Here the $\sin\theta/2$ and $\cos\theta/2$ are related to the parameters of the Hamiltonian and is given by

$$\sin\theta/2 = \frac{\omega-\Delta/2}{[2\omega(\omega-\Delta/2)]^{1/2}},\ \cos\theta/2 = \frac{\lambda}{[2\omega(\omega-\Delta/2)]^{1/2}} \text{ and } \omega^2 = \lambda^2 + \Delta^2/4.$$

Now the state vector $|\psi(t)\rangle$ undergoes a cyclic evolution over a period $T=\pi/\omega$. So that interval $[0,T]$ the state acquires a phase of π. During the evolution the dynamical phase is $\pi\cos\theta$ and the geometric phase is $\pi(1-\cos\theta)$. Now we calculate the lengths and the energies of the various curves. The total length of the dynamical curve is just π, whereas the energy associated with the dynamical curve is $\hbar\omega\pi$. The total length of the geometric curve is $[\pi 2\pi(1-\cos\theta)]^{1/2}$, whereas the associated energy is $\hbar\omega\Omega$, $\Omega = 2\pi\,(1-\cos\theta)$. Since the geometric length of the curve is equal to the square root of π times the total solid angle Ω subtended by the orbit of motion in a unit sphere, it justifies the name. The total length of the natural curve is equal to $\pi\sin\theta$. The CF for the dynamical curve is $\cos\theta$ and for the geometric curve is $\sin\theta/2$. This shows that the phases are proportional to the length of the curves.

Note that the dynamical phase and the geometric phase calculated on using (12) and (13) are $\pi\cos\theta$ and $\pi(1-\cos\theta)$ respectively. Using the states $|\psi_\pm(t)\rangle$ we calculate the total length of the curve $t\rightarrow|\psi_\pm(t)\rangle$. Now $l(\psi_+)|_0^T$ is given by $\pi^2(1+\sin\theta)^{1/2}$. Its associated energy is $\hbar\omega\pi(1+\sin\theta)$. Here, we can also see that the total phase calculated on using (18) is exactly what was expected. Finally $l(\psi_-)|_0^T$ is found to be $[\pi^2(2+3\cos\theta-4\cos\theta)]^{1/2}$. Its associated energy is $\hbar\omega\pi(2+3\cos\theta-4\cos\theta)$. Once again we can calculate the difference phase on using (18). Thus, this simple example demonstrates all the essential features of our formulation of the phases in terms of the length of the curves.

7. Conclusion

To conclude this section, various curves such as the dynamical, geometric and natural curves for an arbitrary cyclic evolution of a quantum system are introduced. Their lengths and energies are defined. It is proved that the phases can be expressed as the integral of the contracted length of some (suitably-defined) curves. Some inequalities among the phases, lengths and energies are shown to be valid. We established the equivalence between the phases and lengths of the curves. Thus wherever we measure the (relative) phase of a state vector undergoing a cyclic evolution, it is nothing but the length of the curve traced by the state vector (with a multiplicative CF). Since the non-adiabatic Berry phase has been measured experimentally, in a sense the contracted length of the geometric curve has been actually measured. So what remain to be measured are the total length of the dynamical curve, the geometric curve and the natural curve.

References

[1] M V Berry, *Proc. R. Soc.* (*London*) **392**, 45 (1984)
[2] B Simon, *Phys. Rev. Lett.* **51**, 2167 (1983)
[3] Y Aharonov and J Anandan, *Phys. Rev. Lett.* **58**, 1595 (1987)
[4] J Samuel and R Bhandari, *Phys. Rev. Lett.* **60**, 2339 (1988)
[5] V Bargmann, *Ann. Math.* **59**, 1 (1954)
[6] J P Provost and G Valle, *Commun. Math. Phys.* **76**, 289 (1980)
[7] J Anandan and Y Aharonov, *Phys. Rev. Lett.* **65**, 1697 (1990)
[8] R Montgomery, *Commun. Math. Phys.* **128**, 565 (1990)
[9] J Anandan, *Phys. Lett.* **A147**, 3 (1990)
[10] J Anandan, *Found. Phys.* **21**, 1256 (1991)
[11] A K Pati, *Phys. Lett.* **A159**, 105 (1991)
[12] A K Pati, *Europhys. Lett.* **18**, 285 (1992)
[13] A K Pati, *J. Phys.* **A25**, (1992)
A K Pati and A Joshi, *Phys. Rev.* **A47**, 98 (1993)
[14] S Abe, *Phys. Rev.* **A46**, 1667 (1992)
S Abe *Phys. Rev.* **A48**, 4102 (1993)
[15] Y Choquet-Bruhat, C Dewitt-Morette and M Dillard-Bleick, *Analysis, manifold and physics*, (North- Holland Publication, 1982) p. 321
[16] N Mukunda and R Simon, *Ann. Phys.* **228**, 205 (1993)
[17] Y Matsushima, *Differentiable manifolds* (Marcel Dekker, Inc. New York, 1972) p. 41
[18] L Allen and J H Eberly, *Optical resonance and two level atoms.* (New York: Wiley) (1975)

PRAMANA
— journal of
physics

© Printed in India

Vol. 42, No. 6,
June 1994
pp. 467–472

On a time-dependent system of noncentral anharmonic oscillators in two dimensions

R S KAUSHAL
Department of Physics and Astrophysics, University of Delhi, Delhi 110007, India

MS received 6 January 1994; revised 29 April 1994

Abstract. A new system of time-dependent anharmonic and anisotropic oscillators in two space-dimensions which corresponds to unequal but related spring constants, having Hamiltonian structure, admitting quadratic invariants and accounting also for the fractional powers in the coupling terms, is found.

Keywords. Time-dependent systems; dynamical invariants; hamiltonian structure.

PACS Nos 03·40; 03·20; 02·30

From several points of view the study of a system of coupled, nonlinear second order oscillators possessing at least one invariant has become quite interesting. Ermakov [1] originally suggested a connection between the solutions of such a pair of coupled equations. In recent years, Ray and Reid [2–6] and others [7–12] have studied these systems in the context of time-dependent (TD) harmonic oscillator and with different degrees of generalizations. As a matter of fact, in their course of study Ray and Reid have evolved a method of constructing the invariant for one-dimensional TD systems known as the Ermakov method and accordingly the invariant so constructed as the Ermakov invariant. The study of these systems is not only interesting as a mathematical exercise in its own right but it may also be useful in such disciplines as laser physics [13], quantum optics [13] and fluid dynamics [23].

The most studied system is the TD harmonic oscillator, which is described by [3]

$$\ddot{x} + \omega^2(t)x = 0, \tag{1}$$

and admits an invariant

$$I = (1/2)[(x/\rho)^2 + (x\dot{\rho} - \dot{x}\rho)^2], \tag{2}$$

where $x(t)$ satisfies (1) and $\rho(t)$ satisfies the auxiliary equation

$$\ddot{\rho} + \omega^2(t)\rho = 1/\rho^3. \tag{3}$$

Following Ermakov [1], Ray and Reid have studied various types of generalization of eqs (1) and (3), and obtained [4, 5] the solutions of a specific class of nonlinear equations. Besides accounting for the damping terms in (1) and (3), the most common generalization considered by them is the following:

For the forms of (1) and (3) as [2]

$$\ddot{x} + \omega^2(t)x = g(\rho/x)/(x^2\rho), \tag{4a}$$

$$\ddot{\rho} + \omega^2(t)\rho = f(x/\rho)/(x\rho^2), \tag{4b}$$

the invariant (2) takes the form

$$I = (1/2)[\phi(x/\rho) + \theta(\rho/x) + (x\dot{\rho} - \dot{x}\rho)^2] \tag{5}$$

with

$$\phi(x/\rho) = 2\int^{(x/\rho)} f(u)\mathrm{d}u; \quad \theta(\rho/x) = 2\int^{(\rho/x)} g(u)\mathrm{d}u.$$

As a special case while $x(t)$ satisfies (1), $\rho(t)$ is also found [4] to satisfy

$$\ddot{\rho} + \omega^2(t)\rho = 1/(x\rho^2)\sum_i c_i(x/\rho)^{2m}i^{-1}, \quad (i = 1, 2, \ldots) \tag{6}$$

where c_i and m_i are arbitrary constants. For $i = 1$ and 2, and with $m_1 = (m-2)/2$, $m_2 = (2m-2)/2$, eq. (6) becomes

$$\ddot{\rho} + \omega^2(t)\rho = c_1 x^{m-4}\rho^{1-m} + c_2 x^{2m-4}\rho^{1-2m}. \tag{7}$$

Among other generalizations considered by Reid and Ray [5], one is in connection with the nonlinear superposition law for the solutions of higher order nonlinear equations. Such a generalization however is not of much interest in the present context. It may be mentioned that all the above generalizations of Ermakov systems are essentially for one-dimensional TD systems (in fact, for the one-dimensional TD harmonic oscillator) and $\rho(t)$ appears as an auxiliary variable needed to provide the invariant for the corresponding TD system. On the other hand, $\rho(t)$ also plays a specific role while looking for a physical interpretation of the derived invariant [12]. In any case, it does not imply the generalization of Ermakov systems to higher space-dimensions. Further, in obtaining (7) the choices of m_1 and m_2 in (6) seem rather ad hoc.

Other generalizations of Ermakov systems have recently been considered by Leach [10] and Athorne [11]. Leach finds an explanation for the nature of the Ermakov system described by

$$\ddot{x}_1 + \omega^2(t)x_1 = g_1(x_2/x_1)/x_1^3, \tag{8a}$$

$$\ddot{x}_2 + \omega^2(t)x_2 = f_1(x_2/x_1)/x_2^3, \tag{8b}$$

in terms of a symmetry algebra. In this case, a transformation of time- and space-variables, namely $T = \cot(\int\rho^{-2}\mathrm{d}t)$; $X = \rho^{-1}x_1\csc T$; $Y = \rho^{-1}x_2\csc T$, eliminates $\omega^2(t)$ from eqs (8) and the newly introduced variable ρ is found to satisfy an equation of the type (3). On the other hand, Althorne makes use of this symmetry algebra of Leach to analyse a Kepler–Ermakov system of the type $\ddot{\mathbf{x}} + \omega^2(t)\mathbf{x} = v(\mathbf{x})/r^3$, by setting $\omega^2(t) = 0$. Another interesting system studied in this context is that of coupled Pinney's equations [15, 16]

$$\ddot{x}_1 + \omega^2(t)x_1 = \beta x_1^{-3} - \alpha x_1 x_2^{-4}, \tag{9a}$$

$$\ddot{x}_2 + \omega^2(t)x_2 = \delta x_2^{-3} - \gamma x_2 x_1^{-4}. \tag{9b}$$

In this case, however, there remains [14], in general, a difficulty of finding a Hamiltonian structure. In the absence of such a structure the system remains of least physical interest. For example, for the system (9) the Hamiltonian structure exists

[16] only for $\alpha = 3\delta$, $\gamma = 3\beta$ and with a kinetic term of hardly any physical interest. In spite of the fact that the invariant associated with this system can be constructed explicitly, this system does not turn out [11] to be integrable even for $\omega(t) = \text{constant}$, i.e. even in a time independent case.

It may be mentioned that the variable $x_2(t)$ in (9) can, in principle, be regarded as $\rho(t)$ of (3) or of (6), and is, in fact, a variable in the second space dimension. On the other hand, the system studied by Leach (cf. eqs (8)) no doubt reduces to the Ray and Reid-form (4) on redefining g_1 and f_1 as

$$g_1(x_2/x_1) = (x_1/x_2)g(x_1/x_2), \quad f_1(x_2/x_1) = (x_2/x_1)f(x_2/x_1)$$

but is structurally different from (4) in the sense that ρ-equation now appears as a by-product of the transformation. Also, in the work of Ray and Reid the ρ-equation (3) is a prerequisite for the existence of the invariant (2). Thus, eqs (8) and (9) although describe certain TD coupled oscillators in two dimensions (with equal spring constants along each dimension) but without any auxiliary equation. Now the question arises as to what are the Ermakov systems in two dimensions which remain integrable and also retain the Hamiltonian structure at the same time. In what follows we suggest a class of Ermakov-type systems in two dimensions which (i) deals with unequal but related spring constants, (ii) ensures, in general, a Hamiltonian structure, (iii) admits quadratic (in momenta) invariants, (iv) can involve fractional powers in the coupling terms, and (v) involves a pair of auxiliary equation in a natural manner. To the best of our knowledge, all these features in a time-dependent system have not been considered so far.

In the present work, we consider a two-dimensional system,

$$V(x_1, x_2, t) = \alpha_1(t)x_1^2 + \alpha_2(t)x_2^2 + \beta(t)x_1^m x_2^n. \tag{10}$$

It is found [17] that this system admits a quadratic invariant only for the case when the arbitrary numbers m and n satisfy the condition $m + n = -2$ and β is a constant. Due to symmetry considerations, we investigate here a system described by the Lagrangian,

$$L = (1/2)(\dot{x}_1^2 + \dot{x}_2^2) - \alpha_1(t)x_1^2 - \alpha_2(t)x_2^2 - \beta_{10}x_1^{-2-n}x_2^n - \beta_{20}x_1^n x_2^{-2-n}. \tag{11}$$

Before we proceed further a few remarks about this general form are in order: (i) Invariants corresponding to some special cases of (11) (particularly, when n is an integer, namely $n = -1, 0$ and $+1$) are derived earlier [17] using the rationalization method [17–19]. In (11) while β_{10} and β_{20} are constants, they can be time-dependent for $n = 0$. The results corresponding to fractional values of n will be discussed later as a special case. (ii) The dynamical algebraic approach [9] when extended to two-dimensional systems also leads [20] to the form (11) as a result of the closer property of the associated Lie algebra. From the rationalization of the 'potential' equation [17–19] for the system (11), the coefficient functions $a_i(x_1, x_2, t)$ and $a_{ij}(x_1, x_2, t)$ in the invariant

$$I = a_0 + a_1\dot{x}_1 + a_2\dot{x}_2 + (1/2)(a_{11}\dot{x}_1^2 + 2a_{12}\dot{x}_1\dot{x}_2 + a_{22}\dot{x}_2^2) \tag{12}$$

turn out to be

$$a_{11} = a_{22} = \psi_3(t); \quad a_{12} = 0,$$

$$a_1 = -(1/2)(\dot{\psi}_3 x_1 + c_5 x_2 - \psi_7); \quad a_2 = -(1/2)(\dot{\psi}_3 x_2 - c_5 x_1 - \psi_6),$$

where c_i are the arbitrary constants and $\psi_i \equiv \psi_i(t)$, are the arbitrary functions. A unique expression for a_0 can be obtained from the integration of the equations [17, 18]

$$\partial a_0/\partial x_1 = a_{11}(\partial V/\partial x_1) - \partial a_1/\partial t; \quad \partial a_0/\partial x_2 = a_{22}(\partial V/\partial x_2) - \partial a_2/\partial t,$$
$$\partial a_0/\partial t = a_1(\partial V/\partial x_1) + a_2(\partial V/\partial x_2)$$

as

$$a_0 = \{\alpha_1\psi_3 + (1/4)\ddot{\psi}_3\}x_1^2 + \{\alpha_2\psi_3 + (1/4)\ddot{\psi}_3\}x_2^2 + \beta_{10}\psi_3 x_1^{-2-n}x_2^n + + \beta_{20}\psi_3 x_1^n x_2^{-2-n}, \tag{13}$$

provided ψ_3, α_1 and α_2 satisfy the equations

$$(1/4)\dddot{\psi}_3 + 2\alpha_1\dot{\psi}_3 + \dot{\alpha}_1\psi_3 = 0; \tag{14a}$$

$$(1/4)\dddot{\psi}_3 + 2\alpha_2\dot{\psi}_3 + \dot{\alpha}_2\psi_3 = 0. \tag{14b}$$

and $c_5 = \psi_6 = \psi_7 = 0$. Equations (14a) and (14b) further provide $\psi_3(t)$ as

$$\psi_3(t) = c_3(\alpha_1 - \alpha_2)^{-1/2}, \tag{15}$$

with a constraint on the potential parameters α_1 and α_2 of the form

$$4(\dddot{\alpha}_1 - \dddot{\alpha}_2)(\alpha_1 - \alpha_2)^2 - 18(\alpha_1 - \alpha_2)(\dot{\alpha}_1 - \dot{\alpha}_2)(\ddot{\alpha}_1 - \ddot{\alpha}_2) + 15(\dot{\alpha}_1 - \dot{\alpha}_2)^3 = 32(\alpha_1 - \alpha_2)^2(\alpha_1\dot{\alpha}_2 - \dot{\alpha}_1\alpha_2). \tag{16}$$

Finally, the invariant (12) for the system (11) becomes

$$I = \{\alpha_1\psi_3 + (1/4)\ddot{\psi}_3\}x_1^2 + \{\alpha_2\psi_3 + (1/4)\ddot{\psi}_3\}x_2^2 + \beta_{10}\psi_3 x_1^{-2-n}x_2^n + + \beta_{20}\psi_3 x_1^n x_2^{-2-n} - (1/2)\dot{\psi}_3(x_1\dot{x}_1 + x_2\dot{x}_2) + (1/2)\psi_3(\dot{x}_1^2 + \dot{x}_2^2), \tag{17}$$

which, in fact, is in conformity with $\mathrm{d}I/\mathrm{d}t = \partial I/\partial t + [I, H]_{PB} = 0$.

Several remarks about the form (11) and the corresponding invariant (17) are in order:

(1) For $n = -1$ and $+1$, the form (17) not only reduces to the results obtained earlier [17] but also provides the invariants for a class of systems characterized by the arbitrary number n including its fractional values. For example, for $n = -3/2$ in (11) the invariant (17) takes the form

$$I = \{\alpha_1\psi_3 + (1/4)\ddot{\psi}_3\}x_1^2 + \{\alpha_2\psi_3 + (1/4)\ddot{\psi}_3\}x_2^2 + \beta_{10}\psi_3 x_1^{-1/2}x_2^{-3/2} + \beta_{20}\psi_3 x_1^{-3/2}x_2^{-1/2} - (1/2)\dot{\psi}_3(x_1\dot{x}_1 + x_2\dot{x}_2) + (1/2)\psi_3(\dot{x}_1^2 + \dot{x}_2^2) \tag{18}$$

with ψ_3 again given by (15) and α_1 and α_2 again related through (16). In this case, however, the invariant I is constrained by the values of x_1 and x_2, particularly when they are negative. In fact, one should consider $|I|$ here for negative values of x_1 or of x_2.

(2) The pair of coupled equations of motion corresponding to the system (11) can be written as

$$\ddot{x}_1 + 2\alpha_1(t)x_1 = (n+2)\beta_{10}x_1^{-3-n}x_2^n - n\beta_{20}x_1^{n-1}x_2^{-2-n}, \tag{19a}$$

$$\ddot{x}_2 + 2\alpha_2(t)x_2 = -n\beta_{10}x_1^{-2-n}x_2^{n-1} + (n+2)\beta_{20}x_1^{n}x_2^{-3-n}. \tag{19b}$$

It is interesting to note that eqs (19a) and (19b) while providing a physically acceptable Hamiltonian structure also offer a Pinney type system [11] for $n = 1$. Further, these equations alongwith eqs (14) not only suggest a new class of time-dependent systems for any finite n but can also be regarded as a generalization of eqs (1) and (7) to higher space-dimensions. In this latter case $\psi_3(t)$, satisfying a pair of third-order equations (of, eq. (14)), can be considered as playing the role of an auxiliary variable (just like $\rho(t)$ in one dimension).

(3) In order to get (7) from (6) the choice of m_1 and m_2 in terms of m seems rather ad hoc in the method of Ray and Reid; whereas here in the two-dimensional case there exists [17] a rationale for such a choice which, in fact, reflects the characteristic of the dynamical system (10).

(4) The invariant (17) is also obtained using other [20] methods and it can be expressed as

$$I = \psi_3(t)H(t) + (1/4)\mathrm{d}[\dot{\psi}_3(x_1^2 + x_2^2)]/\mathrm{d}t - \dot{\psi}_3(x_1\dot{x}_1 + x_2\dot{x}_2) \tag{20}$$

where $H(t)$ is the Hamiltonian corresponding to the system (11). Equation (20) implies that for $\dot{\psi}_3 = 0$, the invariant I reduces to $H(t)$ and α_1 and α_2 become time-independent (cf. eq. (14)).

To summarize, we mention that there exists a new class of time-dependent systems in two dimensions which not only possesses Hamiltonian structure and admits quadratic invariants but can also account for the fractional powers in the coupling terms. Further, there exists a rationale for the powers of the coupling terms in these systems. While all these features could be important in characterizing the new Ermakov-type systems, they are somehow not exhibited by some of the known systems like Pinney's equations. For the complete integrability of these systems, however, there is a need for one more invariant to exist [21]. Such studies with reference to higher order [22] (in momenta) invariants are in progress.

Acknowledgements

The author wishes to record his sincere thanks to Dr D Parashar for several discussions and for critical reading of the manuscript. Several useful suggestions by the referee are gratefully acknowledged. Financial grant from UGC, New Delhi in the form of Research Scientist Scheme is also acknowledged.

References

[1] V Ermakov, *Univ. Izv. Kiev series III* **9**, 1 (1880)
[2] J R Ray and J L Reid, *Phys. Lett.* **A71** 317 (1979)
[3] J R Ray and J L Reid, *Phys. Lett.* **A74**, 23 (1979)
[4] J R Ray and J L Reid, *J. Math. Phys.* **20**, 2054 (1979)
[5] J L Reid and J R Ray, *J. Math. Phys.* **23**, 503 (1982)
[6] J L Reid and J R Ray, *J. Phys.* **A15**, 2751 (1982)
[7] H Lewis and W Riesenfeld, *J. Math. Phys.* **10**, 1458 (1969)
[8] M Lutzky, *Phys. Lett.* **A71**, 317 (1979); **A78** 301 (1980)
[9] R S Kaushal and H J Korsch, *J. Math. Phys.* **22** 1904 (1981)
[10] P G L Leach, *Phys. Lett.* **A158**, 102 (1991)

[11] C Athorne, *Phys. Lett.* **A159**, 375 (1991)

[12] C J Eliezer and A Gray, *SIAM J. Appl. Math.* **30**, 463 (1976)

[13] J M Cervero and J D Lejarreta, *Quant. Opt.* **2**, 333 (1990)

[14] J M Cervero and J D Lejarreta, *Phys. Lett.* **A156**, 201 (1991)

[15] E Pinney, *Proc. Am. Math. Soc.* **1**, 681 (1950)

[16] J Douglas, *Trans. Am. Math. Soc.* **50**, 71 (1941)

[17] R S Kaushal, D Parashar and S C Mishra, *Second order invariants for two dimensional classical dynamical systems* to be published in *Fortschritte der Physik* **42** (1994) #5 (in press)

[18] R S Kaushal, S C Mishra and K C Tripathy, *Phys. Lett.* **A102**, 7 (1984)
S C Mishra, R S Kaushal and K C Tripathy, *J. Math. Phys.* **25**, 2217 (1984)

[19] S C Mishra *Some aspects of two dimensional classical integrable systems*, Ph D Thesis (Univ. of Delhi, 1985), unpublished

[20] R S Kaushal and S C Mishra, *J. Math. Phys.* **34**, 5843 (1993)

[21] E T Whittaker, *Analytical dynamics* (University Press, Cambridge, 1927)

[22] R S Kaushal, *Pramana – J. Phys.* **24**, 663 (1985)

[23] For other applications of these systems, see, for example, the unpublished recent work cited in [11]

PRAMANA
— journal of
physics

© Printed in India

Vol. 42, No. 6,
June 1994
pp. 473–481

Cosmological models with constant deceleration parameter in Nordtvedt's theory

V B JOHRI and KALYANI DESIKAN
Cosmology Group, Department of Mathematics, Indian Institute of Technology, Madras 600036, India

MS received 26 November 1993; revised 5 March 1994

Abstract. Exact solutions of the field equations of Nordtvedt's theory for spatially flat FRW models with constant deceleration parameter have been obtained. Singular solutions with (i) power-law (ii) exponential expansion have been studied in Nordtvedt's theory where the coupling parameter ω is a function of the scalar field ϕ.

Keywords. Cosmology; power-law and exponential expansion; general scalar-tensor theory.

PACS No. **98·80**

1. Introduction

The success of the inflationary scenario has made it an important milestone in the evolution of the early universe. The phenomenon of cosmological inflation requires a finite period of accelerated expansion in the early universe. Several variants of the original inflationary scenario given by Guth (1981) now exist.

La and Steinhardt [1, 2] proposed a new type of inflationary scenario based on BD theory of gravity known as extended inflationary scenario. Unlike previous inflationary models based on general theory of relativity, here the inflationary phase transition can be completed via bubble nucleation. It provides a new solution to the graceful exit problem. Hence, the fine tuning of an effective potential to obtain a slow-roll over transition is not required. But the original idea of extended inflation has its own problems.

If the BD parameter ω is chosen to satisfy constraints from light-deflection and time-delay experiments ($\omega > 500$) [3], the original model leads to excessive distortions in the cosmic microwave background radiation. Weinberg [4] obtained upper bounds on the BD parameter ($\omega < 76$) by requiring that the recovery from the supercooled regime be such that the presently observed universe might emerge. La *et al* [5] discussed a number of astrophysical and cosmological constraints ($\omega < 25$) that significantly limit the types of workable theories and the allowed range of physical parameters. A successful inflationary scenario would require a value of $\omega < 25$ in the early universe. Several means have been devised in order to circumvent this problem.

In order to reconcile the notion of extended inflation with limits obtained from measurements of the microwave background anisotropies, several authors have considered extending the gravitational action beyond the BD action functional used in the original extended inflation model. The first method of evading the microwave bounds was to introduce a potential term $V(\phi)$ for the BD field [5, 6]. This model, however, has a drawback since it requires the BD potential to be very flat so that it does not dominate over false-vacuum energy and disrupt the first-order inflation [7]. Another alternative invokes different couplings of the BD field to visible and invisible matter [8] though these have recently been more tightly constrained [9]. The most popular alternative is to make further modifications to the gravitational action leading to models referred to as hyperextended inflation [10, 11]. Barrow and Maeda [12] have found examples of a new type of inflation intermediate between the power-law and exponential types. They assumed ω as a function of the scalar field ϕ which increases during the evolution of the universe. The functional dependence of ω was taken to be

$$\omega(\phi) = \omega_m \phi^m + \omega_0$$

were ω_m and ω_0 are dimensionless positive constants and the power index m is a real number. Bellido and Quiros [13] proposed a solution to extended inflation by choosing ω as

$$2\omega(\phi) + 3 = 2\beta(1 - \phi/\phi_c)^{-\alpha}$$

where $\phi_c \equiv M_c^2$ with M_c a mass scale close to the Planck mass M_{pl} today.

The most general example of scalar-tensor theories is the Bergmann–Wagoner theory [14, 15, 16] in which the coupling of the scalar field ϕ to the curvature and the cosmological term both depend upon ϕ. This class of theories encompasses other scalar-tensor theories such as Brans–Dicke theory and Nordtvedt's, theory and can be shown to be a low-energy limit of certain superstring theories [17]. Here since the coupling parameter $\omega = \omega(\phi)$ evolves with time, ω could be small initially ($\omega < 25$) and it could increase with the evolution of the universe to a large value ($\omega > 500$) at the present epoch. Hence, general scalar-tensor theories like the Nordtvedt's theory, which overcome the problem inherent in working with the BD theory have caught the fascination of cosmologists [18, 19].

It is worthwhile to observe that most of the well-known models of Einstein's theory and Brans–Dicke theory with curvature parameter $k = 0$, including inflationary models, are models with constant deceleration parameter. The models with constant deceleration parameter form an interesting class of models in cosmology. This has provided us the motivation to study models with constant deceleration parameter in Nordtvedt's theory. Moreover, the number of equations in Nordtvedt's theory is less than the number of unknowns. Hence, an additional assumption in the form of a constant deceleration parameter would suffice to make the system of equations well defined and obtain a unique solution.

In § 2, the field equations of Nordtvedt's theory are given. Section 3 deals with the general solution of Nordtvedt's theory with constant deceleration parameter.

2. Field equations of Nordtvedt's theory

The gravitational field equations of Nordtvedt's theory are given by

$$G_{ab} = -\frac{8\pi}{\phi} T_{ab} - \frac{\omega}{\phi^2}[\phi_{;a}\phi_{;b} - \tfrac{1}{2} g_{ab}\phi_{;c}\phi^{;c}] - \frac{1}{\phi}[\phi_{;a;b} - g_{ab}\Box^2\phi] \tag{1}$$

$$\Box^2\phi = \frac{1}{3 + 2\omega}[8\pi T^{a}_{.a} - \omega' \phi_{;c}\phi^{;c}] \tag{2}$$

where $\omega' \equiv \mathrm{d}\omega/\mathrm{d}\phi$ and T_{ab}, the energy-momentum tensor for a perfect fluid, is given by

$$T_{ab} = (\rho + p)u_a u_b - p g_{ab}. \tag{3}$$

We now restrict our attention to space-times which are homogeneous, isotropic and flat, for which the line element is just the FRW line element (with $k = 0$)

$$\mathrm{d}s^2 = \mathrm{d}t^2 - R^2(t)[\mathrm{d}r^2 + r^2(\mathrm{d}\theta^2 + \sin^2\theta\,\mathrm{d}\phi^2)] \tag{4}$$

where $R(t)$ is the scale factor.

The field equations (1) and (2) with the above metric and the barotropic equation of state

$$p = \gamma\rho, \quad 0 \leqslant \gamma \leqslant 1 \tag{5}$$

now become

$$3\left(\frac{\dot{R}}{R}\right)^2 + 3\frac{\dot{R}}{R}\frac{\dot{\phi}}{\phi} - \frac{\omega}{2}\left(\frac{\dot{\phi}}{\phi}\right)^2 = \frac{8\pi\rho}{\phi} \tag{6}$$

$$2\frac{\ddot{R}}{R} + \left(\frac{\dot{R}}{R}\right)^2 + \frac{\ddot{\phi}}{\phi} + \frac{\omega}{2}\left(\frac{\dot{\phi}}{\phi}\right)^2 + 2\frac{\dot{R}}{R}\frac{\dot{\phi}}{\phi} = -\frac{8\pi\gamma\rho}{\phi} \tag{7}$$

$$\ddot{\phi} + 3\frac{\dot{R}}{R}\dot{\phi} = \frac{8\pi}{3 + 2\omega}(1 - 3\gamma)\rho - \frac{\omega'}{3 + 2\omega}\dot{\phi}^2. \tag{8}$$

Equations (6–8) lead to the continuity equation,

$$\dot{\rho} + 3(1 + \gamma)\rho H = 0 \tag{9}$$

where $H = (\dot{R}/R)$ is the Hubble's function.

Here there are only three independent equations in four unknowns viz., R, ϕ, ρ and ω. Therefore, one more relation is necessary to obtain a unique solution, for which we assume the deceleration parameter to be constant.

Equation (9) on integration yields

$$\rho = \rho_0 R^{-3(1+\gamma)}. \tag{10}$$

3. Exact solutions with constant deceleration parameter

Consider a model with constant deceleration parameter, i.e.,

$$q = -(R\ddot{R})/(\dot{R})^2 = \beta(\text{constant}). \tag{11}$$

Equation (11) can be rewritten as

$$\frac{\ddot{R}}{R} + \beta\left(\frac{\dot{R}}{R}\right)^2 = 0. \tag{12}$$

On integration the above equation gives the exact solution

$$R(t) = \begin{cases} (A + Bt)^{1/(1+\beta)}, & \beta \neq -1 \quad (13a) \\ C\exp(\chi t), & \beta = -1 \quad (13b) \end{cases}$$

where A, B, C and χ are constants of integration. Also, when $\beta = -1$, $H = \chi =$ constant.

The above solutions may be relevant during different eras of evolution in Nordtvedt's theory. For example, we can assume the power-law expansion following the big bang, culminating in exponential expansion during inflationary era and reverting to power-law expansion again after exit from inflation.

For singular models (big bang cosmology with $R(0) = 0$), the expression (13a) for the scale factor may be rewritten as

$$R(t) \sim t^{1/(1+\beta)}, \quad \beta \neq -1 \tag{14}$$

but during the course of evolution, for instance during inflation,

$$R(t) \sim \exp(\chi t) \tag{15}$$

Now equation (10) together with (14) yields

$$\rho = \rho_0 t^{-3(1+\gamma)/(1+\beta)}, \tag{16}$$

Equation (6) coupled with (7) gives

$$2\frac{\ddot{R}}{R} + 4\left(\frac{\dot{R}}{R}\right)^2 + \frac{\ddot{\phi}}{\phi} + 5\frac{\dot{R}}{R}\frac{\dot{\phi}}{\phi} = \frac{8\pi(1-\gamma)\rho}{\phi}. \tag{17}$$

Case (*i*), $\beta \neq -1$

Using (14) and (16) in (17) we have

$$t^2\ddot{\phi} + \frac{5t}{(1+\beta)}\dot{\phi} + \frac{2(2-\beta)}{(1+\beta)^2}\phi = 8\pi\rho_0 t^{2-[3(1+\gamma)]/(1+\beta)}. \tag{18}$$

Equation (18) can be readily integrated to give

$$\phi = \frac{8\pi(1-\gamma)\rho_0(1+\beta)^2}{[2\beta+1-3\gamma][\beta+1-3\gamma]} t^{2-[3(1+\gamma)]/(1+\beta)} + a_1 t^{-2/(1+\beta)} + a_2 t^{(\beta-2)/(1+\beta)} \tag{19}$$

a_1 and a_2 being constants of integration.

Using the expressions for $R(t)$, $\rho(t)$ and $\phi(t)$ from (14), (16) and (19) in (6) we get $\omega(t)$ as

$$\frac{\omega}{6}(1+\beta)^2[\dot{\phi}]^2 = [A_1(t)A_2(t) + A_3(t)A_4(t) - A_5(t)A_6(t)] \tag{20}$$

where

$$[\dot{\phi}]^2(1+\beta)^2 = \{(2\beta-1-3\gamma)Kt^{1-[3(1+\gamma)/(1+\beta)]} - 2a_1 t^{-2(2+\beta)/(1+\beta)} + (\beta-2)a_2 t^{-3/(1+\beta)}\}^2$$

$$A_1(t) = \{2Kt^{1-[3(1+\gamma)/(1+\beta)]} + a_1 t^{-(3+\beta)/(1+\beta)}\}$$

$$A_2(t) = \left\{K\left[(2\beta-3\gamma) - \frac{(2\beta+1-3\gamma)(1+\beta-3\gamma)}{3(1-\gamma)}\right]t^{1-[3(1+\gamma)/(1+\beta)]} - \frac{a_1}{2}t^{-(3+\beta)/(1+\beta)}\right\}$$

$$A_3(t) = \left\{\frac{a_1}{2} t^{-(3+\beta)/(1+\beta)} + a_2 t^{-[3/(1+\beta)]}\right\}$$

$$A_4(t) = \left\{2(\beta - 1) a_2 t^{-[3/(1+\beta)]} - a_1 t^{-(3+\beta)/(1+\beta)}\right\}$$

$$A_5(t) = \left\{K\left[(2\beta - 3\gamma) - \frac{(2\beta + 1 - 3\gamma)(1 + \beta - 3\gamma)}{3(1-\gamma)}\right] t^{1-[3(1+\gamma)/(1+\beta)]} - (\beta - 1) a_2 t^{-[3/(1+\beta)]}\right\}$$

$$A_6(t) = \left\{K t^{1-[3(1+\gamma)/(1+\beta)]} - a_2 t^{-[3/(1+\beta)]}\right\}$$

with

$$K = \frac{8\pi(1-\gamma)\rho_0(1+\beta)^2}{(2\beta + 1 - 3\gamma)(1 + \beta - 3\gamma)}. \tag{21}$$

When $a_1 = a_2 = 0$, the above solution for ϕ reduces to that in BD theory and the coupling parameter ω become invariant with respect to time, also (20) reduces to [20]

$$\omega = \frac{2(1-\beta)}{(1-\gamma)(2\beta - 1 - 3\gamma)} \tag{22}$$

From expression (20), it might look formidable to study the behaviour of ω. But as shown below the expression for ω reduces to simpler forms for two different ranges of the deceleration parameter β. In the following analysis, we consider the relative contributions of the second term with co-efficient a_1 and the third term with co-efficient a_2 in (19). The term with dominant contribution is retained while the other term is dropped.

Case(i) (a) $-1 < \beta < 1$

It is evident, by comparing the exponents of the second and third terms in equation (19), that for values of β lying in the range $-1 < \beta < 0$ (accelerated expansion), the third term in (19) decreases faster with time than the second term and can therefore be neglected for large times. Further, for values of β in the range $0 < \beta < 1$ (decelerated expansion), the exponent of the third term in (19) is comparable to that of the second term. Therefore, any one of the two terms would suffice. Hence, without loss of generality, we have retained the second term in (19). Therefore, for $-1 < \beta < 1$ we have

$$\phi \sim K t^{(2\beta - 1 - 3\gamma)/(1+\beta)} + a_1 t^{-2/(1+\beta)}. \tag{23}$$

Neglecting a_2 in (20), we find

$$\frac{\omega}{6} = \frac{B_1(t) B_2(t)}{[B_3(t)]^2} \tag{24}$$

where

$$B_1(t) = \left\{K + a_1 t^{-(2\beta + 1 - 3\gamma)/(1+\beta)}\right\}$$

$$B_2(t) = \left\{K\left[(2\beta - 3\gamma) - \frac{(2\beta + 1 - 3\gamma)(1 + \beta - 3\gamma)}{3(1-\gamma)}\right] - a_1 t^{-(2\beta + 1 - 3\gamma)/(1+\beta)}\right\}$$

$$B_3(t) = \left\{K(2\beta - 1 - 3\gamma) - 2a_1 t^{-(2\beta + 1 - 3\gamma)/(1+\beta)}\right\}$$

The first derivative of ω with respect to time is given by

$$\dot{\omega} = \frac{C_1(t)C_2(t)}{[C_3(t)]^3} \tag{25}$$

where

$$C_1(t) = 4\pi\rho_0 a_1(1+\beta)(2\beta+1-3\gamma)t^{-(3\beta+2-3\gamma)/(1+\beta)}$$

$$C_2(t) = \left\{K\frac{\beta(2\beta-1-3\gamma)}{2(1+\beta-3\gamma)} + a_1 t^{-(2\beta+1-3\gamma)/(1+\beta)}\right\}$$

$$C_3(t) = \left\{\frac{K}{2}(2\beta-1-3\gamma) - a_1 t^{-(2\beta+1-3\gamma)/(1+\beta)}\right\}.$$

The solutions of Banerjee *et al* [19] can be obtained as a particular case by substituting $\beta = -(1/2)$ and $\gamma = -1$ in (23) and (24).

For small values of time a similar analysis can be done. It can be readily seen that for small times the third term in (19) is the dominant contributor. Hence, in the analysis the third is to be retained.

Case (*i*) (*b*) $\beta > 1$

Here, the second term decreases faster with time than the third term in (19) and hence can be neglected for large times. Therefore, we have

$$\phi \sim Kt^{(2\beta-1-3\gamma)/(1+\beta)} + a_2 t^{(\beta-2)/(1+\beta)}. \tag{26}$$

Putting $a_1 = 0$ in (20), we get

$$\frac{\omega}{6} = \frac{D_1(t)D_2(t)}{[D_3(t)]^2} \tag{27}$$

where

$$D_1(t) = \{K + a_2 t^{-(\beta+1-3\gamma)/(1+\beta)}$$

$$D_2(t) = \left\{K\left[(2\beta-3\gamma) - \frac{(2\beta+1-3\gamma)(1+\beta-3\gamma)}{3(1-\gamma)}\right] \times (\beta-1)a_2 t^{-(\beta+1-3\gamma)/(1+\beta)}\right\}$$

$$D_3(t) = \{K(2\beta-1-3\gamma) + (\beta-2)a_2 t^{-(\beta+1-3\gamma)/(1+\beta)}\}$$

Here $\dot{\omega}$ is given by

$$\dot{\omega} = \frac{E_1(t)}{[E_2(t)]^3} \tag{28}$$

where

$$E_1(t) = -4\pi\rho_0 a_2^2 \frac{(1+\beta)(1+\beta-3\gamma)(2\beta-1-3\gamma)}{(2\beta+1-3\gamma)} t^{-1},$$

$$E_2(t) = \left\{\frac{K}{2}(2\beta-1-3\gamma) + (\beta-2)\frac{a_2}{2} t^{-(\beta+1-3\gamma)/(1+\beta)}\right\}.$$

It can be easily observed that for small times the second term of (19) is to be retained and a similar analysis can be carried out.

It can be seen from the above expressions that the behaviour of ϕ and ω are determined by various parameters such as γ, β, a_1 and a_2. The signature of various quantities like β, a_1, a_2, $(2\beta + 1 - 3\gamma)$, $(1 + \beta - 3\gamma)$, $[3(1-\gamma)(2\beta - 3\gamma) - (2\beta + 1 - 3\gamma)(1 + \beta - 3\gamma)]$ should be considered while studying the evolution of ϕ and ω. Also the signature of the exponents of t in the above expressions plays a crucial role in determining the behaviour of these quantities. As such, there is a variety of models wherein ω increases or decreases with time. There also exists models in which ω decreases (or increases) up to a certain time and thereafter increases (or decreases). Moreover, for ω to be positive, the products of the terms in the numerator of (24) or (27) should be positive. The first derivative of ω with respect to time is useful in determining the behaviour of ω. As such we restrict our attention to that particular class of models for which ω increases with time.

Consider $a_1 < 0$ and $a_2 = 0$ with

$$\begin{aligned} &(2\beta + 1 - 3\gamma) > 0 \\ &(\beta + 1 - 3\gamma) < 0 \\ &(2\beta - 1 - 3\gamma) < 0 \end{aligned} \tag{29}$$

then β would lie in the range

$$\frac{3\gamma - 1}{2} < \beta < 3\gamma - 1 \tag{30}$$

with $\frac{1}{3} < \gamma < 1$. Therefore, from (25) it can be seen that $C_1(t) < 0$, $C_2(t) < 0$ and $C_3(t) > 0$, $\forall t$. Hence, $\dot{\omega} > 0$ i.e. ω increases with time.

Case ii: $\beta = -1$

From equation (13) we see that the scale factor is given by

$$R(t) = Ce^{\chi t}. \tag{31}$$

Using this in (10) we obtain

$$\rho = \rho_0 e^{-3(1+\gamma)\chi t} \tag{32}$$

Now using (31) and (32) in (17) we have

$$\ddot{\phi} + 5\chi\dot{\phi} + 6\chi^2\phi = 8\pi(1-\gamma)\rho_0 e^{-3(1+\gamma)\chi t}. \tag{33}$$

The above equation on integration yields

$$\phi = \frac{8\pi(1-\gamma)\rho_0}{3\chi^2\gamma(1+3\gamma)} e^{-3(1+\gamma)\chi t} + Ae^{-2\chi t} + Be^{-3\chi t} \tag{34}$$

where A and B are constants of integration.

Using (31), (32) and (34) in (6), ω is given by

$$\frac{\omega}{6}[\dot{\phi}]^2 = -\chi^2[X_1(t)X_2(t) + X_3(t)X_4(t) + X_5(t)X_6(t)]^2 \tag{35}$$

where

$$[\dot{\phi}]^2 = \chi^2\{3(1+\gamma)K'e^{-3(1+\gamma)\chi t} + 2Ae^{-2\chi t} + 3Be^{-3\chi t}\}$$

$$X_1(t) = \{2K'e^{-3(1+\gamma)\chi t} + Ae^{-2\chi t}\},$$

$$X_2(t) = \left\{\frac{K'(1+\gamma)(3\gamma-1)}{(1-\gamma)}e^{-3(1+\gamma)\chi t} + \frac{A}{2}e^{-2\chi t}\right\},$$

$$X_3(t) = \left\{\frac{A}{2}e^{-2\chi t} + Be^{-3\chi t}\right\},$$

$$X_4(t) = \{Ae^{-2\chi t} + 4Be^{-3\chi t}\},$$

$$X_5(t) = \left\{2Be^{-3\chi t} - \frac{K'(1+\gamma)(3\gamma-1)}{(1-\gamma)}e^{-3(1+\gamma)\chi t}\right\},$$

$$X_6(t) = \{K'e^{-3(1+\gamma)\chi t} + Be^{-3\chi t}\},$$

with

$$K' = \frac{8\pi(1-\gamma)\rho_0}{3\chi^2\gamma(1+3\gamma)}.$$

It would be very difficult to analyse the general behaviour of ω from the above expression. But a simpler form for ω can be obtained as shown below.

The third term in (34) decreases faster than the second term and therefore it can be neglected. Hence,

$$\phi \sim K'e^{-3(1+\gamma)\chi t} + Ae^{-2\chi t} \tag{36}$$

Therefore, the expression for ω simplifies to

$$\frac{\omega}{6} = -\frac{Y_1(t)\,Y_2(t)}{[Y_3(t)]^2} \tag{37}$$

where

$$Y_1(t) = \{K' + Ae^{(1+3\gamma)\chi t}\}$$

$$Y_2(t) = \left\{\frac{K'(1+\gamma)(3\gamma-1)}{(1-\gamma)} + Ae^{(1+3\gamma)\chi t}\right\}$$

$$Y_3(t) = \{3K'(1+\gamma) + 2Ae^{(1+3\gamma)\chi t}\}.$$

When $\gamma = -1$, the above solutions (36) and (37) reduce to the solutions obtained by Banerjee *et al* [19].

4. Conclusions

In this paper, we have obtained exact solutions of the field equations of Nordtvedt's theory for constant deceleration parameter and $k = 0$. We have considered only singular solutions with (i) power-law, (ii) exponential expansion and have examined the particular class of models in which the BD parameter ω might increase with time. It is found that there exists a variety of models in which ω might increase initially and decrease subsequently and vice versa.

Acknowledgement

We thank the Department of Science and Technology, New Delhi, India for providing financial support.

References

[1] D La and P J Steinhardt, *Phys. Rev. Lett.* **62**, 376 (1989)
[2] D La and P J Steinhardt, *Phys. Lett.* **B220**, 375 (1989)
[3] R D Reasenberg *et al*, *Astrophys. J.* **234**, L219 (1979)
[4] E J Weinberg, *Phys. Rev.* **D40**, 3950 (1989)
[5] D La, P J Steinhardt and E W Bertschinger, *Phys. Lett.* **B231**, 231 (1989)
[6] F S Accetta and J J Trester, *Phys. Rev.* **D39**, 2854 (1989)
[7] F C Adams, K Freese and A H Guth, *Phys. Rev.* **D43**, 965 (1991)
[8] R Holman, E W Kolb and Y Wang, *Phys. Rev. Lett.* **65**, 17 (1990)
[9] T Damour and C Gundlach, *Phys. Rev.* **D43**, 3873 (1991)
[10] P J Steinhardt and F S Accetta, *Phys. Rev. Lett.* **64**, 2740 (1990)
[11] A R Little and D Wands, *Phys. Rev.* **D45**, 2665 (1992)
[12] J D Barrow and K Maeda, *Nucl. Phys.* **B341**, 294 (1990)
[13] J G Bellido and M Quiros, *Phys. Lett.* **B243**, 45 (1990)
[14] P G Bergmann, *Int. J. Theor. Phys.* **1**, 25 (1968)
[15] R V Wagoner, *Phys. Rev.* **D1**, 3209 (1970)
[16] K Nordtvedt Jr, *Astrophys. J.* **161**, 1059 (1970)
[17] M M Green, J H Schwarz and E Witten, *Superstring theory* (Cambridge University Press, Cambridge, 1988)
[18] A Burd and A Coley, *Phys. Lett.* **B267**, 330 (1991)
[19] A Banerjee, S B D Choudhury, N Banerjee and A Sil, *Pramana – J. Phys.* **40**, 31 (1993)
[20] V B Johri and Kalyani Desikan, Communicated, (1993)

PRAMANA
— journal of
physics

© Printed in India

Vol. 42, No. 6,
June 1994
pp. 483–489

Some exact solutions in Bianchi VI_0 string cosmology

RAMESH TIKEKAR and L K PATEL*
Department of Mathematics, Sardar Patel University, Vallabhvidyanagar 388 120, India
*Department of Mathematics, Gujarat University, Ahmedabad 380 009, India

MS received 23 September 1993; revised 29 March 1994

Abstract. Following the techniques used by Letelier and Stachel some new physically relevant explicit Bianchi VI_0 solutions of string cosmology with magnetic field are reported. They include two models describing distributions of Takabayashi strings and geometric strings respectively.

Keywords. Exact solutions; string cosmology.

PACS No. 04·20

1. Introduction

The study of cosmic strings has received considerable interest. Existence of large scale networks of strings in the early universe is confirmed by the present day observations of the universe [1]. The cosmic strings are believed to give rise to density perturbations leading to galaxy formations [2]. Cosmic strings possess stress-energy and are coupled to the gravitational field. The gravitational effects of such strings have been studied by several authors (Vilenkin [3], Gott [4] and Garfinkle [5]).

Letelier [6] and Stachel [7] have developed general relativistic treatment of strings. Letelier [8] obtained relativistic cosmological models in Bianchi I and Kantowski-Sachs space-times adopting the energy-momentum tensor as given by

$$T_{ik} = \rho u_i u_k - \lambda w_i w_k, \tag{1}$$

$$u_i u^i = -w_i w^i = 1, \quad u^i w_i = 0,$$

as the source term in Einstein's field equations

$$R_{ik} - (\tfrac{1}{2}) R g_{ik} = -8\pi T_{ik}. \tag{2}$$

In (1), ρ represents energy density for a cloud of strings with particles attached to them, λ denotes the string tension density, the space-like vector w_i represents the direction of the string and the unit time-like vector u_i is the flow vector of matter.

There is no direct evidence of strings in the present-day universe. Accordingly, cosmological models evolving from the string dominated era and ending up in particle dominated era seem to be of physical relevance. In accordance with Melvin's argument [9] for a large part of the history of evolution of the universe, the matter was in a highly ionized state, smoothly coupled with field, subsequently forming neutral matter as a result of universe expansion. Hence presence of magnetic field in a string-dust universe is not beyond reality. Relativistic models in the context of Bianchi type II,

VI_0, VIII and IX space-times describing cosmological distributions of massive strings have been discussed by Krori *et al* [10]. Banerjee *et al* [11] have studied the effects of presence of magnetic field in the context of the string cosmological models in the Bianchi type I space-times. A class of solutions in the context of Bianchi VI_0 string cosmology has been obtained by Chakraborty [12]. In this paper we have reported some new exact solutions of string cosmology with and without magnetic fields respectively in the context of the Bianchi type VI_0 space-times. Further these solutions have been compared with those obtained by Chakraborty and their physical relevance discussed.

2. Field equations

The metric of Bianchi VI_0 space-time has the general form

$$ds^2 = A^2(t)(dt^2 - dx^2) - B^2(t)e^{2mx}dy^2 - C^2(t)e^{-2mx}dz^2, \tag{3}$$

where m is a constant. The energy-momentum tensor for a cloud of string dust with magnetic field along string direction, given by

$$T_{ik} = \rho u_i u_k - \lambda w_i w_k + \frac{1}{4\pi}\left[-g^{lm}F_{il}F_{km} + \frac{1}{4}g_{ik}F_{lm}F^{lm}\right], \tag{4}$$

where u_i and w_i satisfy the conditions stated in (1) and F_{ik} is the Maxwell's stress tensor, is taken as the source term in (2). We choose x-direction as the direction of strings along which the magnetic field is assumed to be present. In comoving coordinates

$$u^i = (0,0,0,1/A), \quad w^i = (1/A,0,0,0). \tag{5}$$

Maxwell's equations $F_{(i,k;l)} = 0$ and $(F^{ik}\sqrt{-g})_{;k} = 0$, imply that

$$F_{23} = K(\text{constant}) \tag{6}$$

is the only surviving component of F_{ik}. Equations (5) and (6) on substitution in (4) imply that $T_{14} = 0$. The field equations (2) consequently require that $R_{14} = 0$. In the context of the metric (3) this implies

$$R_{14} = -m\left[\frac{B'}{B} - k\frac{C'}{C}\right] = 0. \tag{7}$$

Here and in what follows a prime indicates a differentiation wth respect to t. For Bianchi VI_0 space-times $m = 0$ and subsequently equation (7) implies that $B = C$.

Einstein's field equations (2) then lead to

$$\frac{1}{A^2}\left[\frac{A''}{A} - \frac{A'^2}{A^2} + 2\frac{A'B'}{AB} + \frac{B''}{B} + \frac{B'^2}{B^2} - 2m^2\right] = 8\pi\rho, \tag{8}$$

$$\frac{1}{A^2}\left[-\frac{A''}{A} + \frac{A'^2}{A^2} - 2\frac{A'B'}{AB} + \frac{B''}{B} + \frac{B'^2}{B^2} - 2m^2 - 2\frac{K^2A^2}{B^4}\right] = 8\pi\lambda, \tag{9}$$

$$\left[\frac{A''}{A} - \frac{A'^2}{A^2} + \frac{B''}{B} - m^2 + \frac{K^2A^2}{B^4}\right] = 0. \tag{10}$$

Let ρ_p denote the particle energy density of the configuration so that

$$\rho = \rho_p + \lambda. \tag{11}$$

Equations (8) and (9) accordingly give

$$8\pi\rho_p = \frac{1}{A^2}\left[2\frac{A''}{A} - 2\frac{A'^2}{A^2} + 4\frac{A'B'}{AB} - 4m^2 + 2\frac{K^2A^2}{B^4}\right]. \tag{12}$$

The velocity field u^i, described by (5) is irrotational. The expansion parameter θ and the shear parameter σ^2 for the metric (3) with $B = C$ are given by

$$\theta = \frac{1}{A}\left[\frac{A'}{A} + \frac{2B'}{B}\right], \tag{13}$$

$$\sigma^2 = \frac{1}{3A^2}\left[\frac{A'}{A} - \frac{B'}{B}\right]^2 \tag{14}$$

Raychaudhuri equation [13] in view of the field equations (8)–(10) can be written as

$$\theta' = -\frac{1}{\theta^2} - 2\sigma^2 - 4\pi\rho_p - \frac{K^2}{B^4}, \tag{15}$$

where $R_{ik}u^iu^k = (-K^2/B^4) = -4\pi\rho_p$. The energy conditions imply that $\rho_p \geqslant 0$. The above expression accordingly indicates that the gravitational collapse of the system cannot be avoided in the presence of strings and the magnetic field. The energy conditions do not put any restriction on the sign of the string tension density λ.

3. Explicit solutions

The field equations (8)–(10) constitute a system of three equations with four unknown parameters ρ, λ, A and B. An additional constraint equation relating these parameters is necessary to obtain explicit solutions of the system. Equation (10) cannot be integrated in general unless $A(t)$ or $B(t)$ is specified. Assuming $A(t) = 1$, Chakraborty [12] obtained a class of Bianchi VI_0 solutions of these equations with and without magnetic field. Several assumptions can be made in this regard and explicit solutions can be obtained. We discuss here two fairly simple and physically relevant solutions of this system which are distinct from those reported by Chakraborty.

Solution 1

The Bianchi VI_0 space-time with metric

$$\begin{aligned} \mathrm{d}s^2 = {} & (A_0)^2 e^{4(m^2-K^2)^{1/2}t}(\mathrm{d}t^2 - \mathrm{d}x^2) \\ & - A_0 e^{2(m^2-K^2)^{1/2}t}(e^{2mx}\mathrm{d}y^2 - e^{-2mx}\mathrm{d}z^2) \end{aligned} \tag{16}$$

where A_0 is an arbitrary constant of integration, is a solution of equation (10). The physical and the kinematical parameters corresponding to this model are

$$8\pi\rho = \frac{2}{(A_0)^2}(m^2 - K^2)e^{-4(m^2-K^2)^{1/2}t},$$

$$8\pi\lambda = -\frac{2m^2}{(A_0)^2}e^{-4(m^2-K^2)^{1/2}t},$$

$$8\pi\rho_p = \frac{2(2m^2-3K^2)}{(A_0)^2}e^{-4(m^2-K^2)^{1/2}t},$$

$$\theta = \frac{4(m^2-K^2)^{1/2}}{A_0}e^{-2(m^2-K^2)^{1/2}t},$$

$$\sigma^2 = \frac{(m^2-K^2)^{1/2}}{3(A_0)^2}e^{-4(m^2-K^2)^{1/2}t}. \tag{17}$$

It can be observed that the energy conditions $\rho > 0$, $\rho_p > 0$ are satisfied when $K^2 < 2m^2/3$. The expansion scalar θ is always positive. The Bianchi VI_0 space-time of metric (16) describes an expanding string cosmological model without singularity. For $K = 0$, the model degenerates into a Bianchi VI_0 model of string cosmology without magnetic field.

Solution 2

When $m^2 = K^2$, a solution of (10) can be obtained in the form $A = B^2 = (\alpha t)^6$ without any loss of generality, where α is an arbitrary constant. The Bianchi VI_0 space-time of this solution has the metric

$$\mathrm{d}s^2 = (\alpha t)^{12}(\mathrm{d}t^2 - \mathrm{d}x^2) - (\alpha t)^6(e^{2Kx}\mathrm{d}y^2 + e^{-2Kx}\mathrm{d}z^2). \tag{18}$$

In this model the Bianchi VI_0 nature of the space-time is directly linked with the presence of the magnetic field. In the absence of magnetic field i.e., $K = 0$ the metric (18) becomes of Bianchi I type, representing a string model without magnetic field. The physical and the kinematical parameters of this model have the explicit expressions

$$8\pi\rho = \frac{45 - 2K^2t^2}{\alpha^{12}t^{14}}, \quad 8\pi\lambda = -\frac{15}{\alpha^{12}t^{14}}, \quad 8\pi\rho_p = \frac{60 - 2K^2t^2}{\alpha^{12}t^{14}}, \tag{19}$$

$$\theta = \frac{12}{\alpha^6 t^7}, \quad \sigma^2 = \frac{3}{\alpha^{12}t^{14}}. \tag{20}$$

The model begins with a singularity at $t = 0$ and complies with the requirement $\rho > 0$ inherent in the energy conditions until the epoch $t = \frac{3}{K}\sqrt{\frac{5}{2}}$, where $\rho = 0$. The expressions further indicate that the model remains physically significant for weak magnetic fields i.e. $K \ll 1$. The string tension density is always negative.

4. Explicit solutions in the absence of magnetic field

In the absence of the magnetic field, the field equations (8)–(10) become

$$\left[\frac{A''}{A} - \frac{A'^2}{A^2} + 2\frac{A'B'}{AB} + \frac{B''}{B} + \frac{B'^2}{B^2} - 2m^2\right] = 8\pi\rho A^2 \tag{21}$$

$$\left[-\frac{A''}{A}+\frac{A'^2}{A^2}-2\frac{A'B'}{AB}+\frac{B''}{B}+\frac{B'^2}{B^2}+2m^2\right]=8\pi\lambda A^2, \tag{22}$$

$$\left[\frac{A''}{A}-\frac{A'^2}{A^2}+\frac{B''}{B}-m^2\right]=0, \tag{23}$$

In this case also explicit solutions of (23) can be obtained by assuming an additional relation between the parameters ρ, λ, A and B. We report here two solutions which lead to physically relevant models of string cosmology.

We split equation (23) so that either

$$\frac{A''}{A}-\frac{A'^2}{A^2}=m^2$$

and

$$B''=0 \tag{24}$$

or

$$\frac{A''}{A}-\frac{A'^2}{A^2}=0$$

and

$$B''-m^2B=0. \tag{25}$$

Equations (24) admit the solution

$$A=\exp(\tfrac{1}{2}m^2t^2+at),\ B=\alpha t+\beta, \tag{26}$$

where a, α and β are constants of integration. Without any loss of generality we can choose $\beta=0$ and $\alpha=1$, so that the metric corresponding to this solution reads

$$ds^2=\exp(m^2t^2+2at)[dt^2-dx^2]-t^2(e^{2mx}dy^2+e^{-2mx}dz^2). \tag{27}$$

The space-time is singularity-free. The physical and the kinematical parameters associated with this model are obtained as

$$8\pi\rho=\frac{(1+2at+m^2t^2)}{t^2}\exp(-m^2t^2-2at),$$

$$8\pi\lambda=\frac{(1-2at-m^2t^2)}{t^2}\exp(-m^2t^2-2at),$$

$$8\pi\rho_p=\frac{2(m^2t+2a)}{t}\exp(-m^2t^2-2at),$$

$$\theta=\frac{(2+at+m^2t^2)}{t}\exp(-m^2t^2-2at)/2$$

$$\sigma^2=\frac{(1-at-m^2t^2)}{3t^2}\exp(-m^2t^2-2at). \tag{28}$$

These expressions clearly indicate that all the parameters diverge as $t\to 0$. Accordingly the space-time of this model evolves from the singularity at $t=0$ undergoing expansion. If $a\geqslant 0$, the conditions $\rho>0$, $\rho_p>0$ are satisfied at all epochs.

Equation (25) leads to the solution

$$A = e^{\alpha t + \beta}, \; B = C_1 e^{mt} + C_2 e^{-mt}, \tag{29}$$

where α, β, C_1 and C_2 are constants of integration. Without any loss of generality we can choose $\beta = 0$ and $C_1 = 1$. It is found that if $C_2 = 0$, the above solution leads to a physically relevant model with the metric

$$ds^2 = e^{2\alpha t}[dt^2 - dx^2) - e^{2m(t+x)}dy^2 - e^{2m(t-x)}dz^2. \tag{30}$$

The space-time metric is singularity-free. The physical and the kinematical parameters in this case have the explicit expressions

$$\begin{aligned} &\frac{\rho}{m(2\alpha - m)} = \frac{\lambda}{m(3m - 2\alpha)} = \frac{\rho_p}{4m(\alpha - m)} = e^{-2\alpha t}, \\ &\theta = (\alpha + 2m)e^{-\alpha t}, \\ &\sigma^2 = \frac{(\alpha - m)^2}{3} e^{-2\alpha t}. \end{aligned} \tag{31}$$

The energy density ρ and the particle energy density ρ_p are positive for $m < \alpha$. The string dust distribution has the equation of state

$$\rho = (1 + W)\lambda \tag{32}$$

with $W = 4(m - \alpha)/(2\alpha - 3m)$, characterizing Takabayashi strings [14] for which $W > 0$. This implies the restriction $2\alpha < 3m$. For $\alpha = m$ the kinematical parameter $\sigma = 0$. Further $\rho_p = 0$ and

$$8\pi\rho = 8\pi\lambda = m^2 e^{-2\alpha t}.$$

The model subsequently describes a cosmological distribution of geometric strings characterized by equation of state $\rho = \lambda$.

Acknowledgement

The authors express their sincere thanks to the Director, IUCAA, Pune for providing facilities for the work and referee for valuable suggestions.

References

[1] T W S Kible, *J. Phys.* **A9**, 1387 (1976)
[2] Ya B Zeldovich, *Mon. Not. R. Astron. Soc.* **192**, 663 (1980)
[3] A Vilenkin, *Phys. Rev.* **D24**, 2082 (1981)
[4] J R Gott, *Astrophys. J.* **288**, 422 (1985)
[5] D Garfinkle, *Phys. Rev.* **D32**, 1323 (1985)
[6] P S Letellier, *Phys. Rev.* **D20**, 1294 (1979)
[7] J Stachel, *Phys. Rev.* **D21**, 2171 (1980)
[8] P S Letellier, *Phys. Rev.* **D28**, 2414 (1983)
[9] M A Melvin, *Ann. N.Y. Acad. Sci.* **262**, 253 (1975)
[10] K D Krori, T Chaudhuri, C R Mahanta and A Mazumdar, *Gen. Relativ. Gravit.* **22**, 123 (1990)

[11] A Banerjee, A K Sanyal and S Chakraborty, *Pramana – J. Phys.* **34**, 1 (1990)
[12] S Chakraborty, *Indian J. Pure Appl. Phys.* **29**, 31 (1991)
[13] A K Raychaudhuri, (Clarendon Press, Oxford, 1979)
[14] T Takabayashi, edited by M Flato (Holland, Reidel, Dordrecht)

PRAMANA
— journal of
physics

© Printed in India

Vol. 42, No. 6,
June 1994
pp. 491–494

Quark distribution in light nuclei

NAZAKAT ULLAH
Tata Institute of Fundamental Research, Colaba, Bombay 400005, India

MS received 30 September 1993; revised 24 January 1994

Abstract. The distribution of quarks in light nuclei is given using the quark cluster wave function. An analytic expression for the nucleus ^{4}He is obtained. The distribution so obtained is compared with the one obtained using a different theoretical formulation called mapping.

Keywords. Quark shell model; light nuclei.

PACS No. 21·60

1. Introduction

Since the discovery of quarks, there has been tremendous interest in studying nuclear structure using quarks as building blocks. The non-relativistic shell model of quarks proposed by Isgur and Karl [1] provides a simple framework to construct the wave function of a nucleus using clusters of quarks, in which each quark moves in a simple harmonic oscillator potential. Since the single particle density plays a key role in a many-body problem, one quantity of great interest is the distribution of quarks in nuclei. In an earlier paper [2] we had shown how to construct a many-nucleon wave function using clusters of three quarks. A general expression for the density of quarks was derived for closed shell nuclei and certain conclusions were drawn about the average distance between quarks in a heavy nucleus. Much work still remains to be done about the distribution of quarks in nuclei particularly light nuclei where one hopes to use quark-quark interaction to derive expressions for the binding energy and electric and magnetic moments for these nuclei. In all these calculations one needs the oscillator parameters in which quarks move. The purpose of the present work is to see how one could get this information by comparing the distribution of quarks in the present model with another theoretical formulation which makes use of a procedure called mapping [3] and which has been applied to the ground state of light closed shell nuclei.

In the next section we give essential formulation and in § 3 the conclusions.

2. Formulation

The density of quarks $\rho(r)$ for closed shell nuclei, using non-relativistic quark shell model is given by [2]

$$\rho(r) = K\left[\exp\left(-\frac{r^2}{2b^2}\right)\int \mathrm{d}R\,R^2 P(R)\,j_0\left(\frac{Rr}{b^2}\right)\exp\left(-\frac{R^2}{2b^2}\right)\right.$$

$$+\sqrt{2}\exp\left(-\frac{r^2}{4b^2}\right)\int \mathrm{d}R R^2 P(R) j_0\left(\frac{Rr}{2b^2}\right)\exp-\left(\frac{R^2}{4b^2}\right)\Bigg], \tag{1}$$

Where K is the normalization constant, which in the present work is fixed by the condition

$$\int_0^\infty \mathrm{d}r r^2 \rho(r) = 1. \tag{2}$$

j_0 is the spherical Bessel function of order zero [4] and $P(R)$ is the probability of finding a nucleon at R.

For comparison with mapping formulation, we shall calculate $\rho(r)$ for the light closed shell nucleus ^{4}He. For light nuclei one takes $P(R)$ to be Gaussian given by

$$P(R) = N_0 \exp\left(-\frac{R^2}{\alpha^2}\right), \tag{3}$$

Where N_0 is the normalization constant and α is a parameter.

Using the integral [4]

$$\int_0^\infty \mathrm{d}x x^2 j_0(\lambda x)\exp(-ax^2) = \frac{\sqrt{\pi}}{4}\frac{1}{a^{3/2}}\exp\left(-\frac{\lambda^2}{4a}\right). \tag{4}$$

We can write $\rho(r)$ as

$$\rho(r) = K_0\Bigg[\left(1+\frac{2b^2}{\alpha^2}\right)^{3/2}\exp\left(-\frac{1+(b^2/\alpha^2)}{1+(2b^2/\alpha^2)}\cdot\frac{r^2}{b^2}\right)$$

$$+4\left(1+\frac{4b^2}{\alpha^2}\right)^{3/2}\exp\left(-\frac{1+(2b^2/\alpha^2)}{1+(4b^2/\alpha^2)}\cdot\frac{r^2}{2b^2}\right)\Bigg], \tag{5}$$

where the new normalization constant K_0 is given by

$$K_0 = \frac{4}{\sqrt{\pi}}\frac{1}{b^3}\left[\left(1+\frac{b^2}{\alpha^2}\right)^{-3/2} + 8\sqrt{2}\left(1+\frac{2b^2}{\alpha^2}\right)^{-3/2}\right]^{-1}. \tag{6}$$

Before we give the calculated values of $\rho(r)$, we mention that in the mapping procedure one constructs a nucleon creation and annihilation operator using three quark operators, the expectation value of which is related to the density of quarks.

We have calculated $\rho(r)$ using two physical pictures. In the first one we assume that the parameter α is related to parameter b by the relation $\alpha = b/\sqrt{3}$ which one will get if one transforms the radial wave function of three particles in terms of relative and center-of-mass wave functions. By looking at figure 1, we find that this value of α gives the density of quarks $\rho(r)$ very close to the one obtained in the mapping procedure the h.o. parameter b in both being $(1{\cdot}25)^{-1}$ which gives the r.m.s. radius of the nucleon to be 0·8 fm. But this value of α makes the r.m.s. radius of ^{4}He to be 0·980 which is much smaller than 1·61 extracted from experimental data [5].

In the second picture we keep b the same, but take the value of α from the r.m.s. radius of ^{4}He, the ratio α/b then becomes $\sqrt{2{\cdot}035}$ much larger than the earlier value

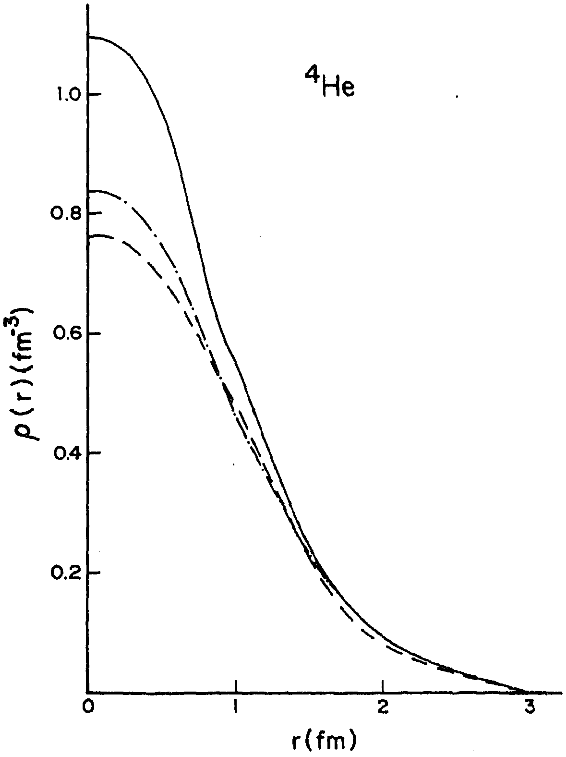

Figure 1. Density of quarks $\rho(r)$ in ^{4}He normalized to $\int_0^\infty dr r^2 \rho(r) = 1$. The solid curve (————) represents $\rho(r)$ when α is chosen to fit the r.m.s. radius of ^{4}He, the dashed (-------) is the one obtained by mapping procedure and the dash-dot (–·–·–) curve is the one obtained using c.m. wave function of three quarks.

of $1/\sqrt{3}$. The quark density $\rho(r)$ as shown in figure 1 then becomes somewhat bigger between $r = 0$ and $r = 1$ fm.

As is obvious from figure 1, $\rho(r)$ using antisymmetric quark wave function is larger at short distances than the one obtained using mapping implying that quarks in the antisymmetric wave function formalism are on the average closer than in the mapping procedure. In future such questions can only be decided by a variational calculation of the ground state energy. At present all one could say is that the exchange effect due to antisymmetry of the wavefunction causes this difference.

3. Conclusion

We have calculated and compared quark density in ^{4}He with the one obtained using mapping procedure to see how quark cluster wave function compares with other formulations. In many-body physics it is always advantageous if one could construct a good many-body wave function. The present study shows that the harmonic oscillator parameters of relative motion of quarks should be chosen differently than the nucleon radial wave function for the best fit to both the nucleus r.m.s. radius and the distribution of quarks.

As is well-known the nonrelativistic quark shell model (NRQSM) has its limitations as it does not take into account multiquark bags and paired quarks. Because of this one cannot use the present model for deep inelastic scattering [6]. Further developments are needed for this purpose.

For calculation of binding energy, one will also need the two-point quark correlation function. For a single nucleon it can easily be found to be a sum of Gaussians but it starts becoming quite complicated as the number of quarks start increasing. Moreover this quantity is not available for comparison in mapping formalism. Therefore, we have not pursued its study beyond single nucleon in the present brief report.

References

[1] N Isgur and G Karl, *Phys. Rev.* **D18**, 4187 (1978)
[2] Nazakat Ullah, *Pramana - J. Phys.* **35**, 325 (1990)
[3] F Catara and M Sambataro, *Phys. Rev.* **C46**, 754 (1992)
[4] M Abramowitz and I Stegun, *Handbook of mathematical functions* (Dover, New York, 1985)
[5] M A Preston, *Physics of the nucleus* (Addison-Wesley, Reading Massachussetts 1962)
[6] R L Jaffe, *Relativistic dynamics and quark-nuclear physics*, edited by M B Johnson and A Picklesimer (John Wiley, New York, 1986) p. 537

SUBJECT INDEX

General and Mathematical Physics

An identity for R_n embedded into E_{n+1} *Guillermo González, José L López-Bonilla and Marco A Rosales* 85–88

The Maxwell tensor for the Lienard–Wiechert field as an exact divergence *José L López-Bonilla, Jesús Morales and Marco A Rosales* 89–95

Generation of ultrasonic waves in water by an elliptical Gaussian laser beam *M S Sodha, S Konar, M P Verma and V Rai* 141–148

Non perturbative effective potentials of quantum oscillators *Rose P Ignatius and K Babu Joseph* 285–297

Coherent states and squeezed states of real q-deformed quantum oscillators *G Vinod, K Babu Joseph and V C Kuriakose* 299–309

Squeezed vacuum as an eigenstate of two-photon annihilation operator *C L Mehta, Anil K Roy and G M Saxena* 311–314

A note on the harmonic plus inverse-harmonic potential in quantum mechanics *R S Kaushal* 315–318

WKB approximation in complex time II *S Biswas, J Guha and N G Sarkar* 319–332

Ensemble interpretation of the EPR-Bell correlations *Ravi K Menon and V K Thankappan* 341–348

Universality in the length spectrum of integrable systems *Debabrata Biswas* 447–453

On phases and length of curves in a cyclic quantum evolution *Arun Kumar Pati* 455–465

On a time-dependent system of noncentral anharmonic oscillators in two dimensions *R S Kaushal* 467–472

Relativity and Gravitation

Cosmological models with constant deceleration parameter in Nordtvedt's theory *V B Johri and Kalyani Desikan* 473–481

Some exact solutions in Bianchi VI_0 string cosmology *Ramesh Tikekar and L K Patel* 483–489

Particle Physics

Photon polarisation asymmetries in $(p, p'\gamma)$ experiments *A R Usha Devi, A Sudha Rao and G Ramachandran* 97–105

Nuclear Physics

Leptodermous expansion of nuclear ground state energies and the anomaly in the nuclear curvature energy *S K Kataria, Aruna Nijasure, V S Ramamurthy and A K Dutta* 107–122

Mass asymmetry dependence of fusion time-scales in $^{11}B + ^{237}Np$ and ^{12}C, ^{16}O, $^{19}F + ^{232}Th$ reactions in a dynamical trajectory model *Kiran Kumar, R K Choudhury and A Saxena* 123–133

Pre-equilibrium effects in the formation of meta stable states *R Upadhyay, Ch V Sastry, R K Jain and J Rama Rao* 135–139

Analysis of the excitation functions of (α, *xnyp*) reactions on natural copper *N L Singh, B J Patel, D R S Somayajulu and S N Chintalapudi* 349–363

Atomic and Molecular Physics

Molecular dynamics in chloronitrobenzenes using NQR data *Shanta Sastry, R Shantha Kumari and R Chandramani* 1–7

Estimation of rotational temperature of the source emitting the spectrum of PbO molecule *A B Darji, T M Patel, M B Sureshkumar, N R Shah and P M Shah* 33–40

Local scaling transformation function and atomic shell structure in density functional theory *B M Deb and Bijoy Kr Dey* 149–157

Hypervirial perturbation theory for eigenenergies for two types of atomic potentials *M R M Witwit* 159–165

An application of hypervirial perturbation theory to calculate energy eigenvalues of the Morse potential for various diatomic molecules *M R M Witwit* 333–340

Multiple scattering of gamma rays in water, concrete and sand
G S Bhandal, Vijay Kumar, Rama Rani, Kawaldeep and K Singh 365–374

Lasers, Optics and Spectroscopy

Self focusing of elliptic Gaussian laser beams: Saturable nonlinearity
S Konar and A Sengupta 223–230

High resolution optogalvanic spectrum of N_2-rotational structure of (11, 7) band in the first positive system *P R Sasi Kumar, S S Harilal, V P N Nampoori and C P G Vallabhan* 231–237

New band system of YbI molecule *K N Uttam and M M Joshi* 239–243

CH local mode overtone excitations in benzyl chloride—a conformational study *T M A Rasheed and V P N Nampoori* 245–250

Modification of spectral characteristics and optogalvanic response in neon hollow cathode under laser excitation *P R Sasi Kumar, V P N Nampoori and C P G Vallabhan* 427–434

Plasma Physics

Plasma-maser interaction of Langmuir wave with kinetic Alfven wave turbulence *Bipuljyoti Saikia, B K Saikia, S Bujarbarua and M Nambu* 435–446

Condensed Matter Physics

Lattice vibrational properties of uranium pnictides
Prafulla K Jha and Sankar P Sanyal 9–14

Electronic structure and high pressure phase transition in LaSb and CeSb
Sankar P Sanyal and S Mathi Jaya 15–22

The white line in *L* absorption spectra of rare earth oxides
N V Moghe, V S Pai, G G Sahasrabudhe and V B Sapre 23–31

Oxide films of copper prepared by the oxidation of copper sulphide films
K S Joseph and B Pradeep 41–47

Photoelasticity in quasicrystals *K Rama Mohana Rao and P Hemagiri Rao* 167–173

Elastic anomalies in strontium titanate *K S Viswanathan and B Subramanyam* 175–185

Relation of coordination number to memory and threshold switching in chalcogenides *Manohar Lal, Navdeep Goyal and Anil Vohra* 187–191

Magnetic phase diagram of anisotropic layered superconductors via magnetization measurements for $H \parallel c$ in Bi2212 *A K Grover, F Iga, Y Yamaguchi, N Aoki, K Ino, N Goyal and Y Nishihara* 193–222

Structure and vibrational properties of carbon tubules *N Chandrabhas, A K Sood, D Sundararaman, S Raju, V S Raghunathan, G V N Rao, V S Sastry, T S Radhakrishnan, Y Hariharan, A Bharathi and C S Sundar* 375–386

The elastic moduli, the volume contribution and the Cauchy ratio for d and f shell metals *N Singh and B S Yadav* 387–394

Temperature dependence of low angle structure factors of liquid alkali metals using electron-ion plasma model *A Bari, P Pal and R N Joarder* 395–404

Electronic structure of non-magnetic impurities in dilute alloys of A1 *P Singh and S Prakash* 405–420

Transport phenomena of $SmSe_{1-x}As_x$ *S Ariponnammal and S Natarajan* 421–426

Experimental Techniques and Instrumentation

Optical design of a toroidal grating monochromator based beam line on Indus-1 *K J S Sawhney and R V Nandedkar* 49–64

Ray tracing studies of a complete plane grating monochromator beam line *V S Edlabadkar and Ashok Pimpale* 65–77

A calorimeter for operation in the temperature range 2–150 K *I Das and E V Sampathkumaran* 251–260

Losses in pendular suspensions due to centrifugal coupling *Sangita N Pitre, S V Dhurandhar, D G Blair and Ju Li* 261–270

High pressure measurement with simple piston gauge in static condition *J K N Sharma, Kamlesh K Jain and H N P Poddar* 271–282

Brief Reports

Photoionization processes in F aggregate of LiF crystal *S V Godbole and A G Page* 79–84

Quark distribution in light nuclei *Nazakat Ullah* 491–494

AUTHOR INDEX

Aoki N
  see Grover A K 193
Ariponnammal S
  Transport phenomena of $SmSe_{1-x}As_x$ 421

Babu Joseph K
  see Ignatius Rose P 285
  see Vinod G 299
Bari A
  Temperature dependence of low angle structure factors of liquid alkali metals using electron-ion plasma model 395
Bhandal G S
  Multiple scattering of gamma rays in water, concrete and sand 365
Bharathi A
  see Chandrabhas N 375
Biswas Debabrata
  Universality in the length spectrum of integrable systems 447
Biswas S
  WKB approximation in complex time II 319
Blair D G
  see Pitre Sangita N 261
Bujarbarua S
  see Saikia Bipuljyoti 435

Chandrabhas N
  Structure and vibrational properties of carbon tubules 375
Chandramani R
  see Sastry Shanta 1
Chintalapudi S N
  see Singh N L 349
Choudhury R K
  see Kiran Kumar 123

Darji A B
  Estimation of rotational temperature of the source emitting the spectrum of PbO molecule 33
Das I
  A calorimeter for operation in the temperature range 2–150 K 251
Datta N Sambhu
  Erratum 283
Deb B M
  Local scaling transformation function and atomic shell structure in density functional theory 149
Desikan Kalyani
  see Johri V B 473
Dey Bijoy Kr
  see Deb B M 149
Dhurandhar S V
  see Pitre Sangita N 261
Dutta A K
  see Kataria S K 107

Edlabadkar V S
  Ray tracing studies of a complete plane grating monochromator beam line 65
Godbole S V
  Photoionization processes in F aggregate of LiF crystal 79
González Guillermo
  An identity for R_n embedded into E_{n+1} 85
Goyal N
  see Lal Manohar 187
  see Grover A K 193
Grover A K
  Magnetic phase diagram of anisotropic layered superconductors via magnetization measurements for $H \| c$ in Bi2212 193
Guha J
  see Biswas S 319

Hariharan Y
  see Chandrabhas N 375
Harilal S S
  see Sasi Kumar P R 231

Iga F
  see Grover A K 193
Ignatius Rose P
  Non perturbative effective potentials of quantum oscillators 285

Ino K
see Grover A K 193

Jain Kamlesh K
see Sharma J K N 271
Jain R K
see Upadhyay R 135
Jha Prafulla K
Lattice vibrational properties of uranium pnictides 9
Joarder R N
see Bari A 395
Johri V B
Cosmological models with constant deceleration parameter in Nordtvedt's theory 473
Joseph K S
Oxide films of copper prepared by the oxidation of copper sulphide films 41
Joshi M M
see Uttam K N 239

Kataria S K
Leptodermous expansion of nuclear ground state energies and the anomaly in the nuclear curvature energy 107
Kaushal R S
A note on the harmonic plus inverse-harmonic potential in quantum mechanics 315
On a time-dependent system of noncentral anharmonic oscillators in two dimensions 467
Kawaldeep
see Bhandal G S 365
Kiran Kumar
Mass asymmetry dependence of fusion time-scales in ^{11}B + ^{237}Np and ^{12}C, ^{16}O, ^{19}F + ^{232}Th reactions in a dynamical trajectory model 123
Konar S
see Sodha M S 141
Self focusing of elliptic Gaussian laser beams: Saturable nonlinearity 223
Kuriakose V C
see Vinod G 299

Lal Manohar
Relation of coordination number to memory and threshold switching in chalcogenides 187
Li Ju
see Pitre Sangita N 261
López-Bonilla José L
see Gonzalez Guillermo 85
The Maxwell tensor for the Lienard-Wiechert field as an exact divergence 89

Mathi Jaya S
see Sanyal Sankar P 15
Mehta C L
Squeezed vacuum as an eigenstate of two-photon annihilation operator 311
Menon Ravi K
Ensemble interpretation of the EPR-Bell correlations 341
Moghe N V
The white line in L absorption spectra of rare earth oxides 23
Erratum 283
Morales Jesús
see López-Bonilla José L 89

Nambu M
see Saikia Bipuljyoti 435
Nampoori V P N
see Sasi Kumar P R 231
see Rasheed T M A 245
see Sasi Kumar P R 427
Nandedkar R V
see Sawhney K J S 49
Natarajan S
see Ariponnammal S 421
Nijasure Aruna
see Kataria S K 107
Nishihara Y
see Grover A K 193

Page A G
see Godbole S V 79
Pai V S
see Moghe N V 23, 283
Pal P
see Bari A 395
Patel B J
see Singh N L 349
Patel L K
see Tikekar Ramesh 483
Patel T M
see Darji A B 33
Pati Arun Kumar
On phases and length of curves in a cyclic quantum evolution 455
Pimpale Ashok
see Edlabadkar V S 65
Pitre Sangita N
Losses in pendular suspensions due to centrifugal coupling 261
Poddar H N P
see Sharma J K N 271

Pradeep B
  see Joseph K S 41
Prakash S
  see Singh P 405

Radhakrishnan T S
  see Chandrabhas N 375
Raghunathan V S
  see Chandrabhas N 375
Rai V
  see Sodha M S 141
Raju S
  see Chandrabhas N 375
Rama Rani
  see Bhandal G S 365
Ramachandran G
  see Usha Devi A R 97
Ramamurthy V S
  see Kataria S K 107
Rao A Sudha
  see Usha Devi A R 97
Rao G V N
  see Chandrabhas N 375
Rao J Rama
  see Upadhyay R 135
Rao K Rama Mohana
  Photoelasticity in quasicrystals 167
Rao P Hemagiri
  see Rao K Rama Mohana 167
Rasheed T M A
  CH local mode overtone excitations in benzyl chloride—a conformational study 245
Rosales Marco A
  see Gonzalez Guillermo 85
  see López-Bonilla José L 89
Roy Anil K
  see Mehta C L 311

Sahasrabudhe G G
  see Moghe N V 23, 283
Saikia B K
  see Saikia Bipuljyoti 435
Saikia Bipuljyoti
  Plasma-maser interaction of Langmuir wave with kinetic Alfven wave turbulence 435
Sampathkumaran E V
  see Das I 251
Sanyal Sankar P
  see Jha Prafulla K 9
  Electronic structure and high pressure phase transition in LaSb and CeSb 15
Sapre V B
  see Moghe N V 23, 283
Sarkar N G
  see Biswas S 319
Sasi Kumar P R
  High resolution optogalvanic spectrum of N_2-rotational structure of (11, 7) band in the first positive system 231
  Modification of spectral characteristics and optogalvanic response in neon hollow cathode under laser excitation 427

Sastry Ch V
  see Upadhyay R 135
Sastry Shanta
  Molecular dynamics in chloronitrobenzenes using NQR data 1
Sastry V S
  see Chandrabhas N 375
Sawhney K J S
  Optical design of a toroidal grating monochromator based beam line on Indus-1 49
Saxena A
  see Kiran Kumar 123
Saxena G M
  see Mehta C L 311
Sengupta A
  see Konar S 223
Shah N R
  see Darji A B 33
Shah P M
  see Darji A B 33
Shantha Kumari R
  see Sastry Shanta 1
Sharma J K N
  High pressure measurement with simple piston gauge in static condition 271
Singh K
  see Bhandal G S 365
Singh N
  The elastic moduli, the volume contribution and the Cauchy ratio for *d* and *f* shell metals 387
Singh N L
  Analysis of the excitation functions of (α, *xnyp*) reactions on natural copper 349
Singh P
  Electronic structure of non-magnetic impurities in dilute alloys of Al 405
Sodha M S
  Generation of ultrasonic waves in water by an elliptical Gaussian laser beam 141
Somayajulu D R S
  see Singh N L 349
Sood A K
  see Chandrabhas N 375

Subramanyam B
see Viswanathan K S 175
Sundar C S
see Chandrabhas N 375
Sundararaman D
see Chandrabhas N 375
Sureshkumar M B
see Darji A B 33

Thankappan V K
see Menon Ravi K 341
Tikekar Ramesh
Some exact solutions in bianchi VI$_0$ string cosmology 483

Ullah Nazakat
Quark distribution in light nuclei 491
Upadhyay R
Pre-equilibrium effects in the formation of meta stable states 135
Usha Devi A R
Photon polarisation asymmetries in $(p, p'\gamma)$ experiments 97
Uttam K N
New band system of YbI molecule 239

Vallabhan C P G
see Sasi Kumar P R 231
see Sasi Kumar P R 427
Verma M P
see Sodha M S 141
Vijay Kumar
see Bhandal G S 365
Vinod G
Coherent states and squeezed states of real q-deformed quantum oscillators 299
Viswanathan K S
Elastic anomalies in strontium titanate 175
Vohra Anil
see Lal Manohar 187

Witwit M R M
Hypervirial perturbation theory for eigenenergies for two types of atomic potentials 159
An application of hypervirial perturbation theory to calculate energy eigenvalues of the Morse potential for various diatomic molecules 333

Yadav B S
see Singh N 387
Yamaguchi Y
see Grover A K 193